

# **BULGARIAN CHEMICAL COMMUNICATIONS**

**2017** Volume 49 / Special Issue L

Selection of papers presented on the IX National Conference on  
Chemistry, 29 September – 1 October, 2016, Sofia, Bulgaria

*Journal of the Chemical Institutes  
of the Bulgarian Academy of Sciences  
and of the Union of Chemists in Bulgari*

**BULGARIAN CHEMICAL COMMUNICATIONS**

**A quarterly published by**

**THE BULGARIAN ACADEMY OF SCIENCES**

**and**

**THE UNION OF CHEMISTS IN BULGARIA**

**Volume 49, Special Issue L**

**ИЗВЕСТИЯ ПО ХИМИЯ**

**Тримесечно издание на**

**БЪЛГАРСКА АКАДЕМИЯ НА НАУКИТЕ**

**и**

**СЪЮЗ НА ХИМИЦИТЕ В БЪЛГАРИЯ**

**Том 49, Специален брой L**

**2017**

**Editor-in-Chief:**

*V. Beschkov*

**EDITORIAL BOARD**

*Ch. Bonev, P.R. Bontchev, L. Boyadzhiev, I. Gutzow, I. Havezov, E. Ivanova, K. Petkov, K. Petrov, L. Petrov, I. Pojarlieff, S. Rakovsky, D. Stoychev, P. Petrov, D. Tsalev, D. Vladikova, D. Yankov*

*Members from abroad:*

*J. M. Albella (Spain), S. Berger (Germany), J. C. Breakman (Belgium), J. Etourneau (France), M. Farina (Italy), K. Friedrich (Germany), J. Gyenis (Hungary), A. J. Kirby (United Kingdom), T. Kowalska (Poland), K. Kutchitsu (Japan), A. Lasia (Canada), O. V. Mazurin (Russia), B. Mutaftschiev (France), E. Peter Kündig (Switzerland), S. De Rosa (Italy), T. F. Tadros (United Kingdom), K. Valko (Hungary)*

*The annual subscription (for 4 issues) for vol. 49 (2017) is € 160. – including postage, handling and packaging charge.*

*Payments should be delivered to:*

*Editorial Board of Bulgarian Chemical Communications, Institute of Chemical Engineering,  
Unicredit Bulbank, IBAN: BG65 UNCR 7630 3400 0017 48; SWIFT/BIC - UNCRBGSF (for Euro €).*

*Unicredit Bulbank, IBAN: BG18 UNCR 9660 3119 9033 12; SWIFT/BIC - UNCRBGSF (for local currency BGN).*

## Hemocyanin from *Rapana thomasiana* – structure and anti-breast cancer activity in a presence of cholinium amino acids

Y. Raynova<sup>1</sup>, K. Idakieva<sup>1</sup>, M. Guncheva<sup>1\*</sup>, V. Uzunova<sup>2</sup>, P. Ossowicz<sup>3</sup>, E. Janus<sup>3</sup>,  
I. Angelov<sup>1</sup>, R. Tzoneva<sup>2</sup>

<sup>1</sup>Institute of Organic Chemistry with Centre of Phytochemistry, Bulgarian Academy of Sciences, Sofia, Bulgaria

<sup>2</sup>Institute of Biophysics and Biomedical Engineering, Bulgarian Academy of Sciences, Sofia, Bulgaria

<sup>3</sup>Institute of Organic Chemical Technology, West Pomeranian University of Technology Szczecin, Szczecin, Poland

Submitted November 7, 2016; Revised February 2, 2017

The focus of the present research is a hemocyanin, isolated from the hemolymph of marine snails *Rapana thomasiana* (RtH), and its interactions with ionic liquids, based on a cholinium cation and a non-polar amino acid as an anion [Chol][AA]. Six RtH-[Chol][AA] complexes have been obtained. Fragmentation and structural changes in the protein, even at low protein to ionic liquid ratios, were observed using static light scattering and fluorescence spectroscopy. For the first time the cytotoxicity of RtH, [Chol][AA] and their complexes on adenoma breast cancer MDA-MB-231 cells was tested. All protein-ionic liquid complexes reduced moderately the cell viability of MDA-MB-231 cells, however, the effect was weaker than those estimated for the pure RtH or [Chol][AA].

**Keywords:** hemocyanin, ionic liquids, conformational changes, anti-breast cancer activity.

### INTRODUCTION

Development of new types of human therapeutics is a fast growing field. Recent trends in the drug development are biotechnological drugs; incl. protein drugs [1]. It is noteworthy to be mentioned that the therapeutic activity of proteins is highly dependent on their conformational structure and maintaining a correct (specific) three-dimensional structure is a key to its biological activity [2].

In the recent years hemocyanins, large respiratory proteins that are found in the hemolymph of mollusks and arthropods, are intensively studied in view of their potential against various socially significant diseases like tumors, viral infections, etc., or of their possible application as vaccine adjuvants [3, 4].

The marine snail *Rapana thomasiana* is an invasive marine species in the Black Sea, Marmara Sea and Mediterranean Sea [5]. The hemocyanin isolated from the hemolymph of this mollusk has been extensively studied and very well structurally characterized [6-12]. During the last decade, a great attention has been paid on its biomedical application. For example, there are reports that the hemocyanin from *Rapana thomasiana* (RtH) possesses an anti-viral activity against herpes and Epstein-Barr viruses [13, 14]. On the other hand, RtH exhibits a radioprotective effect upon radiation-induced injuries and facilitates post-radiation recovery in gamma induced acute radiation syndrome in male albino mice [15].

Elsewhere it was reported that RtH, tested in vitro, has shown a good cytotoxic effect against two human bladder cancer cell lines: CAL-29 and T-24 [16]. In addition, in vivo RtH expresses strong anti-cancer and anti-proliferative effects in the mice challenged with colon carcinoma [17]. Furthermore, in vivo RtH and its subunits act as a non-specific immunostimulators i.e. induce a strong humoral immune response and can serve as vaccine-carriers [18]. In recent studies, we have demonstrated that the modification of RtH with ionic liquids (ILs) containing imidazolium or choline cation and amino acid anions alter or enhance its cytotoxicity against hormone-dependent breast cancer cells (MCF-7) [19, 20].

There is no literature data on the effect of RtH on the highly invasive MDA-MB-231 breast cancer cells. This cell phenotype is known as triple negative breast cancer (TNBC) because these breast cancer cells do not express on their surface estrogen receptors (ER), progesterone receptors (PR) and human epidermal growth factor receptor 2 (HER2) [21]. TNBC is aggressive, hard to be treated because it does not respond to normal hormone therapy and chemotherapeutics that target HER2, thus they have a poor prognosis [22].

In the view of the above-mentioned, the aim of this study is to assess the effect of RtH and its complexes with choline amino acids on MDA-MB-231 cell viability. In addition, we are seeking a correlation between the IL-induced changes in the protein structure and activity.

\*) To whom all correspondence should be sent:

E-mail: maiag@orgchm.bas.bg

## EXPERIMENTAL

### Materials

The hemocyanin was isolated from marine snails *Rapana thomasiana* as described earlier [6]. The ionic liquids: (2-hydroxyethyl)trimethylammonium glycinate [Chol][Gly], (2-hydroxyethyl)trimethylammonium L-valinate [Chol][Val], (2-hydroxyethyl)trimethylammonium L-leucinate [Chol][Leu], (2-hydroxyethyl)trimethylammonium L-isoleucinate [Chol][Ile], (2-hydroxyethyl)trimethylammonium L-methionate [Chol][Met], (2-hydroxyethyl)trimethylammonium L-tryptophanate [Chol][Trp] were synthesized following the previously published procedure [19]. Human breast cancer (MDA-MB-231) cell line was purchased from American Type Culture Collection (ATCC). Thiazolyl Blue Tetrazolium Bromide (MTT) (98%) was purchased from Sigma. RPMI-1640, DMEM high glucose media, L-glutamine, and sodium bicarbonate were purchased from PAN-Biotech GmbH, Aidenbach, Germany.

### Scattering experiments

The scattering measurements were performed on a fiber optics specifically elaborated spectrophotometer on the basis of Ocean Optics QE 65000 spectrophotometer (Ocean Optics Inc., Dunedin, FL, USA) with Spectra Suite Software (Ocean Optics Inc., Dunedin, USA) set-up as it is described in [23] and with excitation at 660 nm. The data were analyzed and graphically represented by means of computer programme Origin 8.0 (Microcal Software, Inc., Northampton, MA, USA).

According to the theory, if the size of a spherical particle is much less than the wavelength of light in the surrounding medium and if the refractive index of the sphere divided by the refractive index of the

surrounding medium,  $m = \frac{n_{sph}}{n_{md}}$ , is not too large,

the calculation can be simplified and scattering in such conditions is widely referred to as Rayleigh scattering [24].

In such conditions, if  $r$  is the radius of the sphere and  $\lambda$  is the free-space wavelength and  $\pi r^2$  is the effective scattered area, then the cross sections for absorption and scattering are [25, 26]

$$C_{abs} = (\pi r^2) \cdot 4x \operatorname{Im} \left( \frac{m^2 - 1}{m^2 + 2} \right) = (\pi r^2) \cdot Q_{abs} \quad (1) \text{ and}$$

$$C_{scat} = (\pi r^2) \cdot \left( \frac{8}{3} \right) \cdot x^4 \left| \frac{m^2 - 1}{m^2 + 2} \right|^2 = (\pi r^2) \cdot Q_{scat}, \quad (2)$$

where  $x$  is the size parameter and equals to  $\frac{2\pi r n_{med}}{\lambda}$  and  $Q$  is scattering or absorption efficacy

where  $r$  is the particle radius.  $Q_{scat}$  compares the scattering cross section to the physical cross sectional area  $\pi r^2$  of the particle.  $Q_{scat}$  is actually not an efficiency (because it can have values greater than 1), but that is the terminology used in light-scattering theory. For values of  $Q_{scat}$  a greater than 1, the particle is able to scatter photons which are outside the physical cross-sectional area of the particle. If the sample is excited far from absorption spectral maximum, then the intensity of scattered light ( $I_{scat}$ ) is given by:

$$I_{scat} \approx (C_{scat} \cdot (1 + \cos 2\theta) + C_{abs}) \cdot I_0 \quad (3),$$

where  $I_0$  is the intensity of incident monochromatic light, and  $\theta$  is angle between excited light beam and direction at which the intensity of scattered light is detected.

On the basis of literature data for the size and shape of a protein, by means of static light scattering measurements it is enough to determine scattered intensities at same conditions for investigated protein and for his products due the investigated processes. On the base of dependence on scattered intensity  $I_{scat}$ , due to  $N$  molecules in a scattered volume ( $V$ ) and environment the equivalent radius of sphere for scattering at  $\theta = 90^\circ$  will be:

$$R_x = R_0 \cdot \frac{I_{sx}}{I_{so}} \cdot \frac{1}{2} K_{1/2} \quad (4)$$

$$K = \frac{(Q_{0scat} + Q_{oabs})}{(Q_{xscat} + Q_{xabs})} \quad (5)$$

where  $R_0$  and  $I_{so}$  are the effective radius of known initial compound and measured intensity of scattered light in solution with this compound,  $R_x$ ,  $I_{sx}$  – respectively for product obtain at corresponding process. In (4) the term  $K$  depends on many parameters, inherent for light scattering process as it can be seen from equation (1) and (2). According to the definition of  $Q_{scat}$  and  $Q_{abs}$  and (5) it can be expected that the value of square root of  $K$  will be near one.

### Absorption spectroscopy

Evolution™ 300 UV-Vis spectrophotometer (Thermo Electron Corporation), equipped with a Peltier temperature control accessory with the highest resolution (1 nm), was used to monitor the formation of the protein-IL

complexes. The changes in the intensities of the absorption bands typical for the aromatic amino acid residues ( $\lambda_{\max}$  at 280 nm) and the copper active site ( $\lambda_{\max}$  at 345 nm) were followed [27]. RtH concentration was kept constant–1.52 mg/mL (0.17  $\mu$ M), while the concentration of [Chol][AA] was varied in the range 0.01–0.4 M.

#### *Fluorescence spectroscopy*

Steady-state fluorescence measurements were conducted on Perkin Elmer LS-5 spectrofluorometer equipped with a data station model 3600. All fluorescence spectra were collected using 1 cm quartz cuvette with excitation and emission band-width set at 2.5 and 20 nm, respectively. The emission spectra were recorded over the range 310–450 nm at a fixed excitation wavelength of 295 nm. The instrument was calibrated using 10  $\mu$ M N-acetyl-L-tryptophanamide dissolved in MilliQ water. Solution of RtH (11 nM) and [Chol][AA] (5 mM) in PBS (25 mM, pH 7.2) were mixed and incubated for 60 min at room temperature prior to measurements.

#### *Cell culture*

The human adenocarcinoma breast cancer cell line, MDA-MB-231 was cultured in DMEM high glucose medium containing L-glutamine, penicillin, streptomycin, amphotericin B, and 10% fetal bovine serum, and maintained in a humidified incubator at 37°C in an atmosphere of 5% CO<sub>2</sub>.

#### *Cell viability assay*

The viability of MDA MB-231 cells after their incubation with RtH, [Chol][AA] and RtH-[Chol][AA] complexes was assessed in MTT colorimetric test [28].

Briefly, 1x 10<sup>4</sup> cells were seeded in each well of a 96-well plate and maintained for 24 h at 37°C and 5% CO<sub>2</sub>. Then, the cells were incubated for additional 24 h with RtH, pure [Chol][AA] or RtH-[Chol][AA] complexes, at concentrations ranging from 100–700  $\mu$ g/mL and 0.67–4.7 mM for the protein complexes and pure ILs, respectively.

Finally, 20  $\mu$ L of MTT was added directly to all 96-wells plates with the adherent cells. They were incubated for 3 h at 37°C and 5% CO<sub>2</sub>, and the absorbance at 570 nm that is due to the formation of a purple blue formazan product was recorded with a 96-well plate reader Tecan Infinite F200 PRO (Tecan Austria GmbH, Salzburg). The quantity of formazan is directly proportional to the number of viable cells.

Blank experiments containing only reaction medium as well as control experiments with not-

treated MDA MB-231 cells were performed. The data from two independent experiments were used.

The viability of the MDA MB-231 cells that are treated with the tested compounds is presented in percentages from the control.

Data were analyzed using Graph Pad Prism software (Graph Pad Software Inc., San Diego, USA). Statistical test one-way ANOVA and Tukey–Kramer post-hoc test was conducted for pairwise comparison. P-value less than 0.05 was considered statistically significant.

## RESULTS AND DISCUSSION

### *Absorption spectroscopy*

The absorption spectrum of the oxy-form of RtH is characterized with two maxima. The first one is centered at 280 nm and is due mainly to the side-chains of Tyr, Trp and Phe comprising the protein molecule, while the absorption band at 345 nm is due to the copper active site and is assigned to O<sup>2-</sup><sub>2</sub> ( $\pi_{\sigma}^*$ ) Cu(II) charge transfer transition [29]. The absorbance ratio of  $A_{345}/A_{280} = 0.25$  is a common characteristic for the fully oxygenated RtH [27]. In presence of [Chol][AA], we observed a decrease in the intensity of the two absorption bands of RtH in a concentration-dependent manner (Fig. 1). The effect is simultaneous and of the same order of magnitude for the two absorption bands, which suggests that in spite of the observed IL-induced conformational changes in the RtH, the active site remains preserved.

Interestingly, the strongest protein-IL interactions were observed for the choline glycinate.

The further structural and biological studies were performed with protein-IL complexes prepared at a molar ratio of 1:6000.

### *Fluorescence spectroscopy*

Tryptophyl (Trp) fluorescence was used to monitor the conformational changes or unfolding of the RtH molecules in various media. Fig. 2 shows the emission spectra of RtH in a native state (25 mM PBS buffer, pH 7.2) in the absence and in presence of choline amino acids. Interestingly, the intensity of Trp fluorescence increased in all media containing ILs. Red-shift in the wavelength maximum of about 3 to 5 nm was observed in presence of [Chol][Val], [Chol][Met] and [Chol][Ile], while in [Chol][Gly] and [Chol][Leu] no shift was detected. In comparison to the emission spectra of the native RtH, the emission spectra of RtH-[Chol][Trp] characterizes with marked red-shift of about 31 nm.

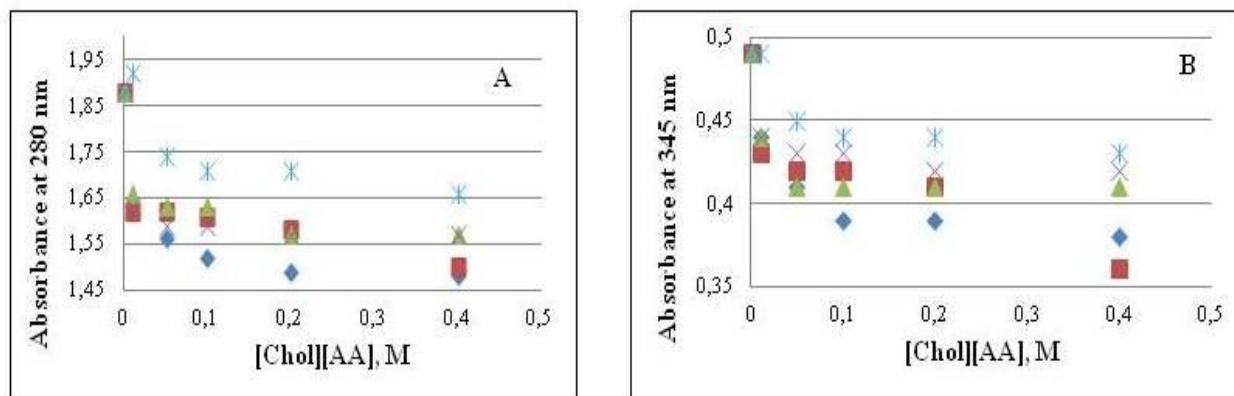


**Fig. 1.** Changes in the absorbance spectra at 280 nm (A) and 345 nm (B) of RtH (1.5 mg/mL) as a function of the [Chol][AA] concentration.

◆ RtH-[Chol][Gly]    ■ RtH-[Chol][Val]    ▲ RtH-[Chol][Leu]    × RtH-[Chol][Ile]    \* RtH-[Chol][Met]

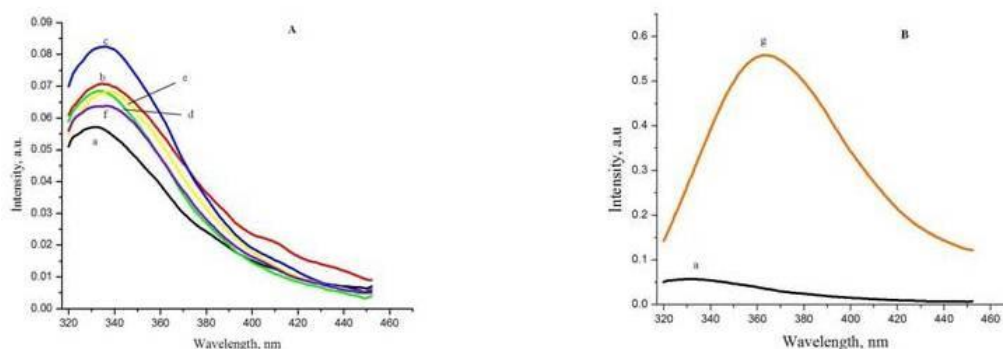


**Fig. 2.** Fluorescence emission spectra of RtH (11nM) in 25 mM PBS buffer (pH 7.2) (a) and in presence of 5mM [Chol][AA] (b-g).  $\lambda_{ex} = 295$  nm,  $\lambda_{em}$  310–460 nm. A) RtH (a), RtH-[Chol][Gly] (b), RtH-[Chol][Val] (c), RtH-[Chol][Leu] (d), RtH-[Chol][Ile] (e), RtH-[Chol][Met] (f); B) RtH (a), RtH-[Chol][Trp] (g).

To evaluate the cytotoxic effect of the ILs on MDA-MB-231 cells we carried out an experiment with [Chol][AA] in concentrations of 0.67 mM and 4.7 mM, corresponding to the lowest and the highest amount of ILs introduced into the system with the RtH-complexes. As can be seen in Fig. 4, most of the tested ILs had moderate cytotoxic effects. However, a strong cell growth inhibition was observed in presence of [Chol][Trp]. The observed effect is time- and dose-dependent. It is noteworthy to be mention that in presence of 4.7 mM of [Chol][Trp] the reduction of cell viability for 48 h exceeded to 90 %.

This may be due to changes in electronic transitions in RtH molecules as a result of electrostatic interactions between ILs and protein molecules. Typically, the red-shift in Trp fluorescence is associated with a presence of positively charged residues near the benzene ring and/or negatively charged residues near the pyrrole end of the Trp [30]. The increase in fluorescence intensity and the red-shift in the  $\lambda_{max}$  can be also a consequence of IL-induced protein unfolding,

which makes Trp residues more exposed to the polar solvent (water). Reports for a red-shift of the Trp peak of cytochrome C in presence of 1-butyl-1-methyl imidazolium chloride and an increase in its fluorescence intensity in presence of alkyl ammonium formates can be found in the literature [31]. In contrast, some authors observed a blue shift in the Tyr emission spectra and decrease in fluorescence intensity for insulin in presence of 1, 3- dialkyl-imidazolium salts [32]. The Trp emission spectra of monellin in presence of 1,1-dialkyl pyrrolidinium based ILs is also blue-shifted [33]. In addition, Fan et al reported a decrease in Trp fluorescence intensity of trypsin in respect to the concentration of the added 1-methyl-3-alkyl imidazolium salts [34].

#### Static light scattering

SLS experiments were performed in order to assess the effect of the tested ILs on the oligomeric state of RtH. The hydrodynamic radii value for oxy-RtH (23.6 nm) [11] in Tris/HCl buffer (pH 7.0) was taken from the literature and was used as a

basis for estimation of the parameters for protein-IL complexes. The calculated effective radius ( $R_x$ ) of RtH in presence of [Chol][AA] are given in Table 1.

**Table 1.** The effective radius ( $R_x$ ) of RtH at presence of [Chol][AA].

RtH in 0.01M Tris/HCl buffer, pH 7.0	$R_x$ , nm
IL-free medium	23.6[11]
[Chol][Gly]	10.1
[Chol][Val]	6.0
[Chol][Leu]	6.0
[Chol][Ile]	6.0
[Chol][Met]	4.1
[Chol][Trp]	6.0

In all SLS experiments the amount of RtH (0.1 mg/mL; 1nM) and ILs (5mM) were kept constant.

All tested ILs caused changes in the protein supramolecular assembly. The estimated decrease in  $R_x$  of RtH is two- to six-fold in comparison to the value set for the protein dissolved in the IL-free medium. We assume that due to strong electrostatic interactions between [Chol][AA] and RtH, the protein molecules undergo fragmentation (dissociation). The result correlates with the observed increase in Trp fluorescence i.e. more Trp residues become exposed to the protein surface. We did not find, however, a linear dependence between the two effects – decrease in the  $R_x$  and the increase in the Trp fluorescence. Probably, along with the dissociation of the RtH in presence of ILs, a rearrangement in the protein molecules occurs. This conclusion is in agreement with the earlier reported distinct differences in RtH calorimetric profiles in presence of [Chol][AA], which we ascribed to the presence in the hemocyanin molecule of more than one structural domains undergoing denaturation more or less independently of each other [19].

#### *Cytotoxicity of RtH, [Chol][AA] and their complexes*

The effects of RtH on MDA-MB-231, hormone-independent breast cancer, cell growth were assessed using concentrations ranging from 100 to 700  $\mu\text{g/mL}$  after 24 and 48 h. RtH exhibited moderate cytotoxic effect on the tested cancerous cells as compared to the control consisting of non-treated with RtH cells (Fig. 3). The observed effect is concentration independent. Our earlier studies have shown that RtH stimulates the proliferation of fibroblasts and in presence of 700  $\mu\text{g/mL}$

hemocyanin, we estimated an increase in cell viability up to 40% in comparison to the control (100%) [19]. In addition, we have shown that RtH does not affect significantly MCF-7 cells (hormone dependent breast cancer). This means that RtH is highly selective and inhibit only the more resistant to various chemotherapies triple negative breast cancer cell line.

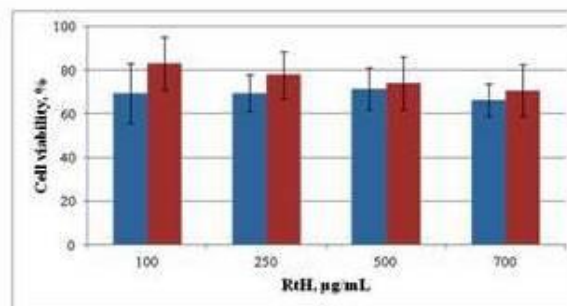


**Fig. 3.** Viability of MDA-MB-231 cells incubated for 24 and 48 h with various concentrations of RtH. The statistic was performed by ANOVA test. \*\*-  $p < 0.01$ , \*\*\*-  $p < 0.001$ . ■ 24 h ■ 48 h

To evaluate the cytotoxic effect of the ILs on MDA-MB-231 cells we carried out an experiment with [Chol][AA] in concentrations of 0.67 mM and 4.7 mM, corresponding to the lowest and the highest amount of ILs introduced into the system with the RtH-complexes. As can be seen in Fig. 4, most of the tested ILs had moderate cytotoxic effects. However, a strong cell growth inhibition was observed in presence of [Chol][Trp]. The observed effect is time- and dose-dependent. It is noteworthy to be mention that in presence of 4.7 mM of [Chol][Trp] the reduction of cell viability for 48 h exceeded to 90 %.

The RtH-[Chol][Trp] complex is more cytotoxic to MDA-MB-231 cells than the non-modified native RtH (Fig. 5). RtH's potential to inhibit the cell growth of this hormone independent breast cancer cells, however, is not influenced from the modified with the rest of the tested ILs protein. On the other hand, comparing these results with our previous findings it is interesting to note that RtH-[Chol][AA] complexes are two times more effective against MCF-7 than MDA-MB-231 cells [19].

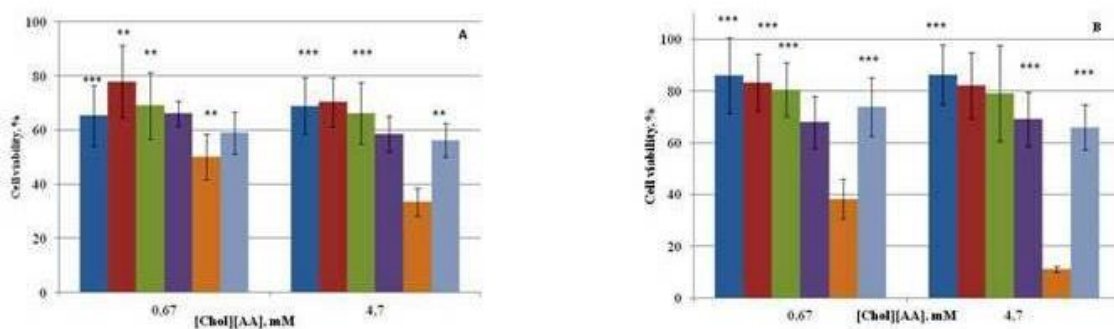


**Fig. 4.** Viability of MDA-MB-231 cell line incubated for 24 h(A) and 48 h (B) with 0.67 and 4.7 mM [Chol][AA]. Data are means±SD of eighth replicates. The statistic was performed by ANOVA test. \*\*- p<0.01, \*\*\*- p<0.001.

■ [Chol][Gly] ■ [Chol][Ile] ■ [Chol][Leu] ■ [Chol][Met] ■

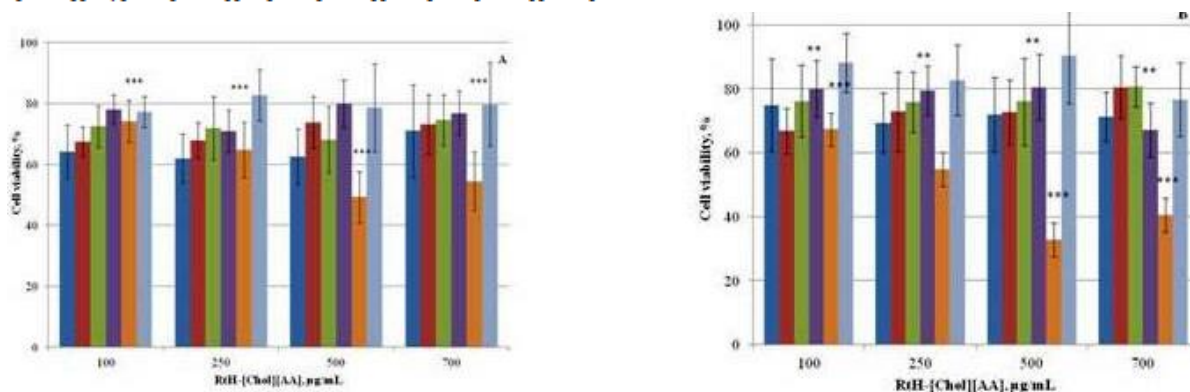


**Fig. 5.** Viability of MDA-MB-231 cells after incubation with various concentrations of RtH-[Chol][AA] complexes for 24 h (A) and 48 h (B). Data are means ± SD of eighth replicates. The statistic was performed by ANOVA test. \*\*- p<0.01, \*\*\*- p<0.001.

■ RtH-[Chol][Gly] ■ RtH-[Chol][Ile] ■ RtH-[Chol][Leu] ■ RtH-[Chol][Met] ■ RtH-[Chol][Trp] ■ RtH-[Chol][Val]

## CONCLUSION

In this study, we showed that RtH-[Chol][AA] complexes had reduced cytotoxic effect on MDA-MB-231 cells as compared with separate applications of the pure RtH or ILs when the latter were applied at the same concentrations. Probably, the induced by [Chol][AA] conformational changes in the secondary structure of RtH hinders the effective binding of the protein on the cell surface. On the other hand, in a previous study, we have shown that the growth of MCF-7 cells was significantly reduced by RtH-[Chol][AA], which may be an indication for a different mechanism of anti-tumor activity of these complexes. The obtained results testified the cell specific effect of RtH which could be explored in treatment of the different tumors.

**Acknowledgements.** This work was supported by research grants DFNP 152/12.05.16 and DFNP-128/12.05.2016 from the Program for career development of young scientists, BAS, Bulgaria.

## REFERENCES

1. O'Connor, *Regulatory Rapporteur*, **6**, 4 (2009). (<http://www.topra.org/>)
2. S. Frokjaer, D. Otzen, *Nat.Rev.Drug Discov.*, 299 (2005).
3. J.R. Harris, J. Markl, *Micron*, **30**, 597 (1999).
4. S. Arancibia, C.Espinoza, F. Salazar, M. Del Campo, R. Tampe, T.-Y. Zhong, P. De Ioannes, B. Moltedo, J. Ferreira, E. C. Lavelle, A. Manubens, A. E. De Ioannes, M. I. Becker, *PLOS One*, **9**, e87240 (2014).
5. M. Gomoiu, B. Alexandrov, N. Shadrin, Y. Zaitsev in *Invasive Aquatic Species of Europe. Distribution, Impacts and Management*, E. Leppäkoski, S. Gollasch, S. Olenin (eds.) Kluwer Academic Publishers, Netherlands, 2002, p. 346.
6. K. Idakieva, S. Severov, I. Svendsen, N. Genov, S. Stoeva, M. Beltramini, G. Tognon, P. Di Muro, B. Salvato, *Comp. Biochem. Physiol. Part B: Comp. Biochem.*, **106**, 53 (1993).
7. R. Boteva, S. Severov, N. Genov, M. Beltramini, B. Filipii, F. Ricchelli, L. Tallandini, M. M. Pallhuber, G. Tognon, B. Salvato, *Comp. Biochem. Physiol. Part B: Comp. Biochem.*, **100**, 493 (1991).
8. S. Stoeva, P. Dolashka, K. Pervanova, N. Genov, W. Voelter, *Comp. Biochem. Physiol. B Biochem. Mol. Biol.*, **118**, 927 (1997).



9. W. Gebauer, S. Stoeva, W. Voelter, E. Dainese, B. Salvato, M. Beltramini, J. Markl, *Arch Biochem Biophys.*, **372**, 128 (1999).
10. M. Perbandt, E.W. Guthoehrlein, W. Rypniewski, K. Idakieva, S. Stoeva, W. Voelter, N. Genov, C. Betzel, *Biochemistry*, **42**, 6341 (2003).
11. D. Georgieva, D. Schwark, P. Nikolov, K. Idakieva, K. Parvanova, K. Dierks, N. Genov, C. Betzel, *Biophys J.*, **88**, 1276 (2005).
12. K. Idakieva, S. Stoeva, W. Voelter, C. Gielen, *Comp. Biochem. Physiol. B Biochem. Mol. Biol.*, **138**, 221 (2004).
13. P. Genova-Kalou, D. Dundarova, K. Idakieva, A. Mohammed, S. Dundarov, R. Argirova, *Z Naturforsch C.*, **63**, 429 (2008).
14. P. Dolashka, N. Nesterova, S. Zagorodnya, A. Dolashki, G. Baranova, A. Golovan, W. Voelter, *Global J. Pharmacol.*, **8**, 206 (2014).
15. I. Kindekov, M. Mileva, D. Krastev, V. Vassilieva, Y. Raynova, L. Doumanova, M. Aljakov, K. Idakieva, *Biotechnol. Biotechnol. Eq.* **28**, 533 (2014).
16. O. Boyanova, P. Dolashka, D. Toncheva, H-G. Rammensee, S. Stevanovic, *Biomed. Rep.*, **1**, 235 (2013).
17. V. Gesheva, S. Chausheva, N. Mihaylova, I. Manoylov, L. Doumanova, K. Idakieva, A. Tchorbanov, *BMC Immunol.*, **15**, 34 (2014).
18. A. Tchorbanov, K. Idakieva, N. Mihaylova, L. Doumanova, *Int. Immunopharmacol.*, **8**, 1033 (2008).
19. M. Guncheva, K. Paunova, P. Ossowicz, Z. Rozwadowski, E. Janus, K. Idakieva, S. Todinova, Y. Raynova, V. Uzunova, S. Apostolova, R. Tzoneva, D. Yancheva, *RSC Adv.*, **5**, 63345 (2015).
20. M. Guncheva, K. Paunova, P. Ossowicz, Z. Rozwadowski, E. Janus, K. Idakieva, S. Todinova, Y. Raynova, V. Uzunova, S. Apostolova, R. Tzoneva, D. Yancheva, *Int. J. Biol. Macromol.*, **82**, 798 (2016).
21. D. Holiday, V. Speirs, *Breast Cancer Res.*, **13**, 215 (2011).
22. T. Ovcaricek, S. G. Frkovic, E. Matos, B. Mozina, S. Borstnar, *Radiol. Oncol.*, **45**, 46 (2011).
23. V. Enchev, I. Angelov, V. Mantareva, N. Markova, *J. Fluoresc.* **25**, 1601 (2015).
24. C.B. Pasternak, P. Collings, A. Giannetto, E. Gibbs, *J. Am. Chem. Soc.*, **115**, 5399 (1993).
25. C. F. Bohren, D.R. Huffman, Absorption and Scattering of Light by Small Particles; John Wiley and Sons: New York, 1983; p. 134-136.
26. R.L Xu, In Particle Characterization: Light Scattering Methods, B. Scartett (Ed) Kluwer Academic Publishers, New York, 2000.
27. K. Idakieva, I. Chakarska, P. Ivanova, A. Tchorbanov, I. Dobrovolev, L. Doumanova *Biotechnol. Biotechnol. Equip.*, **23** (3), 1364 (2009).
28. T. Mosmann, *J. Immunol. Methods*, **65**, 55 (1983).
29. M. Beltramini, L. Bubacco, L. Castella, G. Alzuet, M. Gullotti, B. Salvato, *Eur. J. Biochem.*, **232**, 98 (1995).
30. J. Vivian, P. Callis, *Biophys. J.*, **80**, 2093 (2001).
31. W. Wei, N. Danielson, *Biomacromolecules*, **12**, 290 (2011).
32. A. Kumar, P. Venkatesu, *RSC Adv.*, **4**, 4487 (2014).
33. S. Baker, T. M. McCleskey, S. Pandey, G. Baker, *Chem. Commun.*, **8**, 940 (2004).
34. Y. Fan, X. Dong, L. Yan, D. Li, S. Hua, C. Hu, C. Pan, *Chemosphere*, **148**, 241 (2016).

## СТРУКТУРА И АНТИГУМОРНА АКТИВНОСТ НА ХЕМОЦИАНИН ОТ *Rapana thomasiana* В ПРИСЪСТВИЕ НА ЙОННИ ТЕЧНОСТИ НА ОСНОВАТА НА ХОЛИН И АМИНОКИСЕЛИНИ

Юл. Райнова<sup>1</sup>, Кр. Идакиева<sup>1</sup>, М. Гунчева<sup>1\*</sup>, В. Узунова<sup>2</sup>, П. Осовиц<sup>3</sup>, Е. Янус<sup>3</sup>, Ив. Ангелов<sup>1</sup>, Р. Цонева<sup>2</sup>

<sup>1</sup>Институт по органична химия с Център по фитохимия, Българска академия на науките, София, България

<sup>2</sup>Институт по биофизика и биомедицинско инженерство, Българска академия на науките, София, България

<sup>3</sup>Институт по органична химична технология, Западно-Померански технологичен университет на Шчечин, Полша

Постъпила на 7 ноември, 2016 г.; коригирана на 2 февруари, 2017 г.

(Резюме)

Във фокуса на настоящето изследване са взаимодействията на хемоцианин, изолиран от хемолимфата на морски охлюв от вида *Rapana thomasiana* (RtH) с йонни течности, съдържащи катион и анион, съответно холин и неполярна аминокиселина [Chol][AA]. Бяха получени шест комплекса на протеина с йонните течности [RtH-[Chol][AA]]. За изследвания концентрационен интервал, с помощта на флуоресцентна спектроскопия и светоразсейване беше установено, че RtH претърпява конформационни промени и се наблюдава фрагментация на протеиновата молекулата при добавянето на [Chol][AA]. За първи път е изследвана цитотоксичността на нативния RtH, чистите [Chol][AA] и на техните комплекси спрямо клетки на хормон-независим рак на млечната жлеза (MDA-MB-231). Всички RtH-[Chol][AA] комплекси инхибират умерено клетъчния растеж на MDA-MB-231. Ефектът, обаче е по-слаб от този, който е отчетен при третиране на клетките с немодифициран RtH и с разтвори само на йонните течности.

## Thermal stability of *Helix aspersa maxima* hemocyanin

Y. Raynova<sup>1</sup>, S. Todinova<sup>2</sup>, K. Idakieva<sup>1\*</sup>

<sup>1</sup>*Institute of Organic Chemistry with Centre of Phytochemistry, Bulgarian Academy of Sciences, Acad. G. Bonchev Str., Bl. 9, Sofia 1113, Bulgaria*

<sup>2</sup>*Institute of Biophysics and Biomedical Engineering, Bulgarian Academy of Sciences, Acad. G. Bonchev Str., Bl. 21, Sofia 1113, Bulgaria*

Submitted October 6, 2016; Accepted February 1, 2017

The thermal stability of the hemocyanin, isolated from garden snails *Helix aspersa maxima* (HaH), was studied by differential scanning calorimetry. One transition, with an apparent transition temperature ( $T_m$ ) at 79.8 °C, was detected in the thermogram of HaH in 20 mM HEPES buffer, containing 0.1 M NaCl, 5 mM CaCl<sub>2</sub> and 5 mM MgCl<sub>2</sub> (pH 7.06 at 80 °C), using a heating rate of 1.0 °C/min. The thermal denaturation of HaH was an irreversible process. The scan rate dependence of the calorimetric profiles indicated that the thermal unfolding of the investigated Hc is kinetically controlled.  $T_m$  and  $\Delta H_{cal}$  values for the thermal denaturation of HaH were found to be independent of the protein concentration, suggesting that the dissociation of the Hc into subunits does not take place before the rate-determining step of the process of thermal unfolding started. The thermal denaturation of HaH was described by the two-state irreversible model. On the basis of this model, the parameters of the Arrhenius equation were calculated.

**Key words:** hemocyanin, differential scanning calorimetry, irreversible denaturation

### INTRODUCTION

Hemocyanins (Hcs) are respiratory glycoproteins, isolated from the hemolymph of mollusc and arthropod species [1]. Interest in Hcs is determined not only because of their important biological function, but also because of the opportunities for their successful application in medicine. Hcs, isolated from different organisms, are used in preparation of vaccines, as immunomodulators, as well as in the therapy of bladder cancer [2-6]. Recently, a potential anti-cancer effect of Hcs on a murine model of colon carcinoma was demonstrated, suggesting their use for immunotherapy of different types of cancer [7].

The thermal stability is an important characteristic of proteins having potential therapeutic applications. In the present study, the thermal stability of the Hc, isolated from garden snails *Helix aspersa maxima* (HaH), was studied by differential scanning calorimetry (DSC). This protein can be produced in large quantities for biotechnology and medical use of snails bred in special farms under controlled conditions.

### EXPERIMENTAL

#### *Isolation and purification of hemocyanin*

HaH was isolated according to the procedure described in [8]. Briefly, the native Hc was obtained from the hemolymph, collected from the snails *Helix aspersa maxima*, by ultracentrifugation at 180 000 x *g* (ultracentrifuge Beckman LM-80,

rotor Ti 45), for 4 hours, at 4 °C. The pellets were resuspended in 50 mM phosphate buffer, pH 7.2, and the HaH was further purified by gel filtration chromatography. Protein concentration was determined spectrophotometrically using the specific absorption coefficient  $A_{278}^{0.1\%} = 1.413$  ml.mg<sup>-1</sup>.cm<sup>-1</sup> for HaH [9].

#### *Differential scanning calorimetry*

Calorimetric measurements were performed on a high-sensitivity differential scanning microcalorimeter DASM-4 (Biopribor, Pushchino, Russia). The protein solution in the calorimetric cell was reheated after the cooling from the first run to estimate the reversibility of the thermally induced transitions. The calorimetric data were evaluated using the ORIGIN (MicroCal Software) program package. Molecular mass of 9 000 000 Da for Hc was used in the calculation of molar quantities.

### RESULTS AND DISCUSSION

#### *Irreversibility of the thermal denaturation of HaH*

The thermogram of HaH in buffer 20 mM HEPES (pH 7.06 at 80 °C), at a heating rate of 1.0 °C/min, is shown in Fig. 1 (line a). Heat absorption was observed between 70 and 87 °C, with an apparent transition temperature ( $T_m$ ) at 79.8 °C. Value of 130.5 MJ mol<sup>-1</sup> was calculated for the calorimetric enthalpy ( $\Delta H_{cal}$ ) by an integration of the heat capacity curve. The thermal denaturation of HaH was irreversible as no thermal effect was

\*) To whom all correspondence should be sent:

E-mail: [idakieva@orgchm.bas.bg](mailto:idakieva@orgchm.bas.bg)

detected in a reheating scan (Fig. 1, line b). Irreversibility of the thermal denaturation was observed in the DSC measurements of all of the studied Hcs to date [10-13]. Heat-induced aggregation has been considered to be a major reason for the irreversibility of thermal denaturation of proteins. Indeed, our research on the thermal unfolding of Hc from marine gastropod *Rapana thomasi* ( $T_m$  82.4 °C) by means of Fourier transform infrared (FTIR) spectroscopy clearly demonstrates that above 70 °C the protein irreversibly unfolds with a loss of secondary structure and formation of amorphous aggregates [14].

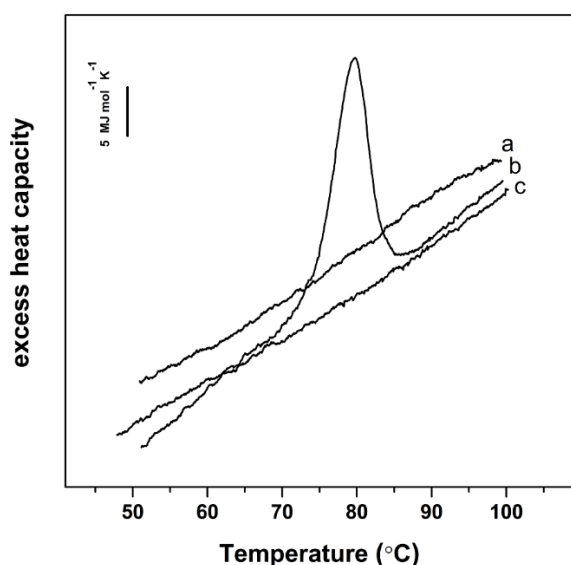


**Fig. 1.** (a) Experimental  $C_p$  transition curve of HaH in buffer 20 mM HEPES, containing 100 mM NaCl, 5 mM  $CaCl_2$ , 5 mM  $MgCl_2$  (pH 7.06 at 80 °C), at a heating rate of 1.0 °C/min; (b) Reheating run; (c) Buffer-buffer base lane.

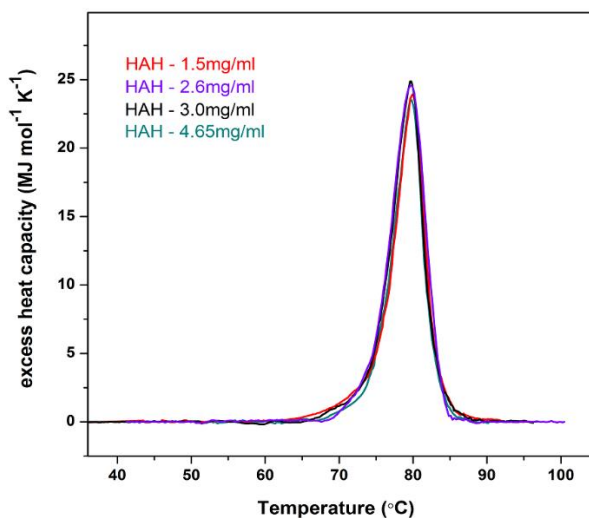


**Fig. 2.**  $C_p$  transition curves of HaH in buffer 20 mM HEPES, containing 100 mM NaCl, 5 mM  $CaCl_2$ , 5 mM  $MgCl_2$  (pH 7.06 at 80 °C), recorded at a heating rate of 1

°C/min and different protein concentrations.

#### Concentration dependence of the temperature of denaturation

The quaternary structure of the molecule of HaH, like in other gastropodan Hcs, represents oligomer of twenty subunits. Dissociation of the Hc molecule to individual subunits may occur during the denaturation process. In order to determine whether this is occurring, DSC traces were collected at varying protein concentrations, at a constant heating rate of 1 °C/min. The  $T_m$  and  $\Delta H_{cal}$  values for the thermal unfolding of HaH were found to be independent of the protein concentration (Fig. 2). Consistent with our previous studies, the oligomeric state of the Hc molecule

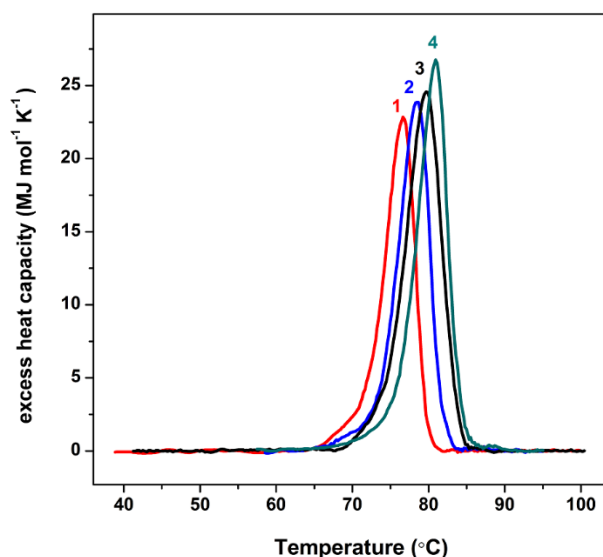


**Fig. 3.** Dependence of the  $C_p$  transition curves of HaH in buffer 20 mM HEPES (pH 7.06 at 80 °C), with heating rate: (1) 0.2 °C/min; (2) 0.55 °C/min; (3) 1 °C/min; (4) 1.8 °C/min. In all cases the protein concentration was 4.65 mg/ml.

does not change during denaturation [11-13]. This indicates that the interaction between subunits, constituting the Hc molecule, is strong enough to prevent protein dissociation before the rate-determining step of the process of thermal unfolding.

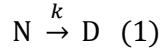
#### Scan rate dependence

Figure 3 shows the excess heat capacity function vs. temperature profiles for HaH at four different heating rates (0.2, 0.55, 1.0 and 1.8 °C/min). The transition temperature of the irreversible thermal denaturation of HaH is scan rate dependent: the maximum of the DSC profiles is shifted toward lower temperatures with a decrease in the heating

rate. The scan rate dependence of the calorimetric traces indicates that the thermal unfolding of the investigated HaH is kinetically controlled [11, 15].

#### Analysis of the calorimetric data

In most cases, the irreversible thermal denaturation of proteins monitored by DSC or other techniques is described using a simple two-state kinetic model, which is a limiting case of the Lumry-Eyring model [16]:



This model considers only two significantly populated macroscopic states, the initial or native state (N) and the final or denatured (D) state. In this case, the process is characterized by a first-order rate constant  $k$  which follows the Arrhenius equation:

$$k = \exp \left[ \frac{E_a}{R} \left( \frac{1}{T^*} - \frac{1}{T} \right) \right] \quad (2),$$

where  $E_a$  is the activation energy of the denaturation process,  $R$  is the gas constant, and  $T^*$  is the temperature at which  $k$  is equal to  $1 \text{ min}^{-1}$ . The two-state irreversible model has been used for

the interpretation of the DSC data for the thermal denaturation of Hcs from different species [11-13, 15]. Four different methods have been devised from Sanchez-Ruiz and co-workers [17] for an evaluation of the activation energy from heat capacity curves.

**Method A.** The rate constant  $k$  (inverse seconds) is obtained at each temperature from the following equation:

$$k = \frac{vC_p}{\Delta H_{\text{cal}} - \Delta H} \quad (3),$$

where  $v$  refers to the heating rate in Kelvin per seconds,  $C_p$  is the molar heat capacity,  $\Delta H$  ( $\text{kJ mol}^{-1}$ ) is the corresponding enthalpy at  $T$ , and  $\Delta H_{\text{cal}}$  is the total molar transition enthalpy. For each heating rate,  $k$  was evaluated for all data in the interval  $(T_m - 2) \leq T \leq (T_m + 2)$ . The Arrhenius plots obtained are shown in Fig. 4A. The mean and standard deviation value of the  $E_a$  determined from the slopes of the Arrhenius plots are as follows

$$E_a = 545 \pm 12 \text{ kJ mol}^{-1}.$$

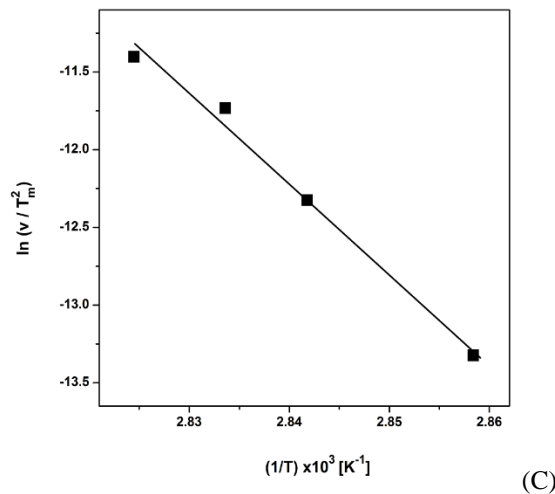
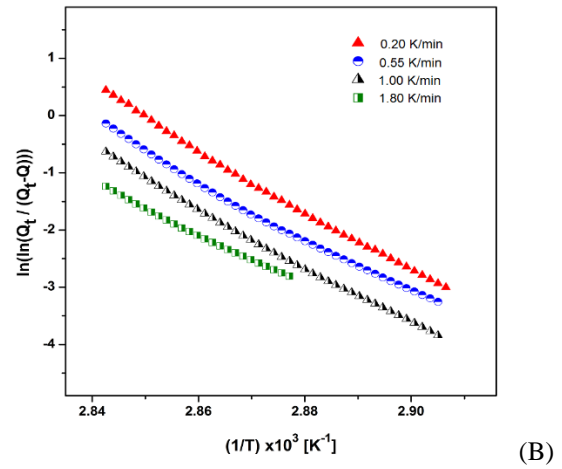
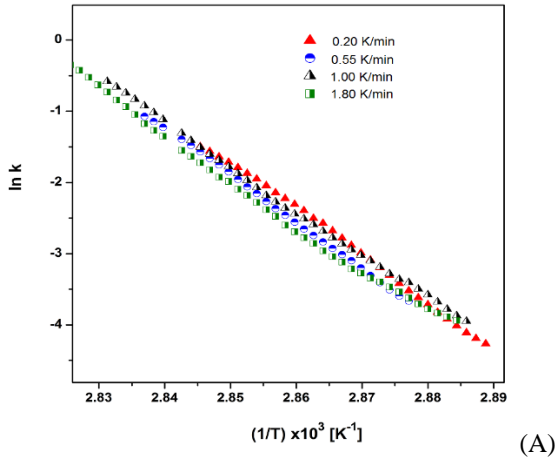


**Fig. 4.** (A–C) Determination of activation parameters for the HaH denaturation from the experimental heat capacity functions. Methods (A–C) are according to Sanchez-Ruiz et al. [17].

**Method B.** The variation of the transition temperature,  $T_m$ , with a heating rate is given by the following relationship:

$$\frac{v}{T_m^2} = \frac{AR}{E_a} \exp\left(-\frac{E_a}{RT_m}\right) \quad (4)$$

If the proposed model is correct a linear dependence of  $\ln(v/T_m^2)$  versus  $1/T_m$  should be established with a slope of  $-E_a/R$ . The value of  $E_a$  determined from the slope of the plot shown in Fig. 4B is as follows

$$E_a = 491 \pm 18 \text{ kJ mol}^{-1}$$

**Method C.** The third estimate of  $E_a$  stems from the following relationship:

$$\ln \left[ \ln \left( \frac{\Delta H_{\text{cal}}}{\Delta H_{\text{cal}} - \Delta H} \right) \right] = \frac{E_a}{R} \left( \frac{1}{T_m} - \frac{1}{T} \right) \quad (5)$$

Plotting the left side of Eq. (7) versus  $1/T$  should yield a straight line with a slope of  $-E_a/R$  for each

heating rate. The results are shown in Fig. 4C. The average value of the  $E_a$  obtained from the four slopes is as follows

$$E_a = 418 \pm 38 \text{ kJ mol}^{-1}$$

**Method D.** Finally, the  $E_a$  can be evaluated from the heat capacity at the transition temperature,  $C_p^m$ , using the equation:

$$E_a = \frac{eRT_m^2 C_p^m}{\Delta H_{\text{cal}}} \quad (6)$$

Using method D the value obtained of the  $E_a$  is as follows

$$E_a = 539 \pm 17 \text{ kJ mol}^{-1}$$

The apparent value of the  $E_a$  averaged over the results obtained from the four methods is as follows

$$E_a = 498 \pm 21 \text{ kJ mol}^{-1}$$

The values of  $T_m$  and  $E_a$  determined for the denaturation of HaH were found to be within the range of the data obtained up to now for other studied gastropodan Hcs (Table 1).

**Table 1.** Parameters for a thermal denaturation of the Hc of *Helix aspersa maxima*, obtained by DSC, at a heating rate of 1 °C/min. Comparison with the data obtained for gastropodan Hcs of *Rapana thomasiana* [11]; *Helix pomatia* [12], *Concholepas concholepas* [13] and *Haliotis rubra* [18].

Hemocyanin species	$T_m$ [°C]	$\Delta H_{\text{cal}}$ [MJ mol <sup>-1</sup> ]	$E_a$ [kJ mol <sup>-1</sup> ]
<i>Helix aspersa maxima</i>	79.8	130 ± 1.0	498 ± 21
<i>Rapana thomasiana</i>	82.4*	195 ± 1.0	597 ± 20
<i>Helix pomatia</i> β-isoform	84.0*	190 ± 1.0	521 ± 7
<i>Concholepas concholepas</i>	78.0*	120 ± 1.0	323 ± 2
<i>Haliotis rubra</i>	78.9*	–	535 ± 65

\* Main transition

In conclusion, the results of the present investigation on the HaH, isolated from snails *Helix aspersa maxima*, allow classifying this Hc as a thermostable protein ( $T_m$  79.8 °C). These data will facilitate the further investigation of therapeutic properties of this respiratory protein.

**Acknowledgements:** This work was supported by research grant DFNP-152/ 12.05.2016 from Program for career development of young scientists, BAS, Bulgaria.

#### REFERENCES

1. K. E. van Holde, K.I. Miller, *Adv. Protein. Chem.*, **47**, 1 (1995).
2. J. R. Harris, J. Markl, *Micron*, **30**, **597** (1999).
3. A. Tchobanov, K. Idakieva, N. Mihaylova, L. Doumanova, *Int. Immunopharmacol.*, **8**, 1033 (2008).
4. V. Gesheva, S. Chausheva, N. Stefanova, N. Mihaylova, L. Doumanova, K. Idakieva, A. Tchobanov, *Int. Immunopharmacol.*, **26**, 162 (2015).
5. C. D. Jurincic, U. Engelmann, J. Gasch, K. F. Klippel, *J. Urol.*, **139**, 723 (1988).
6. Rizvi D. R. Riggs, B. J. Jackson, D. W. McFadden, *Am. J. Surg.*, **194**, 628 (2007).
7. V. Gesheva, S. Chausheva, N. Mihaylova, I. Manoylov, Doumanova, K. Idakieva, A. Tchobanov, *BMC Immunol.*, **15**, 33 (2014).
8. Y. Raynova, L. Doumanova, K. Idakieva, *Protein J.*, **32**, 609 (2013).
9. C. Gielens, J. De Sadeleer, G. Preaux, R. Lontie, *Comp. Biochem. Physiol.*, **88B**, 181 (1987).
10. R. Sterner, T. Vogl, H. J. Hinz, F. Penz, R. Hoff, R. Föll, H. Decker, *FEBS Lett.*, 364, 9 (1995).
11. K. Idakieva, K. Parvanova, S. Todinova, *Biochim. Biophys. Acta*, **1748**, 50 (2005).
12. K. Idakieva, C. Gielens, N. I. Siddiqui, L. Doumanova, B. Vaseva, G. Kostov, V. L. Shnyrov, *Z. Naturforsch.*, 62a, 499 (2007).

13. K. Idakieva, P. Nikolov, I. Chakarska, V. L. Shnyrov, N. Genov, *J. Fluorescence*, **18**, 715 (2008).
14. K. Idakieva, F. Meersman, C. Gielens, *Biochim. Biophys. Acta*, **1824**, 731 (2012).
15. M. Guzman-Casado, A. Parody-Morreale, P. L. Mateo, J. M. Sanchez-Ruiz, *Eur. J. Biochem.*, **188**, 181 (1990).
16. R. Lumry, H. Eyring, *J. Phys. Chem.*, **58**, 110 (1954).
17. M. Sanchez-Ruiz, J.L. Lopez-Lacomba, M. Cortijo, P.L. Mateo, *Biochemistry*, **27**, 1648 (1988).
18. G. Marshall, P. Valtchev, F. Dehghani, G. W. Gomes, *J. Therm. Anal. Calorim.*, **123**, 2499 (2016).

## ТЕРМИЧНА СТАБИЛНОСТ НА ХЕМОЦИАНИН ОТ ОХЛЮВИ *Helix aspersa maxima*

Ю. Райнова<sup>1</sup>, С. Тодинова<sup>2</sup>, К. Идакиева<sup>1\*</sup>

<sup>1</sup>Институт по органична химия с Център по фитохимия, Българска академия на науките, ул. Акад. Г. Бончев, бл. 9, 1113 София, България

<sup>2</sup>Институт по биофизика и биомедицинско инженерство, Българска академия на науките, ул. Акад. Г. Бончев, бл. 21, 1113 София, България

Постъпила на 6 октомври, 2016 г.; приета на 1 февруари, 2017 г.

(Резюме)

В настоящето изследване термичната стабилност на хемоцианин, изолиран от охлюви от вида *Helix aspersa maxima*, беше изследвана с помощта на диференциална сканираща калориметрия. Определена беше температура на топене 79.8 °C на протеина в буфер 20 mM HEPES, съдържащ 0.1 M NaCl, 5mM CaCl<sub>2</sub> и 5 mM MgCl<sub>2</sub> (pH 7.06 at 80 °C), при скорост на нагряване 1.0 °C/мин. Термичната денатурация на хемоцианина беше необратима. Беше установено, че температурата на топене и калориметричната енталпия зависят от скоростта на нагряване, което показва, че процеса на термична денатурация на хемоцианина има кинетичен характер. Калориметричните данни бяха анализирани съгласно “two-state” модела, описващ необратима денатурация на протеини. Изчислена беше активиращата енергия за процеса на термична денатурация на хемоцианина.

## Promoting the oxidative removal rate of 4-chlorophenol on gold-doped TiO<sub>2</sub>/graphene photocatalysts under UV light irradiation

V. I. Iliev\*, D. V. Tomova, V. F. Georgiev, S. K. Rakovsky

*Institute of Catalysis, Bulgarian Academy of Sciences, Acad. G. Bonchev St., Bldg. 11, 1113 Sofia, Bulgaria*

Submitted November 7, 2016; Revised February 2, 2017

4-Chlorophenol photooxidation catalysed by nanosized TiO<sub>2</sub>, Au/TiO<sub>2</sub>, and matching composite materials with reduced graphene oxide (GR) has been studied upon irradiation with UV light. XPS and TEM methods have been applied to characterise prepared photocatalysts. The average size of the titania nanoparticles prepared by the sol-gel method was 20 nm. TiO<sub>2</sub> and Au/TiO<sub>2</sub> particles were randomly distributed on the surface of the graphene nanosheets. The average size of the Au nanoparticles in the modified titania photocatalysts was about 7 nm. XPS measurements confirmed partial thermal reduction or photoreduction of the graphene oxide to graphene. Rate constants of 4-chlorophenol photooxidation catalysed by the studied samples followed the order: Au/TiO<sub>2</sub>/GR > Au/TiO<sub>2</sub> > TiO<sub>2</sub>/GR > TiO<sub>2</sub>. The rate constant of 4-chlorophenol degradation catalysed by an Au/TiO<sub>2</sub>/GR composite was approximately 3.9 times higher than that registered with titania. Enhanced activities of Au/TiO<sub>2</sub>/GR, Au/TiO<sub>2</sub>, and TiO<sub>2</sub>/GR photocatalysts were due to efficient charge carrier separation of the light-generated electron-hole pairs in titania semiconductor. This favoured an additional generation of HO• radicals on the titania valence band.

**Keywords:** photocatalysis, TiO<sub>2</sub>/graphene, Au/TiO<sub>2</sub>/graphene, graphene-semiconductor composite, 4-chlorophenol.

### INTRODUCTION

Photocatalytic reactions over semiconductor materials irradiated with solar or artificial light are of great interest because of their ability to remove a large variety of pollutants in both aqueous and gaseous phase [1,2]. Among various semiconductor photocatalysts, titanium dioxide (TiO<sub>2</sub>) is the most prevalent material for environmental applications [1]. However, a major disadvantage in most semiconductor materials is the high degree of recombination between the photogenerated charge carriers, which ultimately decreases the photocatalyst effectiveness and the photonic efficiency of the redox process. In the case of noble metal modified photocatalysts [3,4] the lifetime of the photogenerated pairs is increased due to efficient separation of the electron-hole charges generated upon irradiation.

In recent years graphene oxide (GO) and reduced graphene oxide (GR) have been used in the design of photocatalysts as a tool for improving the photocatalytic performance of the latter [5–9]. Results from these studies indicate that graphene is an excellent co-catalyst to enhance photocatalytic oxidation and reduction activity. Based on its excellent electron mobility, it is generally believed that graphene can rapidly separate and transfer photogenerated electrons and thus the electron-hole recombination process is impeded [5–8]. Moreover, as a result of  $\pi$ - $\pi$  interactions and formation of hydrogen bonds between organic pollutants and GO

or graphene the local concentration of polluting compounds around the investigated photocatalysts is increased, thus the probability of interaction between substrates and photogenerated active species on the semiconductor interface being increased [5,7,8,10,11].

Many authors have investigated single and coupled graphene-based semiconductor photocatalysts with the purpose of promoting the photonic efficiency of the semiconductors in the decomposition of water and air contaminants [5]. In general, it has been established that the efficiency of graphene-based semiconductor photocatalysts is higher than that of graphene-free catalysts, especially in cases of dye destruction [6]. It was shown that the percentage of graphene content with respect to the photocatalyst plays an essential role on the activity of graphene-based semiconductor photocatalysts. In most cases, a high content of graphene oxide leads to photon scattering and blocking the active sites of the semiconductor photocatalysts [5,12]. So far, the promoting effect of noble metals (gold in particular) on the TiO<sub>2</sub>/GR system efficiency has received little attention in the literature.

This work compares the catalytic activities of TiO<sub>2</sub>, Au/TiO<sub>2</sub>, and corresponding composite materials with reduced graphene oxide in the photocatalytic oxidation of 4-chlorophenol under UV light irradiation. The investigation was carried out using an optimal graphene oxide to semiconductor ratio reported in the literature [13]. A

\*) To whom all correspondence should be sent:

E-mail: iliev@ic.bas.bg

principal aim of this study was to elucidate the effect of GR presence in composite Au/TiO<sub>2</sub> materials and to evaluate rate enhancement of 4-chlorophenol oxidation under UV irradiation.

## EXPERIMENTAL

### *Materials and preparation of photocatalysts*

Titanium (IV) isopropoxide (Sigma-Aldrich), hydrogen tetrachloroaurate(III), H<sub>2</sub>AuCl<sub>4</sub>·3H<sub>2</sub>O (Sigma-Aldrich), and graphene oxide (Grapenea) were used as starting reagents for photocatalyst synthesis. Pollutant 4-chlorophenol (Sigma-Aldrich) was used without further purification.

TiO<sub>2</sub> and TiO<sub>2</sub>/GR photocatalytic materials were synthesised by the sol-gel method. The surface of some samples was modified by gold nanoparticles.

Composite TiO<sub>2</sub>/GO (GO to TiO<sub>2</sub> wt. ratio of 0.05) was prepared by the following procedure. Graphene oxide (87.5 ml) dispersed in water (4 mg ml<sup>-1</sup>) is slowly added dropwise for 2 h to a solution containing 26.9 ml of titanium(IV) isopropoxide dissolved in 30 ml of absolute ethanol. The process is conducted at pH=9 under vigorous stirring followed by ultrasonic dispersion. The resulting transparent colloidal suspension was aged for 30 h until xerogel formation. The obtained gel is filtered and dried at 100°C for 12 h. Further, the dried gel is thermal treated at 450°C for 3 h under argon flow. This temperature is reached at a ramping rate of 5 grad min<sup>-1</sup>. Thermally treated material is then ground in an agate mortar to obtain a fine titania-graphene powder.

Nanosized titania was prepared in a similar way without any addition of graphene oxide.

In the absence of oxygen the prepared photocatalyst samples were modified by nanosized gold particles (0.5 wt.%) by using the photoreduction method [3] at medium pH=7. H<sub>2</sub>AuCl<sub>4</sub>·3H<sub>2</sub>O was used as a precursor at a particular concentration to give 0.5 wt.% Au on the support. A 4-W capacity UV-C lamp (Philips, TUV 4W) was used as the light source to reduce Au<sup>3+</sup> into its metallic state Au<sup>0</sup>. This amount of noble metal was selected based on previous investigations, which reported to be optimal [3,14].

### *Photocatalyst characterisation*

BET specific surface area of the samples was measured by nitrogen adsorption from N<sub>2</sub>+He mixture at the liquid nitrogen boiling temperature using a Micromeritics FlowSorb II 2300 apparatus based on adsorption data in the partial pressure (P/P<sub>0</sub>) range of 0.05–0.35.

4-Chlorophenol adsorption on TiO<sub>2</sub>, TiO<sub>2</sub>/GR, and gold-modified semiconductor materials was

measured at pH=4 in the dark. In each experimental run, 350 mg of photocatalytic material were added to 350 ml of aqueous 4-chlorophenol solution (4×10<sup>-3</sup> mol L<sup>-1</sup>). The suspension was then magnetically stirred for 60 min at 20°C in the dark and in the absence of oxygen to attain adsorption-desorption equilibrium [15]. Afterwards the photocatalytic material was separated by filtration (Whatman, Grade 42). A Shimadzu VCSH total organic carbon (TOC) analyser was used to measure the remaining 4-chlorophenol concentration in the filtrate.

A X-ray Bruker D8 Advance diffractometer with Cu-K $\alpha$  radiation and LynxEye detector was applied to study the crystal phase of the synthesised samples.

A JEOL JEM 2100 high resolution scanning transmission electron microscope was applied to study surface morphology and to measure particle size of the synthesised TiO<sub>2</sub> and TiO<sub>2</sub>/GR samples as well as Au nanoparticle size distribution of the gold-promoted photocatalysts. These results were acquired by measuring 100 particles in each sample.

X-ray photoelectron spectroscopy (XPS) measurements were carried out using an ESCALAB Mk II (VG Scientific Ltd.) electron spectrometer under base vacuum of 10<sup>-8</sup> Pa. XPS spectra were recorded using an Mg K $\alpha$  excitation source with photon energy of 1253.6 eV. The carbon 1s line of binding energy of 284.8 eV was used to calibrate the binding-energy scale of the unit.

### *Photocatalytic experiments*

Photodegradation of 4-chlorophenol was studied in a semi-batch photoreactor containing aqueous suspensions of the semiconductor materials at a content of 1 g L<sup>-1</sup>. A constant temperature of 20°C in the reaction vessel was realised. Before catalytic measurements, each sample was dispersed in water by ultrasonic treatment for 20 min. Then the catalyst was placed into the reactor vessel equipped with a magnetic stirrer. Next, 4-chlorophenol from a stock solution was added to achieve an initial concentration of 4×10<sup>-3</sup> mol L<sup>-1</sup> that is equivalent to 290 ppm TOC. The initial volume of the irradiated reaction mixture was 350 ml. During the photocatalytic process, oxygen was bubbled continuously at a flow rate of 12 L h<sup>-1</sup>. The pH of the liquid phase of the suspensions was adjusted to four by adding a buffer solution (Fixanal, Fluka).

The photoreactor was equipped with a 9-W UV lamp (Philips PL-S 2P) for UV-A irradiation ( $\lambda \approx 365$  nm). Photon flux in the UV light region at the external wall of the quartz tube was 10 mW cm<sup>-2</sup> (UV-A) as measured by a microprocessor-controlled radiometer (Cole Parmer, 97503-00). Samples collected during the dark period and during



irradiation were filtered and, as described above, the degree of mineralisation of 4-chlorophenol was assessed by means of a TOC analyser.

## RESULTS AND DISCUSSION

### Catalyst characterisation

Studies [16–18] have proved that catalyst specific surface area, degree of crystallinity, and metal nanoparticle size on the metal oxide surface are factors that can affect significantly the efficiency of photodestruction of water contaminants. In the case of graphene-based semiconductor photocatalysts, pollutant adsorption onto composite catalysts has an essential effect on photocatalytic destruction efficiency in the aqueous phase [5,7,8,10,11].

Regardless of graphene high theoretical specific surface area (2600 m<sup>2</sup> g<sup>-1</sup>) [19], GR composites with

photocatalytic materials demonstrated lower values (Table 1). This is attributed to occurring agglomeration of the photocatalytic materials and changes in pore size distribution during graphene oxide reduction [20,21]. Compared to unmodified samples, TiO<sub>2</sub>/GR surface area was increased by 21%, whereas the Au/TiO<sub>2</sub>/GR sample manifested an increase of 23%. The gold-modified materials, Au/TiO<sub>2</sub> and Au/TiO<sub>2</sub>/GR (0.5 wt.% Au<sup>0</sup>), showed a negligible change of the specific surface area compared to the parent gold-free samples (Table 1), which is in accordance with results reported by other authors [3,15]. Small changes in surface area might be due to blocking of defect sites on the surface and penetration of finely divided gold particles into catalyst pores.

**Table 1.** Physical properties of the photocatalyst samples and pseudo-first order apparent reaction rate constants ( $k_{app}$ )

Sample	BET area <sup>a</sup> (m <sup>2</sup> g <sup>-1</sup> ) ±2%	Average gold particle size <sup>b</sup> (nm) ±10%	4-Chlorophenol adsorption (μmol gcat <sup>-1</sup> ) ±2%	$k_{app}$ (λ=365 nm) (min <sup>-1</sup> ) ±5%
TiO <sub>2</sub>	140	–	280	0.0025
TiO <sub>2</sub> /GR	170	–	540	0.0051
Au/TiO <sub>2</sub>	134	7.2	250	0.0056
Au/TiO <sub>2</sub> /GR	165	7.4	450	0.0098

<sup>a</sup> determined from N<sub>2</sub> adsorption isotherms

<sup>b</sup> determined from TEM images

4-Chlorophenol adsorption in the dark was considerably enhanced upon formation of graphene composites with TiO<sub>2</sub> and Au/TiO<sub>2</sub>, namely, 1.9 and 1.8 times on TiO<sub>2</sub>/GR and Au/TiO<sub>2</sub>/GR, respectively (Table 1). The increase in sample equilibrium adsorption capacity with respect to 4-chlorophenol is due to π-π interactions and formation of hydrogen bonds between 4-chlorophenol and graphene, the local concentration of the pollutant around the investigated photocatalysts being also increased [5,11]. On sample doping by gold the adsorption of 4-chlorophenol was decreased by 12–20% regarding undoped metal oxides (Table 1). This effect has been associated with reduction of the titania or titania/graphene external surface area that is available for adsorption of 4-chlorophenol [22].

An XRD pattern of Au/TiO<sub>2</sub>/GR is shown in Figure 1. A thermally treated sample exhibited only diffraction peaks due to anatase-phase titania (PDF # 841284). Because of low content no XRD diffraction peaks of gold (0.5 wt.%) were registered with the latter sample.

TEM micrographs of GR and composite photocatalytic materials are presented in Figure 2. TEM analysis of the samples showed that the photocatalytic materials are located on graphene surface (Fig. 2b). The average size of the titania

nanoparticles prepared by the sol-gel method was 20 nm, whereas those of the gold particles on Au/TiO<sub>2</sub> and Au/TiO<sub>2</sub>/GR were 7.2 and 7.4 nm, accordingly (Table 1). Such a small difference in gold particle sizes was insignificant as being within experimental error.

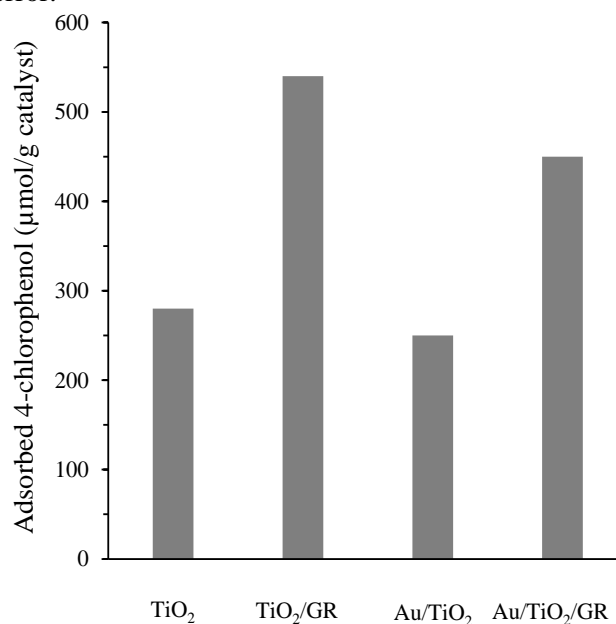


**Fig. 1.** Total amount of 4-chlorophenol adsorbed on the photocatalysts at pH 4 in the dark.

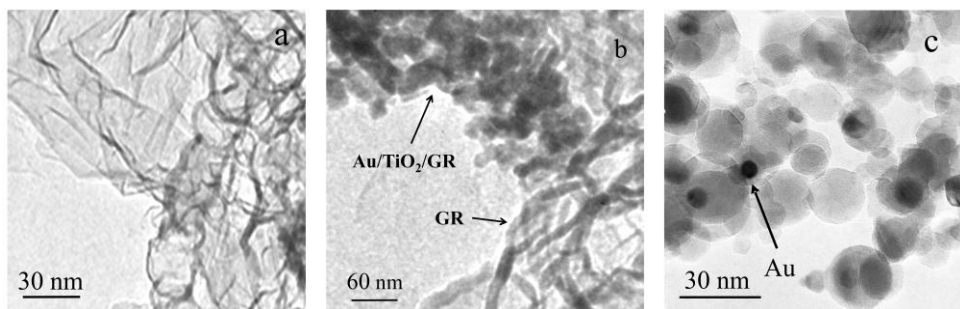


**Fig. 2.** TEM images: (a) graphene; (b) Au/TiO<sub>2</sub>/graphene; (c) Au nanoparticles in Au/TiO<sub>2</sub>/graphene.

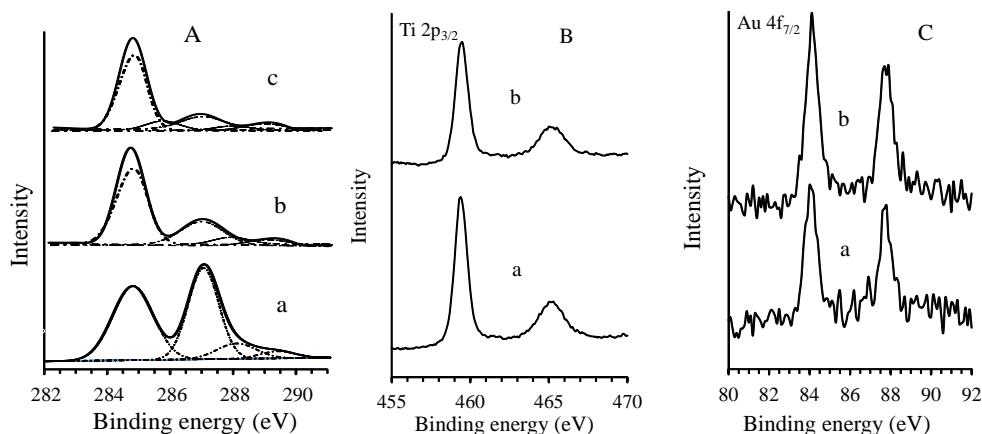


**Fig. 3.** XPS spectra: A – 1 Cs, (a) graphene oxide, (b) TiO<sub>2</sub>/graphene, (c) Au/TiO<sub>2</sub>/graphene; B – Ti 3p: (a) Au/TiO<sub>2</sub>, (b) Au/TiO<sub>2</sub>/graphene; C – Au 4f : (a) Au/TiO<sub>2</sub>, (b) Au/TiO<sub>2</sub>/graphene.

XPS spectra of graphene oxide, graphene, and composite photocatalytic materials are displayed in Figure 3. Figure 3A shows the C 1s spectra of graphene oxide, TiO<sub>2</sub>/GR, and Au/TiO<sub>2</sub>/GR samples. For GO, Fig. 3A (a), four different peaks centred at 284.6, 286.6, 287.8, and 289.0 eV were found, which are related to C=C/C–C bonds in aromatic rings, C–O (epoxy and alkoxy), C=O, and COOH groups, respectively [19]. After thermal treating of the TiO<sub>2</sub>/GO composite at 450°C (Fig. 3A (b)), the intensities of all C 1s peaks of the carbons bonded to oxygen, especially the peak of C–O (epoxy and alkoxy), decreased dramatically because of partial thermal reduction of the graphene oxide to graphene [23]. In contrast to TiO<sub>2</sub>/GR, the Au/TiO<sub>2</sub>/GR sample gave rise to another low intensity C 1s peak at a binding energy of 285.6 eV (Fig. 3A (c)), which indicates an admixture of graphene oxide and entities containing carbon atoms of sp<sup>3</sup> configuration. Most likely, this peak is due to partial destruction of the graphene caused by HO• radicals that are generated upon TiO<sub>2</sub>/GR doping as described above for the photoreduction of the gold precursor. Graphene destruction in aqueous media by HO• radicals generated upon irradiation with UV light over titania surface has already been described in the literature [24].

Neither differences in Ti 2p<sub>3/2</sub> binding energy nor peak broadening in the XPS spectra of TiO<sub>2</sub>,

TiO<sub>2</sub>/GR, and Au/TiO<sub>2</sub>/GR were registered (Fig. 3B) which indicate very weak interactions between titania and graphene.

The binding energies of the Au 4f<sub>5/2</sub> and Au 4f<sub>7/2</sub> peaks positioned at 87.6 and 83.9 eV, respectively, of gold-modified titania and TiO<sub>2</sub>/GR demonstrate that superficially attached gold was completely reduced to metallic Au<sup>0</sup>. In the presence of graphene, no other additional XPS peaks were registered or no broadening of the existing lines was observed (Fig. 3C).

#### Photocatalytic activity

4-Chlorophenol is one of the most used model pollutants for evaluation of the photocatalytic activity of metal oxide catalysts in aqueous solution. The photocatalytic degradation process of 4-chlorophenol in aqueous solution can be interpreted based on the Langmuir-Hinshelwood kinetic model. Under the applied experimental conditions of low 4-chlorophenol concentration and constant UV light flux, the Langmuir kinetic expression [25] can be reduced to a pseudo-first order kinetics equation with respect to the pollutant:

$$\ln C_0/C = k_{app} t, \quad (1)$$

where  $k_{app} = k_r K$ , and  $k_r$  is the rate constant of the limiting step of the reaction at a maximum coverage under the applied experimental conditions,  $K$  is 4-

chlorophenol adsorption-desorption equilibrium constant,  $C_0$  is the initial concentration of 4-chlorophenol, and  $C$  is 4-chlorophenol concentration at a given moment in the course of the photocatalytic reaction. Figure 4 shows a plot of  $\ln C_0/C$  vs. time for the experiments of 4-chlorophenol photocatalytic decomposition. The photocatalytic rates are, therefore, dependent on 4-chlorophenol coverage on the catalysts and 4-chlorophenol concentration.

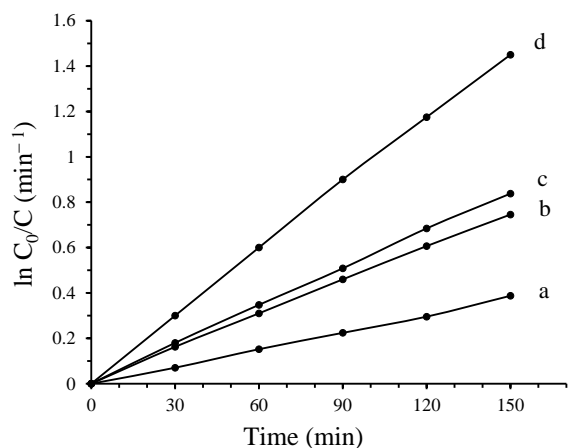


**Fig. 4.** Pseudo-first order kinetics of 4-chlorophenol photocatalytic degradation ( $4 \times 10^{-3}$  mol L<sup>-1</sup>) at pH=4 by irradiation with UV light in the presence of: (a) TiO<sub>2</sub>, (b) TiO<sub>2</sub>/GR, (c) Au/TiO<sub>2</sub>, (d) Au/TiO<sub>2</sub>/GR.

Values of the apparent rate constants of 4-chlorophenol photocatalytic mineralisation over suspended semiconductor materials irradiated with UV-A light are listed in Table 1. The rate constants with UV-A irradiation decrease in the following order: Au/TiO<sub>2</sub>/GR > Au/TiO<sub>2</sub> > TiO<sub>2</sub>/GR > TiO<sub>2</sub> (Fig. 4). Under UV-A irradiation the TiO<sub>2</sub>/GR composite photocatalyst showed a 2-fold increase in the rate of 4-chlorophenol mineralisation compared with the titania photocatalyst. On the other hand, the rate constant values of 4-chlorophenol destruction were increased approximately two times on doping the photocatalysts with gold nanoparticles (Table 1).

Regarding the graphene-free photocatalysts, two principal factors have influence on the increased rate constants of 4-chlorophenol destruction over TiO<sub>2</sub>/GR and Au/TiO<sub>2</sub>/GR. Considering 4-chlorophenol, a higher adsorption capacity of the GR photocatalysts (Fig. 1) is accompanied by enhanced local concentration of the pollutant around the investigated photocatalysts, which facilitates the interaction between photogenerated active species and 4-chlorophenol at TiO<sub>2</sub>/GR and Au/TiO<sub>2</sub>/GR interfaces. A correlation exists between the higher adsorption capacity of the GR composites and their photocatalytic activity (Table 1). On the other hand, it is known that on depositing semiconductor nanoparticles on graphene sheets, the graphene acts

like an electron acceptor by inducing charge carrier separation in the photoexcited semiconductor catalyst [8]. Charge carrier separation also favours an increased activity of the graphene-based semiconductor photocatalysts.

The rate constants of 4-chlorophenol destruction were increased in all cases of photocatalyst modification with gold nanoparticles (Table 1). The effect of gold content and Au nanoparticle size on the photocatalytic activity of modified semiconductor materials under UV and visible light irradiation has been reported in previous works from this laboratory [3,15,17,22]. On depositing noble metal nanoparticles onto the surface of titania and TiO<sub>2</sub>/GR an increase of the quantum yield of the photodestruction reaction of the studied pollutant has been observed. It is due to enhanced separation of electrons and holes and to a higher rate of HO<sup>•</sup> radical formation mainly on the valence band and on the conduction band in the photoexcited semiconductors [26]. Noble metal nanoparticles are highly effective traps for electrons owing to the formation of a Schottky barrier at the metal-semiconductor interface. The Au/TiO<sub>2</sub>/GR system was particularly efficient upon irradiation with UV light and the rate constant of 4-chlorophenol decomposition was approximately 3.9 times higher than that with pure titania (Table 1). In this case, the increased rate constant of 4-chlorophenol decomposition is owing to an enhanced local concentration of the pollutant around the investigated photocatalyst and due to simultaneous charge carrier separation over both gold nanoparticles and graphene (Fig. 5).

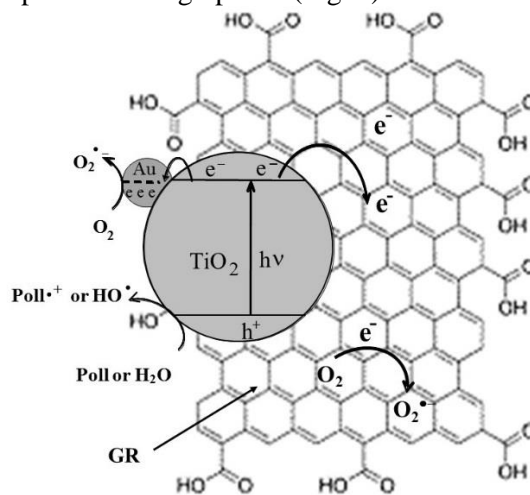


**Fig. 5.** Schematic presentation of charge carrier separation in the photoexcited Au/TiO<sub>2</sub>/GR photocatalyst.

## CONCLUSIONS

4-Chlorophenol photodestruction catalysed by TiO<sub>2</sub>/GR showed a higher rate constant in comparison with titania counterpart which could be

attributed to an enhanced local concentration of the pollutant around the investigated photocatalysts and to an increased probability for interaction between the photogenerated active species and 4-chlorophenol at TiO<sub>2</sub>/GR interface.

In the case of deposited nanosized gold particles (0.5 wt.%) on the surface of the catalysts the higher rate of photocatalytic destruction of 4-chlorophenol is owing to an efficient charge carrier separation, an increase in the lifetime of the excitons, and enhancement of the effectiveness of the interphase charge transfer to adsorbed pollutant molecules. Charge carrier separation was especially efficient during irradiation of the Au/TiO<sub>2</sub>/GR photocatalyst with UV light. In this case, the rate constant of 4-chlorophenol decomposition over the latter was approximately 3.9 times higher than that with pure titania.

**Acknowledgement:** The authors gratefully acknowledge financial support by the Bulgarian Science Fund (Contract DFNI-T02/16).

#### REFERENCES

1. K. Nakata, A. Fujishima, *J. Photochem. Photobiol. C: Photochem. Rev.*, **13**, 169 (2012).
2. H. Park, Y. Park, W. Kim, W. Choi, *J. Photochem. Photobiol. C: Photochem. Rev.*, **15**, 1 (2013).
3. V. Iliev, D. Tomova, S. Rakovsky, A. Eliyas, G. Li Puma, *J. Mol. Catal. A: Chem.*, **327**, 51 (2010).
4. A. Ayati, A. Ahmadvpour, F.F. Bamoharram, B. Tanhaei, M. Mänttari, M. Sillanpää, *Chemosphere*, **107**, 163 (2014)
5. R.K. Upadhyay, N. Soin, S.S. Roy, *RSC Adv.*, **4**, 3823 (2014)
6. S. Chowdhury, R. Balasubramanian, *Appl. Catal. B: Environ.*, **160–161**, 307 (2014)
7. N. Zhang, Y. Zhang, Y-J. Xu, *Nanoscale*, **4**, 5792 (2012)
8. Q. Xiang, J. Yu, M. Jaroniec, *Chem. Soc. Rev.*, **41**, 782 (2012)
9. A.S.A. Shalaby, A.D. Staneva, L.I. Aleksandrov, R.S. Iordanova, Y.B. Dimitriev, *Bulg. Chem. Commun.*, **48**, 38 (2016)
10. Y.H. Ng, I. V. Lightcap, K. Goodwin, M. Matsumura, P.V. Kamat, *J. Phys. Chem. Lett.*, **1**, 2222 (2010)
11. J. Liu, Z. Wang, L. Liu, W. Chen, *Phys. Chem. Chem. Phys.*, **13**, 13216 (2011)
12. S. Morales-Torres, L. M. Pastrana-Martínez, J. L. Figueiredo, J. L. Faria, A.M.T. Silva, *Environ. Sci. Pollut. Res.*, **19**, 3676 (2012)
13. S. Ghasemi, S. Rahman Setayesh, A. Habibi-Yangjeh, M.R. Hormozi-Nezhad, M.R. Gholami, *J. Hazard. Mater.*, **199–200**, 170 (2012)
14. B. Cojocaru, S. Neatu, E. Sacaliuc-Parvulescu, F. Levy, V.I. Parvulescu, H. Garcia, *Appl. Catal. B: Environ.*, **107**, 140 (2011)
15. M. Daous, V. Iliev, L. Petrov, *J. Mol. Catal. A: Chem.*, **392**, 194 (2014).
16. C.G. Granqvist, *Sol. Energy Mater. Sol. Cells*, **91**, 1529 (2007)
17. V. Iliev, D. Tomova, L. Bilyarska, G. Tyuliev, *J. Mol. Catal. A: Chem.*, **263**, 32 (2007).
18. A. Orlov, D.A. Jefferson, N. Macleod, R.M. Lambert, *Catal. Lett.*, **92**, 41 (2004).
19. O. Akhavan, E. Ghaderi, *J. Phys. Chem. C*, **113**, 20214 (2009)
20. H. Adamu, P. Dubey, J.A. Anderson, *Chem. Eng. J.*, **284**, 380 (2016)
21. Md.S.A. Sher Shah, A R. Park, K. Zhang, J.H. Park, P.J. Yoo, *ACS Appl. Mater. Interfaces*, **4**, 3893 (2012)
22. V. Iliev, D. Tomova, R. Todorovska, D. Oliver, L. Petrov, D. Todorovsky, M. Uzunova – Bujnova, *Appl. Catal. A: General*, **313**, 115 (2006)
23. S. Pei, H.-M. Cheng, *Carbon*, **50**, 3210 (2012)
24. J.G. Radich, A.L. Krenselewski, J. Zhu, P.V. Kamat, *Chem. Mater.*, **26**, 4662 (2014)
25. N. Serpone, A. Salinaro, A. Emeline, V. Ryabchuk, *J. Photochem. Photobiol. A: Chem.*, **130**, 83 (2000)
26. V. Subramanian, E.E. Wolf, P.V. Kamat, *Langmuir*, **19**, 469 (2003).

ПРОМОТИРАНЕ НА СКОРОСТТА НА ОКИСЛИТЕЛНО ОТСТРАНЯВАНЕ НА  
4-ХЛОРФЕНОЛ ВЪРХУ ЗЛАТО-ДОТИРАНИ TiO<sub>2</sub>/ГРАФЕН ФОТОКАТАЛИЗАТОРИ  
ПРИ ОБЛЪЧВАНЕ С УЛТРАВИОЛЕТОВА СВЕТЛИНА

В. И. Илиев\*, Д. В. Томова, В. Ф. Георгиев, С. К. Раковски

*Институт по катализ, Българска академия на науките, 1113 София, България*

Постъпила на 9 ноември, 2016 г.; коригирана на 23 март, 2017 г.

Фотоокислението на 4-хлорфенол, катализирано от наноразмерни TiO<sub>2</sub>, Au/TiO<sub>2</sub> и от съответните композитни материали с редуциран графенов оксид (GR) са изследвани при облъчване с ултравиолетова светлина. XPS и TEM методи са използвани за охарактеризиране на получените фотокатализатори. Средният размер на наночастиците от TiO<sub>2</sub> получен по зол-гел метода е 20 nm. TiO<sub>2</sub> и Au/TiO<sub>2</sub> са разпределени на случаен принцип на повърхността на нанолистовете от графен. Средният размер на Au наночастици в модифицираните TiO<sub>2</sub> фотокатализатори е  $\approx 7$  nm. XPS измерванията потвърждават частичната термо- или фото-редукция на графеновия оксид до графен. Скоростните константи на фотоокисление на 4-хлорфенол катализирани от изследваните образци следват реда: Au/TiO<sub>2</sub>/GR > Au/TiO<sub>2</sub> > TiO<sub>2</sub>/GR > TiO<sub>2</sub>. Скоростната константа на деструкция на 4-хлорфенол катализирана от Au/TiO<sub>2</sub>/GR композита е приблизително 3.9 пъти по-висока от тази регистрирана с чист TiO<sub>2</sub>. Повишаването на активността на Au/TiO<sub>2</sub>/GR, Au/TiO<sub>2</sub> и TiO<sub>2</sub>/GR фотокатализаторите е резултат от по-ефективното разделяне на носителите на заряди в генерираните от светлина електрон-дупка двойки в полупроводника TiO<sub>2</sub>. Това благоприятства допълнителното генериране на OH• радикали върху валентната зона на TiO<sub>2</sub>.

## Gas phase ozone decomposition over co-precipitated Ni-based catalysts

T. T. Batakliiev\*, V. F. Georgiev, P. A. Karakashkova, M. V. Gabrovska, D. A. Nikolova,  
M. P. Anachkov, S. K. Rakovsky

*Institute of Catalysis, Bulgarian Academy of Sciences, Acad. G. Bonchev St., Bldg. 11, 1113 Sofia, Bulgaria*

Submitted November 10, 2016; Revised April 6, 2017

The effect of nickel content in the catalyst was investigated in this work in regard to the catalytic activity, stability and mechanical strength of the mixed metal oxides generated by thermal treatment of co-precipitated Ni-Cu-Al samples as catalyst precursors in the reaction of ozone decomposition. The impact of the silver present as a promoter on the catalytic activity was also examined. The catalytic activity of the metal oxide catalysts was estimated by monitoring of the inlet and outlet ozone concentrations and calculating the conversion degree of ozone into molecular oxygen. It was established that at room temperature all the catalysts demonstrate stable and almost constant conversion degree in the course of time on stream. It was found out that all tested catalyst samples have activity in ozone decomposition but the maximal conversion degree (more than 90%) was observed with the catalyst sample impregnated with 3% Ag<sub>2</sub>O. The properties of the catalysts were characterized by using various physical methods such as PXRD, TEM and SEM.

**Keywords:** Ni-Cu-Al metal oxide catalysts, Ag promoter, Co-precipitation, Ozone decomposition

### INTRODUCTION

Ozone is widely used in the industrial and environmental processes more specifically in semiconductor manufacturing, deodorization, disinfection and water treatment [1]. Ozone in the atmosphere protects the Earth's surface against UV radiation, but on the ground level it is accepted to be one of the criteria for air contamination [2].

An effective method for purification of toxic gases containing ozone is the heterogeneous catalytic decomposition [3]. The most effective catalysts for this process are those containing platinum and platinum group metals, however, these metals are very expensive and this fact is limiting their application on a large-scale. Hence, efforts are made to replace precious metals by low cost non-noble transition metals and metal oxides of Mn, Co, Ni, Cr, Ag, Cu, Ce, Fe, V and Mo supported on high specific surface area carriers such as  $\gamma$ -Al<sub>2</sub>O<sub>3</sub>, SiO<sub>2</sub>, TiO<sub>2</sub>, ZrO<sub>2</sub> and charcoal [4]. It has been reported that the transition metals oxides exhibit high catalytic activity in the decomposition of ozone [5]. Among them, the catalysts based on manganese oxide demonstrate the highest activity in the ozone decomposition reaction [3].

The behaviour of silver-containing catalysts in the above mentioned reaction is the subject of several insightful publications. Silver- and nickel-based catalysts deposited on  $\gamma$ -Al<sub>2</sub>O<sub>3</sub> by the impregnation method have been evaluated for the removal of toluene in different plasma catalytic systems. It was reported that NiO/Al<sub>2</sub>O<sub>3</sub> catalyst

displayed a higher enhancement of CO<sub>2</sub> selectivity and ozone decomposition efficiency [6].

Ru-Mn-promoted Ni-based catalysts and commercial Ni-based catalysts have been compared in the reaction of catalytic steam reforming of toluene in the temperatures range 673–1073 K. Generally, it was found out the conversion of toluene and the H<sub>2</sub> content in the product gas increased with the temperature increase [7].

The performance of cassava rhizome gasification has been carried out at high temperatures ranging from 873 up to 1073 K in the presence of Ni/ $\alpha$ -Al<sub>2</sub>O<sub>3</sub> and it was reported that the higher temperature improved the conversion of this material into fuel gas [8].

Efficient degradation of 2,4-dichlorophenoxyacetic acid in aqueous solutions has been achieved on NiO/SiO<sub>2</sub> catalysts in the presence of ozone [9]. In this work NiO nanoparticles have been deposited on the silica surface by impregnation and liquid phase photodeposition in the presence of acetone or benzophenone. The most promising method of preparation appeared to be the sensitized photodeposition allowing a higher reduction degree of the precursor Bis(2,4-pentanedionato)nickel(II) after short irradiation time interval. The authors claim that according to the results on catalytic ozonation of 2,4-dichlorophenoxyacetic acid, the initial specific activity of the photodeposited catalyst was almost 7 times higher compared with that of the impregnated catalyst sample.

The influence of NiO addition on the activity of cement containing catalyst has been studied in the reaction of ozone decomposition [10]. It was found

\*) To whom all correspondence should be sent:

E-mail: todor@ic.bas.bg

out that the addition of NiO to the catalyst system improves its catalytic properties.

In another paper [11] the ability of Ni–Zn ferrite magnetic catalyst in decomposition of dye model contaminants by photocatalytic ozonation has been investigated. Formate, acetate and oxalate anions have been detected as dominant aliphatic intermediates and nitrate, sulfate and chloride ions have been detected as mineralization products of dyes. The results demonstrated that the photocatalytic ozonation using Ni-Zn ferrite magnetic catalyst was a very effective method for dye degradation.

A literature survey suggests that Ag- and Ni-containing catalytic compositions show high activity in the ozone decomposition and most of them have been obtained from impregnated precursor samples [12].

The aim of this paper was to investigate the activity, stability and mechanical strength of the mixed metal oxides promoted by thermal treatment of co-precipitated Ni-Cu-Al samples as catalyst precursors in the reaction of ozone decomposition. Two effects have been observed to have impact on the catalytic activity of the oxide compounds: the nickel content and the silver promoter. For this purpose, two Ni-Cu-Al samples with composition 10%NiO-5%CuO-85%Al<sub>2</sub>O<sub>3</sub> and 20%NiO-5%CuO-75%Al<sub>2</sub>O<sub>3</sub> were synthesized. Studying the influence of the silver addition by co-precipitation or conventional impregnation method on the catalytic activity of the materials would enable to select the optimal catalyst composition with the most advantageous characteristics in the ozone decomposition reaction.

## EXPERIMENTAL

### Sample preparation

All precursor samples were obtained by co-precipitation at 60°C and constant pH=9.0, using ‘*pro analysi*’ purity grade nitrate salts of the corresponding metals: Ni(NO<sub>3</sub>)<sub>2</sub>·6H<sub>2</sub>O, Cu(NO<sub>3</sub>)<sub>2</sub>·3H<sub>2</sub>O, Al(NO<sub>3</sub>)<sub>3</sub>·9H<sub>2</sub>O and AgNO<sub>3</sub>, and Na<sub>2</sub>CO<sub>3</sub> as a precipitating agent. A fixed volume of distilled water was poured in a laboratory synthesis reactor, heated to 60°C, and adjusted with 0.9 M Na<sub>2</sub>CO<sub>3</sub> solution to reach pH=9.0. The mixed nitrate solution (total metal concentration of 0.5 M) and the precipitant were introduced drop-wise simultaneously controlled by two peristaltic pumps during vigorous stirring. The resulting slurry was aged for 60 min in the mother liquor under continuous stirring at 60°C and pH=9.0. Then it was filtered off, washed thoroughly with distilled water until neutral pH value of the filtrate was obtained and absence of NO<sub>3</sub><sup>-</sup> ions - the latter was tested using solution of diphenylamine in H<sub>2</sub>SO<sub>4</sub>. The obtained precipitates were further dried at 100°C for 20 h. The co-precipitated precursors were thermally treated in an air atmosphere at 450°C for 2.5 h before running the catalytic activity test. The calcined products were labeled as Ni10, Ni10Ag and Ni20, where 10 and 20 denote the percentage of NiO in the solids, respectively, and Ag indicate the presence of Ag modifier (Table 1).

The calcined sample Ni10 was impregnated with aqueous solution of AgNO<sub>3</sub> in such quantity as to receive a sample having 3.0 wt % Ag<sub>2</sub>O in its composition. After drying at 100°C, the sample was once more calcined at 450°C for 2.5 h.

**Table 1.** Sample notation and chemical composition of the studied samples

Sample	Chemical composition						
	(wt. %)				(molar ratio)		
	NiO	CuO	Al <sub>2</sub> O <sub>3</sub>	Ag <sub>2</sub> O	Ni <sup>2+</sup> /Al <sup>3+</sup>	Cu <sup>2+</sup> /Al <sup>3+</sup>	M <sup>2+</sup> /Al <sup>3+</sup>
Ni10	10.0	5.0	85.0	–	0.08	0.04	0.12
Ni10Ag	10.0	5.0	82.0	3.0	0.08	0.04	0.12
Ni20	20.0	5.0	75.0	–	0.18	0.04	0.22

### Sample characterization

Powder X-ray diffraction (PXRD) data were collected on a Bruker D8 Advance diffractometer employing CuK $\alpha$  radiation ( $\lambda = 0.15406$  nm), operated at U = 40 kV and I = 40 mA. The crystalline phases were identified using Joint Committee on Powder Diffraction Standards (JCPDS) files. The microstructure of the catalyst was observed using a high-resolution transmission electron microscope (HRTEM JEOL 2100).

A scanning electron microscope (SEM) JSM-5510 of JEOL was used for morphology observations.

The ozone conversion degree measurements were carried out in a tubular glass reactor (6×150 mm) charged with 0.1 g of fixed catalyst bed. The experiments were performed at feed flow rates of 6.0 l h<sup>-1</sup> and inlet ozone concentration of 10 000 ppm. The ozone was generated by passing dry oxygen through a high-voltage silent-discharge ozone generator. The inlet and outlet ozone concentrations

were monitored using a BMT 964 UV absorption-type of ozone analyzer.

## RESULTS AND DISCUSSION

The time–conversion degree dependence measured in the course of 180 min time interval over the studied catalysts is represented in Fig. 1. One can

see that the conversion degree is stable and it remains almost constant with time on stream at room temperature of the catalyst bed. The conversion degree results reveal that the high-loading Ni catalyst (Ni20) demonstrates higher ozone decomposition value (~90%) than that of the low-loading catalysts Ni10 (~77%).

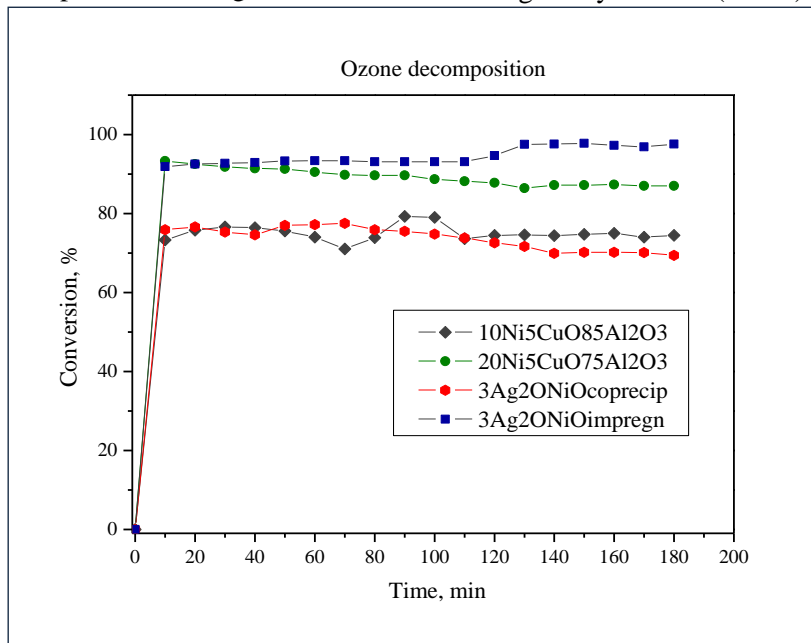


Fig. 1. Ozone conversion as function of ozonation time for the metal oxide catalysts

These results could be explained by considering the most probable mechanism of ozone decomposition including formation of superoxide or peroxide particles on the catalytic surface (Fig. 2). According to this reaction mechanism, ozone is adsorbed on catalytically active site (\*), then O–O bond is cleaved, O<sub>2</sub> is released and atomic oxygen-containing active site O\* is formed as a result (1). These surface sites react again with ozone molecules impinging from the gas phase (2), O<sub>2</sub> is released and an active site containing molecular oxygen O<sub>2</sub>\* is created, and then subsequently it is desorbed (3):

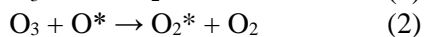
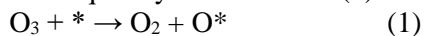
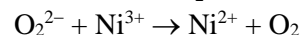
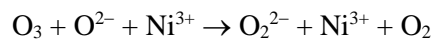
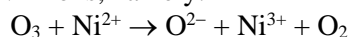


Fig. 2. Mechanism of catalytic ozone decomposition

It could be supposed that during ozone decomposition on transition metal oxides such as NiO-CuO-Al<sub>2</sub>O<sub>3</sub> there occurs formation of intermediate ionic particles possessing either superoxide or peroxide features. The formation of charged chemisorbed oxygen species is accompanied by oxidation of the respective number of cations in the oxide crystal lattice to a higher oxidation state. In our case this will be the oxidation of Ni<sup>2+</sup> to Ni<sup>3+</sup> ions, namely:



The probable reaction scheme of ozone decomposition consists of electron transfer from the Ni<sup>2+</sup> ion to ozone, resulting in formation of higher oxidation state Ni<sup>3+</sup> species and peroxide particles O<sub>2</sub><sup>2-</sup>, followed by reduction of Ni<sup>3+</sup> species back to Ni<sup>2+</sup> ion by desorption of peroxide particle to form oxygen (O<sub>2</sub><sup>2-</sup> → O<sub>2</sub> + 2e<sup>-</sup>) closing the catalytic cycle.

The proposed scheme illustrates the electron transfer ensuring the catalytic ozone decomposition and the necessity of having optimal ratio of the Ni<sup>2+</sup>/Ni<sup>3+</sup> ions and reversible redox Ni<sup>2+</sup>↔Ni<sup>3+</sup> transition. The probability of this kind of association is realized in Ni20 catalyst. Its relatively higher activity could be ascribed to the higher nickel content in this oxide sample, where some Ni<sup>2+</sup> ions are partially oxidized into Ni<sup>3+</sup> oxidation state, enough to form redox Ni<sup>2+</sup>/Ni<sup>3+</sup> couple, hence to realize the reversible redox mechanism of Ni<sup>2+</sup>↔Ni<sup>3+</sup> transition. The lower nickel content in Ni10 catalyst reduces the number of active sites available on the catalyst surface.

An attempt was made to improve the activity of Ni10 catalyst by introduction of silver in the Ni-Cu-Al sample, either by co-precipitation or by impregnation of the calcined Ni10 sample.



The catalytic system containing Ni10 (10%NiO-5%CuO-85% Al<sub>2</sub>O<sub>3</sub>) demonstrates lower degree of ozone decomposition than that of the respective oxide system impregnated with 3.0wt% Ag<sub>2</sub>O, pointing to the high redox properties of Ag in the ozone decomposition [13].

The morphology of the catalytic surface was studied by high resolution transmission electron microscopy (Fig. 3). TEM images reveal an aggregated bundle-like particles and each aggregate is consisting of numbers of nanowires/rods, which are created in the solid solution metal oxide.

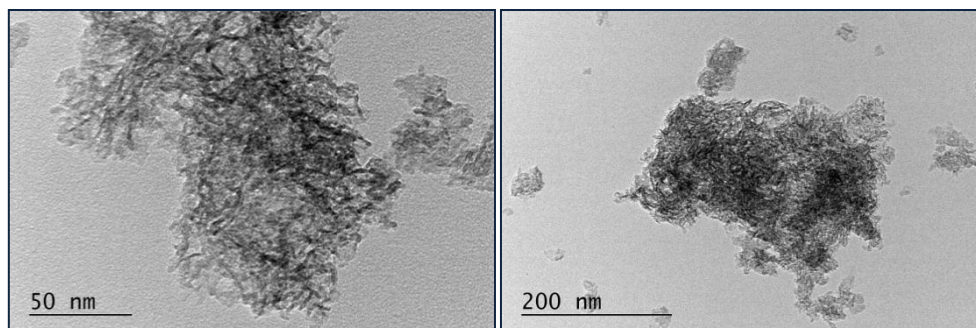


Fig. 3. TEM images of 20Ni catalyst at different magnifications

PXRD patterns of the synthesized metal oxide systems were used for detecting the resultant phases (Fig. 4). The diffractograms reveal that calcination of the co-precipitated precursors at 450°C gives rise to oxide compositions with broad diffraction lines. The recorded badly organized reflections are corresponding to the non-stoichiometric spinel-like NiAl<sub>2</sub>O<sub>4</sub> (JCPDS 00-010-0339) and CuAl<sub>2</sub>O<sub>4</sub> (JCPDS 01-078-0556) phases. The formation of spinel-like Ni- and Cu-aluminate phases could be explained based on the weight content of Ni and Cu in the samples or rather accounting for the superior Al concentration, corresponding to M<sup>2+</sup>/Al<sup>3+</sup> molar ratio from 0.12 to 0.22 (Table 1). It is well-known that the

stoichiometric aluminate spinel M<sup>2+</sup>Al<sub>2</sub>O<sub>4</sub> presents a molar ratio M<sup>2+</sup>/Al<sup>3+</sup> equal to 1:2 [14]. It is necessary to mention that the most intensive peaks of NiAl<sub>2</sub>O<sub>4</sub>, CuAl<sub>2</sub>O<sub>4</sub> and γ-Al<sub>2</sub>O<sub>3</sub> overlap due to the almost identical positions of the various reflections that hamper the accurate identification of the corresponding phases. In addition, the possibility of a mixed spinel (Cu,Ni)Al<sub>2</sub>O<sub>4</sub> formation should not be ignored. Moreover, characteristic patterns of γ-Al<sub>2</sub>O<sub>3</sub> (JCPDS 00-010-0425) are observed. However, some low intensity reflections of γ-Al<sub>2</sub>O<sub>3</sub> phase are absent in the diffractogram of sample Ni20 (higher nickel loading). Reflections of both single NiO and CuO phases are not registered.

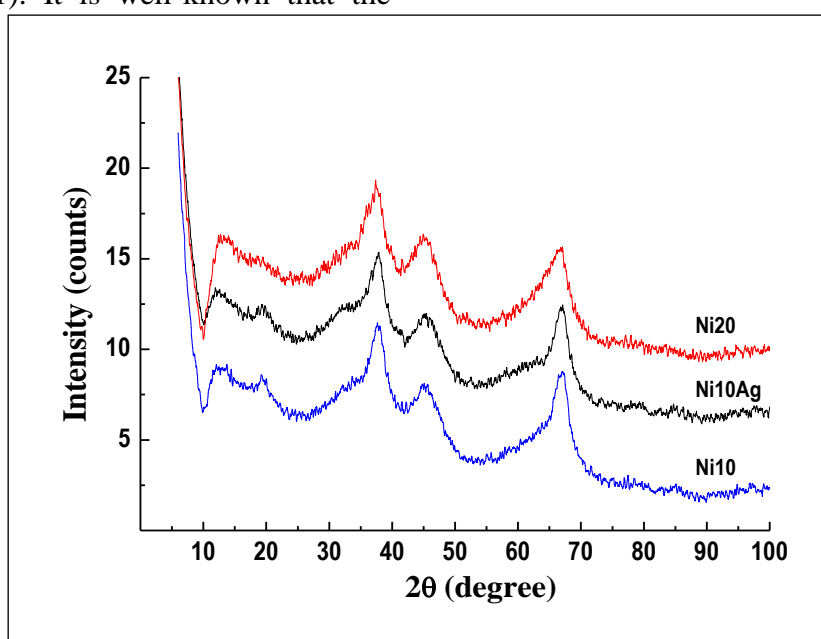


Fig. 4. XRD patterns of nickel, copper, aluminum and silver metal oxide catalysts.

Ag<sub>2</sub>O oxide phase was not observed in the PXRD patterns of silver modified sample (Ni10Ag). This result is not unexpected because AgNO<sub>3</sub> decomposes at 440°C into metallic silver, nitrogen, oxygen, and nitrogen oxide [15]. However, the diffraction lines typical of metal silver (JCPDS 00-004-0783) phase did not appear in the diffractogram of the Ni10Ag sample, most probably due to the small amount of silver or very finely dispersed silver phase.

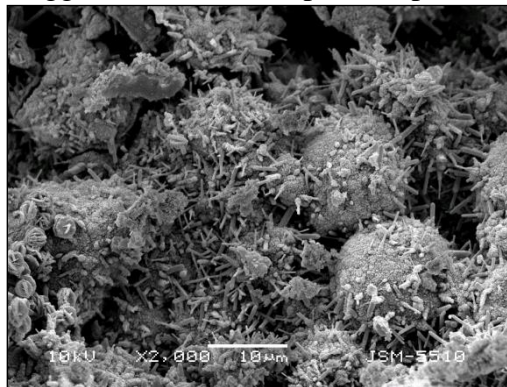


Fig. 5. SEM micrographs of Ni10 catalyst at different magnifications.

The morphology of these particles evidences porous structure of the catalytic surface. The SEM studies are indicative of the influence of the applied preparation method of heterogeneous catalysts with surface roughness which increases the effective surface area of the material. This is essential for the dissociative adsorption of O<sub>3</sub> on the catalytic surface in order to form chemisorbed atomic oxygen in concentrations sufficiently high to promote oxidation.

### CONCLUSIONS

The co-precipitation method turned out to be a very suitable technique for preparation of highly active NiO–CuO–Ag<sub>2</sub>O–Al<sub>2</sub>O<sub>3</sub> catalyst for ozone decomposition.

It was found out that all treated catalytic samples have considerable activity in ozone decomposition but the maximal conversion degree (more than 90%) was observed with the catalyst sample impregnated with Ag<sub>2</sub>O.

The SEM analysis proves the significant role of sample surface morphology in the process of ozone decomposition on the surface of NiO–CuO–Ag<sub>2</sub>O–Al<sub>2</sub>O<sub>3</sub> solid solution oxide catalyst.

The strong synergistic effect due to the formation of NiO–CuO–Ag<sub>2</sub>O–Al<sub>2</sub>O<sub>3</sub> solid solution oxide gave rise to larger number of adsorbed ozone molecules and preferable low temperature redox catalytic cycle, which make a great contribution to its superior activity.

It can be summarized that the ozone decomposition activity increases with the nickel content. This fact

In general, the observed broadening of the diffraction lines indicates that the calcined oxide compositions are poorly crystallized materials, whose average particle size determination is practically impossible.

A wide area of the surface of Ni10 catalyst was scanned by SEM. The illustrations are represented in Figure 5. The so obtained SEM images are exhibiting nanorods-well dispersed particles as well as rounded-like particles agglutinated on mesoporous spheres [16].

is ascribed to the availability of optimal Ni<sup>2+</sup>/Ni<sup>3+</sup> ion pair ratio. A probable scheme is proposed about ozone decomposition composed by the redox couple Ni<sup>2+</sup>/Ni<sup>3+</sup> and reversible redox Ni<sup>2+</sup>↔Ni<sup>3+</sup> transition.

**Acknowledgements:** The authors are grateful to DFNI-T02 16/12.12.14 for financial support.

### REFERENCES

1. S. Rakovsky, G. Zaikov, Kinetic and Mechanism of Ozone Reactions with Organic and Polymeric Compounds in Liquid Phase, monograph (second edition), Nova Science Publishers Inc., New York, 1-340 (2007).
2. S. T. Oyama, *Catal. Rev. Sci. Eng.*, **42**, 279 (2000).
3. B. Dhandapani, S. T. Oyama, *Appl. Catal. B-Environ.*, **11**, 129, (1997).
4. T. Batakliiev, V. Georgiev, M. Anachkov, S. Rakovsky, G. Zaikov, *Interdiscip. Toxicol.*, **7**, 47 (2014).
5. S. Imamura, M. Ikebata, T. Ito, T. Ogita, *Ind. Eng. Chem. Res.*, **30**, 217 (1991).
6. W. Xu, N. Wang, Y. Chen, J. Chen, X. Xu, L. Yu, L. Chen, J. Wu, M. Fu, A. Zhu, D. Ye, *Catal. Commun.*, **84**, 61 (2016).
7. G. Oh, S. Y. Park, M. W. Seo, Y. K. Kim, H. W. Ra, J. Lee, S. J. Yoon, *Renewable Energy*, **86**, 841 (2016).
8. P. Sornkade, D. Atong, V. Sricharoenchaikul, *Renewable Energy*, **79**, 38 (2015).
9. J. L. Rodriguez, M. A. Valenzuela, H. Tiznado, T. Poznyak, E. Flores, *J. Mol. Catal. A-Chem.*, **392**, 39 (2014).

10. I. Martinov, S. Tkachenko, V. Demidyuk, G. Egorova, V. Lunin, *J. Moscow Univ., Ser. 2: Chemistry*, **40**, 355 (1999), in Russian.
11. N. M. Mahmoodi, M. Bashiri, S. J. Moeen, *Mater. Res. Bull.*, **47**, 4403 (2012).
12. I. Stambolova, V. Georgiev, T. Batakliiev, L. Lutzkanov, V. Blaskov, G. Atanasova, S. Vassilev, A. Eliyas, *Journal of Chemical Technology and Metallurgy*, **51** (2), 181 (2016).
13. T. Batakliiev, G. Tyuliev, V. Georgiev, M. Anachkov, A. Eliyas, S. Rakovsky, *Ozone: Science & Engineering*, **37**, 216 (2015).
14. N. Sahli, C. Petit, A.C. Roger, A. Kiennemann, S. Libs, M.M. Bettahar, *Catal. Today*, **113**, 187 (2006).
15. J. He, T. Kunitake, T. Watanabe, *Chem. Commun.*, 795 (2005).
16. J. H. Pan, X. Z. Wang, Q. Z. Huang, C. Shen, Z. Y. Koh, Q. Wang, A. Engel, D. W. Bahnemann, *Adv. Funct. Mater.*, **24**, 95 (2014).

## РАЗЛАГАНЕ НА ОЗОН ВЪРХУ СЪУТАЕНИ НИКЕЛ СЪДЪРЖАЩИ КАТАЛИЗАТОРИ В ГАЗОВА ФАЗА

Т.Т. Батаклиев\*, В.Ф. Георгиев, П.А. Каракашкова, М.В. Габровска, Д.А. Николова, М.П. Аначков,  
С.К. Раковски

*Институт по катализ, Българска академия на науките, ул. Акад. Г. Бончев., Бл. 11, 1113 София, България*

Постъпила на 10 ноември, 2016 г.; коригирана на 6 април, 2017 г.

(Резюме)

В настоящата работа беше изследван ефекта на количеството никел върху активността, стабилността и якостта на смесени метални оксиди получени чрез термична обработка на съутаени Ni-Cu-Al образци като прекурсори на катализатори за реакцията на разлагане на озон. Също така беше изследвано и влиянието на среброто като промотор на каталитичната активност. Каталитичната активност на метал оксидните катализатори беше определена чрез регистриране на озонните концентрации на вход и изход от реактора и изчисляване конверсията на озон до молекулен кислород. В хода на реакцията беше установено, че при стайна температура всички катализатори работят стабилно. Също така беше намерено, че всички третиращи каталитични образци притежават активност в реакцията на разлагане на озон, но най-висока конверсия (над 90%) показва катализатора импрегниран с Ag<sub>2</sub>O.

Свойствата на катализаторите бяха потвърдени чрез използване на различни физични методи за охарактеризиране като ПРД, ТЕМ и СЕМ.

## Effectiveness of TiO<sub>2</sub>-based photocatalysts in the ozone assisted oxidative degradation of model wastewater contaminant adipic acid under UV-light irradiation

V.F. Georgiev<sup>1\*</sup>, V. Iliev<sup>1</sup>, A.E. Elias<sup>1</sup>, T.T. Batakliiev<sup>1</sup>, M.P. Anachkov<sup>1</sup>, V.E. Serga<sup>2</sup>,  
P.A. Karakashkova<sup>1</sup>, S.K. Rakovsky<sup>1</sup>

<sup>1</sup> Institute of Catalysis, Bulgarian Academy of Sciences, Sofia 1113, Bulgaria

<sup>2</sup> Institute of Inorganic Chemistry, Riga Technical University, Riga, Latvia

Submitted November 10, 2016; Accepted February 21, 2017

Palladium and gold modified TiO<sub>2</sub> (Degussa P25) under the effect of feeding oxygen and ozone containing mixture to the reactor under UV-A and UV-C irradiation were examined for their catalytic activity in the reaction of adipic acid oxidation. The samples were synthesized by extractive-pyrolytic method by loading 0.5% of the active metal having particles size varying from 7 to 12 nm. The XRD, TEM and BET methods were employed for their structural and chemical characterization. In the presence of oxygen under UV-A light the apparent first-order reaction rates constants of Pd- and Au-modified TiO<sub>2</sub> samples were respectively 1.7 and 2.3 times higher than that of the pure TiO<sub>2</sub> under the same conditions. These higher reaction rate constants are due to the more efficient separation of the electron-hole charge carriers generated during irradiation. Further, the effectiveness of the catalysts in regard to the photooxidation of adipic acid in the presence of ozone is greater both under UV-C and UV-A light with all the tested samples. The reaction rate constants under monochromatic 254 nm irradiation are about 3 times higher than those evaluated with polychromatic ( $\lambda_{\text{max}}=365$  nm) light. This is due to the additional generation of HO<sup>•</sup> radicals by the ozone on the conduction band of the TiO<sub>2</sub> photocatalysts as well as the result of O<sub>3</sub> photolysis by the UV-C light photons of high energy.

**Keywords:** Photocatalysis, TiO<sub>2</sub>, Ozone, Nanosized photocatalysts

### 1. INTRODUCTION

Adipic acid is used primarily in the manufacture of nylon-6, 6 polyamide, polyester polyols, plasticizers, and lubricant additives. Worldwide demand for adipic acid is about 2 billion tons annually growing up continuously at a steady rate. This could result in its discharging into the environment through various waste streams. Many processes have been proposed over the years and they are being currently used to remove organic toxins from wastewaters. Adipic acid is classified as a hazardous substance and its complete degradation by photocatalytic oxidation is considered to be suitable process. Photocatalysis employing various semiconductors has been the focus of intensive investigations by a number of researchers [1– 6]. A number of metal composite systems have been investigated in degradation of water contaminants by photocatalytic processes through induced redox reactions on the surface of the catalyst. By illumination of the semiconductor catalyst with appropriate light energy, corresponding to the band gap, these processes involve a generation of conduction band electrons and valence band holes and they have been studied sufficiently well. An ideal photocatalyst should be stable, inexpensive, non-toxic and of course highly photoactive. Several semiconductors such as TiO<sub>2</sub>, ZnO, Fe<sub>2</sub>O<sub>3</sub>, WO<sub>3</sub>,

SnO<sub>2</sub>, ZrO<sub>2</sub>, CdS, SrTiO<sub>3</sub>, ZnS have band gap energies sufficient for catalyzing a wide range of chemical reactions. Considerable efforts have been devoted to the design of photocatalytic systems exhibiting a high efficiency for converting light into chemical energy [7 – 9]. Titania, the most thoroughly investigated semiconductor in the literature, seems to be the most promising for photocatalytic destruction of organic pollutants. This semiconductor provides the best combination between catalytic performance and stability in aqueous media. From a practical point of view one of the difficulties in developing a photocatalytic setup including semiconductor dispersion is the separation of the product from the photocatalytic slurry. This implies that the photocatalyst should be fixed on carrier material. It has been reported that TiO<sub>2</sub> is the most suitable because of its good anchoring on the support material [10].

The most important process in photocatalysis employing semiconducting materials is without any doubt the charge separation of electrons and holes. In order to reduce the high recombination rate of photoexcited electron-holes (excitons) and utilize more efficient sunlight, a variety of methods, such as metal and nonmetal doping of TiO<sub>2</sub> have been applied. It has been demonstrated convincingly that the doping with noble metal leads to promotion of its catalytic efficiency in photooxidation processes [11

\*) To whom all correspondence should be sent:

E-mail: vlado@ic.bas.bg

– 13]. Alongside with the employing of TiO<sub>2</sub> in photocatalytic oxidation of water pollutants, the involving of ozone in the process can improve the oxidation processes leading to higher conversion degrees at low cost [14]. The photocatalytic ozonation consists in the simultaneous application of ozone and photocatalysis [15 – 17]. The combination of ozone in photocatalytic systems brings forth a synergistic effect based on the high efficient electron trapping by ozone molecules. In addition to it higher amounts of hydroxyl radicals are being generated when comparing with photocatalysis in the presence of oxygen alone [18].

To investigate the effect of various TiO<sub>2</sub> doped catalysts in the reaction of complete adipic acid oxidation in water under UV light illumination and elucidate the role of ozone in the above reaction, in the present work we successfully synthesized by extractive pyrolytic method Pd/TiO<sub>2</sub> and Au/TiO<sub>2</sub> catalysts with 0.5 % noble metal loading.

## 2. MATERIALS AND METHODS

### 2.1. Chemicals, experimental setup and procedure

Hexanedioic acid (adipic acid 99% purity) was acquired from Merck and it was used in all experiments as received. Paladium powder (≥99.9 %; Aldrich), HCl (35 %) and HNO<sub>3</sub> (65%) (Lachema), *n*-tri-octylamine (C<sub>8</sub>H<sub>17</sub>)<sub>3</sub>N (≥95 %; Fluka) and toluene (analytical grade; Stanchem) were used to produce the precursors. TiO<sub>2</sub> (Degussa, P25) was used as a starting photocatalytic material.

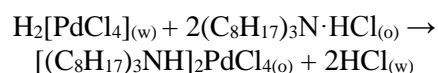
The studies on the photocatalytic oxidation of adipic acid have been performed in a specially designed cylindrical semi-batch reactor (100 mm internal diameter, 150 mm height) affording good absorbance of the incident UV light by the photocatalyst in the solution. In order to uniformly irradiate the entire volume of the solution, Philips (PL-S 2P or TUV PL-S) lamps for UV-A or UV-C irradiation were mounted radially relative to the axis of symmetry of the reactor inside a quartz tube. The photon flux in the UV light region at the external wall of the quartz tube was 10 mW cm<sup>-2</sup> (UV-A) and 14 mW cm<sup>-2</sup> (UV-C), determined by means of a Microprocessor-Controlled Radiometer (Cole Parmer 97503-00). The experiments were performed at a 12 dm<sup>3</sup>h<sup>-1</sup> gas flow rate of oxygen, or an oxygen–ozone mixture, at 293 K, pH 4 and atmospheric pressure. The aqueous suspension containing the respective catalyst sample at content of 1g/L was sonicated for 30 minutes before adding the adipic acid. Previously prepared solution of adipic acid was added to the aqueous slurry of the photocatalyst achieving an initial concentration of 8.3 x 10<sup>-3</sup> mol/L equivalent to 600 ppm TOC (Shimadzu VCSH).

Then the resulting mixture was transferred into the photoreactor and stirred magnetically for 30 min in order to reach the possible adsorption-desorption equilibria onto catalyst surface. The initial volume of the irradiated reaction mixture was 600 ml. During the direct ozonation and the photocatalytic process oxygen or oxygen-ozone mixture feed flow was bubbled continuously through a diffuser at the bottom of the reactor. The ozone concentrations at the reactor inlet and outlet were analyzed by means of an ozone analyzer, whereupon it was established that in the feed O<sub>2</sub>–O<sub>3</sub> gas mixture its concentration was 7.5 x 10<sup>-4</sup> mol/L providing a stoichiometric excess of ozone during the experimental runs. The concentration of the dissolved ozone has been evaluated to be 2.1 x 10<sup>-4</sup> mol/L on the basis of the reactor outlet concentrations by using values of Henry's constants at room temperature [19]. Samples were collected at every 30 min and filtered (Whatman, Grade 42) prior to be analyzed.

### 2.2. Photocatalyst synthesis

The extractive-pyrolytic method (EPM) was used for the catalyst samples preparation. Its simplicity and low cost, characterize the EPM as suitable for nanosized catalysts synthesis. As it can be seen below, this method allows depositing small amounts of noble metals (1–5 %) with particle size ranging from several nanometers to several tens of nanometers onto the surface of the support.

For synthesis of palladium containing catalyst the method can be described as follows: at first a solution of dihydrogen tetrachloropalladate (H<sub>2</sub>[PdCl<sub>4</sub>]) was prepared. An amount of the palladium powder was dissolved in aqua regia and evaporated thereafter upon adding concentrated HCl to the wet salt, which was then diluted with 2M HCl to reach the necessary concentration (0.5 mol.L<sup>-1</sup>). The organic precursor (extract) was prepared by extracting the palladium from the HCl solution using (1 M) *n*-trioctylamine (C<sub>8</sub>H<sub>17</sub>)<sub>3</sub>N solution in toluene. The following chemical interaction is occurring during the extraction:



Where, the subscripts “w” and “o” denote the aqueous phase and organic phase, respectively. As a result, a solution of tri-*n*-octylammonium tetrachloropalladate in toluene was obtained. The results of the analysis of the aqueous solution after extraction using a HITACHI 180-50 atomic absorption spectrometer gave evidence that the palladium amount had been completely extracted into the organic phase. An appropriate volume of the

extract was used to impregnate the TiO<sub>2</sub> in order to produce photocatalyst sample having the required content of 0.5% palladium. After impregnation, the toluene was evaporated by drying at 90–110 °C. Finally, the sample was heated up to 300 °C at a temperature increase rate of 10 °C min<sup>-1</sup>. A similar procedure was employed for synthesis of a 0.5% gold containing catalyst.

### 2.3. Analytical methods

X-ray powder diffraction patterns were recorded on a Bruker D8 Advance powder diffractometer with Cu K $\alpha$  radiation source and SolX detector. The samples were scanned at 2 $\theta$  angles from 10° to 80° at a rate of 0.04° s<sup>-1</sup>. The X-ray power was operated with a current of 40 mA and a voltage of 45 kV.

The metal crystallite size and the metal phase distribution in Au/TiO<sub>2</sub> and Pd/TiO<sub>2</sub> composite samples were examined with a high-resolution transmission electron microscope (HRTEM JEOL 2100).

Ozone was continuously generated by electrical discharges in pure oxygen flow in a self-assembled apparatus having possibility of varying the operating voltage up to 20 kV. Its gas phase concentration was monitored with ozone analyzer BMT 964 based on the absorption of ozone at 254 nm.

The photon flux in the UV light region at the external wall of the quartz tube was 10 mW cm<sup>-2</sup> (UV-A) and 14 mW cm<sup>-2</sup> (UV-C), determined by means of a Microprocessor-Controlled Radiometer (Cole Parmer, 97503-00) fitted with 254 nm and 365 nm sensors.

The specific surface area of the samples was determined on a standard BET apparatus applying the volumetric technique, as the measurements of nitrogen adsorption and desorption were performed at liquid nitrogen boiling temperature of 77 K.

The mineralization degree was analyzed by means of (TOC) analyzer (Shimadzu VCSH).

## 3. RESULTS AND DISCUSSION

### 3.1. Catalysts characterization

The mechanisms of semiconductor photocatalysis are known to involve hydroxyl radicals, trapped electrons, and trapped holes on the particle surface. The processes of entrapping the holes or electrons, and hence a more efficient

generation of OH radicals can be improved further by synthesis of composite materials including noble metal clusters. Of great importance for the effectiveness of these processes is not only the amount of metal loaded onto photocatalyst but also the metal particle size as well. In order to avoid the excessive coverage of the photocatalyst surface, the metal loading must be within the range of 0.5-1 wt.% [20 – 22 ]. In view of above details mentioned we prepared catalysts with 0.5% loadings of gold and palladium onto TiO<sub>2</sub>.

The specific surface areas were determined by nitrogen adsorption to be the following values: TiO<sub>2</sub> – 49.9 m<sup>2</sup>/g; Pd /TiO<sub>2</sub> – 54.5 m<sup>2</sup>/g and TiO<sub>2</sub>/Au – 53.1 m<sup>2</sup>/g. The crystalline phase of the synthesized catalysts was analyzed by X-ray powder diffraction (XRD). Figure 1 represents the XRD spectra of the samples that revealed diffraction peaks corresponding to crystalline palladium and gold phases in separate. The main peaks correspond to a tetragonal TiO<sub>2</sub> – anatase, whose content dominates over that of the rutile, are also represented in the spectra. The crystallite sizes of the palladium and gold particles were calculated to be 10-15 nm. The addition of Au or Pd nanoparticles caused the appearance of small characteristic peaks associated with the dopants. The metal particles have not given rise to any extra strong peaks on the XRD spectra of the doped catalysts. A possible explanation could be that both Au and Pd loading contents of noble metals were too low (0.5% wt.) as well as the formation of small clusters of noble metals with undefined crystalline structure which remain unobserved in the XRD pattern [23].

The ability of the catalyst sample to absorb efficiently photoenergy, depends on the nature of the noble metal and on its content, and it must be sufficiently well dispersed in order to influence the TiO<sub>2</sub>. The morphology of the metal particles on the TiO<sub>2</sub> photocatalyst was studied by transmission electron microscopy (Fig 2). The particle sizes have been estimated by means of the ImageJ software. TEM images show that Pd (Fig. 2a) and Ag (Fig. 2b) nanoparticles are visible as small dark particles with size varying from 5 to 16 nm and a mean diameter of 5.9 and 7.1 nm respectively.

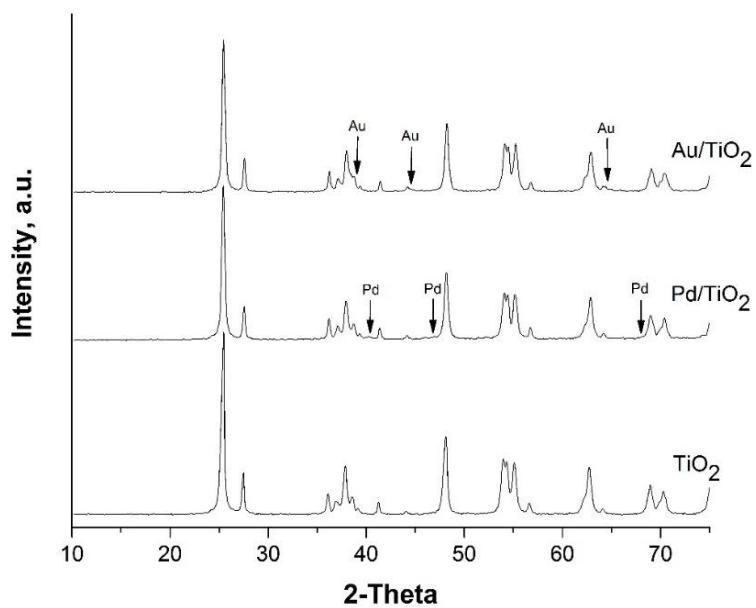


Figure 1. The XRD patterns of the photocatalysts.

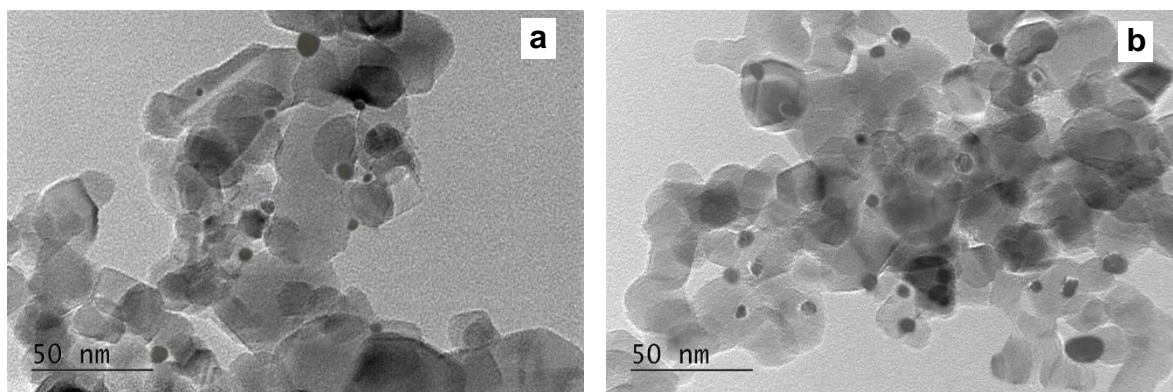


Figure 2. TEM micrographs of Pd/TiO<sub>2</sub> (a) and Au/TiO<sub>2</sub> (b) catalysts.

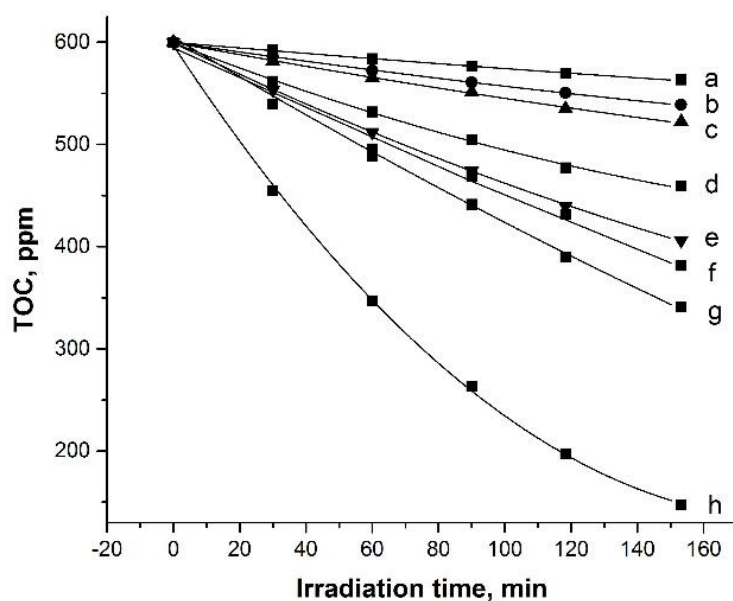


Figure 3. Total degree of mineralization of adipic acid catalyzed by: in the presence of O<sub>2</sub> ( $\lambda = 365$  nm) – (a) TiO<sub>2</sub>, (b) Pd/TiO<sub>2</sub>, (c) Au/TiO<sub>2</sub>; in the presence of O<sub>3</sub> ( $\lambda = 365$  nm) – (d) TiO<sub>2</sub>, (e) Pd/TiO<sub>2</sub>, (f) Au/TiO<sub>2</sub>; in the presence of O<sub>3</sub> ( $\lambda = 254$  nm) – (g) TiO<sub>2</sub>; (h) Au/TiO<sub>2</sub>.

### 3.2. Photocatalytic activity testing

Titanium dioxide doped with 0.5 wt% palladium and gold loading were prepared and tested in degradation of adipic acid in aqueous solution. Further, the ozone-oxygen gas mixture with ozone concentration of  $7.5 \times 10^{-4}$  mol/L was involved in the studied process. Figure 3 represents the kinetic curves of degradation of adipic acid in the presence of the tested samples under UV irradiation.

A number of investigators have reported that the rates of photodegradation of chemical compounds on semiconductor surfaces follow the classical Langmuir-Hinshelwood expression (Eq. (1)) and that the sorption of reactants to the semiconductor surfaces follows Langmuir sorption isotherms [24 – 26].

$$r = \frac{dC}{dt} = \frac{kKC}{1+KC} \quad (1)$$

Where,  $r$  is the oxidation rate of the reactant,  $C$  the concentration of the reactant,  $t$  the illumination time,  $k$  the reaction rate constant, and  $K$  is the adsorption-desorption equilibrium constant. If the initial concentration of the reactant  $C_0$  is of the order of millimoles, the above equation can be simplified to an apparent first-order reaction equation [27 – 29]:

$$\ln\left(\frac{C_0}{C}\right) = kKt = k_{app}t \quad \text{or} \quad C_t = C_0 e^{-k_{app}t} \quad (2)$$

In accordance with this, the rate constant of the adipic acid degradation (fig. 4.) was calculated based on equation (2).

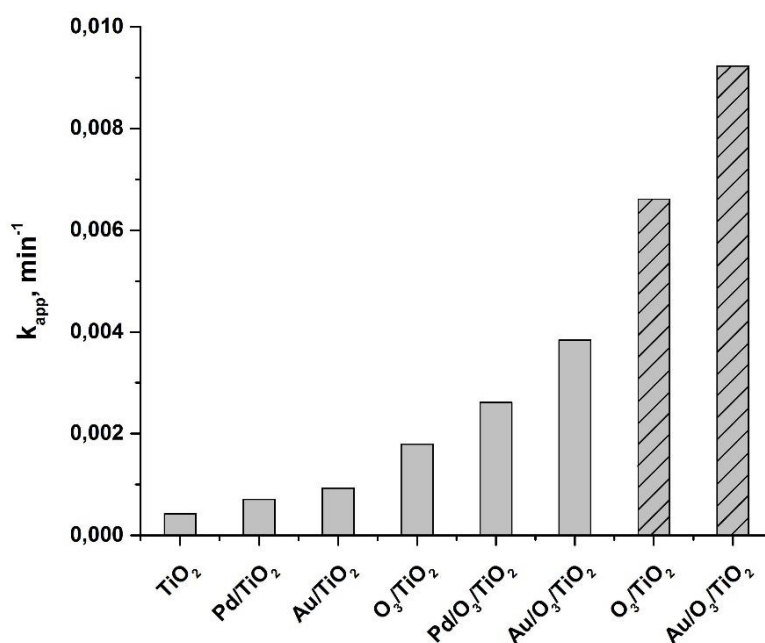


**Figure 4.** Apparent rate constants of adipic acid degradation under UV-light (■ 365 nm) and UV-light (▨ 254 nm).

The photonic efficiency of bare TiO<sub>2</sub> is low (<10%) as the photogenerated e<sup>-</sup>/h<sup>+</sup> pairs (~90%) recombine rapidly after excitation [30] which is evidenced by the results obtained by TOC analysis represented in Fig. 3 and 4. It was observed that the degradation of adipic acid over bare TiO<sub>2</sub> is taking place at a lowest rate constant compared to those achieved in presence of samples doped with noble metals. The principal approach to slow down the electron-hole recombination is based on the loading of electron accepting species on the TiO<sub>2</sub> surface. The sample from composite material containing 0.5% palladium exhibits 1.7 times higher effectiveness in mineralization of adipic acid than that manifested by the pure TiO<sub>2</sub> under irradiation with UV light 365 nm having rate constant of  $4.2 \times 10^{-4}$  min<sup>-1</sup>. The palladium particles having a higher work

function (5.2 – 5.6 eV) relative to those of TiO<sub>2</sub> (4.13 eV) [31] producing a high Schottky energy barrier at the inter-phase boundary facilitating the electron capture. In this case the photonic efficiency is increased by inhibition the electron-hole pair recombination as the photoelectron is transported to the outer system and transfer of holes to the reactants adsorbed on the TiO<sub>2</sub> surface is enhanced. The same tendency was observed in the presence of gold doped TiO<sub>2</sub> catalyst. It was found out that the rate constant of the reaction catalyzed by Au/TiO<sub>2</sub> was 2.3 times ( $9.25 \times 10^{-4}$  min<sup>-1</sup>) higher than that over pure TiO<sub>2</sub>. As it was mentioned above these small metal clusters (5-15 nm.) are regarded as photogenerated electrons scavengers preventing recombination and facilitate the subsequent redox reactions. As it is visible from Fig.3 and Fig.4 the presence of ozone leads to higher



degrees of mineralization of adipic acid. Under irradiation with 365 nm UV light the values of the apparent rate constants of the samples were in order as follows: TiO<sub>2</sub><Pd/TiO<sub>2</sub><Au/TiO<sub>2</sub> which are about 4 times higher than those previously listed. It has been widely accepted that the holes cogenerated together with photoexcited electrons during absorption of UV light can interact with an organic molecule (at high concentration) or, in an aqueous solution, with water forming OH radicals [32] which are powerful oxidizing agents. This consideration indicates that the concentration of hydroxyl radicals

directly influences the rate of the reaction. Herein, by generating hydroxyl radicals appears to be the role of ozone and its impact on the effectiveness of the photocatalytic oxidation because the rate of the reaction of ozone with adipic acid is negligibly small, practically it does not interact with it [33]. Under our experimental conditions (UV-A light, pH=4), the adsorbed ozone is able to interact with deposited metal particle accepting the supplied by the metal photogenerated electrons to give ozonide radicals (O<sub>3</sub><sup>-</sup>) which subsequently form OH radicals (Fig. 5).

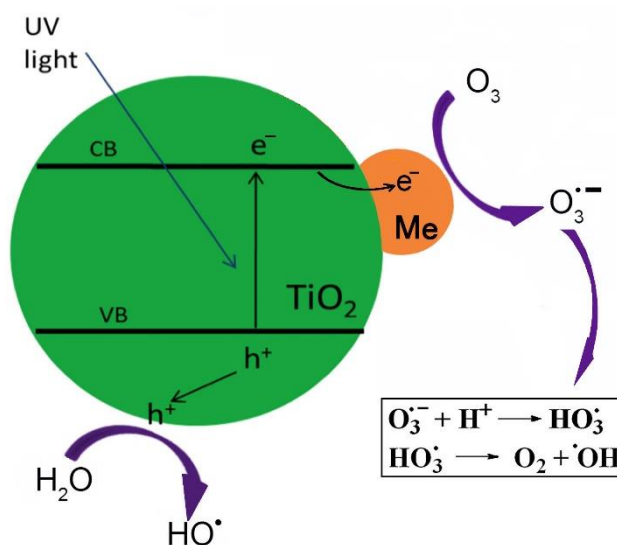
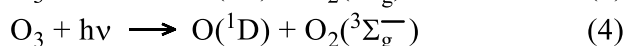
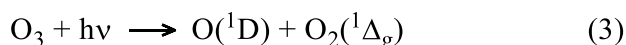
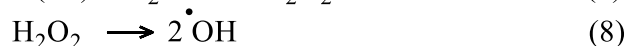
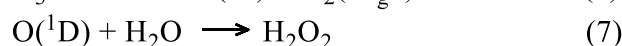
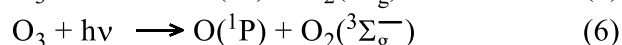
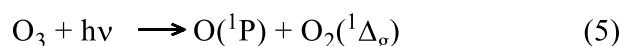


**Figure 5.** Schematic representation of the reduction of ozone on the metal surface.

The highest rate constant  $9.23 \times 10^{-3} \text{ min}^{-1}$  of the adipic acid removal was achieved employing the Au/TiO<sub>2</sub> catalyst in presence of ozone under 254 nm light, which is at about 2,5 times higher, compared to that over the irradiated with 365 nm light (Fig. 4). A possible hypothesis to explain this result could be the involvement the ozone photolysis under UV-C light. Upon photolysis, O<sub>3</sub> is decomposed into O<sub>2</sub> and oxygen atom O (<sup>1</sup>D) and O (<sup>3</sup>P) [34]. The major species formed under irradiation of ozone with UV-C light are excited oxygen atom O(<sup>1</sup>D) with quantum yield,  $\Phi = 0.9$  and singlet dioxygen, O<sub>2</sub>(<sup>1</sup>Δ<sub>g</sub>), as well as oxygen in its ground triplet state, O<sub>2</sub>(<sup>3</sup>Σ<sub>g</sub><sup>-</sup>) as follows:



The competitive reactions are of smaller importance that lead to formation of oxygen atom in its excited state O(<sup>1</sup>P), oxygen singlet O<sub>2</sub>(<sup>1</sup>Δ<sub>g</sub>) and O<sub>2</sub>(<sup>3</sup>Σ<sub>g</sub><sup>-</sup>) according reactions (5) and (6).



As the O(<sup>1</sup>D) is in highly energetic state it reacts very quickly with water molecule to give hydroxyl peroxide which further breaks down into hydroxyl radicals (reaction 7 and 8). It is supposed that H<sub>2</sub>O<sub>2</sub> is formed directly by the addition of O(<sup>1</sup>D) to H<sub>2</sub>O [35]. Upon photolysis of ozone, it is expected that the excited oxygen atom O(<sup>1</sup>P) should react with adipic acid. Hence cyclohexyl radicals and hydroxyl radicals are formed by H atom abstraction, which is promoting the destruction of the organic material by forming hydroxyl radicals through an additional route.

#### 4. CONCLUSIONS

The degradation rates of adipic acid in aqueous solution under irradiation with UV-A and UV-C light in the presence of doped with palladium and gold TiO<sub>2</sub> as well as the enhancement by ozone have

been determined. The characterization of metal-doped TiO<sub>2</sub> using XRD and TEM spectroscopy techniques revealed good degree of dispersion and nanometric size of noble metals clusters on the surface of TiO<sub>2</sub>. Due to the uniform distributions and small size (5-16 nm.) of the metal islands the blocking of fine pores of TiO<sub>2</sub> surface was prevented and the specific surface area of the doped and bare TiO<sub>2</sub> was similar. The photonic efficiency of Au/TiO<sub>2</sub> is almost comparable to that of Pd/TiO<sub>2</sub> but higher than that of Pd/TiO<sub>2</sub>. In general composite catalysts have better activity than pure TiO<sub>2</sub> as their rate constants are 1.7 (Pd/TiO<sub>2</sub>) and 2.3 (Au/TiO<sub>2</sub>) times higher. These results can be explained in terms of trapping of photogenerated electrons on the metal islands leading to better electron-hole charge carriers separation. The highest mineralization rates are achieved involving participation of ozone. Under irradiation with UV-A light in presence of ozone, it was determined that the rate constant of  $3.8 \times 10^{-3}$  employing the Au/TiO<sub>2</sub> and for the process carried under UV-C light the rate constant was about 2.5 times higher. These mineralization rates are due to the powerful capacity of ozone to generate radicals enabling the oxidation of organic pollutants.

**Acknowledgement.** *The authors gratefully acknowledge financial support by State Science Fund, Ministry of Education and Science of Bulgaria (Project DFNI T-02-16/12.12. 14.)*

#### REFERENCES

1. H. Yoneyama, M. Koizumi, H. Tamura, Bull. Chem. Soc. Jpn., **52**, 3449 (1979).
2. J. Kiwi, M. Graetzel, J. Am. Chem. Soc., **101**, 7214 (1979).
3. K. Domen, S. Naito, M. Soma, T. Onishi, K. Tamaru., Chem. Commun., **12**, 543- (1980).
4. L. Krasteva, K. Papazova, A. Bojinova, N. Kaneva, A. Apostolov, Bul. Chem. Comm., **45**, 625 (2013).
5. S. Siuleiman, D. Raichev, A. Bojinova, D. Dimitrov, K. Papazova, Bul. Chem. Comm., **45**, 649 (2013).
6. A. Masakazu, H. Nakaya, s. Kodata, Y. Kubokawa, K. Domen, T. Onishi, J. Phys. Chem., **90**, 1633 (1986).
7. S. Frank, A. Bard, J. Am. Chem. Soc., **99**, 303 (1977).
8. M. Halmann, Nature, **275**, 115 (1978).
9. D. Dimitrov, M. Milanova, R. Kralshvska, Bul. Chem. Comm., **43**, 489 (2011).
10. N. Serpone, E. Borgarello, R. Harris, P. Cahill, M. Borgarello, Solar Energy Materials, **14**, 121 (1986).
11. A. Milis, J. Peral, X. Domènech., Journal of Molecular Catalysis, **87**, 67 (1994).
12. M.I. Litter, J.A. Navío, J. Photochem. Photobiol. A: Chemistry, **98**, 171 (1996).
13. K. Wilke, H.D. Breuer, J. Photochem. Photobiol. A: Chemistry, **121**, 49 (1999).
14. S. Esplugas, J. Giménez, S. Contreras, E. Pascual, M. Rodríguez, Water Research, **36**, 1034 (2002).
15. W. H. Glaze, J. W. Kang, D.H. Chapin, Ozone Sci. Eng., **9**, 335 (1987).
16. G. R. Peyton, W.H. Glaze, Environ Sci. Technol., **22**, 761 (1988).
17. E. Gilbert, Ozone: Science & Engineering, **24**, 75 (2002).
18. S. Esplugas, J. Gimenez, S. Contreras, E. Pascual, M. Rodriguez, Water Research, **36**, 1034 (2002).
19. A. Sullivan, E. Roth, E. Danlel., Ind. Eng. Chem. Fundam, **20**, 137 (1981).
20. V. Kalarivalappil, C. M. Divya, W. Wunderlich, Suresh C. Pillai, Steven J. Hinder, Manoj Nageri, V. Kumar, Baiju K. Vijayan., Catalysis Letters, **146**, 474 (2016).
21. R. Najjar, M. Shokri, S. Farsadi, Desalination and Water Treatment, **54**, 2581, (2015).
22. A. Orlov, D. A. Jefferson, N. Macleod, R. M. Lambert, Cat. Lett., **92**, 4 (2004).
23. P. A. P. Nascente, S. S. Maluf, C. R. M. Afonso, R. Landers, A. N. Pinheiro, E. R. Leite, Appl. Surf. Sci., **315**, 490 (2014).
24. R. McEvoy, R. Matthews, R. Stephen, J. Photochem. Photobiol. A: Chem., **64**, 231 (1992).
25. V. Brezova, A. Stasko, Journal of Catalysis, **147**, 156 (1994).
26. E. Butler, A. Davis, J. Photochem. Photobiol. A: Chem, **70**, 273 (1993).
27. A. Houas, H. Lachheb, M. Ksibi, E. Elaloui, C. Guillard, Applied Catalysis B: Environmental, **31**, 145 (2001).
28. W. Z. Tang, H. An, Chemosphere, **31**, 4157 (1995).
29. I. Konstantinou, T. Albanis, Applied Catalysis B: Environmental, **42**, 319 (2003).
30. H. Zhang, G. Chen, D. Bahnemann., J. Mater. Chem., **19**, 5089 (2009).
31. A. Imanishi, E. Tsuji, Y. Nakato., J. Phys. Chem. C, **111**, 2128 (2007).
32. H. Ceriscber, A. Heller, The Journal of Physical Chemistry, **95**, 5261 (1991).
33. V. Georgiev, S. Rakovsky, K. Stanulov, A. Popov, Oxidation Communications, **31**, 151 (2008).
34. G. Hancock, P. Tyley, Phys. Chem. Chem. Phys., **4**, 4984 (2001).
35. H. Taube, Trans. Faraday Soc., **53**, 656 (1956).

ЕФЕКТИВНОСТ НА ФОТОКАТАЛИЗАТОРИ НА ОСНОВАТА НА TiO<sub>2</sub> В  
ПОДПОМОГНАТО ОТ ОЗОН ОКИСЛИТЕЛНО РАЗГРАЖДАНЕ НА АДПИНОВА  
КИСЕЛИНА КАТО МОДЕЛЕН ЗАМЪРСИТЕЛ В ОТПАДНИ ВОДИ ПРИ ОБЛЪЧВАНЕ С  
УВ СВЕТЛИНА.

В.Ф. Георгиев<sup>1\*</sup>, В. Илиев<sup>1</sup>, А.Е. Елияс<sup>1</sup>, Т.Т. Батаклиев<sup>1</sup>, М.П. Аначков<sup>1</sup>, В.Е. Серга<sup>2</sup>,  
П.А. Каракашкова<sup>1</sup>, С.К. Раковски<sup>1</sup>

<sup>1</sup> *Институт по катализ, Българска академия на науките, София 1113, България*

<sup>2</sup> *Институт по неорганична химия, Технически университет в Рига, Рига, Латвия*

Постъпила на 10 ноември, 2016 г.; приета на 21 февруари, 2017 г.

(Резюме)

Катализатори на основата на паладий и злато модифициран TiO<sub>2</sub> (Degussa P25) бяха изследвани за каталитичната им активност при фоторазграждане на адипинова киселина в присъствието на кислород и озон, под действие на УВ светлина. Пробите бяха синтезирани чрез екстракционно-пиролитичен метод с 0.5% съдържание на активен метал и размер на частиците вариращи от 7 до 12 нм. За установяване на структурните и химични свойства са приложени методите XRD, TEM и BET. В присъствието на кислород и облъчване с UV-A светлината, скоростните константи на реакцията в присъствие на паладий и злато модифицирани TiO<sub>2</sub> материали бяха съответно 1.7 и 2.3 пъти по-високи от тези на чист TiO<sub>2</sub> при същите условия. Това се дължи на по-ефективното разделяне на зарядите (електрон-дупка), генерирани при облъчване. Освен това, ефективността на катализаторите в присъствието на озон е по-голяма, както при облъчване с UV-C така и с UV-A светлина за всички проби. Скоростните константи на реакциите проведени в присъствие на озон при облъчване с 254 нм светлина, са около 3 пъти по-високи, в сравнение с тези облъчени с 365 нанометра. Това се дължи на допълнителното генериране на HO• радикали под действие на озоновия радикал O<sub>3</sub><sup>-</sup>, образуван върху зоната на проводимост на фотокатализатора TiO<sub>2</sub>, от една страна, и в резултат на фотолиза на озона при облъчване с UV-C светлина, от друга страна.

## Kinetics and mechanism of the ozone reaction with cyclohexane in liquid phase

M.P. Anachkov\*, P.A. Karakashkova, V. F. Georgiev, S.K. Rakovsky, L.S. Minchev,  
T.T. Batakliiev

*Institute of Catalysis, Bulgarian Academy of Sciences, 1113 Sofia, Bulgaria*

Submitted November 20, 2016; Revised March 30, 2017

The peculiarities of the ozone reaction with cyclohexane in liquid phase have been studied under conditions of degree of conversion of the cycloalkane lower than 1 %. The ozone solubility in cyclohexane at various temperatures has been characterized by determination of the respective values of the Henry's coefficient. It was found out that the values of the rate constant (at 20 °C) and the activation energy of the reaction were  $0.009 \text{ l}\cdot\text{mol}^{-1}\cdot\text{s}^{-1}$  and  $57.6 \text{ kJ/mol}$  respectively. Dicyclohexyl was identified among the reaction products. The kinetics of formation of the cyclohexanol, cyclohexanone and dicyclohexyl were investigated in details by GC/MSD. A revised scheme of cyclohexane ozonolysis has been proposed.

**Keywords:** ozone, ozonolysis, cyclohexane, liquid phase, oxidation

### INTRODUCTION

An important feature of the ozone reaction with cyclohexane in liquid phase, unlike its oxidation with molecular oxygen, is proceeding of the ozonolysis at ambient temperatures. This reaction is considered in the literature to be a model for the investigation of oxidation processes of alkanes and for polyolefines ageing, and on the other side as a reaction of selective oxidation of cyclohexane to cyclohexanone [1-3]. There are some works, in which kinetics of the reaction and the reaction products are studied depending on the oxidation conditions such as ozone/oxygen ratio, reaction temperature and degree of conversion. Different reaction schemes have been proposed [2, 4], and even a mathematical model of the cyclohexane ozonolysis has been published [3, 5]. The analysis of the literature data shows considerable discrepancies in relation to the kinetic schemes and also in view of the composition of reaction products and the respective proportions within them [1-3]. Probably part of these differences are due to the reactions of ozone with some of the primary products, whose rate constants are considerably higher in comparison with the corresponding value of the ozone-cyclohexane interaction [3, 6].

In the present work, we report a study on the reaction kinetics and the formation of some reaction products during liquid phase ozonolysis of cyclohexane, under conditions of low degrees of conversion.

### EXPERIMENTAL

Ozone was obtained by passing dried oxygen (99.99%) through a 4–9 kV discharge in a self-made design, tubular type of ozone generator.

#### *Ozonation*

The experimental runs were performed in a bubbling reactor, containing 10–15 ml of p.a. grade cyclohexane. An ozone–oxygen mixture with ozone concentration within the range of 1000–25000 ppm ( $4.5 \times 10^{-5}$ – $1.2 \times 10^{-3} \text{ mol l}^{-1}$ ) was passed through the reactor at a flow rate of about of  $(1.3 \pm 0.3) \times 10^{-3} \text{ l s}^{-1}$ . The ozone concentrations in the gas phase at the reactor inlet ( $[\text{O}_3]_0$ ) and outlet ( $[\text{O}_3]_g$ ) were measured spectrophotometrically by BMT model 964 ozone analyzer.

#### *Determination of the amount of consumed ozone and the degree of conversion of cyclohexane*

The ozone absorption process has been studied by continuous monitoring of the ozone concentrations at the reactor outlet, under conditions of constant values of initial ozone concentration at the reactor inlet. The  $[\text{O}_3]_g = f(\tau)$  dependence was recorded on a computer, connected to the ozone analyzer (Fig. 1). The area of the surface enclosed between the curves  $[\text{O}_3]_g = f(\tau)$  and the line  $y = [\text{O}_3]_0$  is proportional to the amount of ozone consumed in the reaction. This amount has been calculated by using the coefficient of ozone extinction at UV wavelength  $254 \text{ nm}$ – $3000 \text{ l cm}^{-1} \text{ mol}^{-1}$  [7] and the respective inlet flow rate of the ozone–oxygen mixture.

\*) To whom all correspondence should be sent:

E-mail: [anachkov@ic.bas.bg](mailto:anachkov@ic.bas.bg)

The real determination of the decrease in cyclohexane concentrations under conditions of extremely low depths of the reaction (< 1%) is inaccurate and practically impossible. In order to realize some kind of objective characteristic of the ozonolysis we will use a special value of "ozone conversion of cyclohexane" (in %), defined as the ratio of consumed ozone (mols) to initial amount of cyclohexane in the bubbling reactor (mols).

GC-MS analyses were performed on Agilent Technologies model 7890A instrument, equipped with mass-selective detector model 5975C. The capillary column DB-WAXETR of 30 m length and 0.25mm i.d., coated with polyethylene glycol (0.25 μm), was used in the experiments.

## RESULTS AND DISCUSSIONS

### Monitoring of the ozone absorption

The kinetic curve of the ozone absorption in cyclohexane is represented in Fig.1. It is seen that the respective curve could be divided into two sections: first one where saturation of cycloalkane with ozone is proceeding and a second one where the curve is parallel to the abscissa as a result of equilibrium between the feeding rate of ozone-oxygen mixture and the rate of the chemical reaction.

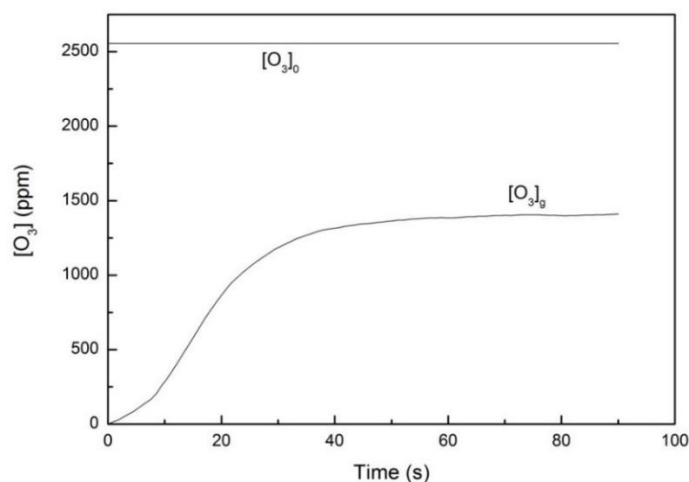


**Fig.1** Dependence of the ozone concentration in gas phase ( $[O_3]$ ) on the bubbling time of the ozone-oxygen gas mixture. Cyclohexane volume-15 ml, gas feeding rate -  $1.18 \cdot 10^{-3}$  l/s, temperature-24 °C.  $[O_3]_0$ -ozone concentration at the reactor inlet,  $[O_3]_g$ -ozone concentration at the reactor outlet.

S.D. Razumovskii et al. [8], which expresses the relationship between the balance of consumed ozone and the rate of the chemical reaction- Eq. (1):

$$\omega([O_3]_0 - [O_3]_g) = k[O_3]_l[RH] \quad (1)$$

where  $\omega$  is the relative flow rate of ozone-oxygen gas mixture (in litres per l of solution per sec);  $[O_3]_0$  and  $[O_3]_g$  are the ozone concentrations at the reactor inlet and outlet, respectively,  $[O_3]_l$  is the dissolved ozone concentration in the liquid phase;  $[RH]$  is the concentration of the reagent. This model is valid in

The reliability of the kinetic results derived from the data about the ozone concentrations in gas phase at the reactor outlet requires validity of Henry's law, which determines quantitatively the ratio between the equilibrium concentrations of ozone in liquid and in gas phase respectively. One of the widely applied criteria with respect to the conditions of validity of Henry's Law is the expression [8]:

$$D_{O_3} \cdot k_1' / k_L^2 \ll 1$$

where  $D_{O_3}$  is the diffusion coefficient of ozone in the solution;  $k_L = D_{O_3} / \delta$  is the coefficient of mass transfer in the liquid phase, and  $\delta$  is the thickness of the boundary layer in the hydrodynamic model of renovation surface; or  $k_L = (D_{O_3} \cdot s)^{1/2}$ , where  $s$  is the time interval of renovation;  $k_1' = k[RH]_0$  where  $k$  and  $[RH]_0$  are the rate constant of ozonolysis of the investigated compound and its initial concentration, respectively. The presented in [6, 8] detailed analysis of the mass transfer of the reagents, under conditions which are practically identical with those in our experiments, shows unconditional applicability of Henry's law to all of those cases ( $\approx 0.01 \ll 1$ ). The determination of rate constants is based on the approach, proposed by

all cases, when the rate of ozone absorption is considerably greater than the rate of the chemical reactions. If in the case of a bimolecular reaction, in accordance with Henry's Law,  $[O_3]_l$  is substituted by  $\alpha[O_3]_g$ , where  $\alpha$  is Henry's coefficient (in mol.l<sup>-1</sup> in liquid/mol.l<sup>-1</sup> in gas phase), then Eq. (1) can be transformed into Eq. (2).

$$k = \omega \cdot \Delta[O_3] / ([RH] \cdot \alpha \cdot [O_3]_g) \quad (2)$$

In order to minimize the influence of the so-called "effect of delay in the response function"- $[O_3]_g = f(\tau)$ ,

upon calculating the values of  $k$  such sections on the kinetic curves are selected, which appear to be practically parallel or only slightly inclined with respect to the abscissa:  $k_1 \cdot \alpha \cdot [O_3]_g \gg d[O_3]_g/d(\tau)$ . The advantages and limitations of this method have been discussed in detail in [8-10]. Despite some contradictory observations, significant number of the rate constants of ozone reactions with organic compounds and polymers are obtained on the basis of Eq. (2) [8].

It follows from equation (2) that for computation of the rate constant, the respective value of Henry's coefficient for cyclohexane should be known. However so far there are no literature data available concerning the solubility of ozone in cyclohexane at all. The most studied cases are the solubility of ozone in water and in chlorinated and fluorinated hydrocarbons [8, 11]. Usually the evaluation of solubility of ozone in liquids is based on the different forms of the Henry's coefficient or some other values, connected with them [11]. There are a little data in the literature about values of Henry's coefficients for hexane, octane and decane with insufficient correlation between them [8, 11].

Our attempt for the determination of  $\alpha$  was based on the proposed by SD Razumovskii equation [8], which describes the balance of consumed ozone for the nonstationary part of the curve in Fig.1 (Eq. (3)).

$$\omega([O_3]_g - [O_3]_g)\tau' = \alpha[O_3]_g + \alpha k[RH] \int_0^{\tau'} [O_3]_g d\tau \quad (3)$$

It follows from Eq. (3) that the  $\alpha$  value is equal to the expression (4):

$$\alpha = \frac{\omega([O_3]_g - [O_3]_g)\tau' - \alpha k[RH] \int_0^{\tau'} [O_3]_g d\tau}{[O_3]_g} \quad (4)$$

where  $\tau'$  is the time interval, necessary of  $[O_3]_g$  to reach its equilibrium value. At this moment

$$d[O_3]_g/d\tau = \omega([O_3]_o - [O_3]_g) - k[O_3]_g[RH] = 0.$$

Therefore  $\alpha \cdot k[RH]$  is equal to  $\omega([O_3]_o - [O_3]_g)$ , and the expression  $\int_0^{\tau'} [O_3]_g \cdot d\tau$  is computed by graphical integration of the respective section of  $[O_3]_g$  curve in Fig.1. The determined, in this way, value of the Henry's coefficient of the ozone solubility in cyclohexane is equal to 1.21 (24 °C). The dependence of  $\alpha$  on the temperature was also investigated in the interval 10-41 °C. Fig. 2 (curve 1) shows that the dependence  $\ln \alpha = f(1/T)$  is linear and the respective values of  $\alpha$  increase with lowering of the temperature.

As it will be shown hereinafter the cyclohexane ozonolysis is a complicated multi stages process. Some of the data concerning values of the rate constant are obtained under different conditions and the attempts to systematize them do not lead to good results [1, 3, 12]. Furthermore the cyclohexane solutions in  $CCl_4$  are usually applied for determination of  $k$ , although it is known that the identified chlorinated derivatives during cyclohexane ozonolysis in  $CCl_4$  show partially participation of the solvent in the reaction [4].

The already determined value of the Henry's coefficient of ozone allows application of eq. (2) for calculation of the respective  $k$  value under conditions of extremely low values of ozone conversion degree of cyclohexane ( $\ll 0.03\%$ ), when involvement of secondary reactions are practically excluded. The value of  $1.25 \cdot 10^{-2} \text{ l} \cdot \text{mol}^{-1} \cdot \text{s}^{-1}$  (24 °C) was obtained. In Fig. 2, curve 2 represents the  $k$  dependence on the temperature in Arrhenius coordinates. The derived from Fig. 2  $k$  value (at 20 °C) and activation energy ( $E_a$ ) are  $0.009 \text{ l} \cdot \text{mol}^{-1} \cdot \text{s}^{-1}$  and 13.78 kcal/mol respectively. These values are in good correlation with some of the literature data for cyclohexane solutions in  $CCl_4$  [1, 12].

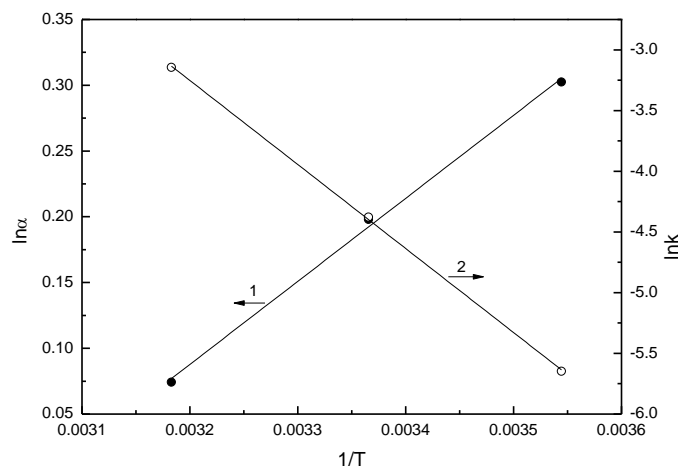


Fig. 2. Dependences of  $\ln \alpha$  (1) and  $\ln k$  (2) on  $1/T$ , where  $\alpha$  is Henry's coefficient (in mol/l in solution / mol/l in gas phase);  $k$  is the rate constant of cyclohexane ozonolysis (in  $\text{l} \cdot \text{mol}^{-1} \cdot \text{s}^{-1}$ ).

*Analysis of the products and the reaction scheme*

It was found out that during cyclohexane ozonolysis a number of organic compounds such as cyclohexanol, cyclohexanone, different kinds of peroxides and hydroperoxides, acids and some others were identified as reaction products; formation of water was also observed [2-4]. However the data concerning the individual yields usually differ from each other and in many cases are contradictory [1-3]. The dependence of the product composition on the reaction conditions such as ozone/oxygen ratio, temperature of the reaction, depth of conversion of cycloalkane has been reported in the literature [3, 5]. At higher degrees of cyclohexane conversion additional compounds are identified, that could be considered as products of ozonolysis of the already mentioned primary reaction products [1, 3].

It has been accepted that cyclohexanol and cyclohexanone are the basic primary products of the ozonolysis and their additive yield, at low degree of conversion, varies within the range of 50-70% [3]. Fig. 3 shows the kinetics of formation of

cyclohexanol; cyclohexanone and dicyclohexil. It is seen that the alcohol concentrations are higher than the respective one of the cyclohexanone.

It is logical that the formation of every reaction product is explained by one or more elementary steps. Also attempts for modeling of the cyclohexane ozonolysis were made [3, 5]. On the basis of the model 28 reactions have been set, but they do not cover all of the identified products, especially at higher degree of conversion. It should be noted that there are serious contradictions with respect to some of the elementary steps, concerning their real existence as well as the values of their rate constants [1-3, 5]. The latest ones determine the contributions of the respective reactions in the formation of considered compounds. Since our aim was to investigate kinetics and mechanism of the formation of primary products at extremely low degrees of conversion, without proposing complete description of the scheme of ozonolysis, we have selected only those elementary steps, for which we suppose that they exert significant influence on the formation of the reaction products under our experimental conditions. They are represented in Scheme 1.

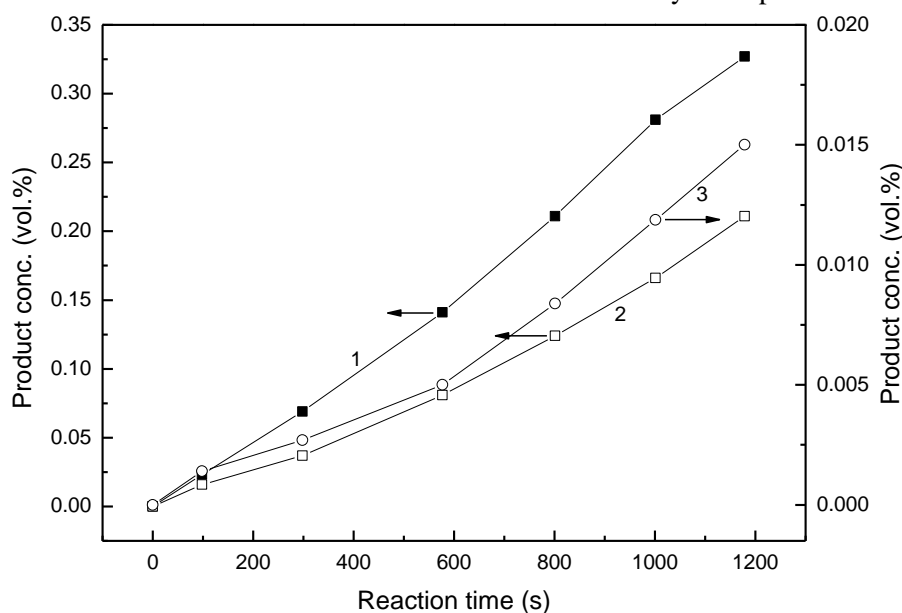
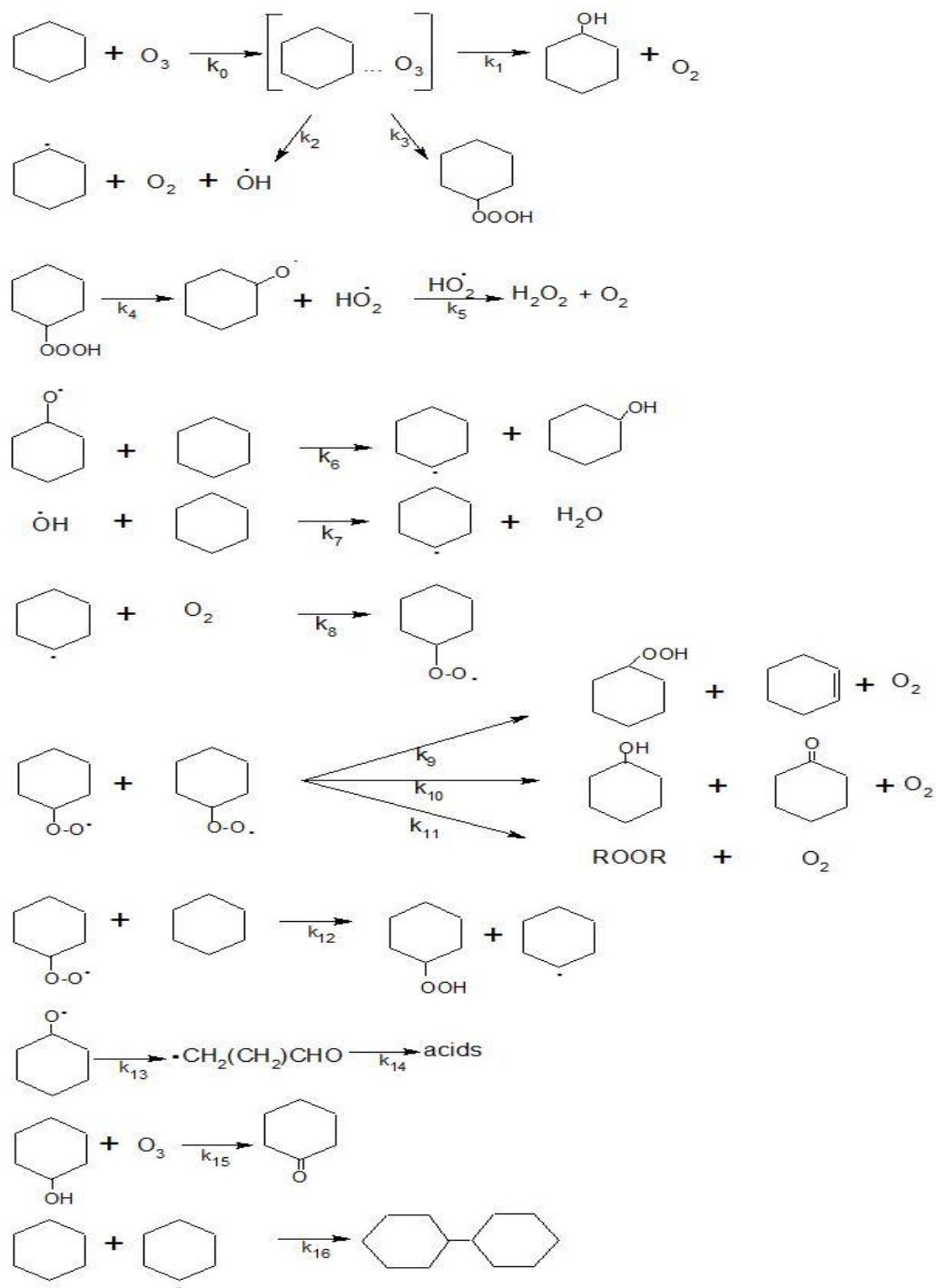


**Fig. 3.** Dependence of the product concentrations on the reaction time for 1- cyclohexanol; 2-cyclohexanon; 3- dicyclohexil. Cyclohexane volume-10 ml,  $[O_3]_0$ -17600 ppm, gas feeding rate -  $1.30 \cdot 10^{-3}$  l/s, temperature-24 °C.

It is seen from Scheme 1 that the products of the disproportionation of two peroxy radicals are cyclohexanol and cyclohexanone (Scheme 1, reaction 10). Additional quantities of cyclohexanol can be formed during the reactions 1 and 6 and in this way the higher yield of the alcohol, compared with the respective ketone (Fig 3), could be

explained. When the ratio cyclohexanol/ cyclohexanone is considered, especially at higher degrees of conversion, the values of the rate constants of the reactions of ozone with alcohol and ketone, which are at 20 °C  $2.65$  (reaction 15) and  $1.6 \cdot 10^{-2} \text{ l} \cdot \text{mol}^{-1} \cdot \text{s}^{-1}$  respectively [1], should also be taken into account.



**Scheme 1.** Cyclohexane ozonolysis.

Particular attention is paid to the third component in the Figure 3- dicyclohexil. Although most of the proposed schemes suggest the formation of alkyl radicals (Scheme 1, reactions 2, 6, 7, 12), there are no reports about possible interaction between them. Till now the presence of dicyclohexil among the identified reaction products is not mentioned in the

literature (reaction 16). In the cases of ozonolysis in  $\text{CCl}_4$  it is known only that there occurs the formation of small amounts of chloroderivates of the cyclohexane [1, 4]. As it is seen in Fig.3 the shape of the respective curve is similar to that of cyclohexanone, but the dicyclohexil concentrations are approximately 20 times of magnitude lower.



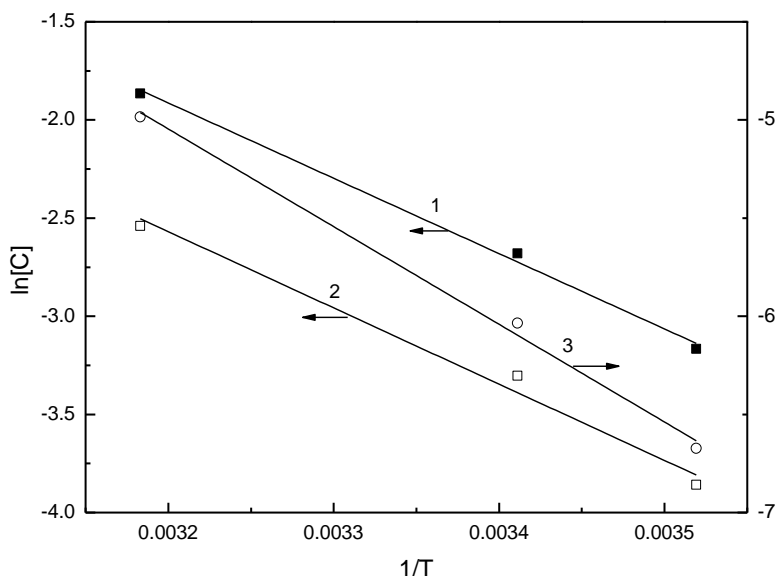


**Fig. 4.** Dependence of  $\ln[C]$  on  $1/T$  for 1- cyclohexanol; 2-cyclohexanon; 3-dicyclohexil. Cyclohexane volume-10 ml, gas feeding rate -  $1.30 \cdot 10^{-3}$  l/s, reaction time-300 s,  $[O_3]_0$ -17600 ppm.

The dependences of cyclohexanol, cyclohexanone and dicyclohexil concentrations on the temperature and ozone concentrations were also investigated. Fig. 4 represents the concentrations of respective reaction products in Arrhenius coordinates. It is found out that all three dependences are linear, as the concentrations of the cyclohexanol, cyclohexanone within the interval 10-41 °C, increase 367 and 374 % respectively, and that of dicyclohexil 540 %. The dependences of the concentrations of reaction products on the ozone concentration, under ozone

conversion of 0.1 %, are represented on Fig. 5. It is characteristic for the three curves that in the 0 -7500 ppm intervals a significant increase in the respective concentrations is observed, whereas from 7500 to 25 000 ppm there are no noticeable changes. This feature most probable is due to the requirement of achievement of "critical values" of the steady state concentrations of the peroxy and alkyl radicals or other precursors of the investigated reaction products.

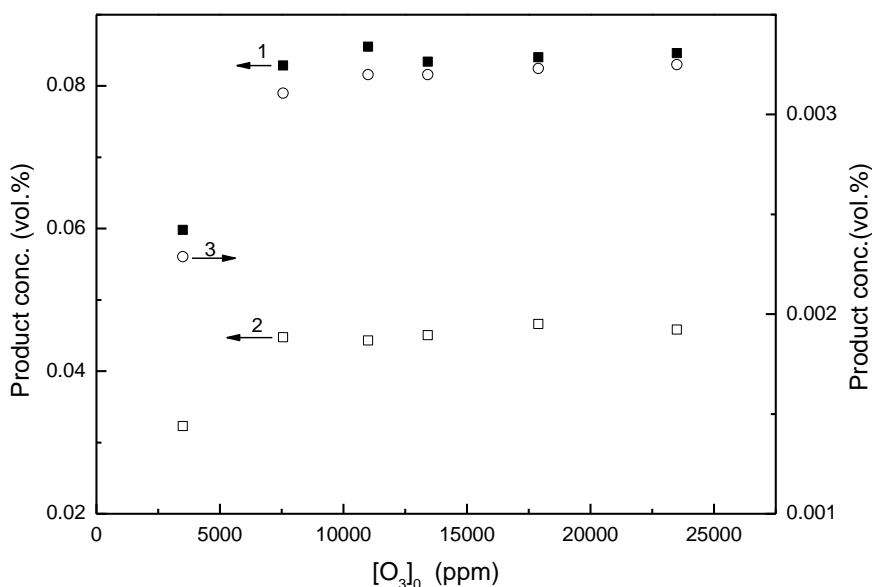


**Fig. 5.** Dependence of the product concentrations on the ozone concentration at the reactor inlet ( $[O_3]_0$ ) for 1- cyclohexanol; 2-cyclohexanon; 3-dicyclohexil. Cyclohexane volume-10 ml, gas feeding rate -  $1.30 \cdot 10^{-3}$  l/s, ozone conversion of cyclohexane-0.1%

## CONCLUSIONS

The peculiarities of the ozone reaction with cyclohexane in liquid phase have been studied under conditions of degrees of low ozone conversion degrees of the cycloalkane between 0.03 and 0.43%.

The ozone solubility at various temperatures has been characterized by determination of the respective values of Henry's coefficient (1.25 at 20 °C). It was found out that the values of the rate constant (at 20°C) and the activation energy of the reaction were 0.009 l.mol<sup>-1</sup>.s<sup>-1</sup> and 57.6 kJ/mol respectively.

Dicyclohexyl was identified among the reaction products. The kinetics of formation of the cyclohexanol, cyclohexanone and dicyclohexyl were investigated in details by GC/MSD. A revised scheme of the cyclohexane ozonolysis has been proposed.

**Acknowledgements.** *The authors gratefully acknowledge financial support by National Science Fund, Ministry of Education and Science of Bulgaria (Contract DFNI-T-02-16/12.12. 14).*

## REFERENCES

1. G.E. Zaikov, S.K. Rakovsky, *Ozonation of Organic & Polymer Compounds*, Smithers, Shrewsbury, 2009.
2. Denisov, E.T., *Mechanism of Liquid-Phase Homolysis of Molecules*, Itogi Nauki Tekh., Ser.: Kinetik. Katal., v. 9, 1981.
3. A.M. Syroezhko, V.A. Proskuryakov, and O.Yu. Begak, *Russ. J. Appl. Chem.*, **75**, 1296 (2002).
4. L.V. Ruban, S. K. Rakovski, and A. A. Popov, *Izv. Akad. Nauk SSSR, Ser. Khim.*, **No 9**, 1950 (1976).
5. A.M. Syroezhko, V.A. Proskuryakov, and O.Yu. Begak, *Russ. J. Appl. Chem.*, **75**, 1448 (2002).
6. S. Rakovsky, M. Anachkov, V. Iliev, A. Eliyas, *J. Adv. Oxid. Technol. (JAOTs)*, **16**, 31 (2013).
7. International Ozone Association Standardization Committee-Europe 002/87 (F), 1987.
8. S.D. Razumovskii, S.K. Rakovski, D.M. Shopov, G.E. Zaikov, *Ozone and Its Reactions with Organic Compounds*, Publ. House Bulg. Acad. Sci., Sofia, 1983 (In Russian).
9. A. Ja. Rozovskii, *Heterogeneous Chemical Reactions (Kinetics and Macrokinetics)*, Nauka, Moscow, 1980 (In Russian).
10. M. M. Rozenberg, E. B. Brun, *Teor. Osn. Khim. Teknol.*, **24**, 198 (1990).
11. A.K. Bin, *Ozone Sci. Eng.*, **28**, 67 (2006).
12. A.M. Syroezhko, V.A. Proskuryakov, *Zh. Prikl. Khim.*, **71**, 1168 (1998).

## КИНЕТИКА И МЕХАНИЗЪМ НА РЕАКЦИЯТА НА ОЗОНА С ЦИКЛОХЕКСАН В ТЕЧНА ФАЗА

М.П. Аначков\*, П.А. Каракашкова, В.Ф. Георгиев, С.К. Раковски, Л.С. Минчев, Т.Т. Батаклиев

*Институт по катализ, БАН, София 1113, България*

Постъпила на 20 ноември, 2016 г.; коригиране на 30 март, 2017 г.

(Резюме)

Изследвани са особеностите на реакцията на озона с циклохексан в течна фаза при степени на конверсия на въглеродородо по-ниски от 1 %. Разтворимостта на озона в циклохексан при различни температури е охарактеризирана посредством определянето на съответните стойности на коефициента на Хенри. Установено е, че стойностите на скоростната константа при 20 °C и на енергията на активация на реакцията са съответно 0.009 l.mol<sup>-1</sup>.s<sup>-1</sup> and 57.6 kJ/mol. Дициклохексил е идентифициран сред продуктите на озонизирания. Кинетиката на образуване на циклохексанол, циклохексанон и дициклохексил е изследвана посредством GC/MSD хроматография. Предложена е ревизирана схема на озонизацията на циклохексан.

## Study of CoNi catalysts for ethanol steam reforming

A.H. Braga<sup>1</sup>, J.B.O. Santos<sup>1</sup>, J.M.C. Bueno<sup>1</sup>, S. Damyanova<sup>2\*</sup>

<sup>1</sup>*Departamento de Engenharia Química, Universidade Federal de São Carlos, Box 676, 13565-905 São Carlos, SP, Brazil*

<sup>2</sup>*Institute of Catalysis, Bulgarian Academy of Sciences, Acad. G. Bonchev Str. Block 11, 1113 Sofia, Bulgaria*

Submitted December 10, 2016; Accepted February 13, 2017

The effect of Co addition to Ni-based catalysts on the change of their structure and electronic properties was studied, as well as how this change influences on catalytic properties in ethanol steam reforming. Two series of MgAl<sub>2</sub>O<sub>4</sub>-supported bimetallic CoNi catalysts with different metal loading of 8 and 15 wt% were prepared. The dependence of ethanol conversion and product distribution as a function of metal loading and temperature reaction was evaluated. Different techniques were used for physicochemical characterization such as: XPS, in situ XAS and HRTEM. Catalytic test was ethanol steam reforming carried out in a wide temperature region from 250° to 650°C. It was shown that a spinel-like Ni<sub>2</sub>CoO<sub>4</sub> was formed in oxide bimetallic CoNi systems, which leads to an alloy formation after reduction. The presence of alloy in bimetallic CoNi catalysts leads to different reaction pathways and to improving the catalyst stability.

**Key words:** CoNi catalysts, hydrogen, ethanol steam reforming, XPS, in situ XANES, TEM.

### INTRODUCTION

Great efforts are currently undertaken to produce hydrogen, for example, for fuel cell applications and for ammonia synthesis by heterogeneously catalyzed processes from renewable sources. This demand inspired studies of the dehydrogenation of oxygenated hydrocarbons. In particular, the light alcohol ethanol (“bioethanol”) is an important candidate as a chemical hydrogen carrier. It is well known that the surface properties of the metal and the oxide support, as well as the metal/oxide interface determine the formation and stability of the intermediates present in the ethanol transformation process. It is generally accepted that the primary step in alcohol activation is the formation of alkoxide [1]. Depending on the particular metal, dehydrogenation and C–C bond scission lead to the formation of alkoxide, aldehyde, acyl, and coke on the surface and mostly H<sub>2</sub>, CH<sub>4</sub>, CO, and aldehyde in the gas phase [2, 3]. Therefore, an efficient catalyst for hydrogen production from ethanol reforming has to dissociate the C–C bond at reasonably low temperatures, to maintain a low CO concentration and to be stable under catalytic reaction. Many studies have been focused on the ethanol steam reforming (ESR) over supported nickel, cobalt or noble metal catalysts. The major drawback of the catalytic systems is their deactivation caused by the coke deposition. It was shown [4] that the noble metals, like Rh and Ru can successfully break the C–C bond leading to less coke deposition and to formation of more stable catalysts.

However, alumina-supported Ni catalysts, due to their low cost and wide availability, as well as due to their capability of C–C bond capture, are the most used catalysts for reforming processes. In addition, ESR over nickel catalysts takes place at moderate temperatures. But, during the ESR the acidity of alumina favors the ethanol dehydration and thereby, increase the tendency for coke formation due to the polymerization of ethylene [5, 6]. In opposite to noble metals, the nickel particles tend to sinter under ESR reaction conditions. Therefore, to avoid the both, nickel metal sintering and alumina acidity, leading to carbon formation and catalyst deactivation, different supports and/or promoters have been added to nickel-based catalysts. For example, on ceria (CeO<sub>2</sub>) support, which is considered to be a basic support, the dehydration was limited and the coke formation was limited due to the redox properties of ceria [7]. Addition of Cu to Ni-based catalyst promotes the water gas shift reaction (WGS) reaction, which is a site reaction of ESR, to produce hydrogen and to avoid the growth of nickel particles [8, 9].

The low-cost cobalt based catalysts are promising catalysts for ESR since they are very selective to H<sub>2</sub> and CO<sub>2</sub> because the reforming temperature can be as low as 623 K in such a way that WGS occurs simultaneously with the steam reforming and, consequently the CO concentration is kept low. Recent studies suggested that the Co<sup>2+</sup> sites are the active centers in ESR, and the Co<sup>0</sup> sites are

responsible for coke formation [3,10]. However, other authors considered that the metallic cobalt plays a key role in ESR [11]. High-pressure X-ray photoelectron spectroscopic studies (HPXPS) demonstrated that during the ethanol reaction over Co/CeO<sub>2</sub>(111) model catalyst the amount of Co<sup>2+</sup> was decreased drastically with increasing the temperature, and at 600 K the majority of Co was metallic; this process was accompanied by the ceria reduction [12]. On the other hand, in-situ studies by FTIR with CO as a probe molecule suggested that the redox pair Co<sup>0</sup> ⇌ Co<sup>2+</sup> is responsible for the activity of cobalt in ESR [13]. Several strategies have been attempted to minimize the coke formation over Co-based catalysts under ESR conditions. It has been demonstrated [14] that alloying the cobalt with other metals promotes the redox pair Co<sup>2+</sup> ⇌ Co<sup>0</sup>, both in terms of lower cobalt reduction temperature, as well as a fast re-oxidation that results in a better catalyst stability.

The synergetic effect of the combination of two active elements like Ni and Co was investigated in the present work. It was attempted to discuss the effect of metal content on the change in the structure and electronic properties of MgAl<sub>2</sub>O<sub>4</sub>-supported monometallic Co and Ni and bimetallic CoNi catalysts with different metal loading under reductive atmosphere and ESR conditions. Different techniques were used for sample characterization such as: X-ray photoelectron spectroscopy (XPS), in situ X-ray adsorption near edge structure (XANES) and transmission electron microscopy (TEM).

## EXPERIMENTAL

### *Sample preparation*

Two series of MgAl<sub>2</sub>O<sub>4</sub>-supported monometallic Ni(Co) and bimetallic CoNi catalysts with different total metal loading of 8 and 15 wt.% were prepared by incipient wetness impregnation of the carrier with aqueous solution of Ni(NO<sub>3</sub>)<sub>2</sub>·6H<sub>2</sub>O (Aldrich, 99%) and/or Co(NO<sub>3</sub>)<sub>2</sub>·6H<sub>2</sub>O (Aldrich, 99%). MgAl<sub>2</sub>O<sub>4</sub> carrier was prepared by sol-gel method described elsewhere [15]. The obtained solids were dried and calcined in air flow at 110° and 500°C for 12 and 6 h, respectively. The first series of samples was labeled as 8Ni, 4Co4Ni and 8Co and the second one as 15Ni, 7.5Co7.5Ni and 15, where the number represents the nominal content of each metal.

### *Sample characterization*

XPS of calcined and reduced samples were registered using SPECSLAB II Phoibos-HS 3500 150 analyzer, employing Al K $\alpha$  (1486.6 eV) radiation. Self-supported pellets of the samples were prepared and reduced in a pretreatment chamber at 750°C for two hours under hydrogen flow. The

spectra were fitted with CASA XPS software, with Shirley background subtraction, and using a convoluted Gaussian/Lorentzian function. Binding energies of Ni 2p, Co 2p, Al 2p and O 1s core electron levels were referred to the C<sub>1s</sub> level at 248 eV.

XANES analyses of the samples were performed at the K edge of Co (7709 eV) and Ni (8333 eV) using D06A - DXAS beamline of Brazilian Synchrotron Light Laboratory at Campinas. The sample was first crushed and sieved to particle sizes smaller than 20  $\mu$ m and pressed into self-supporting pellets. Then the pellets were placed inside a tubular quartz reactor equipped with refrigerated kapton windows transparent to the X-ray beam. In situ temperature-resolved XANES spectra were acquired during temperature programmed reduction (TPR) of the samples (XANES-TPR), which was achieved by heating from room temperature to 750°C, at 10°C/min, with a holding time of 60 min, under a 200 ml/min flow of H<sub>2</sub>/He (5 vol.%). Energy calibration of the XANES spectra was performed with open source ATHENA/IFEFFIT software. A linear combination analysis was performed using Co<sup>0</sup>, CoO, Co<sub>3</sub>O<sub>4</sub>, Ni<sup>0</sup> and NiO references [15].

In situ XANES spectra at the K edge of Co and Ni of the catalysts under ethanol steam reforming conditions were also realized (XANES-ESR). The reactor with previously reduced samples at 750°C under hydrogen stream was cooled to room temperature under a flow of helium. Then a flow of 3.9 ml/min of the ESR mixture (H<sub>2</sub>O/ethanol molar ratio of 3:1), diluted in 133 ml/min of He, was started. The samples were heated from room temperature to 500°C, kept for 30 min, and then more than 30 min at 550°C. The XANES spectra were acquired 10 min after reaching steady state. The reaction products were analyzed by mass spectrometry.

TEM images of reduced and spent catalysts were acquired in a Jeol 2010F microscope, with a Schotcky field emission gun operating with 200 kV of acceleration voltage. The bright field and high resolution images were acquired in a Gatan Tridien CCD detector (2k x 2k pixels). Scanning TEM (STEM) images in bright field and high-angle annular darkfield were obtained using a spot size of 1 nm. Energy filtered TEM (EFTEM) images were acquired in a Gatan Image Filter prism using the Ni and Co L<sub>2,3</sub> core-losses, and O and C K core -losses to generate the energy-filtered image.

Activity test of the catalysts in ESR was realized in a quartz reactor. After reduction of the samples at 750°C for 1 h under hydrogen stream, the reactor was cooled to r.t. and the mixture of H<sub>2</sub>O/ethanol in

molar ratio of 3/1 was past. The temperature was increased in steps of 50°C when the GC analysis was made. For stability test, the ESR stream was admitted at 550°C, the temperature at which the reforming reaction was at maximum, and kept for 6 h on steam in the same conditions of  $W_{\text{cat}}/F_{\text{EtOH}}$  and a mixture composition ( $W_{\text{cat}}/F_{\text{EtOH}} = 114.7 \text{ g}_{\text{cat}} \cdot \text{min} \cdot \text{g}_{\text{EtOH}}^{-1}$ ).

## RESULTS AND DISCUSSION

### XPS analysis

The BEs values of Co 2p<sub>3/2</sub> and Ni 2p<sub>3/2</sub> core electron levels, as well as the atomic XPS Ni/Co ratios for calcined and reduced monometallic and bimetallic CoNi samples with different metal loading are shown in Table 1. In addition, the average particle size of reduced catalysts at 750°C, defined by HRTEM, is included in the Table. 1. The XPS spectra (not shown) of calcined Ni-containing samples exhibited peaks of Ni<sup>2+</sup> accompanied with their satellites. The BE value of 855.48-955.51 eV of calcined monometallic Ni samples means the presence of Ni<sup>2+</sup> ions [16]. However, the addition of Co to Ni samples leads to the increase of BE values of Ni 2p<sub>3/2</sub> electrons for calcined bimetallic CoNi samples with different metal content by approximately of 0.5 eV (from Table 1). The observed phenomena should be explained by the presence of Ni ions in a more electron deficient environment, i.e. Ni<sup>3+</sup> ions could be existing. In opposite to that, the BEs of Co 2p<sub>3/2</sub> electrons for both bimetallic CoNi samples are shifted to lower BE values that suggests a higher concentration of Co<sup>2+</sup> in the spinel, more evidently for sample with the higher metal loading of 15 wt%. (Table 1). The shift in the BEs values of the calcined samples should be caused by the interaction between the components and support surface, as well as by the strong interaction between Co and Ni and formation

of some distorted structure like NiCo<sub>2</sub>O<sub>4</sub> spinel [17]. It was supposed [17] hat this spinel could be formed by the insertion of Ni<sup>2+</sup> into octahedral sites in Co<sub>3</sub>O<sub>4</sub> spinel structure because the ion radius of Ni<sup>2+</sup> (0.069 nm) is larger than that of Co<sup>3+</sup> (0.055 nm).

The XPS of reduced samples are more complex. With exception of the XPS of 8Co sample, all spectra exhibited components assigned to metallic Ni with BEs of 852.52-853.24 eV or metallic Co with BEs of 778.40-778.61 eV, as well as components of 2+ oxidation state. It means that the surface of reduced catalysts is still oxidized even after treatment in a hydrogen atmosphere at 750°C. The more difficult reduction of Co oxide species in these samples, probably is due to their metal dispersion (Fig. 1).

The observed shift in the BEs of reduced samples (Table 1) should be related to the electron interaction between Co and Ni that depends on the composition and metal loading. The shift of BE of Co 2p<sub>3/2</sub> for monometallic Co samples from 781.76 to 778.40 eV with the increase of Co content from 8 to 15 wt% should be connected with the increase of metal particle size (from 4.4 to 11 nm for 8Co and 15Co, respectively, Table 1), followed by the decrease of electron density and reduction of Co nanoparticles. After addition of Co to Ni catalysts the interaction between Co and Ni for reduced high metal-loaded sample of 15 wt% results in a decrease of BE of Ni 2p<sub>3/2</sub> and in a slight increase of BE of Co 2p<sub>3/2</sub>. In opposite to that, an increase of BE of Ni 2p<sub>3/2</sub> for low metal-loaded 4Co4Ni sample is observed, accompanied with the decrease of BE of Co 2p<sub>3/2</sub> (Table 1). It means a deficient of electrons in the environment of Ni in opposite to that observed for Co, most probably caused by the interaction between Co and Ni and an alloy formation similar to that observed by other authors [18].

**Table 1.** Some physicochemical properties of the oxide and reduced monometallic and bimetallic CoNi catalysts

Sample	$D_{\text{metal}}^a$ , nm	Binding Energy, eV		Ratio
		Ni 2p <sub>3/2</sub>	Co 2p <sub>3/2</sub>	
<i>Calcined samples</i>				
8Ni		855.48	-	
4Co4Ni		855.98	780.83	1.6
8Co		-	781.05	
15Ni		855.51	-	
7.5Co7.5Ni		855.90	780.62	1.8
15 Co		-	779.71	
<i>Reduced samples</i>				
8Ni	5.2	852.52	-	
4Co4Ni	4.2	852.84	778.47	2.8
8Co	4.4	-	781.76	
15 Ni	16.8	853.24	-	
7.5Co7.5Ni	9.9	852.99	778.61	1.7
15Co	11.0	-	778.40	

<sup>a</sup>Average particle size or reduced catalysts defined by HRTEM

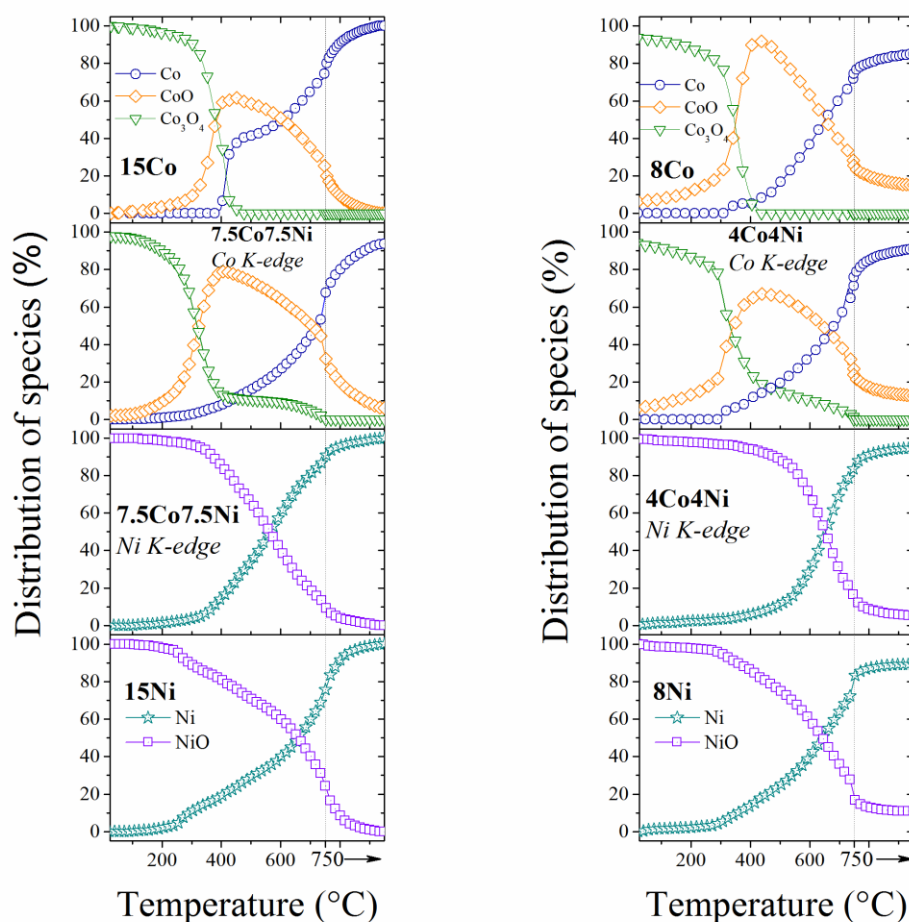


**Fig. 1.** Percentage change of species as a function of reduction temperature defined by in situ temperature resolved XANES spectra of monometallic Co and Ni and bimetallic CoNi samples with different metal loading during the TPR.

The XPS Ni/Co ratios values of both calcined bimetallic CoNi samples are approximately the same and are higher than 1, which means some enrichment of the surface with Ni. The reduction of bimetallic CoNi sample with the higher metal loading of 15 wt% does not change the atomic Co/Ni ratio in relation to that of the respective calcined sample (Table 2). However, the reduction leads to a significantly increase of the Ni/Co ratio of reduced bimetallic 4Co4Ni system (from 1.6 to 2.8, Table 2), which is almost in two times higher than that of the reduced 7.5Co7.5Ni (1.7). It suggests that the treatment of the bimetallic catalyst system with lower total metal loading of 8 wt% under hydrogen atmosphere leads to a re-dispersion of the small nanoparticles, which provokes a segregation of Ni at the surface and leaving Co in the interior, similar to formation of a *core shell* like structure, as the nickel possess a higher affinity to hydrogen than cobalt.

#### *In situ XANES-TPR*

The change of the oxidation state of metal components in both series of catalysts was investigated by in situ temperature-resolved XANES spectra at K-edge of Ni and Co registered during the TPR. The respective semi quantitative change in the percentage of different Co and Ni species as a function of reduction temperature up to 750°C is shown in Fig. 1. It should be noted that the fitting of XANES spectra of calcined Co-containing samples with a higher metal loading of 15 wt% showed mainly the presence of  $\text{Co}_3\text{O}_4$  species, whereas a mixture of 10% CoO and 90%  $\text{Co}_3\text{O}_4$  in the samples of 8 wt% was detected.

The reduction process of cobalt oxide species consists of two reduction processes, being seen in Fig. 1: the first process is the reduction of  $\text{Co}_3\text{O}_4$  to CoO and the second one is the transformation of CoO to metallic cobalt,  $\text{Co}^0$ . It is important to note that the second reduction process for monometallic

Co samples is occurred after finishing the first reduction process at about 400°C. However, for both bimetallic CoNi samples there is a coexisting of transitions  $\text{Co}_3\text{O}_4 \rightarrow \text{CoO}$  and  $\text{CoO} \rightarrow \text{Co}^0$  in a wide temperature region. The reduction of  $\text{Co}^{2+}$  species to  $\text{Co}^0$  for bimetallic systems starts to occur at lower temperature, compared to that observed for monometallic Co samples (Fig. 1). The latter is due to the activation of  $\text{H}_2$  over the surface of metallic nickel species and the hydrogen atoms are transferred to cobalt oxide by spillover effect. It can be concluded that more easy reduction of Co oxide to  $\text{Co}^0$  is observed in the presence of nickel that is more visible for high metal-loaded bimetallic 7.5Co7.5Ni system. At the end of reduction process the monometallic Co catalyst with higher metal content of 15 wt% is totally reduced, whereas the low metal-loaded Co catalyst shows about of 15 wt.% CoO at 750°C (Fig.1).

The reduction of NiO species for both monometallic Ni samples is beginning at lower reduction temperature compared to that observed for the corresponding bimetallic CoNi samples with the same total metal loading (Fig. 1). In addition, there is no significant alteration in the percentage of Ni species of monometallic Ni samples at low reduction temperature (up to 250°-300°C). However, more visible change is observed at temperature higher than 300°C: the percentage of NiO species decreases with increasing the reduction temperature, while that of metallic nickel component ( $\text{Ni}^0$ ) increases, which is well visible for sample with a higher metal loading of 15 wt% (Fig. 1). The percentage of metallic nickel at the end of reduction of 15Ni is approximately of 100 %.

The reduction of NiO species to  $\text{Ni}^0$  for bimetallic CoNi samples is beginning at significantly higher temperatures compared to those of the corresponding monometallic Ni samples, which is more visible for 4Co4Ni (above 400°C, Fig. 1). This means that the presence of Co suppress the reduction of nickel oxide species in the bimetallic system, probably, due to the strong interaction between Co and Ni and formation of the phase similar to  $\text{NiCo}_2\text{O}_4$ .

It is interesting to note that the transition  $\text{Ni}^{2+} \rightarrow \text{Ni}^0$  for both bimetallic CoNi systems is occurred simultaneously with the reduction of  $\text{CoO}$  to  $\text{Co}^0$ . These dynamics suggest the interaction between the both metals cations, and the higher spinel content indicates a coexistence in the same crystallographic phase, like  $\text{Co}^{2+}_{\text{tet}}[\text{Ni}^{2+}\text{Co}^{3+}]_{\text{oct}}\text{O}_3^{2-}\cdot\text{O}$ , as was proposed by other authors [19, 20]. In addition, the shift of the values of reduction temperature of nickel oxide species to higher values with decrease of metal

content is a typical behavior of the small nanoparticles, which are highly reactive.

#### *In situ XANES-ESR*

The change in the oxidation state of metal components (Co, Ni) of both series catalysts as a function of reaction temperature under ethanol steam reforming was evaluated by in situ XANES, being seen in Fig. 2. With exception of 15Co the degree of reduction of high metal-loaded samples (15Ni, 7.5Co7.5Ni) decreases slightly up to about 250°C with the admission of reactants and after that the particles became reduced again as the ethanol molecule activation is occurred. Monometallic 15Co catalyst continues to suffer oxidation up to 350°C followed by the surface reduction of  $\text{CoO}$  to  $\text{Co}^0$  when the atmosphere is turned more reductive (Fig. 2). The oxidation level of Ni particles for both monometallic Ni samples at low reaction temperatures up to around 200°-250°C is lower compared to that observed for bimetallic CoNi systems. This means that the monometallic Ni samples exhibit a higher number of metallic centers, more pronounced for high metal-loaded sample. However, addition of Co to Ni catalysts leads to an increase of the oxidation level of Ni particles, more visible for bimetallic CoNi system with lower total metal loading of 8 wt%. In addition, the presence of nickel oxide species in the low metal-loaded 8Ni and 4Co4Ni samples continue up to a higher reaction temperature of 500° and 400°C, respectively, as the concentration of NiO is much higher for the second one up to 250°C. Since an enrichment of Ni on bimetallic catalysts surfaces was detected by the XPS, especially in the case of 4Co4Ni sample (Table 1), it is reasonable a higher level of oxidation of Ni in relation to that of Co to be observed when  $\text{H}_2\text{O}/\text{C}_2\text{H}_5\text{OH}$  mixture was admitted. Nickel oxide species are well reduced for all samples at reaction temperature above 450°-500°C, being seen in Fig. 2.

The oxidation level of Co particles for both monometallic Co catalysts is higher compared to that of bimetallic CoNi systems (Fig. 2), which can be related to the high affinity of Co to be oxidized. The low metal-loaded 8Co sample suffers a deep Co oxidation where some equilibrium of  $\text{Co}^0$  and  $\text{Co}^{2+}$  would be observed up to 450°-500°C. It is important to note that when Ni of both bimetallic CoNi samples is well reduced at 500°-550°C, Co is partially oxidized (around 5 % and 15 % of  $\text{CoO}$  for 7.5Co7.5Ni and 4Co4Ni, respectively, Fig. 2).

It is interesting to note that the oxidation level of Ni in bimetallic 4Co4Ni system is higher than that of Co at the beginning of reaction. Co is oxidized up to 300°C, whereas Ni reaches the maximum level of oxidation at about 150°-250°C and after that it starts

to be reduced (Fig. 2). It can be concluded that the oxidation level of CoNi catalysts up to about of 300-400°C with the high metal loading of 15 wt% is smaller than that of low metal-loaded samples (8 wt%), most probably, due to some reconstruction in

the particle size of catalysts under reaction conditions of ESR.

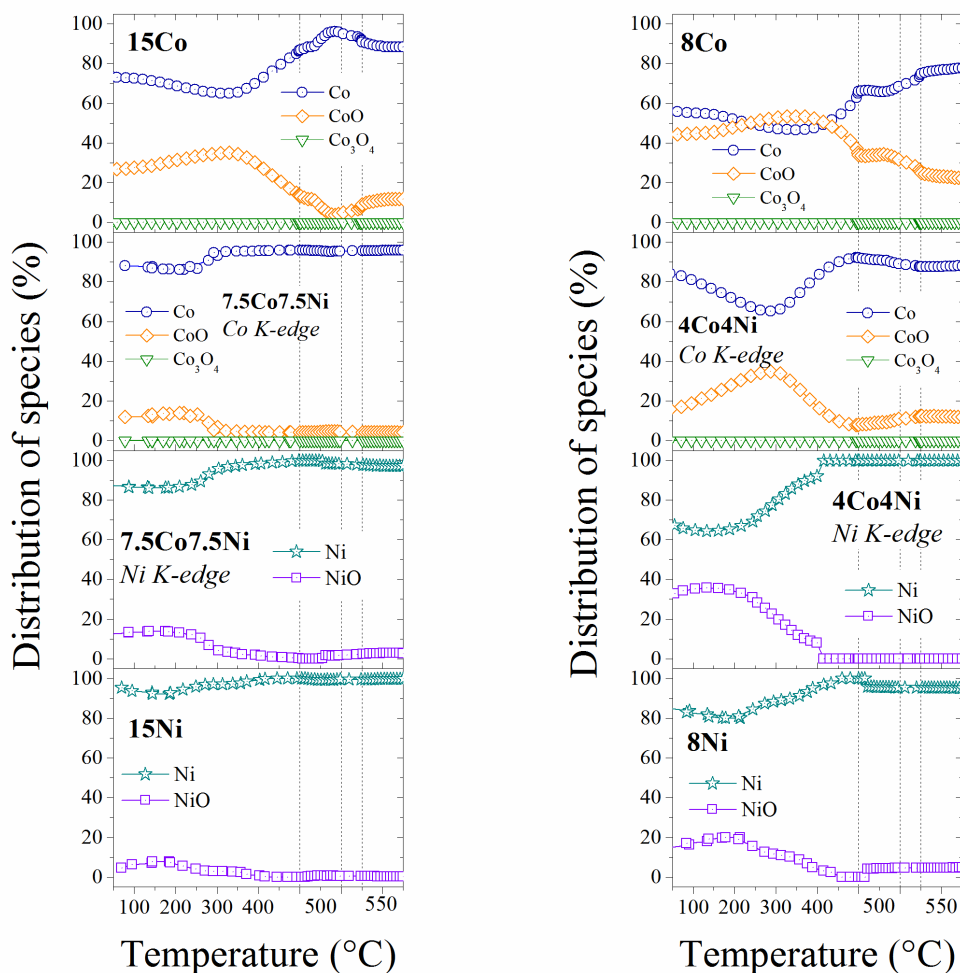


**Fig. 2.** The percentage change of species as a function of reaction temperature defined by in situ temperature resolved XANES spectra of monometallic Co and Ni and bimetallic CoNi catalysts with different metal loading under ethanol steam reforming.

#### Catalysts behaviors in ethanol steam reforming

The evolution of the change of ethanol conversion and products distribution for both series of catalysts as a function of reaction temperature in ethanol steam reforming is shown in Fig. 3. Monometallic Ni catalysts at lower reaction temperature region of 300°-450°C produce methane in a great degree due to the hydrogenation of CH<sub>x</sub> radicals formed by the C-C bond breakage of ethanol molecule. Ni catalyst with a high metal content of 15 wt% exhibits a higher percentage of CH<sub>4</sub> at 300°-

350°C compared to that observed for low metal-loaded 8Ni. This can be related to the higher metallic character of 15Ni at low reaction temperatures, being seen in Fig. 1. In addition, up to 350°-450°C the methane formation is accompanied with the formation of CO<sub>2</sub> in a great degree, which is probably caused by the occurring of the WGSR, due to the increased degree of metallic character of nickel particles. However, above 500°C there is some inversion in the formation of CO<sub>2</sub> and CO not only for both monometallic Ni catalysts, but for all other monometallic Co and bimetallic CoNi systems,



which can be a consequence of the reverse of WGS. The highest selectivity to hydrogen for monometallic Ni catalysts is observed at about 350°C.

The high level of Co oxide species in both monometallic Co catalysts, more visible for 8Co, makes them less active in ethanol reforming reaction (Fig. 3). It was shown [21] that Co particles smaller than 5 nm are unstable and undergoes oxidation easily in the presence of water vapor. The addition of Co to Ni catalysts and the decrease of metal loading leads to less methane formation, which indicates that the methyl radicals formed by the C-C bond breakage are easily hydrogenated over metallic Ni sites. Acetaldehyde is the major product formed at low reaction temperature of 300°C due to the ethanol dehydrogenation, involving O-H bond cleavage of ethanol molecule, which is caused by the high concentration of Co oxide species detected by in situ XANES-ESR (Fig. 2). It is well known [22] that the presence of Co and CoO species are very active for the oxidation of the adsorbed ethoxide

species to produce acetaldehyde. For monometallic Co catalysts (Fig. 3) the activity to C-C bond cleavage accompanied with formation of CO, CH<sub>4</sub> and CO<sub>2</sub> is poorly observed at 300-350°C, more visible for low metal-loaded 8Co sample. The production of CH<sub>4</sub> is very low for Co catalysts, showing that the CH<sub>x</sub> radicals remain adsorbed and suffer successive dehydrogenation, in opposite to that observed for 8Ni. At 400°-450°C the high concentration of CO<sub>2</sub> for both Co catalysts accompanied with the highest degree of hydrogen production is due to the WGS. At temperatures above 450°C there is some inversion in the ratio of CO/CO<sub>2</sub> that could be related to methane reforming with CO<sub>2</sub> [23]. The increase of the rate of C-C bond cleavage with the temperature should be provoked by the increased fraction of Co<sup>0</sup> (Figs. 1 and 2). The reforming reactions on monometallic Co catalysts dominate at temperature above 500°C and the high ethanol conversion is reached at higher temperatures than those for monometallic Ni-containing catalysts; H<sub>2</sub> yield also follows the same trend.

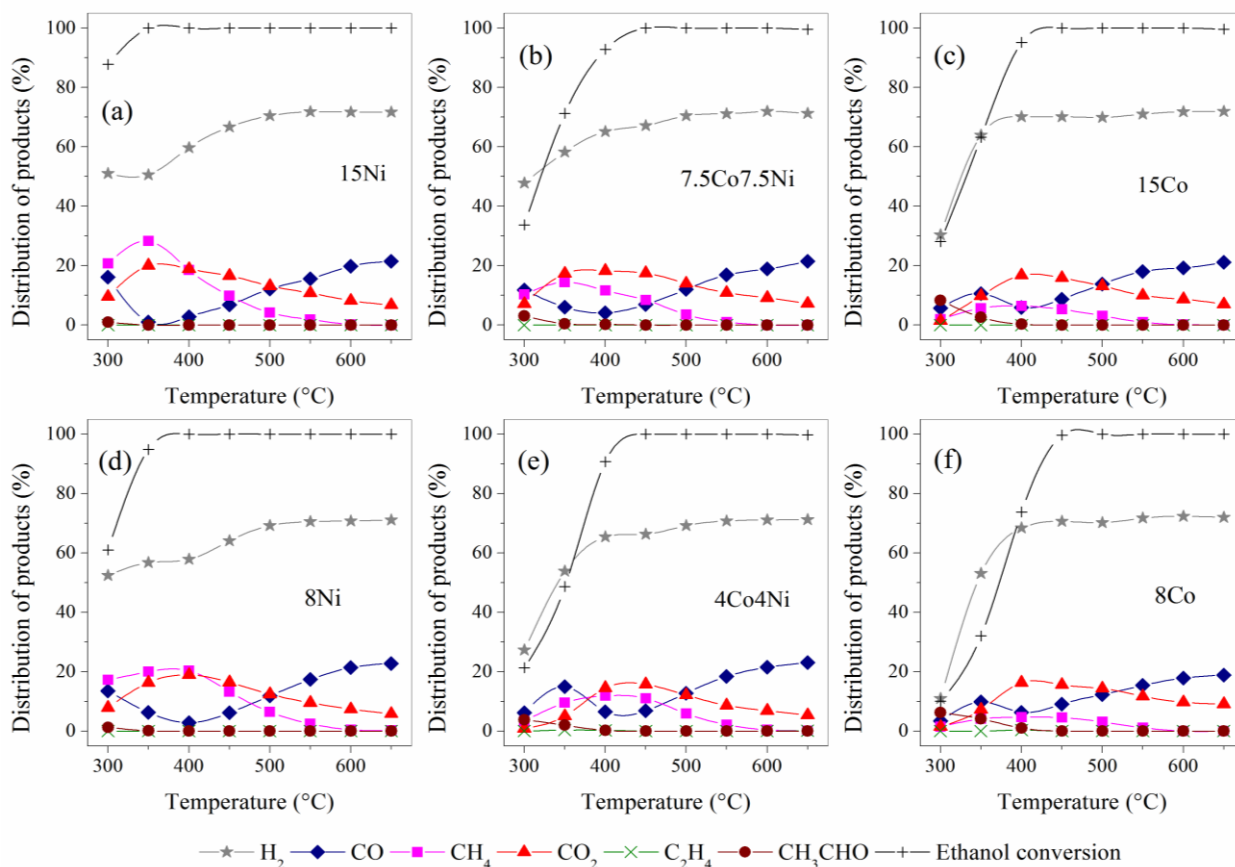


**Fig. 3.** Ethanol conversion and products distribution as a function of reaction temperature in ethanol steam reforming over monometallic Co and Ni and bimetallic CoNi catalysts with different metal loading.

The both bimetallic catalyst systems show an intermediate behavior between those of the bare Co and Ni. At low reaction temperature of 300°C acetaldehyde over CoNi catalysts is formed in a higher concentration than over monometallic Ni, but in a lower concentration than that on monometallic Co (Fig. 3). This is due to the better reducibility of Co and Ni sites of bimetallic CoNi catalysts as was observed by in situ XANES-TPR (Fig. 1). At temperatures above 300°C the route for bimetallic CoNi catalysts run like monometallic Ni ones, but the formation of CH<sub>4</sub> is lower. This suggests that the electronic modification caused by the Co-Ni interaction modifies also how the CH<sub>x</sub> radicals kept adsorbed on the surface.

The bimetallic CoNi catalysts revealed a high stability with time on stream under ESR reaction conditions at 650°C for 8 h. However, the HRTEM images of spent 4Co4Ni catalyst in Fig. 4 show the presence of carbon filaments, on the top of which the particle is situated that give accessibility of the reaction molecule to the catalytic active center. It is well known [24] that the carbon accumulation on the catalyst surface is a function of metal particle size. As was shown [24] the large metal particles in the reaction of methane reforming are encapsulated by carbon species; small nanoparticles due to its reactivity formed low carbon assemblies and the particles with medium size formed well defined carbon nanofilaments. The smallest nanoparticle size (4.2 nm) is detected for reduced 4Co4Ni catalyst (Table 1).

On the other hand, in the case of 4Co4Ni catalyst the electronic properties of the small nanoalloy

detected by the XPS analysis can make the surface oxygen more available to oxidize the carbon coming from the reforming reaction, and making by this way the catalyst more stable.

## CONCLUSIONS

The dependence of ethanol conversion and product distribution as a function of metal loading and temperature reaction was evaluated. The results show that MgAl<sub>2</sub>O<sub>4</sub> is a suitable support for monometallic Co and Ni and bimetallic CoNi catalysts for ethanol steam reforming. The both monometallic Ni systems exhibit the highest ethanol conversion at lower reaction temperature of about 350°C, accompanied with the highest methane yield due to the high metal character of catalysts. The high level of oxide species of monometallic Co catalyst with lower metal loading of 8 wt% makes them less active in reforming reaction at low reaction temperature. The addition of Co to Ni catalyst leads to alloy formation, which leads to the change of electronic properties of bimetallic CoNi catalysts revealed by the decrease of methane selectivity and increase of catalyst stability. The bimetallic CoNi systems exhibit different redox properties than monometallic catalysts, being easily oxidized than monometallic Ni and controlling better the oxidation level than monometallic Co.

**Acknowledgments:** The authors kindly acknowledged to project DFNI E02/16 for financial support and to Brazilian Synchrotron Light Laboratory for XAS beamline experiments.

## REFERENCES

1. M. Mavrikakis, M. Barteau, *J. Mol. Catal. A*, **131**, 135 (1998).
2. C.J. Weststrate, H.J. Gericke, G.M. Verhoeven, I.M. Ciobica, A.M. Saib, J.W. Niemantsverdriet, *J. Phys. Chem. Lett.*, **1**, 1767 (2011).
3. E. Martono, J.M. Vohs, *J. Catal.*, **291**, 79 (2012).
4. S.J. Morrison, H. Idriss, *Catal. Today*, **63**, 327 (2000).
5. M. Badlani, I.E. Wachs, *Catal. Lett.*, **75**, 137 (2001).
6. D. Kulkarni, I.E. Wachs, *Appl. Catal. A*, **237**, 121 (2002).
7. L.V. Mattos, B.H. Jacobs, F.B. Noronha, *Chem. Rev.* **112**, 4094 (2012).
8. A. Bshish, Z.Yahkkob, B. Narayanan, R. Ramakrishnan, A. Ebshish, *Rev. Chem. Papers*, **65**, 251 (2011).
9. M.H. Youn, J.G. Seo, P. Kim, J.J. Kim, H. Lee, I.K. Song, *J. Power Sources*, **162**, 1270 (2006).
10. M.P. Hyman, J.M. Vohs, *Surface Sci.*, **605**, 383 (2011).
11. M.S. Batista, R.K.S. Santos, E.M. Assaf, J.M. Assaf, E.A. Ticianelli, *J. Power Sources*, **124**, 99 (2003).
12. L. Óvári, Krick S. Calderon, Y. Lykhach, J. Libuda, A. Erdöhelyi, C. Papp, J. Kiss, H.-P. Steinrück, *J. Catal.*, **307**, 132 (2013).
13. J. Llorca, N. Homs, P. Ramírez de la Piscina, *J. Catal.*, **227**, 556 (2004).
14. A. Casanovas, M. Roig, C. de Leitenburg, A. Trovarelli, J. Llorca, *Int. J. Hydrogen Energy*, **35**, 7690 (2010).
15. C.N. Avila-Neto, J.W.C. Liberatori, A.M. da Silva, D. Zanchet, C.E. Hori, F.B. Noronha, J.M.C. Bueno, *J. Catal.*, **287**, 124 (2012).
16. S. Andonova, C.N. de Ávila, K. Arishtirova, J.M.C. Bueno, S. Damyanova, *Appl. Catal. B: Environ.*, **105**, 346 (2011).
17. C.F. Windisch, G.J. Exarhos, R.R. Owings, *J. Appl. Phys.*, **95**, 5435 (2004).
18. J.H. Zhang, A. K. Wang, K.A. Dalai, *Ind. & Eng. Chem. Res.*, **48**, 677 (2009).
19. W.J. King, A.C.C. Tseung, *Electrochim. Acta*, **19**, 493 (1974).

20. A. Verma, , D. Kumar, A. Pravarthana, S.B. Deshpande, S.M. Ogale, *J. Phys. Chem. C*, **118**, 16246 (2014).
21. E. van Steen, M. Claeys, M.E. Dry, J. van de Loosdrecht, E.L. Viljoen, J.L. Visage, *J. Phys. Chem. B*, **109**, 3575 (2005).
22. E. Martono, J.M. Vohs, *J. Catal.*, 291, 79 (2012).
23. I. Tankov, K. Arishtirova, J.M.C. Bueno, S. Damyanova, *Appl. Catal. A: Gen.*, **474**, 135 (2014).
24. W.H. Cassinelli, S. Damyanova, N.V. Parizotto, D. Zanchet, J.M.C. Bueno, C.M.P. Marques, *Appl. Catal. A: Gen.*, **475**, 256 (2014).

## ИЗСЛЕДВАНЕ НА КАТАЛИЗАТОР ОТ КОБАЛТ И НИКЕЛ ЗА СТИЙМ-РЕФОРМИНГ НА ЕТАНОЛ

А.Х. Брага<sup>1</sup>, Ж.Б.О. Сантуш<sup>1</sup>, Ж.М.К. Буено<sup>1</sup>, С. Дамянова<sup>2\*</sup>

<sup>1</sup>Департамент по инженерна химия, Федерален университет „Сао Карлуш“, Сао Карли, Бразилия

<sup>2</sup>Институт по катализ, Българска академия на науките, София 1113 България

Постъпила на 10 декември 2016 г.; приета на 13 февруари, 2017 г.

(Резюме)

Изследван е ефектът на добавен Со в Ni катализатори върху измененията в структурата и електронните свойства на катализаторите, както и върху тяхното каталитично поведение в реакцията паров реформинг на етанол. Получени са две серии биметални CoNi катализатори, нанесени върху носител MgAl<sub>2</sub>O<sub>4</sub>, с различно съдържание на металните компоненти в тях (8 и 15 тегл.%). Използвани са различни техники за тяхното физико-химично охарактеризиране: рентгенова фотоелектронна спектроскопия, *in situ* рентгенова абсорбционна спектроскопия и трансмисионна електронна микроскопия с висока резолюция. Каталитичният тест на образците е проведен в реакцията паров реформинг на етанол в широк температурен интервал от 250° до 650°C. Установено е, че шпинел подобна структура на Ni<sub>2</sub>CoO<sub>4</sub> се образува в оксидни биметални CoNi системи, което след редукция води до получаването на сплав. Присъствието на сплав в биметални катализатори е отговорна за високата им стабилност по време на протичане на реакцията.

## Cold plastic deformation effects on the mechanical properties and corrosion behaviour of low-alloyed (2% Cr) steel

D. I. Ivanova\*, G. P. Ilieva, L. B. Fachikov

University of Chemical Technology and Metallurgy, 8 Kliment Ohridsky Blvd., Sofia 1756, Bulgaria

Submitted November 21, 2016; Accepted February 3, 2017

The effect of the cold plastic deformation (0–80 %) on the main mechanical characteristics, microstructure and the residual stresses of low-alloyed (Cr~2 %) carbon steel have been investigated applying various physical and electrochemical methods.

The results revealed that with increase in the degree of deformation there was significant enhance in the ultimate tensile strength, the yield strength and the hardness of the steel tested. The relative elongation reduces at about one order of magnitude.

The model aqueous solutions of sulfuric acid allow observing the effect of the plastic deformation on the corrosion behavior of the steel: It was established that the highest corrosion rates corresponded to deformation range 40–50 %. The general corrosion behavior of the untreated steel alters in localized attack in the deformed steel along the elongated grains having shapes of scratches.

**Keywords:** low-alloyed steel, mechanical properties, corrosion

### INTRODUCTION

The development and practical realization of new steels require various methods allowing deep understanding of the effects of many factors on the steel properties [1–4, 10–11]. In this context, experiments allowing seeing how the assurance and the long-lasting of equipments based on such steels and on the corrosion losses are dependent are highly required.

The contemporary worldwide practice applying steels with increased content of chromium (less 3 %) is mainly for welded constructions working under corrosion attacks of sea water, contaminated atmospheres, mineralized industrial waters, underground and waste waters. The alloying metal (chromium) does not change essentially the mechanical and technological properties of the steels but leads to two or three-fold increases in the intensities of the corrosion attacks, compared to similar cases with non-alloyed steels.

The effect of the cold mechanical treatment as well as the degree of plastic deformation on the corrosion behaviour of various steels commonly have been investigated with respect to the corrosion rates, corrosion potentials, anodic dissolution, etc. [5–9].

This work presents results obtained during studies addressing effects of the degree of cold plastic deformation on both the mechanical properties and microstructure of low-alloyed by chromium steel related to their corrosion resistance in model aqueous solutions of sulfuric acid.

### EXPERIMENTAL

Low-alloyed by chromium steel samples of flat profiled hot rolled sheets (of 3 mm thickness and chemical content, wt. %: C – 0.07; Cr – 1.88; P – 0.017; Mn – 0.67; Ni – 0.06; Cu – 0.15; Si – 0.22; Al – 0.081) were tested.

The cold rolling was carried out by a laboratory scale rolling mill „KWARTO”, with the following characteristics:

- Diameter of the cold-rolling work-rolls –  $130 \cdot 10^{-3}$  m
- Diameter of the supporting rolls –  $320 \cdot 10^{-3}$  m
- Roll width in the working zone –  $180 \cdot 10^{-3}$  m
- Power of the motor – 170 kW
- Rolling rate – 0.1–5.0 m/s
- Maximum roller force applied – 80 t
- Maximum gap between the rolls –  $45 \cdot 10^{-3}$  m
- Hardness of the surface of the rollers – HR = 52–56

The maximal degree of deformation obtained after the rolling (determined by measurements of the reduction in the sheet thicknesses) was about 80 %.

The tests to receiving the mechanical properties such as ultimate tensile strength  $R_m$ , the yield strength limit  $R_{e,0.2}$  and the relative percentage elongation  $A_5$ , of cold-rolled steels used flat samples are conducted in accordance with the Bulgarian standard recommendations (BDS EN 10002-1: 2004) using tensile strength equipment FPZ-100.

The hardness of the rolled samples was

\*) To whom all correspondence should be sent:

E-mail: dimkaivanova@uctm.edu

measured by the Brinell method and assessed in accordance with Bulgarian standard BDS EN ISO 6506-1: 2014.

The effects of the degree of the plastic deformation on the changes in the steel microstructures were determined by metallographic studies. The metallographic specimens were prepared in two orthogonal directions: parallel to

the deformation plane and in the transversal plane. All samples were treated by grinding paper and polished by aqueous suspension of  $\text{Cr}_2\text{O}_3$  and then revealed by a Nital solution. The observations were carried out with optical microscope EPITYP – 2. The original steel microstructure (ferito-pearlitic) of grade 7-8 and the microstructure of the deformed (about 50.18 %) one are shown in Fig. 1.

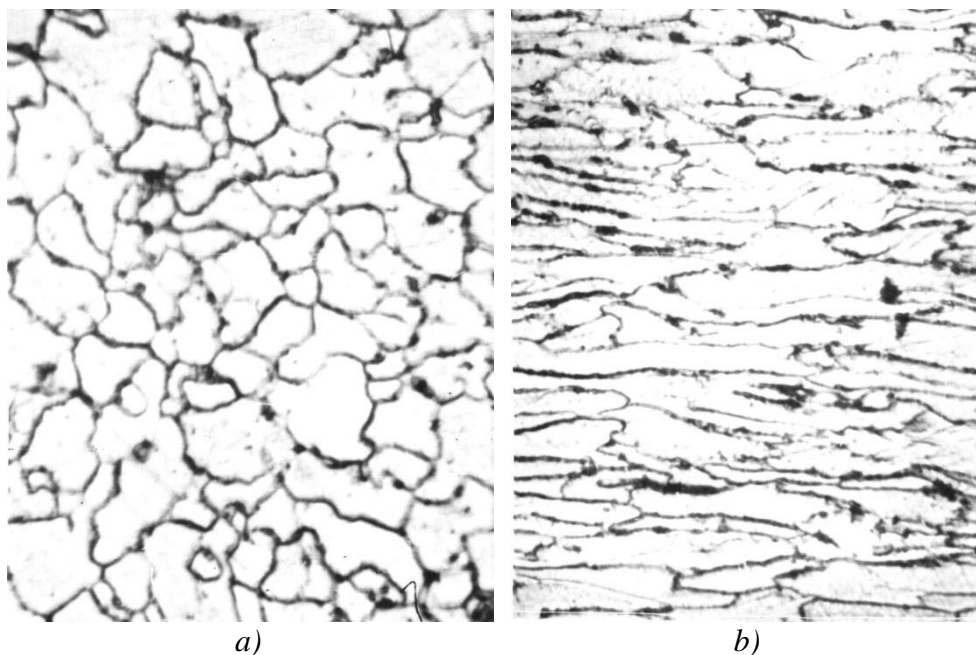


**Fig. 1.** Microstructures of the tested steel samples  
a) original samples ; b) rolled samples (50.18 % longitudinal deformation, x400)

The metallographic analysis allowed determining the grain sizes (Jeffries method) and the length of the lines at the boundaries (the method of Saltikov) [3].

It is well-known that the work of plastic deformation is greater than the liberation of heat under the body deformation. A part of this heat remains into the bulk of the deformed body and increases its internal energy. Metallographic methods such as the inverse photos of the moments allow determining the changes in the lattice structure after the steel deformation. Moreover, the metallographic method of the inverse pole figures allowed identification the texture developed as a result of the plastic deformation [4].

The effect of the cold-rolling on the corrosion behaviour of the steel was determined by the potentiodynamic polarization studies. The method, the equipment and preparation of the samples are described elsewhere [10]. The character of the corrosion attack was examined by scanning

electron microscopy, using a EM-400 “Philips” electron microscope.

## RESULTS AND DISCUSSION

The ultimate tensile strength  $R_m$ , the relative yield strength limit  $R_{e,0.2}$ , the hardness  $HB$  and the relative percent extension  $A_5$  of the treated samples against the degree of plastic deformation  $\varepsilon$  are presented graphically in fig. 2. The plots reveal that  $R_m$ ,  $R_{e,0.2}$  и  $HB$  grow almost parabolically in the entire range of variations of  $\varepsilon$ . All parameters, i.e.  $R_m$ ,  $R_{e,0.2}$  и  $HB$  increase about twofold with a maximal degree of deformation comparing to samples without plastic treatment. The relative extension  $A_5$  decreases almost exponentially and beyond  $\varepsilon > 50\%$  there are practically negligible changes in  $A_5$ .

The curves presented in Fig. 2 were approximated by quadratic polynomials [3], namely:

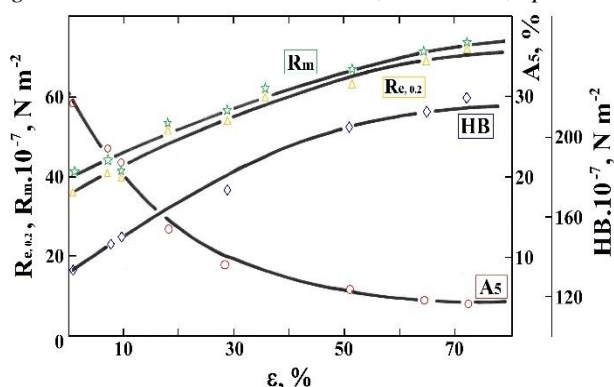


**Fig. 2.** Effect of the degree of deformation,  $\epsilon$  on the mechanical parameters  $R_m$ ,  $R_{e,0.2}$ , HB and  $A_5$

$$y = a + b\epsilon + c\epsilon^2$$

The coefficients  $a$ ,  $b$  and  $c$  are constants specific for each material and mechanical characteristic approximated, and they form sets of normal equations.

The changes in the mechanical characteristics of the deformed steel could be attributed to delayed slipping due to increased density of dislocations and re-orientation of the grains.

The microstructure changes observed as well as the consequent analyzes allow to state that the increase in the degree of deformation there is elongation of the grains and this effect is more pronounced for  $\epsilon > 40\%$ . When the deformation is beyond 60% the grains elongate about 3-4 times and there are onsets of bending and break-ups. At the same time, the deformation practically has no effect on the mean surface  $S_{av}$  and the diameter of the grains  $d_{av}$  as it is demonstrated in Fig. 3.

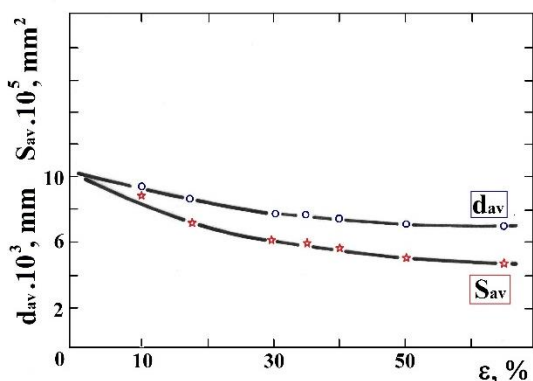


**Fig. 3.** The mean grain surface  $S_{av}$ ,  $\text{mm}^2$  and mean grain diameter  $d_{av}$ , mm as functions of the degree of grain deformation  $\epsilon$ , %

The changes in the mean length of the grain boundary  $\Sigma P$  with the deformation degree are presented in Fig. 4. The plots indicate that  $\Sigma P$  increases strongly at  $\epsilon > 35\%$  when detectable elongations of the grains start. The maximum in the grain elongation  $\Sigma P$  is about threefold the initial size.

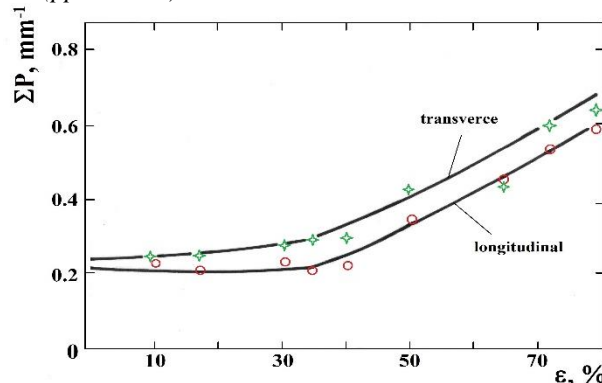


**Fig. 4.** Effect of the degree of deformation  $\epsilon$  on the length of the grain boundary  $\Sigma P$ ,  $\text{mm}^{-1}$

The effect of the degree of plastic deformation on the internal stresses in the steel, represented by the ratio  $\Delta a/a$  ( $\Delta a$  – is the maximal deviation of lattice period from its mean value  $a$ ) and the dimensions of the mosaic blocks  $D$  is demonstrated in Fig. 5. The data presented reveal that the dimension of the mosaic blocks decreases exponentially with the degree of deformation as a result of the blocks break-ups. The ratio  $\Delta a/a$  as a function of  $\epsilon$  exhibits a maximum at about  $\epsilon \approx 50\%$  and a fall beyond this point. This behaviour could be attributed to excess of heat dissipated during the deformation process taking beyond 50% and this heat enhance the diffusion processes in the steel structure with minor changes in the lattice thereof.

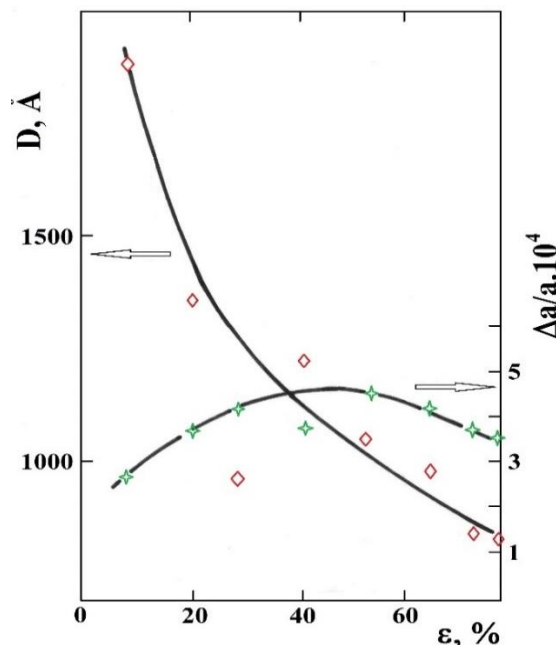


**Fig. 5.** Effect of the degree of deformation  $\epsilon$ , % on the size of mosaic blocks  $D$ , Å and the ratio  $\Delta a/a$

The studies on the texture of the deformed steel reveal that the preferred orientation of the grain slipping is the plane [100].

The corrosion behaviour of the low-alloyed steel and especially the effect of the cold deformation on

it was studied in a model 1.0 M solution of sulfuric acid. In general, the plastic deformation increases the corrosion rate and this process is strongly exhibited in the deformation range 30-50 %.

Further, there is a strong effect of the degree of deformation on the anodic passivity of the steel, precisely, the passive current increases with increase in the deformation. At  $\varepsilon = 50.18\%$ , for example, the passive current is about 2 times greater than that when the original no-treated steel is tested (see Fig.6). This is quite important in cases

of anodic protection of equipment using this steel, where due to local plastic deformations it would be possible to the passive state to be destroyed and the rapid dissolution of the steel on sulfuric acid media to be started.

The deformation of the steel does not affect strongly the corrosion potential  $E_{corr}$ , mV and its values remain almost equal to the ones corresponding to the non-deformed steel under the same conditions (see Fig. 6).

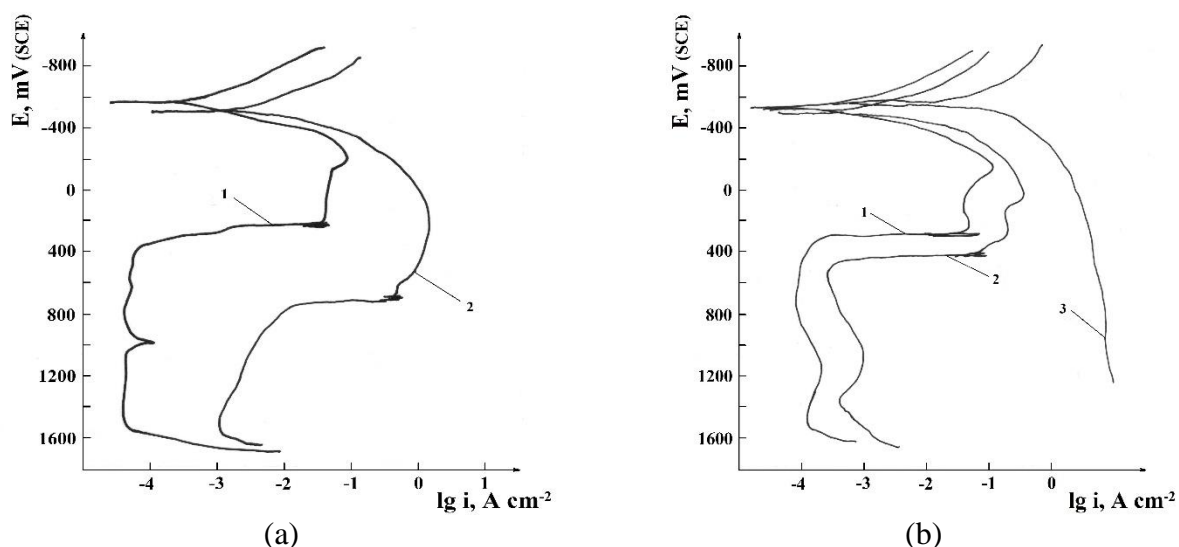


**Fig. 6.** Potentiodynamic polarization relationships  $E$ , mV –  $\lg i$ ,  $A\ cm^{-2}$  obtained in 1.0 M  $H_2SO_4$ : a) non-deformed steel 1 - 20°C, 2 - 60°C; b) deformed steel ( $\varepsilon = 50.18\%$ ) 1 - 20°C, 2 - 40°C, 3 - 60°C

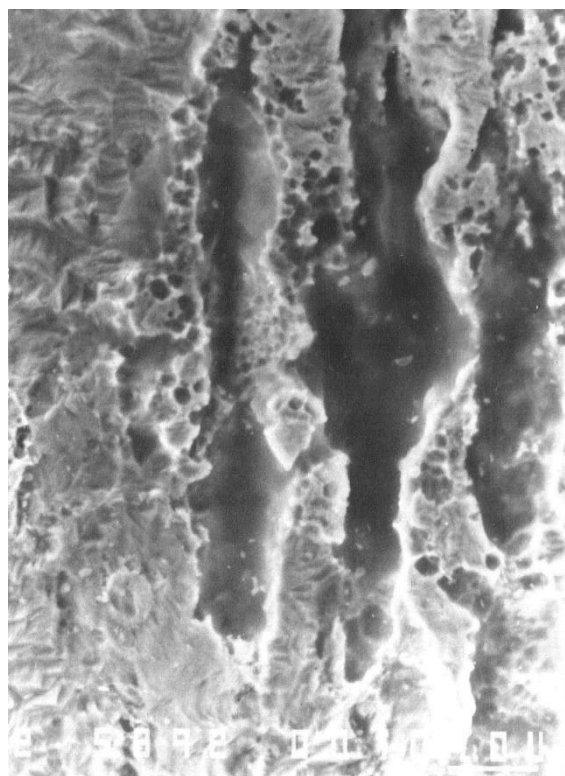


**Fig. 7.** Typical corrosion attack at 64.55 % deformation degree.

The character of the corrosion attack was determined visually by microscopic observations. In cases of both the non-deformed samples and deformed samples the low degrees of corrosion when low degrees of deformation take place the corrosion attacks is over the entire surfaces with slightly increases activity at the central parts of the samples and increased activity at the boundaries of the grains. With increase in the deformation degree, parallel to increased corrosion rate, strong local attacks take place; mainly as scratched strips oriented along the axis of the grain elongation (see Fig. 7).

## CONCLUSIONS

Investigation of the degree of cold plastic deformation on the mechanical properties, microstructure and corrosion behaviour (in model sulfuric acid solutions) of low-alloyed by chrome mild steel was carried out. It was established that with increase in the degree of deformation the tensile strength and the yield strength, as well as the hardness (about 2 times) increase. At the same time, the relative extension reduces at about one order of magnitude. The grain lengths increase

about 3 times while the residual stresses increase when the deformation rises to about 50 % degree of deformation. Beyond the 50% deformation the residual stresses reduces. The most preferred orientation of slipping during deformation is on the plain [100].

In the corrosion tests in model sulfuric acid solutions it was established that the highest corrosion rate was observed in the deformation range 40-50 %. With the non-deformed samples a general corrosion attack took place, but when the deformation was applied the corrosion attack was localized at the boundaries of the elongated grains and the affected areas were formed as scratched strips.

#### REFERENCES

1. A.P. Gulyaev, Metal Science (in Russian), Metalurgia, Moscow, 1977.
2. J. Kuchukov, Plastic Deformation of Metals (in Bulgarian), Technika, Sofia, 1976.
3. G. Belchenko, S. Gubenko, The Basic Metallography of Plastic Steel Deformation, Vishta Schola, Kiev, 1987.
4. A. Russakov, *Roentgenography of metals*, Atomizdat, Moscow, 1977 (in Russian)
5. W.D. France Jr., *Corrosion*, **26**, 189 (1970).
6. Z. A. Foroulis, H.H. Uhlig, *J. Electrochem. Soc.*, **111**, 522 (1964)
7. O.V. Kasparova, A.V. Pleskaev, *Zashchita Metallov*, **19**, 541 (1983)
8. D.M. Dražić, S. Gojković, S.K. Zečević, V. Radmilović, *Corrosion Sci.*, **33**, 791 (1992).
9. L. Fachikov, R. Raichev, *Chemistry and Industry* (in Bulgarian), **62**, 19 (1991).
10. R. Yordanova, D. Angelova, Plastic Deformation and Fracture of Metals. Physical Basis and Technological Descriptions. Methods for Mechanical Testing, Textbook for Laboratory Seminars and Experimental Work (in Bulgarian), UCTM, Sofia, 2010, p. 284.
11. D. Angelova, D. Kolarov, K. Philipov, R. Yordanova, Handbook in Metallurgy, Volume II: Metal Science and Plastic Deformation (in Bulgarian), Scientific editor Prof. D. Angelova, Academic Publishing House "M. Drinov", Sofia, 2009, p. 348.

## ВЛИЯНИЕ НА СТУДЕНАТА ПЛАСТИЧНА ДЕФОРМАЦИЯ ВЪРХУ МЕХАНИЧНИТЕ СВОЙСТВА И КОРОЗИОННОТО ПОВЕДЕНИЕ НА НИСКОЛЕГИРАНА (2% Cr) СТОМАНА

Д. И. Иванова, Г. П. Илиева, Л. Б. Фачиков

*Химикотехнологичен и металургичен университет, бул. „Кл. Охридски” 8, София 1756, България*

Постъпила на 21 ноември, 2016 г.; приета на 3 февруари, 2017 г.

(Резюме)

С помощта на разнообразни физични и електрохимични методи е изследвано влиянието на студената пластична деформация (0÷80%) върху най-важните механични показатели, микроструктурата, остатъчните след деформацията напрежения на нисколегирана с хром (~ 2%) стомана. Установено е, че с нарастване степента на деформация значително се повишават якостта на опън, границата на провлачване и твърдостта на стоманата, а относителното удължение се понижава близо с порядък. В моделни сернокисели разтвори най-висока скорост на корозия се наблюдава в деформационния диапазон 40-50%, когато от обща, корозионната атака се локализира по границите на удължените зърна под формата на бразди.



## CO and VOCs oxidation over alumina supported Cu-Mn catalysts modified by cerium

E.N. Kolentsova<sup>1,\*</sup>, D.Y. Dimitrov<sup>1</sup>, K.I. Ivanov<sup>1</sup>, T.T. Tabakova<sup>2</sup>, Y.G. Karakirova<sup>2</sup>,  
K.K. Tenchev<sup>2</sup>, G.V. Avdeev<sup>3</sup>

<sup>1</sup> Department of Chemistry, Agricultural University, 4000 Plovdiv, Bulgaria

<sup>2</sup> Institute of Catalysis, Bulgarian Academy of Science, 1113 Sofia, Bulgaria

<sup>3</sup> Institute of Physical Chemistry, Bulgarian Academy of Science, 1113 Sofia, Bulgaria

Submitted November 26, 2016; Accepted April 6, 2017

Catalytic oxidation is considered as one of the most promising and environment-friendly technologies for the abatement of CO and VOCs. The aim of this investigation was to study the effect of chemical composition, in particular the modification by cerium, on the activity and selectivity of the selected  $\gamma$ -alumina supported CuO-MnO<sub>2</sub> catalysts (Cu/Mn molar ratio 2:1 and 1: 5) in total oxidation of CO, dimethyl ether (DME) and methanol. The samples were characterized by BET, XRD, EPR and TPR. Structure-reactivity relationship was analyzed in order to explain the role of cerium.

**Keywords:** Copper-manganese-cerium catalyst, CO and VOCs oxidation.

### INTRODUCTION

The study of lanthanides for various catalytic processes has been the subject of increasing interest over the past few decades [1, 2]. It is well known that CeO<sub>2</sub> is widely used as a promoter and/or carrier in many catalytic oxidation reactions, due to the facilitated redox transition Ce<sup>4+</sup>/Ce<sup>3+</sup> and the high oxygen capacity [3]. Trovarelli [4] analysed in details the catalytic properties of CeO<sub>2</sub> and CeO<sub>2</sub>-containing materials and concluded that some of the most important factors determining the suitability of CeO<sub>2</sub> for complete oxidation of volatile organic compounds are the reducing capability and high instability of oxygen in its lattice. The addition of cerium oxide to catalysts based on transition metals deposited on aluminum oxide may improve the ability to store oxygen [5] and the dispersion of the metal particles [6], to stabilize the carrier [4], to increase the rate of reaction of CO with water vapor through the water-gas shift reaction and to provide lattice oxygen for the oxidation of adsorbed reagents [7]. Other publications showed that cerium oxide can improve the activity in complete oxidation reactions not only over catalysts containing noble metals, but also over catalysts based on transition metals [8]. The advantage of the catalysts based on transition metal oxides as compared to catalysts based on noble metals is associated with the lower cost, but also with higher thermal stability and resistance to catalyst poisons, which is essential for their performance [9]. At low

temperatures, they are less active than the catalysts based on noble metals but certain specific combinations of metal oxides can lead to an improvement of the activity in the reactions for volatile organic compounds (VOCs) elimination [10]. Many authors have reported that the mixed metal oxides are more active in the oxidation of VOCs in comparison with the single-component oxides. It has been found that the combinations of MnO<sub>x</sub>, Co<sub>3</sub>O<sub>4</sub>, CeO<sub>2</sub> and MnO<sub>x</sub>-CeO<sub>2</sub>, are just as active as deposited metal catalysts in the oxidation reaction of certain compounds [11]. The copper-containing catalysts for the elimination of CO from gaseous emissions are a subject of extensive studies in the scientific literature. Studies of Rao *et al.* [12] have shown that the oxide CuO-CeO<sub>2</sub> system is an effective catalyst in CO oxidation at low temperature due to the strong synergistic effect between the copper and CeO<sub>2</sub>. Shi *et al.* [13] have studied CuO and the catalytic system based on CeO<sub>2</sub> for the reduction of CO, NO and C<sub>3</sub>H<sub>6</sub>. Their results showed that CuO, distributed in CeO<sub>2</sub>/ $\gamma$ -Al<sub>2</sub>O<sub>3</sub>, increases the thermal stability of catalysts. According to [14], the introduction of small amounts of CeO<sub>2</sub> in CuO<sub>x</sub> leads to an increase in the dispersion of copper oxide.

The aim of present work was to study the modification of alumina supported mixed Cu-Mn oxides by introducing cerium and its effect on the activity and selectivity of the catalysts in total oxidation of CO, methanol, and dimethyl ether (DME).

\*) To whom all correspondence should be sent:

E-mail: [elitsa\\_kolentsova@abv.bg](mailto:elitsa_kolentsova@abv.bg)

## EXPERIMENTAL

### *Catalysts preparation*

Copper-rich Cu-Mn/ $\gamma$ -Al<sub>2</sub>O<sub>3</sub> sample with Cu/Mn molar ratio 2:1 and manganese-rich sample with Cu/Mn molar ratio 1:5 were modified by replacing manganese by Ce in the whole concentration range from 0 to 100%. All catalysts were prepared by wet impregnation of  $\gamma$ -Al<sub>2</sub>O<sub>3</sub> with fraction 0.6-1.0. Prior to the impregnation, the carrier was calcined for 2 hours at 450°C in a ceramic furnace. After keeping it at a room temperature, previously prepared solutions of copper, manganese and cerium nitrates were added. The support remained immersed for 12 hours in the salt solution at 80°C. After the impregnation samples were dried and calcined in the following sequence: 12 h drying at room temperature, followed by heating at 120°C for 10 h, after which the temperature was increased with 10°C/min up to 450°C and kept constant for 4 hours.

### *Sample characterization*

**Texture measurements.** The texture characteristics were determined by low-temperature (-196°C) nitrogen adsorption in a Quantachrome Instruments NOVA 1200e (USA) specific surface area&pore analyser. Pore diameter and total pore volume were determined in accordance with the Gurvich rule at a relative pressure close to 0.99, while the specific surface areas ( $S_{\text{BET}}$ ) were estimated through the Brunauer, Emmett and Teller (BET) method in a standard pressure range  $p/p_0=0.10-0.30$ .

**Powder X-ray diffraction (XRD).** X-ray powder diffraction (XRD) patterns for phase identification were recorded on a Philips PW 1050 diffractometer, equipped with Cu K $\alpha$  tube and scintillation detector. Data for cell refinements were collected in  $\theta$ -2 $\theta$ , step-scan mode in the angle interval from 10 to 90° (2 $\theta$ ), at steps of 0.03° (2 $\theta$ ) and counting time of 3 s/step. The cell refinements were obtained with the PowderCell program. The size-strain analysis was carried out using the BRASS-Bremen Rietveld Analysis and Structure Suite.

**Temperature programmed reduction (TPR).** Temperature-programmed reduction (TPR) of the samples was carried out in the measurement cell of

a differential scanning calorimeter model DSC-111 (SETARAM) directly connected to a gas chromatograph. The measurements were performed in the 30–650°C range at 15°C/min heating rate in flow of 10% H<sub>2</sub>/Ar, the total flow rate being 25 ml/min, sample amount 0,05g.

**Electron paramagnetic resonance (EPR).** The EPR spectra were recorded at JEOL JES-FA 100 EPR spectrometer operating in X-band with standard TE<sub>011</sub> cylindrical resonator under following conditions: modulation frequency 100 kHz, microwave power 1 mW, modulation amplitude 0.2 mT, sweep 500 mT, time constant 0.3 s and sweeping time 4 min.

**Catalyst testing.** The catalytic measurements of CO, methanol and DME oxidation were carried out on continuous flow equipment with a four-channel isothermal stainless steel reactor, containing 1.0 ml catalyst at atmospheric pressure and space velocity (GHSV) of 10000 h<sup>-1</sup>, allowing simultaneous examination of four catalysts under the same conditions. The flow of ambient air (40 – 50% humidity) and CO (final concentration 2.0%) were fed using mass flow controllers (GFC Mass Controller AABORG, Germany). Liquid methanol was cooled to 0°C in evaporator through which the stream of air was passing and additional air was added before reaching the preheater to final concentration of methanol 2.0%. DME (final concentration 0.8–1.0%) was obtained by dehydration of methanol in nitrogen flow on  $\gamma$ -Al<sub>2</sub>O<sub>3</sub> in tubular isothermal reactor. Gas mixtures on the input and output of the reactor were analyzed with a gas chromatograph HP 5890 Series II, equipped with FID and TCD detectors, column Porapak Q (for methanol, CO<sub>2</sub> and DME) and column MS-5A (for CO, oxygen and nitrogen).

## RESULTS AND DISCUSSIONS

### *Texture characteristics*

Table 1 shows the specific surface area, pore volume and average pore diameter of the support, samples with Cu/Ce 2:1 и 1:5 and modified sample Cu/(Mn+Ce) 1:5, in which 20% manganese is replaced by Ce. It is seen that the specific surface of the modified sample increases compared to the basic one. The pore volume and average pore diameter of catalyst samples are nearly identical.

**Table 1.** Specific surface, pore volume and average pore diameter of selected catalyst.

Composition	$S_{\text{BET}}$ [m <sup>2</sup> /g]	$V_{\text{total}}$ [cm <sup>3</sup> /g]	$D_{\text{aver.}}$ [nm]
Al <sub>2</sub> O <sub>3</sub>	219	0.40	7.40
Cu/Ce 2:1	156	0.29	7.30
Cu/Ce 1:5	165	0.29	7.00
Cu/(Mn+Ce) 1:5 20% Ce	193	0.30	6.10

## Powder X-ray diffraction (XRD)

The phase composition of the samples was analyzed on the basis of powder X-ray diffraction data. In Fig. 1 (a) are compared the XRD patterns of the catalysts with Cu:Mn molar ratio 2:1, in which manganese is replaced partially (20, 40, 60 and 80 %) or completely by cerium. The X-ray diffractogram of  $\text{CeO}_2/\text{Al}_2\text{O}_3$  is also shown for comparison. The reflections typical for CuO at  $2\theta = 35.6, 38.8, 48.6$  and  $61.8$  (marked with \*, JCPDS 02-1040) were observed in the X-ray diffractogram of the sample with Cu:Mn ratio 2:1. The

replacement of Mn by cerium led to decreased intensity of these peaks, due to partial amorphization of CuO phase. This phenomenon could be attributed to the formation of small CuO crystallites in agreement with well-known property of ceria to favor high dispersion of CuO particles. New peaks appeared at  $2\theta = 28.5, 33.1, 47.5$  and  $56.3$ , related to fluorite oxide-type diffraction pattern of  $\text{CeO}_2$  (marked with o, JCPDS 43-1002). These peaks are better discernible in the XRD pattern of Cu-Mn (60 and 80 wt.% Ce) due to the increased amount of separate phase of ceria.

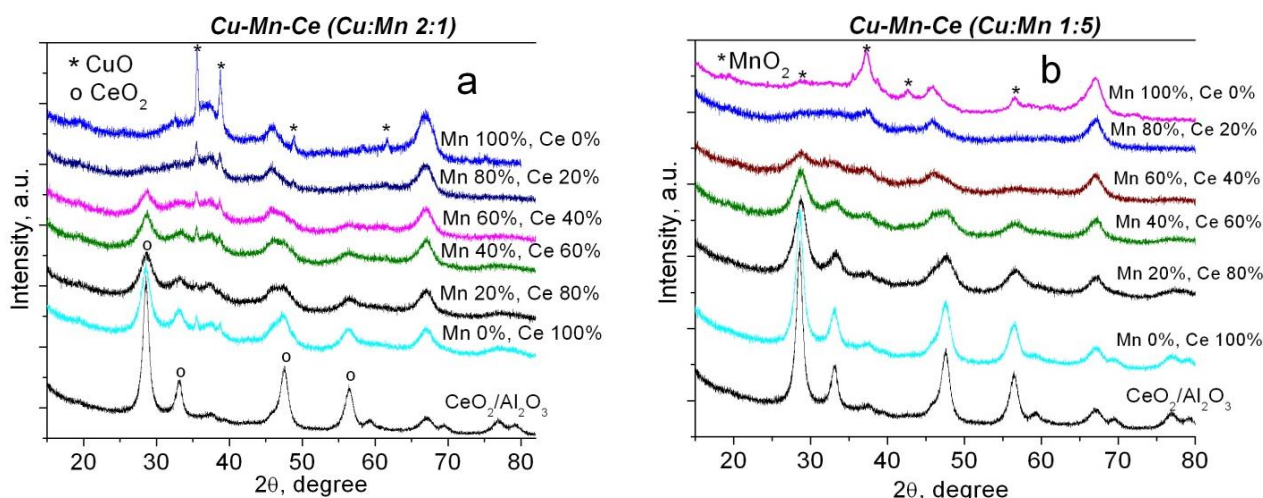


Fig. 1. XRD patterns of Cu-Mn-Ce catalysts with Cu/(Mn+Ce) molar ratio 2:1 (a) and 1:5 (b) after partial or total replacement of Mn by Ce.

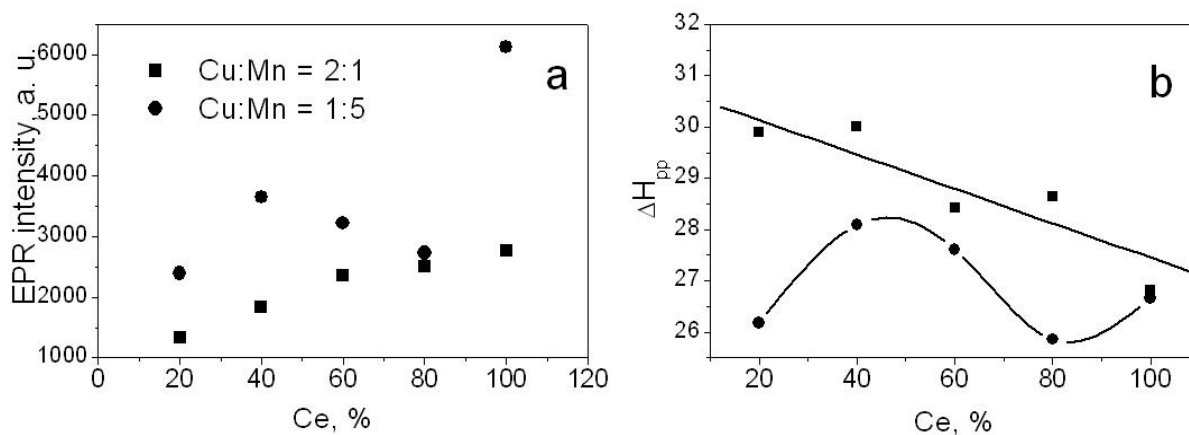


Fig. 2. EPR spectra intensity (a) and line width (b) of Cu-Mn-Ce catalysts with Cu/(Mn+Ce) molar ratio 2:1 (squares) and 1:5 (circles) depending on the content of Ce.

The XRD patterns of alumina supported catalysts with Cu:Mn molar ratio 1:5 after partial or total substitution of Mn by Ce are shown in Fig. 1 (b). Similarly to the observed above differences, the intensity of the reflections of  $\text{MnO}_2$  at  $2\theta = 28.6, 37.2, 42.8$  and  $56.5$  (marked with \*, JCPDS 24-0735) decreased upon replacement of Mn by Ce.

Obviously, the presence of separate phase of ceria was beneficial for dispersion of  $\text{MnO}_2$ .

## Electron paramagnetic resonance (EPR)

Experimental evidences for the role of cerium on the structural features of all samples were provided by EPR spectroscopic study. The EPR spectra of Cu-Mn/ $\gamma$ - $\text{Al}_2\text{O}_3$  samples with Cu/Mn

molar ratio of 2:1 and 1:5 with spectral parameters  $g_{\parallel} = 2.3572$  and  $g_{\perp} = 2.1025$  (not shown) were interpreted as arising from the distorted octahedrally coordinated  $\text{Cu}^{2+}$  ions. The four-line hyperfine splittings indicated presence of isolated  $\text{Cu}^{2+}$  ions ( $I=3/2$ ) on the  $\gamma$ -alumina surface. In Fig. 2 (a) is shown the dependence of the EPR spectrum intensity on the content of Ce. The results clearly demonstrated that the effect of cerium was closely related to Cu:Mn molar ratio. A gradual increase of the spectrum intensity due to higher content of cerium was observed for copper-rich Cu-Mn/ $\gamma$ - $\text{Al}_2\text{O}_3$  samples with Cu/Mn molar ratio of 2:1 (square symbol). This result indicated that the replacement of Mn with higher amount Ce was favorable for increasing of the number of isolated  $\text{Cu}^{2+}$  ions. Isolated  $\text{Cu}^{2+}$  ions can strongly interact with the support because they have no spin-spin interaction. This finding is in agreement with the tendency of decreasing EPR line width (Fig. 2, b) and could be related to improved distribution of

isolated  $\text{Cu}^{2+}$  ions in octahedral coordination with tetragonal distortion. The lack of dipole-dipole interaction may be considered as evidence for better dispersion of CuO in the presence of higher amount  $\text{CeO}_2$ . This suggestion agrees well with analysis of XRD data.

In the case of manganese-rich Cu-Mn/ $\gamma$ - $\text{Al}_2\text{O}_3$  samples with Cu/Mn molar ratio of 1:5, both dependences (Fig. 2 and b, circle symbols) passed through a maximum at 40 % Ce and a minimum at 80 % Ce. The relationship between catalytic activity and Ce content followed similar trend (Fig. 10). Considering higher amount of Mn in the samples with Cu/Mn molar ratio 1:5, it could be hypothesized that these complex dependences are related to the changes in the oxidation state of Mn. Another reason could be the dipolar coupling arising from the strong interaction of near-neighbor copper atoms and formation of clusters possessing antiferromagnetic couplings, which make them undetectable by EPR.

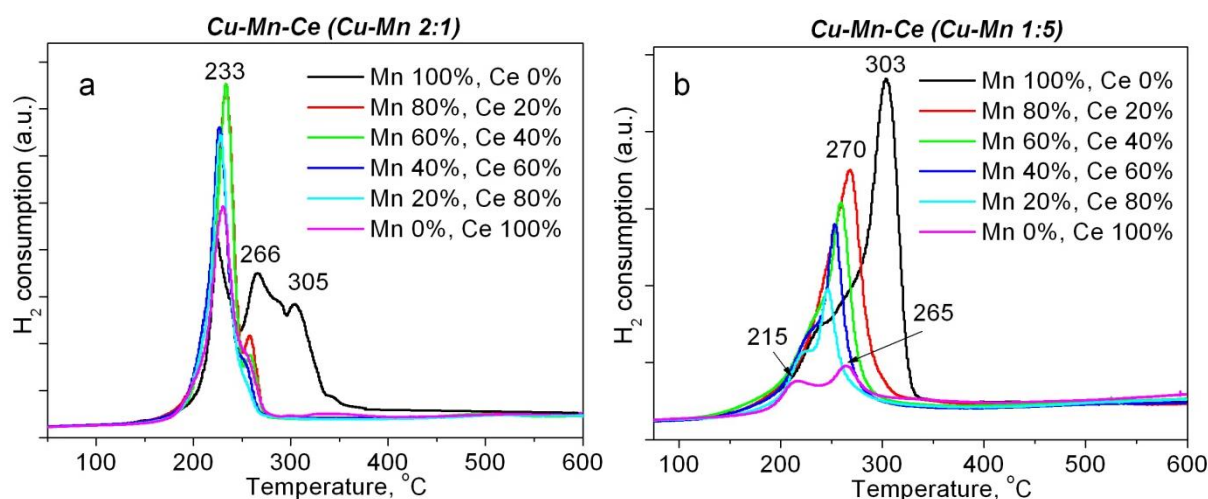


**Fig. 3.** TPR profiles of Cu-Mn-Ce catalysts with Cu/(Mn+Ce) molar ratio 2:1 (a) and 1:5 (b) after partial or total replacement of Mn by Ce.

#### *Temperature programmed reduction (TPR)*

The  $\text{H}_2$ -TPR was used to study the reducibility of the catalysts. As can be seen in Fig. 3, the TPR profiles are complex due to the reduction of  $\text{CuO}$  or  $\text{MnO}_2$  in addition to that of surface oxygen of ceria. The complex TPR profile of Cu-Mn with ratio 2:1 (black curve in section a) may be assigned to the reduction of separate  $\text{CuO}$  phase ( $T_{\max} 230^\circ\text{C}$ ), highly dispersed Cu-Mn spinel phase ( $T_{\max} 266^\circ\text{C}$ ) and some transition of  $\text{Mn}^{4+}$  to  $\text{Mn}^{3+}$ . The peak with well-defined maximum at  $303^\circ\text{C}$  in the profile of Cu-Mn with ratio 1:5 (black curve in section b) should be ascribed to reduction of  $\text{MnO}_2$ , while a

broad shoulder at the low-temperature side of the profile could be related to the reduction of  $\text{CuO}$ .

The analysis of TPR profiles of alumina supported Cu-Mn-Ce samples indicated that the reduction behavior was affected by the presence of separate ceria phase. It is known from the literature that  $\text{H}_2$ -TRP profile of ceria contains two major peaks, one at lower temperature (around  $500^\circ\text{C}$ ), assigned to the reduction of surface oxygen, and one at higher temperature (around  $800^\circ\text{C}$ ), attributed to the removal of bulk oxygen from the ceria structure [14]. Many authors have shown that some transition metals (Cu, Ni) [15] promote the surface reduction of  $\text{Ce}^{4+}$  to  $\text{Ce}^{3+}$ . The first reduction peak can be shifted to much lower

temperature, while the high-reduction peak remains unchanged.

The general finding in this work was the decreased hydrogen consumption in the samples containing Ce. However, it should be considered that the theoretical values of hydrogen consumption for ceria surface layers reduction (which is of interest in present case) according to literature data is limited to 17 % [16] or 20 % [17]. Stronger effect on samples reducibility due to replacement of Mn by Ce was observed for Cu-Mn-Ce samples with Cu/Mn molar ratio of 1:5. A significant shift of  $T_{max}$  to lower temperature was registered with increase of Ce content. The complex shape with two maxima in the profile of sample with 100% Ce (pink curve) could be explained with reduction of CuO ( $T_{max}$  215°C) and ceria surface oxygen ( $T_{max}$  265°C).

The results for CO, methanol and DME oxidation over Cu-Mn-Ce/ $\gamma$ -Al<sub>2</sub>O<sub>3</sub> catalyst with molar ratio Cu/(Mn+Ce) 2:1 and 1:5, in which Mn is replaced by Ce in the whole concentration range from 0 to 100%, are presented in Figs. 4-7. The results, presented in Fig. 4 (a) indicated that the catalytic activity of the samples with molar ratio Cu/(Mn+Ce) 2:1 varied significantly at the whole temperature range depending on the catalysts composition. There is a clear trend of increased activity by increasing the content of cerium. The oxidation reaction started above 80°C, while on the all mixed Cu-Mn-Ce/ $\gamma$ -Al<sub>2</sub>O<sub>3</sub> samples complete CO oxidation was achieved in the temperature range 180 - 200°C. For nonmodified Cu-Mn/ $\gamma$ -Al<sub>2</sub>O<sub>3</sub> catalyst this temperature was 200°C and for sample with total replacement of Mn, i.e. Cu-Ce/ $\gamma$ -Al<sub>2</sub>O<sub>3</sub> - significantly lower (160°C).

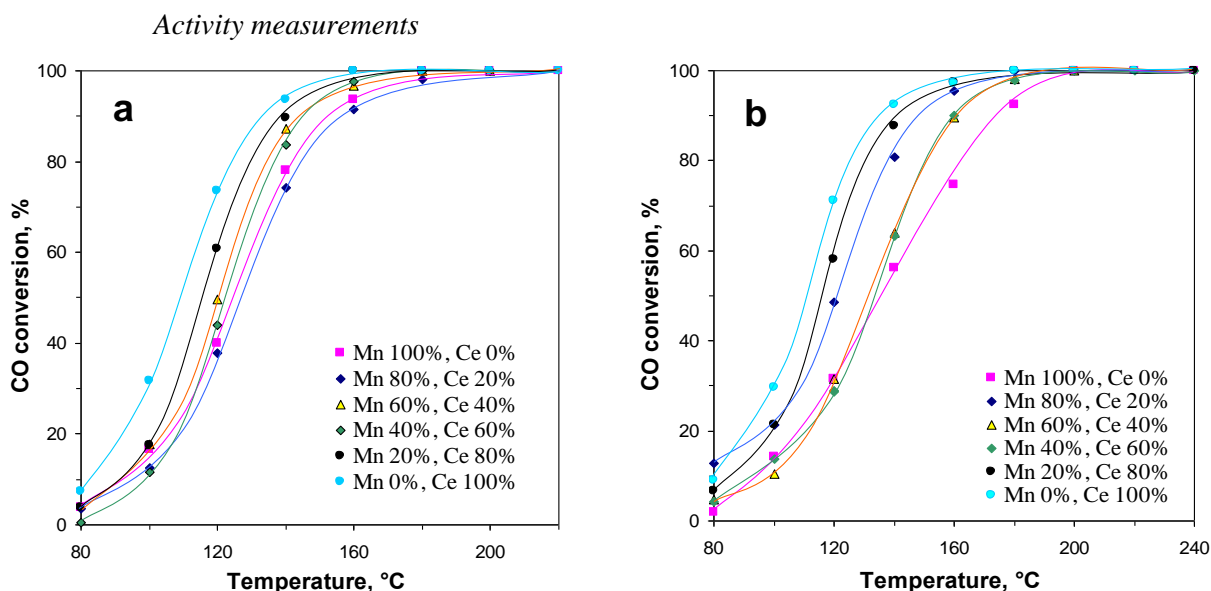


**Fig. 4.** Temperature dependence of CO oxidation over Cu-Mn-Ce/ $\gamma$ -Al<sub>2</sub>O<sub>3</sub> catalyst with Cu/(Mn+Ce) molar ratio 2:1 (a) and over Cu-Mn-Ce/ $\gamma$ -Al<sub>2</sub>O<sub>3</sub> catalyst with Cu/(Mn+Ce) molar ratio 1:5 (b).

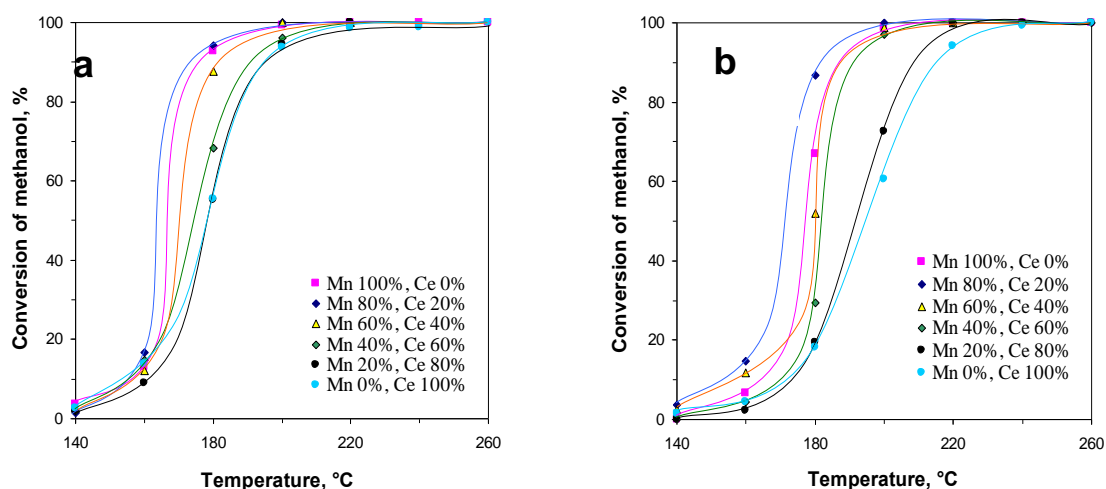


**Fig. 5.** Temperature dependence of methanol oxidation over Cu-Mn-Ce/ $\gamma$ -Al<sub>2</sub>O<sub>3</sub> catalyst with Cu/(Mn+Ce) molar ratio 2:1 (a) and Cu-Mn-Ce/ $\gamma$ -Al<sub>2</sub>O<sub>3</sub> catalyst with Cu/(Mn+Ce) molar ratio 1:5 (b).

The trend in the CO oxidation (Fig. 4, b) over the samples with molar ratio Cu/(Mn+Ce) 1:5 is similar to those represented in Fig. 4 (a). The samples with a high content of cerium showed high catalytic activity, while Cu-Mn/ $\gamma$ -Al<sub>2</sub>O<sub>3</sub> exhibited the lowest activity.

The oxidation of methanol (Fig. 5 a and b) over all samples started at 140°C and complete oxidation was reached at 220 - 240°C, observing the opposite tendency than in CO oxidation. In this case the

most active were the manganese-rich Cu-Mn/ $\gamma$ -Al<sub>2</sub>O<sub>3</sub> samples and the lowest activity demonstrated Cu-Ce/ $\gamma$ -Al<sub>2</sub>O<sub>3</sub>.

The oxidation of DME (Fig. 6 a, b) began at 220°C, and complete oxidation was attained at about 360°C except for the samples, containing a large amount of Ce (Mn20%/Ce80% and Ce100%). Unlike of CO and methanol oxidation, the best performance for DME oxidation was demonstrated by the sample modified with 20% Ce.

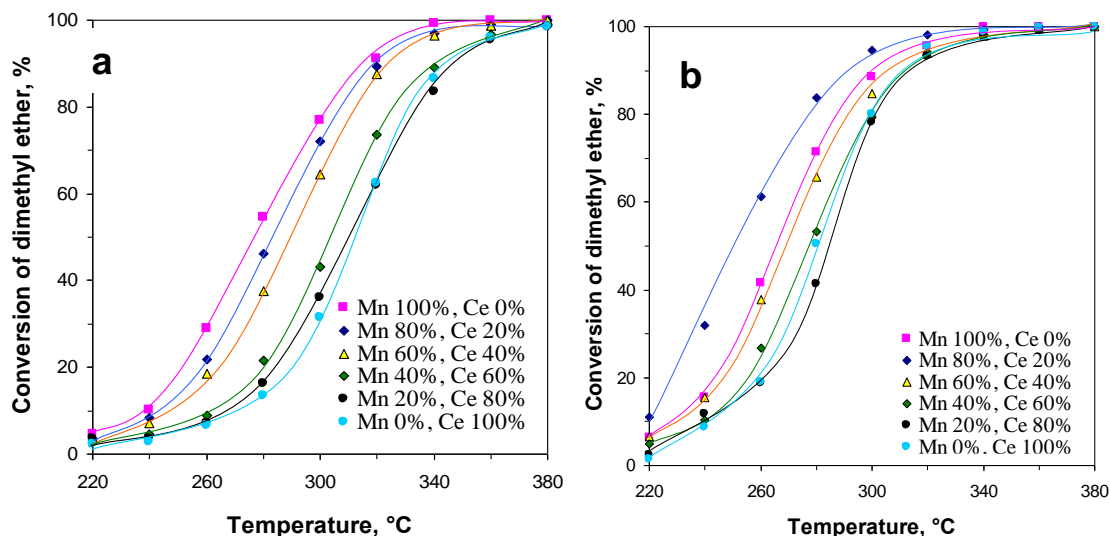


**Fig. 6.** Temperature dependence of DME oxidation over Cu-Mn-Ce/ $\gamma$ -Al<sub>2</sub>O<sub>3</sub> catalyst with Cu/(Mn+Ce) molar ratio 2:1 (a) and Cu-Mn-Ce/ $\gamma$ -Al<sub>2</sub>O<sub>3</sub> catalyst with Cu/(Mn+Ce) molar ratio 1:5 (b).

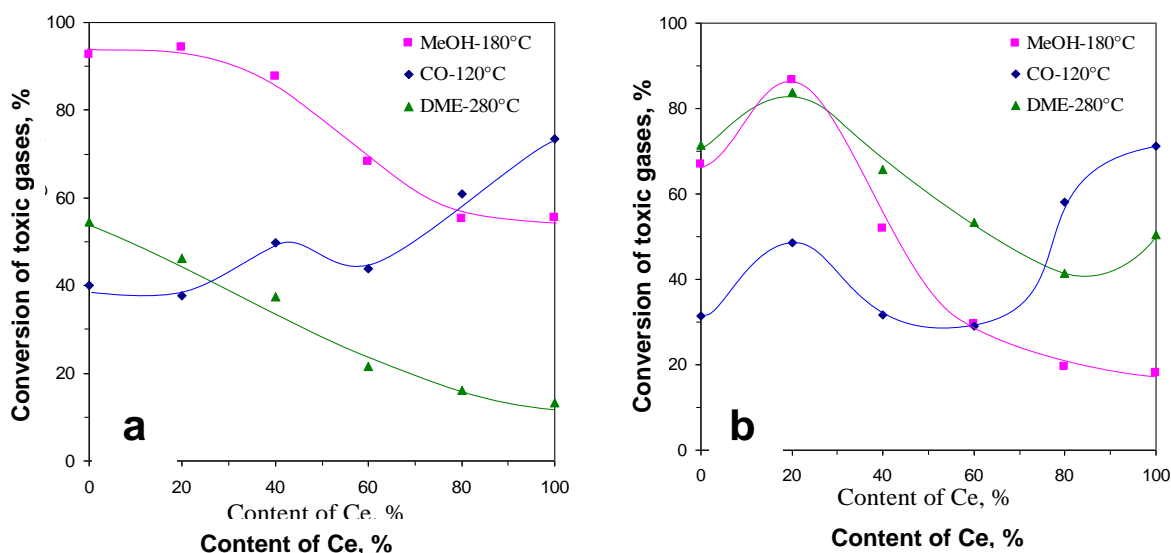


**Fig. 7.** Effect of ceria amount in the active component of Cu-Mn-Ce/ $\gamma$ -Al<sub>2</sub>O<sub>3</sub> catalysts with a molar ratio Cu/(Mn + Ce) 2:1 (a) and 1:5 (b) on CO, CH<sub>3</sub>OH and DME oxidation ( $T_{CO} = 120$  °C,  $T_{MeOH} = 180$  °C,  $T_{DME} = 280$  °C).

For easier interpretation of the results and assessment of the impact of manganese substitution

by cerium in the mixed Cu-Mn-Ce catalysts, part of the data are summarized in Figs. 7.

The results showed a general trend of increasing activity in CO oxidation and decreasing activity in methanol and DME oxidation with the increase of cerium content for both groups of catalyst. This general trend, however, contains specific features, depending on the composition of the catalyst and the type of the oxidized compound. The samples composed predominantly of copper (Cu/Mn molar ratio 2:1) exhibited increased degree of CO oxidation in the whole concentration region. This performance could be attributed to the formation of smaller CuO crystallites in the presence of ceria, in accordance with XRD and EPR results. Additionally, it should be considered the ability of ceria to provide active oxygen species via Mars–van Krevelen mechanism. As concerns the manganese-rich samples (Cu/Mn molar ratio 1:5) the slope of the curve is a little bit different and catalysts behavior should be related to very complex composition of these materials. Indeed, in XRD pattern of the sample Cu/Mn with molar ratio 1:5 (Fig. 1 b, pink line) were clearly observed reflections due to the presence of MnO<sub>2</sub>. Additionally, selected area of the image, obtained by TEM was carefully analyzed (not shown). The distances among the fringes were measured and the spacing of the fringes 0.293 and 0.250 nm closely corresponded to the (2 2 0) and (3 1 1) lattice plane of Cu<sub>1.5</sub>Mn<sub>1.5</sub>O<sub>4</sub>. Partial replacement of Mn by Ce led to formation of new phase of ceria, but this process was accompanied with decreased amount of separate MnO<sub>2</sub> phase and probably with lower content of spinel phase. Our very recent results indicated that alumina supported single Cu and Mn oxide catalysts were less active than mixed ones and the synergistic effect between copper and manganese oxides played a key role for increased CO oxidation activity [18]. In the samples with gradual increased content of ceria obviously were available diverse amounts of MnO<sub>2</sub>, Cu<sub>1.5</sub>Mn<sub>1.5</sub>O<sub>4</sub> and CeO<sub>2</sub> with different impact on the catalytic performance. The sample, in which Mn was totally replaced by Ce, exhibited more than twice higher degree of CO oxidation, indicating that the synergism between copper and cerium is more favourable for CO oxidation, than in the case of Cu and Mn.

With respect to methanol oxidation, the trends are in the reverse direction. The replacement of manganese with cerium led to decrease in the activity, more significant pronounced for the copper-rich samples.

In the case of copper-rich samples, the activity decreased insignificantly up to 40 % manganese replacement by Ce and further increase of Ce

content caused gradual loss of about 30 % degree of CH<sub>3</sub>OH conversion. In contrast to the performance in CO oxidation, the increased amount of separate CeO<sub>2</sub> phase does not contributed for better CH<sub>3</sub>OH oxidation activity. Although XRD and EPR results revealed better dispersion of CuO in the samples with higher content of ceria, obviously the composition, i.e. twice higher amount of CuO is not beneficial for the catalytic performance. The activity of manganese-rich catalysts passed through a maximum at 20 % Mn replacement by Ce, after which followed rapid decrease. This is in agreement with EPR results, showing formation of CuO clusters and decreasing the number of the isolated Cu<sup>2+</sup> ions in the presence of CeO<sub>2</sub>.

The activity in the oxidation of DME followed the same tendency of decreasing with Mn replacement for both groups of catalysts and this is more pronounced for the copper-rich samples. The activity of the samples with Cu-Mn molar ratio 1:5 is much higher than that of the samples with Cu-Mn molar ratio 2:1. This behavior should be related to the substantial difference in the individual activity of copper and manganese toward DME oxidation, recently reported [18]. As in the cases of CO and methanol oxidation the replacement of small amount of manganese with cerium (to 20% Ce) led to an increase in activity of the samples with Cu/Mn molar ratio 1:5, after which the activity decreases significantly because of the reasons, described above.

The results for CO, methanol and DME oxidation can not be connected with the texture characteristics, presented in Table 1. Obviously, the catalysts composition is the decisive factor controlling the catalytic activity.

Summarizing the analysis of catalytic measurements data, it was found that the presence of separate phase of ceria affected positively mainly the CO oxidation activity. The interpretation of the relationship between composition and catalytic activity inferred the role of the reducibility on the different performance in oxidation of CO, CH<sub>3</sub>OH and DME. The amount of consumed hydrogen during TPR measurements of all Ce-containing samples was lower than the one of alumina supported Cu-Mn samples. In a recent paper, the MeOH oxidation activity of these samples was correlated with better reducibility due to the presence of structural defects, in particular oxygen vacancies [18]. The availability of lower amount mobile lattice oxygen in the case of Cu-Mn-Ce samples could be the reason for observed trends in catalysts behavior.

## CONCLUSIONS

The results presented showed that:

- The substitution of manganese by cerium in the mixed Cu-Mn-Ce/ $\gamma$ -Al<sub>2</sub>O<sub>3</sub> catalysts with molar ratio Cu/(Mn + Ce) 2:1 and 1:5 resulted in materials with very complex composition.
- The presences of a separate phase of ceria affected favorably the CO oxidation activity. This finding could be explained by the ability of ceria to take part in the oxidation reaction providing active oxygen species via Mars–van Krevelen

mechanism. The replacement of small amount of manganese with cerium (up to 20% Ce) was beneficial for an increase in CO, methanol and DME oxidation activity of the samples with Cu/Mn molar ratio 1:5.

The reducibility, i.e. mobility of lattice surface oxygen, influenced catalytic performance in methanol and DME oxidation.

**Acknowledgement.** The authors acknowledge the support by the Bulgarian NSF (Project DFNI T 02/4).

## REFERENCES

1. A. Urbutis, S. Kitrys, *Chemija*, **24**, 117 (2013).
2. G.S. Gallego, J.G. Marin, C. Batiot-Dupeyrat, J. Barrault, F. Mondragon, *Appl. Catal. A*, **369**, 97 (2009).
3. G. Rattan, R. Prasad, R.C. Katyal, in 21<sup>th</sup> Thai Institute of Chemical Engineering and Applied Chemistry International Conference (TICChE 2011), Hatyai, Songkhla, Thailand, 2011.
4. Trovarelli, *Catal. Rev. Sci. Eng.*, **38**, 439 (1996).
5. D. Leitenburg, A. Trovarelli, F. Zamar, S. Maschio, G. Dolcetti, J. Llorca, *J. Chem. Soc. Chem. Comm.*, **21**, 2181 (1995).
6. Holmgren, B. Andersson, D. Duprez, *Appl. Catal. B*, **22**, 215 (1999).
7. W. Liu, M. Flytzani-Stephanopoulos, *Chem. Eng. J.*, **64**, 283 (1996).
8. S.C. Kim, W.G. Shim, *Envir. Techn.*, **29**, 535 (2007).
9. R. Prasad, P. Singh, *Catal. Rev. Sci. Eng.*, **54**, 224 (2012).
10. A.H. Ulukardesler, *Energy Sources, Part A*, **35**, 1218 (2013).
11. X.F. Tang, Y.G. Li, X.M. Huang, Y.D. Xu, H.Q. Zhu, J.G. Wang, W.J. Shen, *Appl. Catal. B*, **62**(3-4), 265 (2006).
12. K. Rao, P. Bharali, G. Thirumurthulu, *Catal. Commun.*, **11**, 863 (2010).
13. Shi, L. Xu, A. Zhu, Y. Zhang, C.T. Au, *Chin. J. Catal.*, **33**, 1455 (2012).
14. H.C. Yao and Y.F. Yu Yao, *J. Catal.*, **86**, 254 (1984).
15. Y. Li, Q. Fu, M. Flytzani-Stephanopoulos, *Appl. Catal. B*, **27**, 179 (2000).
16. M.G. Sanchez, J.L. Gazquez, *J. Catal.*, **104**, 120 (1987).
17. Laachir, V. Perrichon, A. Bardi, J. Lamotte, E. Catherine, J. Lavalley, J. El. Faallah, L. Hilaire, F. Normand, E. Quemere, G. Sauvion, O. Touret, *J. Chem. Soc. Faraday Trans.*, **87**, 1601 (1991).
18. K. Ivanov, E. Kolentsova, D. Dimitrov, G. Avdeev, T. Tabakova, *Int. J. Chem. Molec. Nuclear Mater. Metallurg. Eng.*, **9**, 669 (2015).

## ОКИСЛЕНИЕ НА СО И ЛОС ВЪРХУ НАНЕСЕНИ НА АЛУМИНИЕВ ОКСИД Cu-Mn КАТАЛИЗАТОРИ, МОДИФИЦИРАНИ С ЦЕРИЙ

Е.Н. Коленцова<sup>1,\*</sup>, Д.Я. Димитров<sup>1</sup>, К.И. Иванов<sup>1</sup>, Т.Т. Табакова<sup>2</sup>, Й.Г. Каракирова<sup>2</sup>, К.К. Генчев<sup>2</sup>, Г. В. Авдеев<sup>3</sup>

<sup>1</sup> Катедра „Обща химия“, Аграрен университет, 4000 Пловдив, България

<sup>2</sup> Институт по катализ, Българска академия на науките, 1113 София, България

<sup>3</sup> Институт по физикохимия, Българска академия на науките, 1113 София, България

Постъпила на 26 ноември 2016 г.; приета на 6 април 2017 г.

(Резюме)

Каталитичното окисление се счита за една от най-обещаващите и екологично чисти технологии за намаляване съдържанието на СО и летливи органични съединения. Целта на това проучване е да се изследва ефекта на химичния състав, по точно модифицирането с церий, върху активността и селективността на нанесени върху  $\gamma$ -алуминиев оксид CuO-MnO<sub>2</sub> катализатори (молно съотношение Cu/Mn 2:1 и 1:5) по отношение на пълното окисление на СО, диметилов етер (DME) и метанол. Катализаторните образци са охарактеризирани с рентгеноструктурен анализ (XRD), текстурни изследвания, електронен парамагнитен резонанс (EPR) и температурно-програмирана редукция (TPR). Зависимостта между структурата и реактивоспособността на изследваните образци е анализирана с цел обяснение на ролята на добавката от церий.



## Synthesis and photophysical properties of a novel benzanthrone pH sensor based on internal charge transfer

P.M. Miladinova<sup>a\*</sup>, D.A. Todorova<sup>b</sup>

<sup>a</sup> Department of Organic Synthesis and Fuels, University of Chemical Technology & Metallurgy, 8 Kliment Okhridski Blvd, 1756 Sofia, Bulgaria

<sup>b</sup> Department of Pulp, Paper and Printing Arts, University of Chemical Technology & Metallurgy, 8 Kliment Okhridski Blvd, 1756 Sofia, Bulgaria

Submitted December 1, 2016; Accepted May 18, 2017

A novel fluorescence sensing derivative of 3-aminobenzanthrone configured as a “fluorophore-receptor” system was synthesized by nucleophilic substitution of 3-aminobenzanthrone with benzoyl chloride. Synthesized compound was isolated, characterized and identified by TLC, UV-vis, IR and <sup>1</sup>H NMR spectra. Due to the internal charge transfer, the designed fluorophore was able to act as a pH-probe via an “off-on” fluorescence sensing mechanism. The sensor activity toward protons as cations and hydroxide as anions in solution of DMF/water (1:1) and on cellulose paper was studied by monitoring the changes of the fluorescence intensity. The fluorescence changes indicated that the compound would be able to act as an efficient “off-on-off” switch for pH determination, for monitoring of aggressive environment, e.g., in concrete and industrial pollutants.

Keywords: 3-aminobenzanthrone derivative, ICT (internal charge transfer), pH sensor.

### INTRODUCTION

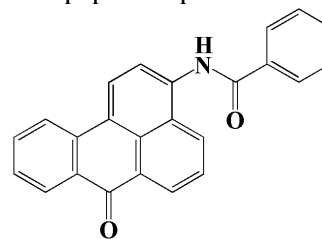
pH is a key parameter for a wide range of applications in the medical field, in environmental and life sciences or for regulation and routine monitoring in industrial processes and in sewage purification plants [1-12]. Fluorescent pH probes usually suffer from optical changes in terms of emission spectra variation and fluorescence intensity. Optical pH sensors based on changes of emission intensity and lifetime have been intensively studied as they can be non-invasive or minimally invasive, disposable, easily miniaturized (down to sub-micrometer), and simple to process (as a coating or solid layer on optical fibers and certain surfaces) for environmental analysis, medical diagnosis, and process control [13-25].

Internal charge transfer (ICT) is one of common principles used for fluorescence molecular switches [26-31]. In the ICT chemosensors the receptor is directly attached to the electron-donating/withdrawing unit that is conjugated to the fluorophore an electron-withdrawing/electron-donating unit. During excitation of the system the fluorophore undergoes donor-acceptor intramolecular charge transfer. The subsequent change in the dipole moment results in a Stokes shift that depends on the microenvironment of the fluorophore. In addition to these shifts, changes in quantum yields and lifetimes are often observed [31-38].

Benzanthrone derivatives attract particular

interest due to their favorable spectral properties - large extinction coefficient, marked Stokes shift, high sensitivity of fluorescence parameters to environmental polarity, etc. [39-43]. Derivatives of benzanthrone are well known as fluorophores emitting fluorescence from yellow-green to orange-red. Bright color and intense fluorescence of benzanthrone gave the impetus to their use as disperse dyes for textiles, daylight fluorescent pigments, dyes for polymers [44-54], lasers, as components in liquid-crystalline systems for electro-optical displays [46, 47, 55-57] or as sensors for biological important metal ions and amines [58-62]. The amidinobenzanthrone derivatives have showed potential as biomedical probes for proteins, lipids, and cells. Such dyes can be also utilized as suitable sensing probes for checking solvent polarity [63-67].

This paper reports on the design and synthesis of novel ICT based amidinobenzanthrone fluorophore (**1**). Also, the photophysical properties of the new compound in presence of protons as cations and hydroxide as anions in solution of DMF/water (1:1) and on cellulose paper are presented.



Formula 1 (**1**).

\*) To whom all correspondence should be sent:

E-mail: ppolya@uctm.edu

## EXPERIMENTAL

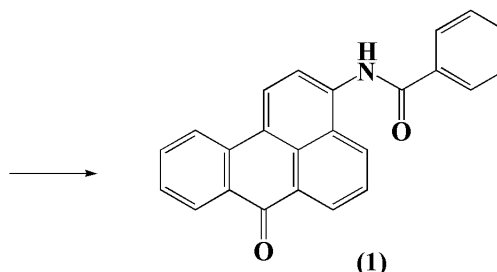
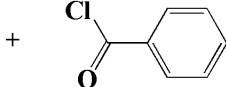
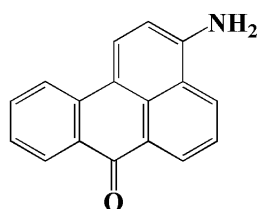
### Materials and methods

3-Aminobenzanthrone was prepared [55] by nitration of benzanthrone with fuming nitric acid and subsequent reduction of the nitro group from the 3-nitrobenzanthrone by Na<sub>2</sub>S. M.p. = 245–246 °C (cc. [55] 246 °C). Solvents are of p.a or analytical grade (Fluka).

The melting point was recorded on a Büchi 535 apparatus (Switzerland). TLC was made on silica gel plate (Merck, 60 F 254, 20x20 cm, 0.2 mm thickness, ready-to-use).

A pH meter Metrohm 704 coupled with combined pH electrode for the pH measurement was used. The commercial standard buffers for pH 2, 7 and 10 (Aldrich) were used for calibration. The absorption spectra were acquired on Hewlett Packard 8452A spectrophotometer. The fluorescent spectra were recorded on a Scinco FS-2 fluorescence spectrophotometer. The excitation source was a 150 W Xenon lamp. Excitation and emission slits width were 5 nm. Fluorescence measurement was carried out in right angle sample geometry. A 1×1 cm quartz cuvette was used for the spectroscopic analysis of the solutions. Fluorescence measurements on the previously dyed paper were carried using standard buffers.

The fluorescence quantum yields ( $\Phi_F$ ) were measured relatively to Coumarin 6 ( $\Phi_F = 0.78$  in ethanol [68] as a standards. All experiments were performed at room temperature (25 °C).



**Scheme 1.** Synthesis of 3-benzamidobenzanthrone (**1**).

### Characteristics of the compound (**1**)

Acylation of the primary amino group with benzoyl chloride was carried out (at reflux during 2 h in dioxane solution). By pouring the reaction mixture into water and filtration the precipitate was obtained. The product was purified by preparative TLC. FT-IR and <sup>1</sup>H NMR spectroscopic studies confirmed the chemical structure of new product.

The photophysical properties of compound (**1**) were investigated in different of polarity solvents at concentration of  $1 \times 10^{-5}$  mol l<sup>-1</sup>. Table 1 summarizes the basic spectral characteristics of (**1**) in chloroform, acetone and dimethylformamide (DMF) solutions: the values of absorption ( $\lambda_A$ ) and fluorescence ( $\lambda_F$ ) maxima, molar extinction

### Synthesis of *N*-(7-oxo-7H-benzo[de]anthracen-3-yl)benzamide or 3-benzamidobenzanthrone (**1**)

3-Aminobenzanthrone [2.45g (0,01 mol)] was dissolved in dioxane (50 mL) and to this solution at 50 °C benzoyl chloride [2.81ml (0,02 mol)] was added drop wise. The temperature was raised to boiling and the mixture was stirred at this temperature for 2 hours. The target compound (**1**) was obtained by pouring into water and filtering. It was purified by preparative thin-layer chromatography (TLC) (n-hexane:acetone = 2/1, v/v) on silica gel.

Yield for crude product 84%, m.p. = 177 °C, R<sub>f</sub> = 0.62 (n-hexane:acetone = 2/1, v/v), IR (KBr) cm<sup>-1</sup>: 3434 (ν-NH), 3055 (ν<sup>as</sup> ArCH), 1719 (ν-C=O), 1647 (νC=O), 1598 and 1576 (δ-NH), 1303 and 1277 (ν-C-N-), 779 (δArCH);

<sup>1</sup>H NMR (CDCl<sub>3</sub>, 600 MHz), ppm: 8.80–8.79 (ds, 1H, NH), 8.50–8.46 (m, 4H, ArH), 8.33–8.29 (m, 3H, ArH), 8.10–8.06 (m, 2H, ArH), 7.84–7.81 (t, 1H, ArH), 7.78–7.76 (t, 1H, ArH), 7.67–7.66 (m, 1H, ArH), 7.62–7.60 (m, 1H, ArH), 7.57–7.55 (m, 1H, ArH).

## RESULTS AND DISCUSSION

### Synthesis of 3-benzamidobenzanthrone (**1**)

The synthetic route used for the preparation of 3-benzamidobenzanthrone (**1**) is outlined in.

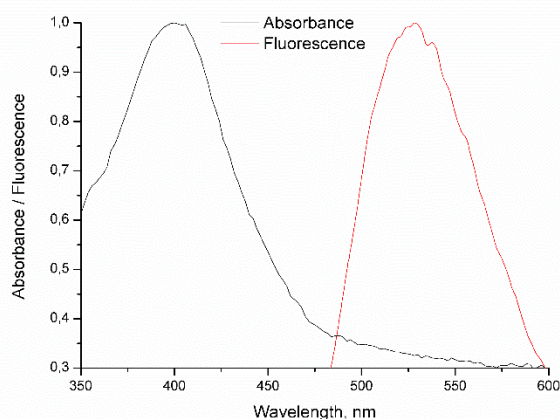
coefficient ( $\epsilon$ ), Stokes shift ( $\nu_A - \nu_F$ ) and quantum yield of fluorescence ( $\Phi_F$ ).

The absorption maximum of (**1**) is shifted hypsochromically if compared to that of 3-aminobenzanthrone (522 nm in dimethylformamide), due to the weaker electron donating ability of the amide group than the amino group.

At room temperature, a weak emission is observed between 480 and 600 nm with  $\lambda_F$  at 515.2 nm (chloroform) till 528.2 nm (dimethylformamide), corresponding to a S<sub>1</sub>/S<sub>0</sub> transition. Fig. 1 presents the normalized absorption and fluorescence spectra of (**1**) in dimethylformamide solution as an example.

**Table 1.** Photophysical characteristics of compound (**1**) in different solvents

Solution	$\lambda_A$ (nm)	$\epsilon$ ( $l \text{ mol}^{-1} \text{ cm}^{-1}$ )	$\lambda_F$ (nm)	$\nu_A - \nu_F$ ( $\text{cm}^{-1}$ )	$\Phi_F$
Chloroform	394	10290	515.2	5971	0.29
Acetone	390	11840	517.8	6328	0.21
Dimethylformamide	396	11560	528.2	6320	0.22

**Fig. 1.** Normalized absorption and fluorescence spectra of (**1**) in dimethylformamide solution.

As seen from Fig. 1, the absorption and fluorescence spectra have bands with a single maximum. The fluorescence curve is an approximately equal mirror image of the absorption curve which is indicative of the molecular structure of compound in excited state and prevailing fluorescence emission. The overlap between absorption and fluorescence spectra is low and an aggregation effect for the concentration at about  $1 \times 10^{-5} \text{ mol l}^{-1}$  has not been observed.

#### *Influence of pH on absorption and fluorescent properties of probe (1)*

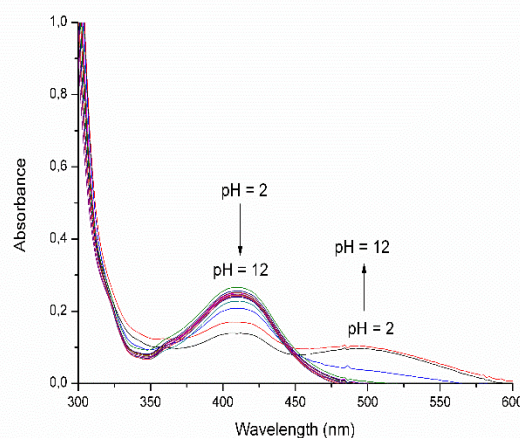
**Investigations in solution.** The compound under study was designed as fluorescence sensor for determining pH changes over a wider pH scale. This was the reason to investigate the photophysical behaviour of probe (**1**) in water/DMF (1:1, v/v) solution at different pH values.

The basic spectral characteristics of 3-benzamidobenzanthrone depends on the polarization of benzanthrone molecule, due to the electron donor-acceptor interaction occurring between the amino substituent and the carbonyl groups from the chromophoric system. Thus it can be predicted that the interaction of a guest with the donor moiety will change the photophysical properties of the fluorophore.

The amide fragments are widely used functional group in anion recognition. They can recognize anions through hydrogen-bonding and deprotonation interactions [69, 70]. As a result it is expectable that synthesized compound is able to detect anions. When an anion interacts with the benzanthrone

fluorophore amide, the carbonyl electron-accepting ability is reduced due to the deprotonation of the amides which generates a strong electron density near the carbonyl group. In a result the ICT efficiency in the 3-amidobenzanthronic fluorophore increases and red shifting and higher quantum yield are expectable.

With regard to the practical application of (**1**) as a pH sensor, absorption spectra in solution of DMF/water (1:1, v/v) at different pH have been investigated (Fig. 2).

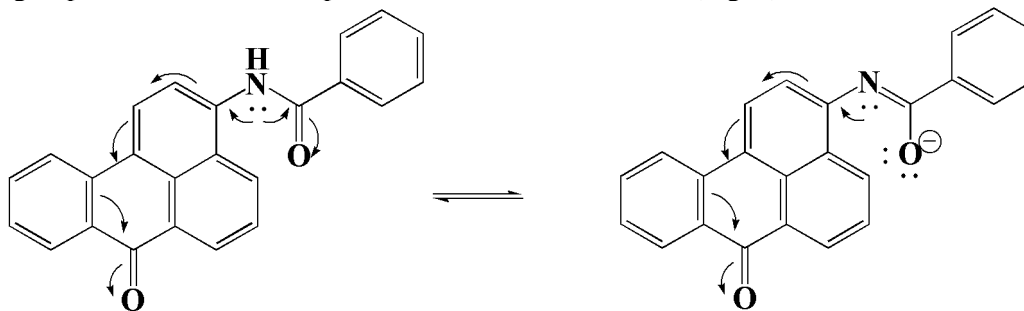
**Fig. 2.** Absorption spectra of compound (**1**) in DMF/water (1:1, v/v) at different pH.

In DMF/water (1:1, v/v) solution compound (**1**) shows longest-wavelength absorption band in range 350-500 nm (in pH range 2-9) and 350-600 nm (in pH range 10-12), which is attributed to the typical for the 3-aminobenzanthrone ICT process. With

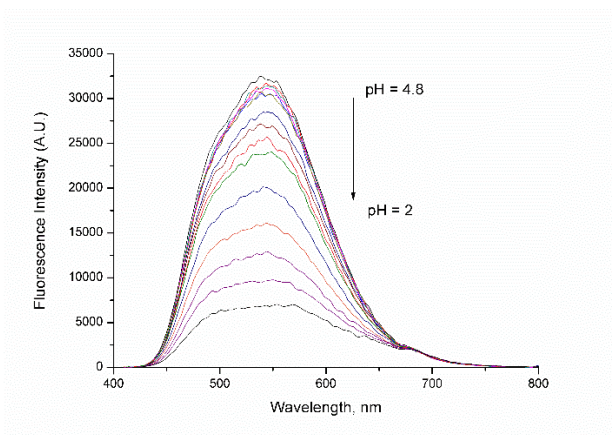
increasing of the alkalinity, the absorption maximum is shifted bathochromically, which corresponded on the deprotonation of the imino group and restores the ICT.

Scheme 2 shows the option for a significant interaction between benzanthrone chromophor and the amide group as receptor via nitrogen atom existing in the molecule of the compound. In this case the unshared electron pair of nitrogen atom interacts with p-electron system of the carbonyl from the amide group, which leads to a partial double

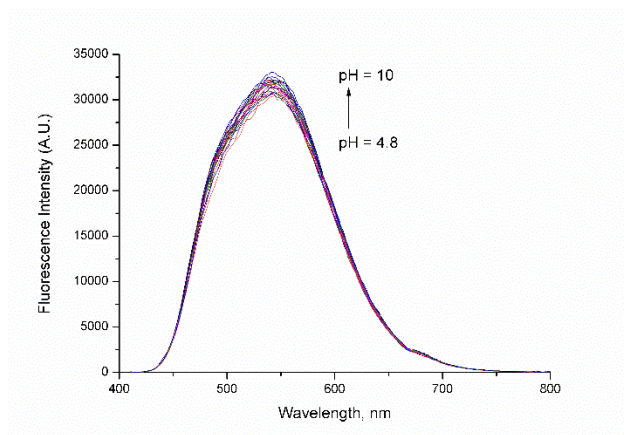
character of the C-N bond. The amide group atoms are located on the same plane and the wide-angle rotation around the C-N amide bond is hindered. In contrast, the unshared electron pair of nitrogen atom interacts with p-electron system of the aromatic chromophore. This leads to an increase in the electron donating properties of the substituent at 3 position of the chromophore molecule and to an increase in the conjugated chromophoric system. As a result, the bathochromic shift in absorption spectra is observed (Fig. 2).



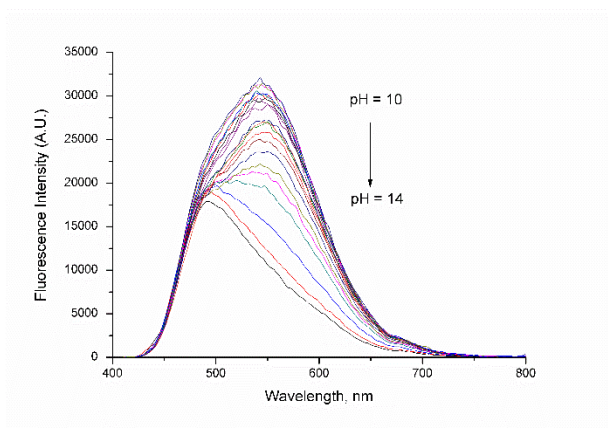
**Scheme 2.** Schematic presentation of protonated and deprotonated forms of compound (1).



(a)



(b)



(c)

The changes in the fluorescence spectra of compound (1) in water/DMF (1:1, v/v) solution at different pH values are depicted in Fig. 3a-c.

**Fig. 3.** Fluorescence spectra of probe (1) in water/DMF (1:1, v/v) solution at different pHs.

The emission spectra of compound under study showed that the compound (1) has fluorescence in the range between 430 and 700 nm.

The strongest fluorescence was observed at pH window 4.8-10 with maximum 538.7-541.4 nm (Fig. 3b). At this pH window the molecule is in "on state". The addition of HCl (pH 4.8-2) to probe (1) converts the imino group in quaternary ammonium cation which strongly decreases the electron donating ability of the nitrogen atom in receptor moiety and decreased the ICT process. At this pH window the compound (1) has fluorescence with maximum at 534.9 nm and the molecule is in "off state" (Fig. 3a). The addition of KOH (pH 4.8-10) to

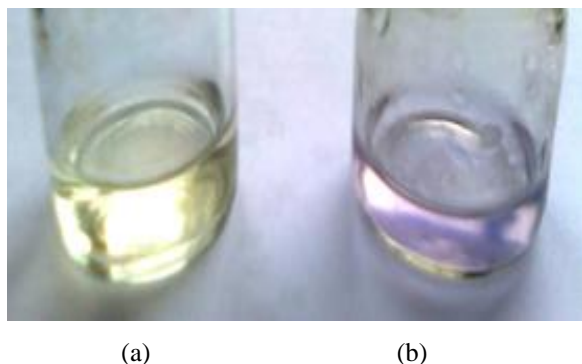


**Fig. 4.** Change in color of the tested compound in a solution of DMF / water = 1: 1 of neutral (pH 7) (a) in an alkaline (pH 12) (b) medium.

As a whole, a pH titration curve reflecting the "off-on-off" fluorescence response for compound (1) was achieved (Fig. 5). The analysis of the fluorescence changes as a function of pH according to the Eq. (1) gives two pKa values for the compound, for protonated (pKa = 3.55) and deprotonated (pKa = 8) forms respectively.

$$\log [(IF_{\max} - IF) / (IF - IF_{\min})] = \text{pH} - \text{pKa} \quad (1)$$

The calculated quantum yields of fluorescence are: 0.06 (pH 2), 0.17 (pH 8) and 0.04 (pH 12).

#### Investigations on paper

Because the compound under study was designed as fluorescence sensor for determining pH changes we decided to investigate the photophysical behaviour of compound (1) on paper at different pH values. The obtained paper samples consist of bleached hardwood and softwood pulp in ratio 1:1. The paper weight was 76 g/m<sup>2</sup>. The changes in the fluorescence spectra of compound (1) on paper previously dyed with dye solution with concentration 1.10<sup>-4</sup> g/ml in chloroform at different pH values are depicted in Fig. 6. The emission spectra of compound under study showed that the compound (1) has fluorescence in the range between 430 and 650 nm. The strongest fluorescence was

probe (1) increases the electron donating ability of the nitrogen atom in receptor moiety and increased the ICT process. At this pH window the compound (1) has fluorescence with maximum at 541.4-548.8 nm and the molecule is in "on state" (Fig. 3b). At pH over 10 the fluorescence decreases, because the reduction of carbonyl group occurs probably ( $\lambda_{\max}^{\text{fl}} = 492$  nm) (Fig. 3c). There is a visible change in the color of the solution of the tested compound, which is typical for the reduction of the carbonyl group at benzanthrone (Fig. 4).

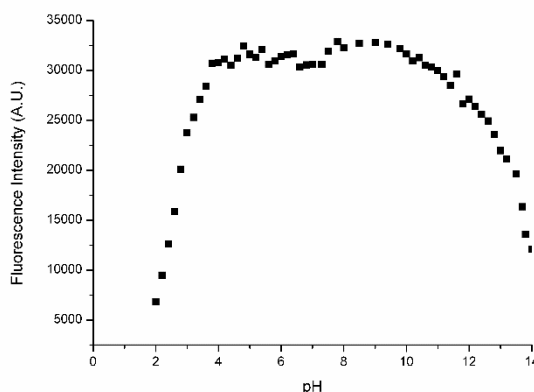


**Fig. 5.** Fluorescence intensity of compound 1 at 540 nm in water/DMF (1:1, v/v) as a function of pH.

observed at pH 4.5 with maximum 494.2 nm (Fig. 6). At pH 2 the fluorescence was lowest and with maximum at 483.7 nm. The investigation on the paper show similar results as the investigation in solution of water/DMF (1:1, v/v).

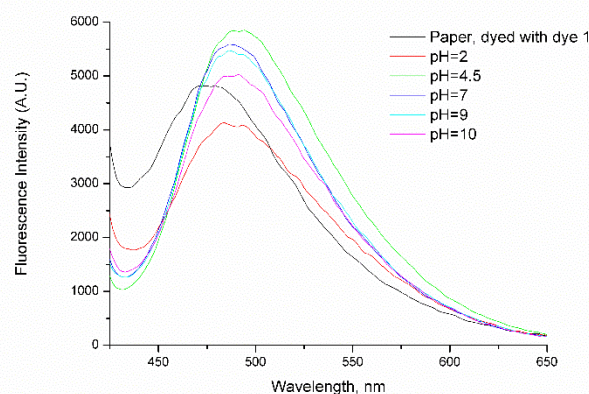


**Fig. 6.** Fluorescence spectra of probe 1 on paper at different pHs.

#### CONCLUSIONS

The synthesis and characterization of new 3-benzamidobenzanthrone has been described. The photophysical behavior of new fluorescent pH sensor in DMF/water and on paper as a function of pH was studied. The system is in "on-state" in the

range of pH 4.5-10. The effect was supposed to be related to the deprotonation of the amide receptor in this pH window. The fluorescence changes indicated that the sensors (**1**) would be able to act as an

efficient “off-on-off” switch for pH determination, for monitoring of aggressive environment, e.g., in concrete and industrial pollutants.

#### REFERENCES

1. R. Wang, C. Yu, F. Yu, L. Chen, *Trends in Analytical Chemistry*, **29**, 1004 (2010).
2. Z.-Q. Hu, M. Li, M.-D. Liu, W.-M. Zhuang, G. Li, *Dyes Pigm.*, **96**, 71 (2013).
3. W. Jin, J. Jiang, X. Wang, X. Zhu, G. Wang, Y. Song, C. Ba, *Respir. Physiol. Neu-robiol.*, **177**, 183 (2011).
4. S. Grant, K. Bettencourt, P. Krulevitch, J. Hamilton, R. Glass, *Sens. Actuators B: Chem.*, **72**, 174 (2001).
5. S. A. Grant, R. S. Glass, *Sens. Actuators B: Chem.*, **45**, 35 (1997).
6. J. Han, K. Burgess, *Chem. Rev.*, **110**, 2709 (2010).
7. A. Wu, L. Duan, *Turk. J. Chem.*, **35**, 475 (2011).
8. M. H. Lee, *J. Fluoresc.*, **26**, 807 (2016).
9. L. Ferrari, L. Rovati, P. Fabbri, F. Pilati, *Sensors*, **13**, 484 (2013).
10. O. Young, R. Thomson, V. Merhtens, M. Loeffen, *Meat Sci.*, **67**, 107 (2004).
11. X. Zhang, H. Jiang, J. Jin, X. Xu, Q. Zhang, *Atmos. Environ.*, **46**, 590 (2012).
12. A. S. Jeevarajan, S. Vani, T. D. Taylor, M. M. Anderson, *Biotechnol. Bioeng.*, **78**, 467 (2002).
13. R. G. Haugland, Handbook of Fluorescent Probes and Research Products, ninth ed., Molecular Probes Inc., Eugene, OR, USA, 2002.
14. B. M. Weidgans, New Fluorescent Optical pH Sensors with Minimal Effects of Ionic Strength, Dissertation zur Erlangung des Doktorgrades der Naturwissenschaften, September 2004.
15. Y. Tian, F. Su, W. Weber, V. Nandakumar, B. R. Shumway, Y. Jin, X. Zhou, M. R. Holl, R. H. Johnson, D. R. Meldrum, *Biomaterials*, **31**, 7411 (2010).
16. C. Ju, H. Yin, C. Yuan, K. Wang, *Spectrochim. Acta Part A*, **79**, 1876 (2011).
17. C. Li, Y. Zhou, F. Xu, Y. Li, C. Zou, C. Weng, *Anal. Sci.*, **28**, 743 (2012).
18. T. R. Martz, J. J. Carr, C. R. French, M. D. DeGrandpre, *Anal. Chem.*, **75**, 1844 (2003).
19. X. H. Yang, L. L. Wang, *Optics Express*, **15**, 16478 (2007).
20. H. N. Kim, K. M. Swamy, J. Yoon, *Tetrahedron Lett.*, **52**, 2340 (2011).
21. C.-Y. Li, Y. Zhou, F. Xu, Y.-F. Li, C.-X. Zou, C. Weng, *Anal. Sci.*, **28**, 743 (2012).
22. Y. Wang, B. Tang, S. Zhang, *Dyes Pigm.*, **91**, 294 (2011).
23. V. Bojinov, N. Georgiev, P. Nikolov, *J. Photochem. Photobiol. A: Chem.*, **197**, 281 (2008).
24. X. Qian, Y. Xiao, *Tetrahedron Lett.*, **43**, 2991 (2002).
25. S. Nagl, O. S. Wolfbei, *Analyst*, **132**, 507 (2007).
26. B. Valeur, J.-C. Brochon (eds), New Trends in Fluorescence Spectroscopy: Applications to Chemical and Life Sciences, Springer Science & Business Media, Dec 6, 2012.
27. C. D. Geddes, J. R. Lakowicz, Advanced Concepts in Fluorescence Sensing: Part B: Macromolecular Sensing, Springer Science & Business Media, Jul 18, 2010.
28. B. Valeur, I. Leray, *Coord. Chem. Rev.*, **205**, 3 (2000).
29. A. de Silva, T. Vance, M. West, G. Wright, *Org. Biomol. Chem.*, **6**, 2468 (2008).
30. V. Bojinov, N. Georgiev, *J. Univ. Chem. Technol. Met.*, **46**, 3 (2011).
31. P. Panchenko, O. Fedorova, Y. Fedorov, *Russ. Chem. Rev.*, **83**, 155 (2014).
32. Y. Mei, P. A. Bentley, *Bioorg. Med. Chem. Lett.*, **16**, 3131 (2006).
33. X. Chen, J. Wang, J. Cui, Z. Xu, X. Peng, *Tetrahedron*, **67**, 4869 (2011).
34. J. Lee, H. Kim, S. Kim, J. Y. Noh, E. J. Song, C. Kim, J. Kim, *Dyes Pigm.*, **96**, 590 (2013).
35. S. Arimori, L. I. Bosch, C. J. Ward, T. D. James, *Tetrahedron Lett.*, **42**, 4553 (2001).
36. S. Arimori, L. I. Bosch, C. J. Ward, T. D. James, *Tetrahedron Lett.*, **43**, 911 (2002).
37. L. Wang, J. Yan, W. Qin, W. Liu, R. Wang, *Dyes Pigm.*, **92**, 1083 (2012).
38. R. Hosseinzadeh, M. Mohadjerani, M. Pooryousef, *Anal. Bioanal. Chem.*, **408**, 1901 (2016).
39. B. Krassovitski, B. Bolotin, Organic luminophores, Chimia, Москва, 1984 [in Russian].
40. D. Wróbel, A. Boguta, E. Mykowska, D. Bauman, I. Grabchev, *Mol. Cryst. Liq. Cryst.*, **427**, 57 (2005).
41. M. S. Refat, A. S. Megahed, I. M. El-Deen, I. Grabchev, S. El-Ghol, *J. Korean Chem. Soc.*, **55**, 28 (2011).
42. E. Kirilova, I. Ivanova, *Sci. J. of Riga Tech. Univ., Material Science and Applied Chemistry*, **23**, 29 (2011).
43. M. El-Sedik, N. Almonasy, M. Nepraš, F. Bureš, J. Cermák, M. Dvorák, M. Michl, R. Hrdina, *Dyes Pigm.*, **97**, 250 (2013).
44. T. Konstantinova, P. Meallier, H. Konstantinov, D. Staneva, *Polym. Degrad. Stab.*, **48**, 161 (1995).
45. T. Konstantinova, H. Konstantinov, T. Kaneva, A. Spirieva, *Polym. Degrad. Stab.*, **62**, 323 (1998).
46. I. Grabchev, V. Bojinov, I. Moneva, *J. Mol. Struct.*, **471**, 19 (1998).
47. I. Grabchev, V. Bojinov, I. Moneva, *Dyes Pigm.*, **48**, 143 (2001).
48. V. Bojinov, T. Konstantinova, *Polym. Degr. Stab.*, **68**, 295 (2000).
49. I. Grabchev, I. Moneva, I. Kozlov, G. Elyashevich, *Mater. Res.*, **4**, 301 (2001).
50. T. N. Konstantinova, R. A. Lazarova, *Dyes Pigm.*, **74**, 208 (2007).
51. T. N. Konstantinova, R. A. Lazarova, *Polym. Degr. Stab.*, **92**, 239 (2007).

52. M. Nepraš, O. Machalický, M. Šeps, R. Hrdina, a P. Kapusta, V. Fidler, *Dyes Pigm.*, **35**, 31 (1997).
53. S. Gonta, M. Utinans, G. Kirilov, S. Belyakov, I. Ivanova, M. Fleisher, V. Savenkov, E. Kirilova, *Spectrochim. Acta Part A*, **101**, 325 (2013).
54. B. Siddlingeshwar, S. M. Hanagodimath, E. M. Kirilova, G. K. Kirilov, *J. Quant. Spectr. Rad. Transfer*, **112**, 448 (2011).
55. I. Grabchev, I. Moneva, *Dyes Pigm.*, **38**, 155 (1998).
56. I. Grabchev, I. Moneva, E. Wolarz, D. Bauman, S. Stoyanov, *Polym. Film Liquid Cryst. Z. Naturforsch.*, **56**, 291 (2001).
57. V. Bojinov, I. Grabchev, *Org. Lett.*, **5**, 2185 (2003).
58. D. Staneva, R. Betsheva, J.-M. Chovelon, *J. Photochem. Photobiol. A*, **183**, 159 (2006).
59. D. Staneva, R. Becheva, *Dyes Pigm.*, **74**, 148 (2007).
60. D. Staneva, R. Betsheva, J.-M. Chovelon, *J. Appl. Polym. Sci.*, **106**, 1950 (2007).
61. S. Dumas, I. Grabchev, P. Stoikova, J. Chauvin, J.-M. Chovelon, *J. Photochem. Photobiol. A: Chem.*, **201**, 237 (2009).
62. G. Zhang, Y. Wen, C. Guo, J. Xu, B. Lu, X. Duan, H. He, J. Yang, *Anal. Chim. Acta*, **805**, 87 (2013).
63. E. M. Kirilova, I. Kalnina, T. Zvagule, N. Gabruseva, N. Kurjane, I. Solomenikova, *J. Fluoresc.*, **21**, 923 (2011).
64. S. Gonta, M. Utinans, G. Kirilov, S. Belyakov, I. Ivanova, M. Fleisher, V. Savenkov, E. Kirilova, *Spectrochim. Acta Part A*, **101**, 325 (2013).
65. O. Zhytniakivska, V. Trusova, G. Gorbenko, E. Kirilova, I. Kalnina, G. Kirilov, P. Kinnunen, *J. Lumin.*, **146**, 307 (2014).
66. K. Vus, V. Trusova, G. Gorbenko, R. Sood, E. Kirilova, G. Kirilov, I. Kalnina, P. Kinnunen, *J. Fluoresc.*, **24**, 493 (2014).
67. O. Zhytniakivska, V. Trusova, G. Gorbenko, E. Kirilova, I. Kalnina, G. Kirilov, J. Molotkovsky, J. Tulkk, P. Kinnunen, *J. Fluoresc.*, **24**, 899 (2014).
68. G. Reynolds, K. Drexhage, *Opt. Commun.*, **13**, 222 (1975).
69. T. Gunnlaugsson, M. Glynn, G. Tocci, P. Kruger, F. Pfeffer, *Coord. Chem. Rev.*, **250**, 3094 (2006).
70. J. Shao, H. Lin, H.-K. Lin, *Talanta*, **75**, 1015 (2008).

## СИНТЕЗА И ФОТО-ФИЗИЧНИ СВОЙСТВА НА НОВ pH-СЕНЗОР С БЕНЗАТРОН НА ОСНОВАТА НА ВЪТРЕШЕН ПРЕНΟΣ НА ЗАРЯДА

П.М. Миладинова<sup>a\*</sup>, Д.А. Тодорова<sup>b</sup>

<sup>a</sup> Департамент „Органичен синтез и горива“

<sup>b</sup> Департамент „Целулоза, хартия и полиграфия“

Химикотехнологичен и металургичен университет, бул. Климент Охридски 8, София 1756, България

Постъпила на 1 декември, 2016 г.; приета на 18 май, 2017 г.

(Резюме)

Синтезиран е нов флуоресцентен сензор, произведен на 3-аминобензантрона, използвайки реакция на нуклеофилно заместване на 3-аминобензантрон с бензоил-хлорид. Сензорът е проектиран като система “флуорофор-рецептор”. Полученото съединение е изолирано и охарактеризирано чрез ТСХ и УВ-Вид спектър, а структурата му - потвърдена с ИЧ и <sup>1</sup>H ЯМР спектри. Поради наличния в молекулата вътрешномолекулен пренос на заряд, синтезираният флуорофор може да се използва като pH проба, оперираща на принципа на “off-on” сензорен механизъм. Изследвана е сензорната активност по отношение на H<sup>+</sup> и OH<sup>-</sup> в разтвор ДМФ/вода (1:1) и върху целулоза (хартия), отчитайки промяната във флуоресцентната интензивност. Изследванията показат, че съединението може да бъде използвано като ефективен “off-on-off” превключвател за определяне на pH на среда, за следене на замърсители в околната среда, такива като например индустриални замърсители.

## A study of the energy potential of vinasse

P.G. Velichkova, T.V. Ivanov, I.G. Lalov\*

*Department of Biotechnology, UCTM, Kl. Ohridsky 8, 1756 Sofia, Bulgaria*

Submitted March 2, 2017; Revised March 16, 2017

The by-product remaining after distillation during the production of wine brandies is called vinasse. It is characterized mainly by a high content of organic matter (proteins, VFA, amino acids) and its typically balanced composition. The aim of this study is to determine the energy potential of organic waste from the production of wine brandy, i.e. vinasse, and to optimize the process of vinasse biomethanation. Process thermal stability was also investigated.

The main characteristics of vinasse as a substrate for biomethanation (pH 3,17, 6,34 g l<sup>-1</sup> protein, 296 gO<sub>2</sub> l<sup>-1</sup> COD, etc.) were determined. A high specific yield of methane was reached by appropriate adapted methanogenic consortium. Biochemical methane potential (BMP) of vinasse was determined at a value of 0,36 lCH<sub>4</sub> gCOD<sup>-1</sup>. A BMP assay provides a measure of the anaerobic digestibility of a given substrate. The BMP test was carried out in batch mode at mesophilic temperature (35°C). The information provided by BMPs is valuable when evaluating potential anaerobic substrates and for optimizing the design and operation of an anaerobic digester. Biomethanation process was optimized by adding appropriate microelements in the medium as the production of methane increased significantly. In a study of thermal stability of the process it was found that biomethanation takes place also under psychrophilic conditions (20 °C), but the period for methane production is extended.

The results showed that the vinasse is a valuable substrate for biomethanation and the process is successfully optimized by adding appropriate microelements in the medium.

**Keywords:** biochemical methane potential, vinasse, biomethane, methanogenic consortium

### INTRODUCTION

In recent years the use of the anaerobic digestion as process to treat organic solid wastes became more frequent. The reason of this new tendency in treatments of solid wastes can be explained considering mainly three factors: 1) the need to apply a process to dispose of organic solid wastes more environmental friendly than landfills as requested by the latest rules concerning the environmental protection in many countries in the world; 2) the opportunity to obtain from this process a renewable fuel called biogas alternative to fossil ones; 3) the advantage of relatively low costs in starting up and managing this process. Biomethanation is the formation of methane by microbes, known as methanogens, in the decomposition of biomass to a final energetically worthwhile gaseous product, called biogas. Biogas production is an efficient method of reducing greenhouse gas emissions (GHG) [1].

The biochemical methane potential (BMP) assay is best suited when used to elucidate what types of substrates, from an array of potential substrates, have the highest biomethane potential. In addition, BMP assays can be used to estimate the optimum ratios between co-substrates when co-digestion is intended. Lastly, BMP assay results can be used to

determine the extent of anaerobic biodegradability of substrates, and thus, relative residence times required for complete digestion. The determination of the BMP of an organic residue can help in the design and economic evaluation of a biogas plant [2]. In this analysis by stoichiometric conversion production of methane is associated directly with the degree of degradation of the organic mass. BMP - test requires a minimum of equipment and tools for organizing and monitoring compared to similar more extensive research and provides more accurate information regarding the specific organic waste that available in the literature. The BMP tests are conducted in batch conditions and in bench scale, measuring the maximum amount of biogas or biomethane produced per gram of biodegradable biomass contained in the organics used as substrates in the biomethanation process. In literature there are different attempts to define a standard protocol in order to gain comparable results but so far such standardization has not been reached.

The by-product remaining after distillation during the production of wine brandies is called vinasse. It is characterized mainly by a high content of organic matter (proteins, VFA, amino acids) and its typically balanced composition. The aim of this study is to determine the energy potential of organic

---

\*) To whom all correspondence should be sent:

E-mail: ivo.lalov@abv.bg



waste from the production of wine brandy, i.e. vinasse, and to optimize the process of vinasse biomethanation.

## MATERIALS AND METHODS

### *Vinasse*

The model vinasse substrate used in the study was laboratory prepared by distilling red wine. The distillate was then concentrated. It has the same properties as industrial. The substrate was stored in the refrigerator at 4 °C.

### *Methanogenic consortia*

Methanogens were obtained as activated sludge from a factory producing bioethanol “Almagest”, Ihtiman, Bulgaria.

### *Analytical methods*

The chemical oxygen demand (COD), total suspended solids, volatile suspended solids (VSS) and volatile fatty acids (VFA) were determined according to APHA (1992) [3]. The protein content

was determined according to the method of Lowry et al. (1951) [4]. Gas production rate measurements were performed using a manual constant pressure liquid displacement system. The biogas composition was estimated using the absorptive method as was described previously by Lalov et al. [5].

### *Procedure for BMP test*

There is no detailed standard procedure for conducting BMP – test, but most studies used very similar procedures. In our BMP – test was used a batch process of biomethanation of vinasse at 35 °C. Test bottles (500 ml) were filled with 300 ml activated sludge mixed methanogenic consortium and 10 ml neutralized vinasse (pH 7). Test bottles were flushed out with nitrogen for 15 minutes and then placed in a thermostat at 35 °C. Scheme of laboratory biomethanation system used in BMP test experiments is shown on Fig. 1

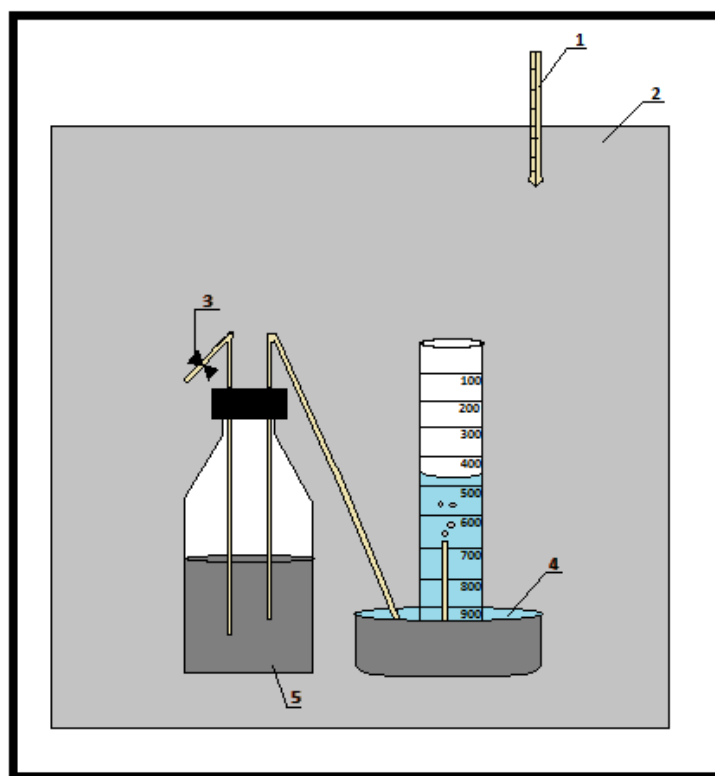


**Fig. 1.** Installation scheme of biomethanation; Legend: 1 – thermometer, 2 – thermostat, 3 – closing clip, 4 – gas holder, 5 – bioreactor

## RESULTS AND DISCUSSION

### *Characteristics of vinasse*

Vinasse is a residual liquid remaining from the fermentation and distillation of alcoholic liquors. It has low total solids content and total solids ranging from 5-10 %. Vinasse has high levels of potassium, calcium and organic matter in its chemical composition as well as moderate amounts of nitrogen and phosphorus and could represent an

alternative to supply such nutrients in crop production. It is characterized mainly by a high content of organic matter (proteins, VFA, amino acids) and its typically balanced composition. With aim to characterize this industrial waste as a potential substrate for methanation many analyses were conducted and the results of which are summarized in Table 1.

**Table 1.** Characteristics of vinasse

Parameter	Value
pH	3.17
COD, gO <sub>2</sub> l <sup>-1</sup>	270
Protein content, g l <sup>-1</sup>	6.34
Volatile fatty acids, mg l <sup>-1</sup>	8.45

As can be seen from the results presented in the table 1 vinasse is characterized by a high organic load. Therefore its anaerobic treatment to generate energy in the form of biogas would be efficient.

#### Characteristics of activated sludge

Mixed methanogenic consortium isolated from industrial wastewater treatment plant was used as standard inoculum in our experiments. The initial characterization of the mixed anaerobic culture included a study of its structure (morphological analysis) as well as determination of its microbial content.

The type of methanogenic culture is demonstrated in Fig. 2. As it can be seen culture is granulated in the form of spherical flocs (soft pellets). The particles have diameters varying in the range of 2-3 mm. The pellets displayed good mechanical stability, maintaining its intact structure at low stirring speeds, especially if no direct mechanical impact was applied. Thus structured consortium has a number of advantages such as rapid sedimentation ability to be retained in the reactor volume at relatively high flow rates, increased resistance to toxic shock, etc. which makes it suitable for use in numerous reaction systems.

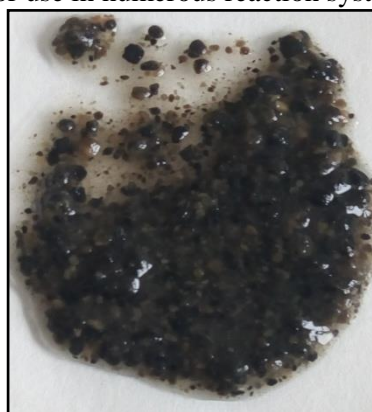


Fig. 2. Photo of activated sludge

An analysis to determine the organic content of the sludge (as VS) showed that the granules contain about 87% organic matter and 13% mineral mass. This feature further confirmed the good qualities of the consortium selected item as it is evident mainly the presence of biomass and EPS as opposed to sludge from a natural source, wherein the

mineral component reaches 70%. Dry weight (D/W) was 4.06 %.

#### Optimization of the BMP test procedure

In order to determine the real (maximum) achievable BMP of vinasse preliminary experiments for optimization of the process have been conducted. The volume of the biogas (methane) produced per unit of converted organic matter was used as optimization criterion. Two parameters were subjected to optimization: the composition of the medium and process temperature.

The lack of appropriate amounts of trace elements in the medium could be a significant barrier in determining the real BMP of the substrate. On the other hand BMP tests have to be carried out keeping the pH around the neutral point (values ranging between 7,0 to 7,8). Drop of the pH value below 6,0-6,5 will inhibit the methane bacteria activity. To avoid drops in pH chemicals are added to the organic substrate to supply a buffer capacity. Sodium bicarbonate, sodium hydroxide, sodium carbonate and sodium sulphide are the most used chemicals [6].

To evaluate the effect of the presence of appropriate micronutrients in the biomethanation medium two different batch processes were carried out simultaneously. Processes of biomethanization of 10 ml vinasse in presence and absence of micronutrients, respectively, were repeated three times. Composition of mineral contents is presented in the Table. 2. A comparison of the kinetics of biogas production during the two biomethanation processes is shown in Fig. 3.

Table 2. Concentrations of nutrients in the middle.

Displacement		500 ml
Activated sludge		300 ml
Minerals	NH <sub>4</sub> Cl	107.73 mg
	KCl	351.14 mg
	(NH <sub>4</sub> ) <sub>2</sub> HPO <sub>4</sub>	21.62 mg
	CaCl <sub>2</sub> . 2H <sub>2</sub> O	67.64 mg
	MgCl <sub>2</sub> . 6H <sub>2</sub> O	486.00 mg
	MnSO <sub>4</sub> . H <sub>2</sub> O	5.39 mg
	H <sub>3</sub> BO <sub>3</sub>	1.54 mg
	ZnCl <sub>2</sub>	0.57 mg
	CuCl <sub>2</sub> . 2H <sub>2</sub> O	0.73 mg
	NaMo <sub>4</sub> . 2H <sub>2</sub> O	0.69 mg
	CoCl <sub>2</sub> . 6H <sub>2</sub> O	8.10 mg

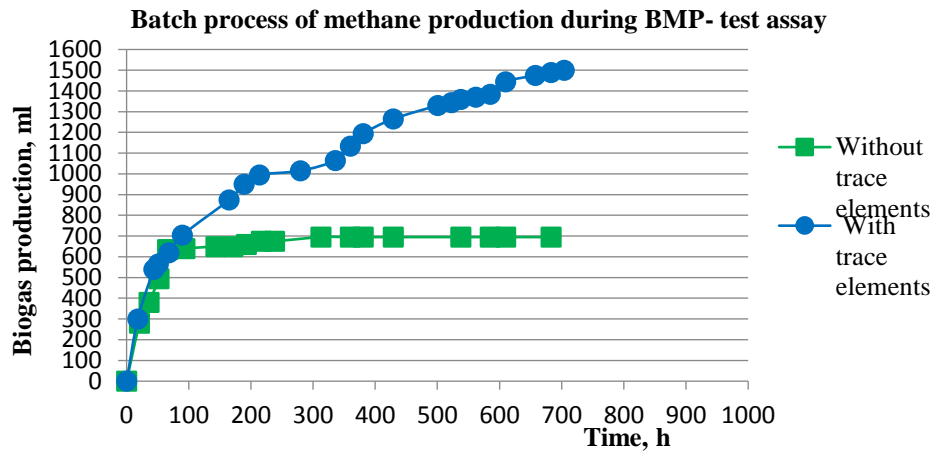


Fig. 3. Batch process of biogas production during BMP-test assay with and without trace elements

As can be seen from the graphs the process of biogas generation strongly depends on the presence of a suitable mineral composition. Obviously, the addition of trace elements resulted in a twofold increase in the yield of biomethane.

Temperature also affects the biomethanation rate and usually higher temperatures imply greater methane yields in a shorter digestion time. Nevertheless sharp increases of temperature should be avoided because they can cause a decrease in biomethane production due to the death of specific bacteria strains, particularly sensitive to temperature changes [7]. To keep constant the temperature during BMP tests it is needed to submerge the reactors in a water bath kept at the selected temperature [8] or to incubate them in a

thermostatically controlled room [9]. Anaerobic digestion of biomass can be performed in three different ranges: psychrophilic (10-20 °C), mesophilic (20-45 °C) and thermophilic (45-68 °C). Most often, the temperature range used in the anaerobic reactor is mesophilic (with optimum at 35 °C) [10].

The study of the temperature optimum of the process was related to the establishment of boundaries of temperature stability of methanogenic consortium. During the experiment temperature was increased with stepwise increments of 5 °C in the range 20-60 °C. After each establishment of the new temperature value a batch methanation of 10 ml vinasse containing trace elements has been carried out for a week (Fig. 4).

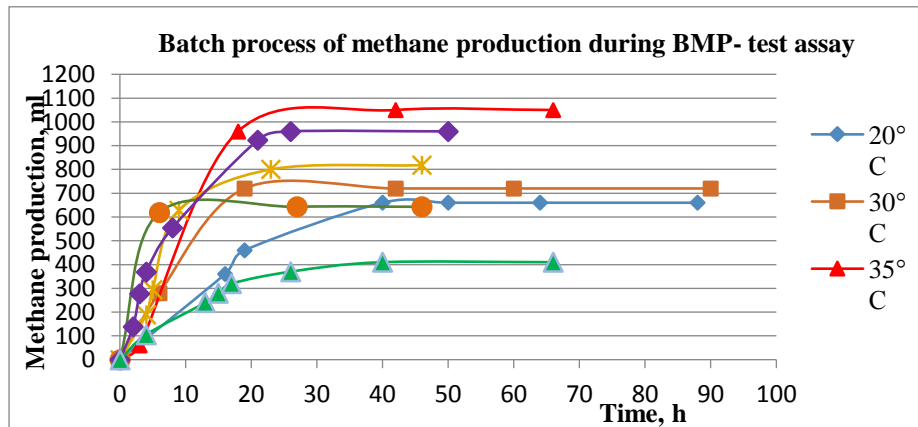


Fig. 4. Batch process of methane production during BMP-test assay at different temperatures

As a result of carried out studies it was found that the optimum temperature of the process is 35 °C. Paradoxically to some extent, additional temperature optimum was observed when temperature was increased to 50 °C. The occurrence of this lower additional optimum could be attributed to the probable processes of temperature adaptation of the methanogenic consortium as a result of gradual increase of the reactor temperature. Additional proof of the presumed successful adaptation was the fact

that the consortium demonstrated metabolic activity even at a subsequent rise in temperature to 60 °C.

#### Calculation of BMP of vinasse

After the above described optimization of the BMP test procedure, the process was repeated four times at optimal conditions. The obtained results were used in the final determination of the real energy potential of vinasse. BMP was determined according to the following Eq.(1).

$$BMP = \frac{V_{\text{biogas}} \cdot C_{\text{methane}}}{V_{\text{sub}} \cdot COD_{\text{sub}}} \quad (1)$$

where:

- BMP – biochemical methane potential, lCH<sub>4</sub> gCOD<sup>-1</sup>;
- V<sub>biogas</sub> – volume of produced biogas, l;
- C<sub>methane</sub> – methane concentration, %;
- V<sub>sub</sub> – volume of the substrate used in the BMP-test, l;
- COD<sub>sub</sub> – chemical oxygen demand of the substrate, gO<sub>2</sub> l<sup>-1</sup>.

To determine the BMP a batch process of biomethanation at 35°C was repeated four times. BMP of vinasse is 0,36 l CH<sub>4</sub> gCOD<sup>-1</sup>.

### CONCLUSION

The test methanogenic consortium keeps good metabolic activity in psychrophilic conditions at 20 °C. During the optimization of the BMP test procedure it was found that the yield of methane can be doubled by the adding of appropriate trace elements in the medium. The process of biomethanation of vinasse occurs most optimally in the presence of suitable microelements in the medium at mesophilic conditions (35 °C).

Determined under the above described conditions BMP of vinasse reached 0,36 lCH<sub>4</sub> gCOD<sup>-1</sup>. The occurrence of the second temperature optimum at 50 °C lead us to hypothesis that even higher value could

be reached in the case of thermophilic methanogenic consortium.

As a result of this study it can be concluded that the vinasse has high bioenergy potential and it is a valuable substrate for biomethanation.

### REFERENCES

1. G. Esposito, L. Frunzo, F. Liotta, A. Panico, F. Pirozzi, *The Open Environ.Eng. J.*, **5**, 1 (2012).
2. E. Elbeshbishy, G. Nakhla, H. Hafez, *Bioresource Technol.*, **110**, 18 (2012).
3. APHA, WPCF, AWWA, Standard methods for examination of water and wastewater, 18th ed. Washington: American Public Health Association, 1992.
4. O. Lowry, N. Rosebrough, A. Farr, J. Randall, *J. Biol. Chem.*, 1951, vol. 193, pp 265-275.
5. I.G. Lalov, M.N. Kamburov, T.V. Ivanov, P.G. Velichkova, *Scientific Works of University of food technologies*, **LXII**, 540 (2015).
6. W. Owen, D. Stuckey, J. Healy Jr., L. Young, P. McCarty, *Water Resour.*, **13**, 485 (1979).
7. J. Chae, A. Jang, S. Yim, S. Kim, *Bioresource Technol.*, **99**, 1 (2008).
8. A. Del Borghi, A. Converti, E. Palazzi, M. Del Borghi, *Bioprocess Eng.*, **20**, 553 (1999).
9. G. Gungor-Demirci, G. Demirci, *Bioresource Technol.*, **93**, 109 (2004).
10. M. Gerardi, *The microbiology of Anaerobic Digesters*, A John Wiley & Sons, Inc. Publication, 2003, pp 89-92.

## ИЗСЛЕДВАНЕ ЕНЕРГИЙНИЯ ПОТЕНЦИАЛ НА ВИНАСА

П.Г. Величкова, Т.В. Иванов, И.Г. Лалов\*

Катедра „Биотехнология“, ХТМУ, бул. „Климент Охридски“ 8, 1756 София, България

Постъпила на 2 март, 2017; приета на 16 март, 2017

(Резюме)

Вторичният продукт, оставащ след дестилацията при производството на винено бренди, се нарича винаса. Тя се характеризира главно с високо съдържание на органични вещества (протеини, летливи мастни киселини, аминокиселини) и със своя балансиран състав. Целта на това изследване е да се определи енергийният потенциал на течния органичен отпадък от производството на винено бренди, т.е. винасата, и да се оптимизира процесът на неговата биометанизация. Изследвана е и термалната стабилност на процеса.

Определени са основни характеристики на винасата като субстрат за биометанизация (рН 3,17, белтък 6,34 г л<sup>-1</sup>, 296 гО<sub>2</sub> л<sup>-1</sup> ХПК и др.). Постигнат е висок специфичен добив на метан посредством използването на подходящо адаптиран метаногенен консорциум. Определен е биохимичният метанов потенциал (БМП) на винасата - 0,36 лCH<sub>4</sub> гХПК<sup>-1</sup>. Анализът на БМП представлява мярка за анаеробната разградимост на даден субстрат. Тестът за БМП се провежда в периодичен режим при мезофилна температура (35 °C). Информацията, предоставена от БМП, е ценна при оценката на потенциални анаеробни субстрати и за оптимизиране дизайна и работата на анаеробния биореактор. Процесът на биометанизация е оптимизиран чрез добавяне на подходящи микроелементи в средата като производството на метан се увеличи значително. При изследване на термичната стабилност на процеса е установено, че биометанизация се извършва и при психрофилни условия (20 °C), но периодът на производство на метан се удължава.

Резултатите показват, че винасата е ценен субстрат за биометанизация и процесът е оптимизиран успешно чрез добавяне на подходящи микроелементи в средата.

## The effect of ultrasound treatment on soy protein and chitosan coating solution for packaging paper

U. Vrabič Brodnjak\*

University of Ljubljana, Faculty of Natural Sciences and Engineering, Department of Textiles, Graphic Arts and Design, Snežniška 5, SI-1000 Ljubljana, Slovenia

Submitted October 20, 2016 ; Accepted February 12, 2017

From the presented research, bio-based polymers (soy protein and chitosan) were used as coatings on packaging paper. Ultrasound treatment was used for the preparation of the coating solution. The coating solution was consisted from chitosan and soy protein in ratio 1:1. The goal of the research was to make a paper coating, which will be biodegradable, will have an improved mechanical and barrier (grease, water vapour transmission) properties. The focus of the use of ultrasound was meant to reduce the production costs and to make paper with better barrier properties, compared to uncoated and coated paper, which solution was not pre-treated. The tensile properties (tensile stress and strain) of pre-treated, solution-coated paper have improved. Due to protein addition in the coating, the strength and toughness of the paper (pre-treated and not pre-treated solution), compared to uncoated enhanced. Furthermore, the surface of treated, coated paper was more even, without many defects, pinholes or cracks. It was observed that the surface of untreated, coated paper is less smooth. The results have shown that grease migration was detected, but very small amount of the stained percent area of untreated and coated paper was detected, about 1%. The detected stained percent area for ultrasound treated coated paper was less, about 0.5%. The results have shown that coating without ultrasound treatment is acceptable, but with ultrasound treatment, the properties of packaging paper have improved even more.

**Key words:** ultrasound treatment, soy protein, chitosan, grease, tensile properties

### INTRODUCTION

Recently, bio based polymers are very popular in different fields of materials science. The annual worldwide paper and board production is more than 370 million tons, where 40 % of these refer to paper and board for packaging [1]. Special attention should be given in the field of packaging, since the use of these polymers is important due to influence on the packed material. Natural polymers are already used as barrier coatings on packaging materials and in recent years, there has been a focus on renewable polymers, mostly as edible films and coatings [2-4]. Bio based coatings, such as starch (rice, corn, potato etc.), proteins (soybean etc.), polysaccharides (chitosan and chitin) and lipids are extracted directly from the biomass. Their advantage is that they are non-toxic, environmentally friendly and have great grease, gas and aroma barrier properties [3, 4].

Isolated soy proteins (ISP) have great film-forming property and are most commonly used as edible wraps for meat, vegetables etc. [5-9]. However, ISP is not expensive biopolymer, it's produced from extraction of soybean oil and it is compatible with commonly used packaging material polyethylene [10]. Chitosan, a polysaccharide, which is derived from crustacean chitin, is commonly used in the food packaging. Some studies have considered proteins and chitosan as coatings on

paper [11-15]. In this study chitosan (CH) was also included as paper coating, because it is readily compatible with paper and has great antimicrobial and mechanical properties as coating material [13-15]. The main objective of producing blend coatings is to improve the permeability and mechanical properties according by the needs of applications. Many studies have been focused mostly on grease resistance, water permeability or improving mechanical properties of coated papers, but no attempts to develop coating using ultrasound treatment have previously been reported. Ultrasound is known as environmentally friendly process, used in many fields of materials science [16-17]. As it can be read in the literature, the positive effect of ultrasonic treatment on the starch dispersions and the application of ultrasonic treatment to starch films improves the moisture properties and provides stronger structure [18, 19].

The current study was thus conducted to investigate the possibility of improving paper coating solution using ultrasound as treatment technique.

### EXPERIMENTAL

#### Materials

Kraft paper, with grammage 80 g/m<sup>2</sup>, chitosan with molecular weight 20kDa (purchased from Sigma Aldrich, Austria), 98% malic acid (purchased

\*) To whom all correspondence should be sent:

E-mail: [urska.vrubic@ntf.uni-lj.si](mailto:urska.vrubic@ntf.uni-lj.si)

from Sigma Aldrich, Austria), glycerol as plasticizer (purchased from Sigma Aldrich, Austria) and isolated soy protein (purchased from Sigma Aldrich, Austria) have been used in this study.

#### *Preparation of blend coating solutions*

Firstly solutions of each compound (chitosan and soy protein) have been prepared. The chitosan solution was prepared by dissolving 2g of chitosan in 100 ml of 98% malic acid. The solution was mixed at 90°C for 5 minutes until chitosan was not dispersed. Before cooling down, coating solution was filtered through a polyester screen (mesh no. 140 with mesh opening 160 µm), by aspiration to remove small lumps in the solution.

Separately soy protein solution was prepared by dissolving soy protein (5g) in distilled water (100 ml). The solution was kept at 85°C for 30 minutes and then in a water bath at 45°C for 2h [25]. After that it was pH-adjusted to 10±0.1 1N NaOH. Soy protein coating solution was also filtered through a polyester screen, to remove undissolved materials.

After that chitosan and soy protein solutions were mixed together and glycerol as plasticizer (40 % w/w of total solid weight in the solution) was added.

#### *Ultrasound treatment of coating solutions*

The blend solution was put into ultrasonic bath (Asonic, Ultrasonic bath, Slovenia) for 15 minutes, using constant 35 kHz frequency. After the ultrasound treatment, the solution was left in the bath for another 15 minutes.

#### *Coatings on paper*

After the solutions were prepared and treated with ultrasound, the coating with a coater proceeded. Kraft paper was coated with hand coater, at ambient temperature, using 120 µm blade. On each paper 5 g/m<sup>2</sup> was applied. The untreated and ultrasound treated solution coated papers were dried at 50°RH and 23°C.

### ANALYSIS METHODS

#### *Grammage and thickness*

The grammage was determined in accordance with ISO 536 standard. Density and specific surface volume were calculated from the grammage and thickness, according to standard ISO 534. The thickness of sample papers was measured with a precision digital micrometre (Mitutoyo Corporation, Japan), to the nearest 0.0001 µm at 10 random locations on each paper.

#### *Tensile properties*

Tensile strength and elongation at break were determined on a tensile testing machine Instron 6022. The samples were analysed at standard atmosphere 23°C ± 1°C of temperature and 50% ± 2% of relative humidity. The cross speed head was 0.1 mm/s. Paper stripes of 18 cm in length and 1.5 in width were used. Ten probes of each sample in the machine direction (MC) and cross machine direction (CD) were tested.

#### *Grease barrier properties*

Grease resistance of paper coated with untreated and ultrasound treated blend solution of ISP and CH, was determined using a modified TAPPI test T-507, which was presented from Park et al. [10]. Smaller stained areas per hour on coated paper indicated greater grease resistance.

#### *Water vapour properties*

Thickness of the films has an influence on water vapor properties [20, 21]. Coatings from biopolymers have mostly hydrophilic nature and also the thickness of the coating influences on water barrier and mechanical properties. In our research thickness (mean values) of the coated papers were used in calculations for water vapour properties.

To determine WVP of the coated paper, the ASTM E96 standard method was used. To ensure the best results of the WVP, the silicone sealant was applied around the cup edge. Samples with exposed area of 50 cm<sup>2</sup> were tested at 90 ± 2% RH and 38 ± 2°C for 24 hours. The WVP was expressed in gram units, per square meter per day. Three samples per each paper sample were tested.

#### *Surface*

The SEM micrographs of coated paper surfaces were taken with a scanning electron microscope (JSM-6060 LV). The instrument operated at 10 kV and 1000X magnification.

### RESULTS AND DISCUSSION

#### *Basic paper properties*

Grammage and thickness influence the physical, optical and water barriers. The thickness has an effect on stiffness of the paper. Table 1 presents determined properties of uncoated and coated paper (with and without ultrasound treatment of the solution).

It can be seen from Table 1 that on coated paper 5 g/m<sup>2</sup> of blend coating solution was applied onto the surface of the paper. As expected, the thickness increased and there are also changes in density and specific volume.

**Table 1.** Determination of grammage, thickness, density and specific volume of uncoated, coated and coated-ultrasound treated paper

Sample	Grammage [g/m <sup>2</sup> ]	Thickness [μm]	Density [g/m <sup>3</sup> ]	Specific volume [m <sup>3</sup> /g]
Uncoated	80	122	655.74	0.00153
Coated	85	132	644.94	0.00155
Coated-treated	85	130	653.85	0.00153

*Mechanical properties*

Tensile properties such as tensile strength and elongation are very important for packaging materials. With coating, tensile properties can be improved. Therefore it can be more flexible, stiff etc. The results of the effects of the coating are shown in Figure 1, where it can be seen that elasticity increased, but tensile strength decreased in both

directions. Nevertheless, elongations at break were better at all coated samples. In general, the behaviour and properties of paper are less flexible in machine direction (MD) as in cross direction (CD). In CD direction papers are more extensible and stiff. It can be proved that coating improved elasticity of sample papers and even more at papers, which coating was pre-treated with ultrasound.

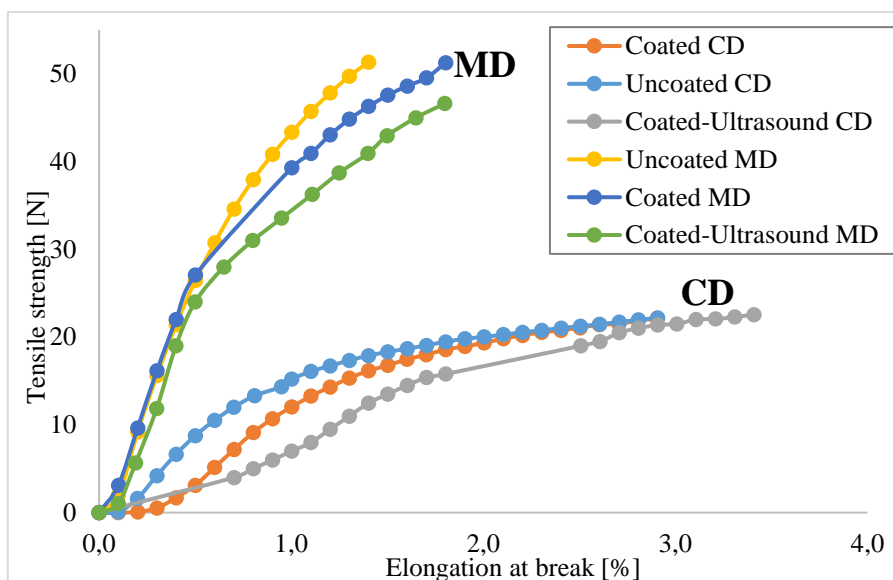


**Figure 1.** Tensile strength and elongation at break for uncoated, coated and coated-ultrasound treated paper in MD and CD directions

*Grease barrier and water vapour properties*

Grease barrier properties of analysed papers were affected by the coatings. In the first 1h the percent of stained area was at uncoated paper much higher than at both coated samples (Figure 2). The results of grease migration at coated samples are probably due to very small pinholes, cracks, where grease could permeate through the coating. After 5h of the test, the grease migration increased at uncoated paper (for 18 %), as well as at both coated papers. Still, there was less stained area detected at coated paper with ultrasound (6%), in comparison to coated sample (8%).

Defects on the coating surface might explain why the percent of stained area are still detected after 8 hours.

It is known that paper has certain grade of moisture, which depends on relative humidity, types

of used pulp, degree of refining and types of used coatings. For packaging materials it is very important to have excellent barrier properties. One of them is also water vapour permeability (WVP). WVP is determined as the amount of water that permeates through the paper of certain thickness per unit time. From Figure 3 it can be seen that ultrasound treatment increased WVP barrier of coated paper, compared to coated, untreated or uncoated sample. The moisture at both coated samples decreased. Reducing of moisture was small, at coated paper moisture decreased for 0.6%% and coated, ultrasound treated for 1%. The influence of ultrasound led to improved surface distribution of the coating, where less pores were detected as well as cracks and other deformations. It was proved that such coating had denser structure, which also increased water vapour barrier. Thus, ultrasound treatment caused rearrangement of free mobile

chains of the polymer matrix of the coating, which for that reason more homogeneous formation of the coating has been made. On moisture and WVP soy protein and chitosan as polymers had influence. Soy protein is known that it exhibits poor WVP properties due to its hydrophilic nature [22].

However, chitosan has hydrophobic nature, it is the only positively charged, naturally occurring polysaccharide [13]. Coatings in combination with chitosan and proteins can give effective water barriers with other prospective properties, which are important for packaging materials.

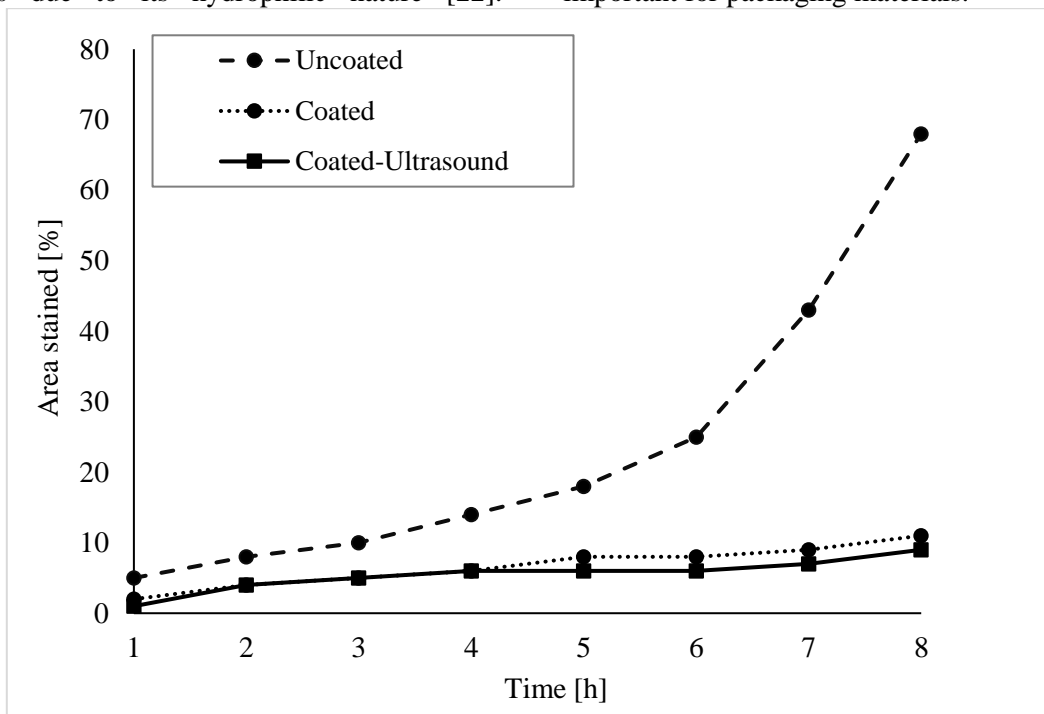


Figure 2. Grease permeation of uncoated, coated and coated-ultrasound treated paper.

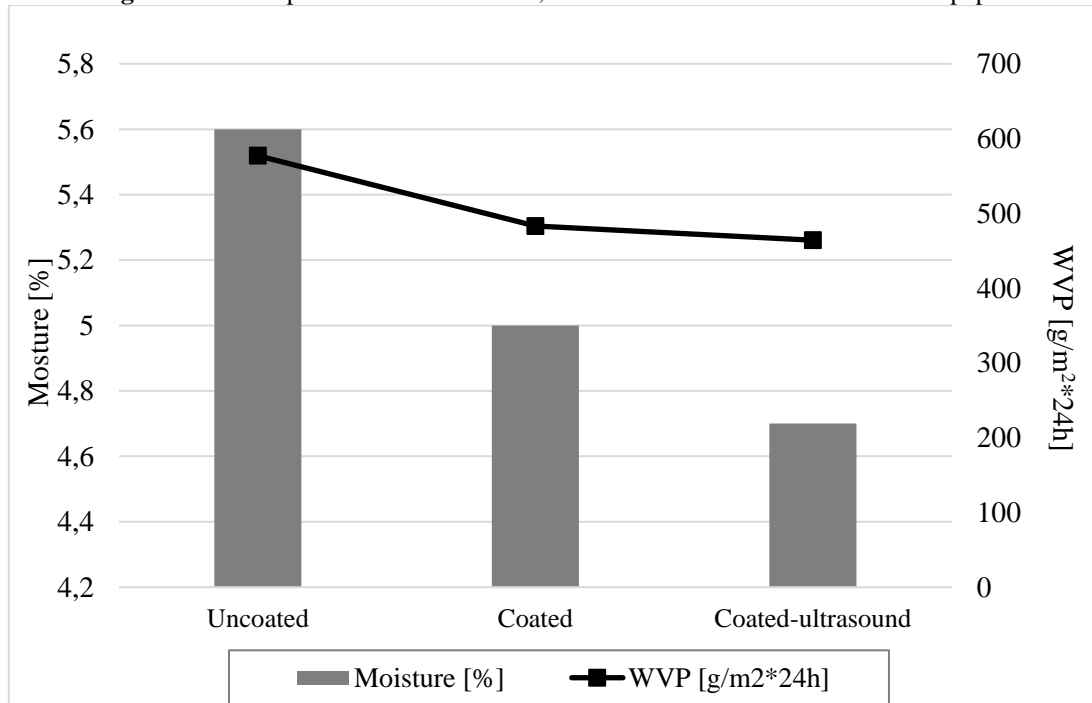
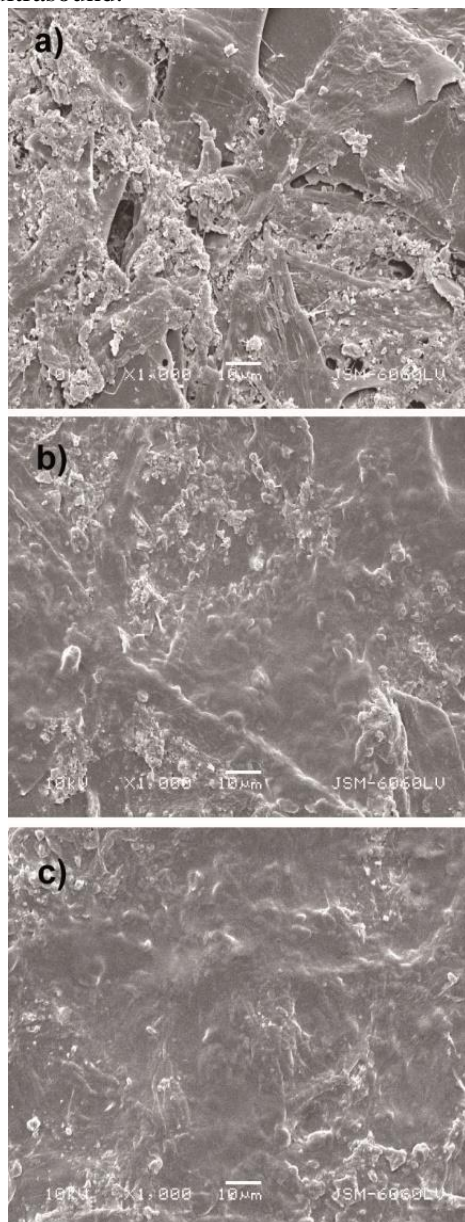


Figure 3. Moisture and water vapour permeability (WVP) of uncoated, coated and coated-ultrasound treated paper.



### Surface

All micrographs show paper surface at 1000x magnification and are presented in Figure 4 (a-c). As expected, the surface of coated paper revealed smoother surface, compared to uncoated paper, which was also proven with other presented analysis in this paper. Even more can be seen at coated paper (Figure 4c), where coating solution was pre-treated with ultrasound.



**Figure 4.** SEM micrographs of uncoated (a), coated (b) and pretreated coated (c) paper.

### CONCLUSIONS

In recent years, various bio-based coatings for packaging materials have been developed, which have different barrier properties. Therefore the

concept of coatings with biodegradable polymers represent stimulating route to create new packaging materials, with improved properties. Bio polymers used in our research are available in the market and their properties can help to improve the packaging paper. With ultrasound treatment we proved that it is effective procedure to improve coating solution and coating itself. In the literature, there are no reported studies of ultrasound treatment of soy protein and chitosan solution suitable as coating for packaging paper. Blend soy protein and chitosan coating possesses good grease and water vapour barrier properties and mechanical properties, which are useful for packaging materials. From the research it was proven that mentioned properties improved even more at solution, which was pre-treated with ultrasound.

### REFERENCES

1. D. A. Todorova, *J. Chem. Technol. Metall.*, **51**, 514 (2016).
2. V.K. Rastogi, P. Samyn, *Coatings*, **5**, 887 (2015).
3. P. Saym, *J Mat Sci*, **48**, 6455 (2013).
4. U. Vrabič Brodnjak, *Prog Org Coat*, **112**, 86 (2017).
5. H. O. Jaynes, W. N. Chou, *Food Prod Dev*, **9**, 86 (1975).
6. A. H. Brandenburg, C. L. Weller, R. F. Testin, *J Food Sci*, **58**, 1086 (1993).
7. H. J. Park, M. S. Chinnan, *J Food Eng*, **25**, 497 (1995).
8. A. B. Arfa, L. Preziosi-Belloy, P. Chalier, N. Gontard, *J Agric Food Chem*, **55**, 2155 (2007).
9. A. B. Arfa, Y. Chrakabandhu, L. Preziosi-Belloy, P. Chalier, N. Gontard, *Food Res Int*, **40**, **22** (2007).
10. H. J. Park, S. H. Kim, S. T. Lim, D. H. Shin, S. Y. Choi, K. T. Hwang, *JAOCs*, **77**, 269 (2000).
11. J. W. Rhim, C. L. Weller, K. S. Ham, *Food Sci and Biotechnol*, **7**, 263 (1998).
12. S. Wang, Y. Jing, *BioResources*, **11**, 1868 (2016).
13. F. Ham-Pichavant, G. Sèbe, P. Pardon, V. Coma, *Carbohydr Polym*, **61**, 259 (2005).
14. W. Zhang, H. Xiao, L. Qian, *Carbohydr Polym*, **101**, 401 (2014).
15. A. B. Reis, C. M. P. Yoshida, E. S. D. Vilela, R. S. Nascimento, I. S. Melo, T. T. Franco, *Journal of Research updates in Polymer Science*, **2**, 122 (2013).
16. T. Bourtoom, M. S. Chinnan, *J Food Sci Technol*, **41**, 1633 (2008).
17. J. Shen, P. Fatehi, Y. Ni, *Cellulose*, **21**, 3145 (2014).
18. W. Zhang, H. Xiao, L. Qian, *Carbohydr Polym*, **101**, 401 (2014).
19. W. J. Cheng, J. C. Chen, D. H. Liu, X. Q. Ye, F. S. Ke, *Carbohydr Polym*, **81**, 707 (2010).
20. H. Aloui, K. Khwaldia, B. Slama, M. Hamdi, *Carbohydr Polym*, **86**, 1063 (2011).
21. K. Khwaldia, *BioResources*, **8**, 3438 (2013).
22. M. Gällstedt, A. Brottman, M. S. Hedenqvist, *Pack Technol Sci*, **18**, 161 (2005).

## ЕФЕКТ НА УЛТРАЗВУКОВОТО ТРЕТИРАНЕ НА РАЗТВОРИ ОТ СОЕВ ПРОТЕИН И ХИТОЗАН, ПРЕДНАЗНАЧЕНИ ЗА ПОКРИТИЯ НА ОПАКОВЪЧНА ХАРТИЯ

У. Врабич Бродняк

*Департамент по текстил, графика и дизайн, Факултет по природни науки и инженерство, Университет в Любляна, Словения*

Постъпила на 20 октомври, 2016 г.; приета на 12 февруари, 2017 г.

(Резюме)

В настоящето изследване се използват полимери на биологична основа (соев протеин и хитозан) за покрития на опаковъчна хартия. Приложено е ултразвуково третиране за подготовка на полимерния разтвор. Този разтвор се състои от хитозан и соев протеин в отношение 1:1. Цел на изследването бе да се постигне биоразградимо покритие с подобрени механични и предпазни свойства (срещи масла, влага). Фокусът на ултразвуковото третиране бе в намаляването на производствените разходи и подобряването на защитните свойства спрямо хартия без покритие или с покритие без такова третиране. Свойствата на опън (напрежения и деформация) се подобряват при покрития с предварително третиране. Поради добавянето на протеин в покритието (с и без третиране) здравината и твърдостта на хартията се подобряват спрямо хартията без покритие. Освен това, повърхността на третираната хартия е по-еднородна, без много дефекти, дупчици и пукнатини. Повърхността на не-покритата хартия е по-малко гладка. Резултатите показват, че е налице миграция на мазни петна, но повърхността им не превишава 1% при покритата и непокрита хартия. Когато разтворите са третирани с ултразвук, площта на петната е около 0.5%. Покритията без ултразвуково третиране са приемливи, но свойствата им се подобряват след такава обработка.

## Printing quality of chitosan-rice starch coated packaging paper

U. Vrabič Brodnjak\*, D. Muck

*University of Ljubljana, Faculty of Natural Sciences and Engineering, Department of Textiles, Graphic Arts and Design, Snežniška 5, SI-1000 Ljubljana, Slovenia*

Submitted October 26, 2016; Accepted January 25, 2017

Biopolymers used as coatings on packaging paper can provide sufficient barriers (water, gas, etc.). Increased environmental concerns, synthetic packaging and coatings are nowadays getting replaced with bio based materials. Therefore thermoplastic starch and chitosan can be good replacements of petroleum based products in packaging industry. In our research chitosan and rice starch were used as coatings on packaging paper. The aim of the research was to determine printing quality on coated paper, which could be used for further applications. The influence of coated thickness on the printing quality was also investigated. Paper was coated with two different coating mixtures. The first was only chitosan coating and the other one was mixture of chitosan and rice starch (ratio 50:50). Coating was applied with two different bars to achieve two different thickness of the coating: 40µm and 80µm. The ink rub test was proceeded using rub tester and the procedure was made according to standard TAPPI T830. Dry rub test showed that all coated samples achieved better results (optical density), in comparison to uncoated paper. In our research two stroke (Rubbing Times) were determined: 25 and 50 cycles, at rubbing speed 106cpm. After 25 cycles sample paper coated with chitosan and rice starch achieved the best quality, according to uncoated and chitosan coated paper. After 50 cycles, the chitosan and rice starch coating still had better abrasion resistance, but it could not be sufficient for further use. The research has proven increased printing quality of coated paper, especially the coating with mixture of chitosan and rice starch.

**Key words:** chitosan, rice starch, coatings, packaging paper, printing quality

### INTRODUCTION

Bio based polymers are in recent years used in many fields, especially at packaging. Packaging research is focused to develop the use of bio plastics which are useful in reducing waste disposal and are good replaces of petroleum and a non-renewable resource with diminishing quantities [1]. Paper, board and cardboard are widely used packaging materials in many shapes and products (boxes, folding cartons, corrugated boxes, paper bags, cups etc.) and their biodegradability, barrier and mechanical properties are of prime importance. Its main components are the renewable materials and used paper can be unfenced in natural conditions if it's not being used again for the production of recycled paper or some other method [2]. In recent years there has been a research focus on renewable biopolymers used as edible films and coatings [3-5]. Bio based coatings, such as starch, proteins and polysaccharides are extracted directly from the biomass. Their advantage is that they are non-toxic, environmentally friendly and have great grease, gas and aroma barrier properties [5-7]. Chitosan exhibits good moisture properties, but it is not sufficient for food applications, because of its hydrophilic nature which attracts moisture [8]. To improve the moisture properties and functional properties of chitosan

coatings, blending it with other biopolymers, hydrophobic substances have been proposed [8, 9]. In previous research numerous of chitosan films and chitosan blends with other natural polymers have been made [10, 11]. Because of high amount of amylase, rice starch is attractive for food packaging as a film barrier or coatings [12]. It has been used also to replace plastic film barriers due to good mechanical properties [12-14]. Based on the literature findings, there has not been done analysis of printing quality of chitosan and/or rice starch coatings on paper.

Inkjet printing is still a growing printing business area, also in the field of packaging. At the same time this printing technique has been used in office and home applications. The properties of coating layer of paper are effecting the inkjet process [15]. The material properties, coatings, capillary structure, temperature and moisture content are important for the topography of the surface [16]. The spreading, penetration and final printing quality are affected by porosity, permeability, thickness, fibre type, moisture content and capillary structure [17, 18]. The printing machine variables can also affect the final droplet setting, but those variables have not been defined in our research.

The goal of our research was to determine printing quality on coated paper with different bio

\*) To whom all correspondence should be sent:

E-mail: urska.vrabc@ntf.uni-lj.si

based polymers, which could be used for further applications.

## EXPERIMENTAL

### *Materials*

Uncoated, unglazed paper, with grammage 80 g/m<sup>2</sup>, chitosan with molecular weight 20kDa (purchased from Sigma Aldrich, Austria), 98% malic acid (purchased from Sigma Aldrich, Austria), glycerol as plasticizer (purchased from Sigma Aldrich, Austria) and rice starch (purchased from Farmalabor Srl, Italy) have been used in this study.

### *Preparation of blend coating solutions*

*Preparation of chitosan coating solution.* The chitosan solution was prepared by dissolving 2g of chitosan in 100 ml of 98% malic acid and 40% w/w of glycerol was added. The solution was mixed at 90°C for 5 minutes until chitosan was not dispersed. Coating solution was after cooling filtered through a polyester screen (mesh no. 140 with mesh opening 160µm) and aspirated in order to remove small lumps in the solution.

### *Preparation of blend solution with chitosan and rice starch*

Firstly solutions of each compound (chitosan and rice starch) have been prepared. The chitosan solution was prepared by dissolving 2g of chitosan in 100 ml of 98% malic acid. The solution was mixed at 90°C for 5 minutes until chitosan was not dispersed. Before cooling down, coating solution was filtered through a polyester screen (mesh no. 140 with mesh opening 160µm), by aspiration to remove small lumps in the solution.

Separately rice starch was prepared by dissolving 2g of rice starch in 100 ml of distilled water. The solution was mixed until it gelatinized (85°C for 20 min) and then cooling to the room temperature. After that chitosan and rice starch solutions were mixed together and glycerol as plasticizer (40% w/w of total solid weight in the solution) was added.

### *Coatings on paper*

After the solutions were prepared, the coating with a coater proceeded. Paper was coated with hand coater, at ambient temperature, using bars with 2 different wire diameters: 0.51mm (with 40µm of wet film deposit) and bar with wire diameter 1.00mm (with 80µm of wet film deposit). On each paper 5 g/m<sup>2</sup> and 10 g/m<sup>2</sup> were applied. The coated papers were dried at 50°RH and 23°C.

### *Printing*

Printing was proceeded on inkjet printer HP Officejet Pro at ambient conditions (T=22±2°C; RH=45±3%) by a drop-on-demand mode with

replaceable cartridges. All samples, uncoated and coated were printed with this technique.

### *Analysis methods*

*Grammage, thickness, density, moisture, smoothness and porosity.* The grammage was determined in accordance with ISO 536 standard. Density was calculated from the grammage and thickness, according to standard ISO 534. The thickness of sample papers was measured with a precision digital micrometre (Mitutoyo Corporation, Japan), to the nearest 0.0001 µm at 10 random locations on each paper. Moisture of paper samples was determined according to ISO 287. Smoothness is an indirect measure and it was analysed according to Bendtsen method (ISO 8791-2). The same as smoothness, porosity was analysed with the Bendtsen method.

*Abrasion resistance of printed and coated papers.* The abrasion resistance of uncoated, coated and printed papers were made on rub tester Labthink (China), according to TAPPI T830 standard. The test was proceeded on dry samples and two of each paper samples were tested. The procedure was carried out on dual stations with arc movement. In our research two stroke (Rubbing Times) were determined: 25 and 50 cycles, at rubbing speed 106cpm and rub pressure 8.9N. For determination of print abrasion, optical density was measured before and after rubbing.

*Surface and image segmentation.* The pictures of uncoated and coated paper surfaces were taken with the digital camera Cannon. After that image segmentation and surface analysis with the ImageJ program has been done.

## RESULTS AND DISCUSSION

### *Basic paper properties*

Grammage and thickness influence the physical, optical, water barriers. The thickness has an effect on stiffness of the paper. Table 1 presents determined properties of uncoated and coated paper, but not printed (with 2 different coating bars: 40µm and 80µm).

From Table 1 it can be seen that 5 g/m<sup>2</sup> and 10 g/m<sup>2</sup> of blend coating solution was applied onto the paper surface. As expected, the thickness increased at 80µm bar, for 5% more than at 40µm bar. With 40µm bar 5g/m<sup>2</sup> of coating has been applied onto the paper surface and with 80µm 10 g/m<sup>2</sup>. Therefore also changes in density were detected.

Moisture content of papers varies depending on used pulp, relative humidity, degree of refining, types of coating and additives used. It has one of the

biggest effects on mechanical properties as well as on other properties (printing quality, gloss etc.). The different effect of biopolymer coating on moisture of the paper, depended on the type of paper, which reflected the difference of interaction between the bio-based coating and cellulose fibres of the paper. From the results presented in Table 1 it can be seen that uncoated paper had the highest moisture content (6.7%), compared to all coated samples, but not significantly. Less moisture had papers, which were coated only with chitosan solution, as well as coatings which were applied with 80µm bar. Smoothness is important parameter for printing paper, which controls the contact between the paper, printing form and thus the transfer of the ink. It

determines roughness, levelness and compressibility. As expected, coated papers (between 370 and 420 ml/min) have higher smoothness, compared to uncoated (510 ml/min) paper. There is difference between chitosan coated and blend coated papers, using different bars. Coating with chitosan is less smooth then blend coating. The results showed that rice starch in mixture with chitosan improved the surface properties of coated paper. From the results it can be obtained that coating generally improved smoothness, which also had further effect on abrasion resistance.

**Table 1.** Determination of grammage, thickness, density, moisture and smoothness of uncoated and coated paper with 2 different coating bars (CH-chitosan, CHR-blend solution of chitosan and rice starch).

Sample	Grammage [g/m <sup>2</sup> ]	Thickness [µm]	Density [g/m <sup>3</sup> ]	Moisture [%]	Smoothness [ml/min]	Porosity [ml/min]
Uncoated	80	122	655.74	6.7	510	1300
Coated CH-40µm bar	85	132	643.94	6.3	460	0
Coated CH-80µm bar	90	140	642.86	6.1	420	0
Coated CHR-40µm bar	85	133	639.10	6.5	380	0
Coated CHR-80µm bar	90	140	642.86	6.3	370	0

It is known that paper is composed of a felted layer of fibres and therefore the structure has a varying degree of porosity. Paper is highly porous material and this property has important influence of printing quality as well. Porosity of paper is an indicator of absorptivity to absorb or water and it is also important in a vacuum feeding process during printing. Results of porosity has shown that uncoated sample had the highest porosity (1300 ml/min), but on coated papers it was unable to measure it. The surface of the coated papers was even and filled, therefore the porosity showed that the porosity in ml per minutes was 0 at all coated samples.

*Abrasion resistance of printed and coated papers*

The abrasion resistance was used to evaluate the resistance of printed surfaces to rubbing abrasion. Coating failures or damages on paper are related to coating-substrate adhesion, coating thickness and internal stress in coating. It should be noted that there are several methods that can characterize other aspects of imaging materials degradation as result of frictional contact with various surfaces under different conditions. Therefore the use of specific methods are depending on end-user applications, such as type of packaging materials and coatings, requirements for coating barriers, etc. In our study

TAPPI standard was used as standard method for determination of printing quality of rubbed coated papers.

Dry rub test showed that all coated samples achieved better results (optical density), in comparison to uncoated paper. In our research two stroke (Rubbing Times) were determined: 25 and 50 cycles, at rubbing speed 106cpm. After 25 cycles (Figure 1) sample paper coated with chitosan and rice starch achieved better quality, according to uncoated and chitosan coated paper. Before rubbing, the highest optical density (1.49) had sample, which was coated with blend coating (chitosan and rice starch) and where 10g/m<sup>2</sup> coating was applied to the paper. At uncoated paper smaller amount of colour has been applied and fixed to the surface and after rubbing, the optical density was the lowest (1.13), compared to other treated samples after 25 cycles. Paper, where only chitosan was used as coating, achieved lower results before and after rubbing, of the optical density (before 1.43 and after 1.14) in comparison to blend coating, but the difference was not so major. From this part it can be concluded that rice starch as coating component influences on more stable and durable coating. However, only chitosan coating had worse abrasion resistance.

After 50 cycles (Figure 2), the chitosan and rice starch coating still had better abrasion resistance (optical density was 1.23) according to other analysed samples, but it could not be sufficient for further use. The difference between 25 and 50 cycles showed that blend coating, which was applied to the

paper surface with two different bars, achieved almost the same values at both rubbing times. As expected, the rubbing abrasion has worsened after 50 cycles at uncoated paper. At chitosan coated paper also the optical density decreased.

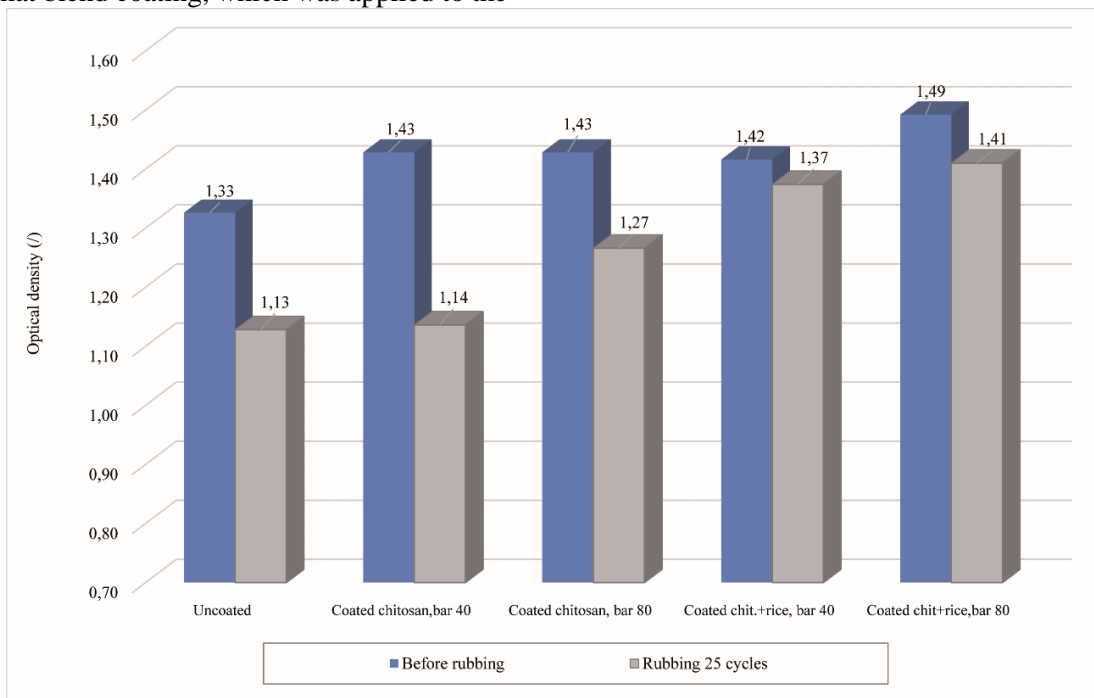


Figure 1. Optical density of uncoated and coated paper samples after rubbing 25 cycles

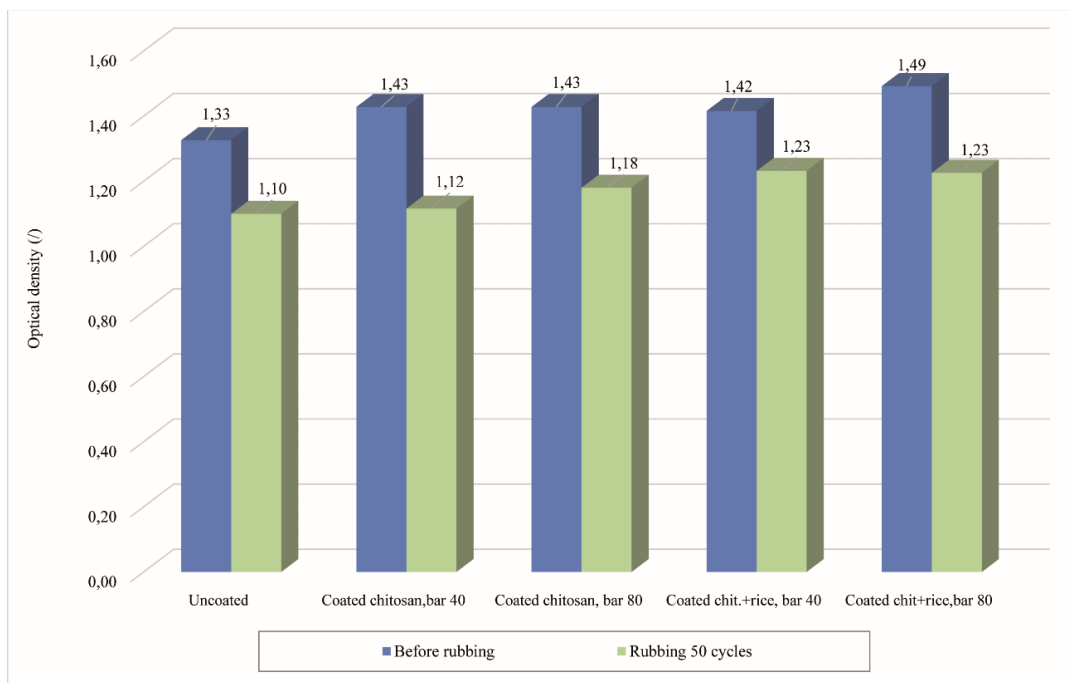


Figure 2. Optical density of uncoated and coated paper samples after rubbing 50 cycles

### Surface

All pictures present paper surface after 25 (Figure 3) and 50 cycles (Figure 4). As expected, the surface of coated paper revealed smoother surface, compared to uncoated paper as seen at both figures.

After 25 cycles at uncoated paper more damages could be seen, compared to coated paper, which was also proven with determination of optical density. In comparison between coated papers, the best results achieved paper, which was coated with blend

solution and the coating has been applied with 80  $\mu\text{m}$  bar.

As expected, all samples rubbed for 50 cycles revealed more damaged surface. At both rubbing times, uncoated sample had the worse surface (more white dots, scraped surface), compared to other tested papers. The best results at both rubbing times

achieved paper, which was coated with blend solution and where 10g/m<sup>2</sup> of coating was applied. The research has proven increased printing quality of coated paper, especially at the coating with mixture of chitosan and rice starch.

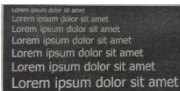
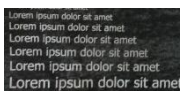
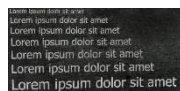
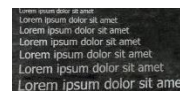
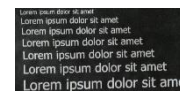
UNCOATED	COATED chitosan, 25 cycles, 40 $\mu\text{m}$	COATED chitosan, 25 cycles, 80 $\mu\text{m}$	COATED chitosan+rice, 25 cycles, 40 $\mu\text{m}$	COATED chitosan+rice, 25 cycles, 80 $\mu\text{m}$
				

Figure 3. Paper printed surface after 25 cycles

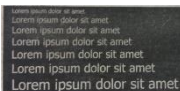
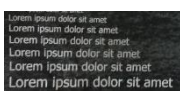
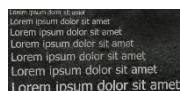
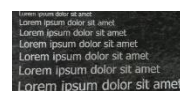
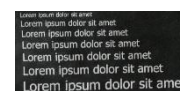
UNCOATED	COATED chitosan, 50 cycles, 40 $\mu\text{m}$	COATED chitosan, 50 cycles, 80 $\mu\text{m}$	COATED chitosan+rice, 50 cycles, 40 $\mu\text{m}$	COATED chitosan+rice, 50 cycles, 80 $\mu\text{m}$
				

Figure 4. Paper printed surface after 50 cycles

### Image segmentation

Image segmentation is one of the most common techniques to process a separating an image into different areas on various features of the analysed image.

Figures 5 and 6 present a histograms of Grey-Scale image-printed surface of each paper sample with different coatings and rubbing cycles. At analysed papers the pixels of foreground had different grey value compared to pixels belonging to the background. The image segmentation technique assumes that pixels above certain threshold on grey level (0-255), belong to the analysed object-image foreground and pixels below that threshold are belonging to the background [19]. At our study images have similar grey levels, as seen in both

presented figures. According to that the changes at all presented histograms were detected. Grey level histograms from papers analysed at 25 cycles (Figure 5) showed that uncoated paper had more damages on the surface and less colour was on it after rubbing. On the other hand more pixels were detected at grey level between 50 and 80. Less damages had paper, which was coated with blend solution (chitosan and rice starch) with 80 $\mu\text{m}$  bar. At this sample the most pixels detected were between 15 and 60 of grey level, meaning that more colour was still applied at the surface, compared to other tested papers. Papers which had coatings of only chitosan and blend coatings showed that had less colour and they were more rubbed after 25 cycles, compared to blend coating with used 80 $\mu\text{m}$  bar.

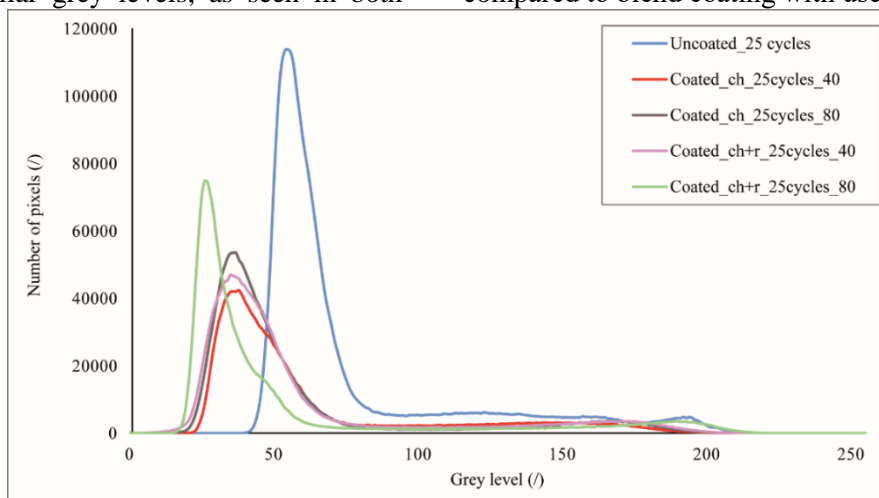
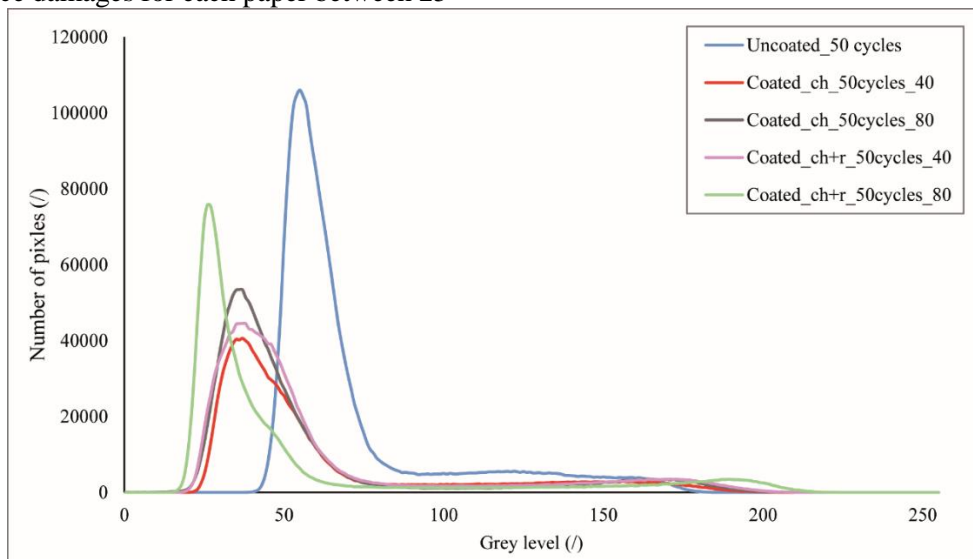


Figure 5. Grey level histograms for paper surface of uncoated and coated samples after 25 cycles of rubbing and 2 different blades (40 $\mu\text{m}$  and 80 $\mu\text{m}$ ).

Figure 6 presents histograms of paper surface for all tested papers at rubbing time 50 cycles. The results have shown similar trend as at 25 cycles. The most damaged surface was again at uncoated paper, where the damages were also confirmed with determination of optical density. The most durable paper surface was again at paper, which was coated with 80 $\mu$ m bar with blend solution. Thus differences between surface damages for each paper between 25

and 50 cycles did not show significant difference, according to image segmentation with this method. For future findings different thresholding methods should be defined, in order to find the most suitable image segmentation for this kind of coatings. Despite this, it can be stated that the analysis has shown differences at uncoated and coated papers, where 2 different bars were used.



**Figure 6.** Grey level histograms for paper surface of uncoated and coated samples after 50 cycles of rubbing and 2 different blades (40 $\mu$ m and 80 $\mu$ m).

## CONCLUSIONS

In this research different coatings, concerning also the different amount of it, its durability and printing quality were prepared. Coatings were successfully prepared and the results have shown that with coatings paper surface properties have improved. Dry rub test showed that all coated papers achieved better results in comparison to uncoated paper. After 25 cycles paper, which was coated with blend solution of chitosan and rice starch achieved the best printing quality (smoothness, porosity, abrasion resistance), according to uncoated and only chitosan coated paper. This was also confirmed with determination of optical density and image segmentation. After 50 cycles, the chitosan and rice starch coating still had better abrasion resistance compared to other analysed samples. For further use the coatings (chitosan and rice starch) should be modified and then they will have a potential for the use in packaging. It was proven, that the properties of ink and printed surface influenced the interactions between coating and ink, which could be seen from presented results. On the other hand pore surface, the pore size, permeability, together with material, ink components and printing process (pressure, speed, etc.) are important coating properties, for achieving good printing quality.

As a subject of a further paper to enhance coatings for better abrasion resistance is to prepare coatings with different ratios of analysed components or to include other biopolymers, which will have better rubbing resistance.

## REFERENCES

1. D.A. Todorova, S.P. Bencheva, *Bul. Chem. Commun.*, **47**, 45 (2015).
2. U. Vrabič Brodnjak, *J. Compos. Biodegrad. Polymers*, **4**, 32 (2016).
3. J. M. Krochta, C. De Mulder-Johnston, *Food Technol*, **51**, 61 (1997).
4. M.S. Rao, S.R. Kanatt, S.P. Chawla, A. Sharma, *Carbohydr Polym*, **82**, 1243 (2010).
5. P. Saym, *J Mater Sci*, **48**, 6455 (2013).
6. N. Bordenave, S. Grelier, V. Coma, *Biomacromol.*, **11**, 88 (2010).
7. S. Wang, Y. Jing, *BioResources*, **11**, 1868 (2016).
8. M.B. Vásconez, S.K Flores, C.A. Campos, J. Alvarado, L.N. Gerschenson, *Food Res Int*, **42**, 762 (2009).
9. J.W. Rhim, C. L. Weller, K. S. Ham, *Food Sci. Biotechnol.*, **7**, 263 (1998).
10. T. Bourtoom, M.S. Chinnan, *Food Sci. Technol.*, **41**, 1633 (2008).
11. M. Jaworska, K. Sakurai, P. Gaudon, E. Guibal, *Polym Int*, **2**, 198 (2003).
12. Z. Zhou, K. Robards, S. Helliwell, C. Blanchard, *Int J. Food Sci Tech*, **37**, 849 (2002).



13. H. Dai, P. R. Chang, F. Geng, J. Yu, X. Ma, *Carbohydr Polym*, **79**, 306 (2010).
14. N. Follain, C. Joly, P. Dole, C. Bliard, *Carbohydr Polym*, **60**, 185 (2005).
15. R. Bollström, A. Määttänen, P. Ihalainen, J. Peltonen, M. Toivakka, *Patent application PCT/FI2010/050056*, (2009).
16. R. Bollström, A. Määttänen, D. Tobjörk, P. Ihalainen, N. Kaihoviirta, R. Österbacka, J. Peltonen, M. Toivakka, *Org. Electron.*, **10**, 1020 (2009).
17. M. von Bahr, F. Tiberg, B. Zhmud, *Langmuir*, **15**, 7069 (1999).
18. J. Kettle, T. Lamminmäki, P. Gane, *Surf Coat Tech*, **204**, 2103 (2010).
19. A. Drobchenko, J. K. Kamarainen, L. Lensu, J. Vartiainen, H. Kälviäinen, T. Eerola, *Frontiers Electr. Electron. Eng. China*, **6**, 328 (2011).

## ПЕЧАТАРСКИ КАЧЕСТВА НА ОПАКОВЪЧНА ХАРТИЯ, ПОКРИТА С ХИТОЗАН И ОРИЗОВА СКОРБЯЛА

У. Врabiч Бродняк\*, Д. Мук

*Департамент по текстил, графика и дизайн, Факултет по природни науки и инженерство, Университет в Любляна, Словения*

Постъпила на 26 октомври, 2016 г.; приета на 25 януари, 2017 г.

(Резюме)

Биополимерите, използвани като покрития на опаковъчна хартия, могат да осигурят значителна защита от влага, газове и пр. Поради екологични съображения синтетичните опаковки сега се заменят с материали на биологична основа. Термопластичната скорбяла и хитозанът могат да бъдат добър заместител на опаковките, базирани на петрола като суровина при опаковките. В това изследване се използват оризова скорбяла и хитозан като покритие на опаковъчна хартия. Цел на изследването е да се определи печатарското качество на така покритата хартия. Изследвано е и влиянието на дебелината на покритието върху печатарското качество. Хартията е покривана с две различни смеси. Първата е само с хитозан, а втората е смес от хитозан и оризова скорбяла в отношение 50:50. Покритията са правени при различни налягания, за да се постигне различна дебелина на покритието: 40µm и 80µm. Извършено е изпитание за изтриване по стандарта TAPPI T830. Тестът на сухо триене показва, че всички образци с покритие дават по-добри резултати (по оптична плътност) в сравнение с непокритите проби. В нашите изследвания две серии (по време на триене) са определени: 25 и 50 цикъла при скорост на триене 106 rpm. След 25 цикъла пробата, покрита с хитозан и оризова скорбяла показва по-добри резултати спрямо необработената хартия или обработена само с хитозанов разтвор. След 50 цикъла покритието от хитозан и оризова скорбяла още има по-добро съпротивление на изтриване, но не достатъчно за по-дълга употреба. Изследването показва повишено печатарско качество на покритата хартия, особено при покрития от смес на хитозан и оризова скорбяла..

## Lignosulphonate and waste technical hydrolysis lignin as adhesives for eco-friendly fiberboard

N. Yotov\*, I. Valchev, S. Petrin, V. Savov

*University of Chemical Technology and Metallurgy, 8 St. K. Ohridski Blv., 1756 Sofia, Bulgaria,*

Submitted November 30, 2016; Revised May 30, 2017

In this study is shown survey about possibility of utilization of Lignosulfonate and waste technical hydrolysis lignin within composition of medium density fiberboards (MDF) produced by dry method.

For the purpose of the study in the laboratory, they are produced MDF with different percentage participation of binder - phenol formaldehyde resin and input supplements lignosulfonate and Technical hydrolysis lignin in their composition. Identified are the main operational features of the boards and are compared with reference ones, without participation of the technical hydrolysis lignin and lignosulfonate. On this base is made analysis of results and are displayed adjacent conclusions and recommendations.

**Keywords:** Medium density fiberboards; MDF; lignosulfonate; technical hydrolysis lignin; phenol formaldehyde resin.

### INTRODUCTION

Wood-based panels are versatile products which made a number of requirements in terms of the environment. In recent years, increasing pressure to develop and produce environmentally friendly technologies for processing and wood products, create new demands on them.

Fiberboard, a structural and decorative material, is a fibrous-felted, homogeneous panel made from lignocellulosic fibers that are combined with a synthetic resin or other suitable bonding system and then bonded together under heat and pressure [1].

Consumption and production of the product MDF increased by continuous pace as in 2012 the consumption of MDF in Europe amount to 10.3 million m<sup>3</sup>, overtaking the need for chipboard [2].

The advantages of this type of boards as a building material and engineering possibilities are many, but there are drawbacks to natural wood. To improve the mechanical properties of the boards (MDF) wood pulp needs to be added adhesives such as emulsions. As adhesives are used water-emulsion synthetic resins having thermosetting properties and strong adhesion to wood. In addition are observed some disadvantages - high value materials contamination of manufacturing equipment, emissions in the environment and toxicity [3].

Wood composite boards are made based on phenol- or urea- formaldehyde resin and they attach to certain levels and amounts of formaldehyde. The process of the emission depends on the exogenous (temperature, relative humidity, air exchange) and endogenous (woody species, the amount of added binders, type of binder, the production conditions, etc. factors [4].

Numbers of the board are made with phenol-formaldehyde resin. Phenol-formaldehyde resins (PFR) compared to other resins have many advantages such as low cost, ease of use when incorporated in the wood mass, rapid gel time in hot pressing, low temperature curing, resistance to microorganisms and mostly water repellent ability and strength characteristics of the finished boards. MDF boards produced by the PFR are suitable for use in both internal and external conditions. One major drawback of the PFR is the given free formaldehyde into the environment when used as a component in the production of MDF.

This determines the relevance of research on the possibility of reducing content of synthetic resins in the wood panels (MDF) through the use of products where there are no harmful emissions. And research related to the possibility of recovery of products dropped by other wood processing industries are included in the wood boards.

Many products are manufactured based on Phenol Formaldehyde resin that vapors of free formaldehyde, which can cause health problems or illnesses in humans. Emissions of free formaldehyde most common causes: irritation of the eyes and upper airways, when the human body is exposed to the emission of formaldehyde in high doses there is a risk of severe poisoning, and prolonged exposure may result in chronic toxicity and even cancer.

For these reasons, worldwide continuously is conducted research to reduce and eliminate the release of free formaldehyde from wood-composite plates. One of the effective methods to reduce the amount of free formaldehyde in fiberboard is the addition of lignosulfonate or technical hydrolysis lignin in the role of binders to appear partial or

\*) To whom all correspondence should be sent:

E-mail: [niko\\_yotov@abv.bg](mailto:niko_yotov@abv.bg)

complete replacement of phenol-formaldehyde resins. On the other hand, it has a negative impact on the physical and mechanical properties of the resulting boards (MDF).

Globally experiments were performed in order to produce dry-formed fiberboards without a resin binder and they have generally been unsuccessful. In recent decades an old process has been re-investigated [1]. This process involves steam explosion of raw lignocellulosic material, thus hydrolyzing most of the hemicelluloses and plasticizing the lignin. The result of this pretreatment is a fiber that can be hot-pressed to produce fiberboard without the need for synthetic binders. Due to the important role of lignin in fiberboard manufacture, several studies have investigated the use of lignin as a natural adhesive and the possibility of replacing fibers with lignin [5].

There are studies in which are successfully produced medium density fiberboards (MDF) without the participation of synthetic resins. As a binder used is an enzymatic lignin [6-8].

A team of researchers from China have produced fiberboards with 10% enzymatic hydrolysis lignin activated at a temperature of pressing than 210° C and a cycle time of 60 s.mm<sup>-1</sup>. The water content of the fiber mass is at relatively high levels by 10 to 18 percent, in order to assist pseudo-phase transition of lignin. These plates with physical and mechanical indicators are close to the standard required and are completely non-toxic, as they are made of biological, natural, ingredients. Studies are still at the stage of laboratory research [6].

The object of this study is to investigate the use of lignosulphonate product and waste technical hydrolysis lignin as adhesives for eco-friendly fibreboard.

## MATERIALS AND METHODS

### Materials

**Wood fiber mass.** For the production of MDF in the laboratory were used wood fibers of mixed species - hardwood, 80% (Fagus sylvatica= 60% and Populus Alba = 40%) and softwood 20% (Pinus sylvestris).

**Bonding agent and other chemicals.** Lignosulphonate - Obtained from spruce wood with low hygroscopicity and average sugar content is used as an additive to replace a part of used Phenol Formaldehyde resin.

Chemical data: Calcium = 6%; Sugars = 7%; Ash = 16%; Solids = 93%; pH = 4.3 ± 0.8; Bulk density 550 kg/m<sup>3</sup>.

Technical hydrolysis lignin (THL) - Waste hydrolyzed lignin produced in the manufacture of

fodder yeast. Chemical analyses of technical hydrolysis lignin were determined according to the follow methods: cellulose (Kurshner); lignin (Klason), ash (TAPPI T-15m) [9] and Elemental Analyzer Euro EA 3000 used for analysis of C, N, S and H.

Chemical data: C - 44.6%; S - 0.7%; H - 8.6%; N - 0.16%; Solids - 92.1%; Lignin - 78%; Cellulose - 12.8%; Ash - 9.1%.

Phenol formaldehyde resin: Solids = 48%; Molecular ratio = 1: 1.3 Density = 1,1780 g.cm<sup>-3</sup>; pH 7.1-7.9; Viscosity at 25°C = 1,400 cps.

For the purpose of the study it was carried out a varying of the amount of the phenol formaldehyde resin from 5 to 15% used for producing of fiberboards (MDF). To determine the influence of the content of the lignosulphonate on the performance of the MDF panels are produced in the laboratory in modifying the content of lignosulphonate from 0 to 20% in increments of 5%. Control boards were made containing only the PFR of 5, 10 and 15%. At these concentrations were conducted experiments with the addition of THL and lignosulphonate.

**MDF panel manufacture.** Pre-prepared wood fiber mass (garnetted stock to the point of 11° Schopper-Riegler method and dried to 8% moisture content) was mixed with Phenol Formaldehyde resin. In some of the experiments the use of additives THL and lignosulphonate was conducted after preliminary gluing and other event together with resin. After subsequent drying of the wood fiber mass, to prepare a carpet timber, which is compressed in a hot press at a temperature of 200° C and 90 s/mm of the boards' thickness. Predefined density is 800 ± 20 kg.m<sup>-3</sup>.

### Methods

**Producing of MDF.** The experiment was designed to study the effect of two factors (percentage of added waste technical hydrolysis lignin and lignosulphonate) on four levels, and to compare fiberboards only with phenol formaldehyde resin. These levels were chosen on the basis of the literature review and on the research group's previous experiences in producing fiberboards (MDF) with externally added technical hydrolysis lignin. The test results of physical and mechanical properties of boards are displayed through specialized testing machine (Zwick Roell) and software to it (TestXpert® II).

Bonding of lignocelluloses material is essential for the manufacture of particleboard, fiberboard, OSB, laminated wood products and plywood. bonding of wood fibers or particles can be achieved by high pressure and temperatures, a phenomenon

known as auto-adhesion [10]. The effect can be used for making binderless boards and panels, but compared to boards made with synthetic adhesives the mechanical properties are inferior.

Technical hydrolysis lignin was injected to the wood fibers by two methods - dry and wet method. The maximum concentration is 10%. PFR's concentration varies from 5 up to 15%. Lignosulphonate has concentration of 5 or 10%.

**Test methods of physical and mechanical properties of MDF.** There were held 50 attempts and produced 50 pieces samples of MDF. All samples were cut before testing by saw and prepared according to the international standard ISO EN 325[11]. The MDF boards were annealed under conditions of 65% humidity and 25 ° C for a period of 72 h. until it reaches the equilibrium humidity and the adhesion in all processes finish before being conducted to a physical-mechanical test. The mechanical properties such as bending strength, modulus of elasticity, water absorption and swelling are determined in accordance with international

standards EN 310 [12], EN 317 [13], EN 622-5 [14]. The physical properties such as thickness swelling and water absorption are determined after 24 hours immersion in water requirements of EN 317.

## RESULTS AND DISCUSSION

### Mechanical properties of the MDF

Figure 1 and 2 shows the change in the indicator values Bending strength and Modulus of elasticity in the production of MDF with PFR and Lignosulphonate.

When added lignosulphonate as a binder to 5% were not observed significant changes in indicators of the boards produced with the PFR. By increasing the percentage of Lignosulphonata between 10 - 15% clearly stands increasing of bending strength of the samples. Respectively the trend is to carry on indicators modulus of elasticity for the same samples. Compared to the control samples the amendment is within 62% [12].

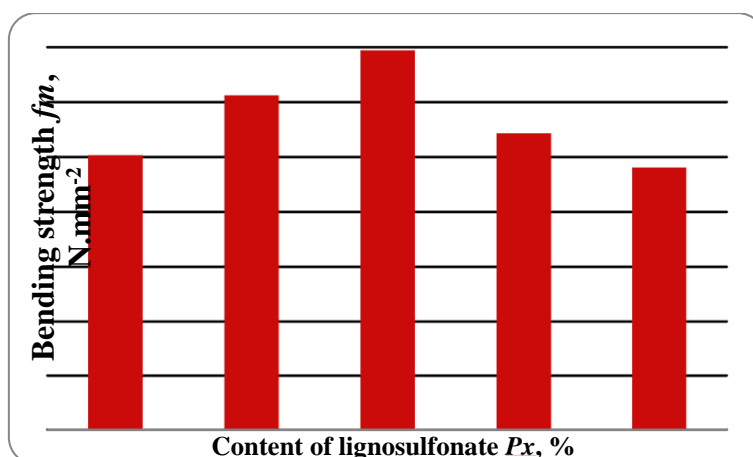


Figure 1. Bending strength of MDF, depending on the content of the lignosulphonate.

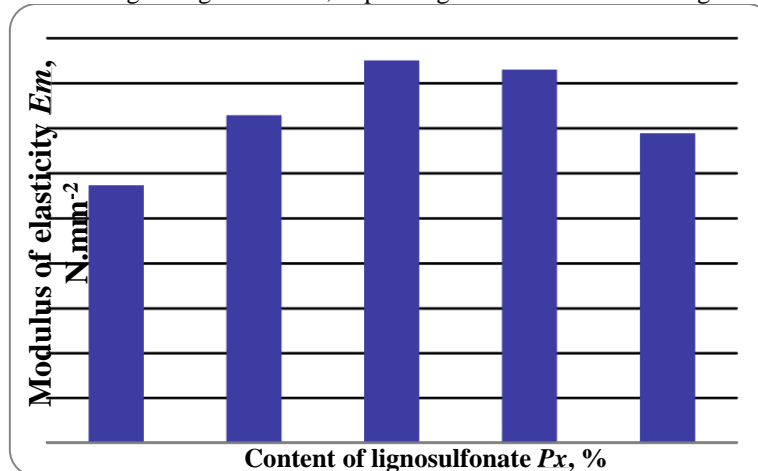


Figure 2. Modulus of elasticity in bending of MDF, depending on the content of the lignosulphonate.

In the indicator for thickness swelling, boards without lignisulphonat are approximately 50%, while the addition of 15 to 20% sensitively is reduced to

20% of swelling (Figure 3). The improvement is 40% on the sampled magnitude [13]. Concerning the water absorption without lignosulphonate MDF value

is above 85%, but with the addition of lignosulphonate from 15 to 20% of the indicator is reduced to 60%

water absorption (Figure 4). The improvement is 73% on research magnitude [13].

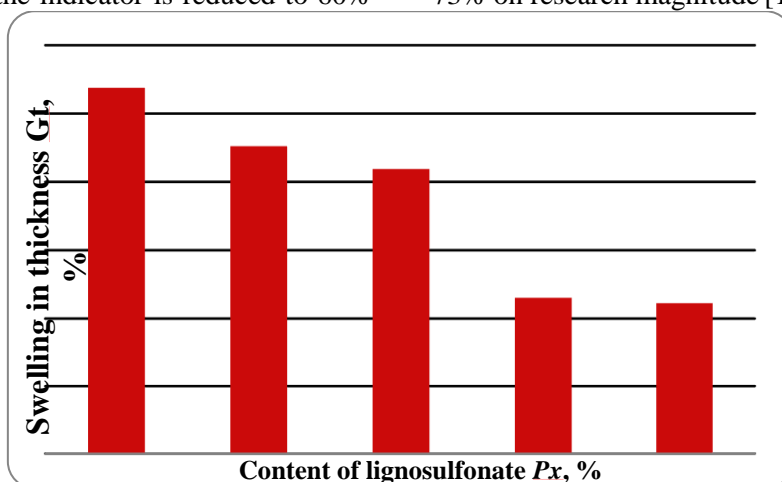


Figure 3. Thickness swelling of MDF, depending on the content of the lignosulphonate.

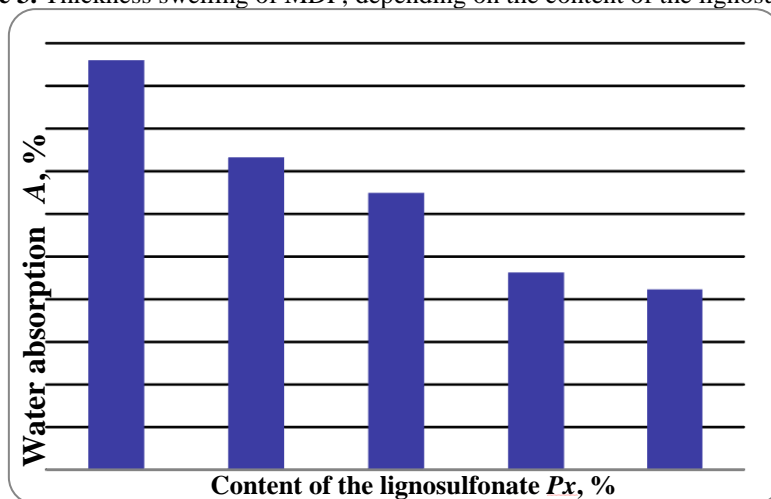


Figure 4. Water absorption of MDF, depending on the content of the lignosulphonate.

It is interesting that in the production of fiberboards (MDF) without the PFR, but only a 10% contribution from the lignosulphonate is obtained bending strength of  $22 \text{ N}\cdot\text{mm}^{-2}$ , which is a value very close to the required standard (Figure 5) [13].

Participation of 5% PFR and 5% Lignosulphonate follow the trend of increasing bending strength. The trend is maintained by increasing the content of the resin with 15% and 10% lignosulphonate. After exceeding the participation of the PFR with more than 15% effect is negative and the participation of lignosulphonata of 10% does not change the performance of research parameter (Figure 6).

Additional positive feature is the reduction of free formaldehyde, because it reduces the total quantity of Phenol Formaldehyde resin used in achieving the same, even more favorable physical and mechanical properties.

## CONCLUSIONS

Fibreboards obtained by the addition of lignosulphonate as a natural adhesive have good mechanical and water resistance properties that fully satisfy the relevant standard specifications.

Lignosulphonates can successfully be used as substitutes for conventional binders used in the production of fiberboards.

In the preparation of medium density fiberboard, with scientific purposes it is found that the waste technical hydrolysis lignin is more like active additive than a binder. By proper technique to use in the composition of wood fiber mass, ensuring proper mixing with the fibers and the resin it is possible to reduce the involvement of phenolic resins, and hence the free formaldehyde in the finished product.

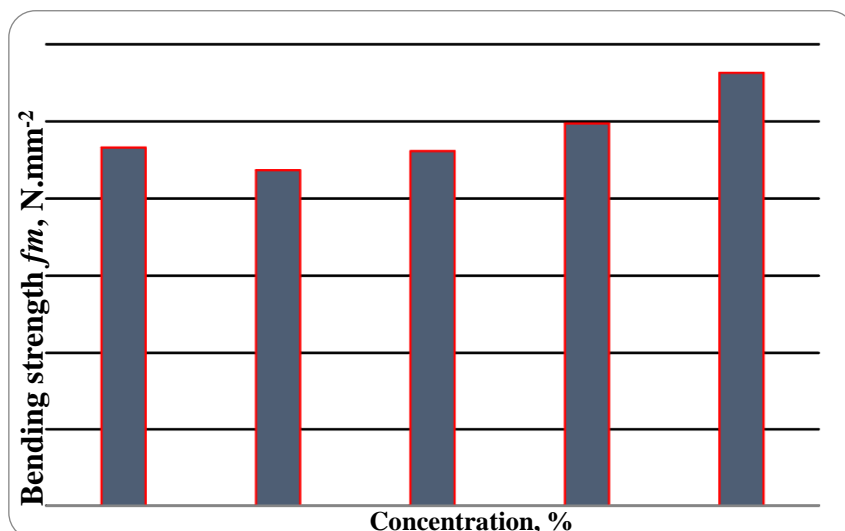


Figure 5. Bending strength of MDF depending on the content of the PFR and lignosulphonate.

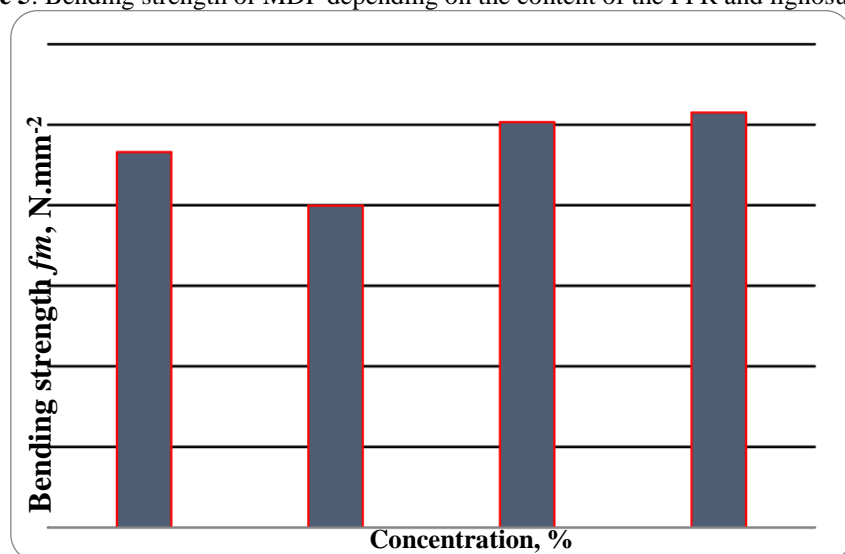


Figure 6. Bending strength of MDF with continuous content Technical hydrolysis lignin and various content of PFR.

#### REFERENCES

1. American National Standard for Containment System Leakage Testing Requirements, Approved August 4, 1994 by the American National Standards Institute, Inc.
2. www.europanel.org
3. S. Boran, M. Usta, E. Gümüřkaya, *Int. J. Adhesion Adhesives*, **31**, 674 (2011).  
<http://www.sciencedirect.com/science/article/pii/S0143749611000819>
4. E. Roffael, *Holz als Roh- und Werkstoff*, **64**, 144 (2006).  
[https://www.researchgate.net/publication/225822907\\_Volatile\\_organic\\_compounds\\_and\\_formaldehyde\\_in\\_nature\\_wood\\_and\\_wood\\_based\\_panels](https://www.researchgate.net/publication/225822907_Volatile_organic_compounds_and_formaldehyde_in_nature_wood_and_wood_based_panels)
5. C. Mancera, N.-E. El Mansouri, F. Vilaseca, F. Ferrando, J. Salvado, *Bioresources*, **6**, 2851 (2011).
6. X. Zhou, et al., *Waste Management*, **32**, 1962 (2012).  
<http://www.sciencedirect.com/science/article/pii/S095653X12002280>
7. M. Sedliacik, J. Sedliacik, Lignin-based wood adhesive, Technicka Univerzita Vozvolene, Zvolen 1997
8. N. El Mansouri, A. Pizzi, J. Salvadó, *Holz als Roh- und Werkstoff*, **65**, 65 (2007). doi:10.1007/s00107-006-0130-z  
<http://link.springer.com/article/10.1007/s00107-006-0130-z>
9. Technical Association of the Pulp and Paper Industry (TAPPI) Standard.
10. E. Farima, B. Rustam, A. Khan, *J. Appl. Polymer Sci.*, **108**, 624 (2008).  
[http://umpir.ump.edu.my/4571/1/cd6490\\_ema\\_farima\\_rustam\\_ali\\_khan.pdf](http://umpir.ump.edu.my/4571/1/cd6490_ema_farima_rustam_ali_khan.pdf)
11. EN 325. (1993). "Wood-based panels. Determination of dimensions of test pieces"
12. EN 310. Wood based panels, determination of modulus of elasticity in bending and bending strength
13. EN 317. Particleboards and fiberboards, determination of swelling in thickness after immersion
14. EN 622-5. Fibreboards, specifications. requirements for dry process boards (MDF)

**ЛИГНОСУЛФОНАТ И ОТПАДЪЧЕН ТЕХНИЧЕСКИ ХИДРОЛИЗЕН ЛИГНИН В РОЛЯТА НА СВЪРЗВАЩО ВЕЩЕСТВО ПРИ ПРОИЗВОДСТВОТО НА ЕКОЛОГИЧНИ ПЛОЧИ ОТ ДЪРВЕСНИ ВЛАКНА**

Никола Йотов\*<sup>1</sup>, Иво Вълчев<sup>2</sup>, Стойко Петрин<sup>3</sup>, Виктор Савов<sup>4</sup>

*Химикотехнологичен и металургичен университет, бул. „Св. Климент Охридски” № 8  
1756 София, България*

Постъпила на 30 ноември, 2016 г.; коригирана на 30 май, 2017 г.

(Резюме)

В настоящият доклад е представено изследване относно възможността за оползотворяване на лигносулфонат и отпадъчен технически хидролизен лигнин в състава на плочи от дървесни влакна със средна плътност (MDF) произведени по сух метод. За целта на изследването, в лабораторни условия, са произведени плочи с различно процентно участие на свързващо вещество - фенолформалдехидна смола и влаганите добавки лигносулфонат и технически хидролизен лигнин в техния състав. Определени са основните експлоатационни показатели на плочите и са сравненени с тези на еталонни такива, без участие на технически хидролизен лигнин и лигносулфонат. На тази база е осъществен анализ на получените резултати и са изведени прилежащи изводи и препоръки.

## Adhesives based on recycled polyurethane foam for wood based materials

K. Dimitrov<sup>1</sup>, V. Yavorova<sup>2</sup>, M. Herzog<sup>1</sup>, S. Nenkova<sup>2\*</sup>

<sup>1</sup>Technische Hochschule Wildau, DE-15745 Wildau, Germany

<sup>2</sup>University of Chemical Technology and Metallurgy, Sofia, 1756, Bulgaria

Submitted September 26, 2016 ; Revised March 1, 2017

Wood materials are increasingly being used in the construction of structural beams, sports equipment, etc. This study was carried out to investigate a new adhesive materials based on recycled polyurethane (PUR) foam. Mechanical tests, DSC, and FTIR were used to study the properties of the composites. After preparing the two-plate systems (beech, oak, walnut and pine tree) glued by the new adhesives and compared with adhesives based on polyvinyl acetate (PVA) the bonding strength and resistance of delamination were determined. Bond strength and water resistance (resistance of delamination) of two wooden plates bonded by the new adhesives were tested using standard methods. The highest shear strength of 16.1 MPa was received with oak wood bonded by the PUR adhesive. All samples prepared with the PUR adhesive were subjected to shear strength testing showing that the PUR adhesive is superior to PVA. In the water resisting test wood species bonded by PUR adhesive had a higher delamination rate than those bonded using PVA glue.

Keywords: Adhesive, recycling, polyurethane, wood

### INTRODUCTION

Adhesives based on polyurethanes (PUR) are used in a wide range of application such as woodworking, furniture building or restoration, boat building and repair, cabinet making and millwork, stone, tile and masonry processing, light aircraft building and repair, crafts, composites production and many others. With respect to the different composition and applied methods as well as versatility in PUR chemistry, various types of PUR adhesives are available in the market, solvent based, solvent-less or water-borne. PUR adhesives usually contain a number of urethane groups in the molecular backbone or they are formed during processing without consideration of the chemical composition of the chain. Thus, typical polyurethane adhesives may contain in addition to urethane linkages aliphatic and aromatic hydrocarbons, esters, ethers, amides, urea and/or allophanate linkages, which are responsible to establishing the final properties [1].

Wood bonding is based on a complex chemistry considering hydrogen bonding, Van der Waals forces, crystallinity or the like. To bond wood to wood, urea or phenol formaldehyde resin based adhesives are available, but these are generally sensitive towards hydrolysis and also cleavage due to stress i. e. often observed in plywood [2-6]. To increase the mechanical properties of plywood, PUR adhesives were recently introduced [7] giving good results. Some disadvantages, e. g. shorter pot life, durability and higher costs, are observed in acrylate based adhesives [8, 9].

PUR adhesives are made from synthetic, oil based

chemicals. To avoid environmental pollution problems, cost effectiveness, recycling poly(ethylene terephthalate) PET based PUR wood composites and adhesives for rubber are object of current industrial interest [10,11]. The recycling of PET to polyols is a sound way to reduce the cost [12] of raw materials used to produce PUR adhesives.

Another source to produce polyols suitable as basic raw materials of adhesives is the recycling of PUR foams. Generally, there are two ways to recycle PUR foams: physical and chemical.

The chemical recycling of polyurethanes is based on the cleavage of urethane bonds by means of a suitable reagent releasing the polyols of the polymer chain and the oligo-ureas as the reaction product of the isocyanates. Various chemical procedures for decomposing used PUR foams have been developed [13-18]. The processes are usually carried out with solvents, glycols, and/or polyols at elevated temperatures usually in the presence of a catalyst. The solvents used in the decomposition reaction include water, alcohols, diols, polyols, inorganic or organic acids, amines, and alkaline compounds. When alcohols such as low molecule weight glycols are used as decomposing solvents, they transesterify the urethane linkages, resulting in short chain hydroxyl functional urethane oligomers, and the polyols used in the reaction of the original PUR foams are thus released [13]. This process is designated as glycolysis. The polyols recovered from glycolysis were re-used in PUR foam manufacturing, but with limited success. Currently, recovered polyols can only partially replace commercial polyols in a PU

\*) To whom all correspondence should be sent:

E-mail: [nenkova@uctm.edu](mailto:nenkova@uctm.edu)



foam-forming reaction. The main obstacle is the presence of the oligoureas (the isocyanate component constitutes 20 to 50 % of the foams) either in the recycle or as waste product; in some glycolysis processes the oligoureas are further reacting [19, 20].

In this paper we describe an attempt to synthesize polyether polyols out of PUR foams to form the basis of adhesives for gluing wood products. This is a continuation of previous work to develop wood composite materials using polyurethane recycling

polyols as the binder [21-24]. The process used was the glycolysis of PU foam using di-n-butylamine and dipropylene glycol as cleavage reagents and solvent. The oligomers obtained were utilized to synthesize the PUR adhesives. The synthesized adhesives were used the wood to wood bonding system. The bond strength and the delamination strength were measured by shear strength and water resistance delamination tests.

## EXPERIMENTAL

### Materials

For the synthesis of the PUR adhesive, the following materials were used:

The polyol, obtained from the glycolysis of flexible PUR foam (using 60 % of PUR foam, 4 % b. w. of di-n-butyl amine in dipropylene glycol) is characterized by a hydroxyl number of 460 mg KOH/g and an amine number of 46 mg KOH/g, and polymeric diphenylmethane diisocyanate (pMDI) with an isocyanate content of 31,5 %, supplied from BASF Schwarzheide GmbH.

For the preparing of the samples, four sorts of wood were used: beech, oak, walnut and pine.

### Instruments used for characterization

Differential scanning calorimetry was performed by a DSC 204 Phoenix, Netzsch GmbH, and the FTIR analyses were carried out using a Fourier Transform IR spectrometer Varian 600 IR Series in the wave-number range 600 – 4000  $\text{cm}^{-1}$ .

Microscopy was performed using a light digital microscope model VHX-5000 (Keyence). It was used to study and determinate the bond layer and the interfaces of the samples.

Mechanical properties (tensile shear strength test) of the samples were examined on a Zwick Z020. A small pressure tank was used for the water delamination tests.

### Preparation of the PUR adhesives

Preparation of polyurethane adhesives was carried out by reacting the polyol obtained from the glycolysis of the flexible PUR foam with the aromatic polyisocyanate (pMDI) employing an isocyanate index of 120 based on the sum of hydroxyl and amine

number.

### Preparation of the samples

Samples for the tensile shear strength tests were prepared according to DIN EN 204 standard from beech, oak, walnut and pine wood plates (longitudinal) by cutting stripes of 150 mm length, 20 mm width and 3 mm thickness out of blocks. Figure 1 shows the parameters of the samples.

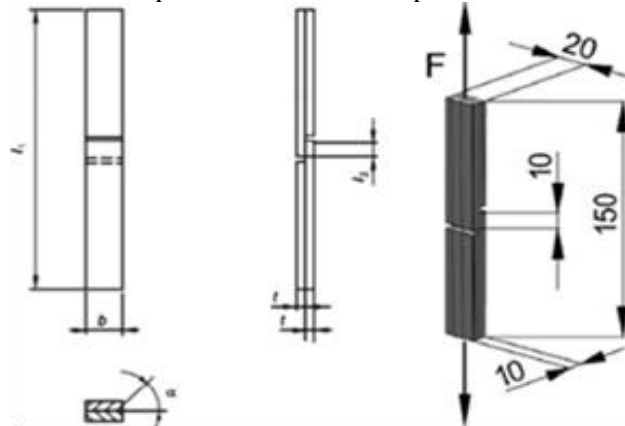


**Figure 1.** Sample parameters for tensile shear strength test according to DIN EN 204. Legend:  $l_1 = 150$  mm,  $l_2 = 7$  mm,  $b = 20$  mm,  $t = 5$  mm.

Samples for water delamination tests were prepared according to DIN EN 302-2 standard from beech, oak, walnut and pine wood.

## RESULTS AND DISCUSSION

### Differential scanning calorimetry

DSC analysis was used to investigate the thermal properties of the PUR adhesive. Figure 2 presents the curves of the DSC analysis.

The sample of the PUR adhesive was placed into DSC pans and sealed. The sealed pan was placed into a DSC instruments and cooled at a rate of  $10^\circ\text{C}/\text{min}$  (with liquid nitrogen as coolant) from room temperature to  $-100^\circ\text{C}$  and then heated at two thermal cycles with  $10$  K/min. The first run of the sample was performed by heating the sample from  $-100^\circ\text{C}$  to  $120^\circ\text{C}$  in the DSC pan, holding for 10 min at this temperature (to erase the thermal history) by slow cooling at  $10$  K/min to  $-100^\circ\text{C}$  and followed heating up to  $+250^\circ\text{C}$ .

The second run was performed by heating from  $-100^\circ\text{C}$  to  $+250^\circ\text{C}$ . The DSC curve in Fig. 2 shows that little gas loss occurs in the range between 50 and  $80^\circ\text{C}$ , while in the second run this peak has disappeared. The gas loss could not be attributed to the polymer structure but probably to gas dissolved in the adhesive or attached to the urea or urethane bonds. Such gas loss is well known to be typical in the case of DSC investigations of polyurethane foams but this is attributed to absorbed water or residual foaming agents. The DSC curve shows furthermore a

relaxation peak in the glass transition region hinting to structural re-arrangements in the polymer structure.

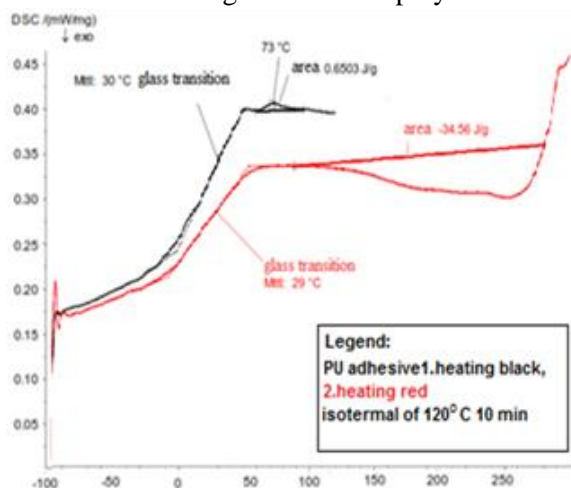


**Figure 2.** Differential scanning calorimetry of PU adhesive

At about 100°C in the first run a post-reaction occurs probably as a result of (probably structurally hindered) free isocyanate groups reaction with the water contained in the wood or with hydroxyl groups of cellulose or lignin catalyzed by the residual amines in the recyclate. It is further assumed, based on the FTIR spectra (see below) that transamination reactions of urethane groups available into urea groups occur with the cleavage of those urethane oligomers in the recyclate polyol which have not been cleaved in the synthesis. In the second run, the glass transition is well defined at +30°C as the transition of the mixed polyetherurethane phase of the glycol used in the recycling process and the liberated long-chain polyether polyol of the foam. Beginning again at 100°C, there is a broad exotherm maximum showing that the post-reaction occurs also in the second run but now with participation of a trimerization reaction of the isocyanate groups or further urea formation by a cleavage reaction of weaker urethane groups. A small endotherm maximum at about 230°C reflects the melting of the crystalline oligourea phase originating from the oligoureas present in the flexible PUR foams with oligomers of 2 to 22 units in case of p-MDI.

### FTIR

Infrared spectroscopy was used for studying the PUR structure of the adhesive. FTIR analysis performed in the polyol and the PUR adhesive is depicted in Figure 3. Characteristic bands of the hydroxyl groups occur at about as a broad peak due to hydrogen bonded and non-bonded hydroxyls at 3400 cm<sup>-1</sup>, at 3353 cm<sup>-1</sup> the maximum of the NH-peak is seen. In the polyol this peak is shifted to 3328 cm<sup>-1</sup> due to hydrogen bonded NH of the oligoureas. At 2280 cm<sup>-1</sup> a very small peak is seen originating from free isocyanate groups due to steric hinderance

in the polymeric MDI. The bands of the carbonyl groups occur at 1726 cm<sup>-1</sup>, and 1706 cm<sup>-1</sup>, resp. The band at the higher wavenumber corresponds to non-hydrogen-bonded urethane CO which is smaller in the adhesive, that at 1706 cm<sup>-1</sup> to the hydrogen bonded carbonyl group of the carbonyl-C=O which is correspondingly stronger in the adhesive. The three bands observed between 2966 cm<sup>-1</sup> and 2869 cm<sup>-1</sup> were attributed to symmetric and non-symmetric stretching of the C-H bonds in the various hydrocarbon groups of the aliphatic chains and the aromatic rings. In Figure 3, the wavenumber of the NCO peak of pMDI should be in the range of 2270-2250 cm<sup>-1</sup> but there is only a very small peak. Further, at 1680 cm<sup>-1</sup> as a shoulder and at 1598 cm<sup>-1</sup> as a band are seen the amid bands of the urea groups present both in the recyclate polyol and the adhesive originating from the decomposition of the PUR foam. At 1412 cm<sup>-1</sup> is the amid IV of the urethane group located.

However, the existence of peaks of amide groups –N-H at 3298 cm<sup>-1</sup>, 1510 cm<sup>-1</sup> and 1530 cm<sup>-1</sup>, the twin carbonyl urethane group at 1706 cm<sup>-1</sup>, 1726 cm<sup>-1</sup>, the carbamate group –CN at 1530 cm<sup>-1</sup> and the –C-O-C group at 1221 cm<sup>-1</sup> proved the urethane formation in the PUR adhesive, the band at 1588 cm<sup>-1</sup> the existence of urea groups derived from the oligoureas in the original foams.

According to Clemitson [25], the existence of the peak at 1730 cm<sup>-1</sup> is designated to a non-hydrogen bonded carbonyl urethane group –C=O while the peak at about 1706 cm<sup>-1</sup> is considered a hydrogen bonded carbonyl urethane group.

The polyol ether group is shown by the peaks at 1083 cm<sup>-1</sup> and 1066 cm<sup>-1</sup>.

### Microscopy

Figure 4 shows the PUR adhesive layer between the wood samples. The microscope investigation was used to calculate the thickness and the structure of the adhesive layer.

The PUR bonding layer in the examples of beech and oak do not show a homogeneous structure, many gas filled cavities were determined. This result can be explained with the availability of water in the raw reagents or, more probable, in the wood. The composites made with PUR adhesive and pine or walnut have a layer of approximately 130 μm for pine and about 30 μm for walnut, respectively.

The composites made with PVA adhesive using beech, oak and walnut (see Figure 5) showed the adhesive layer being between 13 μm and 20 μm. PVA and pine wood has a thickness of ≈ 60 μm.

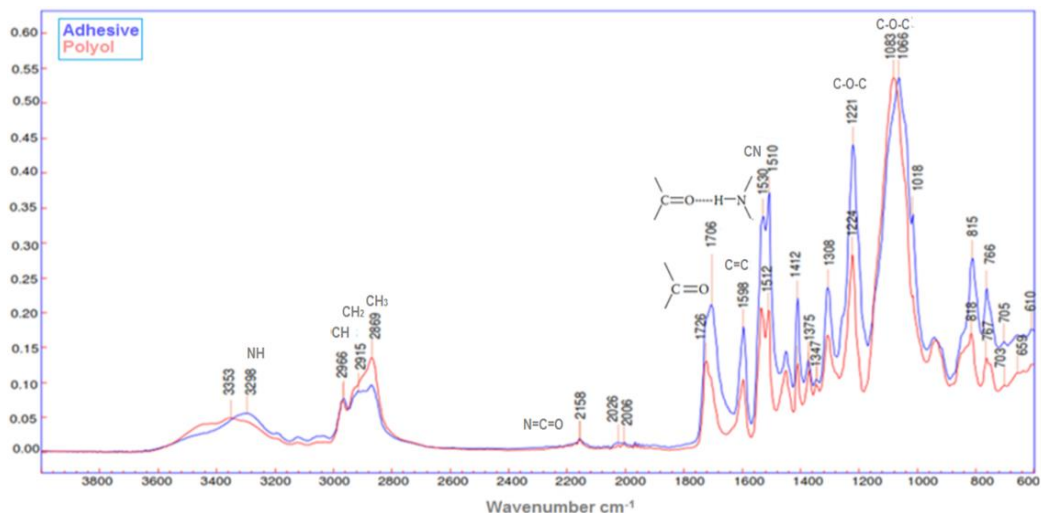


Figure 3. FTIR of the recycling polyol in red and the adhesive in blue.

The tensile shear strength test (see Figure 5) shows that the PUR adhesive is characterized by higher values in case of walnut, oak, or pine wood bonding but in case of beech PVA is superior. Comparing the average values of bonding strength, the highest value (16.11 MPa) was obtained for the oak wood sample bonded by PUR adhesive. The bonding strength of beech wood glued with the PUR adhesive was lower (8.77 MPa) than in case of the other wood types.

The samples of walnut and pine wood bonded by the PUR adhesive were (14.42 MPa) and (11.98 MPa), respectively. However, small differences were observed for different compositions of the adhesives.

### Mechanical properties of materials

The strength of the bonded samples of walnut, oak and pine wood with the PU adhesive gave higher values than the bonded samples using the PVA adhesive.

The information about the bond strength of the adhesives corresponds to the investigation of the surface of the samples after the tensile test, see Figure 7.

In 90 % of the samples the adhesive film was not delaminated from the wood but a cohesive failure of the wood was observed. The orange colouring was used to show the site of destruction of the wood structure. From Figure 7 it is to be seen why the

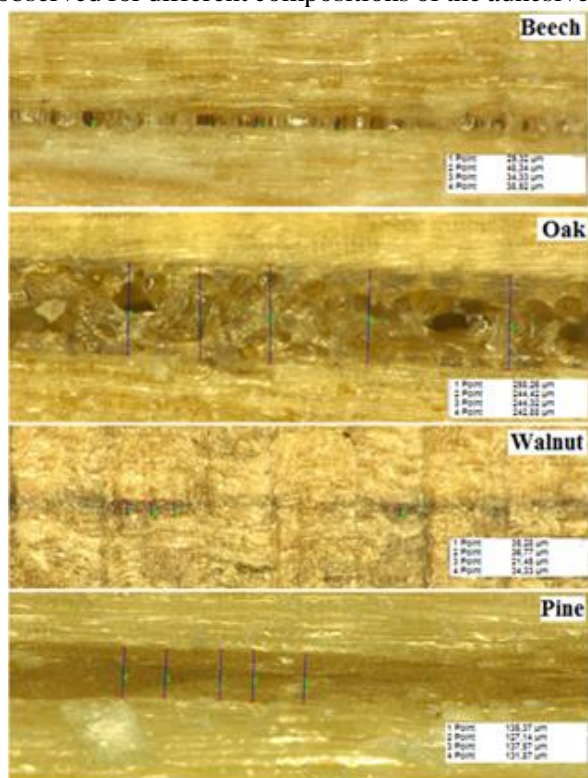


Figure 4. Light microscopy of PU adhesive layer.

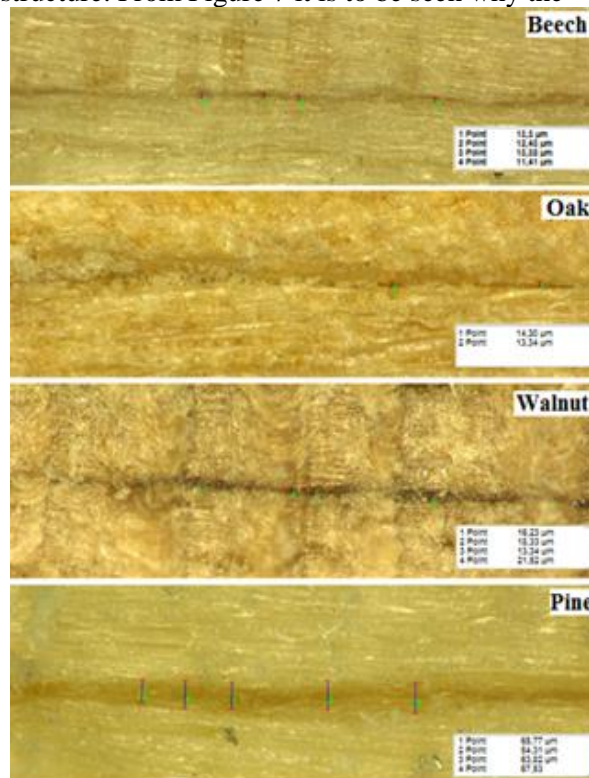


Figure 5. Light microscopy of PVA adhesive layer

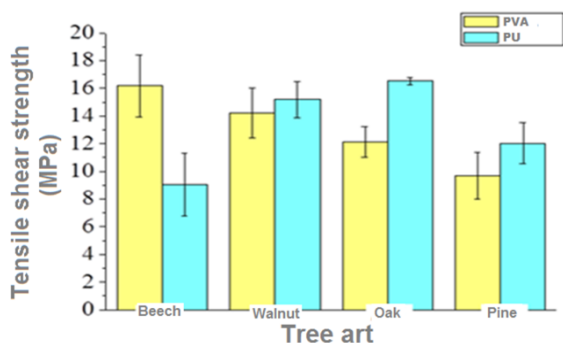


Figure 6. Tensile shear strength test of adhesives.

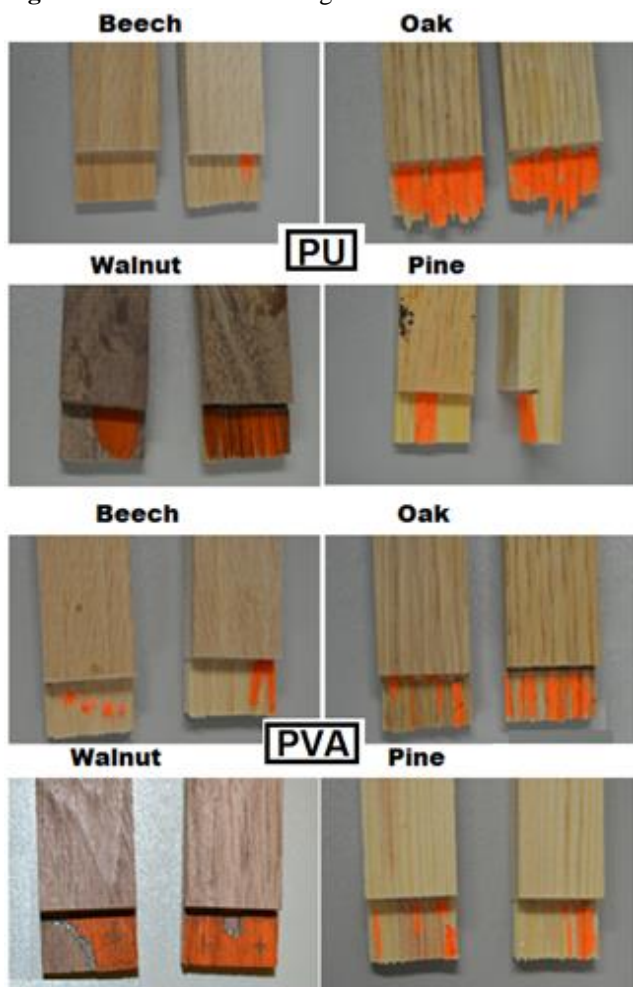


Figure 7. Surface inspection after shear tensile strength test.

samples of beech bonded with the PUR adhesive have lower shear tensile strength than the other samples. The bonding strength between the adhesive and the wood structure was too low to form a stable composite. One reason maybe the surface structure of the wood sample. The beech wood plates had very smooth surfaces.

*Resistance of delamination*

Water resistance of the adhesives (for exterior application) was tested by using the method described in standard DIN EN 302-2. Three cycles according to the conditions shown in Table 1 were

performed.

Table 1. Measurement conditions of delamination test.

Processing	Parameter	Unit	Value
Treatment	Water		
	Temperature	°C	10 – 25
	Duration	min	15
	Pressure	kPa	600±25
	Duration	h	1
Drying	Number of water cycle	-	2
	Air temperatur	°C	65±5
Drying	Duration	h	20
	Number of cycle	-	3
Number of cycle	Number of complete cycle		3
	One cycle consist of two water cycles and drying		

Water-soaking and drying tests of the composites made of the four wood types and the adhesives showed that the adhesive based on PVA had a better water resistance than the PUR adhesive. The results are depicted in Figure 8.

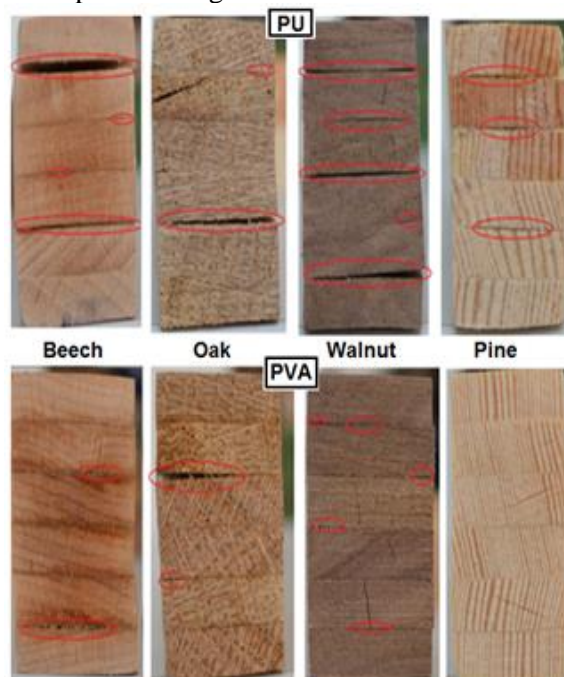


Figure 8. Visual inspection of selected test specimens after the delamination test.

The specimens with PVA adhesive (lower series) showed only a few cracks, while the specimen with the PUR adhesive lead to extensive cracking of the wood material. The highest resistance against delamination was observed in case of the pine wood with both types of adhesives (without delamination for PVA). Only 2 of the 8 samples fulfilled the standard requirements: they suffered less than 5 % delamination.

## CONCLUSIONS

- The recycling method of the flexible PUR foam was successful. The obtained polyol was stable and it has been used in synthesis of adhesive glue for wood based materials.
- Based on the results of this study, PUP foam wastes could be de-composited into recycled polyols and formulated into adhesives for wood with comparable or even improved performances than commercial products. This could help providing a potential new way of utilizing PU wastes as well as developing new adhesive systems for wood or plywood manufacturing.
- The adhesives prepared from recycled polyol presented shorter gel time and greater dry bonding strength than those prepared from PVA.
- The highest resistance against delamination was observed in case of the pine wood with both types of adhesives (without delamination for PVA).

## REFERENCES

1. C. Strobeck, *International Journal of Adhesive & Adhesion*, **10**, 225 (1990).
2. M. Kreneski, F. Johnson, C. Temin, *Polymer Reviews*, **26**, 143 (1986).
3. A. Takemura, H. Mizumaehi, *Technomic Publishing Co.*, 25 (1991).
4. K. Badri, A. Ujar, Z. Othman, F. Sahaldin, *J. Appl. Polymer Sci.*, **100**, 1759 (2006).
5. G. Myres, *Adhesives Age*, **31**, 31 (1988).
6. R. Ebewele, B. River and G. Myres, *Eur. J. Wood & Wood Products*, **52**, 179 (1994).
7. F. Dias and F. Lahr, *Materials Res.*, **7** (3), (2004).
8. M. Vallat and B. Bessaha, *J. Appl. Polymer Sci.*, 76 665 (2000).
9. D. Jia and X. Liang, *J. Appl. Polymer Sci., Part B: Polymer Physics*, **32**, 817 (1994).
10. M. Fornasieri, J. Weiller Alves, E. Muniz, A. Filho, H. Otaguro, A. Rubira, G. Carvalho, *Composites* **42**, 189 (2011).
11. S. Desai, J. Patel<sup>2</sup>, M. Patel, V. Sinha, *Indian J. Chem. Technol.*, **12**, 82 (2005).
12. R. Schaffrath, L. Skokova, G. Behrendt, R. Langenstrassen, *Poliuretanovye Tekhnologii*, **1**, 22 (2006).
13. G. Behrendt, B. Naber, *J. Univ. Chem. Technol. Metall.*, **44**, 3 (2009).
14. R. White, D. Durocher, *J. Cellular Plastics*, **33**, 477 (1997).
15. C. Wu, C. Chang, J. Li, *Polymer Degrad. Stability*, **75**, 413 (2002).
16. C. Wu, C. Chang, C. Cheng, H. Huang, *Polymer Degrad. Stability*, **80**, 103 (2003).
17. J. Lee, D. Kim, *J. Appl. Polymer Sci.*, **77**, 2646 (2000).
18. C. Molero, A. Lucas, J. Rodríguez, *Polymer Degrad. Stability*, **91**, 221 (2006).
19. D. Georgieva, S. Nenkova, G. Behrendt, *J. Univ. Chem. Technol. Metallurgy*, **42**, 345 (2007).
20. D. Georgieva, M. Markwardt, H.-D. Hunger, M. Herzog, G. Behrendt, *Polyurethan-Holz-Komposite und Verfahren zu ihrer Herstellung*, DE-OS 10 (2006) 021 266 (02. 05. 2006/ 23. 11. 2006).
21. D. Georgieva, R. Evtimova, R. Madzharova, G. Behrendt, *Composites Based on Recycling Products, Wood raw materials, and Polyurethanes*, Conference "Organic Precursors", Odessa, (2005).
22. D. Georgieva, S. Nenkova, M. Herzog, G. Behrendt, *BioResources*, **3** (3) 859 (2008).
23. V. Stoychev, B. W. Naber (*Lambda One Isoliertechnik GmbH*), *Verfahren zur Herstellung von Polyolkomponenten für Polyurethane aus Polyurethan-Hartschaumstoffen*, DE-OS 10 2009 026 898 (16. 12. 2010); EP 2 270 083.
24. M. Lezius, B. Naber, Bernhard (*BASF Schwarzheide GmbH*), *Verfahren zur Herstellung von Recyclatpolyolen*, DE 44 45 890 A1 (27. 6. 1996).
25. I.R. Clemitson, *Castable Polyurethane Elastomers*, Second Edition, *CRC Press, Taylor & Francis Group*, (2012).

## ЛЕПИЛА ЗА ДЪРВЕСИНА БАЗИРАНИ НА РЕЦИКЛИРАНИ ПОЛИУРЕТАНОВИ ПЕНИ

К. Димитров<sup>1</sup>, В. Яворова<sup>2</sup>, М. Херцог<sup>1</sup>, С. Ненкова<sup>2</sup>

<sup>1</sup>*Техническо висше училище Вилдау, DE-15745 Вилдау, Германия*

<sup>2</sup>*Химико-технологичен и металургичен университет, София 1756, България*

Постъпила на 26 септември, 2016 г. ; коригирана на 1 март, 2017 г.

(Резюме)

Дървени материали все повече се използват като конструкционни материали, греди, спортни съоръжения, и т.н. Това изследване се провежда, за да се проучи нов залепващ материал базиран на рециклирана полиуретанова пена. Получените материали са охарактеризирани чрез механични тестове, диференциално сканираща калориметрия и трансмисионна инфрачервена спектроскопия. За изследването са използвани четири вида дървесина (бук, дъб, орех и бор). Изготвени са проби с лепилото получено от рециклирани полиуретанови пени и са сравнение със стандартно лепило за дървесина на базата на поливинил ацетат (PVA). Силата на залепване и устойчивост на разслояване бяха определени. Якост и устойчивост на вода (устойчивост на разслояване) на две дървени плочи, свързани с новите лепила са изследвани при използване на стандартни методи. Най-високата якост на опън при срязване (16.1 МПа) е получена с дъбова дървесина, свързан с лепило от рециклирани полиуретанови пени. Всички проби, приготвени с лепилото на PUR бяха подложени на якост на опън при срязване. Изследването показваща, че лепилото получено от рециклирани ПУ пени превъзхожда стандартното лепило базирано на поливинил-ацетат.

## Magnetically assisted fluidized bed bioreactor for bioethanol production

P.G. Velichkova, T.V. Ivanov\*, I.G. Lalov

Department of Biotechnology, University of Chemical Technology and Metallurgy, 8 Kliment Ohridski blvd.,  
1756 Sofia, Bulgaria

Submitted January 24, 2017; Revised May 2, 2017

Ethanol can be produced by fermentation of sugars from agricultural products as wheat and corn, after milling and hydrolysis. The mash after dry mill contains up to 25% reducing sugars, suspended solids and it is very viscous. In this study the effect of a magnetic field on ethanol fermentation with magnetically assisted fluidized bed reactor (MAFBR) was investigated. Magnetically loaded polyurethane foam cubes (3x3x3mm) were used as support material for biofilm formation in a fluidized bed reactor. The magnetite content was 100% wt/wt; density 1050kg/m<sup>3</sup> and immobilized biomass 150mg/g dry support. The polyurethane carriers were stable and had high ethanol fermentation activity. The reticulated structure of the polyurethane foam enabled adherence as well as entrapment of biomass. Magnetically assisted fluidised bed experiments were performed in a glass column 50mm ID and total volume of 1 L, surrounded by a pair of Helmholtz coils with 200mm ID. The performance of ethanol fermentation of mash in the MAFBR was affected by dilution rate and magnetic field intensity. The ethanol productivity reached 17 g/L.h at a feed dilution rate of 0.6 h<sup>-1</sup> with reducing sugars concentration of 150g/L when the magnetic field intensity was 10kA/m.

**Key words:** bioethanol, magnetically assisted, fluidization, magnetic support.

### INTRODUCTION

Ethanol can be produced by fermentation of sugars from agricultural products or waste plant materials [1]. The batch fermentation process is relatively slow process, and continuous fermentation can increase the rate, even higher rates can be achieved if cell retention is also employed. To eliminate inhibition caused by high concentration of substrate and product as well as enhance ethanol productivity, cell immobilization approaches have been applied to produce ethanol continuously in bioreactors [2, 3]. A continuous fluidized bed reactor with the immobilized cell particles was demonstrated to significantly improve ethanol volumetric productivity as compared with the traditional batch systems and other continuous reactor configurations [4]. Magnetically assisted fluidized bed reactor (MAFBR) offers a number of potential advantages over the conventional fluidized bed reactor, such as elimination of solid mixing, low pressure drop through the bed, ease of solid transportation as well as the possibility of operation at increased fluid velocities [5]. The MAFBR has been used as an efficient system coupled with magnetic immobilized cells and enzymes for process intensification of biocatalysis and biotransformation [4, 5]. One of the major problems associated with application of MAFBR is development of suitable supports with magnetic properties. Taking into account that the magnetically stabilized bed

bioreactors operate at velocities greater the minimum fluidization velocity in absence of a field, the bio-support density is of a principal importance. The higher relative fluid/particle velocity (due to density differences) increases the mass transfer efficiency, but this decreases the liquid residence time in the reactor and requires deep beds or recirculation. The employment of polyurethane foam beads with entrapped cells has performed by many researchers [3, 6, 9]. The main purpose of present study was to investigate the influence of hydrodynamic conditions and magnetic field on ethanol productivity in the MAFBR with immobilized *Saccharomyces cerevisiae* cells, in continuous mode of operation.

### MATERIALS AND METHODS

The commercially available wetted polyurethane foam was cut as cubes (3x3x3mm). The magnetite was synthesised by co precipitation of Fe<sup>3+</sup> and Fe<sup>2+</sup> salts [7]. Briefly 5,4 g of FeCl<sub>3</sub>·6H<sub>2</sub>O and 2,78 g FeSO<sub>4</sub>·7H<sub>2</sub>O were dissolved in 20 ml distilled water. The polyurethane foam support (2g) was soaked and mixed well in a solution and heated for 10 minutes to 80 °C. For co precipitation the support cubes were added drop wise into the NH<sub>4</sub>OH (8 M) solution under stirring. After 3 h aging, the magnetic support was collected by external magnet, washed with distilled water to neutral pH and then dried at 60 °C. The procedure was repeated 5 times to obtain magnetic support. The obtained by co precipitation magnetic supports were characterized by XRD, after

\*) To whom all correspondence should be sent:  
E-mail: todorvelikovivanov@abv.bg

heating at 500 °C for 30min. The X-ray powder diffraction pattern of the sample was recorded on a Philips PW1050 diffractometer using  $\text{CuK}\alpha$  (1.5406Å) radiation at room temperature in the range of 10 to 80° in the 2θ scale, with a scanning speed of 0.02°/s and a step time of 3s. The void volume of support was determined by the weighting of dry and saturated with water samples. The cell adsorption and accumulation was carried out on a shaker at 150 rpm and 30°C for 7 days. The culture medium had

the following composition (g/L): 10 yeast extract, 20 peptone, 20 glucose, 1.5  $\text{KH}_2\text{PO}_4$ , 4  $(\text{NH}_4)_2\text{SO}_4$ , and 0.5  $\text{MgSO}_4$ . Every 24 hours the medium was replaced and support washed with fresh medium. The study of ethanol production activity of free and immobilized biomass of *Saccharomyces cerevisiae* was carried out with batch fermentation in shake flasks and corn hydrolysate from bioethanol plant (initial reducing sugars concentration 224g/L) was used as substrate.

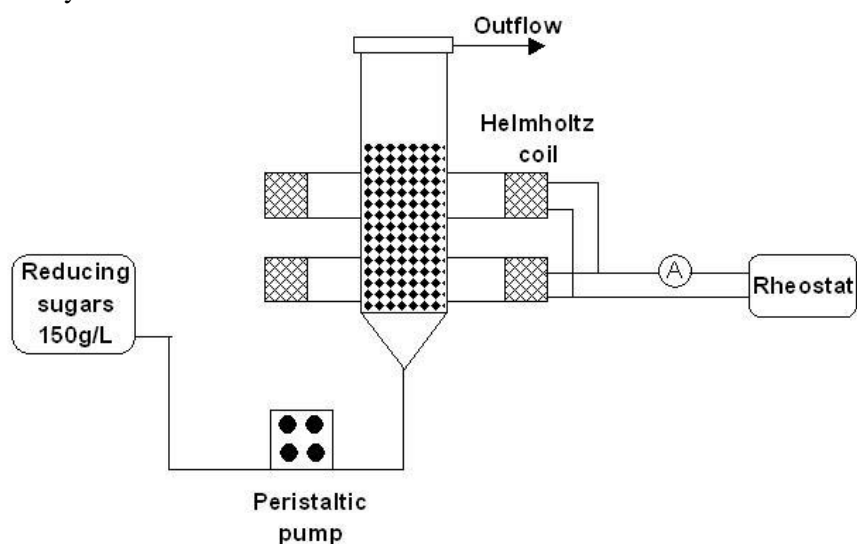


Fig. 1. Experimental set-up for ethanol production in MAFBR.

The magnetically assisted fluidization experiments were performed in a glass column (50mm I.D.) and total volume of 1L. The column was packed with support and substrate with 150g/L glucose was pumped thru the column. In all the experiments a pair of Helmholtz coils was used as a magnetic system. The magnetic field was axially oriented (e.g. parallel to the column axis). The internal coil diameter was 200 mm, distance between symmetry planes - 200 mm. The schematic view of experimental set-up is shown in Fig.1. The concentration of glucose was determined by DNS method. This method tests for the presence of free carbonyl group (C=O), the so-called reducing sugars. This involves the oxidation of the aldehyde functional group. Simultaneously, 3,5-dinitrosalicylic acid (DNS) is reduced under alkaline conditions [3]. The concentration of ethanol was determined by reaction with an excess of potassium dichromate in acid. The reaction was carried out in a special device [8]. The amount of unreacted dichromate is then determined by titration with ferrous ammonium sulphate and the ethanol concentration was calculated as chemical oxygen demand of solution.

#### RESULTS AND DISCUSSION

Whether the expected  $\text{Fe}_3\text{O}_4$  particles rather than other iron species were synthesized was confirmed

via XRD pattern. In order to compare the crystalline structure to define the iron species, XRD characterisation of both commercial  $\text{Fe}_3\text{O}_4$  purchased (Merck) and synthesised were undertaken. In Fig.2, the spectra of synthesized  $\text{Fe}_3\text{O}_4$  indicate similar characteristic peaks with

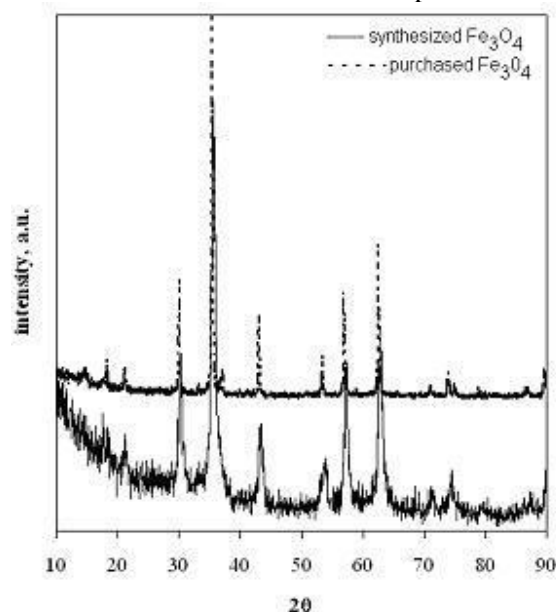


Fig. 2. The X-ray powder diffraction pattern of the synthesized and commercial samples.



commercial Fe<sub>3</sub>O<sub>4</sub> particles at 2θ (Brag angle) values of 30.1, 35.5, 43.2, 53.5, 57.1, 62.6°, which correspond to the typical peaks of Fe<sub>3</sub>O<sub>4</sub> particles [7]. So, there is no doubt that Fe<sub>3</sub>O<sub>4</sub> particles are synthesized successfully.

The main criterion for applicability of obtained support in magnetically assisted bioreactors is magnetic phase content. In order to test the magnetic properties constant magnetic field was applied. The separation of support from substrate under constant magnetic field is shown in Fig.3.



Fig. 3. Magnetic separation of magnetic polyurethane foam particles under an external constant magnetic field

The properties of obtained support and used substrate are summarized in Table 1. The data showed that there are not significant differences between densities of wet biosupport and substrate. The low-density supports allow reduced liquid flow rates and increased substrate residence time in the reactor.

Table 1. Support and substrate properties

Support				
Density dry kg/m <sup>3</sup>	Density wet kg/m <sup>3</sup>	Fe <sub>3</sub> O <sub>4</sub> content kg/kg	Size mm	
100	1050	0,98	3x3x3	Cubes
Liquid phase (substrate)				
Density, kg/m <sup>3</sup>	Reducing sugars, g/l		Suspended solids, g/l	
1030	224		126	

The results from biomass adsorption on magnetic and nonmagnetic polyurethane foam supports are shown in Fig.4. The better results were obtained with magnetite containing polyurethane foam support and

up to 0,15g/g yeast biomass was immobilized for 7 days. A comparison of the experimental results for the batch process using immobilized and free biomass is shown in Fig. 5. The figure shows that there is not difference between activities of free and immobilized cells. The time required for full conversion of hydrolysate to ethanol was 48 hours. Both the free and immobilized cells showed similar properties and this is the evidence that there are not any diffusional limitation, probably due the open pore structure of used support.

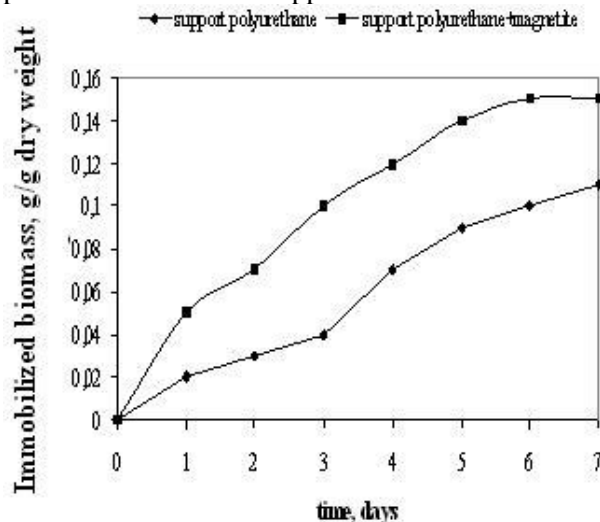


Fig. 4. Effect of incubation time on yeast immobilization.

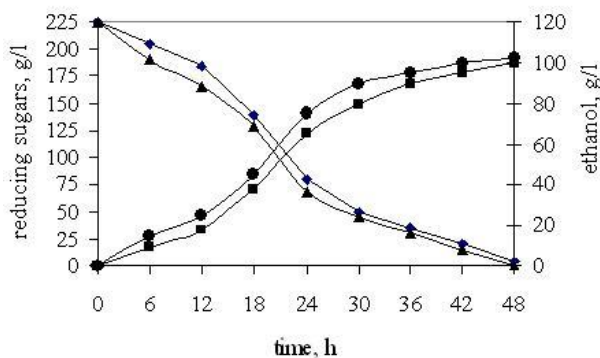


Fig. 5. Ethanol production by batch process with free and immobilized biomass.

In order to determine the hydrodynamic properties of bed the influence of fluid flow speed and magnetic field intensity on fluidisation velocity was examined. The phase diagram of the bed is shown in Fig. 6. It is seen than the fluidisation occurs at fluid velocity over 0,05 mm/s. The bioreactor can be operated as MAFBR at fluid velocities up to 0,2 mm/s and magnetic field intensity 10 kA/m.

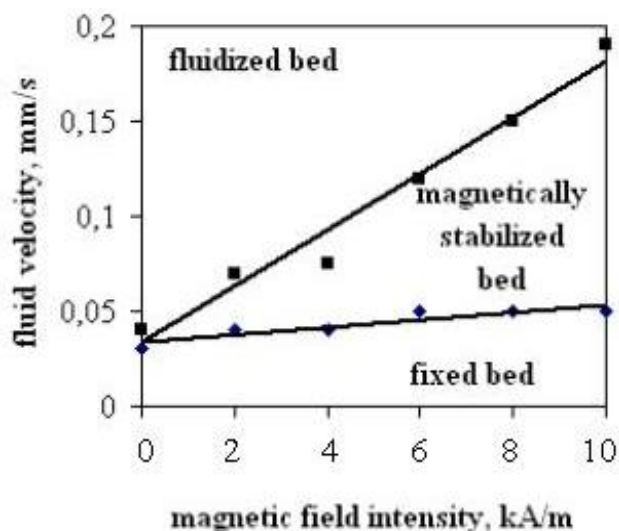


Fig. 6. Phase diagram of the MAFBR

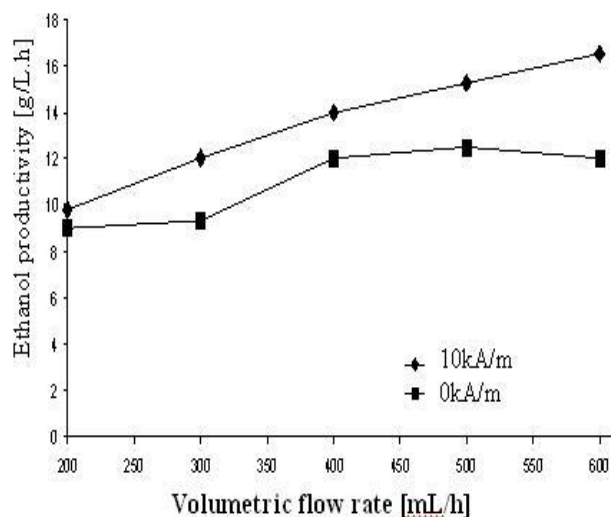


Fig. 7. Ethanol productivity as a function of fluid flow rate.

The results from ethanol production in continuous-flow column reactor are shown in fig. 7. The reactor was run in continuous mode at 25°C, and flow volume speeds from 200ml/h to 600ml/h. The column experiments show that performance of bioreactor increases when magnetic field was applied. The ethanol productivity reached 17 g/L.h, with reducing sugars concentration of 150 g/L when the magnetic field intensity was 10kA/m. The result of this study demonstrated that in MAFBR higher than fluidized bed reactor ethanol productivity can be achieved.

### CONCLUSION

The yeast cells of *S. cerevisiae* were immobilized by adsorption onto magnetite coated polyurethane foam support. An increase in the efficiency of the immobilization was observed in the presence of a magnetite ( $\text{Fe}_3\text{O}_4$  nanoparticles) embedded in a matrix.

Comparison with our previous research [8] showed that on closed pore polyurethane foam up to 0,04g/g dry weight yeast could be immobilized by crosslinking, while up to 0,15g/g yeast biomass was immobilized in open pore polyurethane foam support by biofilm formation. In addition, a slight increase in the performance was observed in non-continuous mode and ethanol productivity reached 7,1 g/L.h. The results obtained in denitrification study [9] showed lower degree of conversion as a result of the small liquid residence time in the bed. Our investigation showed that the use of a MAFBR allow a control of the fermentation process. The main advantage is the ability to decrease the

diffusional mass transfer resistance around the support. However, this effect is limited in particular velocity range. The further increase of the liquid flow rate and magnetic field intensity leads to lower degree of conversion. Other researchers also observed a similar effects [4,5,11].

### REFERENCES

1. S. Ingale, S. J. Joshi, A. Gupte, *Brazilian J. Microbiol.*, **45**, 885 (2014).
2. G. Najafpour, H. Younesi, K. S. K. Ismail, *Bioresource Technol.*, **92**, 251(2004).
3. C. M. S. G. Baptista, J. M. A. Coias, A. C. M. Oliveira, J. M. S. Rocha, M. J. Dempsey, K. C. Lannigan, P. S. Benson, *Enzyme Microbial Technol.*, **40**, 127 (2006)
4. C. Liu, F. Wang, F. Ou-Yang, *Bioresource Technol.*, **100**, 878 (2009).
5. C. Webb, H-K. Kang, G. Moffat, R. A. Williams, A. M. Estevez, J. Cuellar, E. Jaraiz, M. A. Galan, *Chem. Eng. J./Biochem.Eng. J.*, **61**, 241 (2006).
6. N. Abdehagh, M. T. Namini, S. M. Heydarian, B. Bonakdarpour, D. Zare, *Iran. J. Environ. Health. Sci. Eng.*, **8**, 245 (2011)
7. T. Sulistyaningsih, S. J. Santosa, D. Siswanta, B. Rusdiarso, *Int. J. Materials, Mechanics, Manufacturing*, **5**, 16 (2017)
8. A. Caputi, M. Ueda, T. Brown, *Am J Enol Vitic.*, **19**, 160 (1968)
9. T. Ivanov, J. Hristov, S.Petkova, *1st South-East European Symposium on Fluidized Beds in Energy Production, Chemical and Process Engineering and Ecology, Ohrid, Republic of Macedonia*, p. 379, (1997)
10. T. Ivanov, I. Lalov, L. Yotova, *Scientific Works of University of Food Technologies*, **LXII**, 536 (2015)
11. V. Ivanova, P. Petrova, J. Hristov, *Int. Rev. Chem. Eng.*, **3**, 289 (2011).

## ПОЛУЧАВАНЕ НА БИОЕТАНОЛ В БИОРЕАКТОР С МАГНИТНО АСИСТИРАН ФЛУИДИЗИРАН СЛОЙ

П.Г. Величкова, Т.В. Иванов\*, И.Г. Лалов

*Катедра "Биотехнология", Химикотехнологичен и металургичен университет, бул. Кл. Охридски №8,  
1756 София, България*

Постъпила на 24 януари, 2017 г.; коригирана на 2 май, 2017 г.

(Резюме)

Биоетанол може да бъде получен от редица селскостопански продукти, като жито и царевица. При този процес е необходима предварителна хидролиза на суровините. Полученият хидролизат се характеризира с високо съдържание на редуциращи вещества, до 25%, суспендирани частици и е много вискозен. Целта на настоящата работа е да се изследва ефекта на магнитното поле върху алкохолната ферментация в реактор с магнитно асистиран слой.

Като носител за имобилизиране на биомасата е използван пенополиуретан 3x3x3 mm, съдържащ магнетит. Съдържанието на магнетит в носителя е 100%, плътността 1050 kg/m<sup>3</sup>, като имобилизираната биомаса е 150 mg/g сух носител. Получените носители са стабилни и притежават висока ферментационна активност. Структурата на полиуретановата пяна позволява задържане на биомаса в целия обем на частицата. За биореактор с магнитно асистиран слой е използвана колона с диаметър 50mm и общ обем 1L, поставена в центъра на намотка на Хелмхолц с вътрешен диаметър 200 mm. Установено е, че върху производителността на апарата влияние оказват скоростта на разреждане и интензитета на магнитното поле. Производителността по отношение на етанол достига до 17 g/L.h, при скорост на разреждане 0,6 h<sup>-1</sup> и интензитет на магнитното поле 10 kA/m.

## Obtaining of high yield fibrous material from hardwood and evaluation of their optical properties of in process of thermal treatment

R. Boeva<sup>1\*</sup>, I. Spiridonov<sup>1</sup>, G. Radeva<sup>2</sup>

<sup>1</sup>Department of Pulp, Paper and Printing Arts,

<sup>2</sup>Department of Physical Chemistry

University of Chemical Technology and Metallurgy, 8, Kl. Ohridski Blvd., 1756 Sofia, Bulgaria

Submitted November 27, 2016; Revised May 23, 2017

The main fibrous materials used in the pulp and paper industry are: cellulose, semi chemical pulp, high yield fibrous materials (HYFM) and second fibers. All of them are of plant origin. They are obtained mainly from wood and annual plants.

In this study was used poplar wood species with improved density of type - *Populus deltoids cultivar Hunnegem* with density of 504 kg/m<sup>3</sup>. In this research were obtained two types of chemical mechanical pulps (CMP). CMP of Type 1 was obtained with 7% NaOH and 5% Na<sub>2</sub>SO<sub>3</sub>, and CMP of Type 2 was obtained with 7% NaOH, 5% Na<sub>2</sub>SO<sub>3</sub> and 2% H<sub>2</sub>O<sub>2</sub>. The CMP of Type 1 and 2 were received under the same conditions of temperature, hydromodul ratio, duration of process etc.

Both of Chemical Mechanical Pulps have a low degree of brightness, and therefore they are bleached in two stages. The initial process of bleaching was conducted with H<sub>2</sub>O<sub>2</sub> and second stage was performed with Rongalyt C. The samples of both CMP pulps were exposed to artificially thermal ageing at 105°C. The changes of brightness and yellowness in process of the thermal ageing of 105°C at 0, 6, 12, 24, 36 and 48 hours have been measured.

The main goals of this research are obtaining, bleaching in two stages, thermal ageing and evaluating of brightness and yellowness properties of CMP hardwood.

The experimental results of this study shows that the obtained CMP hardwoods could be added to papers for printing, graphic and packaging industry for increasing of printing properties (printability), adhesion of inks and varnishes and optical properties (opacity) of papers.

**Key words:** *hardwood, chemical mechanical pulp, bleaching, thermal ageing, fiber materials*

### INTRODUCTION

The *Populus* are fast-growing species trees. Reaches a height of about 25m and live up to 400 years. The Poplar wood finds wide application for the production of fibrous materials, and the advantage is that they are grown easily and well adapted to soil and climatic conditions of our country [1, 2].

Poplars are found in warm and low parts of our country. In Bulgaria meet basic 4 types of poplar: white poplar (*Populus alba*), black poplar (*Populus nigra*), gray poplar (*Populus canescens*) and aspen (*Populus tremula*) [3-5].

Of all the physical properties of wood most important is density. From her depends on the quantity of expenditure in digesting liquid [6, 7].

### EXPERIMENTAL

Chemical mechanical pulps (CMP) are obtained from the fast-growing hardwood poplar wood from species *Populus deltoids cultivar Hunnegem*. During the process of production of CMP are used: Na<sub>2</sub>SO<sub>3</sub>, analytical grade, NaOH and H<sub>2</sub>O<sub>2</sub>. During the bleached are utilized: H<sub>2</sub>O<sub>2</sub>, analytical grade,

Rongalyte C (NaHS<sub>2</sub>.CH<sub>2</sub>O.2H<sub>2</sub>O), from BASF. The initial material for laboratory experiments is a Poplar



### *Populus*

wood, characterized by higher cellulose content, lower lignin content and higher density.

The reagents Na<sub>2</sub>SiO<sub>3</sub> and MgSO<sub>4</sub> were applied as stabilizers of the H<sub>2</sub>O<sub>2</sub>. NaOH was added to reach a pre-determined pH level (10.5) [2, 5].

The following parameters of the produced CMP have been determined:

- Yield [%], determined by weight method in comparison to the mass of the absolutely dry timber;

\*) To whom all correspondence should be sent:

E-mail: [r\\_boeva@abv.bg](mailto:r_boeva@abv.bg)

- Milling degree, as determined by the device Schopper – Riegler (°SR) as per EN ISO 5267 – 1/AC:2004;
- Microscopic images of the CMP. Used a light microscope OLYMPUS BX 53.

For all used fibrous materials the degree of Brightness R457 and Yellowness (ISO 2470:2002) was determined before and after ageing thanks to the appliance by Spectrophotometer Gretag Magbeth Spectroeye.

#### *Production of CMP*

Wood cleaned from the root part and later shredded into slices with 20mm thickness. After roots removal the wood was chopped into chips of standard dimensions of 15x20x3mm. Used poplar wood species *Populus deltoids* cultivar Hunnegem is 100g in absolutely dry fibrous mass [5].

Obtained two types chemical mechanical pulps:

- CMP of Type 1 is obtained with 8% NaOH and 5% Na<sub>2</sub>SO<sub>3</sub>;
- CMP of Type 2 is obtained with 8% NaOH, 5% Na<sub>2</sub>SO<sub>3</sub> and 2% H<sub>2</sub>O<sub>2</sub>.

The CMP of Type 1 and 2 were received under the same conditions of temperature (80°C), hydromodul ratio 1:5, duration of process 120 min etc.

The preliminary weighted chips have been placed in a thermostatic container with the aim to temper it and to maintain the required permanent temperature.

After retention for a specified period, the used solution was removed and the chips have been washed to reach pH=7. The treatment continued by chips refined in a Sprout-Valdron laboratory mechanical refiner. Further fiber materials it was washed away and sorted out manually between two sieves.

The yield of CMP is calculated by the mass method. After soaking for 24 hours in distilled water, the treated chips were washed to reach neutral pH and dried into a drying apparatus at 105°C to achieve absolute dry state.

#### *Bleaching of fibrous materials*

##### *First stage of bleaching – with 2% H<sub>2</sub>O<sub>2</sub>:*

During the first stage of whitening pH=10.5 and it is maintained thanks to additives like: NaOH 2%, Na<sub>2</sub>SiO<sub>3</sub> 5%, MgSO<sub>4</sub> 0.5%. In order to sequester the ions of the heavy metals - solution of EDTA (ethylenediaminetetraacetic acid) was utilized. The quantities of all reagents are expressed as percentage regarding the absolute dry fibrous material. Separately prepare bleaching solution as a final H<sub>2</sub>O<sub>2</sub> was added and the solution was stirred to homogeneity. The fibrous materials is placed in a polyethylene bag. The content of the bleaching solution is poured at mass for bleaching. During the process, the mass is mix periodically. After the completion of the first stage, the fiber material is washed properly to obtain pH 7 and in this manner it is able to undergo the next phase. The conditions of bleaching are given in Table 1.

**Table 1.** Conditions of bleaching CMP

Type of Bleaching	Quantity of reagent, (%)	T, (°C)	Duration of process, (min)	Concentration of fibrous materials, (%)	pH of the solution
I stage	2% H <sub>2</sub> O <sub>2</sub>	70	120	10	10.5
II stage	1.5% Rongalyt C	70	60	6	5

##### *Second stage of bleaching - Rongalite C*

The conditions of the bleaching in the second stage are presented in Table 1. During the second stage of whitening of the two fiber materials, the reagents utilized are Rongalyt C 1.5% and EDTA 0.5%. The process of bleaching is similar to the one described in the first stage. After completion of the process, the fibrous mass is washed away again to adjust pH 7.

##### *Ageing of fibrous materials*

High-yield fibrous materials contain a lot lignin and therefore faster ageing. Samples of unbleached and both bleached (single-step and two-step) fibrous materials. Obtained are samples which are dried under natural conditions in the dark, without interference by direct sunlight. After drying the samples are subjected to artificial thermal aging at

105°C. In order to characterize the ageing process for bleached and unbleached samples, the degrees of brightness and yellowness for periods of 0, 2, 4, 6, 12, 24, 36, 48 and 72 hours since the commencement of the artificial thermal ageing are determined.

##### *Microscopic analysis of the fiber material*

After obtaining, bleaching and ageing CMP were taken microscopic pictures of apparatus OLYMPUS BX 53. Microscopic analysis was made on the requirements of ISO 8658-71. Prior to this a small amount of each sample was treated to produce a fibrous materials, which was then treated with distilled water aiming to obtain a homogeneous suspension of a concentration of 0.05%. After drying of samples is added solution of Cl-Zn-J (Herzberg reagent) in ISO 9184-3:1990.

**Table 2.** Chemical and physical properties

Wood	Density in air dry state, [kg/m <sup>3</sup> ]	Cellulose, [%]	Lignin, [%]
<i>Populus deltoids cultivar Hunnegem</i>	504	50.4	21.2

RESULTS AND DISCUSSION

The results of the chemical analysis and physical characteristics of the used wood of the species *Populus deltoids cultivar Hunnegem* are presented in Table 2.

From the data in the Table shows that the test species poplar is characterized by much higher density than the usual (about 300-350 kg/m<sup>3</sup>) known species of poplars in Bulgaria. It differs with higher quantity of cellulose than 50% and lignin about 20%. This shows that this type poplar is suitable for obtaining HYFM and its use in the composition of different types of papers and cardboards.

During the study we obtained CMP type 1 - yield is 90% and degree of milling was 13<sup>o</sup>SR, CMP type 2- yield is 88% and degree of milling is 14<sup>o</sup>SR.

The utilization of HYFM in various brands of paper and cardboard is limited because of the low level of whiteness. Therefore, the resulting

chemical mechanical pulp is bleached in two stages.

For CMP type 1 degree of whiteness has increased by about 20 units. Almost the same result was obtained for the other CMP type 2 about 21 units (fig. 1-4).

The degree of yellowness in CMP Type 1 has decreased about 12 units of type 2 about 14 units. It is seen that in the process of aging as time went on, the degree of whiteness decreases and the degree of yellowness increases in all samples.

Furthermore artificial thermal ageing at 105°C is conducted. In order to investigate the impact of this ageing over the parameters of the different fiber materials, bleached and unbleached ones, the levels of whitening and yellowness are measured after various periods of time 0, 6, 12, 24, 36 and 48h. The most intensive in the process of artificial thermal aging change is observed in the early in the process.

On Figs 1 and 2 show the kinetic patterns that show the change of the degree of whiteness and yellowness over time for CMP type 1.

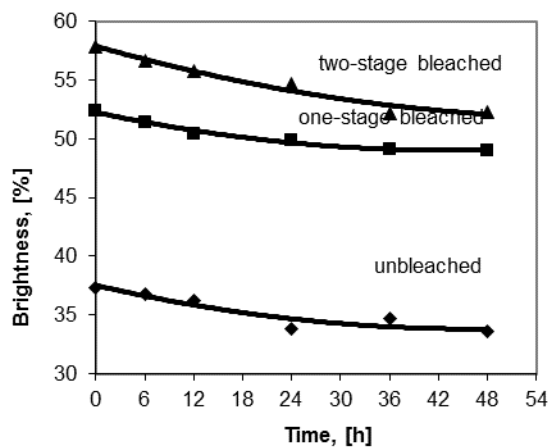


**Fig. 1** Change of the degree of Brightness with time from CMP type 1

From Fig. 1 it can be seen that the degree of whiteness decreases in all fibrous materials, regardless of whether it is unbleached, bleached in two stages or one stage, but to varying degrees. The higher degree of whiteness in the aging process is retained in a two-stage bleached materials.

Fig. 2 shows that regardless of the type of the test samples (bleached or unbleached), yellowness increases with time. Less increase in the degree of

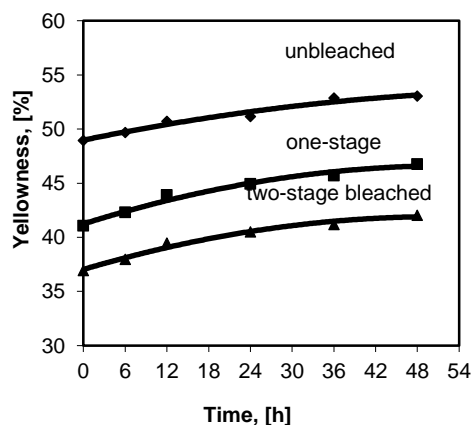


**Fig. 2** Change of the degree of Yellowness with time from CMP type 1

yellowness was observed in a two-stage bleached pulp - about 4 units.

In Fig. 3 are observed the same tendencies. The difference here is that the receiving of CMP type 2 it is treated with H<sub>2</sub>O<sub>2</sub> and another in unbleached type this mass is a degree of whiteness 42.59%. The mass is about 5 units higher brightness compared with CMP type 1.

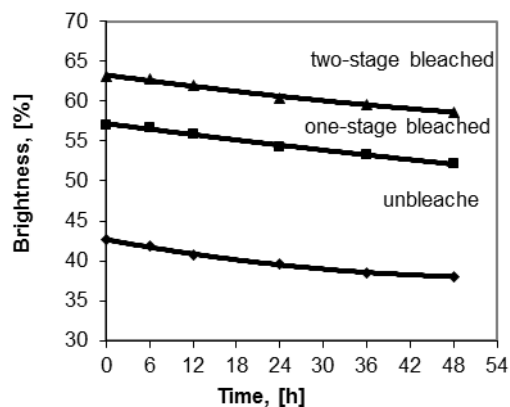


Fig. 3 Change of the degree of Brightness with time from CMP type 2

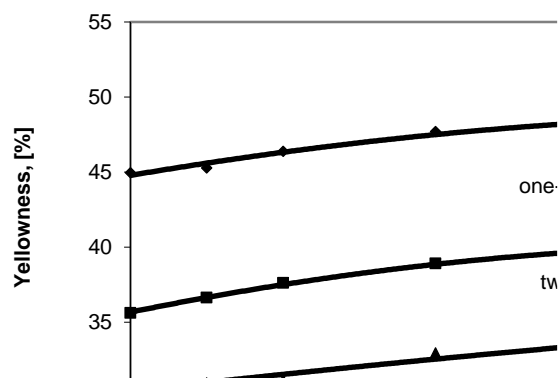
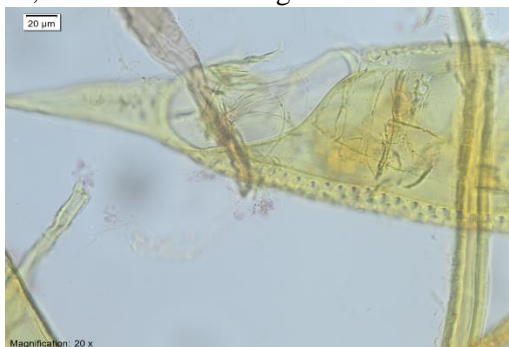


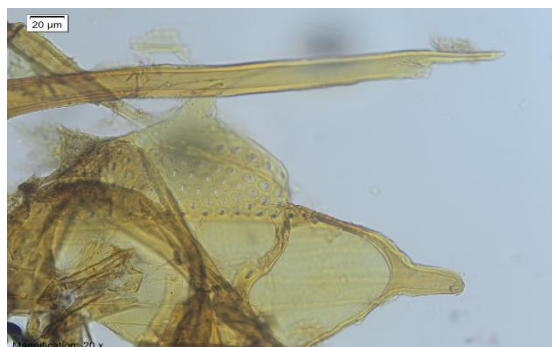
Fig. 4 Change of the degree of Yellowness with time from CMP type 2

Fig. 4 shows the degree of yellowness increases with time in all samples. From figure 2 and Fig. 4 shows the degree of yellowness increases with about 4-6 units, regardless of how it is obtained the mass, whether bleached or unbleached. Fig. 1 and 3 it is seen that when using the bleaching reagent, in this case  $H_2O_2$ , another during the actual obtain the CMP, to increase the degree of whiteness of

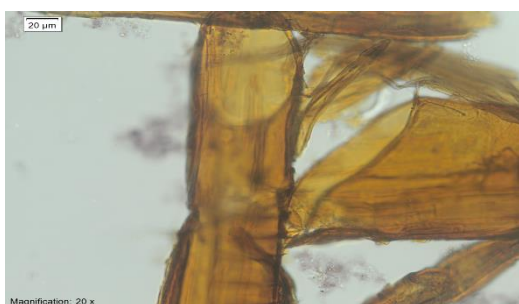
unbleached CMP (type 1 and 2) by approximately 5 units (from 37.37 to type 1 to 42.59 with type 2). The degree of yellowness of the two types CMP are: CMP type 1- 48.95% and CMP type 2 - 44.95%. Of fibrous material from CMP type 1 and CMP type 2 unbleached and two stage bleached type made microscopic images.



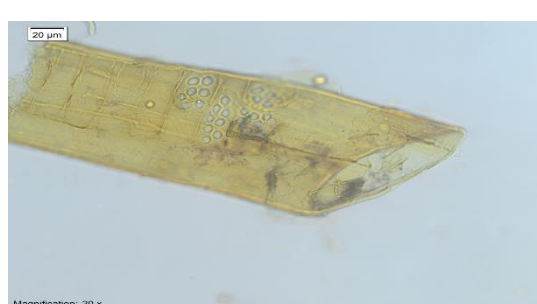
Picture 1. Unbleached CMP type 1



Picture 2. Two bleached CMP type 1



Picture 3. Unbleached CMP type 2



Picture 4. Two bleached CMP type 2

From microscopic images from CMP visible characteristic structural elements of hardwood. There was no difference in the microscopic analysis of fibrous materials in unbleached, bleached a one or two stage types. Perhaps the two stage bleached mass see a chopped

fiber or twisted more and more jagged edges (pictures 1 - 4).

Observed typical HYFM - rough and uneven. They can see the another typical hardwood elements and torn fibers. These ruptures are obtained most likely by – rafined размилане milling or at the very chemical treatment of the

wood during their transformation into a fibrous materials. There are typical dishes with open ends that have the extended typical of the hardwood.

## CONCLUSIONS

➤ *Populus deltoids cultivar Hunnegem* of fast growing species wood, with density of 504 kg/m<sup>3</sup> and rich carbohydrate portion, cellulose (50.4%) and lignin (21.2%). It is therefore suitable for obtaining of high yield fibrous materials.

➤ Obtained two types of works (type 1 and type 2). Type 2 is used in H<sub>2</sub>O<sub>2</sub> at the receiving of the table, and type 1 without H<sub>2</sub>O<sub>2</sub> (other things being equal). Yield CMP type 1 is 90% and degree of milling - 13<sup>0</sup>SR and extraction of CMP type 2 - 88%, and the degree of milling - grinding is 14<sup>0</sup>SR.

➤ Because of the low level of brightness, the CMP was treated by two-stage bleaching. During stage I the agent utilized was an H<sub>2</sub>O<sub>2</sub>, while during stage II reduction agent was applied - Rongalyt C. The final degree of brightness achieved for CMP type 1 (57.88%) and CMP type (63.15%). The obtained CMP has good optical properties and they can be used in the composition of even higher quality types of paper and paperboard.

➤ From microscopic photographs show typical structural elements typical of the hardwood.

In some parts have chopped fibers, twisted or those with jagged ends.

**Acknowledgments:** The authors thank the Scientific Research Centre (contract №11523) at the UCTM Sofia for the financial support of these investigations.

## REFERENCES

1. S.R. Jafari Petroudy, H. Resalati, E. Rasouli Garmaroudi, *J. Wood Forest Sci. Technol.*, **22**, 45 (2015).
2. P. Panayotov, K. Kalmukov, M. Panayotov, "Comparative researching of fast growing species properties from Bulgaria", Scientific-Technical Conference, Innovation in Woodworking Industry and Engineering Design, Sofia, pp. 42–47, 2010.
3. M. Azizi, *Forest Sci. Practice*, **15**, 349 (2013).
4. A. Cafiero, "Poplar trees in the pulp and paper industry and impact of the CAP", *CEPI*, FAO - Roma, pp. 1-19, 2003.
5. R. Boeva, G. Radeva, P. Hinkov, E. Hinkov, *J. Univ. Chem. Technol. Metallurgy*, **47**, 37 (2012).
6. Hybrid Poplar and the pulp and paper industry in North America Implications for a secured supply of quality fiber for papermakers worldwide, Green wood resources, [greenwoodresources.com/wp-content/uploads/.../hybrid-poplar-white-paper.pdf](http://greenwoodresources.com/wp-content/uploads/.../hybrid-poplar-white-paper.pdf), (2014).
7. D. Zamora, G. Wyatt, K. Apostol, U. Tschirner. *Biomass and Bioenergy*, **49**, 222 (2013).

## ПОЛУЧАВАНЕ НА ВИСОКОДОБИВНИ ВЛАКНЕСТИ МАТЕРИАЛИ ОТ ШИРОКОЛИСТНА ДЪРВЕСИНА И ОЦЕНКА НА ТЕХНИТЕ ОПТИЧНИ СВОЙСТВА В ПРОЦЕСА НА ТЕРМИЧНА ОБРАБОТКА

Р. Боева<sup>1\*</sup>, И. Спиридонов<sup>1</sup>, Г. Радева<sup>2</sup>

<sup>1</sup>Катедра „Целулоза, хартия и полиграфия“

<sup>2</sup>Катедра „Физикохимия“

Химикотехнологичен и металургичен университет, бул. „Климент Охридски“ 8, София, 1756, България

Постъпила на 27 ноември, 2016 г.; Приета за печат на 23 май, 2017 г.

(Резюме)

Основните влакнести материали използвани в целулозно-хартиената промишленост са: целулоза, полуцелулоза, високодобивни влакнести материали и вторични влакнести материали. Всички те са от растителен произход. Получават се основно от дървесина и едногодишни растения.

В това изследване е използвана тополова дървесина от вида *Populus deltoids cultivar Hunnegem* с повишена плътност (504kg/m<sup>3</sup>). Получени са два вида химико-механични маси (ХММ). ХММ тип 1 е получена само със 7% NaOH и 5% Na<sub>2</sub>SO<sub>3</sub>, а ХММ тип 2 със 7% NaOH, 5% Na<sub>2</sub>SO<sub>3</sub> и с 2% H<sub>2</sub>O<sub>2</sub>, при еднакви други условия – температура, хидромодул, продължителност на процеса и т.н.

Двете ХММ са с ниска степен на белота и затова след това са избелени двустепенно. При първа степен избелването е проведено с H<sub>2</sub>O<sub>2</sub>, а на втора степен с Rongalyt C. След това е проведено е изкуствено термично стареене при 105°C. Проследена е промяната в белотата и жълтината при термично стареене от 105°C на 0, 6, 12, 24, 36 и 48 час.

Целта на настоящата работа е получаване в лабораторни условия на химико-механични маси от широколистна дървесина, последващо двустепенно избелване и проследяване на изменението на белотата и жълтината с течение на времето при термично стареене от 105°C.

Експерименталните резултати от това проучване показват, че получените ХММ от широколистни дървесни видове могат да бъдат добавени в състава на хартиите за полиграфичната и опаковъчна промишленост. Те подобряват печатните свойства, адхезията с мастила, лакове и оптичните свойства (непрозрачност) на хартиите.



## Evaluation of changes in the optical properties of high yield fibrous materials under thermal treatment

R. Boeva<sup>1\*</sup>, I. Spiridonov<sup>1</sup>, T. Bozhkova<sup>1</sup>, D. Novakovic<sup>2</sup>, B. Banjanin<sup>2</sup>

<sup>1</sup>Department of Pulp, Paper and Printing Arts, University of Chemical Technology and Metallurgy, 8, Kl. Ohridski Blvd., 1756 Sofia, Bulgaria,

<sup>2</sup>Department of Graphic Engineering and Design, Novi Sad, Serbia, University of Novi Sad, Faculty of Technical Sciences, Serbia

Submitted November 27, 2016 ; Revised February 15, 2017

The plants raw materials are huge source with good stock and annually renewable origin of fibers which are needed for different kinds of industries. The wood is one of the most important and easy for processing and treatment raw material for humanity. The wood consists of non-homogenous organic matter, which after chemical and mechanical treatment converts to fibrous materials. The Cellulose is one of the most important components obtained from fibrous materials. Another very actual and usable material in present day is the high yield fibrous material. This material is suitable and perspective for using in composition of packing papers and corrugated boards.

Except the well-known and usable wood species like *Populus* in the last years in many regions like South-East Europe there is a big demand and interest for *Paulownia*. The *Paulownia* belongs to group of fast growing hardwood species, which makes it one of perspective sources of high yield fibrous materials.

In this research chemical mechanical pulps (CMP) from *Populus* and *Paulownia* woods are obtained. Then they were bleached in two stages with H<sub>2</sub>O<sub>2</sub> and Rongalyl C.

The artificial thermal ageing has been made. The measuring, tracing and evaluation of optical properties have been performed of the obtained CMP before and after artificial ageing at temperature of 90°C for 0, 6, 12, 24, 36, 48 and 72h.

The aim of this work is to obtain chemical mechanical masses of *Populus* wood and *Paulownia* wood, to bleach them, to age at 90°C and evaluate their optical and color characteristics.

**Key words:** fiber materials, thermal ageing, corrugated cardboard, packing industry, chemical mechanical pulp

### 1. INTRODUCTION

The timber as natural source and after improving of its properties or after its revision is a universal raw material for meeting various human needs [1, 2].

Fibrous materials with yield of over 65% from the starting raw material are called high-yield. The high yield is due to the initial composition of the starting material or due to partial dissolution of lignin and hemicelluloses [3].

The process of bleaching of high yield fibrous materials differs from bleaching process of pulp. The aim of bleaching of high yield fibrous materials is to discolor lignin and other coloring substances in such manner that they not pass in solution, i.e. without degradation to products with low molecular weight, soluble in water or in alkali solutions [4 - 6].

There are three basic methods for bleaching of high yield fibrous materials: by oxidation, by reducing agents and combined bleaching. To achieve the best results it is preferable to use a combined bleaching.

Over time, during prolonged storage of each fiber material irreversible changes in its properties occur. This process is accompanied by changes in the chemical composition and reduction of mechanical strength of material. Ageing of the fibrous materials is a complex process whose nature has not yet been sufficiently clarified, as in the course of this process many factors influence - the type and chemical composition of the fibrous material, pH of the medium, storage conditions, the degree of impact of light rays on the fibers and microbiological factors.

**The thermal aging** is due to oxidative processes that take place under the action of heat, air oxygen, and hydrolysis under the action of moisture or of their synergy action. Thermal destruction is associated with decrease of strength and causes smaller or greater changes in the chemical composition and properties. The content of lignin is the main factor which depends on the ageing of the fibrous mass [3, 7].

**Features and characteristics of *Paulownia* species.** *Paulownia* from family Scrophulariaceae includes nine highly adaptive species with valuable timber. These are: *P. elongata*, *P. tomentosa*, *P.*

\*) To whom all correspondence should be sent:

E-mail: [r\\_boeva@abv.bg](mailto:r_boeva@abv.bg)



***Paulownia Populus***

All species of the genus *Paulownia* are fast growing with excellent timber, but most promising in this respect are *P. elongata* (the emerald tree) and *P. fortunei*, which for 8-10 years can reach 20m tall and a trunk diameter of 30-40cm.

**Features and characteristics of species *Populus*.** *Populus* are kind of fast-growing wood species. They reach a height of about 25m. They grow quickly and live up to 400 years. Typical for poplar is that it has large number of equally spaced conductive vessels that allow increasing the area of interaction with chemical reagents during chemical processing [2, 4, 5, 7].

## 2. EXPERIMENTAL

### *Used raw materials*

The wood is split into chips with standard size 15x20x3mm [1].

The fibrous materials used in this study are: CMP - chemical mechanical pulp from poplar wood from species *Populus deltoides* clon - 235-15, obtained in the laboratory; CMP – from timber of *P. tomentosa*, obtained in laboratory conditions.

For obtaining CMP the following chemical reagents are used: Na<sub>2</sub>SO<sub>3</sub>, pure analysis, NaOH.

Bleaching reagents are: H<sub>2</sub>O<sub>2</sub>, Rongalyt C (NaHSO<sub>2</sub>.CH<sub>2</sub>O.2H<sub>2</sub>O), supplied by BASF;

The reagents Na<sub>2</sub>SiO<sub>3</sub> and MgSO<sub>4</sub> were applied for stabilization of H<sub>2</sub>O<sub>2</sub>. NaOH was added to reach the pre-determined pH level (10.5). In order to bond the metals ions, the pulp was treated with the complex agent EDTA. The following parameters of the produced CMP have been determined: Yield [%], determined by weight method in comparison to the mass of the absolutely dry timber; Grinding degree, as determined by the device Schopper – Riegler (°SR) per EN ISO 5267 – 1/AC: 2004; Microscopic analysis of the fibers determined on a light microscope OLYMPUS DX53.

For all used fibrous materials the degree of Brightness R457 (ISO 2470:2002) was determined before and after ageing thanks to the appliance by Spectrophotometer Gretag Magbeth Spectroeye.

**A. Production of CMP.** Production of CMP is performed according to preliminary determined optimal regime: NaOH 7%, Na<sub>2</sub>SO<sub>3</sub> 5%, temperature 80°C, treatment duration - 120 min and liquor-to-wood ratio 1:5.

Chips from poplar wood and wood species *Paulownia* with standard size are digested. Chips pour with required amount of solution of NaOH and Na<sub>2</sub>SO<sub>3</sub> and placed in a tempering container to maintain a constant temperature.

After completion of specified period according to the technological regime, the used solution was removed and the chips have been washed to neutral reaction. The treatment continued by chips refining in a Sprout-Valdron laboratory mechanical refiner. Further fiber materials was washed away and sorted out manually between two sieves.

The yield of CMP is calculated by the mass method. After soaking for 24 hours in distilled water, the treated chips were washed to reach neutral pH and dried into a drying apparatus at 105°C to achieve absolute dry state.

The yield of CMP is determined by weight method. After 24 hours soaking in distilled water, chips were washed until neutral reaction and dried to constant weight at 105°C

**B. Bleaching of the different types of fibrous materials.** The samples of CMP are bleached in two-stage: I stage - bleaching with H<sub>2</sub>O<sub>2</sub>, II stage - bleaching with Rongalyt C. The conditions of bleaching are given in Table 1.

**Table 1.** Conditions of bleaching CMP

Type of Bleaching	Quantity of reagent, (%)	T, (°C)	Duration of process, (min)	Concentration of fibrous materials, (%)	pH of the solution
I stage	2% H <sub>2</sub> O <sub>2</sub>	80	120	10	10.5
II stage	1.5% Rongalyt C	80	60	6	5

#### First stage of bleaching

First-degree bleaching is performed with  $H_2O_2$  - 2%. To maintain pH = 10.5 additives of NaOH - 2%,  $Na_2SiO_3$  - 5%,  $MgSO_4$  - 0.5% were used. For binding of heavy metal ions EDTA - 0.5% is used. All reagents are expressed in percent with respect to absolutely dry fibrous material.

Certain amount of fibrous material is weighted and placed in a plastic bag. In it a bleaching solution is added and the mass is stirred to complete homogenization. Then the bag is placed in a thermostatic container that provides a constant temperature in time of bleaching. The fibrous mass in the bag is homogenized periodically to ensure uniform bleaching.

This scheme applies to both fibrous materials. After completion of the first stage of the bleaching fiber material is washed to pH = 7 and then the second stage of bleaching is performed.

#### Second stage of bleaching

In time of bleaching of both fibrous materials in the second stage Rongalit C - 1.5% and EDTA - 0.5% are used under conditions shown in Table 1. The method of bleaching is similar to those used in the first stage. After completion of the bleaching process the fibrous mass is washed again to pH = 7.

Samples of all fibrous materials before and after bleaching have been prepared. After drying of these samples the degree of brightness and yellowness is determined.

**C. Ageing of CMP.** Samples of unbleached, single-step bleached and two-steps bleached CMP were subjected to thermal ageing for 72 hours at temperature of 90°C. For all used fibrous materials the degree of Brightness R457 (ISO 2470:2002) was determined before and after ageing thanks to the appliance by Spectrophotometer Gretag Magbeth Spectroeye. Furthermore, the degree of brightness of bleached samples was determined at the 0th, 6th, 12th, 24th, 36th, 48th and 72th hours from the start of the artificial thermal ageing [2, 3, 5 and 7].

#### Microscopic analysis of fibrous materials

Microscopic images have been made by light microscope OLYMPUS BH 53. Before observations a small part of study mass was taken and placed in a test tube. Distilled water is added and mass is shaken vigorously until a uniform suspension with concentration of about 0.05% is

obtained. A few drops of fibrous suspension are applied to a slide. Excess water is removed with filter paper. Carefully the fibers are distributed in the drop and later the drop is dried under a lamp at a temperature of about 60°C. Once the slide is cooled for a while a drop of staining solution is applied on the fibers and they are covered with a glass roof, making sure no air. As staining solution for identifying the fibrous material a reagent of Herzberg (ISO 9184-3: 1990) - [Cl-Zn-I] is used.

### 3. RESULTS AND DISCUSSION

The results data of the chemical analysis and physical characteristics of the two types of woods are: for *Populus deltoides clon* - 235-15 lignin is (21%), cellulose (50.9%), for *Paulownia Tomentosa* lignin e (20.2%) and cellulose (39.2%). The yield and grinding degree of resulting CMP are defined: the yield of the type *Paulownia tomentosa* is 86% and 13°SR, the yield the type *Populus deltoids clon* -235-15 is 88% and 12°SR.

CMP are bleached in two stages. The artificial thermal ageing of bleached and unbleached under different conditions CMP is made. In order to study the kinetics of the process a thermal aging is carried out at temperature of 90°C. The change of the degree of whiteness with time of 0, 6, 12, 24, 36, 48 and 72 hours was observed. The obtained kinetic curves of Fig 3 and 4 (*Paulownia* and *Populus*) show that whiteness declines over time; the process is accelerated with increasing of temperature.

Figure 1 shows the changes of brightness at the process of artificial ageing. Figure 2 shows the changes of the yellowness at the process of artificial ageing. From Fig. 1 it can be seen that the degree of whiteness decreases for all fibrous materials. In the same conditions of preparation and bleaching of fibrous masses higher degree of whiteness is achieved with the samples of *Paulownia*.

From Fig. 2 it can be seen that regardless of the type of test specimens their yellowness (%) is increased with time. There are almost identical values for yellowness of unbleached CPM of *Paulownia* and two-stage bleached poplar CPM.

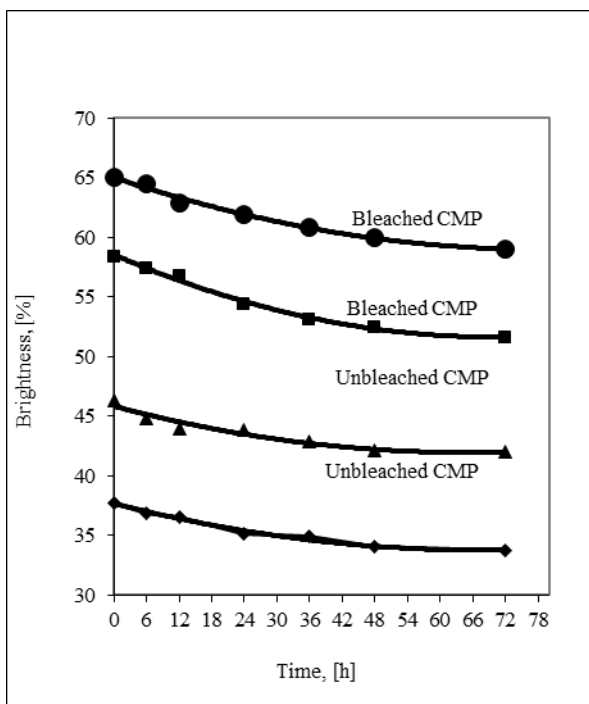


**Fig. 1.** Change in the degree of Brightness of bleached and unbleached CMP samples in artificial thermal ageing at 90°C.

From Figures 1 and 2 (at 90°C) it can be seen that CPM from *Paulownia* in bleached and unbleached state the degree of whiteness is higher and the degree of yellowness is lower compared to bleached and unbleached CPM of *Populus*. CPM from *Paulownia* has better properties regardless of the way they are received and bleached.

Ageing is a complicated process which does not obey formal kinetic principles. The reaction

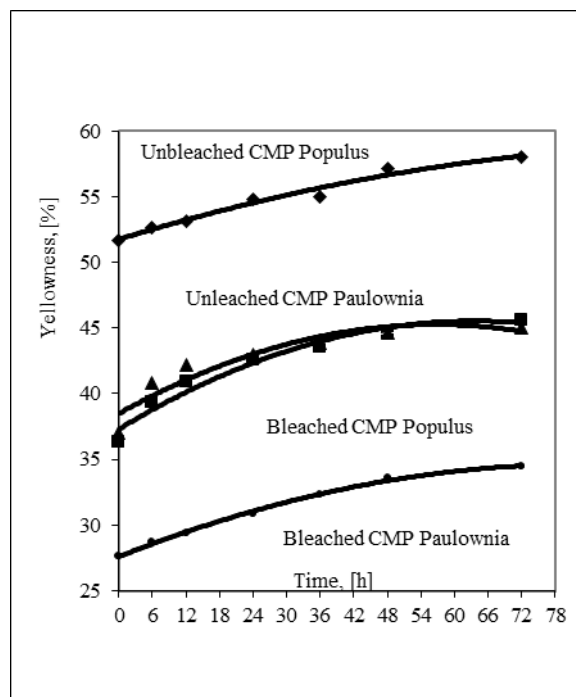
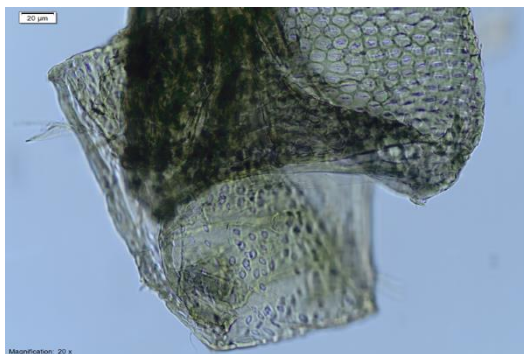
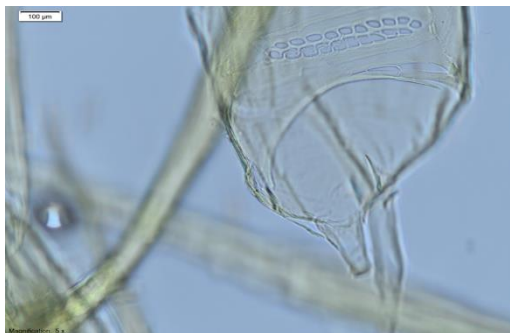


**Fig. 2** Change in the degree of Yellowness of bleached and unbleached CMP samples in artificial thermal ageing at 90°C.

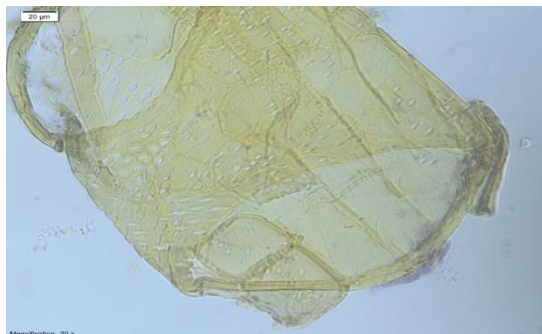
proceeds usually on certain places called active centers, which over time deplete. The active centers are in fact different functional groups primarily of lignin, which in time of the ageing process due the oxidation can form conjugated double bonds with aromatic ring. This way the destroyed during bleaching chromophores can recover. The next microscopic images are made from different CMP.



**Picture 1.** Unbleached CMP of *Paulownia* **Picture 2.** Bleached two-stage CMP of *Paulownia*



Picture 3. Unbleached CMP of *Populus*



Picture 4. Bleached two-stage CMP of *Populus*

At pictures 1 and 3 (unbleached CPM of *Paulownia*) characteristic elements of CPM - coarse fibers with uneven and irregular shape can be seen. They are typical for hardwood structural elements - the trachea, libroform cells and torn fibers, probably from production and grinding of fibrous mass. Tracheas have tapered edges.

Picture 2 shows structural elements which have more twisted and more disorganized parts in comparison to those who did not undergo drastic conditions of bleaching.

Picture 3 shows typical poplar wood vessels with open ends with extensions. There are sections of fibers with torn edges, preferably bundles of fibers and also small particles.

Picture 4 shows samples of poplar after bleaching. Characteristic fibers can be seen: with pores and libroform bundles of fibers and vessels with varying size and shape as thick tubes with mesh construction. More wide and shorter fibers typical for hardwood and wide variety of structural elements are well visible, in comparison with softwood.

If compare structural components of the microscopic images of two types of wood *Populus* and *Paulownia*, we can say that *Populus* has smaller number of pores in the walls of trachea and smaller number of tracheas which leads to higher density of poplar wood. The presence of tracheas negatively affects physical and mechanical properties of fibrous materials, but improves water permeability.

#### 4. CONCLUSIONS

1. Poplar wood and wood from *Paulownia* are fast-growing hardwood species. Poplar wood has a density ( $451\text{kg/m}^3$ ) and rich carbohydrate part, suitable for obtaining of CMP

2. Chemical-mechanical masses of species *Populus deltoides clon - 235-15* and *Paulownia tomentosa* are obtained at pre-established regime with yield respectively 88% and 86%, and degree of grinding respectively  $12^\circ\text{SR}$  and  $13^\circ\text{SR}$ .

3. Microscopic pictures show typical for hardwood species large numbers of structural elements and larger numbers of pores in the walls of the trachea, which is indicative for their lower density, especially for type *Paulownia*;

4. CPM after two-stage bleaching reaches whiteness for *Paulownia tomentosa* 65.6% and for *Populus deltoides clon - 235-15* 57.99%;

5. At the same conditions of obtaining and bleaching *Paulownia tomentosa* has higher degree of whiteness [%] and lower degree of yellowness, which is maintained in the aging process too.

**Acknowledgments:** The authors thank the Scientific Research Centre (contract №11523) at the UCTM Sofia for the financial support of these investigations.

#### REFERENCES

1. P. Panayotov, K. Kalmukov, M. Panayotov, "Comparative researching of fast growing species properties from Bulgaria", Scientific-Technical Conference, Innovation in woodworking Industry and Engineering Design, Sofia, pp. 42 – 47, 2010.
2. R. Boeva, *Food and Packaging Science, Technology and Technologies*, **4**, 15 (2014).
3. R. Boeva-Spiridonova, E. Petkova, *J. UCTM*, **42**, 41 (2007).
4. R. Boeva, Radeva G., P. Hinkov, E. Hinkov, *J. UCTM*, **47**, 37 (2012).
5. S. Ates, Y. Ni, M. Akgul, A. Tozluoglu., *African J. Biotechnol.*, **7**, 4153 (2008).
6. A. Ashori, A. Nourbakhsh, *Eur. J. Wood Product*, **67**, 323 (2009).
7. S. Ates, Y. Ni, M. Akgul, A. Tozluoglu., *African J. Biotechnol.*, **7**, 4153 (2008).

## ИЗСЛЕДВАНЕ НА ПРОМЕНЕТЕ В ОПТИЧНИТЕ СВОЙСТВА НА ВИСОКОДОБИВНИТЕ ВЛАКНЕНИ МАТЕРИАЛИ ПРИ ТЕРМИЧНА ОБРАБОТКА

Р. Боева<sup>1\*</sup>, И. Спиридонов<sup>1</sup>, Т. Божкова<sup>1</sup>, Д. Новакович<sup>2</sup>, Б. Банжанин<sup>2</sup>

<sup>1</sup>Катедра „Целулоза, хартия и полиграфия“,

Химикотехнологичен и металургичен университет, бул. „Климент Охридски“ 8, София, 1756, България

<sup>2</sup> Университет на Нови Сад, Технически факултет, Катедра по графично инженерство и дизайн, Сърбия

Постъпила на 27 ноември, 2016 г.; коригирана на 15 февруари, 2017 г.

(Резюме)

Растителните суровини са голям и ежегодно възобновяващ своите резерви суровинен източник. Дървесината е не само една от най-старите и най-лесно обработваните суровини, но и една от най-важните за човечеството. По своята същност тя е нехомогенна органична материя чрез чиято химична преработка се превръща в различни видове влакнести материали. От тях се използва предимно целулозата, но днес интерес представляват и високодобивните влакнести материали. Този материал е подходящ и перспективен за използване в състава на различни видове опаковъчни хартии и картони.

Освен добре познатия ни дървесен вид *Populus*, през последните години в Югоизточна Европа има интерес към изследване и използване на вида *Paulownia*, който също спада към групата на бързо растящите дървесни широколистни видове и прави този вид един от перспективните източници на високодобивни влакнести материали.

От двете дървесини са получени химикомеханични маси (ХММ). След това те са избелени двустепенно ( $H_2O_2$  and Rongalut C) и подложени на термично стареене.

Проследени са измененията в оптичните свойства на получените ХММ преди и след изкуствено термично стареене от 90°C на 0, 6, 12, 24, 36, 48 and 72h. Направен е микроскопски анализ на получените влакнести материали.

Целта на настоящето изследване е получаване, избелване и стареене при 90°C на химикомеханични маси, получени от тополова (*Populus*) дървесина и дървесина от *Paulownia* и оценяване промените в оптичните и цветови характеристики.

## Fast growing *Paulownia* wood – perspective raw material for production of fibrous materials

R. Boeva<sup>1</sup>, G. Radeva\*<sup>2</sup>, I. Spiridonov<sup>1</sup>

<sup>1</sup>Department of Pulp, Paper and Printing Arts, <sup>2</sup>Department of Physical Chemistry  
University of Chemical Technology and Metallurgy, 8, Kl. Ohridski Blvd., 1756 Sofia, Bulgaria,

Submitted November 26 2016; Revised April 6, 2017

The present paper is intended to make a comparative kinetic analysis of the effect of bleaching pretreatment and temperature increase on the thermal ageing of fiber material derived from fast growth *Paulownia* wood. The brightness reversion of bleached and unbleached samples is followed within the interval from 6 to 72 hours. The temperature values studied refer to 90°C, 105°C and 120°C. Exponential kinetic equation is applied for description of the ageing process kinetics by means of which the initial and current rates of the process are calculated. The values of the activation energy and the pre-exponential factor in the Arrhenius equation applied increase simultaneously in the course of the process.

**Key words:** *Paulownia* wood, Brightness, Thermal aging, Kinetic analysis

### 1. INTRODUCTION

The low-cost raw forest products and the processes providing the use of wood biomass could solve the problem with the scarce natural resources. *Paulownia* is a deciduous tree capable of achieving very height growth rates under favorable conditions. Under good growth conditions these trees will reach 15 m in height and will produce commercially harvestable timber in 7-10 years. This deciduous tree has been widely used for construction, pulping, furniture making and handicrafts [1, 2].

Semi chemical pulping process is a two-stage method. It combines chemical treatment aimed at lignin partial removal and a mechanical refining step leading to defibring [3-5]. The semi chemical pulps produced on the ground of hardwoods have higher strength but relatively low brightness when compared to that obtained from softwoods. Because of the lignin content the unbleached samples of semi chemical pulps (CMP) age faster than the bleached one. The yellowing starts with the oxidation of the lignin phenolic hydroxyl groups, which in turn leads to the subsequent formation of quinones, quinone-methydes and cyclohexadienes [6-8].

Ageing is a complicated process, because the rate of changes in the fiber materials depends on the temperature, on the amount of the bleaching reagents, on the degree of the delignification, on the mass concentration, on the bleaching sequence, on the process duration, as well as on other factors [9].

The study of the kinetics of semi chemical pulp

thermal ageing is expected to provide data whose treatment may facilitate to elucidate its mechanism and hence to optimize the process accounting as well the advantages of the methods of treatment and storage. The problem is that ageing is a complex process which does not obey formal kinetic principles.

The purpose of this study is to investigate and analyze the kinetics of the artificial thermal ageing of bleached and unbleached chemical mechanical pulps obtained from *Paulownia tomentosa*.

### 2. EXPERIMENTAL

The experiments were carried out with a pulp obtained from *Paulownia tomentosa*. Chemical mechanical pulp (CMP) was obtained under the following conditions: 100 g absolutely dry strips, hydromodule of 1:5, treatment temperature of 80°C, duration of 120 min, with addition of 8% NaOH and 5% Na<sub>2</sub>SO<sub>3</sub>. The oxidation reagent: H<sub>2</sub>O<sub>2</sub> was added in concentration of 2%. The concentrations are evaluated in respect to the mass of the absolutely dry strips used. CMP yield was 86% (determined by the weight method), while the degree of refining was 13<sup>0</sup>SR. (the measurements were conducted on a Schopper-Riegler (°SR) equipment in correspondence with the EN ISO 5267 – 1/AC:2004).

CMP prepared under the conditions pointed above was subjected to a two-stage combined bleaching, i.e. bleaching with oxidation reagent: H<sub>2</sub>O<sub>2</sub> (I stage) followed by bleaching with the reducing agent Rongalyt C (II stage). The first stage was applied to CMP at 70°C within 120 min. In this case the pH is 10.5, while the amount of H<sub>2</sub>O<sub>2</sub> was

\*) To whom all correspondence should be sent:  
E-mail: ggradeva@abv.bg

again 2%. The additives used referred to 2% NaOH, 5% Na<sub>2</sub>SiO<sub>3</sub>, 0.5% MgSO<sub>4</sub> and 0.5% EDTA (Na<sub>2</sub>C<sub>10</sub>H<sub>14</sub>O<sub>8</sub>N<sub>2</sub>·2H<sub>2</sub>O) as a complexing agent. All amounts pointed so far were calculated in respect to the absolutely dry fibrous material used. The procedure applied required to place the sample in a polyethylene bag, to bring it to the temperature value envisaged and then to introduce the bleaching solution under constant stirring aiming complete homogenization.

Rongalyt C (NaHSO<sub>2</sub>·CH<sub>2</sub>O·2H<sub>2</sub>O) and EDTA were introduced during the second stage of the bleaching process which was carried out for 60min at 70°C. The consumption of Rongalyt C and EDTA was 1.5% and 0.5%, correspondingly. In this case the pH is 5. The bleaching procedure was analogous to that applied during the first stage. The bleached fibrous material obtained was finally washed until a neutral reaction was obtained.

Samples of unbleached and bleached CMP were subjected to thermal ageing for 72 hours at temperatures of 90°C, 105°C and 120°C. Their brightness and yellowness was determined using “Brightness R<sub>457</sub> (in correspondence with ISO 2470:2002) prior to and after the ageing. Furthermore, the degree of brightness of the bleached samples was determined at the 6-th, 12-th, 24-th 36-th, 48-th and the 72-th hour of the process.

### 3. RESULTS AND DISCUSSION

The effect of ageing of CMP is followed on the ground of the comparative investigation of bleached and unbleached samples. The brightness reversion observed in the course of the thermal ageing of the samples of both types is followed at 90°C, 105°C and 120°C. The values obtained are summarized in Table 1.

**Table 1.** Values of the degree of brightness, *W* (%) of CMP – unbleached and bleached, in the course of the process of ageing (h) at the temperature values studied (T°C).

Time, h	Brightness, <i>W</i> , %					
	T=90°C		T=105°C		T=120°C	
	unbleached	bleached	unbleached	bleached	unbleached	bleached
0	46.31	65.01	46.05	65.60	46.73	65.89
6	44.83	64.47	44.22	63.60	44.26	62.48
12	43.96	62.94	43.57	62.38	43.62	61.57
24	43.85	61.95	43.05	60.79	42.41	60.24
36	42.89	60.85	42.96	60.59	41.75	58.25
48	42.13	59.98	42.76	58.81	41.10	56.74
72	41.98	58.99	42.06	58.03	40.08	56.50

It is seen from Table 1 that the bleached samples have higher degrees of brightness than those of the unbleached one at all temperature values studied. Furthermore, the temperature increase brings about increase of the rate of ageing of the samples of both types. The results presented evidence as well that the brightness of the bleached samples, although higher than that of the unbleached one, shows higher reversion with time and temperature.

The comparative consideration of the characteristics of the thermal ageing kinetics is done with the introduction of the kinetic variable,  $\alpha$ :

$$\alpha = \frac{W_0 - W}{W_0} \quad (1)$$

where  $W_0$  is the initial brightness value in % (ISO), while  $W$  in % (ISO) is the current value connected with the time of the treatment. The variable  $\alpha$  can be also considered as an extent of the thermal ageing proceeding or as a relative decrease of the degree of brightness in the course of the process.

The kinetic curves of the change of  $\alpha$  with time (h) obtained for the bleached and unbleached samples at the three temperature values studied are presented in Fig. 1. As Figure 1 shows  $\alpha$  increases with time and temperature for both types of samples. This increase of the kinetic variable corresponds to the increase of the extent of the process of thermal ageing, i.e. to the corresponding brightness reversion of CMP.

Various kinetic equations describing the kinetics of processes taking place on homogeneous and heterogeneous surfaces [9-12] have been applied aiming to elucidate the specifics of the ageing process. It was found that the process of ageing is best described by the exponential equation (2) valid for heterogeneous processes taking place on uniformly inhomogeneous surfaces:

$$v = v_0 e^{-\alpha\alpha} \quad (2)$$

where the current and the initial rate of the ageing process are designated by  $v = d\alpha/dt$  and  $v_0$ , respectively. In accord with the model of uniformly



inhomogeneous surfaces [10-12] the active centres on the biomass surface are distributed linearly in correspondence with their energy. The kinetic coefficient of inhomogeneity  $a$  in Equation 2 accounts for the energy and entropy inhomogeneity of the heterogeneous system. All kinetic curves are linearized in coordinates  $\alpha - \ln t$  in correspondence with the approximate integral form of the exponential kinetic equation:

$$\alpha = \frac{1}{a} \ln(v_0 a) + \frac{1}{a} \ln t \quad (3)$$

The linear dependences obtained in correspondence with Equation 3 are presented in Figure 2.

The value of the slope of the lines obtained (Figure 2) provides the determination of coefficient of inhomogeneity  $a$  (Equation 3). The values of the latter are presented in Table 3. It is seen that  $a$  decreases with temperature increase.

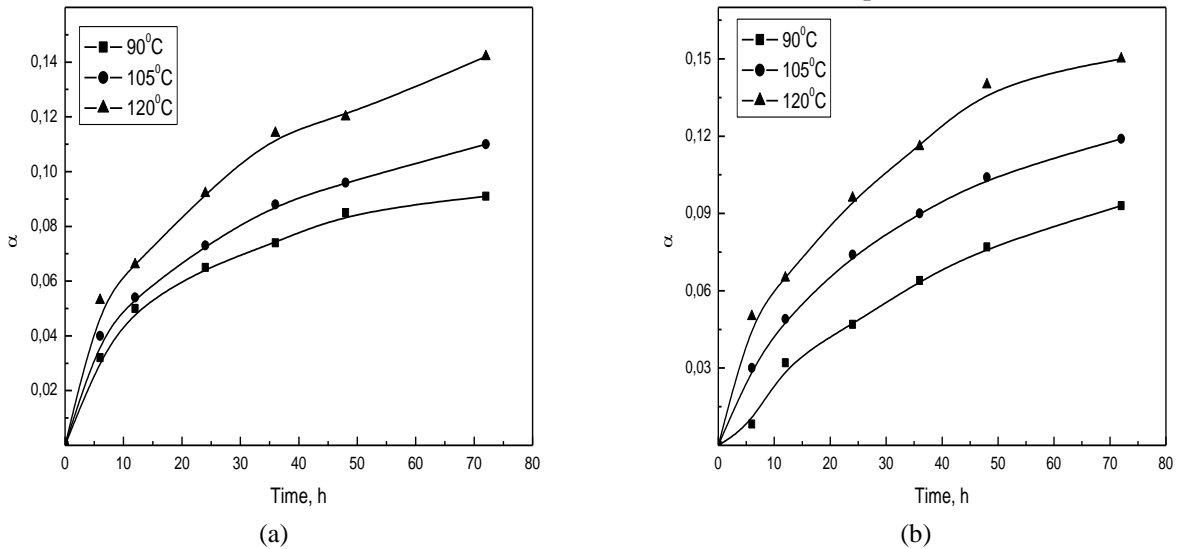


Fig. 1. Kinetic curves of increase of the ageing process extent for: (a) unbleached CMP; (b) bleached CM.

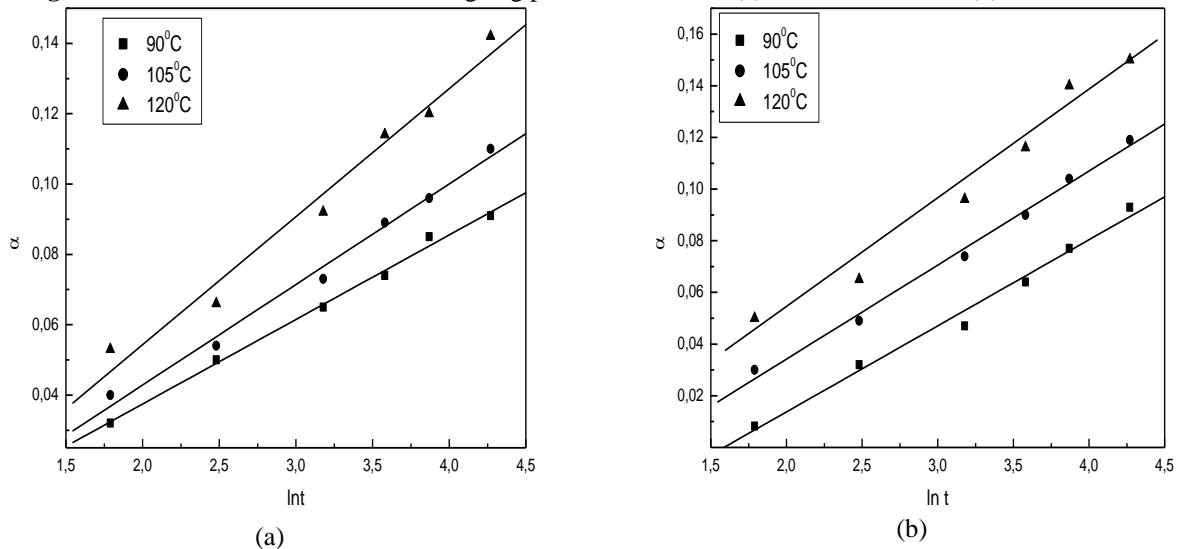


Fig. 2. Linearization of the kinetic curves in coordinates  $\alpha - \ln t$  for: a) unbleached CMP; b) bleached CMP.

Table 2. Initial and heterogeneity characteristics of the artificial ageing processes.

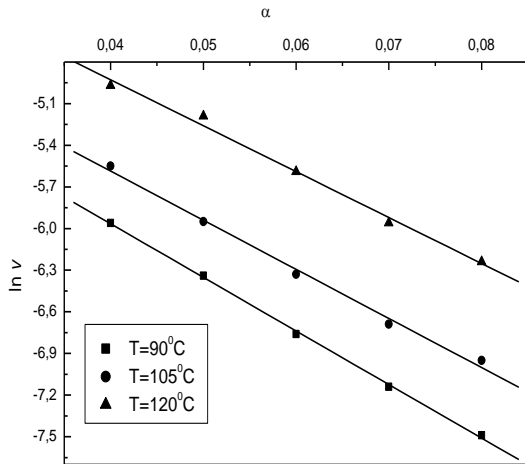
Temperature	90°C		105°C		120°C	
	unbleached	bleached	unbleached	Bleached	unbleached	bleached
$a$	41.66	30.03	31.96	27.48	27.47	23.29
$v_0 \times 10^3, h^{-1}$	12.03	6.73	15.45	10.84	27.30	24.72

The integral form of the exponential kinetic equation (Equation 3) can be used for the determination of the initial rate,  $v_0$  ( $h^{-1}$ ), of the process of thermal ageing at  $\alpha \rightarrow 0$ . The values of  $v_0$  are presented in Table 2. The current rate of the

process,  $v$  ( $h^{-1}$ ), at different time and temperature values is estimated on the ground of Equation 4 at a constant value of the extent of the process proceeding ( $\alpha = \text{const}$ ):

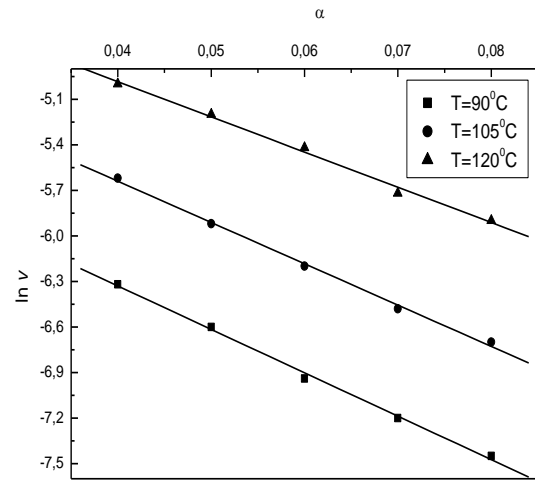
$$v = \frac{1}{at} \quad (4)$$

The temperature effect is outlined in Figure 3 according to the logarithmic form of Equation 2.



(a)

The latter shows that the rate of ageing of both samples types decreases with  $\alpha$  increase and increases with the temperature increase.



(b)

**Fig. 3.** Dependence of the current rate,  $\ln v$  ( $\text{h}^{-1}$ ) on  $\alpha$ , at the temperature values studied for: a) unbleached CMP; b) bleached CMP.

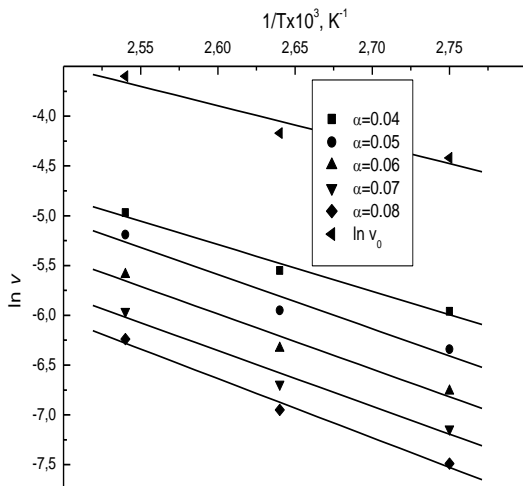
The temperature effect on the process parameters can be followed through the investigation of the temperature dependence of the initial  $v_0$  and the current rate  $v$  on the ground of the Arrhenius equation:

$$\ln v = \ln A - \frac{E}{R} \frac{1}{T} \quad (5)$$

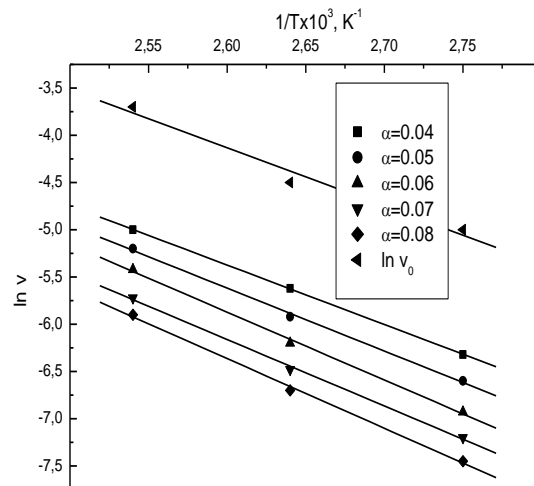
where  $E$  (kJ/mol) is the activation energies of the process at different constant values of  $\alpha$ , while  $A$  is

the pre-exponential factors. The values of the activation energy and the pre-exponential factor and their change at different values of  $\alpha$  are summarized in Table 3 and Figure 4.

As Figure 4 shows the linear dependences obtained have different slopes, i.e. the values of the activation energy and the pre-exponential factor increase with  $\alpha$  increase. That means that the surface is energy and entropy heterogeneous.



(a)



(b)

**Fig. 4.** Temperature dependence of the initial  $v_0$  and the current rate  $v$  at  $\alpha=\text{const}$  in case of: a) unbleached CMP; b) bleached CMP.

The values of the pre-exponential factor and the activation energy increase as well in the course of the process, which indicates that the number of the chromophore groups, responsible for brightness

reversion, increases. The total increase of the energy and entropy factors is greater at the bleached samples. Their rate of ageing is lower and

hence it can be concluded that the bleaching hampers in fact the ageing.

**Table 3.** Values of the activation energy,  $E$ , kJ/mol and the logarithm of the preexponential factor,  $\ln A$  at different values of process proceeding,  $\alpha = \text{const}$ .

$\alpha$	$\ln A$		$E$ , kJ/mol	
	unbleached	bleached	unbleached	Bleached
0	7.38	8.30	36.10	40.20
0.04	8.77	10.97	43.4	52.27
0.05	9.77	11.69	50.55	55.35
0.06	10.07	12.79	51.38	59.70
0.07	10.20	13.20	51.79	61.30
0.08	11.20	13.71	54.77	64.50

#### 4. CONCLUSIONS

A kinetic analysis of the stability to thermal ageing of samples of bleached and unbleached CMP obtained from *Paulownia tomentosa* is presented. The kinetics of the process is best described by an exponential kinetic equation valid for heterogeneous process. The temperature dependence of the rate is followed and the values of the activation energy and the preexponential factor in the Arrhenius equation are estimated. They are found to increase simultaneously with increase of the extent of the process on the bleached and the unbleached samples.

**Acknowledgments.** The authors thank the Scientific Research Centre (contract №11523) at the UCTM Sofia for the financial support of these investigations.

#### REFERENCES

1. C. L., Wu L., Zhu Y., Kim K., Know J., Bae S., *Holzforschung*, **63**, 440 (2009).
2. C. L., Liu Z., Kim K., Bae S., *Holzforschung*, **62**, 197 (2008).
3. N. Oggiano, L. G. Angelini, P. Cappelletto, *Ind. Crops Prod.*, **7**, 59 (1997).
4. M. Rehbein, M. Pereira, G. Koch, *Sci Technol*, **44**, 435 (2010).
5. O. Kordsachia, F. Marin, J.L. Sanchez, J. Arauzo, R. Fuertes, A. Gonzalo, *Bioresource Technol.*, **100**, 3933 (2009).
6. M. Rehbein, M. Petreira, G. Koch, O. Kordsachia, *Wood. Sci Technol*, **44**, 435 (2010).
7. P. Zadorecki, P. Flodin, *J Appl Polym Sci.*, **31**, 1699 (1986).
8. A. Castellan, P. Girard, C. Vanucci, *J. Wood Chem Technol.*, **8**, 73 (2007).
9. R. Boeva, G. Radeva, P. Hinkov, E. Hinkov, "Thermal Ageing of Different Kinds of Fiber Materials: A Kinetic Study", *J. Chem. Technol. Meall.*, 47 (1), 37, 2012.
10. G. Radeva, I. Valchev, S. Petrin, E. Valcheva, P. Tsekova, *Carbohydr Polym.*, **87**, 1280 (2012).
11. S. Veleva, E. Valcheva, I. Valchev, G. Radeva, *React Kinet Catal Lett.*, **72**, 355 (2001).

## БЪРЗОРАСТЯЩАТА ДЪРВЕСИНА ОТ *Paulownia* - ПЕРСПЕКТИВНА СУРОВИНА ЗА ПРОИЗВОДСТВО НА ВЛАКНЕСТИ МАТЕРИАЛИ

Р. Боева<sup>1</sup>, Г. Радева<sup>2\*</sup>, И. Спиридонов<sup>1</sup>

<sup>1</sup>Катедра „Целулоза, хартия и полиграфия“, <sup>2</sup>Катедра „Физикохимия“, Химикотехнологичен и металургичен университет, бул. „Климент Охридски“ 8, София, 1756, България

Постъпила на 26 Ноември, 2016 г., Приета за печат на 6 Април, 2017 г.

(Резюме)

Целта на настоящата работа е да се направи сравнителен кинетичен анализ на ефекта от избелване и от повишаване на температурата върху термичното стареене на влакнест материал, получен от бързорастяща дървесина от вида *Paulownia*. Проследено е изменението на оптичните свойства на избелените и неизбелени образци в интервала от 6 до 72 часа. Проследено е стареенето при три температури от 90°C, 105°C и 120°C. За описание на кинетиката на процеса на стареене е приложено експоненциалното кинетично уравнение. Изчислени са началната и текущите скорости на процеса. Установено е, че стойностите на активиращата енергия и на предекспоненциалния множител, от уравнението на Арениус, нарастват едновременно в хода на процеса.

## Investigation of color characteristics changes of semi chemical pulp samples in process of ageing

R. Boeva<sup>1\*</sup>, I. Spiridonov<sup>1</sup>, Ž. Pavlović<sup>2</sup>, G. Vladić<sup>2</sup>

<sup>1</sup>Department of Pulp, Paper and Printing Art, University of Chemical Technology and Metallurgy, 8, Kl. Ohridski Blvd., 1756 Sofia, Bulgaria

<sup>2</sup>Department of Graphic Engineering and Design, Faculty of Technical Sciences, University of Novi Sad, Serbia

Submitted November 26, 2016; Revised February 3, 2017

The fibrous species are the main raw materials needed for production of the various types of papers for printing and graphic industry, corrugated boards and packaging papers. Because of increasing demands, lack of materials, high value of raw fiber resources and of course of ecological reasons – there is substantial and increasing necessity of processing of wood for manufacturing of high yield fibrous material (HYFM).

In this study was utilized semi chemical pulp which was obtained from hardwood fibrous material.

The semi chemical pulp used in experiment was bleached in two different stages. It have been performed investigation of the changes in the optical properties of bleached and unbleached type of fibrous materials before and after artificially thermal ageing at of 105°C at 0, 6, 12, 24 and 36h.

For complete characterization of obtained and tested materials it have been made a complete characterization and estimating of color characteristics and differences in CIE Lab system during all of processing and ageing. The changes in the optical properties and colors before and after aging have been determined.

The experimental results and properties of samples in this study shows that the tested Semi Chemical Pulp hardwoods could be used completely for producing of corrugated boards and added to packing papers composition. The benefits of replacement of cellulose with semi chemical pulp are leading to cheaper and more ecological products for printing and packing industry.

**Key words:** semi chemical pulp, fiber materials, thermal ageing, corrugated cardboard, packing paper

### 1. INTRODUCTION

The main raw materials for the production of paper and paperboard - fibrous material are derived from various types of wood or annual plant materials by treatment with chemical reagents under certain conditions.

The advantages of HYFM (high yield fiber materials) are almost complete preservation of the original chemical composition of the starting timber or only partial dissolution of lignin and hemicelluloses. The usage of HYFM in the composition of high quality papers and boards are limited by their low degree of brightness. This necessitates them to be bleached [1, 2].

The availability in the mass of HYFM of heavy metal ions such as Fe<sup>3+</sup>, Mn<sup>2+</sup>, Cu<sup>2+</sup> etc., are affecting at the bleaching process. The whitening effect becomes smaller and this causes in increasing expense of bleaching agent. In order to prevent the influence of metal ions are used complexing agents. For this purpose most often are used polyphosphates, EDTA, etc. The result is increasing of degree of brightness with additionally approx. 3%. Ageing processes of HYFM are very intensive, which acceleration is a consequence of the higher content of lignin [5].

In the study an investigation of color characteristics changes of semi chemical pulp samples of in process of ageing after two bleaching process is conducted.

### 2. EXPERIMENTAL

#### *Production of CMP*

As a fibrous material in this work is used neutral-sulphite semi chemical pulp (SCP), produced in the factory conditions from hardwood. Bleaching reagents are used: H<sub>2</sub>O<sub>2</sub>, pure analysis, Rongalylt C from BASF [2, 3].

The composition of the bleaching solution, H<sub>2</sub>O<sub>2</sub> stabilizers are used - Na<sub>2</sub>SiO<sub>3</sub> and MgSO<sub>4</sub>. To achieve the required pH of about 10.5 is added NaOH. As complexing agents for connecting of heavy metal ions is used a solution of EDTA – 0.5%.

#### *Bleaching of the semi chemical pulps*

The conditions of the bleaching process (established in previous investigations) are shown in Table 1. Semi chemical pulps are treated at the two-stage bleaching:

- First stage of bleaching – with H<sub>2</sub>O<sub>2</sub>;
- Second stage of bleaching - Rongalite C from BASF.

\*) To whom all correspondence should be sent:

E-mail: [r\\_boeva@abv.bg](mailto:r_boeva@abv.bg)

**Table 1.** Conditions of bleaching semi chemical pulp

Type of Bleaching	Quantity of reagent, (%)	T, (°C)	Duration of process, (min)	Concentration of fibrous materials, (%)	pH of the solution
I stage	2% H <sub>2</sub> O <sub>2</sub>	75	120	10	10.5
II stage	1.5% Rongalyt C	75	60	6	5

*First stage of bleaching*

In a first degree of bleaching for maintaining pH=10.5 are used additives of: NaOH - 2%, Na<sub>2</sub>SiO<sub>3</sub> - 5%, MgSO<sub>4</sub> - 0.5%. For binding of heavy metal ions is used EDTA - 0.5%.

In order to achieve better degree of brightness, it is required to ensure mixing of the fiber material and facilitating the uniformly distribution of whitening mixture. After completion of the first stage of the bleaching fiber material is washed to pH=7 and then passes to the second degree of bleaching.

The fibrous mass is placed in a polyethylene bag where the bleaching solution is poured. The additional reagents are added and the solution is mixed till reaching complete homogenization. Later the bag is placed in thermostatic container which ensures constant temperature during the whole process of bleaching. In order to achieve better degree of degree of brightness, it is required to ensure mixing of the fiber material, thus facilitating the uniformly distribution of whitening mixture [2, 3, 6, 7].

*Second stage of bleaching*

In the bleaching of SCP in second degree is used Rongalit C (NaHSO<sub>2</sub>.CH<sub>2</sub>O.2H<sub>2</sub>O) and EDTA - 0.5%, and the conditions are shown in Table 1.

The process of bleaching is similar to the one described in the first stage. After completion of the process, the fibrous mass is washed away again to adjust pH 7.

*Ageing of fibrous materials*

The samples of both bleached and unbleached fiber materials, are dried and then submitted to artificial thermal ageing. Are determined the degree of brightness and yellowness for 0, 6, 12, 24 and 36 hours from the beginning of artificial thermal aging at 105°C.

For a more complete characterization the color characteristics are measured with a densitometer-spectrophotometer under the following conditions: standard light illuminant - D65, standard observer - 10°, geometry of measurement 45°/0° or 0°/ 45°, polarizing filter.

In the system CIE L\*a\*b\* are measured the following main parameters: CIE L\* (lightness), CIE a\* - red-green coordinate, CIE b\* - yellow-blue coordinate.

**3. RESULT AND DISCUSSION**

The utilization of HYFM in various brands of paper and cardboard is limited because of the low level of whiteness. SCP is bleached in two stages. After the bleaching is conducted artificial thermal ageing at 105°C.



**Picture1.** Semi chemical pulps.

By advancing the process of artificial thermal ageing change the brightness decreased most at the beginning of the process ageing.

In order to track the influence of ageing at 105°C on the properties of various fibrous materials, bleached and unbleached has traced

change of the degree of Brightness and Yellowness over time (0, 6, 12, 24 and 36h).

On Fig. 1 and 2 are presented the kinetic regularities showing these changes in the brightness and yellowness of SCP depending on time at 90°C.

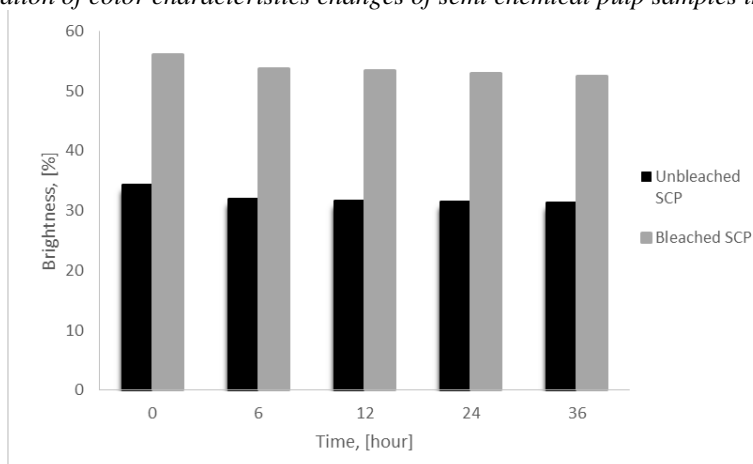


Fig. 1. Change of the Brightness of the bleached and unbleached samples of SCP in artificial ageing of 90°C

Fig. 1 shows that the degree of Brightness decreases at all samples, regardless of the manner of obtaining and bleaching of fibrous materials, but in differing amounts. It is seen further that the higher degree of brightness of the bleached samples were reserves in the process of artificial thermal ageing. There is a difference in the change in the degree of brightness in relation of the starting brightness depending on the conditions of obtaining and type of bleaching of the corresponding fibrous material. All this results shows that the fibrous

materials and their production of paper and paperboard must be used and stored at lower temperatures.

Fig. 2 shows that the degree of Yellowness increase at all samples in the process of artificial thermal aging with the progress of the process.

In Table 2 are presented CIE L\*a\*b\* color characteristics of the bleached and unbleached SCP samples before and after ageing.

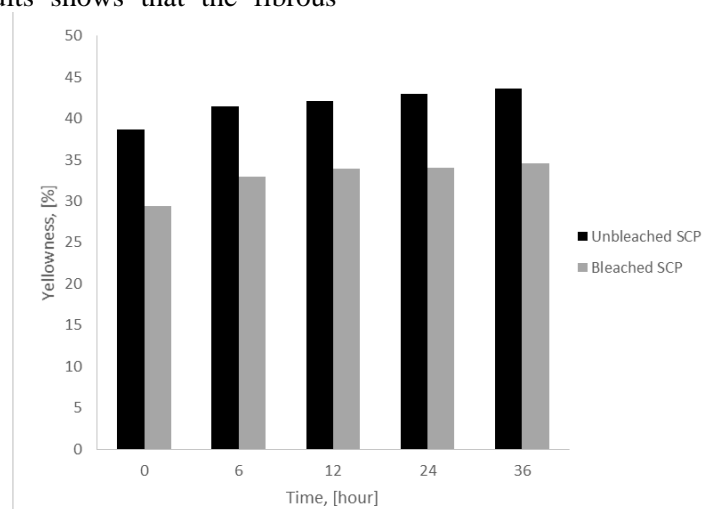


Fig. 2. Change of the Yellowness of the different samples of SCP in artificial ageing of 90°C.

Table 2. Color characteristics of the bleached and unbleached SCP samples before and after ageing

Type of samples	Before ageing			After ageing		
	L*	a*	b*	L*	a*	b*
Unbleached SCP	68.38	7.95	18.61	70.12	7.68	20.54
Bleached SCP	84.41	2.95	17.96	83.71	3.30	19.46

Unbleached semi-chemical pulp has higher values of CIE b\* during the ageing, indicating that there is a color shifting in yellow direction – Db=1.93. Before and after the ageing the CIE a\* coordinate of Unbleached SCP has the relatively same values, comparable to measurement accuracy. The obtained results for Bleached SCP are similar -

higher values of CIE b\* during the ageing, indicates color shifting in yellow direction – Db=1.5.

The value of color difference - DE<sub>ab</sub> before and after ageing of Unbleached SCP (DE<sub>ab</sub>=2.83) is approximately two times bigger than Bleached SCP (DE<sub>ab</sub>=1.69). The reason is better chemical stability resulting at less color shifting at bleached samples during the artificial ageing process.

### 3. CONCLUSIONS

On the basis of the present investigation it is established:

- The conducted two stage bleaching increases the degree of brightness of SCP. This expands the possibilities for its use in preparing various types of paper, cardboard and their production of packaging.

- At ageing of fibrous materials, they modify their optical properties. Conducted artificial thermal ageing at 105°C showed a decrease in the degree of brightness in different degrees in the studied samples.

- Unbleached SCP has higher values of CIE b\* during the ageing, indicating that there is a color shifting in yellow direction. Before and after the ageing the CIE a\* coordinate of Unbleached SCP has the relatively same values, comparable to measurement accuracy. The obtained results for Bleached SCP are similar - higher values of CIE b\* during the ageing, indicates color shifting in yellow direction.

- The value of color difference - DEab before and after ageing of Unbleached SCP is approximately two times bigger than Bleached SCP. The reason is better chemical stability resulting at

less color shifting at bleached samples during the artificial ageing process.

**Acknowledgments:** The authors thank the Scientific Research Centre (contract №11523) at the UCTM Sofia for the financial support of these investigations.

### REFERENCES

1. L. Wilson, What the printer should know about paper, Moscow, 2005.
2. R. Boeva-Spiridonova, E. Petkova, *J. Chem. Technol. Metall.*, **42**, 41 (2007).
3. R. Boeva, G. Radeva, *J. Chem. Technol. Metall.*, **49**, 585 (2014).
4. K. M. Han, R. Dharmawardhana, R. S. Arias, C. Ma, V. Busov, S. H. Strauss, *Plant Biotechnol J*, **9**, 162 (2011).
5. M. El-Sakhawy, *Polymer Degrad. Stability*, **87**, 419 (2005).
6. M. Area, H. Cheradame, *BioResources*, **6**, 5307 (2011).
7. Z. Zhou, A. Jääskeläinen, I. Adorjan, A. Potthast, P. Kosma, T. Vuorinen, *Holzforschung*, **65**, 289 (2011).
8. N. Kachin, I. Spiridonov, *Cellulose Chem. Technol.*, **39**, 255 (2004).
9. N. Kachin, I. Spiridonov, *Printing Processes, Part 1, Theoretical bases, Pleiada, Sofia, 2000.*

## ИЗСЛЕДВАНЕ НА ПРОМЕНИТЕ В ЦВЕТОВИТЕ ХАРАКТЕРИСТИКИ НА ОБРАЗЦИ ОТ ПОЛУЦЕЛУЛОЗНА МАСА В ПРОЦЕСА НА СТАРЕЕНЕ

Р. Боева<sup>1\*</sup>, И. Спиридонов<sup>1</sup>, Ж. Павлович<sup>2</sup>, Г. Владич<sup>2</sup>

<sup>1</sup>Катедра „Целулоза, хартия и полиграфия“, Химикотехнологичен и металургичен университет, бул. „Климент Охридски“ 8, България,

<sup>2</sup>Катедра по графично инженерство и дизайн, Университет в Нови Сад, Факултет по технически науки, Нови Сад, Сърбия

Постъпила на 26 ноември, 2016 г.; приета за печат на 3 Февруари, 2017 г.

(Резюме)

Влакнестите материали са основната суровина, необходима за производството на различни видове хартии и картони за нуждите на полиграфичната и опаковъчната промишленост. Поради нарастващите изисквания към суровинните ресурси и влакнестите материали и разбира се по екологични причини - съществува необходимост от преработването на дървесината за производството на високодобивни влакнести материали (ВДМ).

Като влакнест материал в това изследване е използвана полуцелулоза, получена от широколистна дървесина. Полуцелулозата е избелена двустепенно. Проследени са измененията в оптичните свойства на влакнестите материали (в избелен и неизбелен вид) преди и след изкуствено термично стареене от 105°C на 0, 6, 12, 24 and 36h.

За цялостно охарактеризиране на получените материали е извършена оценка на цветовете характеристики в системата CIE Lab по време на стареене. Определени са промените в оптичните свойства и цветовете характеристики преди и след стареене.

Получените резултати от изследваните образци показват, че полуцелулозата има добри свойства и може успешно да се използва при производството на различни видове хартии и картони. Ползите от замената на целулозата с полуцелулоза водят до получаване на по-евтини и по-екологични продукти за печатната и опаковъчната промишленост и в някои случаи и до по-добри показатели.

## The effect of washing temperature and number of washing cycles on the quality of screen printed textiles materials

N. Kašiković<sup>1</sup>, M. Stančić<sup>2</sup>, I. Spiridonov<sup>3\*</sup>, D. Novaković<sup>1</sup>, R. Milošević<sup>1</sup>, D. Grujić<sup>4</sup>,  
B. Ružičić<sup>2</sup>

<sup>1</sup> University of Novi Sad, Faculty of Technical Sciences, Department of Graphic Engineering and Design, Trg Dositeja Obradovića 6, 21 000 Novi Sad, Serbia

<sup>2</sup> University of Banja Luka, Faculty of Technology, Department of Graphic Engineering, Bulevar Vojvode Stepe Stepanovića 73, 78 000 Banja Luka, Bosnia and Herzegovina

<sup>3</sup> University of Chemical Technology and Metallurgy, Department of Printing Arts, Pulp and Paper, bulevard "Sveti Kliment Ohridski" 8, Sofia, Bulgaria

<sup>4</sup> University of Banja Luka, Faculty of Technology, Department of Textile Engineering, Bulevar Vojvode Stepe Stepanovića 73, 78 000 Banja Luka, Bosnia and Herzegovina

Submitted November 30, 2016; Accepted May 18, 2017

The life standards growth has led to the fact that buyers of textile materials, beside functionality, expect aesthetic value as well. The aesthetic characteristics of the textile materials are often promoted by the printing process of these materials. Printed textile materials, as well as printed surfaces itself, are exposed to various influences during exploitation. One of the most common impacts that these materials are exposed to is the washing process. Washing process causes the change of textile fibers as well as the change of the colour reproduction on these materials, where, as a result, the overall print quality changes. The aim of this research is to determine the effects of the washing process on the colour change in the CIE L\*a\*b\* colour space, as well as the effects of the washing process on water retention value change of screen printed cotton textile materials using black ink. The study included an analysis of two different parameters connected to the washing process: temperature and number of washings. The research results indicate that the washing temperature increase leads to major colour reproduction changes, where beside that, the number of washing cycles has certain influence on the colour reproduction of printed textile materials exposed to washing tests as well. The investigation revealed that the washing process caused washing-out of ink particles which increases the water retention value of the tested printed materials. The research results indicate that the quality of printed textiles, besides the washing process parameters, affects its material characteristics.

**Keywords:** cotton, washing, screen printing, colour reproduction, water retention value

### 1. INTRODUCTION

On the global market are nowadays present garments manufactured by processing of a wide range of textile raw materials. The most frequently used textile material is cotton. The reason of great market share of this material is its excellent properties, such as air permeability, ability to conduct moisture and heat, softness, low-allergen and anti-static properties [1]. Furthermore, cotton materials do not require special care, possess the ability to be washed well and have a relatively long life, which is another reason for their prevalence in the clothing industry. The life standard increase of society, in general, and of individuals, has caused a great turn in the textile and clothing industry because the customer requirements became higher ever before. For today's average buyer it is not enough that the garment meets only basic functions, such as protection of the body and functionality, but the selected garment is expected to meet the fashion and visual requirements (shape, colour, and

material) [2]. The increase of the aesthetic values of textile materials, and therefore of the clothes as a whole, is often carried out with the printing process. Printing of textile materials can be described as the art and science of decorating fabric with a colourful pattern or design [3]. Certain reports indicate that more than 27 billion m<sup>2</sup> of textile material substrates are printed every year [4]. Also, it is considered that printing of textile materials has annual growth of 2% [5]. The most important printing technique of textiles is screen printing technology [6, 7, 4] that is characterized by considerably lower costs for high circulations, and high productivity [8, 9].

The clothes are usually exposed to external influences such as washing, heat, abrasion, UV light, etc. [10]. One of the most influential factors these materials are exposed to is the washing process. It is proved that the washing process causes certain changes in physical and chemical characteristics [11], as well as changes in micro-mechanical properties (permeability, resistance to

\*Corresponding author.

E-mail address: [i\\_spiridonov@abv.bg](mailto:i_spiridonov@abv.bg)



cracking, stiffness) [12]. Also, it was noticed that the washing process causes a colours change [13]. The degree of textile fibers change, as well as the colour change, depends on the washing method, washing temperature, water hardness and washing time. Further, modern detergents consist of bleaching substances and their enzymatic activators as well as inhibitors of the dyes transfer. All of these substances can cause colours change of the printed inks [14].

To achieve the highest possible quality of the prints, there is an increasing trend of using instrumental measuring methods, i.e. spectrophotometric measurements. The instrumental colour measurement methods allow quantification of colour by numerical values. The basis of this process is the determination of the colour difference between the two prints. Determination of the colour differences is based on the calculation of the colour coordinates differences of the CIELab colour space ( $\Delta L^*$ ,  $\Delta a^*$ ,  $\Delta b^*$ ) [15, 16]. It is expressed as a  $\Delta E$  value and corresponds to the visual difference between the two colours. To determine the value of colour differences, it can be used a larger number of formulas, such as CMC (1: c) [17], BFD (1: c) [18], CIE 94 [19] and the newest one CIE  $\Delta E_{2000}$  [20]. Ranges of possible colour differences values are presented in Table 1 [21].

Wearing comfort of a garment, besides other things, is conditioned by the sorption properties of the material [22]. The most important sorption

characteristics are water retention value, air permeability, and relative humidity. Water retention value of textile materials largely depends on the type of fiber or the creation of chemical bonds between water molecules and fibers.

**Table 1.** Ranges of colour differences

$\Delta E$	Effect
< 3	Hardly perceptible
3 < 6	Perceptible, but acceptable
> 6	Not acceptable

This study aims to determine how the parameters of washing, before all temperatures and number of cycles, affect the quality of the prints on the printed textile materials. To obtain more accurate results, a large number of printed samples (three types of textile material surfaces), subjected to a number of washing processes using different temperatures are analyzed.

## 2. METODS AND MATERIALS

The investigation was conducted on the textile materials of different surface structures, thereby three types of cotton knitwear were used: single, pike and interlock. Material characterization was carried out through the following parameters: material composition (ISO 1833), surface mass (ISO 3801) and the knitting density (ISO 7211-2). The materials characteristics are presented in Table 2.

**Table 2.** Properties of the used textile materials

Tests	Type of weaves	Material composition (%)	Fabric weight (g/m <sup>2</sup> )	Thread count (cm <sup>-1</sup> )	
				Vertical	Horizontal
Material A	Single	Cotton 100 %	138	14	19
Material B	Pike	Cotton 100 %	185	15	16
Material C	Interlock	Cotton 100 %	207	12	18
Method		ISO 1833	ISO 3801	ISO 7211-2	

For the study, a special test chart using Adobe Illustrator CS5 software package was developed. The size of test chart is 297 x 420 mm, and it contains different elements for analysis of print quality. In the study were examined solid fields (100% tone value) with the size of 30 x 120 mm, printed using process black ink.

Printing of the samples was carried out using screen printing technique, with six colour printing system M & R Sportsman E Series. Pan et al. have found that the quality of screen printing process is largely influenced by four parameters [23], which is why these parameters were kept constant during the printing process of all the samples. Printing speed was 15 cm/sec, the hardness of the squeegee 80° Shore Type A, the printing pressure 275.8 x 10<sup>3</sup> Pa

and the snap-off distance 4 mm. Printing is done by Sericol Texopaque Classic OP Plastisol ink. Fixing of printed ink was carried out at the temperature of 160° C for 150 seconds.

For the preparation of the printing carrier (printing plate), the mesh with the mesh count of 120 threads/cm was selected. Aluminium screen printing frames with the size of 58 x 84 cm were used as the holders of the printing mesh. The size of the printing plate, without a frame, was 50 x 76 cm. Printing plates have been developed using conventional linearized positive films. The optical density of the transparent and opaque (black) parts of the film was 0.03 and 4.1 respectively. The resolution of the film was five times lower than the mesh count. As a photosensitive layer was used

Sericol Dirasol 915 emulsion. Exposition of the printing plate was done using metal halide UV lamp (1000 W); at a distance of 1 m from the printing mesh. The exposure time was 2.6 minutes that was determined using an Autotype Exposure Calculator (Sericol) control strip.

The printed samples were subjected to ten washing cycles. The washing process is carried out at the two different temperatures according to ISO 105- C10:2006 standard [24]. Washing bath contained 5 g/l of soap for textiles while the solution to cotton material ratio was 50:1. The samples were washed for 30 minutes at the temperatures of 30°C and 60°C. After the washing process, the samples were rinsed twice with distilled water, after which they were rinsed for 10 minutes using cold water. The rinsed samples were drained and dried in the spread-out state at a temperature of 60°C.

Analysis of print quality included an analysis of colour reproduction. The colour reproduction was characterized by the means of 1) CIE L\*a\*b\* colour coordinates measurements of solid patches (100% coverage) printed with black ink, which enabled the calculation of the colour differences ( $\Delta E$ ) between the materials of the same material composition but different characteristics in terms of surface mass and knitting density; 2) relative spectral reflection measurements of the printed samples. All the measurements were done after the printing process as well as repeated after subjecting the samples to a multiple of washing cycles under different temperatures. The CIE L\*a\*b\* colour coordinates were determined using a spectrophotometer HP200 (D65 illumination, 10° standard observer, measuring geometry d/8, aperture 8 mm), while the relative spectral reflectance characteristics were measured using spectro-densitometer Techkon SpectroDens (D50 illumination, the standard observer 2°, measuring geometry 0°/45°, aperture 3mm).

SEM microscopic analysis provides high-quality microscopic images of the fibers [25], thus provides further analysis of the reasons for the textile materials colour change. The analysis was performed using a JEOL electron microscope LV 6460, with the focus on observing the changes on the textile materials surfaces, which are generated by the printed ink and the effects of the washing processes. The samples were classified, labeled and prepared according to the specifications for laboratory measurements. To make the samples become electro conductive and prepared for SEM analysis, they are vaporized using gold.

The sorption properties of textile materials affect both the printing process, and the washing process. Changing the sorption properties of knitwear due to printing and washing processes were determined by measuring the water retention value of the knitwear. Determination of the water retention value in knitwear  $W_{rv}$  was performed according to standard DIN 53814 [26]. Acclimatized fabric sample (approximately 1.6 g) was cut into small pieces. Each sample was examined four times in parallel sessions, where each previously weighed cuvette, contained 0.4 g of a sample. Cuvettes with the samples were placed in a glass and transfused with a previously prepared solution (1g non-ionic agent in 1L of distilled water). Bubbles were expelled from the cuvette by using a needle after which prepared samples were left to rest for 2 hours. Afterwards, the cuvettes were subjected to centrifugal forces for 20 min at 3000 rev/min, using a CENTRIC 150A (Tehtnica) device. After the centrifugation process was done, cuvettes with the samples were weighed and from the mass differences values of cuvettes with the samples after the centrifugation process and empty cuvettes, the mass values of processed samples are generated [26].

The ability to retain water in fabrics  $W_{rv}$  (%) is calculated according to the formula:

$$W_{rv} = \frac{m_c - m_{kl}}{m_{kl}} \cdot 100 \quad (1)$$

where:

$m_c$  - mass of the centrifuged sample [g],

$m_{kl}$  mass of the acclimatized sample [g].

### 3. RESULTS AND DISCUSSION

Results of the spectrophotometric analysis of the samples printed in the experiment are presented in Table 3. For each sample, are determined by CIE L\*a\*b\* colour coordinates, and are calculated the colour difference values. On the basis of these results, it was found out in what extent the colour reproduction of the original had changed after washing cycles with different washing temperatures.

When calculating colour differences ( $\Delta E$ ), as the reference CIE L\*a\*b\* values were taken the CIE L\*a\*b\* values of solely printed samples, and in regard to these values, colour difference values were calculated after a number of washing cycles at different temperatures for each material.

After washing process, in case of all knitted samples it was noticed that the increase of washing temperature causes major changes of the analyzed samples, i.e. colour difference values are greater between the samples before and after washing under the temperature of 60°C comparing to the

colour difference values between the samples that were washed at a temperature of 30°C. Also, it was noticed that with the increase in the number of washing processes major changes of the analyzed samples occur, thus the colour difference values increase with increasing number of washing cycles

**Table 3.** Values of CIE L\*a\*b\* colour coordinates and colour differences after printing process and washing cycles under different temperatures

Sample	L*	a*	b*	ΔE
A- P	22,390	0,180	-0,238	-
A- 30- W1	24,702	0,116	-0,366	2,316
A- 30- W5	28,130	-0,216	-0,448	5,758
A- 30- W10	30,148	-0,258	-0,744	7,787
A- 60- W1	25,522	0,126	-0,366	3,135
A- 60- W5	29,508	-0,170	-0,416	7,129
A- 60- W10	32,438	0,054	-1,154	10,091
B- P	21,506	-0,114	-0,796	-
B- 30- W1	24,628	-0,176	-0,200	3,179
B- 30- W5	27,518	-0,160	-0,492	6,020
B- 30- W10	28,392	-0,296	-0,488	6,895
B- 60- W1	25,662	-0,092	-0,362	4,179
B- 60- W5	29,718	-0,066	-0,500	8,218
B- 60- W10	30,860	-0,236	-0,456	9,361
C- P	26,570	0,158	-0,340	-
C- 30- W1	27,074	-0,090	-0,244	0,570
C- 30- W5	28,284	-0,194	-0,592	1,768
C- 30- W10	28,680	-0,242	-0,308	2,148
C- 60- W1	25,966	0,122	-0,436	0,613
C- 60- W5	29,558	-0,022	-0,508	2,998
C- 60- W10	31,376	-0,270	-0,488	4,827

Analyzing the results of the material A, it can be noticed that the colour difference after the first washing process at a temperature of 30°C is barely noticeable. By increasing the number of washings, colour difference values rise. After the fifth washing process, the colour difference is noticeable, but still acceptable, while, after the tenth washing process, the values of colour differences are too large, thus unacceptable. The washing temperature of 60°C causes major changes of the prints, where after the first washing process at this temperature, the resulting colour difference value is noticeable, but acceptable. By increasing the number of washing processes, produced colour differences can be characterized as significant or unacceptable.

In case of the material B, a similar behaviour of the colour differences values is present, at all washing temperatures. Thus, after the first washing process, a noticeable but acceptable colour difference occurs, while, after the fifth and tenth washing processes, a large and unacceptable colour differences are generated. Although the colour differences behaves in the same manner with the increase of the temperature and the number of washing processes, it can be noticed that the increase of washing temperature generates the greater colour difference change as well.

By reviewing the colour differences results of material C (material with the greatest surface mass and the most pronounced relief surface structure), lower colour difference values were observed, comparing to the other two materials. The influence of washing process at a temperature of 30°C resulted in a barely perceptible colour differences after ten washing processes. Colour difference, under the washing temperature of 60°C, after the first and the fifth washing, is barely noticeable, while after the tenth wash cycle it is noticeable but acceptable.

In addition to CIE L\*a\*b\* colour coordinates and colour differences determination, the relative spectral reflection for all samples were obtained, both after the printing process and after the washing processes. The effect of washing temperature and the number of washing processes on the relative spectral reflectance of the samples surface was monitored. In Figures 1, 2 and 3 are presented the relative spectral reflection curves of samples after printing and washing processes.

Washing process affects the change of the relative spectral reflection curves of the samples, so the relative spectral reflection curves after the washing process exhibit higher degree of reflectivity comparing to the relative spectral reflection curves of the solely printed samples. From the Figures 1, 2 and 3, it can be noticed that the increase in washing

temperature, as well as in the number of washing cycles leads to the higher reflectivity of the sample surface. This can be explained by the fact that during the exposure of the printed samples to washing process, a part of the ink particles is being washed away, which causes a decrease of light absorption and on the other side the increase of light reflection. Thus, it can be concluded that the increase of the washing cycles and the washing temperature leads to washing out of larger quantities of printed ink, and hence to a higher reflectivity of the surface.

Analysis of SEM micrographs (x500 magnification) was conducted on the unprinted samples, samples after printing process, and after the first washing cycle under the tested washing temperatures, Figures 4, 5 and 6.

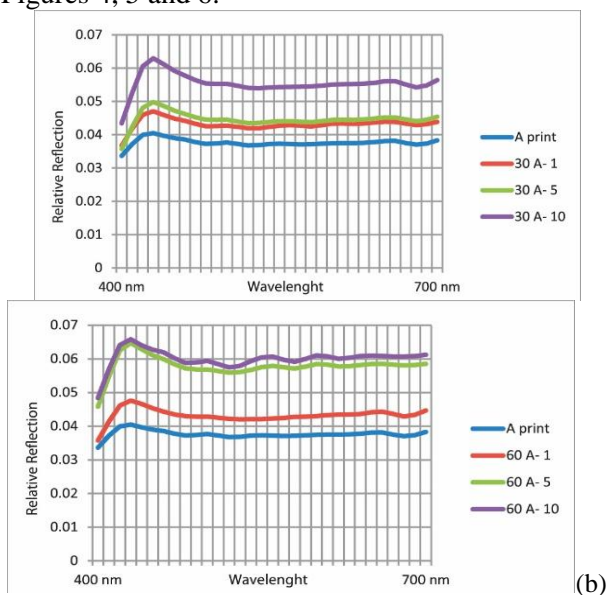


**Fig. 1.** Relative spectral reflection curves obtained after printing and washing cycles for material A at washing temperature of 30°C (a) and 60°C (b)

Remark: Letter A is a material A mark, numbers 30 and 60 represent washing temperature in °C; 1 is sample mark after the first washing, 5 is sample mark after the fifth washing, and 10 is sample mark after the tenth washing.

Figures 4, 5 and 6 indicate that the analyzed samples underwent a change of the surface morphology after the printing process. Figures 4a, 5a and 6a clearly show a smooth fiber structure, whereas in Figure 4b, 5b and 6b can be noticed ink particles on the surface of the fibers which is a result of the printing process. It can be said that the fibers are almost entirely covered in ink due to the high ink deposit. By exposing the printed samples to the washing process, a part of the ink quantity is washed off the fibers surface, which can be seen in

Figures 4c, 4d, 5c, 5d, 6c and 6d. Thereby, it can be seen that the effect of washing process at higher temperatures leads to the removal of larger quantities of printed ink. The consequence of the partially ink removal is that it reduces the amount of ink that absorb a part of the light spectrum, so the surface becomes smoother, and, therefore, more reflective. These conclusions are directly related to the changes in spectral and colour difference values.

Water retention value was measured on the samples before printing, after printing, and after the first, the fifth and the tenth washing processes at all washing temperatures. The results are presented in Table 4.

The water retention value test results indicate that the printing process reduces water retention value, which is valid for all three materials. This phenomenon can be explained by the fact that during the printing process, the ink layer is transferred both onto the material surface and in the material structure. The ink deposition on the material surface covers the hydrophilic cotton fibers, reducing that way the amount of space where the water molecules come in contact with the cotton fibers, which lowers the absorption ability of the fibers and thus the ability to retain water.

After subjecting the samples to the first washing process, no matter the washing temperature is, water retention value is increased.

This is caused by the fact that washing process causes washing out of the printed ink particles. After washing out the ink particles, the hydrophilic surface of cotton fibers is released, this in turn allows greater fiber absorption characteristics and greater water retention value.

By further observation of the water retention values, in case of washing temperature of 30°C, it was noticed that in the case of materials A and B, after the fifth washing cycle there is a decrease in the water retention value in comparison to the same samples, after the first washing cycle.

This phenomenon can be explained by the fact that during the printing process, an uneven clustering of ink particles occurred on the surface of the substrate material, which led to the appearance of mottle or macro nonuniformity on the prints. After the first washing cycle, a complete ink washout from the fibers occurred on the surfaces with a lower concentration of ink, which released the material surface enabling contact of the fibers with water.

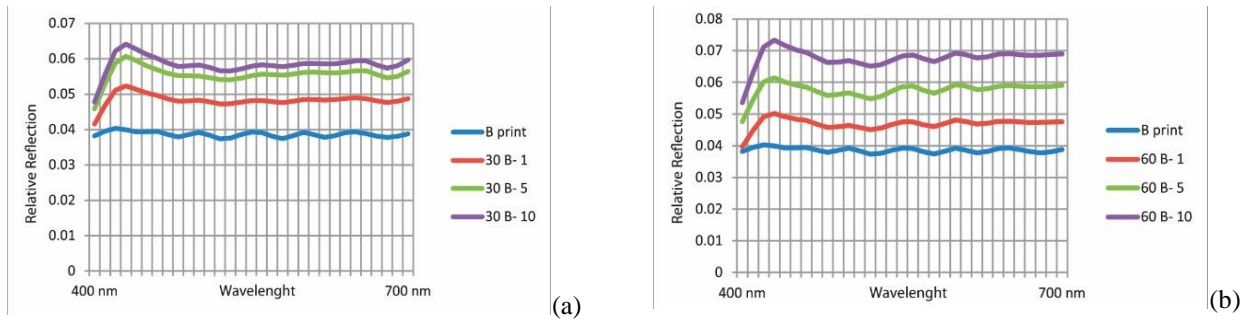


**Fig. 2.** Relative spectral reflection curves obtained after printing and washing cycles for material B at washing temperature of 30°C (a) and 60°C (b). Remark: Letter B is a material B mark, numbers 30 and 60 represent washing temperature in °C; 1 is sample mark after the first washing, 5 is sample mark after the fifth washing and 10 is sample mark after the tenth washing.

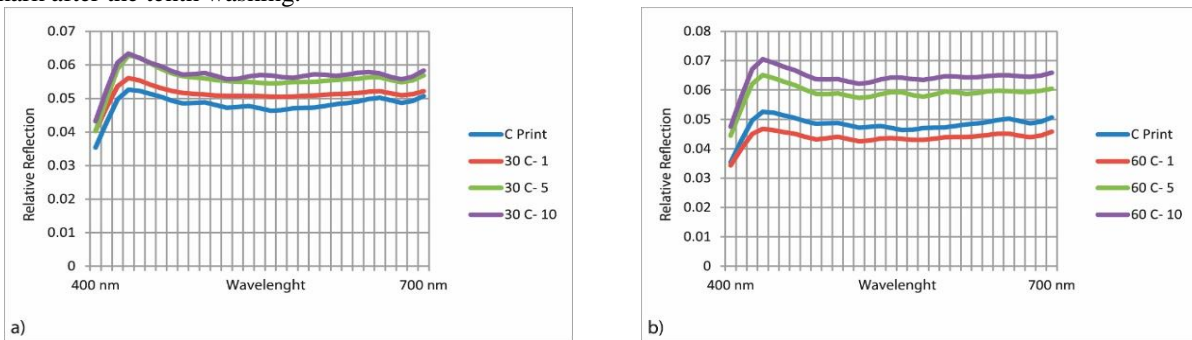


**Fig. 3.** Relative spectral reflection curves obtained after printing and washing cycles for material C at washing temperature of 30°C (a) and 60°C (b). Remark: Letter C is a material C mark, numbers 30 and 60 represent washing temperature in °C; 1 is sample mark after the first washing, 5 is sample mark after the fifth washing, and 10 is sample mark after the tenth washing.

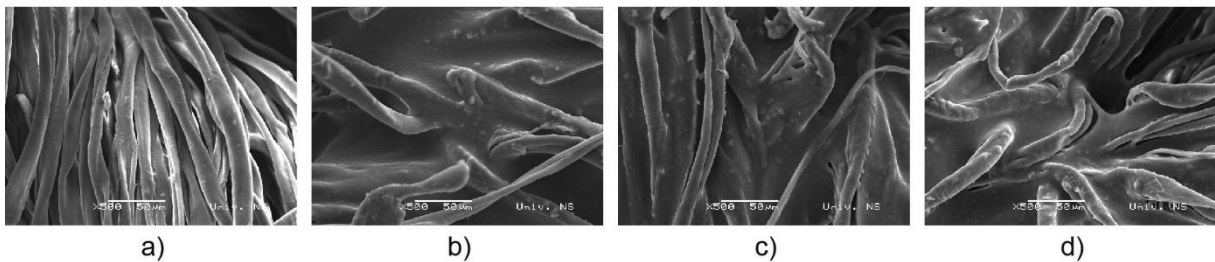


**Fig. 4.** SEM micrographs for material A: a) before printing process, b) after printing process, c) after washing process (30°C), d) after washing process (60°C).

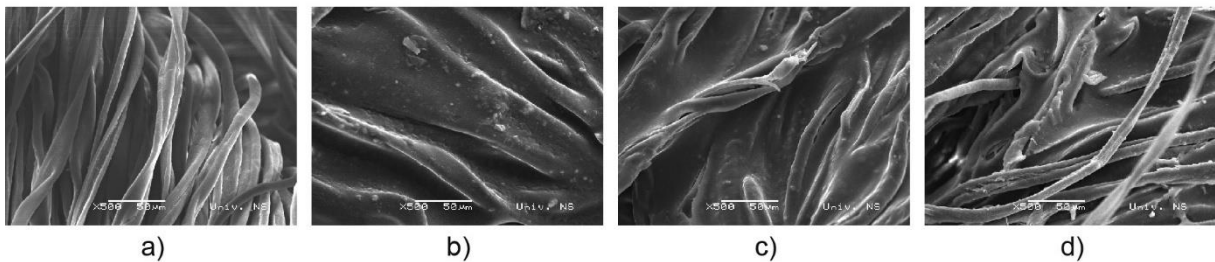


**Fig. 5.** SEM micrographs for material B: a) before printing process, b) after printing process, c) after washing process (30°C), d) after washing process (60°C).

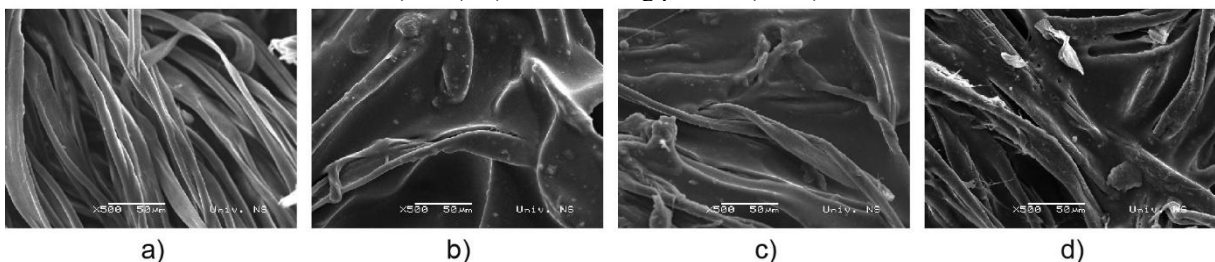


**Fig. 6.** SEM micrographs for material C: a) before printing process, b) after printing process, c) after washing process (30°C), d) after washing process (60°C)

**Table 4.** Water retention value of tested materials

Sample	W <sub>rv</sub> (%)	Sample	W <sub>rv</sub> (%)	Sample	W <sub>rv</sub> (%)
A	33.04	B	33.04	C	28.48
A- P	22.92	B - P	24.42	C - P	22.60
A- 30- W1	23.78	B - 30- W1	28.48	C - 30- W1	23.29
A- 30- W5	22.62	B - 30- W5	27.96	C - 30- W5	24.88
A- 30- W10	24.78	B - 30- W10	28.36	C - 30- W10	22.89
A- 60- W1	24.38	B - 60- W1	26.44	C - 60- W1	23.48
A- 60- W5	25.61	B - 60- W5	26.82	C - 60- W5	23.70
A- 60- W10	27.04	B - 60- W10	27.13	C - 60- W10	23.50

The increasing number of washing cycles affects printed ink particles to remove or regroup from the regions with higher ink concentrations to the regions with lower ink concentration. Free surfaces of the fibers are then recovered with the ink particles that consequently lead to the reduction of water retention value. However, a further increase of washing cycles even further affects ink particles to remove, and thus the water retention value rise. In the case of the material C (material with the greatest surface mass and the most pronounced relief surface structure) the ability to retain water was higher after the first wash than after the fifth wash. However, a further increase of the number of washing cycles brings to the decline of the material ability to retain ink. The initial trend of the water retention value behaviour can be explained by washing out of ink particles, similarly as in the case of two previously analysed materials. However, exceptionally strong relief surface structure of this material leads to the fact that the phenomenon of ink particles regrouping from regions with higher ink concentrations to the regions with lower ink concentrations occurs by exposing samples to higher number of washing cycles, hence this is the reason for water retention value decrease after the tenth washing cycle, comparing to the same value after the fifth washing cycle.

In the case of washed samples at the washing temperature of 60°C it can be noticed that with the

increase of washing cycles number, water retention value rise. It can be assumed that the higher the washing temperature, the better the washing out of ink particles, which will be further rinsed with every following washing cycle without retention. At the same time, as an exception, material C possesses the water retention values that are slightly lower after the tenth washing comparing to the recorded value after the fifth washing. This phenomenon is due to the rougher surface relief structures of this material.

Obtained colour reproduction results were processed using multiple linear regression analysis, where statistically reliable relation of colour differences on the number of washing cycles and washing temperatures was obtained. The resulting statistical models are presented in Tables 5, 6, 7. sing multiple linear regression analysis, mathematical dependence models of the water retention value relative to the number of washing cycles and washing temperature were created, for materials A and B (Tables 8 and 9).

The resulting statistical dependence model of the water retention value on the washing cycles and washing temperature for material C is not statistically significant, because the coefficient of the multiple linear regression is 0.041, for the given mathematical model.

**Table 5.** Multiple linear regression coefficients for the obtained mathematical model that determine dependence of colour difference value ΔE on water temperature T and series of washing WS for all material A

$\Delta E = 0.149 + 0.682 * WS + 0.05 * T$										
Multiple reg. coef.	Std. Error of the Estimate	$b_0 = 0.149$			$b_1 = 0.682$			$b_2 = 0.05$		
		Std. Error	t	p	Std. Error	t	p	Std. Error	t	p
R <sup>2</sup>	s	1.093	0.136	0.900	0.085	7.997	0.004	0.021	2.384	0.097
0.959	0.770									

**Table 6.** Multiple linear regression coefficients for the obtained mathematical model that determine dependence of colour difference value  $\Delta E$  on water temperature T and series of washing WS for all material B

$\Delta E = 0.904 + 0.482 * WS + 0.063 * T$										
Multiple reg. coef.	Std. Error of the Estimate	$b_0 = 0.904$			$b_1 = 0.482$			$b_2 = 0.063$		
		Std. Error	t	p	Std. Error	t	p	Std. Error	t	p
R <sup>2</sup>	s	1.523			0.594			0.120		
0.876	1.072	1.523			0.594			0.120		

**Table 7.** Multiple linear regression coefficients for the obtained mathematical model that determine dependence of colour difference value  $\Delta E$  on water temperature T and series of washing WS for all material C

$\Delta E = - 1.516 + 0.318 * WS + 0.044 * T$										
Multiple reg. coef.	Std. Error of the Estimate	$b_0 = - 1.516$			$b_1 = 0.318$			$b_2 = 0.044$		
		Std. Error	t	p	Std. Error	t	p	Std. Error	t	p
R <sup>2</sup>	s	1.183			0.290			0.148		
0.839	0.833	1.183			0.290			0.148		

**Table 8.** Multiple linear regression coefficients for the obtained mathematical model that determine dependence of water retention value  $W_{rv}$  on water temperature T and series of washing WS for material A

$W_{rv} = 20.658 + 0.210 * WS + 0.065 * T$										
Multiple reg. coef.	Std. Error of the Estimate	$b_0 = 20.658$			$b_1 = 0.210$			$b_2 = 0.065$		
		Std. Error	t	p	Std. Error	t	p	Std. Error	t	p
R <sup>2</sup>	s	1.245			0.120			0.072		
0.801	0.877	1.245			0.120			0.072		

**Table 9.** Multiple linear regression coefficients for the obtained mathematical model that determine dependence of water retention value  $W_{rv}$  on water temperature T and series of washing WS for material B

$W_{rv} = 29.559 + 0.033 * WS - 0.049 * T$										
Multiple reg. coef.	Std. Error of the Estimate	$b_0 = 29.559$			$b_1 = 0.033$			$b_2 = - 0.049$		
		Std. Error	t	p	Std. Error	t	p	Std. Error	t	p
R <sup>2</sup>	s	0.447			0.411			0.011		
0.918	0.315	0.447			0.411			0.011		

4. CONCLUSIONS

Textile products made of cotton fibers are exposed to different environmental influences, out of which the washing process is one of the most frequent. This paper examined the effect of washing cycles at different washing temperatures on the quality of screen printed cotton textile materials. To determine print quality, following measurements were conducted: spectrophotometric analysis of colour reproduction, SEM microscopic

analysis of the samples and water retention value of the samples before and after washing processes.

Investigation revealed that washing process affected the quality of the screen printed textile materials, which was confirmed by spectrophotometric analysis, consisted of CIE L\*a\*b\* coordinates determination (after which  $\Delta E$  values were calculated) and the determination of relative spectral reflection values.

The increase in a number of washing cycles leads to a bigger colour reproduction change in

comparison to the samples that were not subjected to the washing process. Also, a rise of the washing temperature contributes to even bigger colour differences between the samples. This can be explained by the fact that the washing process leads to peeling, i.e. washing out of the printed inks. Rinsing process is supported with the certain amount of heat. Thus bigger deviation of reproduced colours was recorded after washing processes conducted at higher temperatures. Effects of the washing processes are the change of the relative spectral reflectance values of the samples, which is confirmed by generated spectral curves.

It was also proved that the surface mass, knitting density and type of weave, affect the behaviour of printed materials in the process of exploitation. Knitted sample C, that possesses the greatest surface mass, lowest knitting density and relatively rougher surface structure comparing to knitted materials A and B, showed the best service properties with regard to the quality of the printed impression after washing process.

SEM microscopic analysis of samples was monitoring the behaviour of the material before, after printing and after washing process at different temperatures. The analysis showed that after the printing process, the highest amount of ink is present on the sample surface. However, subjecting the samples to washing process leads to washing out of printed ink. SEM analysis also indicates that washing temperature increase leads washing out of larger amounts of printed ink. Due to the reduction of ink amount on the surface of the samples, a greater amount of light is being reflected from the surface, thus perceived differences of colour reproduction on the prints before and after the washing process.

Obtained results indicate that the printing and washing processes, as well as washing temperatures, have an impact on the water retention value of the tested materials. Printing process leads to a reduction of water retention value, while exposure to a larger number of washing cycles leads to increase of water retention value. Washing processes at higher temperatures lead to the improvement of the water retention value as well.

By summarizing all the results, it can be concluded that the effect of washing has an impact on the quality of impressions printed by screen printing technique on textiles. The effect of washing process on the print quality may be reduced by selecting the appropriate materials with respect to the type of applied weaves or its surface structure, as well as selecting the appropriate washing temperature.

By processing the results of the investigation using multiple linear regression analysis, statistically reliable dependence of the water retention value  $W_{rv}$  on the number of washing cycles and washing temperature was obtained, with a very high multiple regression coefficient value for materials A and B, while for the material C statistically reliable model of interdependence of tested parameters was not obtained. Further examination of the results using multiple linear regression analysis led to a statistically reliable dependence model of colour differences  $\Delta E$  on the number of washing cycles and washing temperature, with a very high multiple regression coefficient value for all materials.

In order to broaden current knowledge in this scientific area, it is planned to test how printing parameters, primarily screen mesh count in combination with external factors affect print quality on the textiles. When printing textile materials besides the quality of the image reproduction an important aspect is the comfort that person perceives while wearing a garment made by treating these materials. For this reason, in the future investigations it is planned to examine the impact of printing on thermal and physiological properties of the textile materials.

**Acknowledgments.** The research is supported by Ministry of education, science and technology development of Republic of Serbia, project number: 35027 „Development of software model for scientific and production improvement in graphic industry“ and project CEEPUS III RS – 0704 – 04 – 1516, „Research and Education in the Field of Graphic Engineering and Design“.

#### REFERENCES

1. Lam, Y. L., Kan, C. W., Yuen, C. W. M., *Cellulose*, **18**, 493 (2011).
2. D. Grujić, Ph.D. Thesis. Univerza v Mariboru, Fakulteta za strojništvo, Maribor 2010.
3. M. Stančić, D. Grujić, D. Novaković, N. Kašiković, B. Ružičić, J. Geršak, *J. Graphic Eng. Design*, **5**, 25 (2014).
4. D. Onar Çatal, A.T. Özgüney, E.P. Akçakoca Kumbasar, *Tekstil ve Konfeksiyon*, **22**, 309 (2012).
5. N.H. Momin, PhD Thesis. Melbourne, RMIT University, 2008.
6. N. Kašiković, D. Novaković, I. Karlović, G. Vladić, *Tekstil ve Konfeksiyon*, **22**, 115 (2012).
7. S. Kiatkamjornwong, P. Putthimai, H. Noguchi, *Surface Coatings International Part B: Coatings Transactions*, **88**, 25 (2005).
8. Lee, T. M., Choi, Y. J., Nam, S. Y., You, C. W., Na, D. Y., Choi, H. C., Shin, D. Y., Kim, K. Y., Jung, K. I., *Thin Solid Films*, **516**, 7875 (2008).



9. F. Krebs, M. Jørgensen, K. Norrman, O. Hagemann, J. Alstrup, T. Nielsen, J. Fyenbo, K. Larsen, J. Kristensen, *Solar Energy Materials and Solar Cells*, **93**, 422 (2009).
10. M. Stančić, N. Kašiković, D. Novaković, R. Milošević, D. Grujić, *J. Graphic Eng. Design*, **4**, 27 (2013).
11. S. Kalantzi, D. Mamma, E. Kalogeris, D. Kekos, *Fibres & Textiles in Eastern Europe*, **18**, 86 (2010).
12. B. Tomšič, B. Simončič, B. Orel, M. Žerjav, H. Schroers, A. Simončič, Z. Samardžija, *Carbohydrate Polymers*, **75**, 618 (2009).
13. Xiang, W., Cai, Z.S., *J. Appl. Polymer Sci.*, **108**, 1005 (2008).
14. J. Was-Gubala, *Science and Justice*, **49**, 165 (2009).
15. N.T. Kočevar, *Tekstil*, **55**, 127 (2006).
16. I. Majnarić, S. Bolanča, K. Golubović, *Tekstil*, **59**, 456 (2010).
17. F.J.J. Clarke, R. McDonald, B. Rigg, *J. Soc. Dyers Colourists*, **100**, 128 (1984).
18. M.R. Luo, B. Rigg, *J. Soc. Dyers Colourists*, **103**, 86 (1987).
19. CIE Publication 116, *CIE Central Bureau, Vienna* 1995
20. D.H. Kim, J.H. Nobbs, *Proc. 8<sup>th</sup> Congress AIC Colour 97. Kyoto 1997*: pp. 446-449
21. J. Hardeberg, PhD Thesis, Ecole Nationale Supérieure des Télécommunications, Paris, 1999.
22. B. Das, A. Das, V. Kothari, R. Fanguero, M. Araujo, *Autex Research Journal*, **7**, 100 (2007).
23. J. Pan, G. Tonkay, A. Quintero, *Proc. Int. Symp. Microelectr., San Diego, California, USA, 1998*, pp. 264-269.
24. ISO105-C10:2006, Geneva 2006.
25. F. Bozdoğan, I. Tiyek, G. Özçelik Kayseri, *Tekstil ve Konfeksiyon*, **20**, 87 (2010).
26. DIN 53 814, 1997.

## ИЗСЛЕДВАНЕ НА ВЛИЯНИЕТО НА ТЕМПЕРАТУРАТА И БРОЯ ЦИКЛИ НА ИЗПИРАНЕ ВЪРХУ КАЧЕСТВОТО НА ТЕКСТИЛНИ МАТЕРИАЛИ СЪС НАНЕСЕНИ СИТОПЕЧАТНИ ИЗОБРАЖЕНИЯ

Н. Кашикович<sup>1</sup>, М. Станчич<sup>2</sup>, И. Спиридонов<sup>3\*</sup>, Д. Новакович<sup>1</sup>, Р. Милошевич<sup>1</sup>, Д. Груджич<sup>4</sup>, Б. Ружичич<sup>2</sup>

*Университет на Нови Сад, Технически факултет, Катедра по графично инженерство и дизайн, Сърбия*

<sup>2</sup> *Университет на Баня Лука, Технически факултет, Катедра по графично инженерство, Босна и Херцеговина*

<sup>3</sup> *Химикотехнологичен и металургичен Университет, Катедра „Целулоза, хартия и Полиграфия“, България*

<sup>4</sup> *Университет на Баня Лука, Технически факултет, Катедра по текстилно инженерство, Босна и Херцеговина*

Постъпила на 30 ноември, 2016 г.; Приета за печат на 18 май, 2017 г.

(Резюме)

В съвременното общество се наблюдават все по-високи изисквания към текстилните материали и платове - освен удобно облеклото е необходимо да отговаря и на редица естетични критерии. Външния вид и естетиката на текстилните материали често се определят от качеството на печата върху тях.

Печата и самия текстилен материал са подложени на редица различни въздействия по време на експлоатацията. Едно от най-срещаните и влияещи въздействия е процеса на изпиране, който влияе върху текстилните влакна и цветната репродукция изразена чрез промяна в качеството на отпечатъка.

Целта на настоящото изследване е установяване на влиянието на перилния процес върху изменението на цветовите характеристики в цветово пространство CIE L\*a\*b\* на памучни текстилни материали отпечатани по ситопечатния метод. В изследването е направен анализ на влиянието на два различни параметъра свързани с процеса на изпиране – температурата и брой цикли на изпиране. Получените резултати показват, че увеличаването на температурата на изпиране води до сериозна промяна в цветовите характеристики на ситопечатните изображения и текстила. Броя цикли на изпиране също оказва, макар и по-малко влияние върху цветовите промени. Изследванията показаха, че в процеса на изпиране се отделят частици от мастилата, което води до промяна не само на цветовите характеристики, но и на другите изследвани свойства на текстилния материал.

## Ink - jet imprints in just noticeable color difference evaluation

S. Dedijer<sup>1</sup>, I. Tomić\*<sup>1</sup>, I. Spiridonov<sup>2</sup>, R. Boeva<sup>2</sup>, I. Jurič<sup>1</sup>, N. Milić<sup>1</sup>, S. Đurđević<sup>1</sup>

<sup>1</sup>University of Novi Sad, Faculty of Technical Sciences, Department of Graphic Engineering and Design, Novi Sad, Serbia

<sup>2</sup>University of Chemical Technology and Metallurgy, Department of Printing Arts, Pulp and Paper, Sofia, Bulgaria

Submitted November 30, 2016; Accepted May 18, 2017

In this paper we investigated the possibility of using ink - jet printing technique for the purpose of just noticeable color difference (JND) evaluation. When performing color difference evaluations with printed samples, it is expected that colorimetric values of printed samples exhibit minimal deviation from the established target values. The uniformity of printed area and consistency in colorimetric values is also a must. The printing technique used may significantly influence the color reproduction, thus altering the targeted color difference. In order to evaluate the level of inconsistency influenced by the ink-jet printing technique, we chose five initial color centers, varied their lightness and hue in such a way that color difference between neighboring samples was  $0.25 \Delta E^*_{ab}$ . The samples were printed on uncoated 120 g/m<sup>2</sup> paper. For accurate quantification of color difference, we used CIELAB and CIE2000 color difference formulae as well as MCDM formula. It was shown that the expected color differences were not obtained in all cases and for all colors used. Although the CIE2000 formula gave slightly more accurate results than CIELAB, their performances were shown to be quite similar. It was shown that the variability is dependent on the color center as well as on the degree and direction of variation in lightness and hue. The study indicated that performing color difference evaluations on ink - jet imprints at the level of 0.25 up to 0.75  $\Delta E^*_{ab}$  units will be strongly influenced by printing inconsistency.

**Key words:** ink - jet printing, just noticeable color difference (JND), color difference formulae

### INTRODUCTION

Color is one of the most important visual attributes in many industrial branches and is often associated with the concept of quality. It can be considered as a highly important commercial determinant of quality for a wide range of products. The color can be evaluated by instrumental or visual analysis. Visual analysis, often referred to as subjective, are based on human perception of color while the instrumental analysis are based on physical, objective evaluation of color stimuli using spectral measurements, measurements of the tristimulus values, relating to the quantitative description of the color appearance, lightness/brightness, hue or chroma/saturation [1-3].

Since the color could be measured, the topic of practical importance is the color-difference evaluation - precise definition of the magnitude of color differences between various colored stimuli. For that purpose, the series of color difference equations have been established, with more or less successful correspondence between changes in the physical description of a color stimuli and its appearance [1]. The aim of decades of research in this field was to establish the color difference

formula which would be successfully used in just noticeable, small through moderate to large color differences evaluations with the magnitude which would be correlating the visual one [4-14].

Currently, there are at least six color difference equations available, including the so-called advanced formulae: CIELAB, CIELUV, CMC, BFD, CIE94, CIE00 [6-9,12-28], where most of them are based on CIELAB colorimetric system. From this variety arises several questions that should be attempted to be answered: the decision making criteria for the formula to be used, the compatibility of results accomplished using different formulae, applicability of each one under various conditions. So far, it is established that each of the formulae mentioned above performs best under a specific, more or less similar set of reference conditions. Each formula result in different values, which might, in some color regions, be quite significant [6].

Instrumental color measuring and evaluation processes, based on color-difference calculations, is usually performed between target color stimuli and corresponding reproduced match. The pass/fail decision is made on the basis of the established color difference threshold. The color difference threshold differs in  $\Delta E^*_{ab}$  value depending upon the

\*) To whom all correspondence should be sent:

E-mail: [tomic@uns.ac.rs](mailto:tomic@uns.ac.rs)

area of application and color difference formulae used: a difference of  $5\Delta E^*_{ab}$  may be acceptable in some applications, whereas for other, differences over 1  $\Delta E$  may be unacceptable.

Nevertheless, defined threshold should always be in compliance with an observer's ability to detect a difference in colored stimuli. Thus, in terms of color-difference perceptibility, the smallest perceptible difference by the human eye, detected at 50 % probability, is known as a just-noticeable difference (JND) [7,8,10]. A theoretical CIELAB JND is deemed a difference of 1.0  $\Delta E^*_{ab}$ , with equal contributions from the  $L^*$ ,  $a^*$  and  $b^*$  errors [8,16,30]. In contrast, in another experimental study, encompassing the evaluation of uniform color differences, was reported an average value of 2.3  $\Delta E^*_{ab}$  for JND [24,30]. Color difference of 1  $\Delta E^*_{ab}$  is normally detected in neutral colors, while more saturated colors require a slightly larger  $\Delta E^*_{ab}$  in order to be detected by the untrained observer [24,31]. According to Ebner [32], CIELUV color difference of less than 1  $\Delta E^*_{uv}$  will not be perceptible, as well. The color differences up to 4 may or may not be perceptible, depending on the color itself, while the difference larger than 4, is highly likely to be perceived [32].

If the printed samples are tending to be used in experiments where a series of color tests are to be compared with a color reference in order to establish the color difference threshold (JND), it is obvious that those tolerances for prints cannot be even considered. It is inevitable for reproduced color to be influenced by printing technology, but the magnitude of the influence must be known and taken into consideration if performing color difference evaluations.

Driven by the findings stated above, we investigated the possibilities of using ink - jet printing technique for the purpose of just noticeable color difference (JND) evaluation tending to reveal to which extend the used printing technique alter

the targeted color difference. For the analysis, we have chosen five CIE color centers (gray, green, red, blue and yellow) and varied their lightness and hue in order to achieve targeted color difference. The color difference calculations using  $L^*a^*b^*$  values from ink-jet printed samples were performed using  $\Delta E^*_{ab}$  and  $\Delta E_{00}$  color difference equations.

## METHODOLOGY

In order to evaluate the level of reproduction inconsistency which will be directly influenced by printing technique used, we chose five initial color centre [9] (Table 1). Their lightness and hue were varied in the steps of  $\Delta E^*_{ab} 0.25$ , where the changes were made in both directions i.e. by lowering and increasing the values. When the lightness value was varied, hue value was left unchanged, and vice versa. The smallest color difference from the initial color was 0.25, while the largest was set to be 1.5. Since the lightness and hue were varied independently, we created 5 color test charts (Fig. 1) with lightness and 4 color test charts with hue variations (achromatic, gray color was omitted in hue variation analysis).

The targeted digital  $L^*a^*b^*$  data of each color patch were calculated on the basis of expected color difference value  $\Delta E^*_{ab}$ ,  $L^*a^*b^*/ C^*h^0$  values of five initial color centers and following formulae [2-3,33]:

$$\Delta E^*_{ab} \text{ (CIELAB, } \Delta E76) \text{ color difference: } \Delta E^*_{ab} = [\Delta L^{*2} + \Delta a^{*2} + \Delta b^{*2}]^{1/2} \quad (1)$$

where:

- $\Delta L^*$  - the lightness difference:  $\Delta L^* = L^*_1 - L^*_2$ ,
- $\Delta a^*$  and  $\Delta b^*$  - chromaticity differences:  $\Delta a^* = a^*_1 - a^*_2$ ,  $\Delta b^* = b^*_1 - b^*_2$
- $L_1$ ,  $a_1$ ,  $b_1$  - lightness and chromaticity coordinates of sample 1 (CIE color centre);  $L_2$ ,  $a_2$ ,  $b_2$  - lightness and chromaticity coordinates of sample 2 (targeted color patch).

$$\Delta E^*_{ab} = [\Delta L^{*2} + \Delta C^{*2}_{ab} + \Delta H^{*2}_{ab}]^{1/2} \quad (2)$$

**Table 1.** CIELAB chromaticity parameters of the test color centers. The CIE1931 Standard Colorimetric Observer was used in the calculations

Color center	$L_j^*$	$a_j^*$	$b_j^*$	$C_j^*$	$h_j^o$
Gray	61.65	0.11	0.04	0.12	20
Red	44.38	36.91	23.33	43.67	32
Yellow	86.65	-6.92	47.15	47.66	98
Green	56.09	-32.13	0.44	32.13	179
Blue	35.60	4.83	-30.18	30.56	279

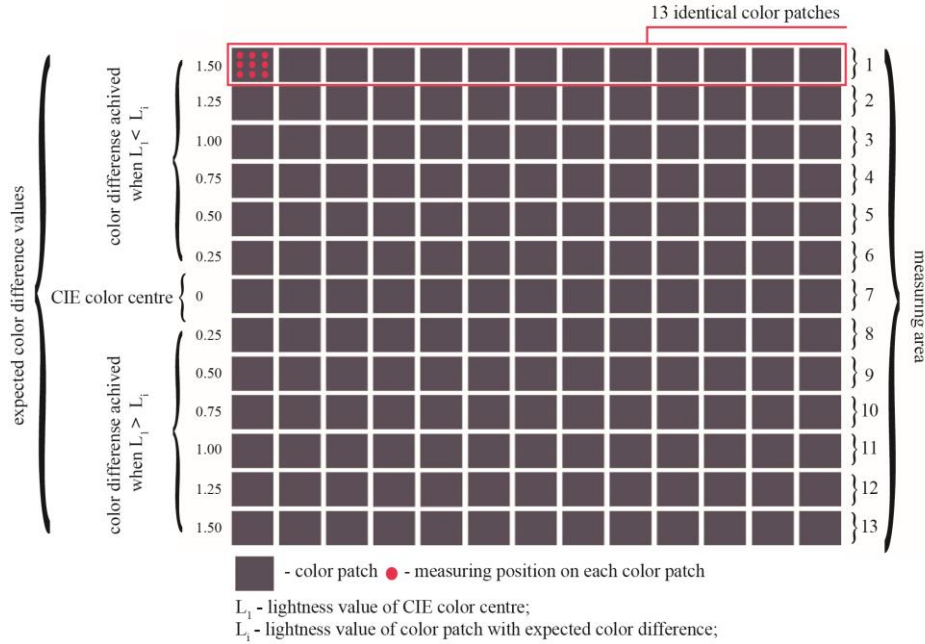


**Figure 1.** Example of generated color test chart and pictorial explanation of relevant elements (one color/variation in lightness value)

Chroma ( $\Delta C^*_{ab}$ ) differences:  $\Delta C^*_{ab} = C^*_{ab,1} - C^*_{ab,2}$  (3)

Hue ( $\Delta H^*_{ab}$ ) differences:

$$\Delta H^*_{ab} = 2(C^*_{ab,1} C^*_{ab,2})^{1/2} \sin(\Delta h_{ab}/2) \quad (4)$$

$$\Delta h^*_{ab} = h^*_{ab,1} - h^*_{ab,2} \quad (5)$$

Chroma ( $C_{ab}^*$ ):  $C_{ab}^* = [(a^*)^2 + (b^*)^2]^{1/2}$  (6)

Hue angle ( $h_{ab}^*$ ):  $h_{ab}^* = \tan^{-1}(b^*/a^*)$  (7)

where  $a^*$ ,  $b^*$  - chromaticity coordinates of the sample;  $C^*_{ab,1}$  is chroma of sample 1 (CIE color centre);  $C^*_{ab,2}$  - chroma of sample 2 (targeted color patch);  $h^*_{ab,1}$  is hue angle of sample 1 (CIE color centre);  $h^*_{ab,2}$  - hue angle of sample 2 (targeted color patch).

The  $L^*a^*b^*$  data were then recalculated to RGB values (CIE D50 standard illuminant and standard 2° observer; 0-1 scale) and used for of the generation of color patches size of 2x2 cm (sRGB, .tiff format). For this purpose, we employed MATLAB® R2013a. The patches were used for color test chart creation in Adobe® Photoshop® CS6 software.

The created color test charts were printed on uncoated, single-weight matte 120 g/m<sup>2</sup> ink - jet paper using calibrated ink-jet printer Epson Stylus Pro 7800. The settings of a printer were according to manufacturers' recommendation for high quality color printing –on the resolution of 720x1440 dpi. Thirteen patches were printed for each color and each lightness/hue variation, whereas each color patch was measured nine times (as depicted in Figure 1) and  $L^*a^*b^*$  values were recorded accordingly. They were used for color difference (averaged) and MCDM calculation ( $L^*$ ,  $a^*$  and  $b^*$

value of 117 measurements per each color/lightness/hue variation). The colorimetric measurements were performed using Techon SpectroDens Advanced spectrophotometer (measurement geometry: 0°/45° with respect to CIE D50 standard illuminant and standard 2° observer). Measurement is performed on black, matte backing.

For accurate quantification of produced color difference on ink-jet imprints, we used  $\Delta E^*_{ab}$  (Eqn.1) and  $\Delta E_{00}$  ( $\Delta E_{2000}$ ) [33,35-36]:

$$\Delta E_{00} = [(\Delta L'/K_L S_L)^2 + (\Delta C'/K_C S_C)^2 + (\Delta H'/K_H S_H)^2 + R_T(\Delta C'/K_C S_C)(\Delta H'/K_H S_H)]^{1/2} \quad (8)$$

where

$$\Delta L' = L'_1 - L'_2$$

$$\Delta C' = C'_1 - C'_2$$

$$\Delta H' = 2(C'_1 C'_2)^{1/2} \sin(\Delta h'/2)$$

$$\Delta h' = h'_1 - h'_2$$

$$S_L = 1 + \frac{0.015(\bar{L} - 50)^2}{\sqrt{20 + (\bar{L} - 50)^2}}$$

$$S_C = 1 + 0.045\bar{C}'$$

$$S_H = 1 + 0.015\bar{C}'T$$

$$T = 1 - 0.17 \cos(\bar{h}' - 30^\circ) + 0.24 \cos(2\bar{h}') + 0.32 \cos(3\bar{h}' + 6^\circ) + 0.20 \cos(4\bar{h}' + 63^\circ)$$

$$R_T = -\sin(2\Delta\theta) R_C$$

$$\Delta\theta = 30 \exp\left\{-\left[\frac{(\bar{h}' - 275^\circ)}{25}\right]^2\right\}$$

$$R_C = 2 \sqrt{\frac{\bar{c}'^7}{\bar{c}'^7 + 25^7}}$$

$$L' = L^*$$

$$a' = (1 + G)a^*$$

$$b' = b^*$$

$$C' = (a'^2 + b'^2)^{1/2}$$

$$h' = \tan^{-1}(b'/a')$$

$$G = 0.5 \left( 1 - \sqrt{\frac{C_{ab}^{*-7}}{C_{ab}^{*-7} + 25^7}} \right)$$

$K_L=1$ ;  $K_C=1$ ;  $K_H=1$  (default values).

Mean Color Difference from the Mean (MCDM) was computed across all repetitions (measuring areas, Fig.1), for each color and each variation in order to give better insight in color variability caused by printing process itself. MCDM value was calculated based on  $\Delta E_{ab}^*$  and  $\Delta E_{00}$ , as well [37-38]:

$$MCDM = \sum_{i=1}^n E_{abi}^* \quad (9)$$

where:

$$\Delta E_{ab}^* = [(L_i^* - L_{mean}^*)^2 + (a_i^* - a_{mean}^*)^2 + (b_i^* - b_{mean}^*)^2]^{1/2}$$

$$L_{mean}^* = \sum_{i=1}^n L_i^* / n;$$

$$a_{mean}^* = \sum_{i=1}^n a_i^* / n;$$

$$b_{mean}^* = \sum_{i=1}^n b_i^* / n;$$

$n = 117$  (the number of samples);

$$MCDM = \sum_{i=1}^n E_{00i}^* \quad (10)$$

where:

$$\Delta E_{00} = [((L_i' - L_{mean}')/K_L S_L)^2 + ((C_i' - C_{mean}')/K_C S_C)^2 + (2(C_i' C_{mean}')^{1/2} \sin((h_i' - h_{mean}')/2)/K_H S_H)^2 + R_T((C_i' - C_{mean}')/K_C S_C) (2(C_i' C_{mean}')^{1/2} \sin((h_i' - h_{mean}')/2)/K_H S_H)]^{1/2}$$

$$L_{mean}' = \sum_{i=1}^n L_i' / n;$$

$$C_{mean}' = \sum_{i=1}^n C_i' / n;$$

$$h_{mean}' = \sum_{i=1}^n h_i' / n;$$

$n = 117$  (the number of samples).

## RESULTS AND DISCUSSION

On Fig. 2 and Fig. 3 are depicted calculated color differences in contrast to expected ones. Figure 2 represent the results where the color difference was obtained by lightness variation, while Figure 3 shows those obtained by hue variations. The gray line represents the ideal color reproduction, thus theoretically achievable targeted/ reproduced color difference ratio.

According to the results presented on Fig. 2, the achieved color differences exhibited moderate to large discrepancies from targeted values. The highest deviations were observed in case of green color by lowering the  $L^*$  value of the color centre. In case of gray, red, blue and yellow CIE color centre, similar trend can be observed: if the targeted color difference value were smaller, the deviations were higher and the

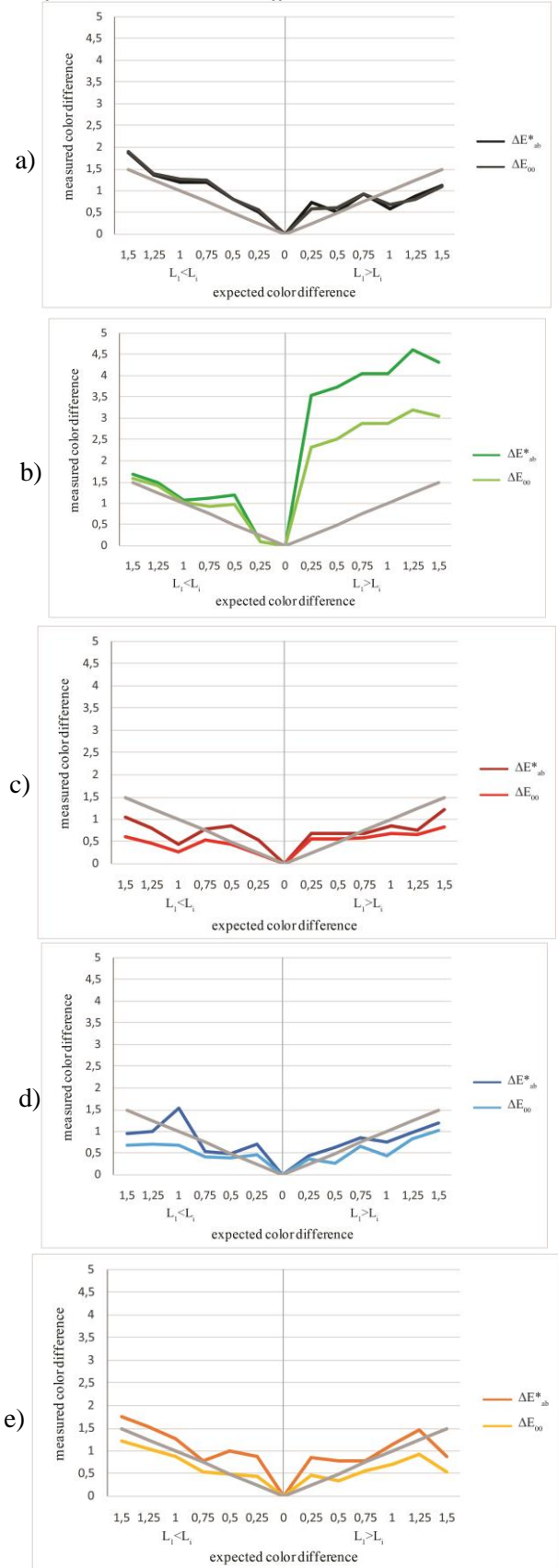


**Figure 2.**  $\Delta E_{ab}^*$  and  $\Delta E_{00}$  color difference values (lightness scale variations): a) gray; b) green; c) red; d) blue; e) yellow.

reproduced values were above the targeted ones; if the targeted  $\Delta E$  values were bigger, the discrepancies were of lower value, while the reproduced  $\Delta E$  values are below the targeted ones. In the case of the smallest initially defined  $\Delta E$  values, the color differences were doubled, or even tripled from the expected ones. The highest discrepancies were reached for color differences ranging from 0.25 to 0.75, for all the colors encompassed in the analysis. The defined trends were observed regardless of the color difference formulae used. The use of  $\Delta E_{00}$  color difference formula resulted in lower  $\Delta E$  values in comparison to  $\Delta E^*_{ab}$ . The exception is achromatic, gray color, where both equations led to almost the same values. Taking into account the way of obtaining the color difference values, this result was expected (see Eqns. 1 and 8).

Overall, if the L value was changed,  $\Delta E^*_{ab}$  presented slightly better performances when evaluating the reproduction closest to target one, but restricted to range of color difference above 0.75. Otherwise, the minor advantage is given to  $\Delta E_{00}$  formula. Comparing the results presented on Fig. 3 with those shown on Fig. 2 it is evident that higher reproduction accuracy was achieved when color difference was obtained by the change in chromacity. Better agreement between targeted  $\Delta E$  values and reproduced ones was obviously achieved in case of green and yellow color. On the other side, quite huge discrepancies were outlined in case of blue and red color. Expressed in  $\Delta E^*_{00}$ , color differences certainly have shown lower deviation range, especially in case of green, yellow and blue. Thus, if the hue value was changed,  $\Delta E_{00}$  is expected to slightly outperform  $\Delta E^*_{ab}$  when evaluating the color reproduction closer to target one.

In order to get better insight in given results, we performed the MCDM calculations based on both used formulae (Eqns. 9 and 10). Mean Color Difference from the Mean was used to express the color variation over each measuring area (see Fig. 1), regardless of predefined  $\Delta E$  values. MCDM, as a pure measure of repeatability, should be able to give an overall overview about expected discrepancies in color difference. The results are presented on Fig. 4 and Fig. 5.

As it can be seen from the presented graphs, MCDM value was ranging from 0.15 to 0.7. This can be easily correlated to poorer reproduction of targeted color differences lower than 0.75  $\Delta E$ , indicating that expected variations in color reproduction could be up to 0.75  $\Delta E$ .

This is not likely to be credited to measuring procedure or measuring device, since the manufacturers guarantees of high measuring precision and repeatability [34] and low coefficient of variation for each measuring field and all three

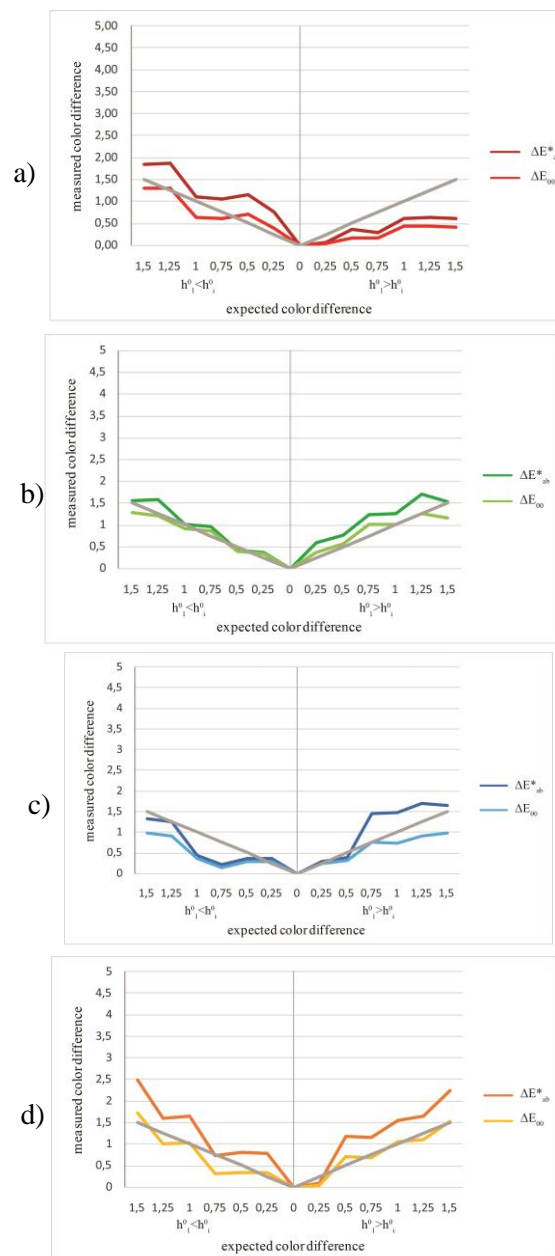


**Figure 3.**  $\Delta E^*_{ab}$  and  $\Delta E_{00}$  color difference values (hue scale variations): a) green; b) red; c) blue; d) yellow

colorimetric values,  $L^*$ ,  $a^*$  and  $b^*$  (below 3%, with the exception of green - below 7%). The results showed that if MCDM calculation is based on  $\Delta E^*_{ab}$  rather than  $\Delta E_{00}$  color difference formula, the color reproduction repeatability will be estimated of lower range (higher MCDM values), and vice versa.

As it was expected, almost the same MCDM values were calculated in case of achromatic gray color. According to MCDM, the lowest color variation was achieved for blue color, whereas the

smallest differences between MCDM  $\Delta E^*_{ab}$  and MCDM  $\Delta E_{00}$  were achieved, as well. On the contrary, obtained results for yellow color centre,

followed by green ones, pointed on higher impact of color difference calculation method on MCDM values.

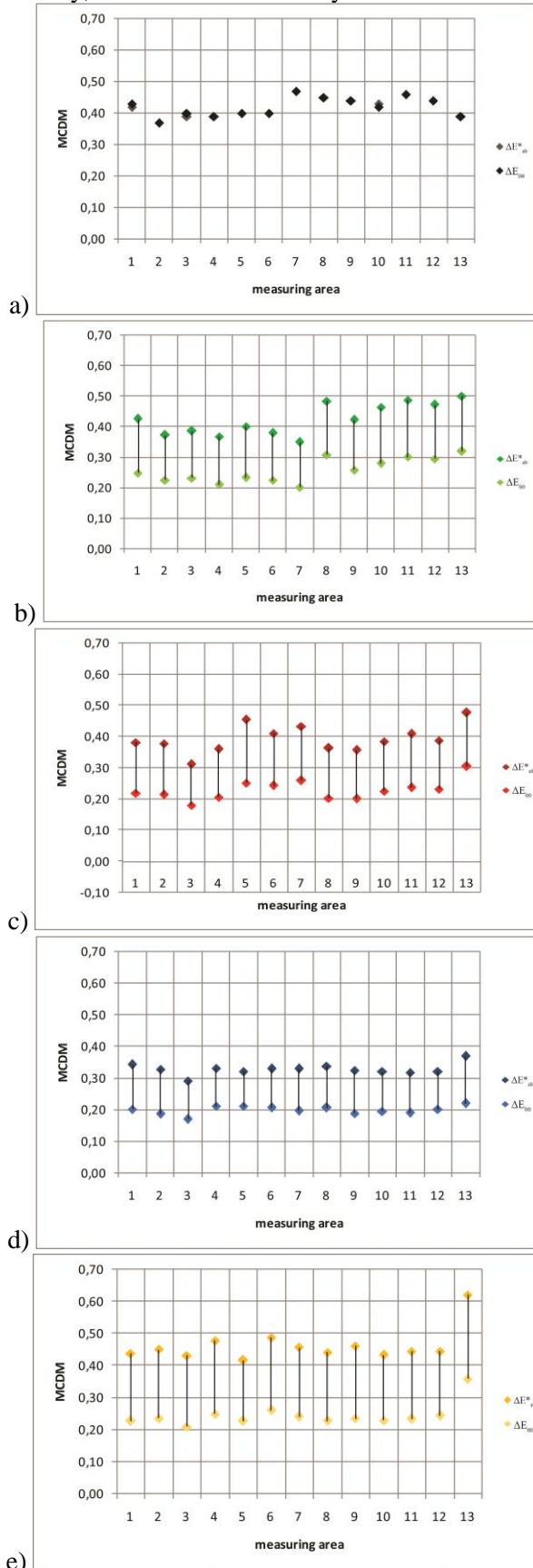


Figure 4. MCDM values /  $\Delta E^*_{ab}$  and  $\Delta E_{00}$  (lightness scale variations): a) gray; b) green; c) red; d) blue; e) yellow.

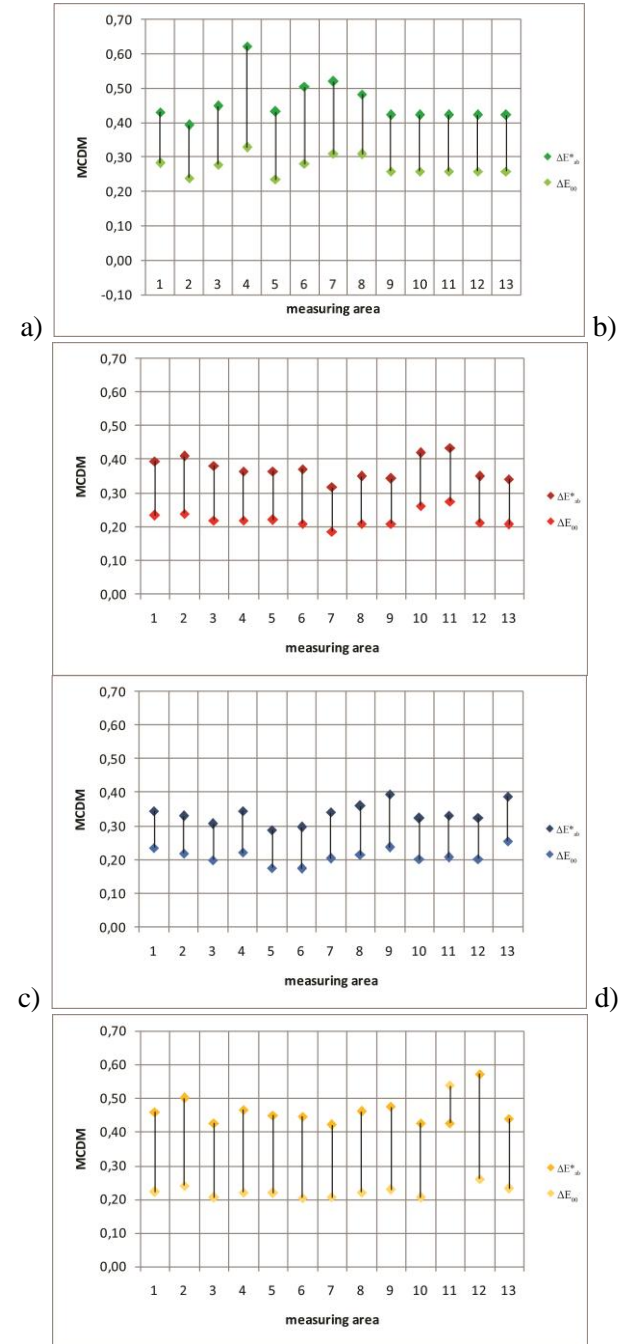


Figure 5. MCDM values /  $\Delta E^*_{ab}$  and  $\Delta E_{00}$  (hue scale variations): a) green; b) red; c) blue; d) yellow.

## CONCLUSIONS

This research aimed to investigate the possibilities of using ink - jet printing technique for the purpose of just noticeable color difference evaluation (JND). We started from the premise that the printing technique used may significantly influence the color reproduction, thus alter the targeted color difference. In order to evaluate the level of discrepancies, we chose five initial color centers and independently varied their lightness and

hue. For color difference calculation we used  $\Delta E^*_{ab}$  and  $\Delta E_{00}$  color difference formulae. The conclusions derived were as follows:

- Results shown that the expected color differences were not obtained in all cases and for all colors used.
- The variability is dependent on whether the color difference was effected by initial variations in color lightness or hue, color itself as well as calculation method used.
- If the controlled color difference change is aimed to be achieved using ink-jet printing technique, the one can expect that the printing process itself will contribute to color shift up to 0.75  $\Delta E$ .
- The larger the initially defined color difference, the more precise reproduction is achieved.
- Slightly higher reproduction accuracy was achieved when color difference was obtained by change in hue, comparing to the case when lightness was altered.
- Although the  $\Delta E_{00}$  formula gave slightly more accurate results than  $\Delta E^*_{ab}$ , their performances are quite similar: if the L value was changed,  $\Delta E^*_{ab}$  presented slightly better performances, but restricted to range of color difference above 0.75. Otherwise, the minor advantage is given to  $\Delta E_{00}$  formula; if the hue value was changed,  $\Delta E_{00}$  slightly outperformed  $\Delta E^*_{ab}$ .
- Both formulas performed better in case of green and yellow color centre when hue was changed, and blue color center, when lightness was changed.
- The obtained results are considered to be attributable to the size of the color difference used, as well.

In the future, we plan to extended this research with the assessment of medium and large color differences and the performance of other color difference formulae, as well.

**Acknowledgement.** This work was supported by the Serbian Ministry of Science and Technological Development, Grant No.: 35027 "The development of software model for improvement of knowledge and production in graphic arts industry".

#### REFERENCES

1. D. H. Brainard, Color Appearance and Color Difference Specification, The Science of Color, Elsevier, 2003.
2. M.L. Gulrajani, Colour measurement principles, advances and industrial applications, Woodhead Publishing Limited in association with The Textile Institute Abington Hall, Granta Park, Great Abington Cambridge CB21 6AH, UK, 2010.
3. M.D. Fairchild, Color Appearance Models, Wiley, 2013.
4. J.A. Martinez, A.J. Poza, M. Melgosa, E. Hita, *J. Opt.*, **28**, 26 (1997).
5. S.S. Guan, M.R. Luo, *Color Res. Appl.*, **24**, 331 (1999).
6. J.H. Xin, C. C. Lam, M. R. Luo, *Color Res. Appl.*, **26**, 376 (2001).
7. B. Laborie, F. Vienot, S. Langlois, *Opht. Physiol. Opt.*, **30**, 568 (2010).
8. <https://arxiv.org/abs/1211.5556>
9. H. Xu, H. Yaguchi, S. Shioiri, *Color Res. Appl.*, **27**, 349 (2002).
10. CIE TN 001:2014:CIE, Technical note (2014).
11. S. S. Guan, M. R. Luo, *Color Res. Appl.*, **24**, 344 (1999).
12. G. Hong, M. R. Luo, *Imaging Sci. J.*, **54**, 86 (2006).
13. K. M. R. Ho, G. Cui, M. R. Luo, B. Rigg, in: Proc. of the Interim Meeting of the International Color Association, Brazil, 2004), P.J. Alessi (eds.), Brazilian Color Association, Lisbon, 2004, p.117.
14. M. Vik, in: Industrial colour difference evaluation: LCAM textile data (Proc. of the Interim Meeting of the International Color Association, Brazil, 2004), P.J. Alessi (eds.), Brazilian Color Association, Lisbon, 2004, p.138.
15. [https://www.researchgate.net/profile/Ming\\_Luo4/publication/254682236\\_Colour\\_Difference\\_Formulae\\_Past\\_Present\\_and\\_Future/links/541e8d330cf241a65a18b591.pdf](https://www.researchgate.net/profile/Ming_Luo4/publication/254682236_Colour_Difference_Formulae_Past_Present_and_Future/links/541e8d330cf241a65a18b591.pdf)
16. <http://www.printing.org/abstract/8754>
17. S. Grgic, M. Grgic, L. Mandic, in: Comparison of Color Difference Equations (Proc. 48th Int. Symposium ELMAR, Zadar, 2006); I. Mustač, B. Zovko-Cihlar, M. Grgić (eds.), Croatian Society Electronics in Marine - ELMAR, Zadar and Department of Wireless Communications, Faculty of Electrical Engineering and Computing, University of Zagreb, Zadar, 2006, p. 107.
18. H. Mangine, K. Jakes, C. Noel, *Color Res. Appl.*, **30**, 288 (2005).
19. H. Xu, H. Yaguchi, s. Shioiri, *Opt. Rev.*, **8**, 487 (2001).
20. M. Melgosa, *Color Res. Appl.*, **25**, 49 (2000).
21. D. R. Pant, I. Farup, in: Riemannian Formulation of the CIEDE2000 Color Difference Formula (Proc. 18th CIC: Color Science and Engineering Systems, Technologies, and Applications, San Antonio, 2010), G. J. Woolfe, F. H. Imai, S. E. Grinnan (eds.), Society for Imaging Science and Technology, San Antonio, 2016, p.103
22. D. R. Pant, I. Farup, *Color Res. Appl.*, **37**, 429 (2012).
23. <http://www.astm.org/Standards/D2244>
24. <http://www.spectralcal.com/Documents/White%20Papers/Visual%20Color%20Comparison.pdf>
25. C. Gómez-Polo, M.P. Muñoz, M. C.L. Luengo, P. Vicente, P. Galindo, A.M.M. Casado, *J. Prosthet. Dent.*, **115**, 65 (2016)
26. B. Ortiz-Jaramillo, A. Kumcu, W. Philips, in: Evaluating color difference measures in images (Proc. 8th Int. Conf. on Qual. Multim. Exp., Lisbon,



- S. Dedijer et al.: Assessment of using ink - jet imprints in just noticeable color difference evaluation* 2016), F. Pereira (eds.), Instituto de Telecomunicações, Lisbon, 2016
27. D. Novaković, N. Kašiković, Ž. Zeljković, D. Agić, M. Gojo, *Tekstil*, **59**, 297 (2010)
28. N. Kašiković, D. Novaković, G. Vladić, M. Klančnik, *J. Graph. Eng. Des.*, **2**, 24 (2011)
29. R.R. Seghi, E.R. Hewlett, J. Kim, *J. Dent. Res.*, **68**, 1760 (1989).
30. [https://research.tableau.com/sites/default/files/2014/CIC\\_48\\_Stone\\_v3.pdf](https://research.tableau.com/sites/default/files/2014/CIC_48_Stone_v3.pdf)
31. W. Collins, A. Hass, K. Jeffery, A. Martin, R. Medeiros, S. Tomljanovic, *Graphic Design and Print Production Fundamentals*, <http://open.bccampus.ca>, 2015.
32. M. Ebner, *Color constancy*, Wiley, 2007.
33. N. Ohta, A. Robertson, *Colorimetry - fundamentals and applications*, Wiley and Sons, 2005.
34. <http://www.techkon.com/spectrodens-en.html>
35. <http://www.brucelindbloom.com/>
36. M. R. Luo, *Encyclopedia of Color Science and Technology: CIEDE2000, History, Use, and Performance*, Springer, 2015.
37. A. Sarkar, L. Blond, P. Le Callet, F. Autrusseau, P. Morvan, J. Stauder, in: *A color matching experiment using two displays: design considerations and pilot test results* (Proc. 5th CGIV, Joensuu, 2010), G. J. Woolfe, F. H. Imai, S. E. Grinnan (eds.), Society for Imaging Science and Technology, Joensuu, 2010, p.8
38. M. Wang, K. Xiao, S. Wuerger, TLV. Cheung, MR. Luo, in: *Measuring human skin colour* (Proc. 23th CIC: Color Science and Engineering Systems, Technologies, and Applications, Darmstadt, 2015), G. J. Woolfe, F. H. Imai, S. E. Grinnan (eds.), Society for Imaging Science and Technology, San Antonio, 2015, p.230.

## ОЦЕНКА И АНАЛИЗ НА СЛАБО ЗАБЕЛЕЖИМИ ЦВЕТОВИ РАЗЛИКИ ПРИ СТРУЕН ПЕЧАТ

С. Дедижер<sup>1</sup>, И. Томич<sup>1</sup>, И. Спиридонов<sup>2</sup>, Р. Боева<sup>2</sup>, И. Юрич<sup>1</sup>, Н. Милич<sup>1</sup>, С. Джурджевич<sup>1</sup>

<sup>1</sup> *Университет на Нови Сад, Технически факултет, Катедра по графично инженерство и дизайн, Нови Сад, Србија*

<sup>2</sup> *Химикотехнологичен и металургичен университет, Катедра „Целулоза, хартия и полиграфія“, Българија*

Постъпила на 30 ноември, 2016 г.; Приета на 18 май, 2017 г.

(Резюме)

В настоящата статия са изследвани възможностите за използване на дигитални струйни печатни системи за оценка на слабо различимите цветови разлики, които са особено важни от гледна точка на зрителния анализатор за получаване на вярна и коректна репродукция на тоновете и цветовете. При оценката на цветовите разлики спрямо зададен еталон се очаква да има коректно зададени референтни стойности още в процеса на предпечат и репродуциране. Равномерността и еднородността на получените печатни изображения е изключително важна и зависи от вида на печатната технология. В настоящия експеримент е направено изследване за дигиталния струен печат като най-качествен и перспективен. Избрани са пет дефинирани еталонни точки с вариране на светлотата и цветовия тон с цел постигане на диапазон от контролни скали и полета с цветови разлики започващи от 0,25 и достигащи до 1,5 единици. Цветовата разлика между 2 съседни полета има стойност 0,25. Използвана е 120 г/кв.м хартия и дигитална струйна система Epson Stylus Pro 7800. Използвани са две от формулите за изчисляване на цветовите разлики - CIELAB и MCDM. От направения анализ на резултатите е установено в кои от случаите се получават коректно зададените цветови разлики от 0,25 единици и репродукцията е вярна. Установено влиянието на светлотата и наситеността на изследваните полета върху получените резултати.

## Characterization of flexo and letterpress printing plate's surface roughness by indirect SEM image-based profilometry

S. Dedijer<sup>1</sup>, M. Pal\*<sup>1</sup>, R. Boeva<sup>2</sup>, I. Spiridonov<sup>2</sup>, T. Bozhkova<sup>2</sup>, V. Zorić<sup>1</sup>, Ž. Zeljković<sup>1</sup>

<sup>1</sup>University of Novi Sad, Faculty of Technical Sciences, Department of Graphic Engineering and Design, Novi Sad, Serbia

<sup>2</sup>University of Chemical Technology and Metallurgy, Department of Printing Arts, Pulp and Paper, Sofia, Bulgaria

Submitted November 30, 2016; Accepted February 3, 2017

In this paper indirect, image-based approach to the characterization of surface structure and roughness of flexographic and letterpress printing plates was investigated. Our previous research have shown that direct stylus profilometric method, when used in flexographic and letterpress printing plates surface roughness characterization, resulted in certain usage difficulties. Being a polymeric structure, surface of plates was scratched by stylus diamond tip and the measuring device has shown alt and slowdown in performance. The solution of such a problem lies in indirect and non-contact profilometry approach. According to literature findings SEM micrographs can be used for non-contact surface topography characterization, since they are excellent tool for visualization and qualitative description of surface topography. The indirect approach was based on use of Gwyddion software functions for analysis of SEM images and calculation of standard profilometric parameters. The results of the study have shown that it is possible to obtain profilometric parameters from analysis of SEM micrographs.

The study also involved analysis of influence of different micrograph magnification on final surface roughness results. It is shown that, with appropriately calibrated grayscale intensity distributions, optimal agreement with expected  $R_a$  value was achieved using indirect profilometric method. The statistical analysis showed that magnification level had no significant influence on obtained results of  $R_a$  parameter (based on p value of 0.05). Its influence was more expressed if the point of interest was shifted toward more specific roughness characteristics like peaks and valleys. Overall, the results indicated that proposed indirect image-based profilometry is a useful tool in the characterization of surface's topographies of flexo and letterpress printing plates.

**Key words:** surface roughness, direct and indirect profilometric method, flexo printing plates, letterpress printing plates

### INTRODUCTION

Surface roughness parameters of the materials are frequently used in many engineering industries as the parameters which clearly depict their surface structure and surface characteristics [1-3]. The surface properties of particular material are defined by its chemical composition and morphology, as well. But, since surface roughness and surface topography often greatly define its functional properties, such as mechanical function, wear, lubrication and appearance, they should not be underestimated and should be precisely determined and characterized [2,3]. In flexography and letterpress printing, printing plates are one of the most influencing on overall printing process. Surface topography of the printing plate highly influence ink transfer during printing process, hence final imprint quality [1,4-9]. Previous research has shown that surface roughness of the printing plate is even more significant than the surface energy when considering print quality [1,10].

There are many methods successfully proposed for the analysis and description of surface roughness and surface topography, where the obtained surface roughness parameters mostly depend upon characteristics of necessary instrument, its settings and data post processing [1,7,9,11]. Well known and widely used surface roughness analyzing methods are imaging (i.e. SEM - scanning electron microscopy or AFM - atomic force microscopy) and profilometric methods (i.e. MSP - mechanical stylus profilometry or non-contact laser profilometry) [1,2,7-9,12,13].

If the primary research goal is visualization of surface topography, then it is recommended to use one of the imaging methods. If the quantitative topographical information is needed, in terms of different surface roughness parameters, than it is more suitable to consider one of the various profilometric methods, contact or non-contact ones [2,14]. The advantage of non-contact ones is in avoiding the potential damages on the specimen's surface associated with the contacting stylus [14]. Namely, in the contact profilometry, the measuring

\*) To whom all correspondence should be sent:

E-mail: apro@uns.ac.rs

unit is equipped with sharp diamond tip mounted on a console which moves along a line on the specimen, measuring directly the surface irregularities, videlicet peaks and valleys. In order to achieve high precision in surface roughness characterization, it is advisable to record a several test lines [1,7,9,12,15]. The average uncertainty in the direct profilometric surface roughness parameters evaluation is found to be up to 6.5% [2].

Even if there is a wide range of parameters which can be used in surface roughness characterization, still the most commonly used ones are amplitude ISO roughness parameters (ISO 4287:1997 and ISO 12218:1997):  $R_a$  (average surface roughness),  $R_q$  ( $R_{ms}$ , root-mean-square deviation),  $R_{zDIN}$  (mean value of the single roughness depths  $Z_i$ ),  $R_p$  (leveling depth) and  $R_v$  (maximum depth of profile valley) [1,7,9,13,14,16-18]. In more specific applications, such as characterization of surfaces with asymmetric roughness, these parameters cannot successfully describe surface irregularity or complexity. Combined with the metrological limitation of used method, such is in stylus profilometry the limitation to reproduce smaller details [2], it is inevitable to resort to another approach in surface roughness characterization, like the concept of fractals. Estimation of surface roughness via fractals is based on SEM or AFM micrographs, and according to findings, it is well correlated to the profilometric parameters. More detailed description and advantages of this particular method are given in [2,13,15].

Another promising approach in surface roughness characterization is software-based extraction of profilometric parameters from SEM or AFM recordings of specimen surface. It seems to be a promising tool, gaining more attention with development of free and open source software for Scanning Probe Microscopy (SPM). This method is based on spatial grayscale intensity distributions

analysis of SEM/AFM micrographs and direct calculation of amplitude ISO roughness parameters. This approach was found to be utilized in surface roughness characterization of wide range of substrates: silicate glasses [19], graphene [20], ZnO thin films [21,22], CL optic surface [23], membranes [24], siliconized cellulosic substrates [25] as well as offset printing plates [2].

In this context, we aimed through this study to present a studious comparison of two basically different approaches to the surface roughness characterization of printing area on polymeric flexo and letterpress printing plates. The research encompassed detailed analysis of surface roughness parameters obtained from indirect SEM image-based profilometry against those obtained with the standard, direct stylus profilometric method. Through the evaluation of the performances and usefulness of indirect, image-based method in the characterization of surface topography of flexographic and letterpress printing plates, we have tried to set a stepping stone towards standardizing the image analysis technique in printing plate's surface roughness characterization.

## EXPERIMENTAL

### Materials

In this paper we have used three type of specimens: two conventional, solvent-washable photopolymer flexographic printing plates (Nyloflex FAH 2.84 mm and Nyloflex FAR 2.84 mm) and one water-washable photopolymer letterpress printing plate (Nyloprint WF-F 0.88). All specimens were prepared by UVA radiation exposure, in order to develop proper hardness of printing elements, followed by conventional developing process, solvent or water based, helped by brushing. [26,27]. The processing parameters used were in compliance with manufacturer's recommendation [28-30] and are given in Table 1.

**Table 1.** Plate processing parameters

Printing plates	Back exposure [s]	Main exposure [min]	Washout speed [mm/min]	Washout time [min] and temperature [°C]	Drying time [min]	Drying temperature [°C]	Post exposure UV-A [min]	Light finishing UV-C [min]
Plate I (FAH)	120	24	160	/	180	60	10	15
Plate II (FAR)	80	24	160	/	180	60	10	15
Plate III (WF-F)	/	4	/	4 (28)	15	60	3	/

Surface roughness analysis

As we have mentioned before, the main scope of this paper was in-depth analysis of possibility to use the indirect SEM image-based profilometry in surface roughness characterization of flexographic and letterpress printing plate.

Albeit, there are many roughness parameters which can be used for the surface characterization, in this investigation the four most common amplitude ISO roughness parameters have been used, namely  $R_a$ ,  $R_q$  ( $R_{ms}$ ),  $R_p$  and  $R_v$ . These parameters are compliant to the geometric product specification standards (ISO4287:1997 and ISO 12218:1997) and they are the most suitable for the aims of this study [7,12,16]. The  $R_a$  and  $R_q$  parameters are two amplitude-averaging quantities, which are the most widely used for the industrial applications, while  $R_p$  and  $R_v$  are two peak-valley parameters, optimal to quantify the importance of extreme peaks and valleys on the surface [14,16].

Thus, surface roughness parameters [1,7, 2,14,16-18] were as follows:

a)  $R_a$ , average surface roughness, defined as the average deviation of the surface profile from the mean line, geometrically represented as a total ruled area divided by the evaluation (sampling) length  $l$ , and analytically given with the expression:

$$R_a = \frac{1}{l} \int_0^l |y(x)| dx \quad (1)$$

b)  $R_q$  ( $R_{ms}$ ), root-mean-square deviation or the rms roughness, represents the square root of the arithmetic mean of the squares of profile deviation from mean within sampling length, mathematically described as:

$$R_q = \sqrt{\frac{1}{l} \int_0^l y^2(x) dx} \quad (2)$$

c)  $R_p$ , leveling depth, is the distance between the highest peak and the reference line (Fig. 1),

d)  $R_v$ , maximum depth of profile valley, measured below the reference line (Fig.1).

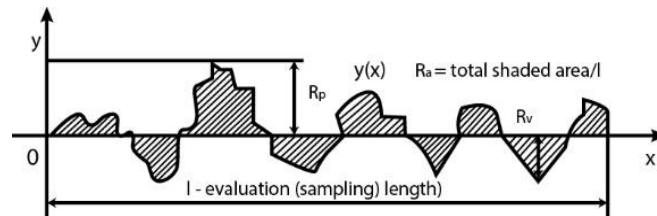


Figure 1. Surface roughness parameters

Direct profilometric surface roughness measurements. For the purpose of direct profilometric measurements, the portable surface roughness tester TR 200 (Micro Photonics, Inc.) was used. It is provided with a 2 mm radius diamond tip. The unit is compatible with ISO 4287, DIN 4768, ANSI B 46.1 and JIS B601 standards [31]. The device measurement parameters were as

presented in Table 2. Measurements of the roughness parameters were carried out on the solid printing area of each specimen by 18 different measuring lines, 9 per in two principal directions, printing and cross printing direction, in order to avoid possible variations caused by the measuring direction.

Table 2. Device measuring parameters

Filtering method	Measuring range	Resolution	Standard	Traversing speed	Cut-off
Gauss filtering	$\pm 20 \mu\text{m}$	$0.01 \mu\text{m}$	ISO 4287 standard	0.135mm/s	0.80 mm

Indirect surface roughness measurements

The indirect determination of the roughness parameters was done based on the analysis of the SEM micrographs in Gwyddion v.2.38 software. It is free and open source software for SPM data visualization and analysis, supported by the Czech Metrology Institute [32-35]. It is rather versatile software, which is not only limited to surface topography characterization. Gwyddion can be successfully used for particle size measurements [36-38], particle automatic counting and covering

area calculation [39,40] as well as line profiling and 3D imaging [32,34,35]. The SEM micrographs were captured on JEOL JSM 6460 LV Scanning Electron Microscope. Before imaging, the samples were gold-coated (15.0 nm thick and  $19.32 \text{ g/cm}^3$  dense layer of gold) in order to enable uniform electrical properties of the surface. For the experiment purposes, the specimens were imaged at three different tilt angles and four different magnification values. The SEM recording parameters are given in Table 3.

Table 3. SEM recording parameters

Working distance	Voltage	Tilt angle	Magnification
15 mm	20 kV	$0^\circ, \pm 5^\circ$	600x; 800x; 1000x; 1500x

Previous research [2, 24] has shown that the precision and certainty of image-based profilometry is highly dependable on several parameters including pixel size, number of pixels, working distance, rotational and tilt angles, but far the most is the intensity or height calibration [2]. The image-based profilometry relies on the analysis of the spatial distributions of intensities in grayscale SEM image whereas the bright areas on the image represent the elevated (peaks) while dark areas represent the depressed areas (valleys) of the imaged surface. Definition of surface roughness follows from the assumption that the intensity in a particular pixel is proportional to its elevation [2]. Thus, the scaling and calibration of SEM images with respect to their intensities are essential for the lowest result uncertainty.

For the scaling procedure in Gwyddion software, three user defined input values are needed: length (x), width (y) and depth (z) of an SEM micrograph, expressed in micrometers. Appropriate scaling of the x and y dimensions of an image is ensured according to the scaling mark on the image (usually a white line), of a known length in micrometers as well as in pixels. The determination of z-value (depth), the maximum roughness value which Gwyddion will calculate [24] is accomplished according to the procedure established for quantitative analysis of SEM images given in [2,41]. We have selected this particular methodology, since the alternative one proposed in [24] based on the effective penetration depth of

secondary electron beam needed to produce the SEM images, directly influence the large discrepancies between the surface roughness values measured experimentally using the AFM profilometer and those quantified using Gwyddion. Conversion of the grayscale intensity (0–255) to the corresponding height scale (z) was accomplished by using the images recorded at three different tilt angles (0°, ±5°), defining the corresponding coordinates of black and white points on the images through the image matrix, calculating the distances between those points and defining z factor as the median value of determined distances [2,41]. Since the black level in the images was not 0 but higher, we have used corrected calibration factor given by:

$$z_{cor} = z * 255 / (255 - x) \quad (3)$$

where  $x$  is the median value of black levels of points used in calculation.

On the appropriately scaled SEM micrographs, further analysis of surface roughness was conducted using software build-in function ISO tool. This tool provides a roughness analysis along the straight-line arbitrarily drawn by the means of cursor over the imported SEM micrograph. Roughness profile (Fig. 2), derived as a one-dimensional texture profile along the cursor line, compounds of high frequency/short wavelength component – roughness and low frequency/long wavelength component – waviness, videlicet form of the profile [2,35,42].

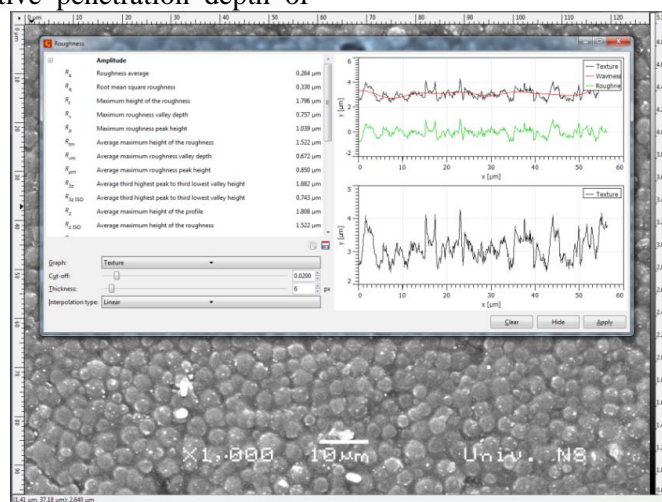


Figure 2. Roughness profile of a particular surface presented in Gwyddion.

Cut-off frequency, thickness value and interpolation type are supposed to be preselected. They are influencing factors on final surface roughness parameters values as well.

The cut-off frequency is specified in the units of the Nyquist frequency and is to be set according to ISO 4287 standard, at 1/5 scan length [2].

Thickness value is in direct proportion to the quantity of data used in the evaluation of one profile point – the higher the value the more neighboring data perpendicular to the profile direction is used in the evaluation [2,43].

Concerning interpolation type, linear interpolation was found as optimal [2,24,35] where

the interpolated value of the point was calculated from the three vertices of the Delaunay triangulation containing that point.

Input x and y values were 213.33  $\mu\text{m}$  and 160  $\mu\text{m}$ , 160  $\mu\text{m}$  and 120  $\mu\text{m}$ , 128  $\mu\text{m}$  and 96  $\mu\text{m}$ , 84.21  $\mu\text{m}$  and 63.16  $\mu\text{m}$  for micrographs imaged at magnification level of 600x, 800x, 1000x and 1500x, respectively. Input z value was 0.23  $\mu\text{m}$ , 0.12  $\mu\text{m}$  and 0.02  $\mu\text{m}$  for micrographs of Plate I, Plate II and Plate III, respectively.

We have used thickness value of 6 px and linear interpolation. Cut-off frequency was set to 0.04 for images magnified 600x and 800x, and 0.02 for images of 1000x and 1500x magnification value.

The profilometric parameters were determined from SEM images recorded at zero tilt, along eight straight horizontal and eight straight vertical lines, each 60  $\mu\text{m}$  long, avoiding apparent fallacies on image, resulting from residual dust or other impurities on specimen surface.

The values of each profilometric parameter used for the graph generation in Results and discussion section represent the average value obtained from the measurements with corresponding standard deviations.

#### RESULTS AND DISCUSSION

SEM micrographs presenting surface topographies of used printing plates taken with magnification of 1000x and corresponding 3D

surface plot, generated in Gwyddion via built-in function for converting 2D captured images into 3D maps of the surface, are given in Fig. 3 and Fig. 4, respectively.

As it was expected, plates' surface topography of flexography Plate I and Plate II is visually pretty similar and manifested as medium rough surface with clearly visible surface cracks. The white areas, as well as easily spotted larger bulges are residual impurities left behind after plates airbrush treatment. The surface of flexographic printing plate can be found to be still partially tacky even after UV-C light post treatment [26, 27] and consequently micro-impurities can easily remain on its surface. The letterpress printing plate (Plate III) has visually somewhat different surface topography with distinguished pores and grainy structure, therefore it was expected to have difference in surface roughness parameters values in comparison with the other two plates.

These imperfections or characteristic areas on the observed printing plates were allowing precise SEM imaging and later on a proper image calibration in Gwyddion. However they should be avoided during the image-based measuring process, since they can lead to misinterpretation of roughness parameters, due to false decrease or increase of the height parameters (shadow area of the impurity particle, the particle itself).

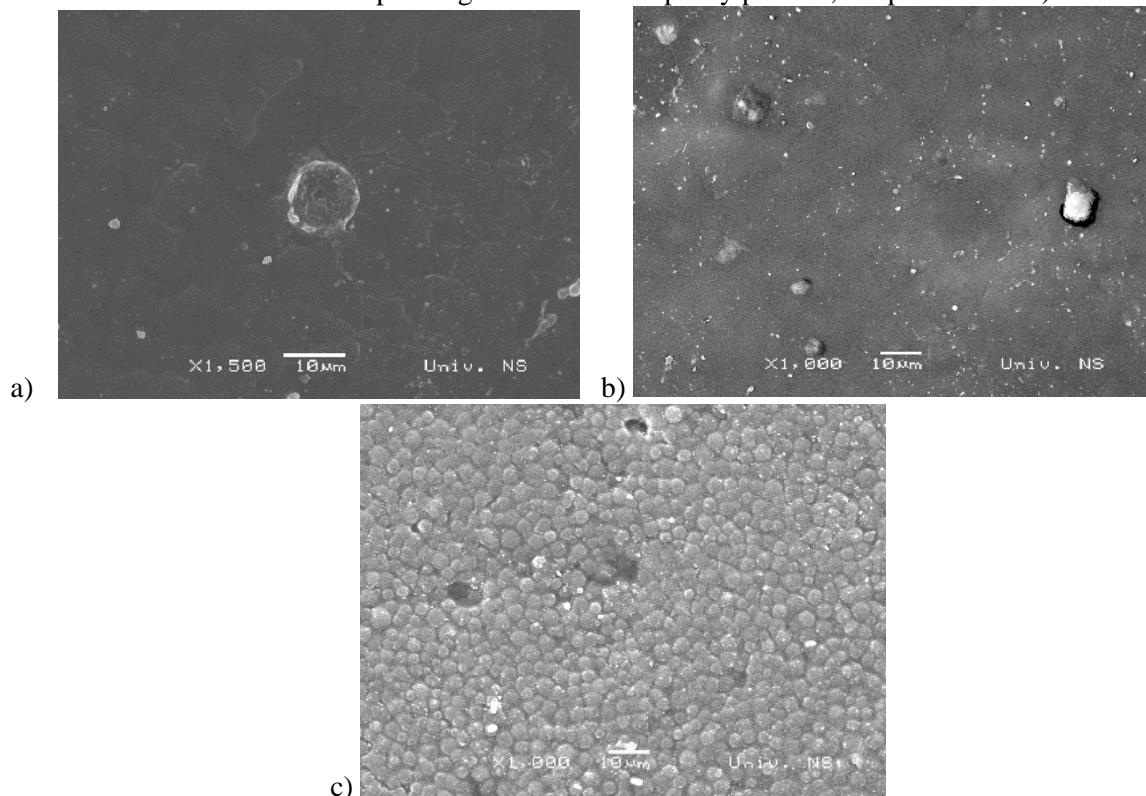


**Figure 3.** SEM images of printing plate' surface topography, magnification 1000x a) Plate I, b) Plate II, c) Plate III.

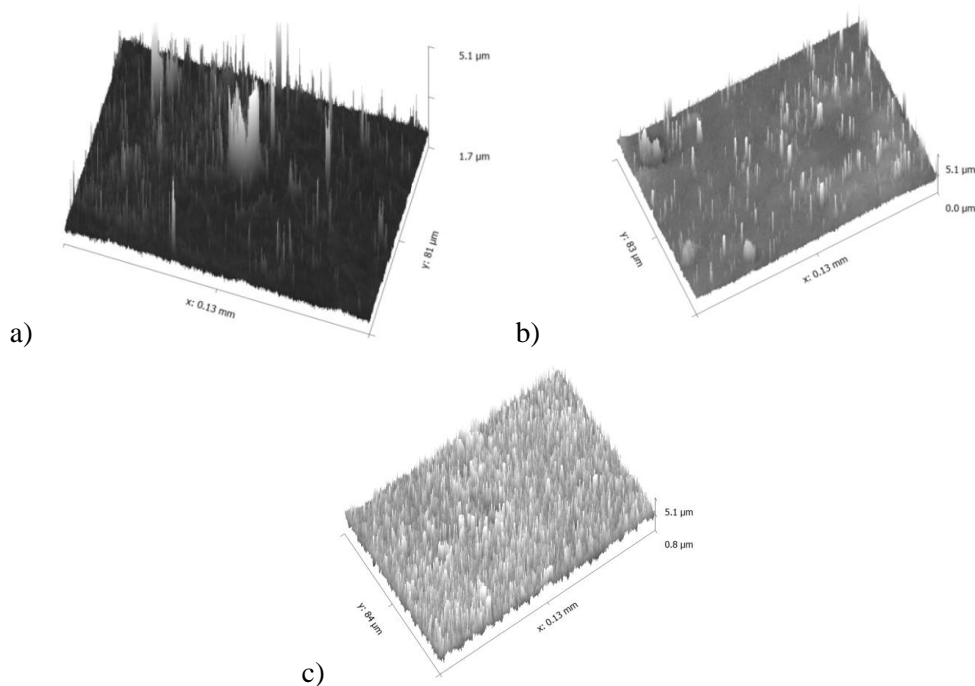


**Figure 4.** 3D surface plot of analyzed printing plates a) Plate I, b) Plate II, c) Plate III.

The 3D images (Fig. 4) represent three-dimensional reconstruction of surface topography providing better understanding of the surface imperfections and also displaying the visual comparison of flexographic and letterpress printing plates. The 3D surface plots, again, illustrate the similarity in a surface topography of two flexo plates, characterized by extremely high, sharp, needle-like pinnacles randomly distributed, which are actually mostly impurities on plate surface. Letterpress printing plate has more uniform structure with deeper valleys, not as sharp, but uniformly distributed peaks, without many extremes.

#### Direct determination of profilometric parameters

Direct profilometric measurements of three different polymeric printing plates resulted in a range of profilometric parameters' values (Fig. 5), providing a basis for a comparison with those obtained with indirect, image-based surface roughness analyzing method. The measured roughness profiles indicate a remarkable similarity in corresponding surface roughness parameters values for flexography printing plates, Plate I and Plate II. Letterpress printing plate, Plate III, has lower average surface roughness and lower maximum peak height but higher maximum valley depth. Decrease in overall surface roughness might be due to different polymeric composition as well as difference in applied processing parameters.

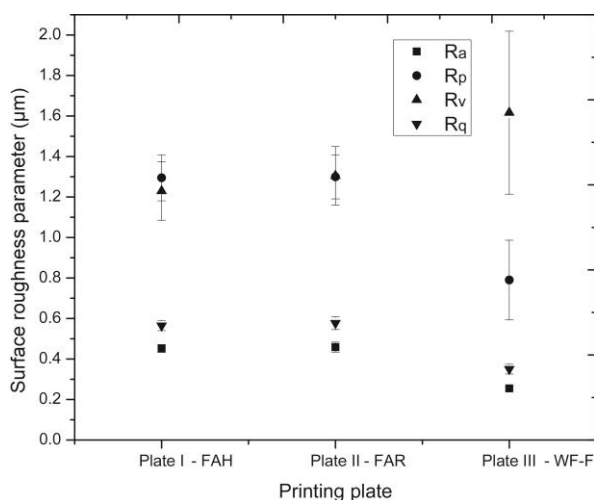


**Figure 5.** Surface roughness parameters of analyzed printing plates – direct profilometry.

During measuring process, we have found that the physical interaction of diamond tip of measuring device and polymeric surface of a printing plate can lead to scratching of the plate surface, interruption in measuring, consequently disable reading, prolong measuring process and potentially causing irretrievable damages on a plate surface.

Higher values of standard deviation can be observed for  $R_p$  and  $R_v$  roughness parameters (Fig. 5). But, it cannot be indicative of problems in the data or experiment disadvantages, considering the parameters nature as well as the fact that the coefficient of variation, as a measure of dispersion of data relative to the mean [44], is not greater than 30% [45].

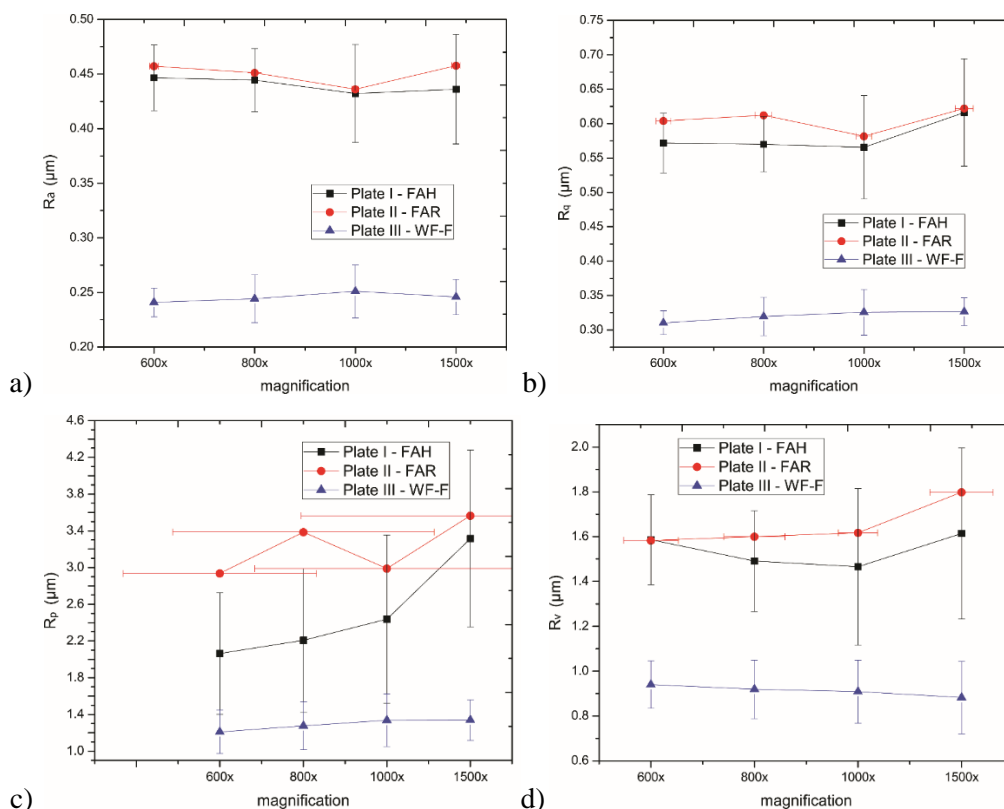


**Figure 6.** Surface roughness parameters of analyzed printing plates – indirect SEM image-based profilometric method  
a)  $R_a$ , b)  $R_q$ , c)  $R_p$ , d)  $R_v$

#### Indirect determination of profilometric parameters

Mean values, with corresponding standard deviation, of surface roughness parameters  $R_a$ ,  $R_q$ ,  $R_p$  and  $R_v$  obtained by indirect, SEM image – based methodology are presented in Fig. 6.

The profilometric parameters, derived from SEM images obtained at zero tilt angle, are discussed in terms of magnification level used during imaging. Graphs presented indicate that with higher magnification level overall surface roughness (reflected through  $R_a$  and  $R_q$  parameter) is slightly changing and exhibit the similar trend for examined specimens. The values of roughness parameters which reflect the deepest valley and highest peak on the surface are much more influenced by the used magnification level during imaging.

This was expected, since the SEM image-based profilometric method is relying on the analysis of

the spatial distribution of gray intensities of an image whereas the gray intensity of each pixel is directly proportional to depressed (valleys: darker pixel, lower grayscale value) or elevated (peaks: lighter pixel, higher grayscale value) areas. The magnification level directly influences the gray intensity value of each pixel which represent the lowest valley ( $R_v$ ) and highest peak ( $R_p$ ) value, but the overall surface roughness will be slightly changed.

It is also noticed that standard deviation as well as corresponding coefficient of variation are higher with higher magnification level, which might indicate significant influence of magnification level on the measuring precision and stability as well as result accuracy. This is especially expressed in case of  $R_p$  and  $R_v$  surface roughness parameter. But again, this can be also partially attributed to methodology itself, as it was already explained, as



well as to the nature of these parameters (representing the highest and deepest point of the profile along measuring line, thus expecting to exhibit a greater variety in comparison to averaged surface roughness).

#### *Statistical analysis of profilometric measurements*

Deeper analysis of surface topography using SEM micrographs of the different magnification levels and their comparison with the corresponding parameters obtained from the measurements with TR 200 was done using statistical technique for testing the equality of means: one – way analysis of variance (one-way ANOVA).

Preliminary analyses of normal distribution and homogeneity of variance have shown that assumption of the homogeneity, according to Levene's test for equality of variances, was violated. Since the literature findings suggest that analysis of variance is reasonably robust to violations of this assumption, if the size of groups is reasonably similar [46] (in our case they are the same size of 18), we have believed that conclusions derived from one-way ANOVA tests are legitimate. According to advisable procedure we have used Dunnett's T3 post hoc test and Welsh and Brown-Forsythe test.

A one-way between-groups analysis of variance indicated that there is no statistically significant difference at the  $p < 0.05$  level for  $R_a$  surface roughness parameter in case of all three printing plates. Practically, this means that mean values of  $R_a$  parameter resulting from different SEM micrographs captured at 4 different magnification levels as well as from TR 200 measuring device do not differ significantly.

The same result was found to be in case of  $R_q$  parameter and flexographic printing plates but not for the letterpress printing plate where statistically significant difference was found at the  $p < 0.05$  level. Posthoc comparisons using the Dunnett's T3 post hoc test indicated that the mean value obtained with TR significantly differ from mean values obtained from SEM micrographs but, importantly, they do not differ from each other, emphasizing once more the insignificant influence of magnification level on overall surface roughness derived using image-based profilometry.

However, the differences between the mean values of  $R_p$  parameter, both for flexographic as well as letterpress printing plate significantly differ at the  $p < 0.05$  level. Dunnett's T3 post hoc test revealed that significant difference is reported between the mean values derived from direct and indirect profilometry. Statistically significant

difference was also established between  $R_p$  values obtained from micrographs captured with magnification of 1500x and other three, lower ones. In the case of two flexo printing plates, the difference between mean values of  $R_p$  parameter obtained from micrographs with 1000x and 1500x magnification was also found to be significant.

The difference between mean values of  $R_v$  parameter are not found to be statistically different in the case of letterpress plate, but in the case of flexographic plates, however, these differences were only established between mean values of direct and indirect profilometry.

This analysis pointed out the greater influence of magnification level of SEM micrographs used for surface roughness analysis if the point of interest is shifted toward more specific roughness characteristics, like peaks and valleys, rather than overall, average roughness. Also, it is rather important to emphasize that the derived significant differences between the mean values of  $R_v$  and  $R_p$  parameters from direct and indirect profilometry are directly reflecting the nature of methodologies themselves. Increased values of  $R_p$  parameter derived from SEM micrographs in comparison to those obtained with stylus profilometer might be direct consequence of rather small pixel dimension (i.e. 100  $\mu\text{m}$  on image magnified 1000x) thus precise registration of the deepest pores, as well as insufficiently small size of a diamond tip of measuring device and thus disability to reproduce the smallest details. The increased values of  $R_v$  parameter might be found in influence of the local tilt angle of the surface structure on brightness level in the SEM micrograph, thus evaluation of the topographic contrast of SEM images [2].

## CONCLUSIONS

In this paper, we have analyzed indirect, image-based approach to the characterization of surface roughness of flexographic and letterpress printing plates against standard, profilometric method. In the analysis we have included SEM micrographs captured at four different magnification levels. The conclusions derived from the conducted research are as follows:

- The average surface roughness values obtained by the indirect profilometric method correspond to average surface roughness ( $R_a$ ) obtained by direct stylus profilometric method. The differences between average values were not found to be statistically different.
- Greater differences were found in case of roughness parameters which describe more specific roughness parameters – peaks and valleys. The

reasons might be found in the methodologies themselves, since determination of these parameters are directly influenced by physical resolution of the measuring device on one side and pixel dimension as well as pixel grayscale level on the other side.

- The higher influence of magnification level of SEM micrographs was established if the point of interest is shifted toward more specific roughness characteristics, rather than overall, average roughness.

- In terms of results consistency, repeatability, accuracy and dissipation, both methodological approaches have exhibited the same trend, where more consistent results were obtained for  $R_a$  and  $R_q$  parameter over the  $R_p$  and  $R_v$  parameter.

- Direct profilometric method has exhibited deficiencies in terms of leaving scratches on the plate surface, interruptions in measuring and prolongs measuring process.

Overall, the results have shown that proposed indirect image-based profilometry can serve as a flexible, valuable and useful tool in the characterization of the average surface roughness of flexo and letterpress printing plates.

**Acknowledgement.** *This work was supported by the Serbian Ministry of Science and Technological Development, Grant No.: 35027 "The development of software model for improvement of knowledge and production in graphic arts industry".*

#### REFERENCES

1. S. Dedijer, M. Apro, Z. Pavlovic, T. Cigula, B., Obrenovic, *Papiripar*, **56**, 24 (2012).
2. Ž. Pavlović, D. Risović, D. Novaković, *Surf. Interface Anal.*, **44**, 825 (2012).
3. Ž. Pavlović, T. Muck, A. Hladnik, I. Karlović, *Acta Polytech. Hung.*, **9**, 181 (2012).
4. S. Dedijer, D. Novaković, M. Pal, Ž. Pavlović, *J. Graph. Eng. Des.*, **3**, 12 (2012).
5. S. Hamblyn, D. Bould, M. F. J. Bohan, T. C. Claypole, D. T. Gethin, in: Consistency of flexographic plate making (Taga Proceedings of the 57th Annual Technical Conference, Toronto, 2005), Toronto, 2005, p. 17
6. J. Johnson, C. Andersson, M. Lestelius, L. Järnström, P. Rättö, P. E. Blohm, *Nord. Pulp Paper Res. J.* (2008).
7. S. Dedijer, D. Novaković, in: Determination of surface roughness factors of solid printing areas on different flexo printing plates (Proc. of the 5th International Symposium on Novelties in Graphics, Ljubljana, 2010), Ljubljana, 2010, p. 806
8. J. Choi, K. O Brate, US patent 2010/0173135 A1 (2010).
9. S. Dedijer S., M. Pal, in: Comparative study of line and dot elements reproduction on flexo printing plates using different film making technologies (Proc. of the 7th International Symposium on Graphics Engineering and Design, Novi Sad, 2014), D. Novaković (eds.), Novi Sad, 2014, p. 77
10. G. G. Barros, C. M. Fahlerantz, P. A. Johansson, *TAGA Journal*, **2**, 43 (2005).
11. P.J. Ramon-Torregrosa, M.A. Rodriguez-Valverde, A. Amirfazli, M.A. Cabrerizo-Vilchez, *Colloids and Surfaces A: Physicochem. Eng. Aspects*, **323**, 83 (2008).
12. N. Milić, S. Dedijer, M. Pal, Ž. Pavlović, in: The statistical analysis of processing conditions' influence on the surface roughness of flexo printing plate (Proc. of the 6th International Symposium on Graphics Engineering and Design, Novi Sad, 2012), D. Novaković (eds.), Novi Sad, 2012, p. 141
13. D. Risovic, S. Mahovic Poljacek, M. Gojo, *Appl. Surf. Sci.*, **255**, 4283 (2009).
14. <https://www.nist.gov/sites/default/files/documents/c-alibrations/osa-92.pdf>
15. D. Chappard, I. Degasne, G. Huré, E. Legrand, M. Audran, M.F. Baslé, *Biomaterials*, **24**, 1399 (2003).
16. S. Mahovic, *PhD Thesis*, UZ - FGA, Zagreb, 2007.
17. Ž. Pavlović, T. Cigula, D. Novaković, M. Apro, in: Influence of printing process on printing plate's surface characteristics (Proc. of the 1th International Joint conference on Environmental and Light Industry Technologies, Budapest, 2010), C. Horvath (eds.), 2010, p. 135
18. Ž. Pavlović, D. Novaković, S. Dedijer, M. Apro, *J. Graph. Eng. Des.*, **1**, 32 (2010).
19. T. Palomar, I. Llorente, *J. Non-Cryst. Solids*, **449**, 20 (2016).
20. Z. Li, R.J. Young, I. A. Kinloch, N. R. Wilson, A. J. Marsden, A. P. A. Raju, *Carbon*, **88**, 215 (2015).
21. C. Shang, Y. Thimont, A. Barnabé, L. Presmanes, I. Pasquet, P. Tailhades, *Appl. Surf. Sci.*, **344**, 242 (2015).
22. T.G. Carvalho, S.C. Fidelis, O.F. Lopes, C. Ribeiro, *Ceram. Int.*, **41**, 10587 (2015).
23. T.G.F. Souza, V.S.T. Ciminelli, N.D.S. Mohallem, *Mater. Charact.* **109**, 198 (2015).
24. F. A. AlMarzooqi, M. R. Bilad, B. Mansoor, H. A. Arafat, *J. Mater. Sci.* **51**, 2017 (2016).
25. P.S. Purohit, P. Somasundaran, *J. Colloid Interface Sci.*, **426**, 235 (2014).
26. FTA, *Flexography: Principles and Practices*, 5th Edition, 1999.
27. H. Kipphan, *Handbook of Print Media, Technologies and Production Methods*, Springer Verlag, 2001.
28. [http://www.flintgrp.com/en/documents/Printing-Plates/nyloflex/nyloflex\\_FAH\\_EN.pdf](http://www.flintgrp.com/en/documents/Printing-Plates/nyloflex/nyloflex_FAH_EN.pdf)
29. [http://www.flintgrp.com/en/documents/Printing-Plates/nyloflex/nyloflex\\_FAR\\_EN.pdf](http://www.flintgrp.com/en/documents/Printing-Plates/nyloflex/nyloflex_FAR_EN.pdf)
30. [http://www.flintgrp.com/en/documents/Printing-Plates/nyloprint/nyloprint\\_techn\\_data\\_EN.pdf](http://www.flintgrp.com/en/documents/Printing-Plates/nyloprint/nyloprint_techn_data_EN.pdf)
31. [https://www.dcu.ie/sites/default/files/mechanical\\_engineering/images/CV\\_TR-200e\\_Manual.pdf](https://www.dcu.ie/sites/default/files/mechanical_engineering/images/CV_TR-200e_Manual.pdf)

32. D. Necas, P. Klapetek, *Cent. Eur. J. Phys.*, **10**,181 (2012).
33. S. Talu, Hab. Thesis, TU - FME, Cluj-Napoca, 2014.
34. A. Kumar, S. Chauhan, M. Kumar, G. Gupta, *Appl. Surf. Sci.* **345**, 156 (2015).
35. <http://gwyddion.net/>
36. T. Zahoranova, T. Mori, P. Yan, K. Sevcikova, M. Vaclavu, V. Matolin, V. Nehasil, *Vacuum*, **144**, 86 (2015).
37. T.G.F. Souza, V.S.T. Ciminelli, N.D.S. Mohallem, *Mat. Charact.*, **109**, 198 (2015).
38. J. Kucerova, Z. Svobodova, P. Knotek, J. Palarcik, M. Vlcek, M. Kincl, D. Horak, J. Autebert, J.-L. Viovy, Z. Bilkova, *Mat. Sci. Eng. C-Mater.* **40**, 308 (2014).
39. J. B. Florindo, M. S. Sikora, E. C. Pereira, O. M. Bruno, *Physica A*, **391**,4909 (2012).
40. B. Liu, X. Wang, H. Du, J. Liu, S. Zheng, Y. Zhang, J. D. Miller, *Int. J. Miner. Process.* **151**, 33 (2016).
41. P. Podsiadlo, G. W. Stachowiak, *Wear*, **206**, 39 (1997).
42. T. R. Thomas, *Rough Surfaces*, Imperial College Press, 1999.
43. <http://lben.epfl.ch/files/content/sites/lben/files/users/179705/AFM%20module%20Handout.pdf>
44. P. Lovie, *Coefficient of Variation*, John Wiley & Sons, Ltd, 2005.
45. C. E. Brown, *Applied Multivariate Statistics in Geohydrology and Related Sciences*, Springer, 1998.
46. J. Pallant, *SPSS Survival Manual*, 5th edition, Open University Press, 2001.

## ИЗСЛЕДВАНЕ НА ПОВЪРХНОСТНИТЕ ХАРАКТЕРИСТИКИ НА ФЛЕКСО И ЛЕТЪРПРЕС ПЕЧАТНИ ФОРМИ ЧРЕЗ SEM БАЗИРАН АНАЛИЗ

С. Деджиер<sup>1</sup>, М. Пал\*<sup>1</sup>, Р. Боева<sup>2</sup>, И. Спиридонов<sup>2</sup>, Т. Божкова<sup>2</sup>, В. Зорич<sup>1</sup>, Ж. Желькович<sup>1</sup>

<sup>1</sup> Университет на Нови Сад, Технически факултет, Катедра по графично инженерство и дизайн, Сърбия

<sup>2</sup> Химикотехнологичен и металургичен университет, Катедра „Целулоза, хартия и полиграфия“, България

Постъпила на 30 ноември, 2016 г.; Приета за печат на 3 февруари, 2017 г.

(Резюме)

В това изследване е използван нов метод базиран на анализ на изображението за оценка на повърхностната структура и неравност (нееднородност) на флексо- и летърпрес печатни форми. Предишни наши изследвания показаха, че директното използване на профилографски метод за анализ на гореспоменатите печатни форми води до редица трудности като отклонения в точността на измерване и забавяне на работата при измерване на полимерни материали. Беше установено, че безконтактните методи като SEM, са особено подходящи за визуализация и количествено описание на повърхностната структура.

Индириктния метод базиран на Gwyddion софтуерни функции за анализ на SEM изображения и изчисляване на стандартни профилографски резултати. Резултатите показаха, че е възможно получаването и използването на данни от SEM анализа на подробни данни за повърхностната структура и профил на изследваните печатни форми.

Извършен е анализ на влиянието на различните увеличения върху анализа на повърхността. Статистическия анализ показа, че различните мащаби и увеличения, не оказват съществено влияние върху получените резултати за Ra.

Като заключение, резултатите показаха, че предложения и изследван индириктен метод за характеризиране на повърхността на печатните форми е особено полезен и достатъчен за точен анализ на интересуващите печатната индустрия параметри.

## The colorimetric and microscopic analysis of differences in colorfastness to rubbing process caused by different composition of screen print inks

G. Vladić<sup>1</sup>, N. Kašiković<sup>1\*</sup>, I. Spiridonov<sup>2</sup>, R. Boeva<sup>2</sup>, I. Pinčjer<sup>1</sup>, M. Stančić<sup>3</sup>

<sup>1</sup> *University of Novi Sad, Faculty of Technical Sciences, Department of Graphic Engineering and Design, Trg Dositeja Obradovića 6, 21 000 Novi Sad, Serbia*

<sup>2</sup> *University of Chemical Technology and Metallurgy, Department of Printing Arts, Pulp and Paper, Bulevard "Sveti Kliment Ohridski" 8, Sofia, Bulgaria*

<sup>3</sup> *University of Banja Luka, Faculty of Technology, Department of Graphic Engineering, Bulevar Vojvode Stepe Stepanovića 73, 78 000 Banja Luka, Bosnia and Herzegovina*

Submitted November 30, 2016; Accepted February 5, 2017

Screen printing is dominant method for textile printing. Wide variety of textile products and their applications demands printing inks of different composition also. These differences among inks cause different exploitation characteristics. Having in mind that textile products are printed mainly in order to achieve aesthetic effect it is important to maintain constant color values throughout the products exploitation period. Among other influencing factors rubbing process is very important factor in color changes of textile products during its exploitation period. This paper aims to conduct the colorimetric and microscopic analysis of colorfastness to rubbing process caused by different the composition of the oil and water based screen print inks. Beside the ink composition, mesh count variation of the screen was also used (43 and 100 threads/cm). 100% cotton based textile material was used as a substrate. Results indicate that oil based inks and lower mesh count of the screen can produce better colorfastness, thus resulting in longer lasting printed products.

**Keywords:** colorfastness, rubbing, screen printing, cotton

### 1. INTRODUCTION

Textile products are most often sold to the final consumer with specific pattern or illustration applied to their surface. This makes textile products more desirable and more valuable. Textile printing can be defined as a process of applying color to fabrics through localized dyeing, or as the art and science of decorating a fabric with a colorful pattern or design [1]. The usual methods for textile printing are flat-bed screen printing and rotary screen printing, these two processes make nearly 80% of the total textile printing output [2]. Recreant introduction of digital ink jet printing provides some advantages, such as simplicity and customization possibilities. Ink jet textile printing is predicted to become even more popular in the near future as production speeds increase. But still screen printing has a great advantage over digital printing in terms of cost when low-circulations are produced [3]. Ink jet printing demands at least three-pass printing on the pretreated cotton fabric in order to produce the same levels of color gamut, volume and saturation as screen prints [4]. A comparison of colorfastness properties between these two techniques proves the differences. Screen printed fabrics have better colorfastness to washing, perspiration and rubbing, while the ink-jet printed

fabrics have better colorfastness to dry-cleaning and light [5].

Cotton is one of the most important fibers in the textile industry and its considered to account for more than 70% of all printed substrates [6]. Coloration of cotton can be achieved with either dyes, by dyeing or printing, or with pigment by using a print paste/ink.. Printing with dyes and pigment inks use different chemical principles. Dye is soluble and has affinity to the fiber on which is applied, while pigments are not soluble and don't show affinity to the fiber [7]. Dye is fixed by the suitable bond formation between dye and fiber usually hydrogen bonds, Ionic or electrostatic bond and covalent bond. On the other hand pigments and fiber have no interaction the pigment is fixed by a binder. Binder is external agent, which provides linkage between pigment and fiber. Although, dyed printing produces soft tactile textures, pigment printing is more popular for textile printing. Factors contributing to the pigment printing popularity are easy application on a variety of fabrics, simple ink preparation recipes, and the absence of fixation after printing are the primary factors contributing to the popularity of the method.

Printing ink also known as printing paste contains pigments, thickeners, binders, and auxiliaries. Depending on the class of pigment used

\*Corresponding author.

E-mail address: [knemanja@uns.ac.rs](mailto:knemanja@uns.ac.rs) (N. Kašiković) © 2017 Bulgarian Academy of Sciences, Union of Chemists in Bulgaria

and style of printing employed ink composition can vary. Therefore, it is worthwhile investigating the colorfastness characteristics of fabric prints achieved through using flat-bed screen printing and pigment dispersion systems.

There are numerous influences on the printed fabric during exploitation such as friction, color adhesion after washing, thermal load, washing process, friction, UV light, etc. [1]. The fastness property of pigment ink on the fabric depends on the adhesion between binder film and fiber and also on the strength of the binder film. Stronger the adhesion and stronger the film better would be fastness property. The binder film can be abraded, thus giving the pigment inks poor rubbing fastness particularly wet rubbing fastness. Characteristics such as softness, elasticity, plasticity, solvent stability, fastness requirements and the production cost of the textile product will most significantly influence the choice of binders [8]. Thickness of the ink film is also a factor, it is dependent on the

pressure applied during the printing process and the mesh count. Fabric or mesh count is one of the most important parameters that influences printing quality. It corresponds to the number of threads/cm. Besides the mentioned printing process parameters, the pretreatment of the textile fabric can also influence the fastness properties [9]. The goal of this paper is to explore colorfastness to rubbing process caused by different composition of screen print inks and screen mesh used in the printing process.

## 2. EXPERIMENTAL

### 2.1. Materials

Printing substrate used for this experiment was 100% cotton material. Deposition of the ink was done using conventional screen printing technique. SEFAR Basic mesh was used, in two variations of screen printing mesh count, 43 threads/centimeter and 100 threads/centimeter, characteristics are shown in Table 1.

**Table 1.** Characteristics of screen printing mesh

Screen printing mesh: SEFAR BASIC									
Mesh number	Mesh count [1/cm]	Thread diameter nominal [μm]	Weave	Tolerance of mesh count [± n/cm]	Mesh opening [μm]	Open area [%]	Mesh thickness (woven) [μm]	Tolerance of mesh thickness [μm]	Theoretical ink volume [cm <sup>3</sup> /m <sup>2</sup> ]
100/25 5-40 PW	100	40	1:1	3.5	55	25	75	6	20
43/110- 80 PW	43	80	1:1	2.0	149	41	130	10	53

Synthetic rubber squeegee 75 shore, was used. Variation of binder type in ink composition and color was used. Specifically Oil based Sericol Texopaque Classic OP plastisol inks (black OP 001 and red OP 134), and water based Taxiscreen Aqua AJ (black WBA 70 and red WBA 22) print inks.

### 2.2. Method

Samples were printed using the variation of the mentioned screen printing mesh, ink composition and color according to ink manufacturer instructions, honoring recommended drying and fixating process. The patches of color were printed on to the substrate, and later cut in to peace's, adequate for testing, dimensions 10 x 10 mm.

Electronic crockmeter Testex textile instrument LTD. TF411, was used for testing colorfastness of textiles to dry rubbing. Rubbing head diameter 16 mm, vertical pressure 9 N, rubbing stroke 104 mm, according to the ISO 105x12/D02 standard. Colorimetric measurements and microscopic analysis of the samples were taken after printing and after 20, 40, 60, 80, and 100 rubbing repetitions.

Colorimetric of the samples were taken using HP200 colorimeter, D65 lighting, 2° standard observer and d/8 measuring geometry. Spectrophotometric measurements using X-Rite Eye One Pro, 0/45° measuring geometry. Microscopic imagery was made using Vitiny VT 300 microscope at 10x optical magnification and 1600 x 1200 px resolution.

After colorimetric measurements were taken, color differences were calculated according to the CIE 1976 ( $\Delta E_{ab}$ ) color difference formula shown below.

$$\Delta E_{ab} = [(\Delta L^*)^2 + (\Delta a^*)^2 + (\Delta b^*)^2]^{1/2}$$

where  $\Delta L^* = L_1 - L_2$ ,  $\Delta a^* = a_1 - a_2$ ,  $\Delta b^* = b_1 - b_2$ ,  $L$  is the brightness value,  $a$  is red/green color value,  $b$  is yellow/blue color value.

Color difference value can be translated to human perception reference as  $\Delta E_{ab} < 0.2$  - the difference is not perceivable,  $\Delta E_{ab}$  between 0.2 and 1 - the difference is noticeable,  $\Delta E_{ab}$  between 1 and 3 - the difference can be seen,  $\Delta E_{ab}$  between 3 and 6 - the difference is easy to see and  $\Delta E_{ab}$  over 6 - obvious color difference [10].

### 3. RESULTS AND DISCUSSION

Results of the color differences analysis between prints just after printing and after rubbing treatment repeated 20, 40, 60, 80 and 100 times are shown in figures 1 and 2 for samples printed using 100 thread/cm screen, black and red Oil based Sericol

Texopaque Classic OP plastisol ink and water based Taxiscreen Aqua AJ ink, respectively. Figures 3 and 4 show the results for samples printed using 43 thread/cm screen with same combination of ink.

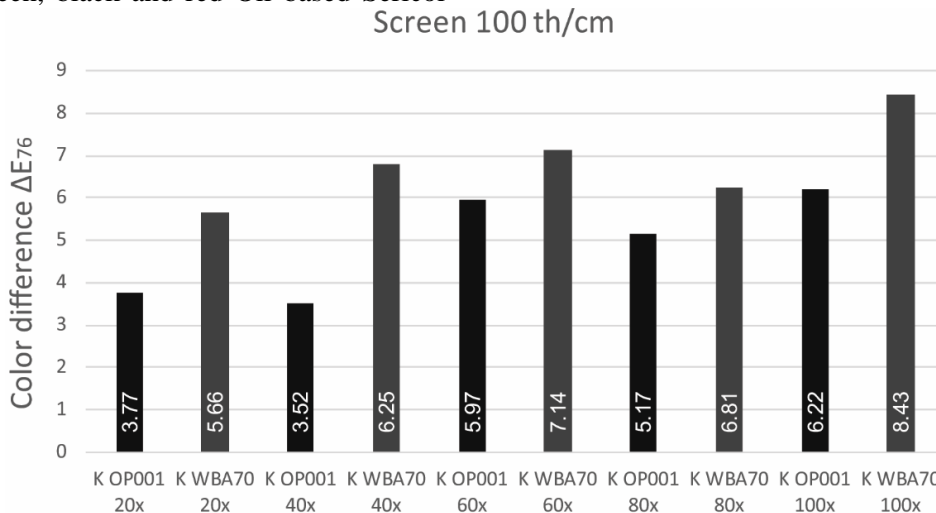


Fig. 1. Comparison of color differences between samples printed using 100 thread/cm screen, black Oil based Sericol Texopaque Classic OP plastisol ink (OP 001) and water based Taxiscreen Aqua AJ ink (WBA 70)

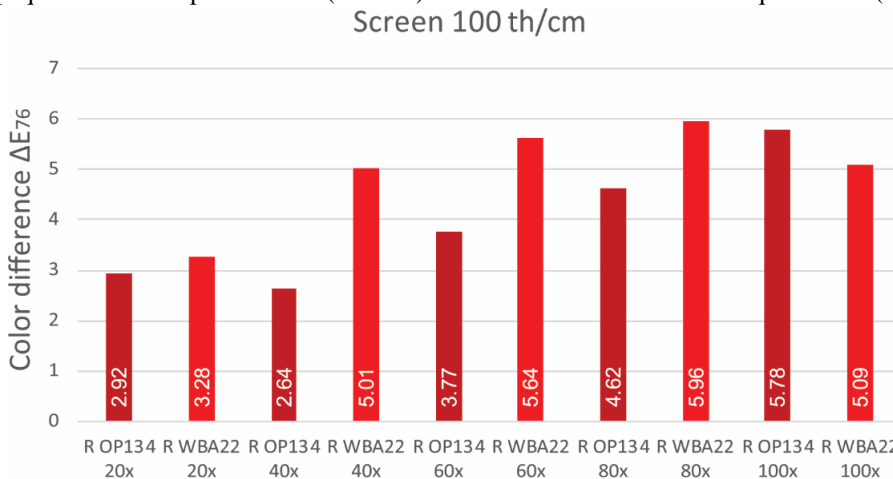


Fig. 2. Comparison of color differences between samples printed using 100 thread/cm screen, red Oil based Sericol Texopaque Classic OP plastisol ink (OP 134) and water based Taxiscreen Aqua AJ ink (WBA 22)

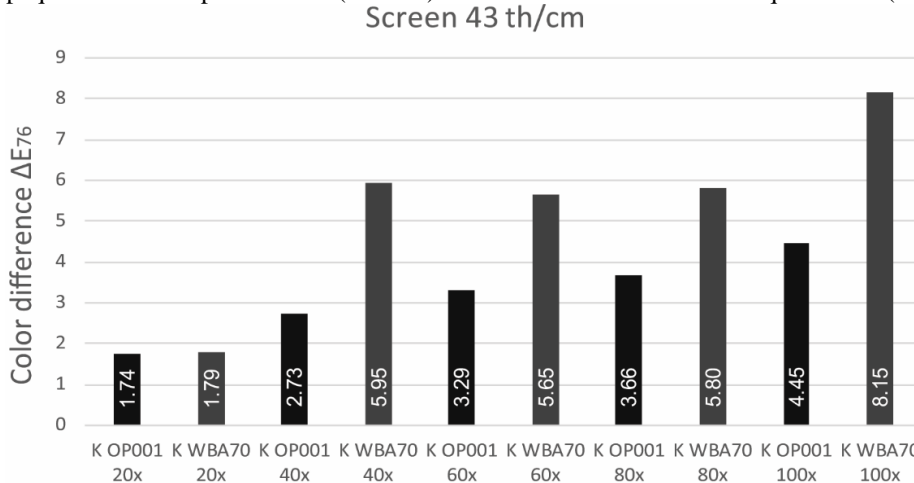
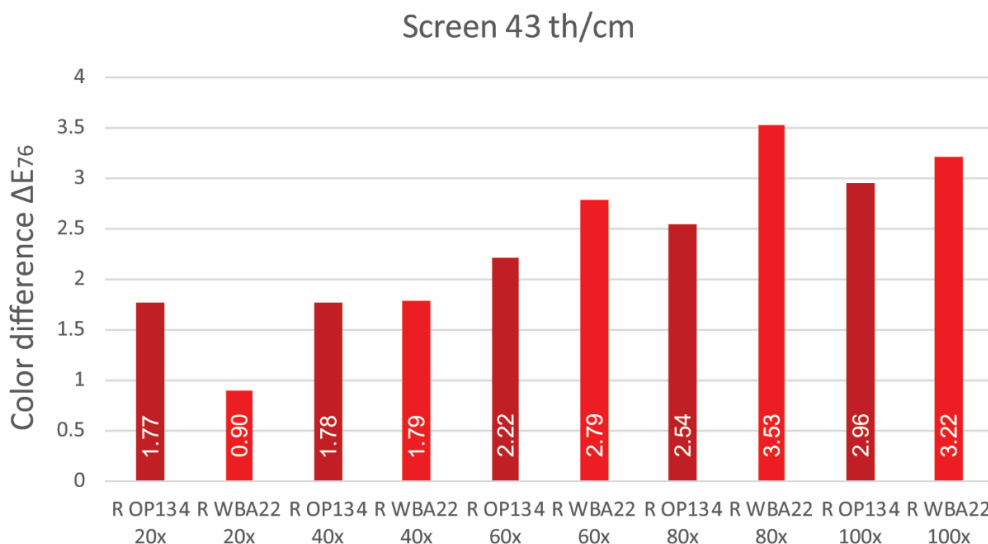


Fig. 3. Comparison of color differences between samples printed using 43 thread/cm screen, black Oil based Sericol Texopaque Classic OP plastisol ink (OP 001) and water based Taxiscreen Aqua AJ ink (WBA 70)



**Fig. 4.** Comparison of color differences between samples printed using 43 thread/cm screen, red Oil based *Sericol Texopaque Classic OP plastisol ink (OP 134)* and water based *Texiscreen Aqua AJ ink (WBA 22)*

Results show significant differences between sample printed with different inks and different print screen mesh count. In case of samples printed using print screen mesh count 100 threads/cm, which causes less ink to be deposited, color differences progress significantly as number of rubbing cycles increases. This is the case in both oil and water based inks. Water based ink shows more changes and some ink smearing. Black colored ink suffers greater changes than red one, presumably because black pigment is soot based.

The samples printed using print screen mesh count 43 threads/cm, with higher ink deposition have proven to be more resilient to the rubbing than

prints made using 100 threads/cm screen. Trends observed for oil and water based inks black and red colored inks are similar as in samples printed using print screen mesh count 100 threads/cm. Black colored ink suffers greater changes than red one.

Analysis of the spectral reflectance did not show significant changes caused by rubbing treatment. Changes in all samples whether printed using 100 threads/cm or 43 threads/cm screen, oil or water based inks, black or red, showed minimal changes in spectral reflectance. Figure 5 shows results for spectral reflection changes of samples printed using 45 threads/cm, oil based black ink.

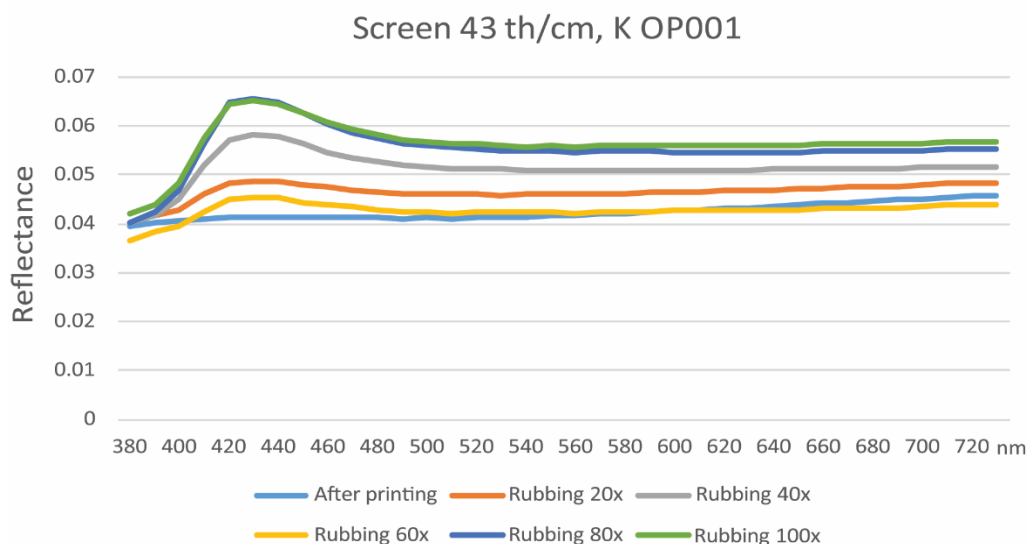


**Fig. 5.** Spectral curves for samples printed using 43 thread/cm screen, black Oil based *Sericol Texopaque Classic OP plastisol ink (OP 001)*

Changes in reflectance under 2% can be observed throughout the whole specter and only in 400 nm segment the changes are nearing the 4%, these small changes are typical for all samples. All

the samples showed good ink penetration into the material and sufficient deposition of ink which could not be rubbed off, exposing the substrate, even submitted to the hundred rubbing strokes.

#### 4. CONCLUSIONS

The study have been made to evaluate the rubbing/crocking fastness properties, of samples printed using screen printing technique varying 100 threads/cm and 43 threads/cm printing screen mesh count, oil and water based and black or red colored inks. Following conclusions are revealed from the results. It is observed that the color fastness to rubbing of printed fabric can be improved by the appropriate selection of ink, mainly having in mind its binder properties. The influence of right amount of ink deposited showed to be crucial for good color fatness to rubbing. Manipulation of the ink deposition is possible by variation of printing screen mesh characteristics. As there are far more mesh characteristics than just mesh count they could be investigated in future studies. Analysis of the spectral reflectance changes showed no significant effect, proving all the samples had good ink penetration into the material and sufficient deposition of ink which could not be rubbed off.

**Acknowledgments.** The research is supported by Ministry of education, science and technology development of Republic of Serbia, project number: 35027 „Development of software model for

scientific and production improvement in graphic industry“.

#### REFERENCES

1. M. Stančić, B. Ružičić, N. Kašiković, D. Grujić, D. Novaković, R. Milošević, *Revista materia*, **21**, 817 (2016).
2. I. Enomoto, H. Itoh, Y. Ikeda, Proc.7<sup>th</sup> International Conference on Radiation Curing, Kualalumpur, Malaysia, pp. 113-117 (1999).
3. M. Stančić, B. Ružičić, N. Kašiković, D. Novaković, R. Milošević, *J. Chem. Technol. Metall.*, **50**, 141 (2015).
4. S. Kiatkamjornwong, P. Putthimai, H. Noguchi, *Surface Coatings Int. Part B: Coatings Transactions*, **88**, B1, 25 (2005).
5. M. Mikuž, S. Š. Turk, P. F. Tavčer, *Coloration Technol., Society of Dyers and Colourists*, **126**, 249 (2010).
6. M. M. Molla, *Dyes and Pigments*, **74**, 371 (2007).
7. S. A. Bahmani, G.C. East I. Holme, *Coloration Technology*, **116**, 94 (2000).
8. G. Hammonds, “Pigment Printing Handbook,” 1st Edition, American Association of Textile Chemist and Colorists, Research Triangle Park, N.C, (1995).
9. N. Yaman, E. Ozdogan, N. Seventekin, *J. Eng. Fibers Fabrics*, **7**, 40 (2012).
10. K. Schläpfer, *Farbmetrik in der Grafischen Industrie (UGRA)*, St. Gallen, 2002.

## КОЛОРИМЕТРИЧЕН И МИКРОСКОПСКИ АНАЛИЗ НА УСТОЙЧИВОСТТА НА ЦВЕТОВЕТЕ НА РАЗЛИЧНИ СЪСТАВИ НА СИТОПЕЧАТНИ МАСТИЛА

Г. Владич<sup>1</sup>, Н. Кашикович<sup>1\*</sup>, И. Спиридонов<sup>2</sup>, Р. Боева<sup>2</sup>, И. Пинчиер<sup>1</sup>, М. Станчич<sup>3</sup>

<sup>1</sup> Университет на Нови Сад, Технически факултет, Катедра по графично инженерство и дизайн, Сърбия

<sup>3</sup> Химикотехнологичен и металургичен Университет, Катедра „Целулоза, хартия и Полиграфия“, Бългрия

<sup>2</sup> Университет на Баня Лука, Технически факултет, Катедра по графично инженерство, Босна и Херцеговина

Постъпила на 30 Ноември, 2016 г.; Приета за печат на 5 Февруари, 2017 г.

(Резюме)

Ситопечатната технология е основен метод за печат върху текстил. Широкото разнообразие на текстилни продукти и тяхното приложение изискват различни състави, а от тук и различни свойства на мастилата за сито печат.

Една от важните характеристики на текстилните продукти е тяхната естетическа стойност, като тук важно условие е максималното запазване на цветовите характеристики на сито печатното изображение през целия експлоатационен период.

Устойчивостта на изтриване и цветови промени по време на експлоатация на текстилните продукти е особено важна характеристика.

В настоящата разработка са направени изследвания на устойчивостта на изтриване на цветовете на различни като композиция сито мастила на водна и маслена основа при линиатури на мрежата от 43 до 100 нишки на см. Използван е 100% памучен материал. Резултатите показаха, че мастилата на маслена основа и с по-ниска линиатура дават по-добра устойчивост на изтриване на цветовете.



## Studies of technologies for exposing photopolymer plates in a controlled atmosphere and their application on a corrugated post print

T. Ts. Bozhkova\*, I. Spridonov, A. Ganchev, R.Boeva- Spridonova

*Department of Pulp, Paper and Printing Arts, University of Chemical Technology and Metallurgy, 8, Kl. Ohridsky Blvd, 1756 Sofia, Bulgaria*

Submitted November 30, 2016; Accepted May 18, 2017

The new technologies for digital plate making proved key to achieving a higher quality of corrugated post print.

The goal of the present study is to examine the technologies of exposing photopolymer plates in a controlled atmosphere and their optimal use in flexo corrugated post print.

The main problem with the flexo corrugated post-print is the flouting effect on the printed image. It is caused by the difference in the impression corresponding with the waves of corrugated board, forming an unstable dot gain in half tone areas of the image and generating visible stripes. The purpose of this study will be to determine whether and to what extent the technology for exposing photopolymer plates with flat top dot technologies in controlled atmosphere can reduce or eliminate these problems.

Keywords: flexo printing, photopolymer plates, corrugated

### INTRODUCTION

The flexographic technology is gaining ground as a major and dominant method for printing on packaging. This applies to both flexible packaging, where flexo successfully overtook gravure printing, as well as to printing of corrugated board, selfadhesive labels and others where it appears as an alternative to offset printing. This huge growth in flexo technology we see in recent years is due to the significant increase in printing quality. By analyzing consumer demand it turns out that their main requirement from flexo is improvement of printing quality, stricter quality control, optimization and standardization of the printing process. This is made possible mainly due to the new technologies, especially in pre-press, which proved key to achieving a higher quality printing. They include some key factors such as dot gain compensation, gradation in highlights, transition to zero, tonal range extension – features, on which designers and print buyers are focused [1].

Some studies report that about 90% of the packaging, produced from corrugated board printing, is full color and in most cases the used print technology was flexo post print. The printed images vary from one- and two-color printing (with just some basic information about the product and the company) to sophisticated four- to seven-color images. The advantages of direct post-print to pre-print on offset or flexo can be achieved only if the used flexo technics provide a significant quality improvement on the reproduction [1,2].

The increase in the quality requirements for

printing on corrugated cardboard also lead to the introduction of new technologies such as using thin photopolymer plates, while compensating the difference in thickness with compressible foam, which allowed for the digital plate making technology to enter this area.

A key issue for quality printing on corrugated board is the so called wash-board, or fluting, effect, which occurs when the flat halftone images are reproduced with stripes that follow the waves of the corrugated board.

In order to make such stripes less visible, the common practice is that the printed liner should be with a higher mass than what is required in order to achieve the desired strength for the corrugated board. The reason is that the liner with a higher mass does not bend as much around the waves of corrugated board, thus reducing the fluting effect on the printed images. However, this raises the cost of production.

### ANALYSIS OF THE PROBLEMS AND PREVIOUS STUDIES

In our previous studies we were testing and analyzing the main screening technologies, including stochastic and hybrid screening as well as HD Flexo technology. They were compared to regular screening with round and circular dot shape, and checking reproduction in highlights and shadows while printed in actual production conditions.

Other things analyzed were if and how much the used methods increase the ink transfer, gradation and tonal range, the maximum optical density and

\*) To whom all correspondence should be sent:

E-mail: t.bozhkova@uctm.edu

color intensity. To increase the ink transfer a different methods to increase roughness by generating microcells on the surface of printing elements were tested

The main problem with printing directly on the corrugated board is the image striping, which occurs due to the copying of the waves of the corrugated cardboard on the image. The effect of image striping when printing on corrugated board is caused by the different effective pressure of the screens in the different areas: depending on whether the waves confront or not, the resistance of the printed material is different, which generates the difference in the effective pressure during printing. The difference in the pressure results in a different dot gain and creates a visible striping on the image.

Therefore, the goal of this research is to study how the different technologies to expose photopolymer plates compare to the conventional plate making in the corrugated post print, in the areas of the floating effect, ink transfer, ink transfer and uniformity and to determine the optimal plate making method for flexo post print for corrugated cardboard in production conditions.

#### TERMS OF THE EXPERIMENT AND ANALYSIS OF RESULTS

##### *Used material*

- Kraftliner White 135g,
- Corrugated board B-Flute 125g
- The control test targets on DPC 155, produced via the conventional digital platemaking technology in the presence of oxygen.
- The control test targets on DPC 155, made via the DigiCorr technology, replacing the air with nitrogen with a nitrogen content of 99.999%.
- The control test target on DS2 45, made via a conventional digital plate making technology in the presence of oxygen.
- The control test target on DS2 45 made via the DigiFlow technology replacing air with inert environment with controlled atmosphere with 1.3%.oxygen

##### *Methods and equipment*

- Printing press BOBST Masterflex HD
- Printing press W&H Primaflex
- VIPflex 333 - tools to control the dot size on the black mask for laser engraving and screen dots.
- FLEX 3 PRO to control the profile of screen elements and microphotography.
- Spectrophotometer CyFOS Spectro 2000.
- Spektrodensitometer PRESTOdE.

All tests were made in accordance with the standard printing conditions used in the factories.

##### *Conducting the study and analyzing the results*

The application of various alternative technologies in a controlled atmosphere was studied against the conventional platemaking for corrugated board, including both direct printing on corrugated board, and pre-print on paper for producing corrugated boards.

The first part of the study was to determine whether and how the flat top dot technologies allow for reduction of the floating effect on corrugated post-print.

In order to determine this, test forms were printed, produced in a controlled atmosphere with a fixed presence of oxygen (DigiFlow), with complete absence of oxygen (DigiCorr), with lamination of a protective membrane on the engraved black mask (LUX), which prevents contact with air, as well as tests whose main exposure was obtained via powerful UV exposure with high intensity - UV LED sources (NExT and Full HD), which significantly limit the impact of oxygen due to the short time of impact were analyzed. To achieve optimal results, the test plates were produced by the developers of the technology and were compared to conventional digital platemaking obtained on the same photopolymer plates. Tests with the usage of laminated membrane and high intensity UV LED sources showed similar results with those using controlled quantity of oxygen (DigiFlow), which is why further researches and comparisons were focused on the DigiCorr and DigiFlow methods.

The test trials were printed on BOBST Masterflex HD in production conditions. The test elements included screen test targets with 32 lpcm screen ruling, oriented parallel and along the waves, as well as full color images. The printed targets were mounted together and the print test was made with both plates (produced via conventional and alternative technologies) to exclude the impact of the specific settings of the printing press on the tested technology. It should be emphasized that in the separate printing of the two plates alone, better results can be expected due to the possibility of setting the printing press according to a specific plate type, but this would lead to doubt whether the difference in results is not due to the printing conditions.

Tests were printed on corrugated boards with B, E and F waves, but for the comparative analysis, the fingerprints on the B waves were used, where the floating effect on the image is the most pronounced. For the purposes of the study, test targets printed on Kraftliner - white 135g and B-Flute 125g were analyzed. For corrugated board

with E and F waves, the difference was not so strongly visible.

The results presented below are for control test targets on DPC 155, made on conventional technology in the presence of oxygen and also with replacing air with an inert gas technology - DigiCorr. The main exposure of digital photopolymer plates was done in the absence of oxygen by replacing the air in the exposure chamber with an inert atmosphere (exposure under a nitrogen atmosphere with nitrogen content 99.999%). In this case, we notice the best

improvement in reducing flout effect and the best results were achieved, compared to the conventional plate making and other alternative methods. Comparison to technologies with a controlled amount of oxygen – DigiFlow, showed no improvement in this parameter.

The results of the direct post-printing on corrugated board using plates made with oxygen-free and conventional technologies are fundamentally different, which is well illustrated by photographs made for flat 30% halftone screens fields (Figure 1).

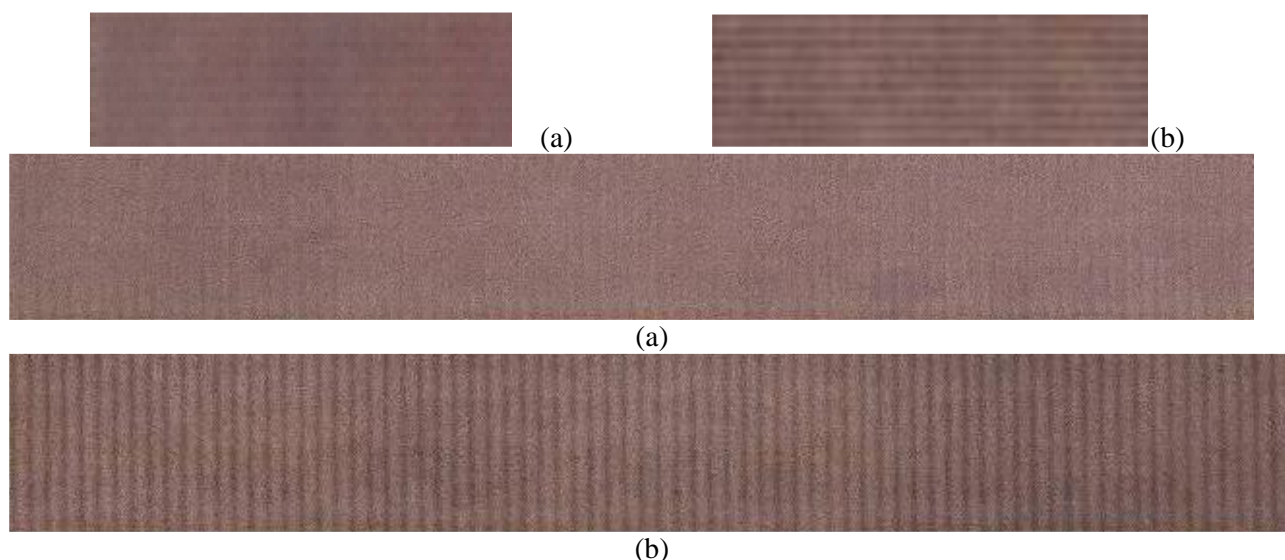


**Fig.1** Printing on corrugated board with test plates made in atmosphere in (a) absence of oxygen and (b) with conventional plate making in the presence of oxygen, when the image is parallel or along to the waves direction.

Studies have shown that the method of plate making has a significant influence on the flouting effect, most visible in flat screen tone, and depends on the gradation of the image. Images printed with plates, produced in the absence of oxygen, look better and are more uniform, and the flouting effect is drastically reduced. The lighter and darker lines on the printed images follow the waves of corrugated board and are the result of different impression during printing. The settings of impression when printing on corrugated board usually exceed the minimum necessary pressure to avoid irregularities in the surface of the print material, which in this case are significant. This is most noticeable in the flat halftone areas.

The printed control strips in the interval 0-100% were analyzed as well. It was found that flouting effect is visually most noticeably in the midtones, in the area of transition from positive to negative dots, where the dot bridging occurs. The impact of technology depends on other factors related to the dot gain, such as plate hardness, the presence of compression pad, ink viscosity and print

impression. Additionally the impact on the gradation in direct post-print on corrugated board was analyzed. It was found that a higher dot gain is typical for the plate making technology without oxygen.

To determine the reasons of these differences in the halftone printing, we compared the microphotography of screen elements reproduced in different technologies – analog, conventional digital and DigiCorr, and analyzed how the profiles of the screen elements will behave during printing in the print contact area and how it could reflect to the dot gain (Figure 2).

The microphotographs of screen elements reproduced in different plate making conditions show a difference in the slopes profile and give reason to assume that this could be the explanation for the different results in corrugated post-print. Comparing the top of the dots in the plates produced by the analog and conventional digital plate making and the ones reproduced in DigiCorr technology in an inert gas outlines the differences in these elements.

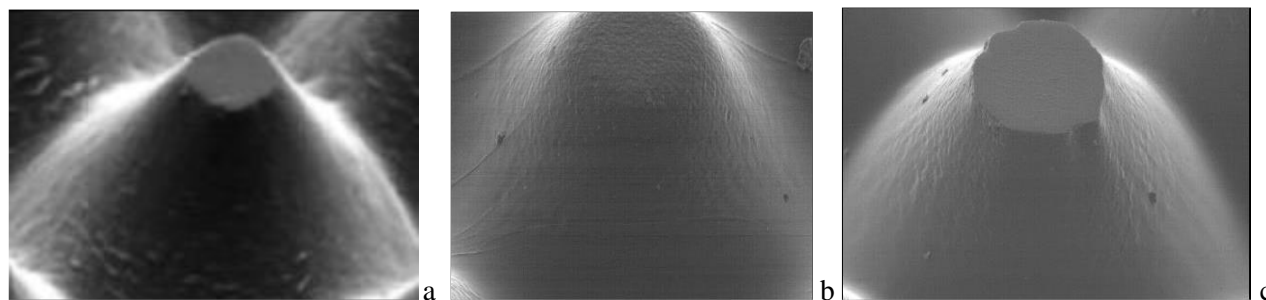


Fig. 2. (a) Analog; (b) Conventional digital; and (c) DigiCorr screen elements

The screen dots on the analog plate are with flat surface and gentle slopes. This will lead to a higher but stable dot gain during printing. This effect is well known since the old times when only analog plates were used.

For the conventional digital platemaking, screens are with the rounded dot profile and steeper slopes. The rounded dot shape makes the dot gain more sensitive to non-uniformity of the print pressure. The steeper dot shoulders of the rounded dots additionally make them more critical to the impression during printing. The combination of both factors makes the print contact of a rounded top dot and wavy corrugated board much more unstable. In the areas of reduced and increased print impression the dot gain will vary significantly.

Similar to the results with analog plates those obtained with platemaking technology when plates are exposed to a controlled atmosphere with oxygen 1.3% (technology DigiFlow). The pixel structure of the dots' edges is reduced and creates better round dot shape, but at the same time makes the slopes gentler and generates some rounded top dots, even if it is not as strongly visible as the standard digital platemaking. However, such technology doesn't show improvement of floating effect and we can't recommend it for corrugated post print.

The dots on the plates with DigiCorr platemaking technology are flat top dots with pixel structure of the edges, which in general will lead to a higher dot gain. But at the same time the top of the dot has a cylinder profile. Such profile of the dot makes the dot gain process less critical to the difference in the impression when printing directly on corrugated board and the printing of the smooth halftone areas is more visually more uniform.

The difference in the print results with plates produced through different platemaking methods is obvious. To find the origin of such effect the chemical process during the plate making was analyzed.

We believe that comparison of the various chemical reactions in the digital to analog

platemaking technology is the key for the explanation of the observed effect.

When analog plates are exposed, there is a limited quantity of oxygen (through vacuum). For digital platemaking it is the opposite – the whole main exposure is taking place in the presence of air, respectively with oxygen. Such chemical reaction during the main exposure is studied in details, when the digital plate-making technology based on engraved black mask was invented. It was found that due to the presence of oxygen during the main exposure, the polymerization process activated by the UV-A energy is accompanied by blocking part of the radicals of the photo-initiator by the oxygen in the air. The process is known as inhibition. Such inhibition of the radicals reduces the polymerization at the edges of the dots and makes them with steep slopes [1].

The shrinking of the dots and the steep slopes, resulting from the processes of inhibition during the main exposure, made such platemaking process preferable to flexo printing for tags and labels, as well as for flexible packaging. It was a revolution in the flexo print quality due to very fine highlights, the transitions to zero and the reduction of dot gain compared to analog plate making. But such plates required more precise printing process as they are more sensitive to the pressure during printing. At the same time the round top dot when is used for corrugated post print is making the floating effect more visible.

On the microphotographs of the plates made in an inert atmosphere the dot profile is very interesting – it is like a cylinder at the top part of the screen dot. The size of the cylindrical profile is only a few tens of microns, but has a significant impact on the printing properties of the plate in corrugated post print. This cylindrical profile can be explained by the presence of a very little amount of oxygen, which limits the inhibition to only a thin surface layer next to the screen and solids and forms the specific cylinder profile of the flat top dot. The use of plates, reproduced in almost

full absence of oxygen and the formation of an area with a vertical profile reduces the sensitivity of dot gain caused by uneven pressure characteristic in direct corrugated post print. This is strongly confirmed by tests and results.

The reduction of fluting effect is different depending on the type of cardboard, but improved print results were observed in the majority of printed products. The differences are obvious and



are illustrated on the print test photos Figure 1.

A comparison of microphotographs screen dots produced in oxygen and an inert environment showed strong reproduction of the pixel structure of the dot's edges. In the oxygen environment the pixel structure disappears due to the dot shrink while in an inert atmosphere the pixels are well copied (Figure 3a,b).

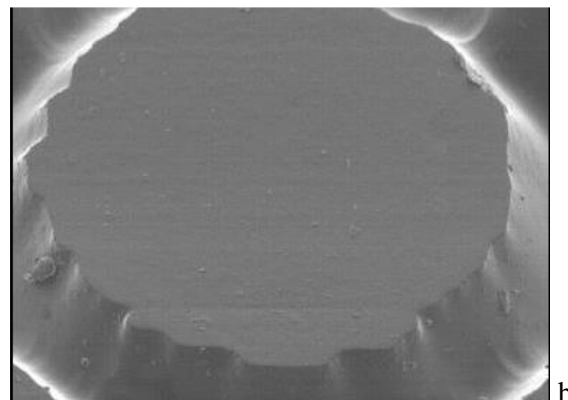


**Fig.3.** Microphotography of dots on plates made in a) oxygen environment, b) in an inert atmosphere.

The pixel structure of the dot edges leads us to the following conclusions. When the main exposure during platemaking is done in a controlled atmosphere at a complete absence of oxygen, then the processes of inhibition is very very limited. This is proven by the pixel structure of dot's edges. At the same time it can be seen, that some less pronounced smoothing of reproduced pixels exists. This fact is practically immaterial in terms of dot shape, but confirms the conclusions for the creation of the cylinder profile on the top of the dot.

At the same time, test trials confirmed that the pixel structure of the dot shape typical for all flat top dot technologies can be ignored for corrugated post print, since the used screen rulings are low, and because of the water-based inks used on the absorbent surface, the pixels structure at the dot edges disappear during printing.

#### *Test trials for corrugated pre-print*

The impact of platemaking technology in corrugated pre-print was also examined. In this case for the test trials was used a DS2 45 plate type, produced in conventional digital and in a controlled atmosphere with 1,3% oxygen - DigiFlow technology with and without structuring the black mask to generate roughness on the solids.

The test was printed on W&H Primaflex printing press on Kraftliner White 135g substrate.

Since it is printed directly on paper for corrugated board, the risk for floating effect is not applicable.

It was tested whether the surface structuring of solids with DigiFlow technology will improve the ink transfer. No increase of optical density or improvement of the ink uniformity was found, which can be explained by the fact that printing is performed with water-based inks on the absorbing substrate, so surface tension on smooth ink transfer had no negative impact unlike what was observed when printing on films. Based on this, further research on the impact of structuring was conducted.

Studies have shown that for the platemaking with flat top dot technologies, creates a dot gain of about 10% in the mid tones compared to conventional digital plate making without an increase of the optical ink density and ink uniformity as it was observed when printed on polymer films. This could be a problem and make the application of alternative platemaking methods unattractive for the corrugated pre-print. These results can be explained by the nature of the ink transfer for the water-based ink on absorbent substrates like paper.

## CONCLUSIONS

The results obtained in this experiment are important for practice.

The examined alternative technologies for platemaking for flexo printing for corrugated significantly improve the image quality by reducing floating effect at corrugated post print. This is most pronounced in the platemaking methods at complete absence of oxygen during the main

exposure.

The results when such technology was used show significantly reduced flouting effect especially in mid and flat tone area.

The effect is varying depending on the type of corrugated board used and is most pronounced in corrugated boards with B wave. In this case, improving the quality of image reproduction is most pronounced and the advantages of the technology are visible.

At the same time, we observe the typical for flat top dot technologies higher dot gain and higher tonal jump in the gradation at the transitional area, where the positive dot is converted to negative at mid and  $\frac{3}{4}$  tonal gradation.

The platemaking technology with controlled presence of 1.3% oxygen worsen rather than improve gradation due to printing with water-based inks on absorbent surfaces, which is why we do not

recommend the use of these technologies in the pre-print for corrugated.

#### REFERENCES

1. Dreher "Systems for flexo printing form production" Flexo & Gravure Global, 2, 2012.
2. V.Jansen, "Elegance on corrugated – the package for a brilliant print run" Flexo & Gravure Global, 1, 2001.
3. V.Jansen, R.Breakspreare, "High quality, cost effective printing with corrugated postprint" Flexo & Gravure Global, 4, 2003.
4. A.R.Kannurpatti, Dr.B.K.Taylor, "Polymerization Timing- The platemaker's role in controlling the process", FLEXO Nov. 2001, pp 12-16.
5. A.R.Kannurpatti, B.K.Taylor, "Polymerization Timing- The platemaker's role in controlling the process", FLEXO Nov. 2001, pp 12-16.

## ИЗСЛЕДВАНЕ НА ТЕХНОЛОГИИ ЗА ЕКСПОНИРАНЕ НА ФОТОПОЛИМЕРНИ ФОРМИ В КОНТРОЛИРАНА АТМОСФЕРА И ТЯХНОТО ПРИЛОЖЕНИЕ ПРИ ДИРЕКТЕН ПЕЧАТ ВЪРХУ ВЪЛНООБРАЗЕН КАРТОН

Т. Божкова\*, И. Спиридонов, А. Ганчев, Р. Боева-Спиридонов

*Катедра »Целулоза, хартия и полиграфия», Химико-технологичен и металургичен университет, бул.Кл.Охридски 8, 1756 София, България.*

Постъпила на 30 ноември 2016 г., приета на 18 май 2017 г.

(Резюме)

Новите технологии за изработване на цифрови форми за флексо печат се явяват ключови за постигането на високо качество при директния печат върху вълнообразен картон.

Целта на настоящата работа е да се изследват технологиите за експониране на фотополимерни печатни форми в контролирана атмосфера и да се определи тяхното оптимално използване при директния флексо печат върху опаковки от вълнообразен картон.

Основният проблем при директния флексо печат върху вълнообразен картон е ефекта на раиране на отпечатваното изображение. Това се дължи на разликата в натиска при печат, съответстващ на вълните на вълнообразния картон, което води до неравномерно нарастване на растерския тон в полутоновите участъци и пресъздаването на вълните на картоната върху изображението. Целта на това изследване е да се определи дали и до каква степен изработването на фотополимерни печатни форми с технологии с плоска точка в контролирана атмосфера може да намали или да премахне този проблем.

## Improvement of physical-mechanical and optical properties of the packaging production through coating with aqueous polymer dispersions in accordance with the environmental protection requirements

T. Ts. Bozhkova<sup>1\*</sup>, R. Boeva<sup>1</sup>, I. T. Spridonov<sup>1</sup>, J. Sapkota<sup>2</sup>, Y. V. Nedelchev<sup>1</sup>, N. Kašiković<sup>3</sup>, S. Dedijer<sup>3</sup>, M. Pal<sup>3</sup>

<sup>1</sup>University of Chemical Technology and Metallurgy, 8 Kl. Ohridski, 1756 Sofia, Bulgaria

<sup>2</sup>Department of Polymer Engineering and Science, Montanuniversität Leoben, 8700 Leoben, Austria

<sup>3</sup>Department of Graphic Engineering and Design, Novi Sad, Serbia, University of Novi Sad

Submitted November 30, 2016; Accepted May 18, 2017

The nowadays growing demands toward sustainable development and environmental protection led to increased interest in bio-degradable materials from renewable sources. Aqueous polymer dispersions are used for surface coating of paper and cardboard in the packaging industry in order to improve the physical-mechanical and optical properties of the production. This article summarizes the main parameters in the preparation, processing and utilization of aqueous dispersions based on synthetic and bio-degradable polymers for coatings in packaging paperboard production. It shows that the bio-sourced aqueous coating have acceptable physical-mechanical properties, but lower gloss than the conventional water based coatings.

**Key words:** bio-degradable polymers, renewable resources, packaging, coating

### INTRODUCTION

The aqueous coatings (also called dispersion coatings) are water-based coatings that are used for protection of the printed material from abrasion, scratches, and finger prints. They provide fast further processing and enhance the optical and physical-mechanical properties of the printing production. The dispersion coatings attract attention to the end-product with gloss, matt, gold, silver and even smell effects and add some valuable functions – barrier, anti-migration, anti-slippery, anti-bacterial etc. [2]

Water-based coatings dry physically by means of the absorption of the coating into the substrate and the evaporation of water (Figure 1). This drying is achieved through hot air and infrared. With the drying, water is extracted from the coating. The

polymer particles approach each other and form the coating film. Water-based coatings, as a result of their many advantages, have become the leading technology in the printing industry: environmentally friendly, odorless, tasteless, no yellowing and reduction of spray powder. [1] Water-based coatings contents 25-35% solids, 60-70% water and 5% additives. Their main ingredients are:

- Dispersions of acrylate and styrene acrylate polymers
- Alkaline-neutralized resins dissolved in water
- Wax dispersions (polyethylene waxes) or/and silicones for scuff and rub resistance
- Film-forming agents
- Additives to enhance certain properties

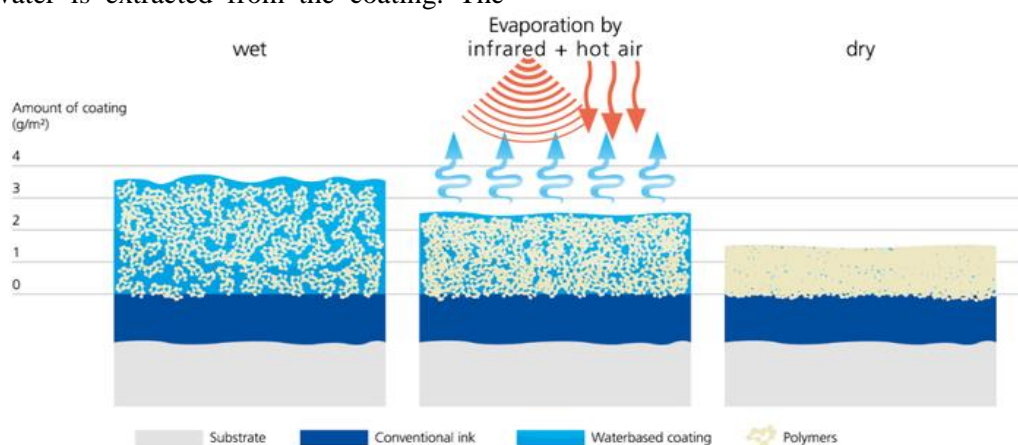


Figure 1. Drying method of water-based coatings [2].

\*) To whom all correspondence should be sent:

E-mail: : t.bozhkova@uctm.edu

© 2017 Bulgarian Academy of Sciences, Union of Chemists in Bulgaria

### Polymer dispersions

Polymer dispersions are stabilized water-borne emulsion polymers with colloidal particles in water. Many polymers are not amendable to emulsion polymerization. In such cases the dispersion must be prepared by dispersing the water insoluble performed polymer into an aqueous phase. These “pseudo dispersions” contain often emulsifying agent, which prevents or slows down agglomeration settling. Polymer dispersions are formulated into coatings with fillers, waxes and additives. All the additives are used to improve barrier properties, runability, decrease blocking and ensure easy post-processing.

As the polymer morphology affects the film formation, the goal is to keep polymer particles amorphous in dispersions. The methods for preparing pseudo dispersions can be divided into two groups: VOC based and thermo/mechanical. [3]

### Biopolymers and bio-coatings

In recent years an increasing interest is observed in development of eco-friendly materials.

Oil-based polymers are slowly being replaced by such from renewable resources. Biodegradability and compostability are playing very important role for environmental sustainability. Some biodegradable polymers possess excellent mechanical properties, thermal and UV resistance, however production capacity, processing challenges, adhesion, barrier properties and the price are not yet on a sufficient level for the demands of the packaging and printing industries. Biopolymer dispersions find use in various applications, such as adhesives, inks, coatings, etc. From the Biopolymers family only few cover the performance requirements for applying on printing products. [2]

According to European directives and EN 13432 standard, the key requirements for biodegradable products are:

- Chemical composition: the standard sets limits for volatile matter, heavy metals (Cu, Zn, Ni, Cd, Pb, Hg, Cr, Mo, Se, As) and fluorine

Biodegradation: chemical breakdown of materials into CO<sub>2</sub>, water and minerals. Pursuant to the standard at least 90% of the materials have to be broken down by biological action within 6 months.

**Table 1.** Composition in traditional water-based coatings vs coatings based on renewable resources

Traditional waterbased coatings	Coatings based on renewable resources
Acrylate / styrol acrylate dispersions	Natural resins
Polyethylene waxes	Natural waxes
Wetting agents and additives	Wetting agents and additives
Water	Water

- Disintegration: the physical decomposition of a product into tiny pieces. After 12 weeks at least 90% of the product should be able to pass through a 2x2 mm. mesh
- Quality of the final compost and ecotoxicity: the quality of the compost should not decline as a result of the added material. [4]

The goal of this study is to compare 2 types of water-based coatings, their properties and characteristics applied with different screen rollers – the reference coating, based on synthetic polymer – and the tested coating, based on biopolymer.

## EXPERIMENTAL

### Materials

Table 1 shows the comparison in composition between conventional water-based coating and coatings based on renewable resources. As a reference has been used conventional acrylic water-based multipurpose, gloss coating with fast drying speed and high wet block resistance – ACTEGA Terra Wet GlossG9/535 (45 sec viscosity). The tested coating was water-based gloss coating, based on renewable resources - ACTEGA Terra Green Gloss G5/200 (45 sec viscosity).



**Table 2.** Physical properties of the materials used.

Physical Properties:	ACTEGA Terra Wet Gloss G9/535 (45 sec)	ACTEGA Terra Green Gloss G5/200 (45 sec)
Boiling temperature / boiling range	( 1013 hPa ) > 100 °C	( 1013 hPa ) > 100 °C
Density :	20 °C - 1,04 g/cm	20 °C - 1,04 g/cm
pH value :	7 - 9,5	7 - 9,5
Solid content:	25 – 45 Wt %	25 – 45 Wt %
Max.VOCcon (EC):	2,322 Wt%	0,278 Wt %

**Table 3.** Composition and characterization of the materials used.

Ingredients:	ACTEGA Terra Wet GlossG9/535 (45 sec)	ACTEGA Terra Green Gloss G5/200 (45 sec)
Styrene Acrylic Resin and/or Emulsion	40- 50%	30-50% (renewable resins)
Polyethylene/wax	1-10%	1-10%
Silicon Defoamer	0-1%	0-1%
Wetting agent/sulfosuccinate	5-10%	1-5%
Water	20-40%	40-50%
Propylene glycol	1-5%	-

*Characteristics of the materials*

Resins and waxes used for Terra Green are amply available and are extracted from the sources that are not competing with the food chain. No plants, trees or animals are eliminated for the waxes and resins used in TerraGreen. Comparable to caoutchouc, the used materials are harvested and

the biomass remains existing. The resins and waxes used grow naturally in the wild or they are harvested at traditionally existing and sustainably cultivated plantations in Europe, South America and Asia. TerraGreen has no negative impact on existing eco systems and is certified to EN 13432. [1]

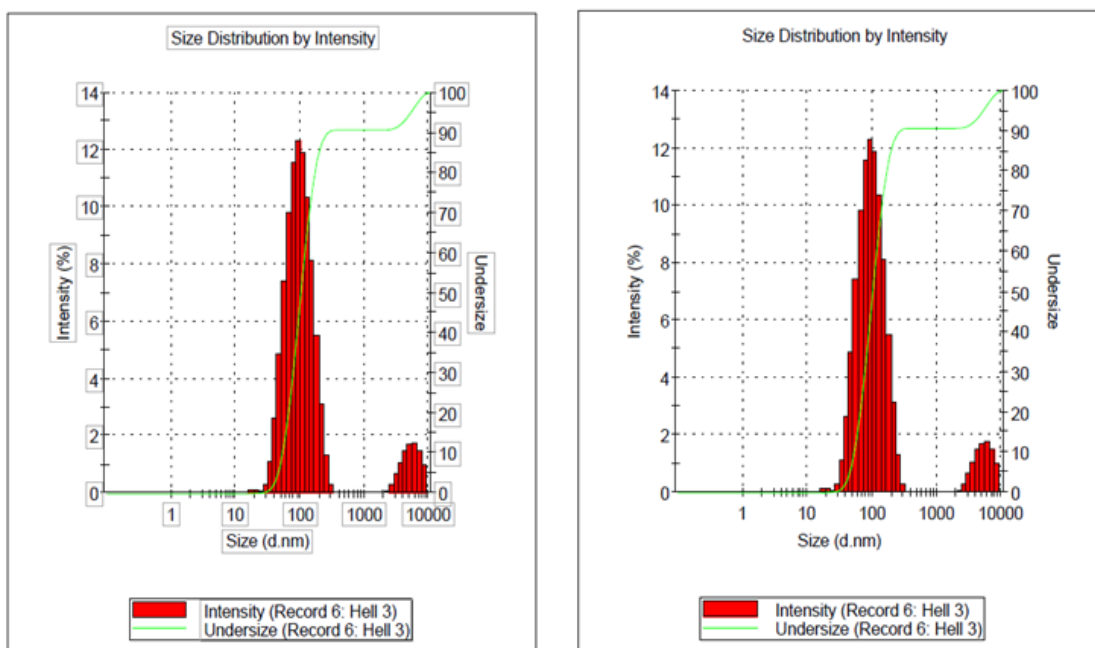


**Figure 2.** Comparison of particles size distributions as a function of intensity.

Table 2 and Table 3 show the properties and characteristic contents of both coatings. From table 2 we can obtain information about the physical properties of both coatings. The only difference is

in Volatile Organic Compounds content, which is much lower in the BIO-Coating. Table 3 shows the detailed information about the ingredients in both coating types. The water content in the BIO-

Coating exceeds the water content in the acrylic one by max. 10%, which could influence the drying and runability. Figure 2 shows the size distribution report with identical peak intensities in both coatings.

*Methods*

Both coatings were applied on offset printing press HEIDELBERG CD74 4+L, under same conditions and initial parameters:

- Material – Cardboard – LWC 170 g/m<sup>2</sup>
- Ceramic Anilox rollers:
  - Zecher, 160L/cm, 60 °, 7,5 cm<sup>3</sup>/m<sup>2</sup> – Wet application – 2,5 g/m<sup>2</sup>
  - Zecher, 100L/cm, 60 °, 13 cm<sup>3</sup>/m<sup>2</sup> - Wet application – 3,8 g/m<sup>2</sup>
  - Zecher, 80L/cm, 60 °, 15 cm<sup>3</sup>/m<sup>2</sup> - Wet application – 5,0 g/m<sup>2</sup>
  - Zecher, 60L/cm, 60 °, 17 cm<sup>3</sup>/m<sup>2</sup> - Wet application – 6,0 g/m<sup>2</sup>

- The wet application amount of varnish is about 1/3 to 1/4 of the theoretical cell volume of the screen roller.
- IR Lamps power – 15 %, hot air – 100 %
- Temperature in stack – 35° C
- Equal press speed – 8 000 sheets/hour

**RESULTS AND DISCUSSIONS**

*Gloss after coating*

Figure 3 shows the gloss changes after application of the coatings with the different anilox rollers. The BIO-coating shows lower gloss in comparison to the conventional one with an 8-10 gloss units (GU) in all applied quantities.

*Adhesion test*

A 5 c. piece of tape TESA Film, 57341 Beiersdorf was applied on the top of the coated materials. The tape was removed by hand from the printed surface. The adhesion of the coating was determined by the amount of coating that was removed when the tape is peeled off. The results are summarized in Table 4.

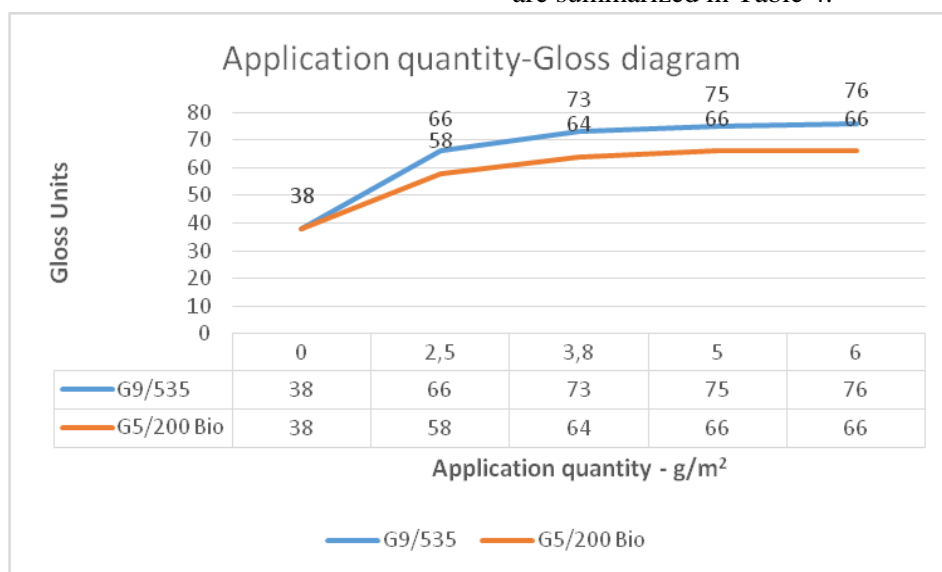


**Figure 3.** Application quantity-Gloss diagram.

**Table 4.** Adhesion test results.

Coating	2,5 g/m <sup>2</sup>	3,8 g/m <sup>2</sup>	5 g/m <sup>2</sup>	6 g/m <sup>2</sup>
G9/535	Average	Good	Good	Good
G5/200 - BIO	Average	Good	Good	Good

There was no performance difference between both coatings on the adhesion test, which indicates good adhesion of the BIO-Coating.

#### *Scratch resistance*

- Industry standard for most application is the scratch test - if the coating/ink is not removed by your fingernail, it is considered to exhibit acceptable adhesion and scratch resistance. If the surface is damaged, it indicates inadequate curing or an excessively soft ink/coating film.

All samples showed good scratch resistance. There was no difference between reference and tested coatings on the scratch resistance test.

I. Rub resistance - Rub resistance describes the ability of printed paperboard to withstand marking, scuffing or smudging during handling in conversion, packaging, distribution and use. Poor rub resistance is apparent if, after normal handling and use, the printed or varnished paperboard surface is marked, scuffed or smudged. An extremely demanding environment or special end use may require extra protection against rubbing. This protection might be provided by such treatments as extrusion coating or lamination. Laboratory rub testing of dry print can be done using an optional number of rubs and pressure. The results are assessed visually against standards. A block is either moved back and forth over an area of printed sample or moved by rotary motion in an orbital path over the print depending on the instrument used. A record is made of the number of

rubs e.g. 50 or 100 and rub pressure 20 N. The degree of surface rub is subjectively compared to reference standards. 4 tests were performed – 50, 100, 200, 500 rubs. All samples showed very good rub resistance with no difference between the reference and tested coatings.

#### CONCLUSIONS

As a result from the tests, it can be concluded, that the biodegradable coating can comply with the main physical-mechanical characteristics required from a water-based coating. However, the bio-based aqueous coating showed lower gloss compared to the conventional water-based coating. The next step in this direction is the improvement of the optical characteristics which would clearly show the increase in the gloss.

#### REFERENCES

1. ACTEGA Terra - [www.actega.com/terra](http://www.actega.com/terra)
2. T. Ts. Bozhkova, I. T. Spridonov, Y. V. Nedelchev, R. K. Boeva, A. M. Ganchev - Improvement of the physical-mechanical and optical properties of printing production with biodegradable overprint varnishes, Bulgarian Chemical Communications, Vol. 47, Special issue A, pp. 60 – 64, , 2015.
3. M. Vähä-Nissi, C.Laine, R. TaIja, H. Mikkonen, S. Hyvärinen, A. Harlin, Aqueous Dispersions from Biodegradable/Renewable Polymers TAPPI PLACE 2010 Conference - April 18-21, 2010, New Mexico, USA.
4. European Directive 94/62/EC on packaging and packaging waste, 20 December 1994.

## ПОДОБРЯВАНЕ НА ФИЗИКО-МЕХАНИЧНИТЕ И ОПТИЧНИТЕ СВОЙСТВА НА ОПАКОВКИТЕ ЧРЕЗ ПОКРИТИЕ С ВОДНИ ПОЛИМЕРНИ ДИСПЕРСИИ В СЪОТВЕТСТВИЕ С ИЗИСКВАНИЯТА ЗА ОПАЗВАНЕ НА ОКОЛНАТА СРЕДА

Т.Божкова<sup>1\*</sup>, Р.Боева<sup>1</sup>, И.Спиридонов<sup>1</sup>, Я. Сапкота<sup>2</sup>, Я.Неделчев<sup>1</sup>, Н. Кашикович<sup>3</sup>, С. Деджиер<sup>3</sup>, М. Пал<sup>3</sup>

<sup>1</sup> Химико-технологичен и металургичен университет, бул.Кл.Охридски 8, 1756 София, България.

<sup>2</sup>Ръководител катедра полимерно инженерство, Montanuniversität Leoben, 8700 Леобен, Австрия

<sup>3</sup>Университет на Нови Сад, Технически факултет, Катедра по графично инженерство и дизайн, Сърбия

Постъпила на 30 ноември 2016 г., приета - 18 май 2017 г.

(Резюме)

Нарастващите изисквания към устойчиво развитие и опазване на околната среда в наши дни доведоха до засилен интерес към биоразградими материали от възобновяеми източници. Водните полимерни дисперсии се използват за повърхностно облагородяване на хартия и картон в опаковъчната индустрия, като целта е да се подобрят физико-механичните и оптичните свойства на печатната продукция. Тази статия обобщава основните параметри при приготвянето, обработката и използването на водни дисперсии на базата на синтетични и биоразградими полимери за покрития в производството на картонени опаковки. Изследването показва, че биоразградимите вододисперсионни лакове имат приемливи физико-механични свойства, но по-нисък блясък от конвенционалните вододисперсионни лакове.

## Preparing, properties and application of waterborne polyurethane-acrylate oligomer as a matrix in UV-cured fiberglasses

A. Matev<sup>1\*</sup>, P. Velev<sup>1</sup>, S. Ismail<sup>1</sup>, M. Herzog<sup>2</sup>

<sup>1</sup>University of Chemical Technology and Metallurgy (UCTM), Sofia 1000, Bulgaria

<sup>2</sup>Technische Hochschule Wildau TH- Wildau, Wildau 15745, Germany

Submitted October 18, 2016 ; Accepted February 12, 2017

Waterborne polyurethane-acrylate oligomer-(WPUA) was prepared via in-situ and anionic self-emulsifying method from Hexamethylene diisocyanate (HDI), polyether polyol (Lupranol 1000/1), dimethylolbutanoic acid (DMBA), and capped with 2-Hydroxyethyl methacrylate (2-HEMA). Then Ultraviolet (UV) curable fibreglass prepreg was obtained from WPUA oligomer, 2-hydroxyethyl acrylate (2-HEA) as reactive diluent, Irgacure 500 as photoinitiator and glass fabric of different weight (81; 163; 660g/m<sup>2</sup>). The physical properties of produced WPUA oligomers, such as IR spectra (by Fourier transform infrared spectroscopy), particle size distribution and apparent viscosity were investigated. Mechanical properties of UV-cured fibreglass composites, such as tensile strength, elongation at break and thermal properties DSC (Differential scanning calorimetry), of UV-cured composites were determined. The specific UV-WPUA was selected as a material with many applications. The results indicate that the prepared UV-WPUA is suitable as matrix material for UV-curable fibreglass composites.

**Keywords:** waterborne polyurethane-oligomer, UV-curable fiberglasses, mechanical and thermal properties

### INTRODUCTION

Polyurethanes (PUs) are used in a surprising array of commercial applications [1]. They are also unique polymeric materials with a wide range of physical and chemical properties [2]. Polyurethanes are usually used as adhesives, coatings, foams, and different kinds of plastics and elastomers, as well as matrix for polymeric composites [3]. Recently, waterborne polyurethane (WPU) has been developed largely because of its excellent mechanical properties, fire resistance, low toxicity and lack of environmental hazards [4]. The waterborne polyurethanes using ultraviolet (UV)-curing technology have gained increasing interests due to their advantages such as low energy consumption, high chemical stability, cost efficient and high curing speed [5]. Light-induced polymerization of multifunctional monomers or oligomers, also called UV-radiation curing, has become a well-accepted technology which has found a large variety of industrial applications because of its unique advantages [6]. UV-radiation curing has been successfully used to produce polymer composites [7]. This is the process of film transformation from a reactive liquid (except a powder) into a solid by radiation in the ultraviolet-energy region rather than by heat. UV cure coatings involve the polymerization and crosslinked polymer network induced by photons and are one of the most

important classes of coatings [8]. The most extensively used UV-curable resins are based on acrylate, which exhibit high reactivity, i.e. short reaction times in the order of magnitude of fractions of a second, and offer a large choice of monomers and telechelic oligomers with functional end groups. Acrylate-based resin systems typically consist of three basic components namely, acrylate functionalised oligomer, which forms the backbone of the polymer network, acrylate monomers (small molecules containing one or more vinyl groups) and photoinitiator, which generates free radicals on UV exposure [9]. Furthermore the high reactivity of acrylates leads to a fast photopolymerization process and saves time in industrial processes [10]. Also in the UV-curing technology of waterborne polyurethanes is usually used acrylates as a reactive diluents. They are some of these ingredients which dilute the oligomer to reduce its viscosity in order to conveniently coat on a suitable substrate prior to making the polymer film, and the second function is the participation of the diluent in the reactive process of the oligomer with a view of making a polymer with a desired property for some specific purpose [11]. In the present study, WPUA was synthesized with polyether polyol, 2,2-dimethylolbutanoic acid 2-hydroxyethyl methacrylate and hexamethylene diisocyanate. WPUA synthesis was carried out in flowing nitrogen atmosphere. These aqueous polyurethane dispersions and their dried polymer

\*) To whom all correspondence should be sent:

E-mail: andrey\_matev@yahoo.com

films were characterized and confirmed for the formation of urethane linkage. Laminated products are prepared from layers of materials bonded together forming a unit body. Laminated plastics are produced in large volumes by the industry in the form of laminated sheets, tubes, rods and a multitude of products employing such materials as paper, asbestos, cloth, wood cellulose, glass fabric (fiberglass), etc., bonded together by synthetic resins [12]. In these case UV-curing waterbased polyurethane is a matrix for bidirectional fiberglass reinforced composites.

## EXPERIMENTAL

The materials, which were used in this experiment are:

- Polyether polyol (Lupranol 1000/1,  $M_n = 2000$ g/mol) was produced by BASF Polyurethanes GmbH, Lemförde, Germany
- 2,2- dimethylolbutanoic acid (DMBA)
- 2- Hydroxyethyl methacrylate (2-HEMA)
- 2-Hydroxyethyl acrylate (2-HEA)
- Triethylamine (TEA) were supplied from Sigma Aldrich Chemie GmbH
- Desmodur N3300 - Aliphatic polyisocyanate (HDI trimer) was produced by Bayer MaterialScience AG, Leverkusen, Germany
- Dibutylbis (lauroyloxy) tin (DBTL) PC CAT T12 was produced by Performance Chemicals Handels GmbH Irgacure 500 were supplied from BASF Schweiz AG, Germany.

### *Preparation of UV- PUA oligomer*

A certain amounts of Lupranol 1000/1 (10.802 g) and HDI (8.325 g) were added into a four-necked flask equipped with a mechanical stirrer, thermometer and reflux condenser. Then, PC CAT T12 was added as catalyst and the mixture was heated to 45-55°C and keeping the temperature for 1 h. to prepare the -NCO terminated prepolymer. Next, the above prepolymer was reacted with a certain amount of DMBA (1.221 g) dissolved in small amount of acetone at 45-55°C for another 2 h, and the -NCO terminated prepolymer containing carboxyl group was obtained. 2-HEMA (4.875 g) was added into the system and reacted at 45-55°C for 3-5 h. When the temperature was cooled down to 40°C, TEA were added into the flask subsequently and reacted at 40°C for 30 min. The mixture was then dispersed into deionized water at 30°C under vigorous stirring for 30 min. The synthetic route of WPUA oligomer is shown in Figure 1.

### *Particle size distribution of the oligomers*

For the determination of the particle size distribution of WPUA oligomers WPUA sample materials were filled to 5-ml test tubes and diluted with deionized water. The particle size was determined by light scattering with the laser particle size analyzer (Zetasizer Nano S Malvern Instruments Limited) according to ISO 13320:2009.

### *The apparent viscosity of WPUA oligomers*

The apparent viscosity of the WPUA oligomer was measured by a rotational viscometer (Anton Paar Physica MCR 301) according to ISO 3219:1993 Plastics-Polymers/resins in the liquid state or as emulsions or dispersions. Determination of viscosity using a rotational viscometer with defined shear rate; when the shear rate was 2000  $s^{-1}$ , the high shear rate warranted highly reliable measurements at a temperature 25°C.

### *IR spectra of the matrix*

FT-IR spectrum of the matrix was obtained according to ASTM E1252 - Standard Practice for General Techniques for Obtaining Infrared Spectra for Qualitative Analysis between 4000 and 400  $cm^{-1}$  with an FT-IR spectrometer (Varian 620- IR, FT-IR). A minimum of 16 scans was signal-averaged with a resolution of 2  $cm^{-1}$  in the 4000 – 400  $cm^{-1}$  ranges.

### *Preparation of UV- curing fiberglass composites*

WPUA fiberglass composites were prepared by casting the newly synthesized oligomer and glass fabric of different weight (81; 163; 660g/m<sup>2</sup>) onto a teflon plate drying at 65°C for 3 h. Because water was used as diluents in this system, a flash-off step is needed, to remove the water by evaporation before UV-curing. During the water removal from the aqueous dispersion, physical entanglement occurred because of the large molecular weight of the prepolymer. Then was irradiated with the UV light from a lamp (main wave length: 365 nm, the power of the lamp: 400 W, Spectral UV-A emission 1200 mW/m<sup>2</sup> and distance between the thin film samples and the center of UV lamp of 15 cm). The Irgacure 500 was activated and radicals for the polymerization could be produced. The formed radicals react at the acrylate double bond of the monomers and oligomers forming polymers under crosslinking and the WPUA fiberglass composite is obtained. The waterborne WPUA matrix was cured through a two-step process. The photo-dissociation mechanism of Irgacure 500 is shown in Figure 2.

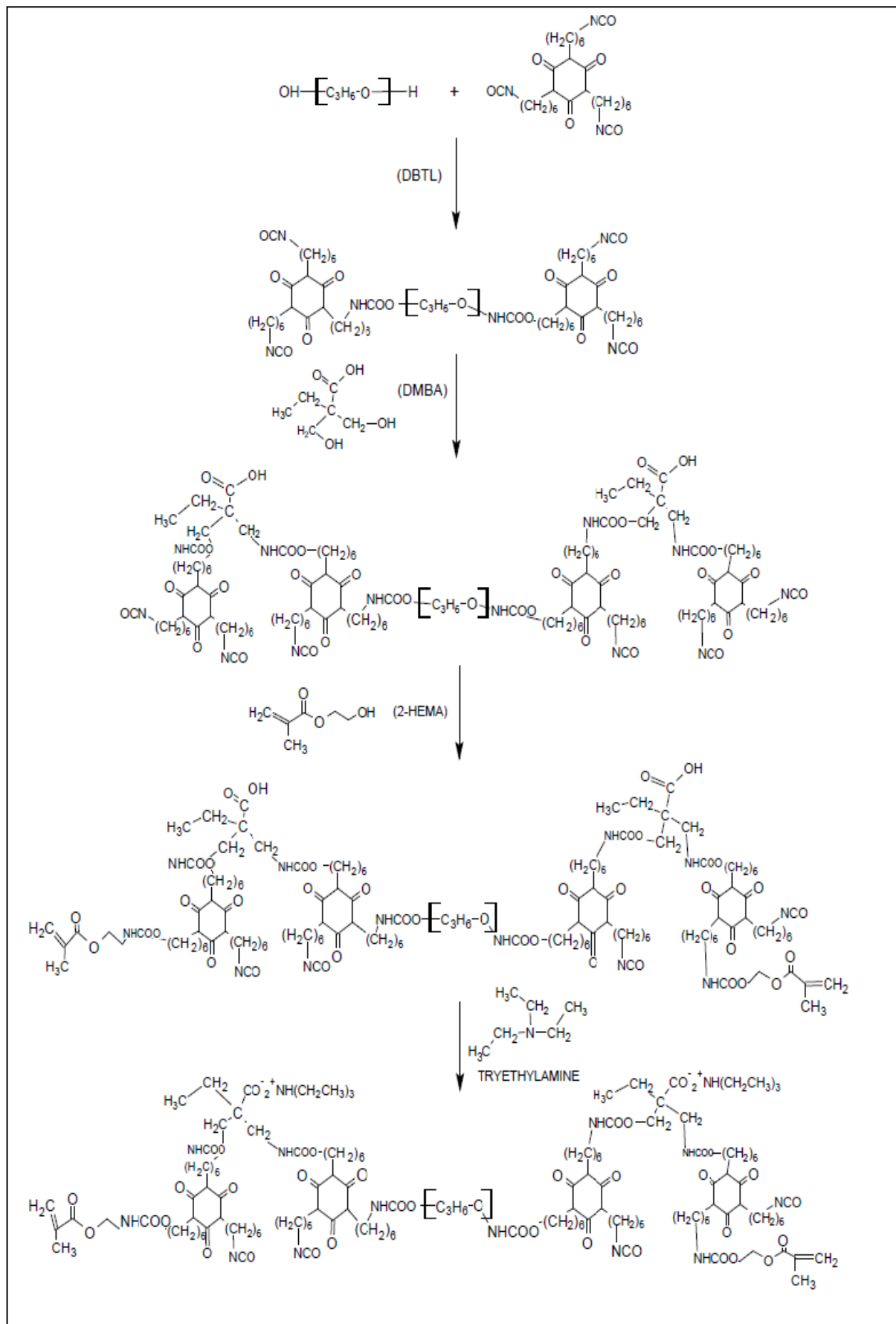
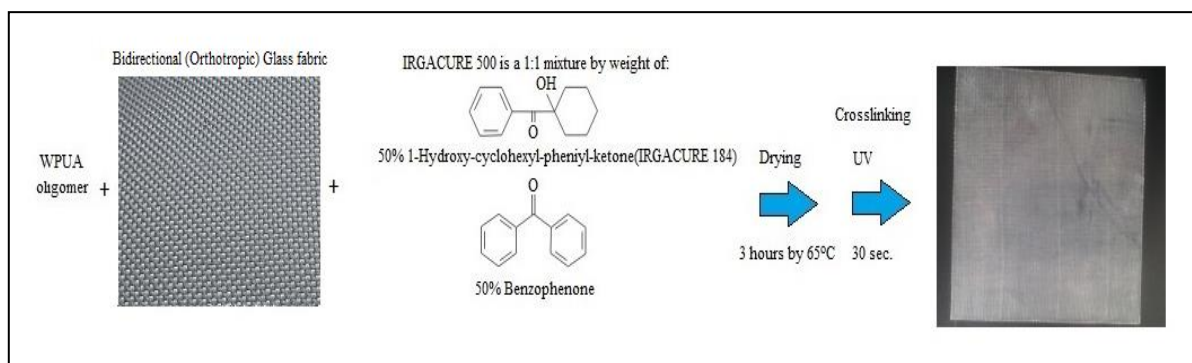


Figure 1. The synthetic route of the UV-WPUA oligomer.



**Figure 2.** Preparation of UV- curing fiberglass composites.

### Mechanical properties of UV- curing fiberglass composites

Tensile strength testing and elongation at break testing for all of the specimens were carried out on „Zwick Z 020 ” Zwick GmbH & Co. KG, Ulm, Germany at room temperature at a speed of 50 mm/ min. All measurements had an average of three runs. The dumbbell- type specimen was prepared according to EN ISO 527-3:1995.

### Fibre and matrix volume of the composites

Fibre volume ratio is easily determined by simple weighing of a defined area of the composite of known glassfiber mass. Typically, an ASTM D3171-15 test method is employed which requires weighting of the sample and knowledge of the density of the components. The resin volume is the difference between the composite and fibre volume and was calculated according to the following formula:

$$V_{fiber} = V_{composite} - V_{matrix}$$

### Thermal properties of fiberglasses (DSC)

Differential scanning calorimetry (DSC) of the UV-cured fiberglass composites were performed on a „DSC 204 Phoenix”, NETZSCH, Germany according to ISO 11357. The programmed heating range was from -100°C to 300°C at a heating rate of 10 °C/min under a nitrogen atmosphere. The measurement was performed at with 6–10 mg samples. DSC curves were recorded.

## RESULTS AND DISCUSSIONS

### Particle size of oligomers

The results from particle size determination are presented at *Figure 3* and *Figure 4*. For WPUA average size is 145 [d.nm] in comparison with Bayhydrol 2317 at about 88, 40 [d.nm]. These strong difference between polyols will affect not only at the physical properties of the

polyols and also of the mechanical properties of the fiberglass samples.

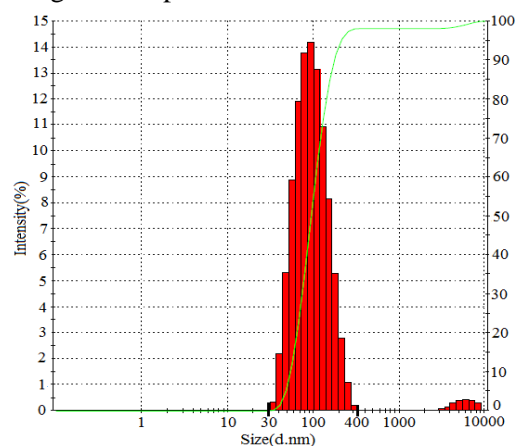


**Figure 3.** Particle Size of Bayhydrol 2317.

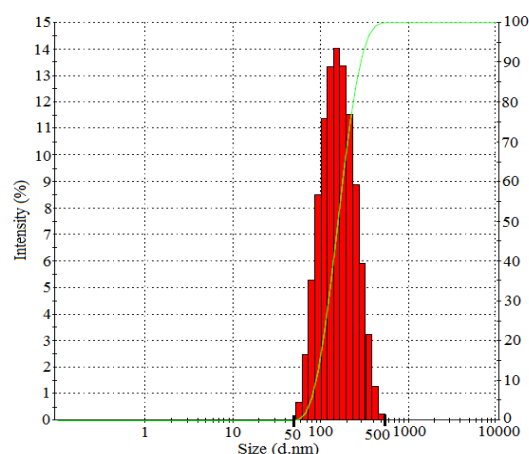


**Figure 4.** Particle Size of WPUA oligomer.

### The apparent viscosity of WPUA oligomers

It can be observed at *Figure 5*, that there is a difference in viscosity between WPUA and Bayhydrol 2317 and WPUA oligomer is preferable not only as a matrix in fiberglass composites and also for a spraying method because of its lower viscosity.

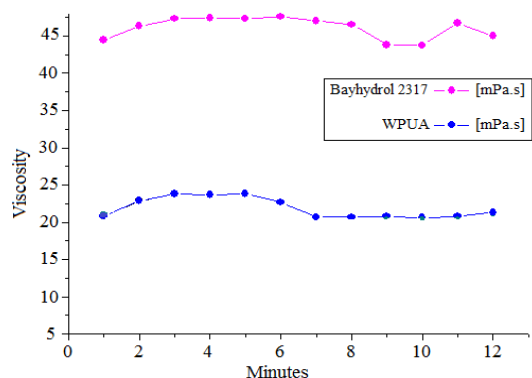


Figure 5. Viscosity of WPUA oligomer.

#### IR spectra of the matrix

The FTIR analysis at Figure 6 was used mainly to check the completeness of the polymerization reaction, in terms of the disappearance of the NCO band at  $2255\text{ cm}^{-1}$  and the appearance of the N-H band at  $3362\text{ cm}^{-1}$ . The result indicated that the NCO had reacted with OH into NHCOO and the NCO groups had been completely bonded. Besides the presence of a band at  $1682\text{ cm}^{-1}$  is characteristic for the urethane group C=O and the band at  $1531\text{ cm}^{-1}$  belongs to C-NH group from the urethane. The strong bands at  $2970$ ,  $2863$ ,  $1462$  and  $1373\text{ cm}^{-1}$  are C-H asymmetric and symmetric vibration, as well as asymmetric and symmetric stretching  $\text{CH}_3$ .

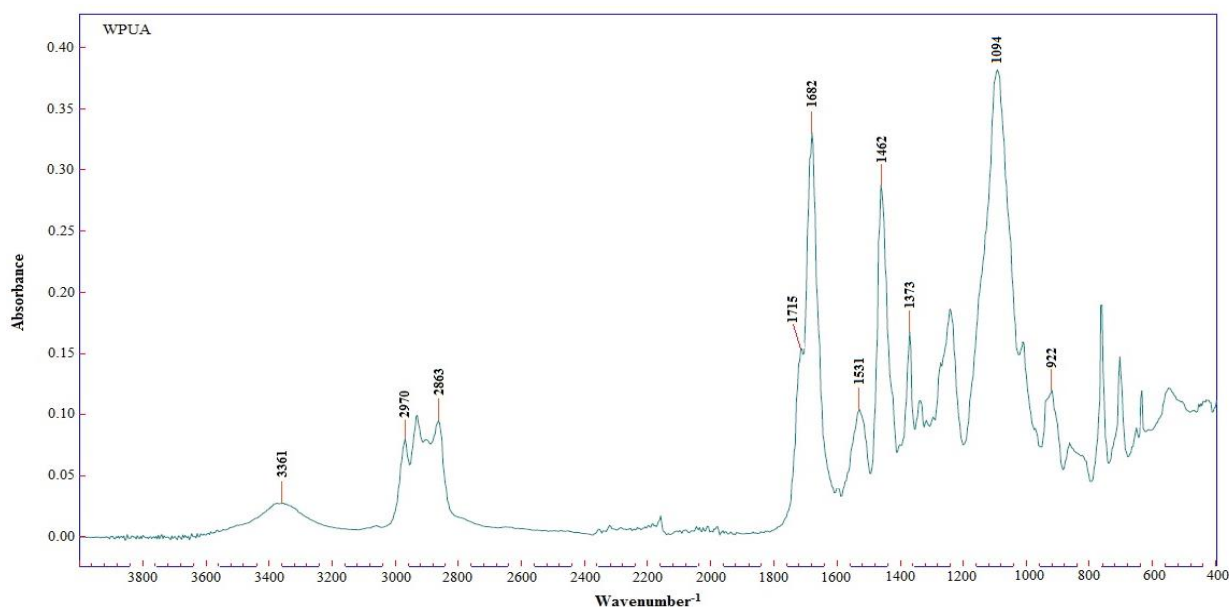


Figure 6. IR spectra of the matrix.

The FTIR spectrum of the matrix: There is a wide peak at  $3375\text{ cm}^{-1}$ , which belongs to the OH groups from 2-HEMA (used by oligomer synthesis). The peak at  $1715\text{ cm}^{-1}$  peak is characteristic for the carbonyl group (C=O), and 2-HEA. The peak at  $1094\text{ cm}^{-1}$  belongs to the (C-O) bond. The intensity decrease of the peak at  $922\text{ cm}^{-1}$  is a polymerization result, whereas the double bond ( $\text{CH}_2=\text{CH}$ ) in the acrylate moiety breaks.

#### Thermal properties of fiberglasses (DSC)

The DSC curves of the WPUA fiberglass composites are shown in Figure 10. From which, it can be seen that the samples (1-3) have one glass transition temperature, around  $21$ ,  $24$ ,  $30^\circ\text{C}$  and exothermal peaks at about  $160^\circ\text{C}$  which is a symbol of reactivity after the UV-curing, expecting affects to the mechanical properties of the samples. The conclusions from the abovementioned results are, that it is recommended not only UV light and also temperature treating for the fully completion of the curing.

#### Fibre volume of the composites

It can be observed from Table 1, that the fiber volume fractions of the samples ranged from  $50,61\%$  to  $69,52\%$ .



**Table 1.** Composite fibre and matrix volume

Sample	Matrix	Fiber grammage	V <sub>fabric</sub>	V <sub>matrix</sub>
1	WPUA	81 g/m <sup>2</sup>	61,84%	38,15%
2	WPUA	163 g/m <sup>2</sup>	50,61%	49,38%
3	WPUA	660 g/m <sup>2</sup>	69,52%	30,47%

*Mechanical properties of UV-curing fiberglass composites*

It can be observed in general from Figure 7- 9, that optimal elongation at break properties was observed in sample 1 glassfiber reinforced

composites with glass fabric weight- 660 g/m<sup>2</sup>, optimal tensile strength and minimal Young's modulus by sample 2 glassfiber reinforced composites with glass fabric weight- 163 g/m<sup>2</sup>.

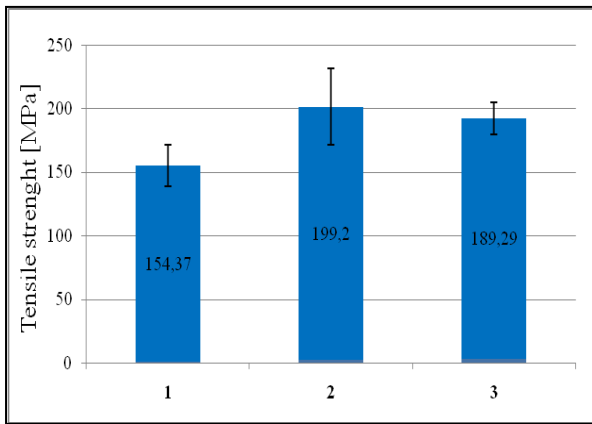


**Figure 7.** Tensile strength of fiberglass composites.

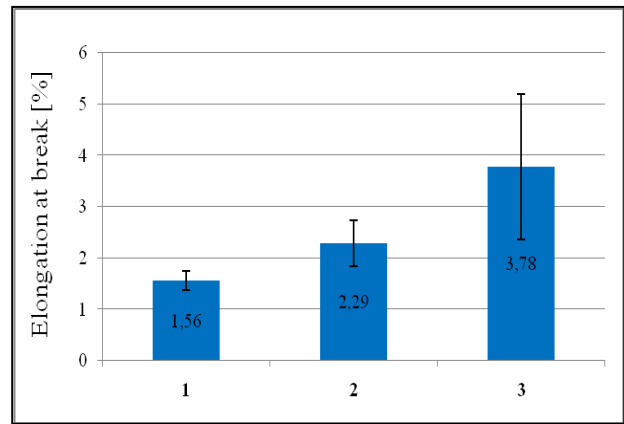


**Figure 8.** Elongation to break of fiberglass composites.

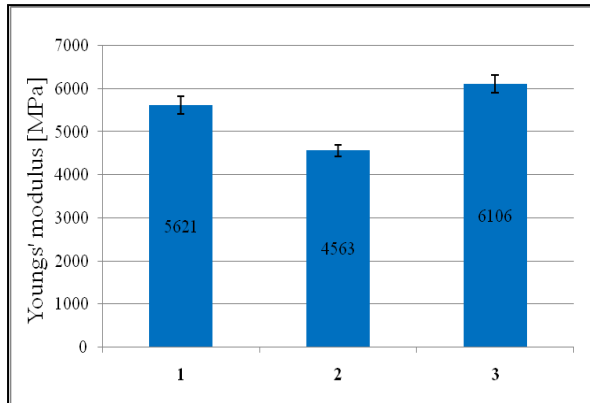


**Figure 9.** Young's modulus of fiberglass composites.

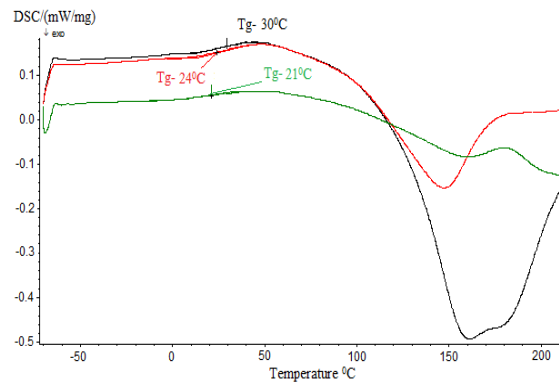


**Figure 10.** DSC curves of the composites

**SUMMARY**

The samples were prepared using UV-PUA oligomer, the Irgacure 500 and the monomer 2-HEA. The quantity of 2-HEA, the content of the Irgacure 500, the drying time of the samples, the temperature and the curing time have important effects on the properties of the UV-cured fiberglasses. The experimental results indicated that the optimum irradiation time was 30- 50s after the UV-PUA being applied on a poly (tetrafluoroethylene) -“TEFLON” plate at room temperature, and catalyst (photoinitiator) dosage was 4% (wt%) of the total amount. Almost all the

UV-cured fiberglasses have a residue bonds and that will be a topic for additional investigations. The UV-curing PUA dispersions are especially advantageous in high production open molding, pultrusion and filament winding processes for many different products and their quick fix, such as boats, skylight panels, shower and tub enclosures, RV and truck panels, poles, tanks, pipes. Manufacturers of these and other products should evaluate photocuring as a way to increase production and lower styrene emissions.

REFERENCES

1. M. Szycher, "Szycher's Handbook of Polyurethanes", Second Edition, CRC Press, 2 (2013)
2. Ho Tak Jeon, Moon Kyong Jang, Byung Kyu Kim, Kwang Ho Kim, *Colloids Surfaces A: Physicochem. Eng. Aspects*, **302**, 559 (2007).
3. Hemul V. Patel, Jignesh P. Raval, Pradip S. Patel, *Archives of Applied Science Research*, **1**, 294 (2009).
4. Minqiang He, Jicheng Xu, Fengxian Qui, Xiaonong Chen, *Int. J. Polymer Anal. Charact.*, **18**, 211 (2013).
5. Heping Xu, Dongya Yang, Qing Guo, Yingying Wang, wenling Wu & Fengxian Qui, *Progress Org. Coat.*, **73**, 47 (2012).
6. Ch. Decker, *Macromol. Rapid Commun.*, **23**, 1067 (2002).
7. Saeed Bastani, Mohsen Mohammad Raei Nayini, Majid Mohseni, UV-curable nanostructural composites: preparation and properties, *Nanofabrication using Nanomaterials*, Chapter 6, 179
8. L. Keller, C. Decker, K. Zahouily, S. Benfarhi, J. M. Le Meins, J. Miehe-Brendle, *Polymer*, **45**, 7437 (2004).
9. G. Mashouf, Ghodsieh Mashouf, Morteza Ebrahimi, Saeed Bastani, *Pigment & Resin Technol.*, **43**, 61 (2014).
10. C. Sow, B. Riedl, P. Blanchet, *Progress in Organic Coatings*, **67**, 188 (2010).
11. M. Idriss Ali, K & Khan, Mubarak & M. Zaman, M & Hossain, Muhammad, Reactive diluent effect on properties of UV-cured films. *Journal of Applied Polymer Science*, **54**, 309 - 315 (1994) 10.1002/app.1994.070540305.
12. Nicholas P. Cheremisinoff, Paul N. Cheremisinoff, *Fiberglass Reinforced Plastics*, 1st Edition (1995), Elsevier

ИЗГОТВЯНЕ, СВОЙСТВА И ПРИЛОЖЕНИЕ НА ВОДОДИСПЕРГИРАН ПОЛИУРЕТАН-АКРИЛАТЕН ОЛИГОМЕР КАТО МАТРИЦА ЗА УВ-ВТВЪРДЯВАЩИ СЕ СЪТЪКЛОПЛАСТИ

А. Матев<sup>1\*</sup>, П. Велев<sup>1</sup>, С. Исмаил<sup>1</sup>, М. Херцог<sup>2</sup>

<sup>1</sup>Химикотехнологичен и металургичен университет (ХТМУ), София 1000, България

<sup>2</sup>Техническо Висше Училище-Вилдау ТХ- Вилдау, Вилдау 15745, Германия

Постъпила на 18 октомври, 2016 г.; приета на 12 февруари, 2017 г.

(Резюме)

Изготвен е вододиспергиран полиуретан- акрилатен олигомер -(ВПУА) чрез анионен самоемулсифициращ метод от Хексаметилен диизоцианат (ХДИ), полиетер полиол (Лупранол 1000/1), диметилбутанова киселина (ДМБК), и се въвеждат акрилатни крайни групи с 2-хидроксиетил метакрилат (2-ХЕМА). След което е получен стъклопласт втвърдяващ се след облъчване с ултравиолетова (УВ) светлина от ВПУА олигомер, реактивен разтворител 2-хидроксиетил акрилат (2-ХЕА), фотоинициатор Иргакюр 500 и стъклени платове с различно тегло (81, 163, 660г/м<sup>2</sup>). Изследвани са физичните свойства на произведените ВПУА олигомери чрез Инфрачервена спектроскопия, определен е размерът на частиците и вискозитетът. Определени са механичните свойства на УВ-втвърдяващите стъклоусилени композити- якост на опън, удължение при скъсване, и термичните свойства чрез ДСК (диференциално сканираща калориметрия). Специфичните УВ-ВПУА са материали с широка област на приложение. Получените резултати определят изготвеният УВ-ВПУА като подходящ за матрица на УВ- втвърдяващи се композити.

## Investigation on the influence of reactive dyes over the colour stability of offset printing paper during ageing

D. A. Todorova\*, P. M. Miladinova

*University of Chemical Technology and Metallurgy, 8 Kl. Ohridski, 1756 Sofia, Bulgaria*

Received November 21, 2016; Accepted May 8, 2017

Contrary to the general belief that coloured papers are mainly used in the field of hygiene and tissue papers, nowadays during the printing process with the new digital technology some of the specialists in the printing and publishing industry prefer to produce special books and journals with specifically coloured paper. Therefore, dyeing of offset paper is reasonable. The reactive dyes are well known mainly as a textile dyes and they have only limited use in paper production. They are capable of forming covalent dye-polymers bonds, for instance, with the hydroxyl groups of cellulose. The purpose of this study was to investigate the influence of reactive dyes over the colour stability during the accelerated ageing of the paper, both at dry heat and at exposure to light.

In this experiment were used two laboratory synthesized reactive dyes, derivatives of chlorotriazine and one of them contains a stabilizer fragment. Dyes were used in the composition of offset printing paper with a fibre content of bleached softwood and hardwood pulp in a ratio of 1:1. The paper was sized with alkyl ketene dimer and as filler was used natural calcium carbonate. The optical properties -  $L^*C^*h^*$  from the CIE Lab colour space have being examined before and after the accelerated ageing of the resulting paper samples.

As a result of the studies carried out it was found out that with both reactive dyes were obtained paper samples with similar colour shades, uniform colouring and stable colour, distinguished by stability under thermal and light accelerated aging.

**Key words:** accelerated ageing of paper, thermal ageing, light ageing, reactive dyes, optical properties

### INTRODUCTION

Contrary to the general belief that coloured papers are mainly used in the field of hygiene and tissue papers, nowadays during the printing process with the new digital technology some of the specialists in the printing and publishing industry prefer to produce special books and journals with specifically coloured paper. Therefore, dyeing of offset paper is reasonable and the use of reactive dyes would have benefits, both for the properties and for the colour stability during ageing of the paper. Generally, paper is colour by dyes of different chemical nature – inorganic pigments; synthetic organic pigments; basic, acid, direct dyes and others.

The reactive dyes are well known mainly as a textile dyes and they have only limited use in paper production. They have been tested in the late 1800s [1]. The first reactive dye is synthesized by IG Farben in 1932, but it first appeared commercially in 1956, after their invention in 1954 by Rattee & Stephenson at the Imperial Chemical Industry (ICI), Dyestuffs Division site in Bleckley, Manchester, UK [2,3]. They stand out from other dyes by their ability to make covalent bonds between carbon atoms of

the dye reactive group and oxygen atoms of pulp hydroxyl groups under alkaline conditions [4]. Reactive dyes are divided, according to their structure of reactive group, in haloheterocycle and vinyl sulfone based dyes, which react with cellulose through nucleophilic substitution and addition mechanisms, respectively. Commercially, the widest used systems are: vinyl sulfone, monochlorotriazine, bifunctional dyes, difluoro chloropyridine, monofluoro triazine and dichlorotriazine. In addition to reacting with fibre, reactive dyes also react with water (dye hydrolysis) in a form which cannot bound to cotton, but behaves as a substantive dye and affects colour fastness, when is used on fabric. The most important parameter affecting exhaustion and „fixation“ of reactive dyes are temperature, salt and alkali concentration and liquid ratio [4].

Because of the limited use of reactive dyes in the paper dyeing process, there are not so much results about the properties of the paper suspension, paper white waters and paper properties.

The quality and long-term stability of paper materials produced from cellulosic fibres with various additives are determined by the extent of oxidative and hydrolytic reactions taking place upon ageing. These processes may considerably reduce the physicochemical and chemical properties of

---

\*) To whom all correspondence should be sent:  
E-mail: [todorova.dimitrina@uctm.edu](mailto:todorova.dimitrina@uctm.edu)

paper, resulting in damage to paper structure, an increase of brittleness, and finally, a total loss on material quality. The hydrolytic and oxidative processes are related to each other, and are affected by various intrinsic factors (sizing, filling, adhesives, the presence of acid groups, metal ions, lignin, etc.) and extrinsic factors (storage conditions, temperature, humidity, the presence of oxygen, light and environmental impurities) [7].

The purpose of this study was to investigate the influence of new reactive dyes over the colour stability during the accelerated ageing of paper, both at dry heat treatment at 105 °C and at exposure to light with intensity of 765±75W/m<sup>2</sup> and wavelength of 290-800nm.

### EXPERIMENTAL

The investigations were carried out with laboratory obtained paper samples (70g/m<sup>2</sup>) from bleached hardwood and softwood pulp in proportion 1:1, with beating degree of 42°SR (Schopper Riegler). The paper samples were sized with Alkyl Ketene Dimer (AKD) – 2% from o.d.f., filled with natural calcium carbonate (CaCO<sub>3</sub>) – 20% from o.d.f. and as a retention additive (RA) was used modified poly acryl amide with cationic charge in consumption 0,05% from o.d.f.

The two examined dyes were laboratory synthesized red reactive dyes. The compounds are

monoazo reactive dyes whose chromophore is an orange acid dye, prepared by diazotization of the amino C acid and subsequently coupling with I acid in slightly alkaline medium. Reactive group (chlorine atom) was introduced into the chromophore by reaction of the acid orange dye with cyanuric chloride and the dichlorotriazine reactive dye was obtained. In the subsequent step by a reaction of the last one with 4-amino-2,2,6,6-tetramethylpiperidine or ammonia the monochlorotriazine reactive orange dyes (1) and (2) were obtained (Fig.1).

The tetramethylpiperidine fragment in the molecule acts as a stabilizer fragment and its introduction was done with purpose - increment of the colour fastness to light (photo-stability). It was expected that the paper dyed with this dyes exhibit also a greater photo-stability. This assumption was made based on the fact that the dyed fibres (cotton and wool) and chemically coloured polymers showed high photo-stability [5,6].

The consumption of Reactive Dye 1 (RD1) and Reactive Dye 2 (RD2) in the paper was 0,2%, 0,4%, 0,6% from o.d.f.

The obtained paper samples were examined for their optical properties – colour coordinates L\*, C\* and h\* before and after the accelerated ageing, by Frank – PTI spectrophotometer / D65\_10.

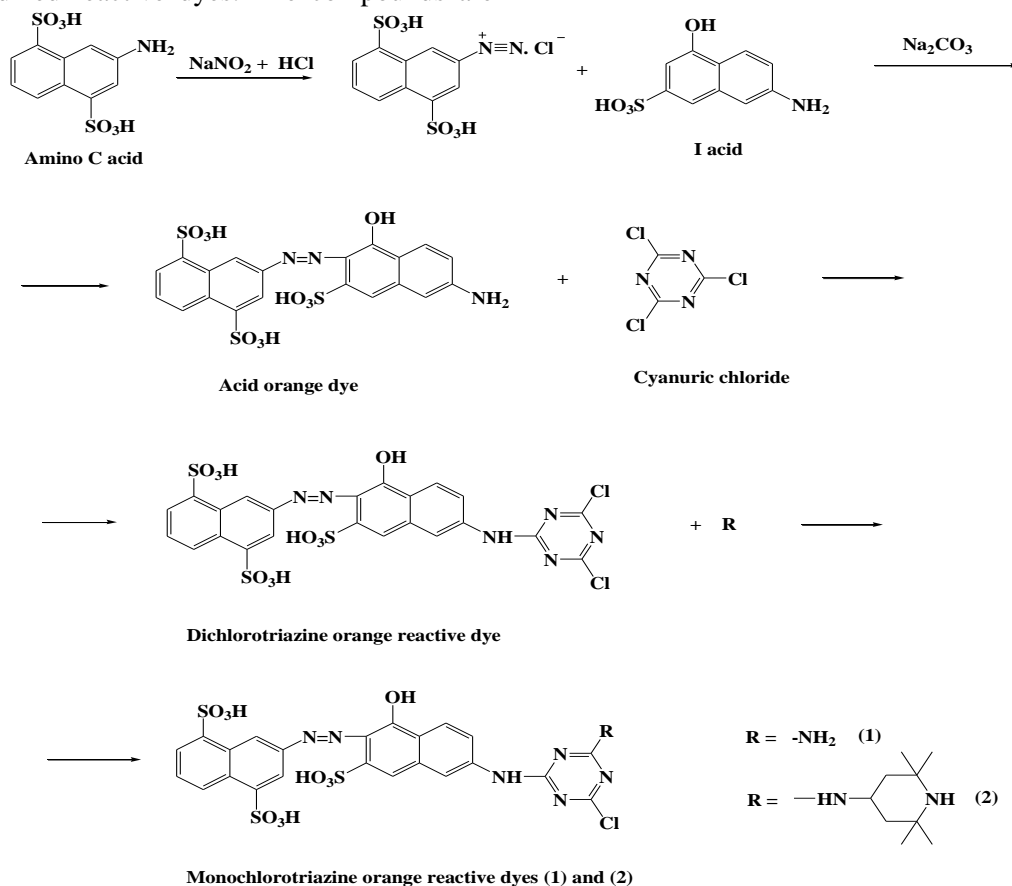


Fig.1 Chemical characteristic of reactive dyes

The thermal ageing was conducted according to ISO 5630-1:2014 [8] at temperature of 105 °C, and duration of 36h.

The light ageing is being conducted according to ISO 5630-7:2014 [9], by exposure to light with intensity of  $765 \pm 75 \text{ W/m}^2$  and wavelength of 290-800nm and duration of 48h.

The CIE  $L^*c^*h^*$  Colour Space is in the form of a sphere and there are three axes;  $L^*$ ,  $C^*$  and  $h^*$  [10].

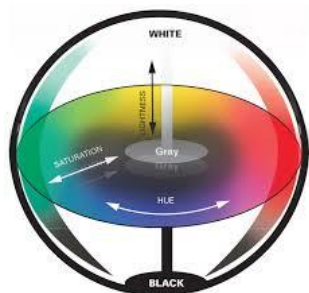


Fig.2 The CIE  $L^*c^*h^*$  Colour Space.

The  $L^*$  axis represents *Lightness*, brightness and the brilliance of the paper. This is vertical; from 0, which has no lightness (i.e. absolute black), at the bottom; through 50 in the middle, to 100 which is maximum lightness (i.e. absolute white) at the top. Just like CIELab, the lighter the colour, the higher the value.

The  $C^*$  axis represents *Chroma* or 'saturation'. This ranges from 0 at the centre of the circle, which is completely unsaturated (i.e. a neutral grey, black or white) to 100 or more at the edge of the circle for very high Chroma (saturation) or 'colour purity'. Chroma, or saturation, describes where a colour falls between the centre and the edge of the sphere. Lower numbers near the centre are more grey and have very little chroma, while higher numbers are purer and saturated.

The  $h^*$  axis represents *Hue*. The units are in the form of degrees° (or angles), ranging from 0° (red) through 90° (yellow), 180° (green), 270° (blue) and back to 0 and all of the colours that fall in-between. [10]. The  $L^*C^*h^*$  colour model is very useful for coloured papers.

## RESULTS & DISCUSSION

The process of natural ageing of paper is too slow to permit observing changes in a reasonable time frame. Thus, different methods of accelerate ageing of paper under dry heat and light exposure have often been used to speed up the process of physic-mechanical and optical changes of properties in the paper. The hydrolytic degradation has been looked as the most important reason for the loss of strength properties of the paper and the lignin content as the most important factor for light ageing. In the present study, the raw material was

bleached pulp, so that the lignin cannot be of an essential factor for the colour change during thermal and light ageing.

The colours with the same hue can further vary - can be very bright and clear or dull and grey - e.g. strong blatant, brilliant red or mat, increscent red. This is characterized by the colour parameter  $C^*$  - colour, saturation, intensity, purity of tone. With increasing  $C^*$ , increases the colour growing, intensity of colour. Similarly, chromaticity  $C^*$ , the colours may in the same colour tone  $h^*$  yet differ in their brightness  $L^*$ .

### *Influence of the quantity and type of reactive dyes, on the colour parameters of the papers during accelerate thermal ageing*

It is known, from the different previous publications, that three days (72h) of accelerated thermal ageing at 105°C is equal to 25 years of natural ageing [11,12]. In view of the fact, that the received by us paper samples were from bleached cellulose and its thermal aging is most noticeable during the first six hours, we assumed that for the colour parameters longer aging than 36h was not necessary.

The colour coordinate -  $L^*$ , which expresses the lightness, brightness and the brilliance of the paper, decreases with adding of both reactive dyes (Fig.3). The colour parameter variation with time is comparatively low, being most sensitive during the first 24 hours. The differences between both reactive dyes are small. But at 0,2% consumption of both RD, the lightness of the paper samples is nearly the same and it stayed stable after 36h accelerated thermal ageing. With increasing the dyes consumption and the duration of the thermal ageing, the colour of the paper samples is slightly getting lighter and the colour difference is getting bigger.

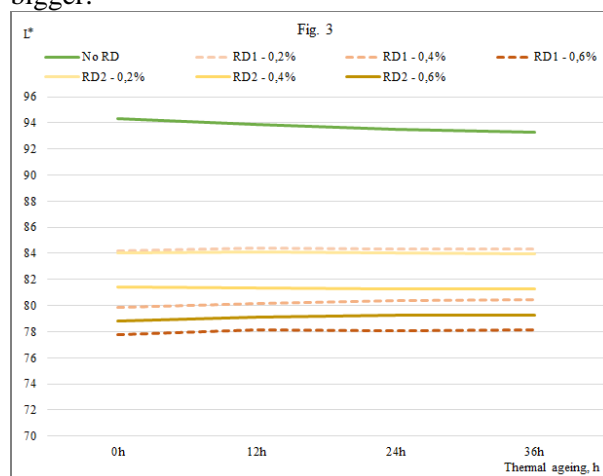
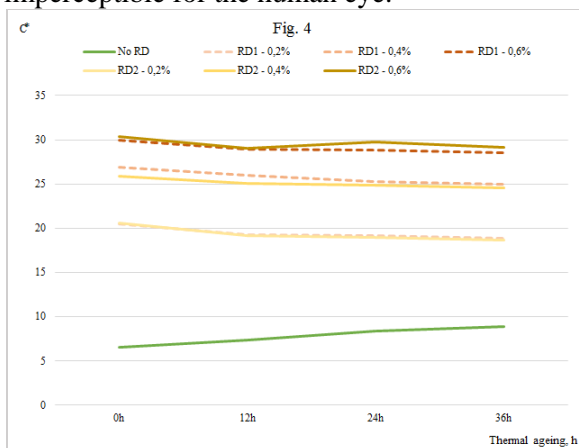


Fig. 3. Dependence of Lightness ( $L^*$ ) of the paper samples at different RD type and consumption, from the duration of the thermal ageing

The colour difference between the samples dyed with the two examined reactive dyes is nearly imperceptible for the human eye.



**Fig. 4.** Dependence of Chroma ( $C^*$ ) of the paper samples at different RD type and consumption, from the duration of the thermal ageing

As it is seen from Fig.4 and Fig.5, which represents the Chroma –  $C^*$  and the Hue –  $h^*$  of the papers samples, with both reactive dyes are obtained paper samples with uniform colouring, which is comparatively stable during thermal ageing. Relatively large changes in the parameter  $C^*$  were observed at the higher consumption of both examined dyes (0.4% and 0.6%), while at consumption 0.2% the values for  $C^*$  are almost the same.

Usually, the hue of the coloured paper samples is the most sensitive parameter during ageing and especially during the first 24h. As it is seen from Fig. 5 the difference between the colour of the paper at 0,4% and 0,6% consumption of the dye is less, than that at 0,2%. With increasing the RD consumption, the colour parameter  $h^*$  is getting less susceptible of accelerated thermal ageing, i.e. the brighter the colour, the bigger the changes.

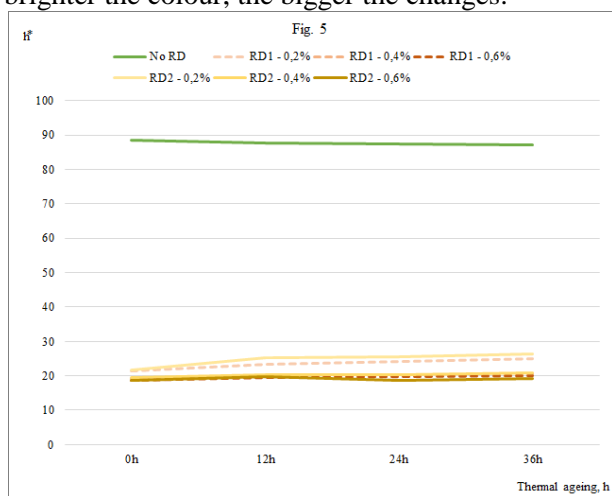


**Fig. 5.** Dependence of Hue ( $h^*$ ) of the paper samples at different RD type and consumption, from the duration of the thermal ageing.

### ***Influence of the quantity and type of reactive dyes, on the colour parameters of the papers during accelerate light ageing***

Light plays an important role in the natural ageing of paper. The effect of light on paper has been reviewed by several authors [13, 14] and a lot of experiments had been made during the natural conditions. Experimental results indicate that the mechanisms for aging with pollutants, light and heat are all different from each other and are also fibre dependent [15].

In our experiment the accelerated light ageing has been conducted in apparatus - Ametek Atlas MTS Suntest CPS+ Benchtop Xenon Exposure Environment Tester Chamber (Fig.6).



**Fig. 6** Paper samples in the Suntest apparatus

The results for the colour parameters of the paper samples are shown on Fig.7, Fig.8 and Fig.9.

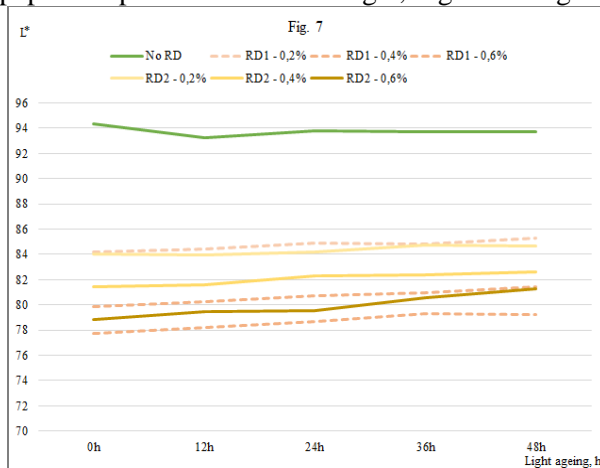


**Fig.7.** Dependence of Lightness ( $L^*$ ) of the paper samples at different RD type and consumption, from the duration of the light ageing

As it is seen from Fig.7, which represents the colour lightness of the paper samples, during the accelerated light aging, the parameter  $L^*$  is amended even for paper without reactive dye, which shows the aggressiveness of this type of aging, compared to the thermal ageing. The first 24 hours of aging also shows most sensitive colour changes. From Fig.7 it is seen that the values of the parameter  $L^*$  decreases, which means that the paper

is getting darker. The results shown on Fig. 9, which represents the hue of the paper, shows that the colour is amended to the yellow hues. With further continuance of the light aging, the paper samples are becoming brighter again, which is associated with the burnout of the colour of the paper.

During the light aging of the paper samples, the largest variation is observed for the parameter  $C^*$ , which represents the saturation of the paper. Fig.8 shows, that the paper samples lose colour saturation, because the values decreases, i.e. the colour is getting more faded. Unlike the thermal

aging, here the changes during the ageing duration, are not so smooth and the susceptibility of RD2 is greater than that of RD1. The paper samples are losing their purity and become grey and turbid.

On Fig.9 is shown the variation of the hue parameter ( $h^*$ ) of the paper samples during accelerated light ageing. As it is seen, most stable was the colour of paper samples dyed with RD2, at consumption of 0.4% of the dye. Obviously at low quantities of the dyes, the colour of the paper samples is more sensitive to light aging, especially in presence of RD1, which do not contain a light-stabilizer fragment in its molecule.

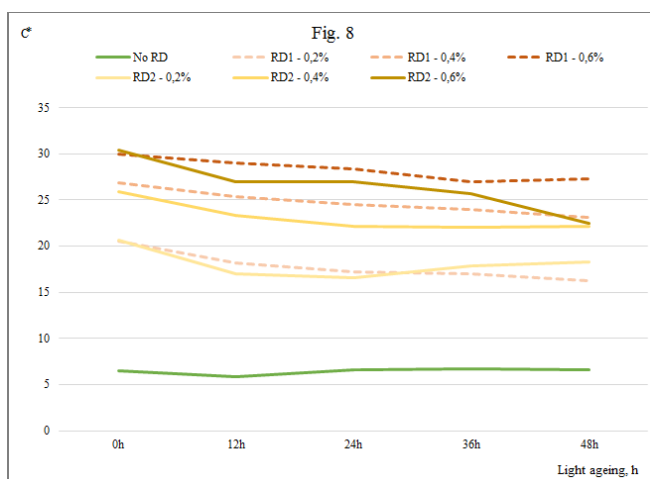


**Fig. 8.** Dependence of Chroma ( $C^*$ ) of the paper samples at different RD type and consumption, from the duration of the light ageing

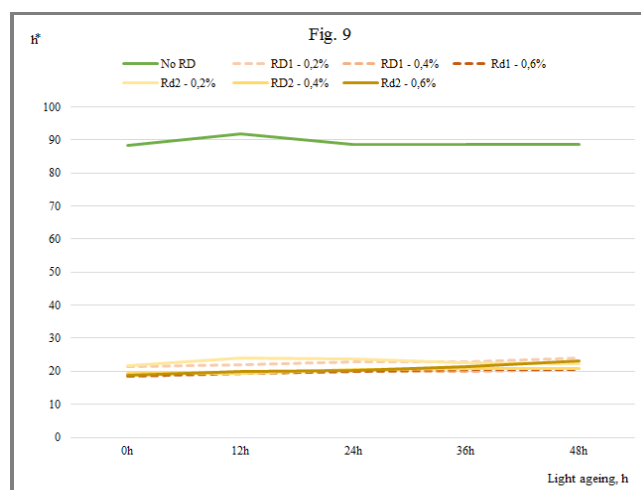


**Fig. 9.** Dependence of Hue ( $h^*$ ) of the paper samples at different RD type and consumption, from the duration of the light ageing

## CONCLUSIONS

On the basis of the results of the studies carried out for dyeing wood free neutrally sized paper by two laboratory synthesized reactive dyes, using cationic polyacrylamide as retention additive and with a view of the complex influence on the colour stability during accelerated ageing the following conclusions can be made:

- With both reactive dyes have been obtained paper samples with uniform colouring.
- The colour difference between the samples dyed with the two examined reactive dyes are nearly imperceptible for the human eye.
- During the accelerated thermal aging, the changes of the colour are smaller and smoother.
- During the accelerated light aging, the changes in the colour are larger and have more variation in the parameters.
- Most variable colour parameter during accelerated aging is the chroma -  $C^*$ .
- During the thermal aging, more stable over time is the colour characteristics of the paper samples dyed with RD1 and those of PD 2 are more

stable during the light aging, demonstrating the positive effect of the presence of light-stabilizer fragment in its molecule.

- Most suitable in terms of colour stability is RD2 at 0,4% consumption.
- Both examined reactive dyes are suitable for dyeing of offset printing paper.

## REFERENCES

1. H. Tappe, W. Helmling, P. Mischke, K. Rebsamen, U. Reiher, W. Russ, L. Schläfer, P. Vermehren "Reactive Dyes" in Ullmann's Encyclopedia of Industrial Chemistry, Wiley-VCH, Weinheim, (2000)
2. K. Venkataraman, The Chemistry of Synthetic Dyes, Vol. 7. Academic Press: New York, (1972).
3. Dyeing of cotton fabric with reactive dyes, textilelearner.blogspot.com, (2012).
4. N. Ristic, I. Ristic, *J. Eng. Fiber Fabrics*, **7**, 113, (2012).
5. P. Petrova-Miladinova, T. Konstantinova, *J. Univ. Chem. Technol. Met.*, **39**, 405 (2004).
6. T. Konstantinova, P. Petrova-Miladinova, *Dyes and Pigments*, **67**, 63 (2005).

7. B. Havlínová, S. Katuščák, M. Petrovičová, A. Maková, V. Brezová, *J. Cultural Heritage*, **10**, 222 (2009).
8. ISO 5630-1:2014. Paper and board — Accelerated ageing — Part 1: Dry heat treatment at 105 °C, International Organization for Standardization, Geneva, Switzerland, (2014)
9. ISO 5630-7:2014. Paper and board — Accelerated ageing — Part 7: Exposure to light, International Organization for Standardization, Geneva, Switzerland, (2014)
10. H. Kipphan, „Hand Book of Print Media”, Heidelberg, Springer, (2001)
11. X. Zou, T. Uesaka, N. Gurnagul, *Cellulose*, **3**, 243, (1996).
12. X. Zou, T. Uesaka, N. Gurnagul, *Cellulose*, **3**, 269 (1996).
13. S. Zervos, A. Moropoulou, *Int. J. Preservation Library Archival Materialc*, **27**, 219 (2006).
14. V. Bukovski, *Restaurator*, **21**, 55 (2000).
15. M. Area, H. Cheradame, *BioResources*, **6**, 5307 (2011).

## ИЗСЛЕДВАНЕ НА ВЛИЯНИЕТО НА РЕАКТИВНИ БАГРИЛА ВЪРХУ СТАБИЛНОСТТА НА ЦВЕТА НА ОФСЕТОВА ХАРТИЯ ЗА ПЕЧАТ ПРИ СТАРЕЕНЕ

Д. А. Тодорова\*, П.М.Миладинова

*Химикотехнологичен и металургичен университет, бул. Климент Охридски №8, София 1756*

Постъпила на 21 ноември, 2016 г.; приета на 8 май, 2017 г.

(Резюме)

Противно на общото схващане, че цветни хартии се използват главно в санитарно-хигиената областта, в днешно време в процеса на печат с новите цифрови технологии, някои от специалистите в полиграфическата индустрия предпочитат да произвеждат уникални книги и списания с специално оцветена хартия. Ето защо, багрнето на офсетова хартия е разумно. Реактивните багрила са добре известни предимно като текстилни багрила и имат ограничено използване при производството на хартия. Те са способни да образуват ковалентни химични връзки (багрило-полимер), например с хидроксилните групи на целулозата. Целта на експеримента е да се изследва влиянието на реактивни багрила върху стабилността на цвета по време на изкуствено топлинно и светлинно стареене на хартията.

В този експеримент се използват две лабораторно синтезира реактивни багрила, производни на хлоротриазин като един от тях съдържа стабилизаторен фрагмент. Багрилата се използват в състава на офсетова хартия за печат от избелена целулоза от иглолистна и широколистна дървесина в съотношение 1: 1. Хартията е с проклеяна с алкил кетен димер, а като пълнител е използван природен калциев карбонат. Оптичните свойства - L\*, C\*, h\* на получените проби хартия, от цветовото пространство CIE Lab са определени преди и след изкуствено стареене.

В резултат на проведените изследвания се установи, че с двете реактивни багрила са получени проби хартия с подобни цветови нюанси, еднородно оцветяване и стабилен цвят, отличаващи се със стабилност при топло и светлинно стареене



## Dyeing of offset printing paper with new reactive dyes - influence over the paper properties and the ageing

D. A. Todorova, P. M. Miladinova, V. N. Blyahovski

University of Chemical Technology and Metallurgy, 8 Kl. Ohridski, 1756 Sofia, Bulgaria

Received November 16, 2016; Accepted May 8, 2017

According to Smithers Pira, the paper and board demand in the region of Central and East Europe, is expected to increase and not a small part is coloured paper mainly because the increased consumption of corrugated board papers, but also because the increased consumption of specially coloured printing papers, for the new digital technology for the printing and publishing industry. Therefore, dyeing of offset paper is reasonable and the use of reactive dyes would have benefits. The aim of this study was to investigate the influence of three new reactive dyes over the main strength and hydrophobic properties of the coloured offset printing paper and colour stability during ageing.

In the present study were used three reactive dyes, both of them were laboratory synthesized monochlorotriazine reactive orange and red dyes, containing stabilizer fragment and the other was commercial reactive red product of Kemira®. Dyes were used in the composition of offset printing paper with a fibre content of bleached softwood and hardwood pulp. The main strength and hydrophobic properties of the coloured papers were examined. The optical properties and colour stability of the paper samples were also being examined before and after the thermal and light accelerated ageing.

As a result of the studies carried out it was found out that with the three reactive dyes were obtained paper samples with uniform colouring. The obtained papers were with stable colour, distinguished by stability under thermal and light accelerated aging. The sizing of the paper was enhanced and the strength was at the same level.

**Key words:** reactive dyes, offset paper, hydrophobic properties, optical properties, thermal ageing, light ageing

### INTRODUCTION

According to Smithers Pira, the paper and board demand in the region of Central and East Europe, is expected to increase with about 2 million tons during 2014 to 2019 [1]. Not a small part of it is coloured paper mainly because the increased consumption of corrugated board papers, but also because the increased consumption of specially coloured printing papers, for the new digital technology for the printing and publishing industry. Therefore, dyeing of offset paper is reasonable and the use of reactive dyes would have benefits.

Reactive dyes are widely used in the textile industries not only for cotton, but also wool and polyamides, because of their wide variety of color shades, simple dyeing procedure and good stability during washing process and brilliant colors, but they have only limited use in paper production [2,3].

Reactive dyes for cellulose resemble acid dyes in their basic structure, but additionally possess one or more reactive groups. Dyes containing a dichlorotriazinyl reactive group are capable of reacting with cellulosic fiber, in the presence of alkali, to form covalent bond between the dye and

the fibre [4].

Reactive dyes are divided, according to their structure of reactive group, in haloheterocycle and vinyl sulfone based dyes, which react with cellulose through nucleophilic substitution and addition mechanisms, respectively. Commercially, the widest used systems are: vinyl sulfone, monochlorotriazine, bifunctional dyes, difluoro chloropyridine, monofluoro triazine and dichlorotriazine. In addition to reacting with fibre, reactive dyes also react with water (dye hydrolysis) in a form which cannot bound to cotton, but behaves as a substantive dye and affects colour fastness, when is used on fabric. The most important parameter affecting exhaustion and „fixation“ of reactive dyes are temperature, salt and alkali concentration and liquid ratio [4,5].

Reactive dyes require high concentrations of an electrolyte to improve dye-fibre interaction. One approach to improve the fixing ability of the dye is by using a fixative agent (cationic chemical reagent) before adding the reactive dye. [6-9]

Because of the limited use of reactive dyes in the paper dyeing process, there are not so much results about the properties of the paper suspensions, paper white waters and paper properties.

\*) To whom all correspondence should be sent:

E-mail: todorova.dimitrina@uctm.edu

This article is a continuation of our previous work to investigate the influence of new reactive dyes over the properties of the paper suspensions and the white waters from the production of coloured offset printing paper [10,11].

The purpose of this study was to investigate the influence of three new reactive dyes over the main strength and hydrophobic properties of the coloured offset printing paper and colour stability during ageing.

## EXPERIMENTAL

In the current experiment were used three reactive dyes, both of them are laboratory synthesized monochlorotriazine reactive orange and reactive red dyes, containing stabilizer fragment and the other was commercial reactive red product from the Levacell® range of Kemira®.

The used Reactive Dye 2 (RD2) was laboratory synthesized and it is compound of monoazo reactive dyes whose chromophore is an orange acid

dye, prepared by diazotization of the amino C acid and subsequently coupling with I acid in a slightly alkaline medium. Reactive group (chlorine atom) was introduced into the chromophore by reaction of the acid orange dye with cyanuric chloride and the dichlorotriazine reactive dye was obtained. In the subsequent step by a reaction of the last one with 4-amino-2,2,6,6-tetramethylpiperidine or ammonia the monochlorotriazine reactive orange dyes (1) and (2) were obtained.

The tetramethylpiperidine fragment in the molecule acts as a stabilizer fragment and its introduction was done with purpose - increment of the colour fastness to light (photo-stability). It was expected that the paper dyed with this dyes exhibit also an enhanced photo-stability. This assumption was made based on the fact that the dyed fibres (cotton and wool) and chemically coloured polymers showed high photo-stability [12,13]. The reactions of the synthesis are shown on Fig. 1.

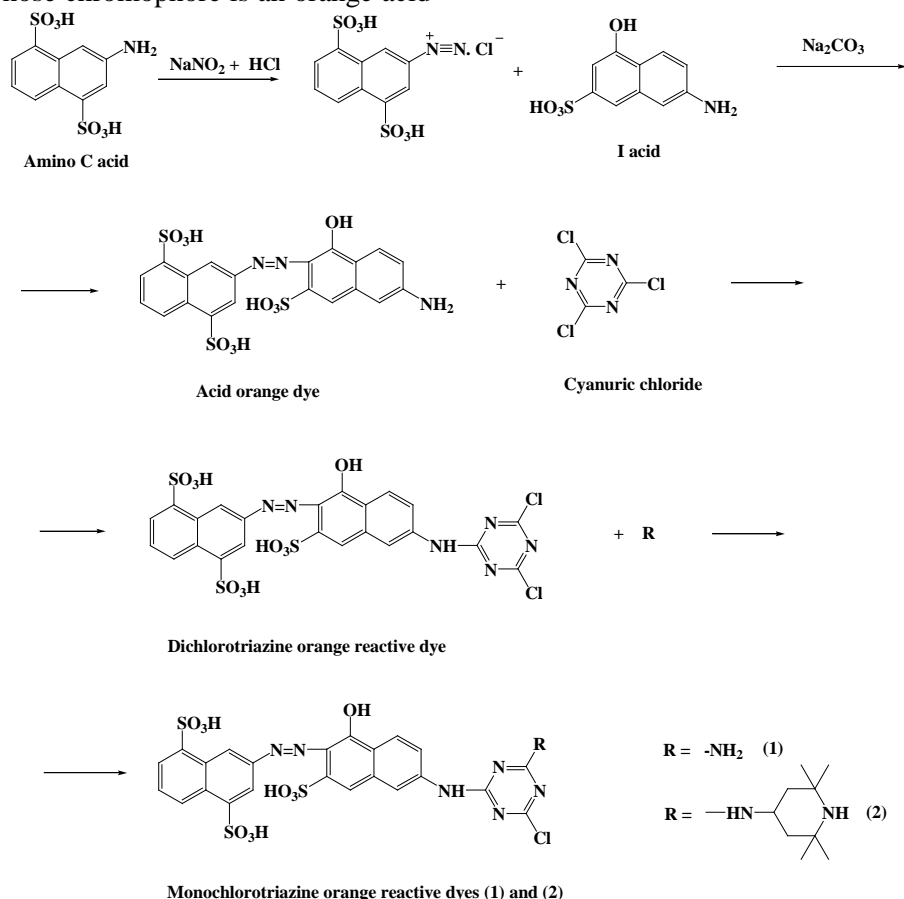


Fig.1 Chemical characteristic of reactive dye 2.

Based on our previous studies [10] conducted with RD1 and RD2, for further research we chose working with RD2.

Reactive Dye 3 (RD3) is commercial reactive red dye from the Levacell® range of Kemira® –

Levacell® Neon Red 2B 05, which is *Azo-reaktivfarbstoff* (azo-reactive dye).

Reactive Dye 4 (RD4) was synthesized similarly to the RD2, where instead of amino C acid and I acid the 2-aminobenzenesulfonic acid and H acid were used (Fig.2).

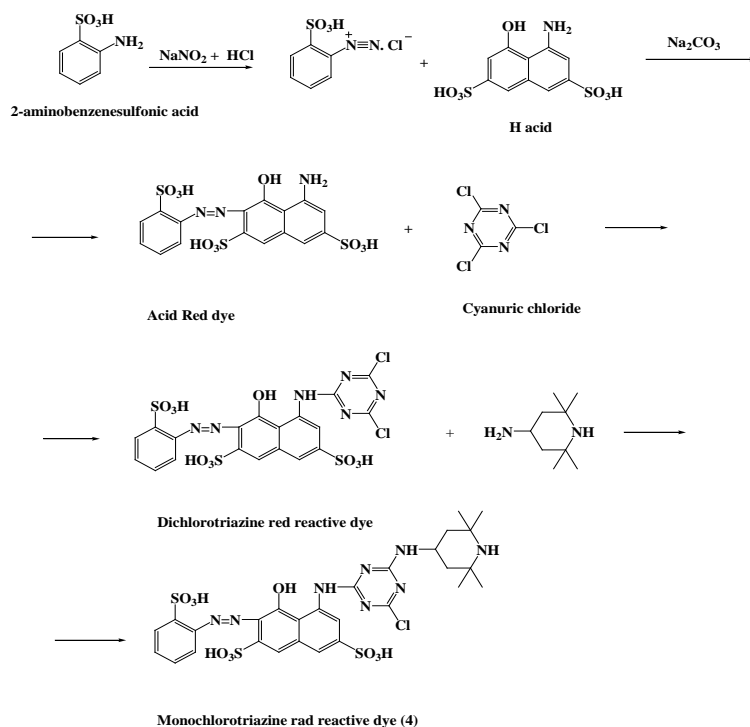


**Fig.2** Synthesis of reactive dye 4.

The consumption of Reactive Dyes in the paper is 0,2%, 0,4%, 0,6% from o.d.f.

The investigations were carried out with laboratory obtained paper samples (70 g/m<sup>2</sup>) from bleached hardwood and softwood pulp in proportion 1:1, with beating degree of 42°SR (Schopper Riegler).

The colour and the wavelength of the dyes are shown on Fig. 3. For fixing the reactive dyes was used cationic polymer fixative on the basis of epichlorhydrin-dimethylamin-copolymer (Levogen E 1063 LQ of Kemira) with a consumption of 1% of o.d.f. The paper was sized with alkyl ketene dimer – 2% of o.d.f (Fennosize KD 157YC of Kemira) and as filler was used ground calcium carbonate – 20% of o.d.f (Hydrocarb V40 of Omya). As a retention additive was used modified polyacrylamide with cationic charge – 0,05% of o.d.f.

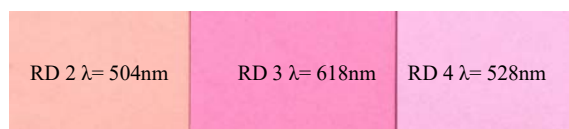


**Fig. 3** Dyed paper samples with the three examined reactive dyes

The obtained paper samples were being examined for its strength properties - the Tensile Index (TI), Nm/g acc. ISO 1924-2:2008 [14], hydrophobic properties – water absorptiveness Cobb<sub>60</sub>, g/m<sup>2</sup> acc. ISO 535:2014 [15], optical properties – colour coordinates L\*, a\* and b\*

before and after the accelerated ageing, by Frank – PTI spectrophotometer / D65<sub>10</sub>.

The thermal ageing was conducted according to ISO 5630-1:2014 [16] at temperature of 105 °C, and duration of 48h.

The light ageing was conducted according to ISO 5630-7:2014 [17], by exposure to light with intensity of 765±75W/m<sup>2</sup> and wavelength of 290-800nm and duration of 48h.

## RESULTS & DISCUSSION

### *Influence of the quantity and type of the reactive dyes, on the properties of the papers*

The parameter Tensile Index (N.m/g), depends primarily on the amount and strength of the bonding forces between the fibres in the finished paper sheet. As it is shown on Fig.4, with adding of reactive dyes, the tensile strength of the paper samples is improved or remained unchanged. It is interesting that RD2 give an enhanced for the tensile index of the paper samples in all three consumptions, and the improvement is with about 2 N.m/g. When adding RD3 the results for this parameter are higher than those with RD2 and RD4. As it is seen from the figure, best result is obtained at 0,4% consumption of RD3. RD 4 give limited effect over the strength properties and just about at 0,4% quantity the parameter is higher that the sample without reactive dye. Probably, with the small consumption of the RD4 the hydrogen bonds between the fibres are less, but after 0,4% dye, the

bonding forces in the paper are also with the participation of the hydroxyl groups from the dye molecule.

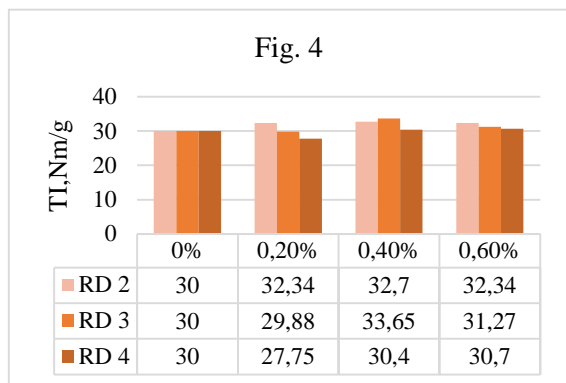


**Fig. 4.** Dependence of Tensile Index (TI) of the paper samples, from the RD type and consumption

On Fig.5 are shown the results for the water absorptiveness  $Cobb_{60}$  ( $g/m^2$ ) of the obtained paper samples. As it is seen from the figure, by adding and increasing the dye consumption, the water absorptiveness decreases, which means that the paper is with higher hydrophobicity. Probably the results are due to the presence of covalent bonds and the less free hydroxyl groups, which can react with the water. Best results are obtained with RD4 even at 0,2% quantity of the dye. According to the positive effect of the reactive dyes, for the water absorptiveness  $Cobb_{60}$ , the dyes can be arranged in the following descending order: RD4 > RD3 > RD2.

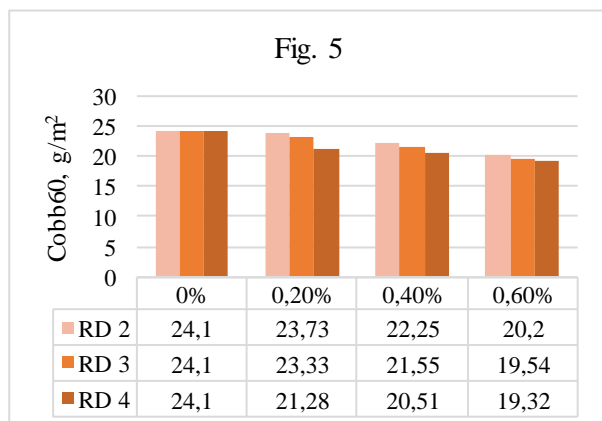


**Fig. 5.** Dependence of water absorptiveness ( $Cobb_{60}$ ,  $g/m^2$ ) of the paper samples, from the RD type and consumption

The water absorption of the paper is one of the most important indicators relating to the good printability of offset papers. Therefore, the effect of the investigated reactive dyes upon water absorptiveness can be considered as a great advantage over the other types of dyes used in the paper industry.

**Influence of the quantity and type of reactive dyes, on the colour stability of the paper samples during accelerated thermal ageing.**

Accelerated ageing of paper is carried out for three major purposes. The first is to establish in a conveniently short time the relative ranking of materials, or physical combination of materials, with respect of their chemical stability or physical durability. The second is to estimate or predict potential long-term serviceability of material systems under expected conditions of use, and the third is to elucidate the chemical reactions involved (the degradation mechanism) and the physical consequences thereof. [18]

It is well known that the main reason for the loss of paper strength, during ageing is the hydrolytic degradation, while for the colour stability is the lignin content.

From different previous publications [19,20] is known, that three days (72h) of accelerated thermal ageing at 105°C is equal to 25 years of natural ageing. In view of the fact, that the received by us paper samples are by bleached cellulose and the thermal aging is most noticeable during the first six hours, we assumed that for the colour parameters longer aging more that 48h is not necessary.

The results for the colour coordinate -  $L^*$ , which expresses the lightness, brightness and the brilliance of the paper, during the accelerated thermal ageing of the paper samples, are presented in Table.1. It is clearly seen that  $L^*$  decreases with adding of the three examined reactive dyes and the biggest difference is in the paper samples dyed with RD 3. The colour parameter variation with time is comparatively low, being most sensitive during the first 24 hours.

**Table 1.** Colour coordinate  $L^*$  during 48h of thermal ageing

Reactive Dye Type	Reactive Dye, %	$L^*$					
		Duration of Thermal Ageing					
		0h	6h	12h	24h	36h	48h
without RD	0%	93,34	92,49	92,93	92,73	92,77	92,67
RD2	0,2%	80,3	80,09	79,6	79,55	79,6	79,65
RD2	0,4%	75,61	75,33	75,26	75	74,95	74,96
RD2	0,6%	72	72,06	71,73	71,73	72,14	72,09
RD3	0,2%	74,87	74,79	74,95	74,9	74,65	74,68
RD3	0,4%	68,81	68,94	68,93	68,82	68,73	68,72
RD3	0,6%	65,02	65,08	64,87	64,95	64,88	64,88
RD4	0,2%	79,71	79,41	79,32	79,34	79,64	79,42
RD4	0,4%	73,79	73,91	73,92	74,1	74	74,2
RD4	0,6%	72,15	72,27	72,30	72,64	73,11	73,24

As regards the influence of the quantity of the dye, it can be said that the variation of this parameter is more sensitive at lower dye consumption. The difference between the lightness of the paper at 0,2% to 0,4% compared to that between 0,4%-0,6% is higher. With increasing consumption of the dyes the parameter changes with smaller variations.

With increasing the dyes consumption and the duration of the thermal ageing, the colour of the paper samples is slightly getting lighter.

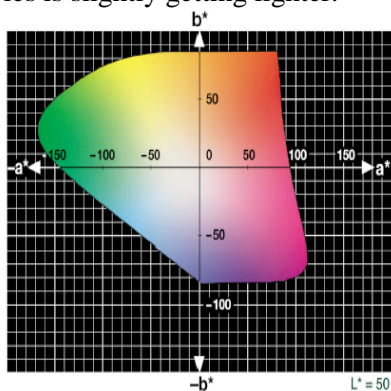


Fig.6 CIE L\*a\*b\* colour space, at L\*=50

With the three examined reactive dyes are obtained paper samples with uniform colouring. If the a\* parameter, in the colour system CIE L\*a\*b\*, is positive the colour is red and if the b\* parameter is also positive the colour is yellow (Fig.6).

The results for the colour coordinates a\* and b\* of the paper samples dyed with the three examined reactive dyes, during the 48h thermal ageing, are presented in Fig. 7, Fig.8 and Fig.9.

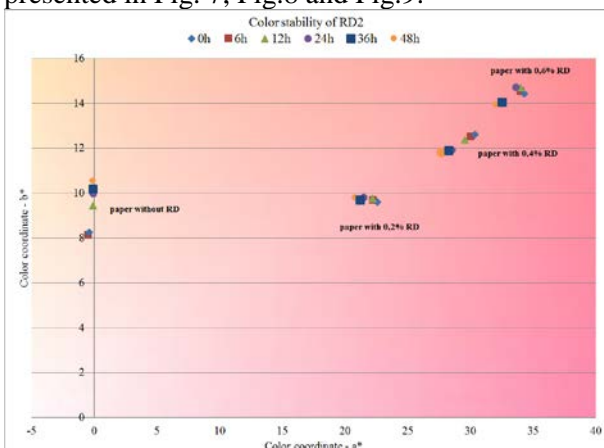


Fig. 7. Color stability, expressed as the a\* and b\* color coordinates of the paper samples dyed with RD2 during the thermal ageing

The general review of the figures shows that the paper samples dyed with RD2 has a substantially different colour from the other two reactive dyes, as both parameters have positive values, hence its colour is red-orange. Reactive dyes 3 and 4 have

negative values of b\*, which means that their colour is in the range of magenta.

From Fig. 7, which represent the stability of the colour paper samples dyed with RD2, it can be seen that the greatest colour change was observed after the first 24 hours of the thermal ageing, and the least is the change in the paper samples at dye consumption of 0.2%. With increasing of the consumption of RD2, the difference in the colour characteristics are increased, as is most apparent at 0.6%. In all three examined reactive dyes, paper becomes darker and the colour shifts to yellow hues. Least change is observed at the low dye quantity.

At RD3 the colour change has a different character than that of RD2 (Fig.8). The points that unsubscribed the chromaticity coordinates of the paper samples with dye consumption of 0.2% are relatively scattered, but with a clear and smooth tendency towards yellowing, while at a rate of 0.6%, are relatively compact, but again with continuous variation. And here, as it is at RD2, the colour of the paper samples is changing to yellow hues. With increasing the dye concentration, the colour stability is increased and the change to yellow hues in the smaller ranges.

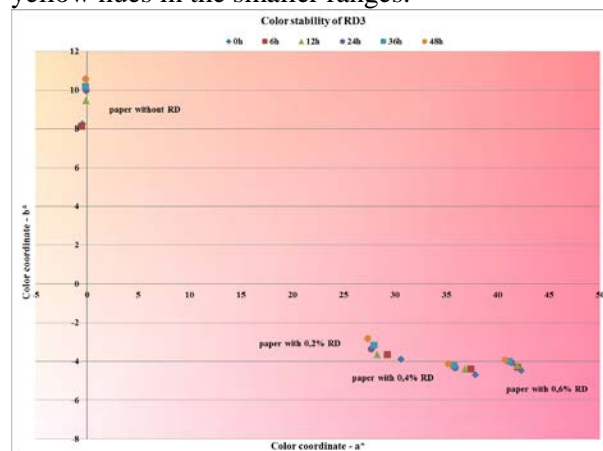
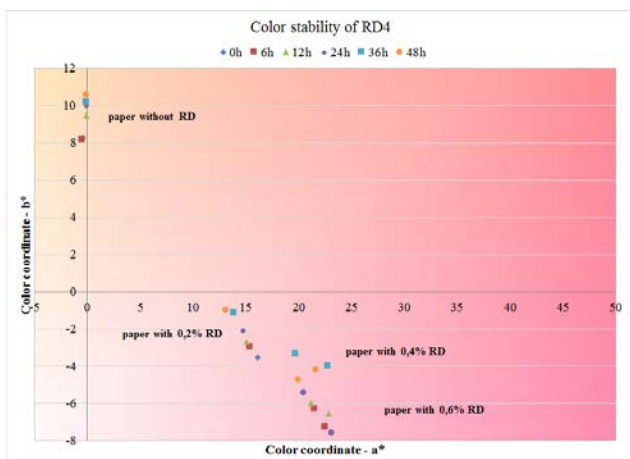


Fig. 8. Colour stability, expressed as the a\* and b\* colour coordinates of the paper samples dyed with RD3 during the thermal ageing

The colour stability of the paper samples, dyed with RD4, during the accelerated thermal ageing is shown on Fig. 9. Regarding the RD4, the results are the most controversial and it is difficult to be defined a clear boundary between the colours of the paper samples at different reactive dye consumption. This is the dye with the lowest colour stability and the greatest change in the direction of yellowing.



**Fig. 9.** Colour stability, expressed as the  $a^*$  and  $b^*$  colour coordinates of the paper samples dyed with RD4 during the thermal ageing

***Influence of the quantity and type of reactive dyes, on the colour parameters of the paper samples during accelerated light ageing***

Light plays an important role in the natural ageing of paper. The effect of light on paper has been reviewed by several authors [13,14] and a lot of experiments had been made during the natural conditions. Experimental results indicate that the mechanisms for aging with pollutants, light and heat are all different from each other and are also fibre dependent [15].

In our experiment the accelerated light ageing is being conducted in apparatus - Ametek Atlas MTS Suntest CPS+Benchtop Xenon Exposure Environment Tester Chamber.

**Table 2.** Colour coordinate  $L^*$  during 48h of light ageing

Reactive Dye Type	Reactive Dye, %	$L^*$					
		Duration of Thermal Ageing					
		0h	6h	12h	24h	36h	48h
without RD	0%	93,34	93,19	93,18	93,32	93,23	93,09
RD2	0,2%	80,3	80,69	80,73	82,58	82,23	84,67
RD2	0,4%	75,61	75,98	75,83	77,41	79,23	81,5
RD2	0,6%	72	72,24	72,43	72,8	74,92	78,89
RD3	0,2%	74,87	74,66	75,32	75,11	75,63	78,35
RD3	0,4%	68,81	68,51	69,52	68,96	69,39	71,54
RD3	0,6%	65,02	64,91	65,01	65,26	65,5	65,51
RD4	0,2%	79,71	79,57	79,88	81,7	81,62	80,7
RD4	0,4%	74,64	74,42	74,86	76,09	76,87	77,33
RD4	0,6%	71,23	71,05	71,43	73,12	73,95	74,41

The results for the colour coordinate -  $L^*$  during the accelerated light ageing of the paper samples, are presented in Table 2. During the light ageing, this parameter is most sensitive. But unfortunately we cannot highlight clear dependence between the dye consumption and the duration of the

light aging. However, it can be said that the paper samples dyed with RD3 are most stable and there is no drastically amending of the lightness. For the other two examined reactive dyes, the colour amending occurs after the 36 hours of light ageing. The values of the parameter  $L^*$  increases, which means that the paper is getting brighter.

The results for the colour parameters of the paper samples, during the accelerated light ageing, are shown on Fig.10, Fig.11 and Fig.12.

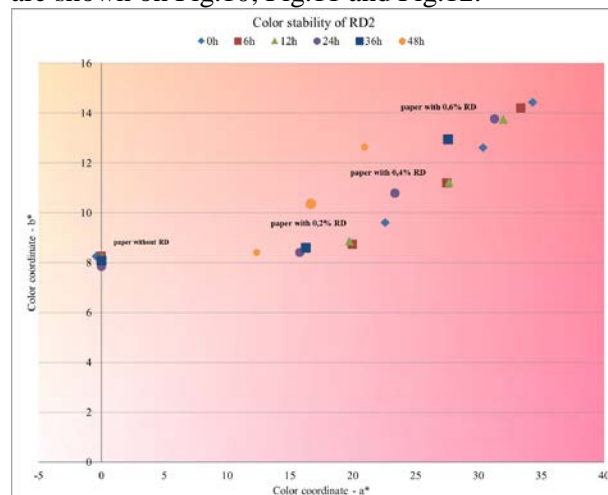


**Fig. 10.** Colour stability, expressed as the  $a^*$  and  $b^*$  colour coordinates of the paper samples dyed with RD2 during the light ageing

From Fig. 10, which represent the stability of the colour paper samples dyed with RD2 it is seen that in this dye the colour change over time is smooth and follows a clear pattern - from left to right, which means that the colour of the paper samples lightens as the greatest change occurred in the first 6 hours of light aging, and between 36<sup>th</sup> and 48<sup>th</sup> hour.

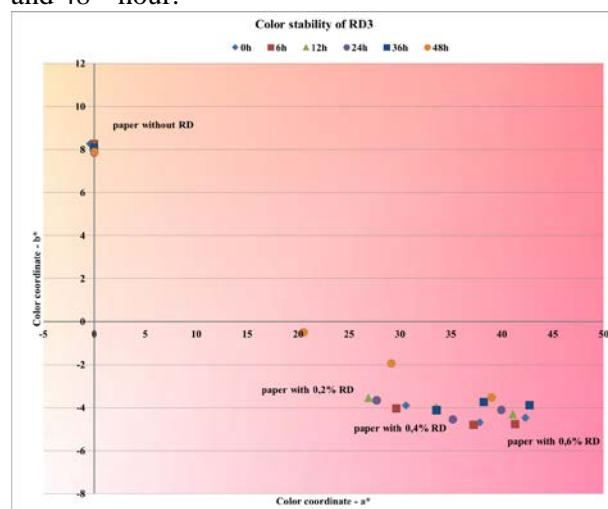


**Fig. 11.** Colour stability, expressed as the  $a^*$  and  $b^*$  colour coordinates of the paper samples dyed with RD3 during the light ageing

The change of the colour parameters  $a^*$  and  $b^*$ , of paper hand-sheets dyed with RD3 are presented

in Fig. 11. As with RD2 here trends in colour changing are again clear and the change is from left to right, but the differences are smaller, probably because the colour is darker and the influence of light is not so intense as in bright shades. The greatest aging was observed at dye consumption of 0,2%. Drastically changes in the colour occurred at the three examined dye quantities after the 36<sup>th</sup> hour of light aging.

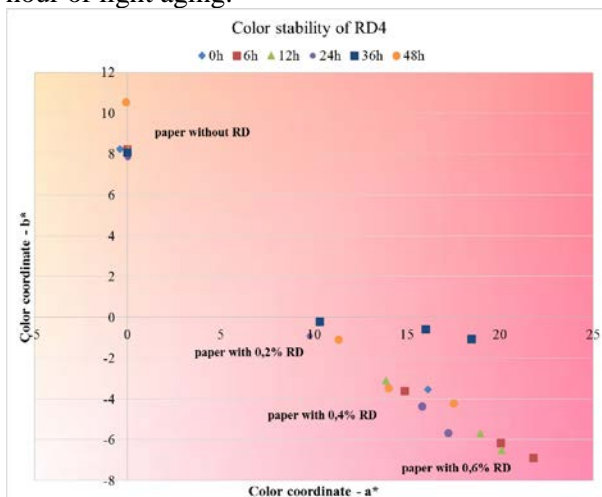


**Fig. 12.** Colour stability, expressed as the a\* and b\* colour coordinates of the paper samples dyed with RD4 during the light ageing

The results for the colour stability of the RD4 during light aging are difficult to be interpret because the colour coordinates of the resulting paper samples are too scattered and cannot define a clear boundary between the individual reactive dye consumptions.

Striking is the fact that unlike RD2 and RD3, even at 36<sup>th</sup> hour of the light ageing the colour of the paper is strongly shifted towards the lighter shades, but the location of the points describing the colour of the paper during the 48 hours run again darkening, which is associated with the burnout of the paper.

During the light aging of the paper samples, the largest variation is observed for the paper samples dyed with RD4. According to the positive effect of the reactive dyes, for the colour stability during light ageing, the dyes can be arranged in the following descending order: RD2 > RD3 > RD4.

## CONCLUSIONS

On the basis of the results of the studies carried out for dyeing wood free neutrally sized paper by three reactive dyes, using cationic polyacrylamide as retention additive and with a view of the complex influence on the properties and colour stability during accelerated ageing the following conclusions can be made:

- With adding of the three examined reactive dyes, the tensile strength of the paper samples is improved or remained unchanged.

- According to the positive effect of the reactive dyes, for the water absorptiveness Cobb<sub>60</sub>, the dyes can be arranged in the following descending order: RD4 > RD3 > RD2.

- The positive effect of the investigated reactive dyes upon water absorptiveness can be considered as a great advantage over the other types of dyes used in the paper industry.

- During the thermal aging, more stable over time is the bright coloured paper samples and the changes are smooth.

- During the accelerated light aging, the changes in the colour are larger and have more variation in the parameters and after the 36-th hour of ageing the paper is burned-out.

- According to the positive effect of the reactive dyes, for the colour stability during thermal and light ageing, the dyes can be arranged in the following descending order: RD2 > RD3 > RD4.

- Both examined laboratory synthesized reactive dyes are suitable for dyeing of offset printing paper.

## REFERENCES

1. <http://www.smitherspira.com>, Paper and Board Market in Central and Eastern Europe to grow by 2% annually from 2013 to 2019, January, (2015)
2. Ali S<sup>1</sup>, Mughal MA<sup>2</sup>, Shoukat U<sup>2</sup>, Baloch MA<sup>2</sup>, Kim SH<sup>3</sup>, Cationic starch (Q-TAC) pre-treatment of cotton fabric: influence on dyeing with reactive dye, *Carbohydr Polym.* 117, (2015), 271-278
3. K.F. Morris, D.M. Lewis, P.J. Broadbent, Society of Dyers and Colourists, *Coloration Technology*, **124**, 186 (2008).
4. H. Tappe, W. Helmling, P. Mischke, K. Rebsamen, U. Reiher, W. Russ, L. Schläfer, P. Vermehren "Reactive Dyes" in *Ullmann's Encyclopedia of Industrial Chemistry*, Wiley-VCH, Weinheim, (2000)
5. K. Venkataraman, *The Chemistry of Synthetic Dyes*, Vol. 7. Academic Press: New York, (1972),
6. A. Tawfik, D.F. Zaki, M.K. Zahran, Degradation of reactive dyes wastewater supplemented with cationic polymer (Organo Pol.) in a down flow hanging sponge (DHS) system, *J. Ind. Eng. Chem.*, **20**, 2059 (2014).
7. I.A. Bhatti, Sh. Adeel, S. Siddique, M. Abbas, *J. Saudi Chem. Soc.*, **18**, 606 (2014).
8. Haiyan Li, Shiyu Liu, Jianhai Zhao, Na Feng, *Colloids & Surfaces A Physicochemical and Engineering Aspects*, , January 2016, 494.
9. K. Chinoune, K. Bentaleb, Z. Bouberka, A. Nadim, U. Maschke, *Appl. Clay Sci.*, **123**, 64 (2016).
10. D. Todorova, P. Miladinova, *Int. Sci. J. Sci.. Business.Soc.*, **Year 1**, 22 (2016).

11. V. Blahovski, D. Todorova, „New reactive dyes for offset paper – influence over the properties of white waters“, XXI international Symposium in the Field of Pulp, Paper, Packaging and Graphics, Proceedings, Zlatibor, 21-24 June, 2016.pp. 59-65.
12. P. Petrova-Miladinova, T. Konstantinova, *J. Univ. Chem. Technol. Metall.*, **39**, 405 (2004).
13. T. Konstantinova, P. Petrova-Miladinova, *Dyes and Pigments*, **67**, 63 (2005).
14. ISO 1924-2:2008 Paper and board -- Determination of tensile properties, International Organization for Standardization, Geneva, Switzerland, (2008)
15. ISO 535:2014. Paper and board -- Determination of water absorptiveness - Cobb method, International Organization for Standardization, Geneva, Switzerland, (2014)
16. ISO 5630-1:2014. Paper and board — Accelerated ageing — Part 1: Dry heat treatment at 105 °C, International Organization for Standardization, Geneva, Switzerland, (2014)
17. ISO 5630-7:2014. Paper and board — Accelerated ageing — Part 7: Exposure to light, International Organization for Standardization, Geneva, Switzerland, (2014)
18. M. Area, H. Cheradame, *BioResources*, **6**, 5307 (2011).
19. X. Zou, T. Uesaka, N. Gurnagul, *Cellulose*, **3**, 243, (1996).
20. X. Zou, T. Uesaka, N. Gurnagul, *Cellulose*, **3**, 269 (1996).
21. B. Havlínová, S. Katuščák, M. Petrovičová, A. Maková, V. Brezová, *J. Cultural Heritage*, **10**, 222 (2009).
22. H. Kipphan, „Hand Book of Print Media“, Heidelberg, Springer, 2001.
23. S. Zervos, A. Moropoulou, *Int. J. Preservation Library & Archival Material*, **27**, 219 (2006).
24. V. Bukovski, *Restaurator*, **21**, 55 (2000).
25. M. Area, H. Cheradame, *BioResources*, **6**, 5307 (2011).

## БАГРЕНЕ НА ОФСЕТОВА ХАРТИЯ ЗА ПЕЧАТ С НОВИ РЕАКТИВНИ БАГРИЛА - ВЛИЯНИЕ ВЪРХУ СВОЙСТВАТА НА ХАРТИЯ И СТАРЕЕНЕТО

Д.А. Тодорова, П.М. Миладинова, В.Н. Бляховски

*Химикотехнологичен и металургичен университет, бул. Климент Охридски №8, София 1756*

Постъпила на 16 ноември, 2016 г.; приета на 18 май, 2017 г.

(Резюме)

Според Смитърс Pira, търсенето на хартия и картон в региона на Централна и Източна Европа се очаква да нарасне и не малка част да е цветна хартия, не само поради увеличеното потребление на вълнообразен картон, но и заради увеличеното потребление на специално оцветени хартии за печат, за новите цифрови технологии и издателската индустрия. Ето защо, багрено на офсетова хартия за печат е разумен подход и използването на реактивни багрила ще има ползи. Целта на това проучване е да се изследва влиянието на три нови реактивни багрила върху основните якостни и хидрофобни свойства на цветни офсетови хартии за печат и цветостабилността им по време на стареенето.

В настоящото изследване се използват три реактивни багрила, като двете от тях са лабораторно синтезиран монохлортриазинови реактивни оранжеви и червени багрила, съдържащ стабилизаторен фрагмент, а другото е реактивно червено багрило, търговски продукт на Kemira®. Багрилата се използват в състава на офсетова хартия за печат от избелена целулоза на иглолистна и широколистна дървесина. Разгледани са основните якостни и хидрофобни свойства на оцветените хартии, техните оптични свойства и стабилност на цвета им преди и след термично и светлинно изкуствено стареене.

В резултат на проведените изследвания се установи, че с трите реактивни багрила се получават хартиени проби с еднородно оцветяване. Получените хартии са със стабилен цвят, отличаващ се със стабилност както при топло, така и при светлинно стареене. Проклейването на хартията се подобрява, а якостта запазва нивото си.



## Overview of security printing types and trends in its future development

T. Bozhkova\*, I. Spiridonov, K. Shterev

University of Chemical Technology and Metallurgy, 1756 Sofia, Bulgaria

Submitted November 30, 2016; Accepted May 8, 2017

In the current research are described various ways to protect secure documents, labels and packages, and the different security printing techniques applied today and the way they will evolve in future.

Security end products constitute a wide variety of different types of documents, packages, labels and cards. The degree to which these need protection from counterfeiters, forgers and terrorists depends upon how deleterious their illegal procurement and misuse is to human welfare and financial stability.

In order to reduce forgery and counterfeiting, the printing industry uses a big range of variable security methods and via different combinations, a high security document is achieved. Security printing devices are often categorized as overt, covert and machine-readable.

Another advantage that the security printer has today is the ability to produce security documents on nontraditional, nonporous substrates such as plastic and polymer - biaxially oriented polypropylene. Due to this complexity in its chemical structure documents and banknotes have a greater abrasion resistance and lower rate of tampering.

**Key words:** security printing, substrates, inks, printing technologies

### INTRODUCTION

Security printing is the field of the printing industry that deals with the printing of items such as banknotes, cheques, passports, tamper-evident labels, product authentication, stock certificates, postage stamps and identity cards. The main goal of security printing is to prevent forgery, tampering, or counterfeiting.

Different types of printing techniques are suited to different applications. Sometimes a heavier weight of ink is needed on the substrate in order for the security feature to work properly. In other instances is needed to use a technique that uses a more delicate approach, so that the detailing in the artwork adds to the security.

In recent days and in an overgrowing market, the industry of Security printing is struggling to bring up new ideas, with more security features and less costs. Vital parts in printing industry play the latest approaches in the field of chemistry. The ability to produce security documents on nontraditional, nonporous substrate such as plastic and polymer is not anymore a futuristic technology, but an adequate solution in several spheres. [1]

### SUBSTRATES IN SECURITY PRINTING

Substrates for printing are mainly paper, polymer and cardboard. Security substrates can be designed and manufactured with special features and considerations to protect documents from counterfeiting or alteration of information (forgery).

**Security fibers.** They are embedded in the upper most layers of the security paper. Usually they can

vary in colors. There are several different types of threads – natural or synthetic materials, and can obtain different spectral features either fluorescent or non-fluorescent. This feature is often used in banknote printing paper (Fig. 1) [1,4].

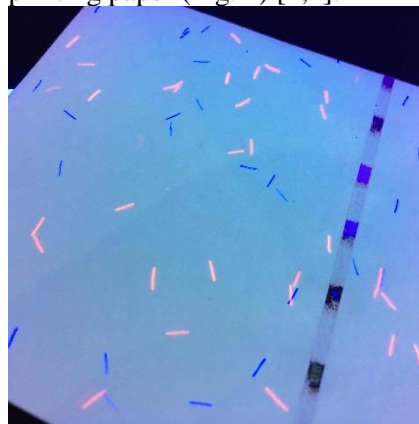


Fig. 1. UV fluorescent threads and hologram thread.

**Security thread:** or also known as hologram thread is an embossed in the paper dark metallic thread, which can contain a micro-text visible by placing the paper to light (Fig 1).[1,4,5]

**Watermark.** A watermark is an identifying image or pattern in paper that appears as various shades of lightness/darkness when viewed by transmitted light (or when viewed by reflected light, atop a dark background), caused by thickness or density variations in the paper.[2] Watermarks have been used on postage stamps, currency, and other government documents to discourage counterfeiting. [5] Watermarks are divided in two types – linear, and halftone watermarks, where as for the halftone watermarks, several levels of

\*) To whom all correspondence should be sent:

E-mail: t.bozhkova@uctm.ed

transparency is observed.

**Planchettes.** Planchettes are tiny paper dots (0.055-in in diameter) that are embedded during papermaking and are not reproducible by scanning, photocopying, or printing (Fig.3). Planchettes can be fluorescent or non-fluorescent.[1]

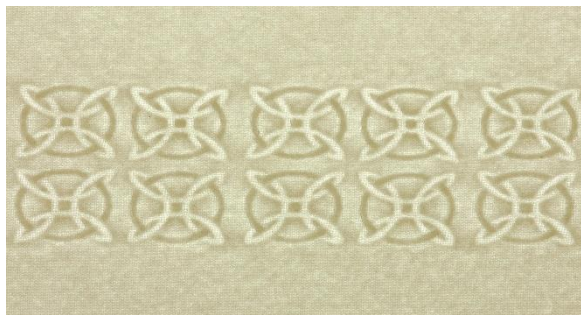


Fig. 2. Watermark.

**Fluorescent planchettes** change color under UV radiation;

**Non-fluorescent planchettes** can be removed from paper surface; resistance to removal provides evidence of counterfeiting.

**Chemically-reactive planchettes** change color upon contact with an alkine solution.

**Thermochromic planchettes** are authenticated through contact with heat, which causes them to

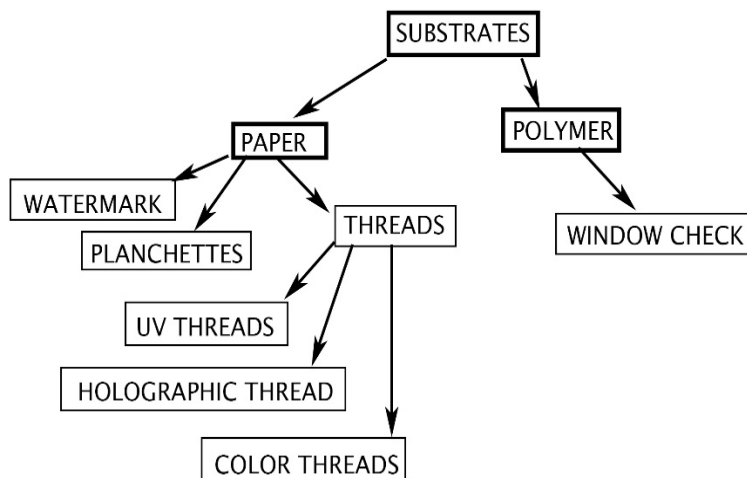
change color. They make it possible to verify a document's authenticity without the aid of special lamps or other tools [1].



Fig. 3. Planchettes.

**Chemically reactive stains:**— the paper is provided with chemically reactive compounds that provide vivid coloration upon application of chemicals used to tamper with documents.[1]

In some specific cases, substrates can be personalized and produced with certain features and unique securities in order to improve the level of protection and to prevent from counterfeiting and forgery. The security features used in substrates are given on Scheme 1.



Scheme 1. Security features in substrates.

Most banknotes are made of heavy paper, almost always from cotton fibres for strength and durability, in some cases linen or speciality coloured or forensic fibres are added to give the paper added individuality and protect against counterfeiting. Some countries, including Nigeria, Romania, Mexico, New Zealand, Israel, Singapore, Malaysia, United Kingdom and Australia, produce polymer (plastic) banknotes, to improve longevity and allow the inclusion of a small transparent window (a few millimeters in size) as a security feature that is difficult to reproduce using common counterfeiting techniques [2,10,11]. Polymer

banknotes are banknotes made from a polymer such as bi-axially oriented polypropylene (BOPP). Polymer banknotes last significantly longer than paper notes, causing a decrease in environmental impact and a reduced cost of production and replacement. In November 2011 Canada joined the list of countries using polymer currency as it began the introduction of a new banknote series.

#### SECURITY INKS

A wide variety of security inks can be used in documents, packages, labels, and cards. In addition to security printing inks, the printer can also use

overprint varnishes and laminates to help deter counterfeiting. It should be noted that many security printing inks depend upon the absorption of UV radiation and its re-emission as visible light. Therefore, to work properly, many security designs and devices must be printed on UV-dead or uncoated paper. On other media they will only work if there are no UV brighteners in the substrates.

**Fluorescent dyes** are dyes which fluoresce under ultraviolet light or other unusual lighting.



Fig. 4. UV fluorescent inks.

**Iridescent inks** contain metallic particles and exhibit a change of color and surface texture when viewed at different angles. They consist of a metallic or pearl-luster type of inks. The iridescent optical variable structures interact with light to give the appearance of fluctuating colors emanating from otherwise colorless matter. Iridescent inks are produced by either Fraunhofer diffraction or Bragg reflectance from multiple thin-film structures that exhibit the desired light-interference patterns [1].

**Photochromic ink.** Photochromic ink changes color when exposed to UV illumination, then reverts to its original color in visible light [1]. Photochromic ink is easy to verify with a UV source or natural sunlight. Inks are available that change from colorless to colored, or that change from one color to another, under UV. This ink is available for waterless offset lithography and flexography.

**Phosphorescent inks:** inks, with compounds that reflect light, after being lit with a certain frequency of light [1].

**Thermochromic ink.** Activated by temperature, thermochromic ink changes from one color to another when exposed to body heat. Documents can be verified by pressing a finger over the ink or by rubbing the printed area by two fingers to trigger the color shift. Inks can change from one color to another or from colorless to a color or the other way around (Fig. 5). Various of colors and

These show up as words, patterns or pictures and may be visible or invisible under normal lighting. This feature is also incorporated into many banknotes and other security documents. Some producers include multi-frequency fluorescence, such that different elements fluoresce under specific frequencies of light. For example there are tri-fluorescent inks that are visible at three different frequencies of the UV light. They are shown in Fig. 4 [1,6,13].

temperatures are available on the market [1,3,9,12].

**Optical variable ink.** The ink changes from one color to another, being observed in a different angle (fig. 6). A common type of optically variable pigment is based on a layered optical interference structure. The interference structure typically has at least one metallic reflecting layer, at least one transparent dielectric layer and at least



Fig. 5. Thermochromic ink.

one semitransparent metal layer. Metals like aluminum, gold, copper or silver are used as the metallic reflecting layer, chemical compounds like magnesium fluoride, silicon dioxide or aluminum oxide are used as the transparent dielectric layer and metals like chromium or nickel are used as the semitransparent metal layer.

Incident white light is partially reflected at the pigment's semitransparent surface layer, and

partially at the underlying metal layer. The difference in optical path between both parts of reflected light results in constructive or destructive interference, depending on the wavelength, i.e. enhances the reflectivity for certain wavelengths and reduces it for others. This spectral discrimination is perceived by the human eye as the appearance of color. For different angles of view, the difference in optical path changes, which makes the layered material exhibit angle-dependent color [6-8].

**Infrared ink:** they become visible, when lit with infra-red light. These inks can react to a certain frequency of light in the IR spectrum.

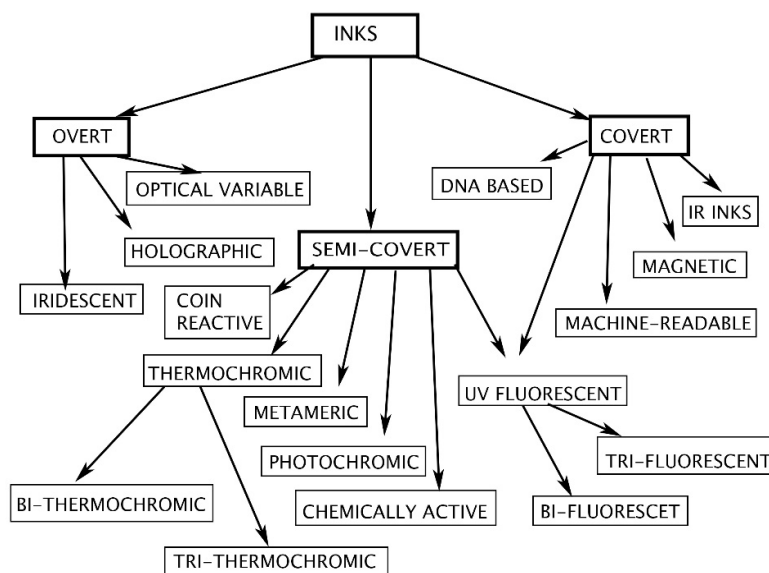
**Machine readable inks** – consist of magnetic pigments. The pigment is dispersed in a binder system or waxy compound and is applied by pressure or by heating to a film – most often polyethylene. Machine-readable inks are used in the

branch of banking security due to their fast processing.[1]

On scheme 2 most of the security inks, divided in three branches: overt, covert, semi-covert can be observed.



Fig. 6. Optically variable inks.



Scheme 2. Security features within inks.

### PREPRESS SECURITY FEATURES FOR EMBEDDING INTO DOCUMENTS

Prepress in security printing plays a vital roll in securing ID cards, passports and other government documents. Designers can apply a vast majority of features, with the help of computer programs, constructed only for the purpose of security printing. A whole departments in each printing house are left to work only over republish.

**Microtext.** Microtext, 15-90 microns high, is usually printed as a repeated alphanumeric message and at normal viewing distance appears to be a a continuous line of some geometric shape. Printers can cleverly design copy with signature lines,

portrait outlines, or pictures with microline text [1].Without a microscope, microtext is difficult to be spotted out. This is an excellent deterrent against counterfeiting documents, currency, and other financial instruments such as checks (Fig. 7) [1,3,9].

**Guilloches patterns.** The guilloche pattern is a unique, nonrepeating spiral design that is carried out to bleed marks, so when the document is trimmed, the lines reach the edge.[1] Using a guilloche pattern as a background can be very effective to protecting a document from counterfeiters (Fig. 8).



Fig. 7. Microtext.



Fig. 8. Guilloches.

**Void pantographs.** Void pantograph is effective against the usual counterfeiter using a photocopier. It is an invisible or barely-visible message hidden in the background of the print. A word such as “photocopy” will appear when the document is being copied. This technique is based on the inability of the copiers to accurately reproduce screen densities of different differing resolutions and dots angles. Unaided eye sees an even color density, unlike the photocopier [1].

**Prismatic color blending.** This technique involves overprinting multiple ink colors to create a third color. When applied to a document, this effect is difficult to match by scanning or copying. At first glance, prismatic color blending looks similar to split-fountain printing. The differences are apparent when two processes are compared under magnification. Prismatic blending requires at least two color printing unites on the press, while split-fountain printing requires one ink unit that is located with multiple ink color separated by a “dam” at the ink rollers [1].

**Digital watermarks.** The digital watermark is a digital image that is embedded in the microstructure of an existing image file, the location and structure of which is known only to the creator of the

original image file [1]. When printed on paper, the watermark becomes a machine-readable feature. A specific software will be needed to see the image.

**Fake watermarks:** faint images of continuous tone or halftone, printed on the back side of a substrate. They imitate a real substrate watermark when observed over transmitted light.

#### SECURITY PRINTING TECHNOLOGIES

Security printing devices are often categorized as either “overt” or “covert”. Overt security devices are integrated into documents and are designed to be easily detectable by the unaided eye under normal daylight or office lighting. Covert devices are usually hidden in the document's design. They can be machine-readable or require special optical aids to be detected and verified.

There are a wide variety of technologies that are used to print materials. The main industrial printing processes are:

**Offset lithographic printing.** This is the most popular and used printing method in all spheres of printing production. The revolution that came with Offset printing has brought a wide variety of possibilities. Not only that it has increased the speed and revolutionized the history of slow and complex printing, but it has played an important roll in security printing as well. One of the advantages over other forms of printing, is high and consistent image quality [3,16].

Offset lithography is a process used for printing on a flat surface, using plates. An image is transferred to an offset plate which is chemically treated so that only image areas (such as type, colors, shapes and other elements) will accept ink [16].

In security printing, offset machines are most suitable for printing in details. It is great for intricate details such as guilloche patterns and security printing artwork. Another option is the split duct printing that gives a unique security mark and can be spotted for unarmed eye. Printing with UV

an IR inks is also a security feature, commonly used in the production of tickets, shares, etc.

**Flexography** (often abbreviated to flexo) is a form of printing process which utilizes a flexible relief plate. It is essentially a modern version of letterpress which can be used for printing on almost any type of substrate, including plastic, metallic films, cellophane, and paper. It is widely used for printing on the non-porous substrates required for various types of food packaging (it is also well suited for printing large areas of solid colour) [3,15].

In security printing, this method is especially good when printing inks such as thermo-chromic or where you need to carry more ink to make the security feature more effective. Unlike offset printing though, flexo is not that detailed and cannot be used for printing micro lines and details.

**Intaglio printing.** Intaglio is a printing technique in which the image is incised into a surface. Normally, copper or zinc plates are used, and the incisions are created by etching or engraving the image, but one may also use mezzotint. In printing, the surface is covered in ink, and then rubbed vigorously with tarlatan cloth or newspaper to remove the ink from the surface, leaving it in the incisions. A damp piece of paper is placed on top, and the plate and paper are run through a printing press that, through pressure, transfers the ink to the paper.

The very sharp printing obtained from the intaglio process is hard to imitate by other means. Intaglio also allows for the creation of latent images which are only visible when the document is viewed at a very shallow angle [3,5,9].

**Screen printing** is a printing technique whereby a mesh is used to transfer ink onto a substrate, except in areas made impermeable to the ink by a blocking stencil. A blade or squeegee is moved across the screen to fill the open mesh apertures with ink, and a reverse stroke then causes the screen to touch the substrate momentarily along a line of contact. This causes the ink to wet the substrate and be pulled out of the mesh apertures as the screen springs back after the blade has passed. [5]

In security printing, screen is very often used for features needing a higher ink thickness. Such security features are optical variable inks and color-

shifting inks.

## CONCLUSIONS

By nature, the security printing industry is a niche marketplace of unique, one-of-a-kind processes, a marketplace that attracts suppliers and manufacturers with specialty and novelty materials, advanced processes, and other enabling technologies outside the realm of general commercial printing.

Future trends in Security Printing are getting on the way with the new nanoprint technologies, printed electronics and revolutionary inventions in digital printing.

These and many more are to become the new security printed features in order to protect the public from illegal activities and bring a more safe and secure future of printed documents.

## REFERENCES

1. R.D. Warner, Introduction to Security Printing, (2005).
2. J. Izdebska, S. Thomas, Printing on Polymers Fundamentals and Applications (2015)
3. <http://www.securityprinting.co.uk/techniques.php>
4. C.J. Biermann, Handbook of Pulping and Papermaking (2 ed.). San Diego, California, USA: Academic Press (1996). p. 171
5. [https://en.wikipedia.org/wiki/Security\\_printing](https://en.wikipedia.org/wiki/Security_printing)
6. R. Richard, UV Printing Comes Alive at Upcoming Print UV Conference, February, 2011, [www.whattheythink.com](http://www.whattheythink.com).
7. E. Nelson, What the Printer Should Know about Ink, GATF Press, Pittsburgh, NPES, 2004.
8. A. Vuarnoz, O. Amrein, P. Veya, Ink composition comprising optically variable pigments, use of the composition, optically variable pigment and method of treating said pigment, (2003)
9. <http://polygrafiamagazine.bg/>
10. [https://en.wikipedia.org/wiki/Polymer\\_banknote](https://en.wikipedia.org/wiki/Polymer_banknote)
11. <https://www.polymersolutions.com/blog/the-state-of-the-art-science-of-polymer-money/>
12. <http://ieeexplore.ieee.org/xpls/icp.jsp?arnumber=6974982>
13. <http://www.tappi.org/content/events/07place/papers/vig.pdf>
14. W.B. Halbrook, Jr., C.L. Langston, Thermal paper with security features US patent 5883043 A (16.03.1999)
15. <http://www.pneac.org/>

## ОБЗОРЕН ПРЕГЛЕД НА ВИДОВЕТЕ ЗАЩИТИ В ЗАЩИТЕНИЯ ПЕЧАТ И ТЕНДЕНЦИИ ЗА БЪДЕЩОТО ИМ РАЗВИТИЕ

Т. Божкова\*, И. Спиридонов, К. Щерев

*Химико-технологичен и металургичен университет, 1756 София, България*

Постъпила на 30 ноември, 2016 г.; приета на 8 май, 2017 г.

(Резюме)

Още една от ключовите промени в индустрията е възможността за печат върху невсмукващи субстрати, като полимери - биаксиално ориентиран полипропилен. Благодарение на тази комплексност в химичните структура на субстратите, документите и банкнотите имат по-голяма износоустойчивост и по-ниска ставка на подправяне. В настоящата разработка е направен обзорен преглед на защитения печат и са описани различните методи и печатни технологии за защита на документи, етикети и опаковки. Разгледано е тяхното приложение и тенденции за бъдещо развитие.

Защитените продукти представляват голямо разнообразие от различни видове ценни книжа и документи. В зависимост от вредите, които фалшифицирането и подмянето могат да нанесат върху благополучието и финансовата стабилност на притежателя им, се определя степента на защита на отделните продукти.

С цел да се намали възможността за подмяне и фалшификация, печатарската индустрия разполага с широк обхват от защитни методи, подбрани в подходящи комбинации, благодарение на които се постигат високо защитени документи. Защитните средства се категоризират като явни, скрити и машиночитаеми.

## New methods of protection during the conservation of books

I. Tzvetanska<sup>1\*</sup>, V.Lasheva<sup>2</sup>

<sup>1</sup>University of Library Studies and Information Technologies

<sup>2</sup>University of Chemical Technology and Metallurgy, 8 Kl. Ohridski, 1756 Sofia, Bulgaria

Submitted December 2, 2016; Accepted June 8, 2017

The libraries storing paper funds are often forced to withdraw from circulation a series of books that have become unusable due to bio-corrosion. Usually destroyed materials are weakened, pigmented paper and crumbling, covered with barnacles, with colorful spots and often with tight glued pages. The species composition of microorganisms that break down the cellulose component of the paper in terms of libraries are not adequately studied and is of interest both in theoretical and in practical terms. In conservation libraries new worldwide environmental technologies are being implemented. For the disinfection of bibliographical and museum cultural heritages are designed especially new specific methods of treatment without toxic substances and chemicals. The method "anoxia" is a non-toxic disinfection by controlled oxygen-free environment and embedded control pest insects, without any risk to the literary heritage of people and the environment. In the method "anoxia" the atmosphere artificially changing, by the removal of oxygen to levels below 0.5%, and is introducing inert gas (nitrogen in most cases). At the same time control the levels of temperature and relative humidity to be maintained within certain parameters for the efficiency of the method. Anoxia eliminate parasites by dehydration and suffocation. The mortality of the pests was 100%, irrespective of their stage of development.

The studies presented in this experiment are the applications of the method "anoxia", which are being carried out in the regional library in Rousse in Bulgaria.

**Key words:** Conservation, books, paper, anoxia

### INTRODUCTION

Preservation of documentary book heritage is a constant challenge for institutions and professionals, responsible for its storage. Efforts are oriented towards identifying agents that cause damage of documents and the application of measures to prevent or combat the attack of these agents. Measures are developed to protect and provide acceptable conditions for storage of documents and ensure their durability.

Creation of microenvironment with oxygen deficiency is a perspective for long-term storage of documents from paper and not only for them. This method is safe, non-toxic and completely inert with respect to the objects to be treated and may delay the degradation and destruction of sensitive and vulnerable documents mainly caused by oxygen, pollutants and inadequate levels of humidity and temperature.

As the most promising non-toxic methods are considered freezing and modified atmosphere with inert gases, carbon dioxide and oxygen absorbers.

The method of anoxia atmosphere / environment without oxygen / is a technique for eradication and control of pests. It consists in removing the oxygen

from enclosed space in which the materials or objects have been isolated for treatment or preventing.

Modified atmosphere anoxia can be made in three versions: with application of CO<sub>2</sub> or inert gas, oxygen absorbers or both processes simultaneously.

The results are dehydration and suffocation of microorganisms and insects no matter in which evolutionary stage of development they are egg, pupa, larva, adult. Nitrogen is often used as an inert gas. It does not kill directly, but prevents the unwanted influence. The anoxia method is applicable to all types of organic / paper, leather, fabric, wood / and inorganic materials. Anoxia method is non-toxic to humans and the environment, and is widespread as a suitable alternative within the concept of protection of collections and cultural heritage. This process requires equipment with high sensitivity and precision control - temperature, humidity, concentration of oxygen and inert gas content.

The purpose of this work is to study feasibility and efficiency of this non-toxic method - anoxia pest control and disinfection, restriction of degradation of documents from biological agents and its implementation in Bulgaria.

\*) To whom all correspondence should be sent:

E-mail: book\_restore@vip.bg



## EXPERIMENTAL

In this work the method of dynamic system anoxia is applied. In this system CO<sub>2</sub> gas and / or inert gases are used for blowing down oxygen from the hermetically sealed space to the oxygen concentration from 0.5 to 0.1%.

In the dynamic system anoxia gas CO<sub>2</sub> is used and the gas flow is controlled by a flow regulator. The most suitable are large reusable cameras. To control the lethal effect the relative humidity, temperature and oxygen levels are constantly monitored by equipment. In cameras can be installed moisturizers and dryers, in order to maintain the natural moisture of the material. Schafer [1] recommends the use of fans inside the large package to avoid formation of gas layers. By air movement the gases are mixed and reach to all levels of materials in the package. According Selwitz and Maekawa [2] CO<sub>2</sub> is effective for insect mortality at a concentration of 60% and 80%. A high accuracy at sealing of packages is not required and fluctuations in the concentration of CO<sub>2</sub> do not affect the effectiveness of treatment. CO<sub>2</sub> is cheaper than N<sub>2</sub>. However, according to Schafer CO<sub>2</sub> at concentration of 100% reduces metabolism of some insects, which leads to a state of latency and does not cause mortality. In addition, if there is moisture in the packing material, removed during the treatment of the exhibits, there is a high risk CO<sub>2</sub> to transform into carbonic acid. This acid will increase the acid content in exhibits causing additional damage of documents on paper, pigments, metal. Therefore, experts should be aware of these consequences and evaluate them before choose a method of processing.

Nitrogen and argon are the most commonly used inert gases. Researches [3,4,5] and publication of Selwitz and Maekawa "Inert gases in pest control in a museum" [2], show 100% mortality under controlled conditions of temperature and relative humidity.

At combinations of temperature, relative humidity and duration of exposure, the results show a complete mortality of the insects after 80 hours at 25 ° C, 75% RH (humidity) and 0.5% of O<sub>2</sub> (99,5% N<sub>2</sub>). Rust and Kennedy [5] report about their in-depth entomological studies of modified system anoxia with nitrogen. They found that using nitrogen in test cameras in which the content of oxygen is strictly controlled below 0.1% only 72 hours at 25° and 55% RH are required for complete destruction of pests of all stages of their development for most types. However, 192 hours / 8 days / have been necessary to achieve the total mortality of the eggs and all forms of *Lasioderma*

*serricorne*. Therefore, minimal exposure of 10 days in 0.1% O<sub>2</sub> containing nitrogen and 25 ° C, 55% humidity is recommended to achieve efficiency of anoxia in museum exhibits.



Researchers and specialists in other institutions [6, 7] reported about success of nitrogen atmosphere in destroying of insects and microorganisms in museum exhibits. Later they made assessments and fulfilled new analyzes using not only nitrogen but also argon. Infected objects were subjected to detailed entomological review. It was found that shorter exposure time is needed for full mortality by argon than by nitrogen.

Figure 1 and Figure 2 show the effect of temperature during exposure / days / needed to achieve complete mortality of insects at 40% RH and a low concentration of O<sub>2</sub> / 0.1% / in a nitrogen and argon atmosphere for the following types: (1) *Hylotrupes bajulus*, (2) *Lasioderma serricorne*, (3) *Anobium punctatum*, (4) *Xestobium rufovillosum*, (5) *Lyctus brunneus*, (6) *Stegobium paniceum*, (7) *Nicobium castaneum*, (8) *Attagenus piceus*.

## RESULTS AND DISCUSSION

The method of dynamic atmosphere anoxia is used in Ruse Regional Library by combination of carbon dioxide and nitrogen and in the National Library of Bulgaria only by nitrogen.

It has been shown that the application of anoxia atmosphere for the treatment and prevention of materials on a protein carrier, when the humidity is in the range 33-40% and the oxygen content is 0.1%. There were no changes in the physicochemical properties of the objects [8].

Argon and nitrogen have proven their effectiveness in the eradication of all forms of life in depriving them of oxygen, leading to anoxia. If the oxygen content of the inert atmosphere is 0.1% argon shows more rapid effectiveness as compared to nitrogen, because it is heavier than nitrogen and more quickly deposits on the objects subjected to anoxia [9].

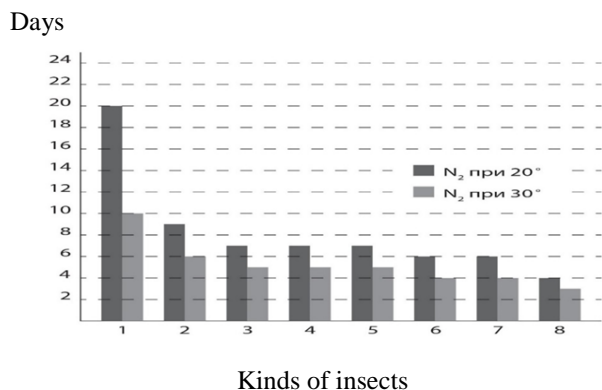


**Figure 1.** Mortality of insects using nitrogen.

The required duration of exposure to this inert environment depends on the types of microorganisms and insects, from their stage of life, oxygen content, and type of inert gas, relative humidity and temperature. According to Selwitz and Maekawa [2] noble inert gas helium can also be effective, but it has a very high rate of diffusion through plastic film and a higher price. According Elert and Maekawa [10], the oxygen concentration must be below 0.3% over a period of 14 days to ensure complete mortality of the insects in all stages /eggs, larvae, pupae and adults/. The temperature inside the system should be about 25-30 C and relative humidity not more than 50%. However, according to Beck [11], the high humidity requires exposure time of 15 to 22 days. According to studies of Elert and Maekawa [10], the species, stage of development and the environmental conditions during the treatments are important factors that must be taken into account in order to achieve a complete liquidation of the microorganisms and insects. According to studies of Selwitz [2], by increasing of temperature the rate of metabolism and oxygen consumption in insects increases, i.e. they consume more oxygen and lose more body fluid, leading to dehydration and death with lower humidity. Another factor is the time of exposure to low concentrations of oxygen. Rust and Kennedy [5] observed mortality at all stages after 192 hours / 8 days / of exposure in an oxygen-free atmosphere at concentration of 0.1% of oxygen, temperature 25,5°C and 55 RH. Elert and Maekawa [10] showed that most microorganisms and insects can be removed after 8 days at oxygen concentration below 0.3%, temperature of 25 ° C and RH 50%. However, these authors recommend a treatment within 14 days under the above mentioned conditions in order to ensure complete destruction. To establish anoxic condition it is desirable to add about 2-3 days safety margin above experimentally proven time of life. However, at temperatures below 25 ° C the processing time

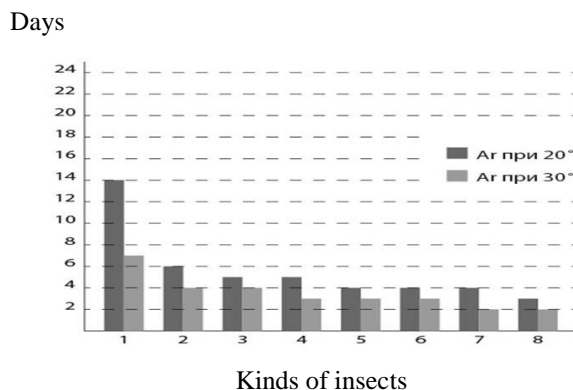


**Figure 2.** Mortality of insects using argon

should be increased, i.e. the treatment will last 22 days at a temperature of 20° C. But the most resistant insects may not be liquidated at 20° C for 22 days [10-14] Therefore, the parameters of temperature, relative humidity and oxygen concentration must strongly comply because the more resistant insects will survive for a longer time under conditions of anoxia.

An extremely important factor for efficient performed anoxia is the camera, etc. balloon or bag, where the materials will be placed for disinfection and treatment. Cameras are made of high barrier plastic or plastic with low oxygen permeability. Originally they were developed for the food industry and pharmacy, so that their products can be transported and stored long-term safe. High barrier materials are made of layers of different plastics such as polyethylene terephthalate RET18; polyvinyl vinylidene, PVDC19; polyamide (nylon) and polyester, joined by co-extrusion.

A new ultra-modern technology for extrusion of material from latest generation of polymers is PET. Its excellent mechanical, thermal and chemical parameters, safety for environment, combined with structural strength, crystalline transparency and gloss make it very valuable for barrier products. Because of its undoubted qualities in comparison with other polymer materials it is recommended by legislation in many European countries. It is necessary these high barrier polymers for anoxia atmosphere to be flexible, transparent and resistant to punctures, not to bend under seal with heat to not compromise the treatment.

## CONCLUSIONS

The microenvironment created by the conditions of anoxia is alternatively proven method for prevention, treatment and long-term storage. Anoxia atmosphere prevents oxidation, biological and microbiological degradation of documents.

Collections of libraries, archives and museums are built from organic materials that are part of diet

of microorganisms and insects so we must take regular preventive measures and treatment of infections if they are identified. It is necessary to know well the agents threatening collections in order to select the most appropriate methods for disinfection and treatment and establish a system for integrated control, adapted to the needs of each institution.

Modified methods atmosphere anoxia show good results in treatment of various kinds of collections, as we found in this study. Its methodology requires knowledge of various procedures, requirements and specific equipment. Through studies and adequate training of staff they can be applied systematically in damaged library collections.

In analysing the methodology of atmosphere anoxia, the key factors that ensure the effectiveness are:

- To maintain the oxygen concentration below 0.3%.
- The exposure time of the microenvironment created by reduced oxygen content.
- To maintain the relative humidity of about 50% inside the hermetic space.

The responsibility to these requirements during the course of treatment will lead to complete liquidation of microorganisms and insects, as above mentioned factors must interact in complete unity.

#### REFERENCES

1. S.Schäfer, Desinfestação com métodos alternativos, atóxicos e Manejo Integrado de Pragas (MIP) em museus, arquivos e acervos & Armazenamento de objetos em atmosfera modificada. Associação Brasileira de Encadernação e Restauro, São Paulo, 2002.
2. Ch. Selwitz, Sh. Maekawa, Inert gases in the control of museum insect pests. Los Angeles: The Getty Conservation Institute (1998).
3. N.Valentin, Fr. Preusser, Controle de insetos por meio de gases inertes em arquivos e bibliotecas. Emergências com pragas em arquivos e bibliotecas. Projeto CPBA. Rio de Janeiro: Arquivo Nacional, (2001).
4. M. Gilberg, *Studies in Conservation*, **36**, 93 (1991).
5. M. Rust, J. Kennedy. The Feasibility of Using Modified Atmospheres to Control Insect Pests in Museums. Marina del Rey, Calif.: Getty Conservation Institute. (1993)
6. G.Hanlon, V. Daniel, N.Ravenel, S. Maekawa, Dynamic system for nitrogen anoxia of a large museum objects: A pest eradication case study. In Proc.2nd Int. Conference on Biodeterioration of Cultural Property, October 5-8, 1992, ed. K. Toishi, H Arai and K. Yamano, 86-90. Tokyo: International Communications Specialists, (1992).
7. R. Koestler, Practical application of nitrogen and argon fumigation procedures for insect control in museum objects. In Proc. 2nd Int. Conference on Biodeterioration of Cultural Property, October 5-8, 1992, ed. K. Toishi, H Arai and K. Yamano, 94-96. Tokyo: International Communications Specialists, (1992).
8. E. Hansen, S. Lee, H. Sobel, *J. Amer. Inst. Conservation*, **31**, 325 (1992).
9. S. Maekawa, F. Preusser, F. Lambert, A hermetically sealed case for the display and storage of mummified objects in a stable inert atmosphere. International congress Tenerife, Spain: Museo Arqueologico de Tenerife. (1992)
10. K., Elert, S. Maekawa, The Use of Oxygen-Free Environments in the Control of Museum Insect Pests. Los Angeles: The Getty Conservation Institute, (2003).
11. I. Beck, (Coord.); trad. Elizabeth Larkin Nascimento e Francisco de C. Azevedo. Rio de Janeiro: Projeto Conservação Preventiva em Bibliotecas e Arquivos/ Arquivo Nacional, (2001).

## НОВИ МЕТОДИ ЗА ЗАЩИТА ОТ БИОФАКТОРИ ПРИ КОНСЕРВАЦИЯ НА КНИГИ

Искра Цветанска<sup>1</sup>, Веска Лашева<sup>2</sup>

<sup>1</sup>Университет по библиотекознание и информационни технологии, София, България  
<sup>2</sup>Химикотехнологичен и металургичен университет, бул. Климент Охридски 8, 1756 София, България

Постъпила на 2 декември, 2016 г.; приета на 8 юни, 2017 г.

(Резюме)

При консервация на библиотечни фондове се прилагат нови световни екологични технологии. За дезинфекция на библиографични и музейни културни наследства специално са разработени нови методи на третиране без токсични субстанции и химикали. Методът „Аноксия“ представлява нетоксична дезинфекция, посредством контролирана безкислородна среда и внедрен контрол на нашествия от насекоми, без никакъв риск за книжовното културно наследство, за хората и околната среда. При метода Аноксия изкуствено се променя на атмосферата, чрез премахването на кислорода до нива под 0,5 % и въвеждане на инертен газ / в повечето случаи азот/. В същото време се контролират нивата на температурата и относителната влажност, които се поддържат в определени параметри за ефективност на метода. Аноксията елиминира паразитите, чрез дехидратация и задушаване. Смъртността на вредителите е 100%, независимо от техния стадий на развитие. В настоящата разработка е представено приложението на метода „Аноксия“ в България в регионалната библиотека в Русе.

## Conservation and restoration of documents from the National Historical Museum fund by appropriate methods

R.T.Cenkova, V. Lasheva\*

*University of Chemical Technology and Metallurgy, 8 Kl. Ohridski, 1756 Sofia, Bulgaria*

Submitted December 1, 2016; Accepted November 14, 2017

Libraries and museums keep in their funds millions of written pages that contain the wealth of Bulgarian cultural and scientific heritage. The conservation and restoration of written materials is associated with preservation, rehabilitation and bringing objects to their original overall condition. To apply the restorative processes it is necessary to have a knowledge of the essential changes of the materials forming written cultural monuments under their long-term preservation, to suspend destructive factors causing accelerated aging of the paper and the inks, and to develop reliable restoration methods. Each object received for restoration and conservation has its own specific value: historical, technical and artistic. The primary task of restoration and conservation of written documents is not only mechanical adhesion of the detached places of separate pages and restoration of missing parts of the documents with new material but also stabilization of material basis of the paper, manuscript or document and termination of further destructive processes aiming their preservation for a maximum possible period of time. The purpose of this work is the study and application of appropriate methods of restoration and conservation of documents. Presented are various documents restored in the laboratory of conservation and restoration at the National Museum of History.

**Key words:** conservation, restoration, paper, documents

### INTRODUCTION

Libraries and museums keep in their funds millions of written pages that contain the wealth of Bulgarian cultural and scientific heritage. The conservation and restoration of written materials is associated with preservation, rehabilitation and bringing objects to their original overall condition.[1] To apply the restorative processes it is necessary to have a knowledge of the essential changes of the materials forming written cultural monuments under their long-term preservation, to suspend destructive factors causing accelerated aging of the paper and the inks, and to develop reliable restoration methods. Each object received for restoration and conservation has its own specific value: historical, technical and artistic.[2,3] The primary task of restoration and conservation of written documents is not only mechanical adhesion of the detached places of separate pages and restoration of missing parts of the documents with new material but also stabilization of material basis of the paper, manuscript or document and termination of further destructive processes aiming their preservation for a maximum possible period of time.[4,5]

In enrichment exposure National Historical Museum, and in the preparation of exhibitions in the studio for restoration and conservation of paper do various monuments such as books, maps, engravings, documents, posters, newspapers,

photographs and more.

This work aims to study and application of appropriate methods of restoration and conservation of certain documents. Thus they are saved, restored, or close to its original state by removing or isolating harmful factors.

### EXPERIMENTAL

The processes of conservation and restoration comprise of both traditional methods of restoration and some new ones, which were introduced in the laboratory practice, name [6,7].

**1. Use of Gore-tex.** Gore-Tex-producing Lascaux Restauro A.Diethelm AG CH-830 Bruttisellen was used for cleaning in the process of restoration and conservation. This is a porous material, which transmits solution in one direction.

**2. Modification process of duplication.** In the experimental work was changed technology of duplication of fragile, crumbling exhibits that need further strengthening was modified in the laboratory. Initially adhesive has been applied on the new basis, then the object has been placed and the restorer with hands or with a roll works on the front of the exhibit to the full application of the adhesive. It was found that in many cases during this operation a fragment of the exhibit might accidentally break away or to become a rupture, which could create additional difficulties to restorer and with extremely fragile objects - even losses. Therefore, when using the technique of doubling,

---

\*) To whom all correspondence should be sent:

E-mail: vesla@uctm.edu

an adhesive layer is applied evenly on the new basis and the object to be restored is placed on it. Then a sheet of melinex is placed and the adhesive layer is evenly spread using a special Japanese brush. Thus avoiding the possibility of direct contact with the exhibit and reducing the likelihood of the formation of blowholes

Three objects for restoration are presented. All exhibits were placed in a chamber with thymol steams for disinfection, mechanically cleaned with soft rubber, scalpel and brush.

### RESULTS AND DISCUSSIONS

Presented are 3 site restoration fund of the National Historical Museum:

- Handwritten prayer book from the 19th century
- Book "Greater Hungary" 1941.
- Photography - Stefan Macedonia in the role of Samson from "Samson and Delilah".

The exhibits were initially placed in a chamber with thymol steams-for disinfection were then mechanically cleaned with soft rubber scalpel and brush. Before the beginning of the restoration procedures the exhibits are photographed.

A Handwritten Prayer book from 19th century before restoration procedures is illustrated on photo 1.



**Photo 1.** Handwritten prayer book before restoration

The Prayer-book was cleaned by gore-tex and various solvents - ethyl alcohol, toluene, ether and others. The Prayer-book was cleaned by gore-tex and various solvents - ethyl alcohol, toluene, ether

and others. Strengthening of the paper was done with low percentage solution of pure cellulose. All missing parts were filled and the torn areas were strengthened with appropriate Japanese paper and adhesive. Finally, the individual sheets were placed under press, face in sequence and stitch.

A Handwritten Prayer book from 19th century after restoration procedures is illustrated on photo2



**Photo 2.** Handwritten prayer book after restoration

Conservation and restoration procedures are performed on the book "The Great Hungary" from 1941. The book is torn pages and cover. For restoration and skills are used to attach each of its pages to the book block by a suitable adhesive and Japanese paper. Fenced areas are fragmented.

The condition of the book before restoration is illustrated on photo 3.

The following stages of work under the classical (manual) method of conservation and restoration are applied:

- photo shooting and visual inspection is done. Prepare a conservation-restoration work plan
- disinfection in chamber with thymol steams.
- mechanical cleaning.
- check for solubility of the inks.
- procedures for the cleaning of polluted areas, treatment with various solvents, washing with water and subsequent drying between filter papers.
- strengthening of paper and filling the missing parts with the appropriate Japanese paper with the necessary density and hue.

- if necessary - duplication on a thin micalet paper with appropriate adhesive.
- taking a picture of the restored object.
- placing under press for further smoothening of the folded sections.



**Photo 3.** Book "Greater Hungary" before restoration.

The results achieved are visible on the attached pictures of the objects after the restoration-photo 4.



**Photo 4.** Book "Greater Hungary" after restoration.

The fund of National Historical Museum is preserved Photography - Stephen Macedonia in the role of Samson from "Samson and Delilah" - Photo 5. The photography was in a relatively good condition, but it was necessary to be cleaned and reinforced. It was pretty dusty from the front side and the passepartout was faded. There were traces of glue on the back side on the passepartout. A careful treatment with bleaching reagents was required for the bleaching. That is why the photography was carefully cleaned from its front and back sides with a scalpel, rubber and brush. The front side was treated with cotton swabs dipped

in pure ethyl alcohol. After this treatment the image became much clearer. The passepartout was also cleaned – treated with bleaching reagents - photo 6.

The fund of National Historical Museum is preserved Photography - Stephen Macedonia in the role of Samson from "Samson and Delilah" - Photo 5. The photography was in a relatively good condition, but it was necessary to be cleaned and reinforced.

It was pretty dusty from the front side and the passepartout was faded. There were traces of glue on the back side on the passepartout. A careful treatment with bleaching reagents was required for the bleaching. That is why the photography was carefully cleaned from its front and back sides with a scalpel, rubber and brush. The front side was treated with cotton swabs dipped in pure ethyl alcohol. After this treatment the image became much clearer. The passepartout was also cleaned – treated with bleaching reagents.



**Photo 5.** Photography - Stefan Macedonsky in the role of Samson from "Samson and Delilah" before restoration.



**Photo 6.** Photography - Stefan Macedonsky in the role of Samson from "Samson and Delilah" after restoration.

The results achieved are visible on the attached pictures of the objects after the restoration, namely:

**Object 1** - filled and reinforced missing parts, bleached contaminated areas, straightened and sewn up sheets.

**Object 2** – the pages are cleaned from stains of different origins, straightened, arranged and fixed.

**Object 3** – the paspartout is cleaned and bleached, the photography is acquired greater contrast and clarity after the cleaning.

The templates, processed by this method meet the basic requirements for durability, safety and reversibility, but the method itself is very slow, low-productive and labor-intensive.

### CONCLUSION

The paper as basis of valuable documents and exhibits is exposed to the effects of time, place of storage, moisture, bacteria, insects, molds and others. Its preservation and protection of all these adverse effects is a major task of its restoration and conservation in order to be preserved a maximum long period of time.

Covered by those major objectives are the numerous of restorations performed by restorers of National Historical Museum of dozens of exhibits and a variety of individuals and institutions. Each case is approached individually, according to the nature of the destruction of the paper, the cover - i.e. the object of restoration.

The common among them all is that the restoration process transparent materials are used Japanese or mica paper, silk veils, adhesives

and stabilizers of the paper, which in most cases ensure the durability of the document.

The basic requirements for the selection of methods for restoration of one or other written material, no matter how individual are for each, comply with the requirement their original form not to be changed, as well as the processes to be reversible. This means that, if necessary, they can get their original form.

Particularly important element of the restoration work is the chemicals and reagents that are used to be harmless for the paper and people.

Furthermore the specialists continuously explore and apply other more modern and more efficient working methods as well as new materials and techniques for restoration of the paper.

### REFERENCES

1. D. Saykova, Basic Methods of Conservation and Restoration of Paper, Sofia (1990).
2. I. Cvetkova, R. Vulkova, *Proc. National Museum of History*, **13**, Sofia (2002).
3. A. Goryaeva, S. Hazova, Methods of Restoration in Restoration Centers in Germany (2009).
4. S.Dobrusina, E. Chernin, Conservation Documents: Science and Practice, St. Petersburg(2013).
5. S.Dobrusina, Stabilization Documents, Moscow (2014).
6. S. Fairbrass, The Institute of Paper Conservation (1992).
7. Dr. N. Pickwood, The paper conservator-Journal of the Institute of Paper Conservator, **11** (1987).

## КОНСЕРВАЦИЯ И РЕСТАВРАЦИЯ НА ДОКУМЕНТИ ЧРЕЗ ПОДХОДЯЩИ МЕТОДИ ОТ ФОНДА НА НАЦИОНАЛНИЯ ИСТОРИЧЕСКИ МУЗЕЙ

Р. Ценкова, В.Лашева

*Химикотехнологичен и металургичен университет, 1756 София, България*

Постъпила на 1 декември, 2016 г.; приета на 14 ноември, 2017 г.

(Резюме)

Библиотеки и музеи съхраняват във фондовете си милиони изписани страници, съдържащи богатството на българската културна и научна мисъл. Консервацията и реставрацията на писмените материали е свързана със запазване, възстановяване и доближаване на обектите до първоначалното им цялостно състояние. За да се приложат възстановителните процеси, е необходимо да се познават същностните изменения на материалите, изграждащи писмените паметници на културата при дълготрайното им съхранение, да се преустанови действието на разрушителните фактори, предизвикващи ускорено стареене на хартията и мастилата и да се разкрият надеждни методи за тяхното възстановяване. Всеки постъпващ обект за реставрация и консервация има своя специфична ценност и особеност - историческа, техническа и художествена. Първостепенна задача на реставрацията и консервацията на писмени документи в такъв случай не е само механичното залепване на разкъсаните места на отделни страници и възстановяване на липсващите части от документите с нов материал, а стабилизация на материалната основа на книгата, ръкописа или документа и прекратяване на по-нататъшните разрушителни процеси с цел запазването им за максимално дълъг срок от време. Целта на настоящата работа е изследване и прилагане на подходящи методи за реставрация и консервация на документи. Представени са различни документи реставрирани в Лабораторията по консервация и реставрация при Националния исторически музей.

## Study the possibilities of using silver nanoparticles in packaging paper

D.A. Todorova\*, V.G. Lasheva

University of Chemical Technology and Metallurgy, 8 Kl. Ohridski, 1756 Sofia, Bulgaria

Submitted December 12, 2016; Accepted May 23, 2017

Nanotechnology offers an enormous opportunity for innovations in food packaging, which can benefit both, the consumers and the industry. The application of nanotechnology shows significant advantages for improving the quality of packaging materials. Innovations related with the use of nanotechnology in food packaging and quality control is a core focus in the modern food industry. The packaging can be made to be "smart", which means that it can ensure the conditions of a safe environment or to send a signal to the user of pollution and pathogens. Silver nanoparticles have become the dependable antimicrobial material with a variety of applications. Packaging materials with nanoparticles of silver or related cationic silver nanocomposites, provide a possibility for effective and safe antimicrobial packaging.

In the present study are examined the opportunities for using silver nanoparticles in the composition of packaging paper. The physic-mechanical properties of laboratory obtained packaging papers, with and without silver nanoparticles, are been examined. Microbiological tests of the paper samples are also been made. The obtained results show bacteriostatic effect of silver nanoparticles over the packaging paper properties.

**Key words:** nanoparticles, silver particles, packaging paper, antimicrobial properties, physic-mechanical properties

### INTRODUCTION

The application of nanotechnology shows significant advantages for improving the quality of packaging materials. Innovation related to the use of nanotechnology in food packaging and quality control is the main focus in the modern food industry. The silver nanoparticles can be relatively uniformly distributed in a matrix of other materials such as pulp, plastics, and others and thus be more effective at killing bacteria and fungi. Packaging materials with nanoparticles of silver, or cationic release of their contents.

associated silver nanocomposites allow to create effective and safe antimicrobial packaging. Similar technology is used in many countries for the production of containers for food storage.

In terms of nanotechnology, the selected key technologies with significant quality and food safety are:

- Nano-encapsulation of biologically active substances (amino acids, vitamins, peptides, proteins, antioxidants, etc.) with the purpose of controlled

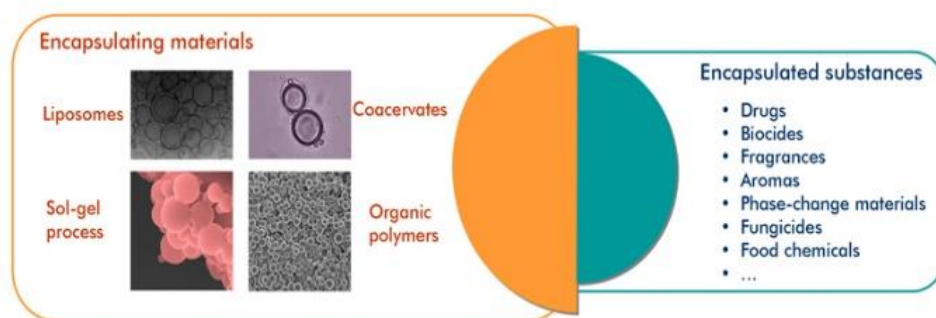


Fig.1. Encapsulation process.

The process is carried out as a fraction of the active substance is surrounded by an encapsulating agent with dimensions of micro and nano particles, thereby isolating the substance from the external environment.

Nano and microsensors are used to detect toxins, pathogenic microorganisms, pesticides,

contaminants and residues of antibiotics in food products throughout their production cycle and storage in the distribution network.

A device based on optical fluorescence biosensors is provided. Each nanoparticle contains thousands of molecules which are suitable to be attached to each bacterium. When antibodies and antigens react efficiently the fluorescent signal

\*) To whom all correspondence should be sent:

E-mail: todorova.dimitrina@uctm.edu



amplified by allowing the bacterial concentration can be readily determined using a fluorescence microscope and spectrum-fluorescence analysis [1-5].

The most popular method for the synthesis of silver nanoparticles is the chemical reduction of silver salts in aqueous solutions in the presence of a stabilizer.

The purpose of this work was to explore the possibilities to obtaining silver nanoparticles using ultrasound and to include them in the composition of wrapping paper. Microbiological tests of the wrapping paper samples were conducted and the physical and mechanical properties with and without silver nanoparticles were studied.

## **MATERIALS AND METHODS**

The silver nanoparticles can be synthesized using a variety of techniques. These include high temperature and a method (such as plasma, for example by formation of films) which are expensive and complicated for realization. The most commonly used methods which allows synthesis at moderate temperature are associated with the chemical reduction of silver ions in water [6-8] or in organic [9,10] solutions.

Because of its low cost and easy implementation, as well as in laboratory and in industrial conditions, the method for the synthesis of silver nanoparticles by means of ultrasound field represents an interesting alternative in comparison with the other known methods.

As a precursor has been used silver nitrate ( $\text{AgNO}_3$ ), as a reducing agent - ethyl alcohol (96%) and ammonia solution 25% as stabilizer.

For obtaining the solutions containing silver nanoparticles the following experimental work has been carried out :

Silver nitrate was dissolved in distilled water at room temperature using a magnetic stirrer. Consecutively has been added ethyl alcohol and ammonia solution. The flask has been placed in an ultrasonic bath with thermostatically controlled temperature, while the color of the solution had been changed from transparent to light yellow or dark yellow. The yellow colour of the solution is a certain sign of the presence of silver nanoparticles.

The effect of time of exposure of ultrasound, the working volume, the concentration of silver nitrate, ammonia and ethanol over the resulting nanoparticles has been investigated. The resulting solutions has been analyzed by atomic-absorption analysis.

The measurements by fluorescence microscopy shows the presence of a very small amount of

aggregated particles with sizes up to several microns. The obtained suspensions has been added into the pulp suspension, in order to obtain wrapping paper samples. They has been subjected to a microbiological and mechanical measurement.

## **RESULTS AND DISCUSSION**

The process of preparing silver nanoparticles through chemical reduction requires the use of various substances performing specific functions. A reducing stabilizing agents are necessarily to be presented into the solution and sometimes also agents to accelerate the process. As a precursor of the silver is selected silver nitrate -  $\text{AgNO}_3$ , as it is relatively inexpensive (compared to other silver compounds or pure silver), widely used, especially for the synthesis of silver nanoparticles by chemical reduction and shows satisfactory results.

The reducing agent influences the size and distribution of the nanoparticles in the suspensions. The absence of a reducing agent in the system limits the yield of nucleus and their further growth due to low concentration or absence of silver atoms. As reducing agents in synthesis of silver nanoparticles are used most commonly ammonia [11] (Fig.2), ethanol [12] as well as sodium citrate [13].

The stabilizing agent is involved in the process by stopping the growth of the nanoparticles, which starts after the formation of germs, but also prevents the agglomeration and precipitation of already formed nanoparticles [8,9]. Ammonium hydroxide has been preferred by us as a stabilizer as it is significantly cheaper.

The accelerate agents, are intended to increase the rate of the reaction when it is too slow. Various salts are used mainly as an accelerate agents in the synthesis of silver nanoparticles. When using silver nitrate as raw material these salts act as catalysts participating in the process of formation of silver ions. When the process of synthesis is exposed to the external field (for example microwaves or ultrasound), it is usually necessary to use an accelerator, since its effect is weaker than that of the field.

The ultrasonic field may affect the mechanism of formation of nanoparticles due to the presumably activating this process thermally, and also it increases the speed of the particles, atoms and ions, as well as collisions between them.

The operating parameters, influencing on the process, the quantity and quality of the obtained silver nanoparticles are the following:

- The water temperature in the ultrasonic bath (40 °C or 50 °C);

- The amount of distilled water (50 ml; 100 ml or 200 ml);
- The concentration of silver nitrate solution;
- Concentration of  $\text{NH}_3\text{OH}$  (25%) in the solution;
- The concentration of ethyl alcohol (96%) in the solution.

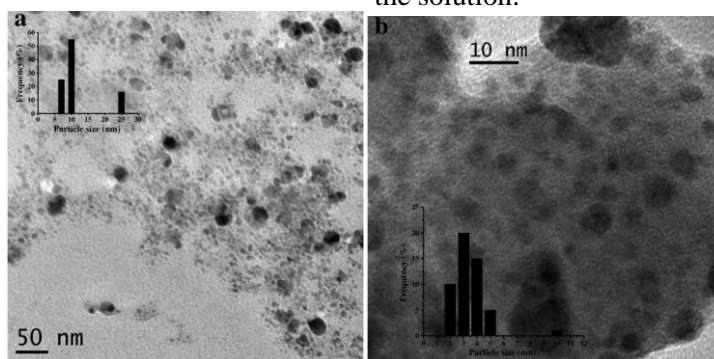


**Fig.2** Transmission electron microscopy of silver nano-particles, prepared by reduction of silver nitrate and a stabilizing agent (a) and sodium borohydride (b) sodium citrate [11].

**Table 1.** Results of the atomic absorption spectrometry

Sample	$\text{AgNO}_3$ concentration in the solution before the synthesis, $\text{mg/l}$	Concentration of unbound silver after AAS analysis, $\text{mg/l}$	Converted silver, %
1.	1700	1110	65
2.	1700	770	45
3.	1700	790	46
4.	1700	1140	67



**Fig.3.** Different colors of suspensions prepared under different operating parameters. a) A solution, which does not change color or pale yellow suspensions; b) suspensions with dark yellow or black colour.

The resulting suspensions were analyzed using Atomic Absorption Spectrometry (AAS) and the results are represented in Table 1.

Between 45 and 65% of the silver in the solution has been gone from associated to free state. This gives us grounds to assume, that has been received solid silver particles that have nano-scale, probably due to the characteristic yellow color of yellow suspensions (Fig.3). The steadfast yellow colour of the slurry indicates the presence of silver nanoparticles.

Several laboratory experiments had been conducted to obtain wrapping paper. The used raw material was unbleached kraft pulp, beaten in "Yokro" grinder to 36°SR. The laboratory obtained paper samples were with a grammage of 70  $\text{g/m}^2$  and sizing degree of  $\text{Cobb}_{60} = 22 \text{ g m}^2$ . As sizing agent is been used rosin size in the amount of 3 %

to o.d.f. and aluminum sulfate 4.5 % from the o.d.f. [14].

During the paper formation process a solution of silver nanoparticles in different quantities were added into the fibrous suspension. The physico-mechanical properties (BDS EN 194-2:2000) of the received laboratory paper samples were examined and the results are represented in Table 2. The resulting samples were subjected also to microbiological tests to establish the barrier properties.

The obtained tensile strength results shows that the tensile length of the of the paper samples containing silver nanoparticles, fell slightly compared to that of a zero sample. Paper samples containing silver nanoparticles virtually has no changes in the physical and mechanical characteristics or has slightly lower values. This decrease is probably due to the weaker hydrogen

bonds between the fibers due to the decrease of the contact surface between the fibers.

**Table 2.** Physico-mechanical properties of the laboratory obtained wrapping paper samples

Sample	Tensile Strength, m	Elongation, %
Zero sample	5500	10.2
Sample 1	5300	10
Sample 2	5400	10.1
Sample 3	5200	10.3
Sample 4	5500	9.9
Sample 5	5500	10.1
Sample 6	4900	9.8
Sample 7	5300	10.2

The resulting paper samples were subjected to microbiological tests to identify the impact of silver nanoparticles. For this purpose single colonies of bacteria *Escherichia coli* strain LE392 were cultured. A solid nutrient medium Luria-Bertrand (LB) agar containing is used [3]. The optical density of the formed bacteria was measured on a spectrophotometer. On the surface of the paper samples are been made lineal strokes with bacteria. The samples were left for two weeks in a thermostat at a temperature of 37°C. Observations shows (see Fig. 4) that *Escherichia coli* bacteria have been penetrated only in the zero sample. All other samples exhibit antibacterial activity, which was substantiate from the absence of gloss and odour of the samples.

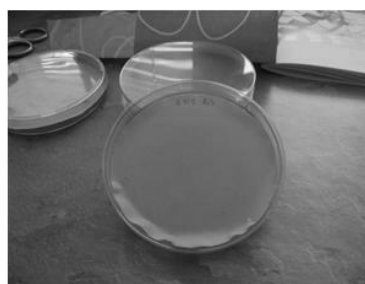
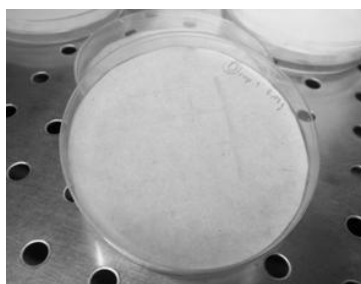


**Fig. 4.** (A) zero-sample showing visible traces of bacteria. (B) Sample containing silver nanoparticles in with no ingress of bacteria.

## CONCLUSIONS

From the studies carried out it has been established that the application of nanotechnology shows significant advantages for improving the quality of packaging materials. The use of packaging paper with silver nanoparticles helps to keep food fresh and the effect of different types of bacteria such as *Escherichia coli*.

The paper acts as a barrier to bacteria and can be used as a material for food packaging.

## REFERENCES

1. V. Popov, I. Hinkov, S. Diankov, M. Karsheva, Y. Handziyski, *Green Processing & Synthesis*, **4**, 125 (2015).
2. I. Hinkov, S. Diankov, M. Karsheva, V. Lasheva, I. Ivanov, Y. Handziyski, *Revue de génie industriel*, № 6, 16 (2011).
3. V. Popov, I. Hinkov, M. Karsheva, S. Diankov, V. Lasheva, Y. Handziyski, *Scientific works ,vol. LX „Food science, engineering and technologies – 2013“ 18-19 october 2013, Plovdiv*, 1010-1013, (2013).
4. R. Gottesman, S. Shukla, N. Perkas, L. Solovyov, Y. Nitzan, A. Gedanken, *Langmuir*, **27**, 720 (2011).
5. <http://www.nanoup.org>
6. N. Leopold, B. Lendl, *J. Phys. Chem. B*, **107**, 5723, (2003)
7. K. Caswell, C.M. Bender, C.J. Murphy, *Nano Letters*, **3**, 667 (2003).
8. Z. Pillai, P.V. Kamat, *J. Phys. Chem. B*, **108**, 945 (2004).
9. D. Chen, Y.W. Huang, *J. Colloid Interface Sci.*, **255**, 299 (2002).
10. I. Pastoriza-Santos, L.M. Liz-Marzan, *Nano Letters*, **2**, 903 (2002).
11. E. Filippo, A. Serra, D. Manno, *Colloids and Surfaces A: Physicochem. Eng. Aspects*, **348**, 205 (2009).
12. A. Pal, S. Shah, S. Devi, *Materials Chem. Phys.*, **114**, 530 (2009).
13. W. Zhang, X.L. Qiao, J.G. Chen, *Colloids Surf. A: Physicochem. Eng. Aspects*, **299**, p.22-28 (2007)
14. N. Ivanova, S. Bencheva, D. Todorova, *Handbook of Chemistry, Technology and Properties of Paper*, Sofia, UCTM, 2009.

## ПРОУЧВАНЕ ВЪЗМОЖНОСТИТЕ ЗА ИЗПОЛЗВАНЕ НА СРЕБЪРНИ НАНОЧАСТИЦИ В ОПАКОВЪЧНА ХАРТИЯ

Д. Тодорова, В. Лашева

*Химикотехнологичен и металургичен университет, Бул. Климент Охридски, 1756 София, България*

Подадено на 12 декември 2016 г. ; Приет на 23 май 2017 г.

(Резюме)

Нанотехнологиите предлагат огромна възможност за иновации в опаковането на хранителни продукти, които могат да бъдат от полза както за потребителите, така и за промишлеността. Прилагането на нанотехнологиите показва значителни предимства за подобряване на качеството на опаковъчните материали. Иновациите, свързани с използването на нанотехнологиите в опаковането на хранителни продукти и контрола на качеството, са основен фокус в съвременната хранително-вкусова промишленост. Опаковката може да бъде направена като "умна", което означава, че може да осигури условия за безопасна среда или да изпрати сигнал до потребителя на замърсяване и патогени. Сребърните наночастици се превръщат в надежден антимикробен материал с разнообразни приложения. Опаковъчните материали с наночастици от сребро или сродни катионни сребърни нанокompозити осигуряват възможност за ефективна и безопасна антимикробна опаковка.

В настоящото изследване са разгледани възможностите за използване на сребърни наночастици в състава на опаковъчна хартия. Изследвани са физико-механичните свойства на получените лабораторни опаковъчни образци - хартия, със и без сребърни наночастици. Извършени са и микробиологични тестове на образците от хартия. Получените резултати показват бактериостатичен ефект на сребърните наночастици върху свойствата на опаковъчната хартия.

## Synthesis and SAR evaluation of the phytochemical activity of new N-pyrrolylcarboxylic acids

S.P. Vladimirova<sup>1\*</sup>, M.B. Georgieva<sup>2</sup>

<sup>1</sup>Department „Organic Synthesis and Fuels”, University of Chemical Technology and Metallurgy, 8 Kl. Ohridski Blvd., 1756 Sofia, Bulgaria

<sup>2</sup>Department „Pharmaceutical Chemistry”, Faculty of Pharmacy, Medical University - Sofia, 2 Dunav str., 1000 Sofia, Bulgaria

Submitted October 10, 2016; Accepted May 8, 2017

Two new N-pyrrolylcarboxylic acids were synthesized via Paal-Knorr cyclization by condensation of  $\gamma$ -aminobutyric acid and 1,4-dicarbonyl compounds. The obtained structures were elucidated by IR and <sup>1</sup>H-NMR spectral data and their purity was proven by TLC characteristics and melting points. The corresponding phytochemical activity of the obtained compounds on wheat and cucumber cultivars in three concentrations was studied. Both molecules were tested at 4 concentrations for herbicidal activity whereat no concentration dependence of the herbicidal effects was established. The inhibition of growth of the aerial parts and roots at the lowest (0.001 mM) and the highest (1 mM) concentration of the compounds was comparable.

In addition a number of structural parameters were calculated for the target compounds and some analogues thereof. A second degree polynomial structure-activity dependency on the herbicidal effects from the corresponding miLogP was observed with R<sup>2</sup> in the range of 0.796 to 0.894.

**Keywords:** pyrroles, phytochemical activity, structure-activity relationship.

### INTRODUCTION

Herbicide use is increasingly being adopted around the world. In many parts of the world, herbicides are being increasingly used to replace tillage in order to improve environmental conditions. In comparison with tillage, herbicide use reduces erosion, fuel use, greenhouse gas emissions and nutrient run-off and conserves water [1,2].

Thousands herbicides are known of the chemists, but widely used in agriculture are approximately 100. After the imposition of the widespread use of herbicide glyphosate, there is no introducing of new herbicides in the last 20 years [3,4]. The search for new herbicides is necessary mainly due to the great "plasticity" of the weeds, which results in adjustment to the herbicides used. In this regard, the synthesis and study of the activity of novel compounds with a potential herbicidal activity is especially important.

As a continuation of previous research in our laboratory [5], the current study offers 2 new derivatives of pyrrole for evaluation of phytochemical activity as potential herbicides.

### RESULTS AND DISCUSSIONS

#### *Synthesis of the targeted structures*

Paal-Knorr pyrrole synthesis, well known as a *powerful reaction* in a retrosynthetic context, was

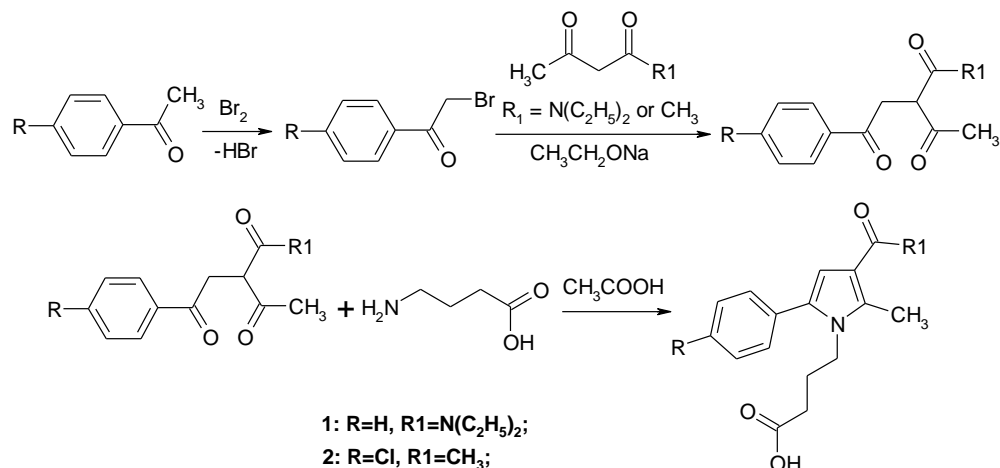
chosen as a reliable access to the targeted structures. The reaction was performed according to Scheme 1 as a cyclization between preliminary prepared 1,4-dicarbonyl compounds and  $\gamma$ -aminobutyric acid. The selection of  $\gamma$ -aminobutyric acid, acting as amino-partner, was based on its involvement of a number of reactions plants such as: control the balance of carbon and nitrogen for the plants, regulate pH of the cells involved in the defense of plants against oxidative stress, and attacks from insects, such as acting osmoregulator, and also as a signal molecule in plants.

The intermediate 1,4-dicarbonyl compounds were synthesized by condensation of R-substituted  $\omega$ -bromoacetophenones with relevantly R1-substituted commercially available  $\beta$ -dicarbonyl compounds [6]. Conditions for C-alkylation were afforded to suppress the concurrent O-targeted reaction intrinsic to this class of ambident compounds [7,8]. The  $\omega$ -bromoacetophenones, well known as strong lachrymators, were prepared in our laboratory [9].

The structural diversity **R1**= N(C<sub>2</sub>H<sub>5</sub>)<sub>2</sub> and **R1**= CH<sub>3</sub> aimed changes in hydrophobicity and molar volume of the molecules:

\*) To whom all correspondence should be sent:

E-mail: vladimirova.s@mail.bg

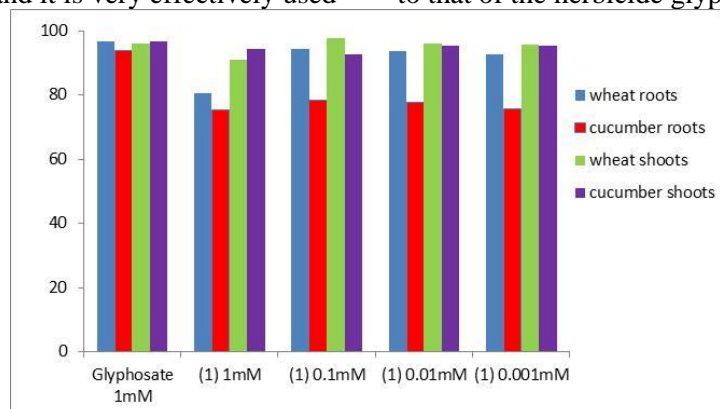


Scheme 1. A synthetic access to the targeted products.

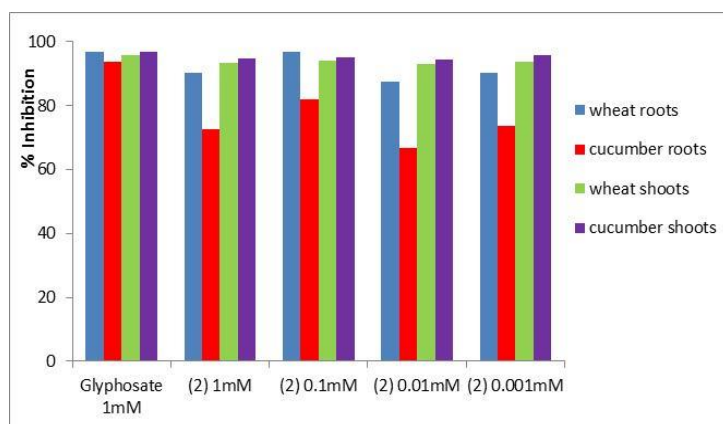
### Phytochemical activity of newly synthesized N-pyrrolylcarboxylic acids

The growth-regulating activity of the newly synthesized N-pyrrolylcarboxylic acids was tested by bioassays with wheat (monocotyledonous) and cucumber (dicotyledonous) cultivars. The phytochemical activity was compared to the activity of herbicide glyphosate [(N-phosphonomethyl)glycine]. Glyphosate was chosen since it is one of the most widely distributed herbicide in the world and it is very effectively used

in both agricultural and nonagricultural lands. It is very toxic to practically all plant species, but monocotyledonous are more sensitive to its action [10,11]. The prime activity of glyphosate is that it inhibits the biosynthesis of proteins that is essential for plant growth. The results of the bioassays showed that both newly synthesized compounds inhibit the growth of the coleoptile (hypocotyle respectively) and roots of seedlings, and in the experiments with wheat, the effect of all compounds was comparable to that of the herbicide glyphosate (Graphics 1,2):



Graphic 1. Influence of compound 1 on the wheat growth (*Triticumaestivum* L.), cv. Sadovo-1 and cucumber growth (*Cucumissativus* L.), cv. Gerganaseedlings, grown in the dark (4 days, 25±1 °C)



Graphic 2. Influence of compound 2 on the wheat growth (*Triticumaestivum* L.), cv. Sadovo-1 and cucumber growth (*Cucumissativus* L.), cv. Gerganaseedlings, grown in the dark (4 days, 25±1 °C)

Both compounds inhibited the growth of the roots and shoots of cucumber to a lesser extent to the one measured for the reference glyphosate, where the influence on the cucumber shoots was the weakest. It is visible, that the inhibition of roots and shoots in the evaluated wheat cultures is comparable with the one for glyphosate.

Although the compounds were tested at 4 concentrations no concentration dependence of the herbicidal effects was established, and the inhibition of growth of the aerial parts and roots at the lowest (0.001 mM) and the highest (1 mM) concentration of the compounds was comparable.

From the results presented here, it is difficult to explain the exact mode of the herbicide action of the newly synthesized compounds tested. Further investigation will give more information on this

problem and will trace the possibilities of their usage in agriculture.

### SAR EVALUATION

In an attempt to identify any structure activity relationships a number of structural parameters were calculated for the synthesized compounds. Some analogues thereof, previously synthesized and analyzed by us [5], were added for statistical evaluation. It was of interest to establish the dependency of the herbicidal activity from the structural parameters as: molecular mass, miLogP, volume. From the obtained results was found, that only in the means of miLogP a structure-activity relationship may be drawn. The corresponding dependencies of the evaluated herbicidal effects from miLogP are presented on Figures 1 to 4 below as follows:

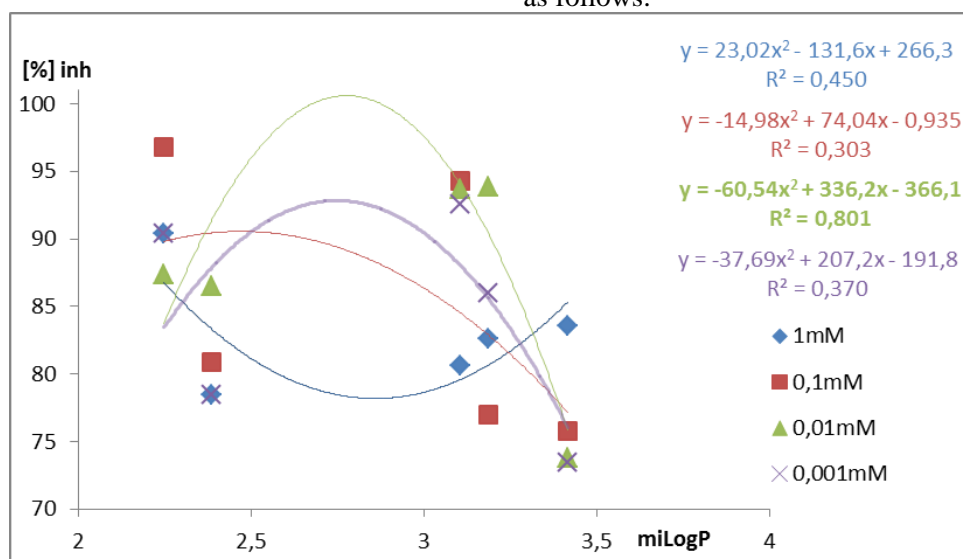


Fig. 1. SAR dependency of inhibition of wheat roots from miLogP.

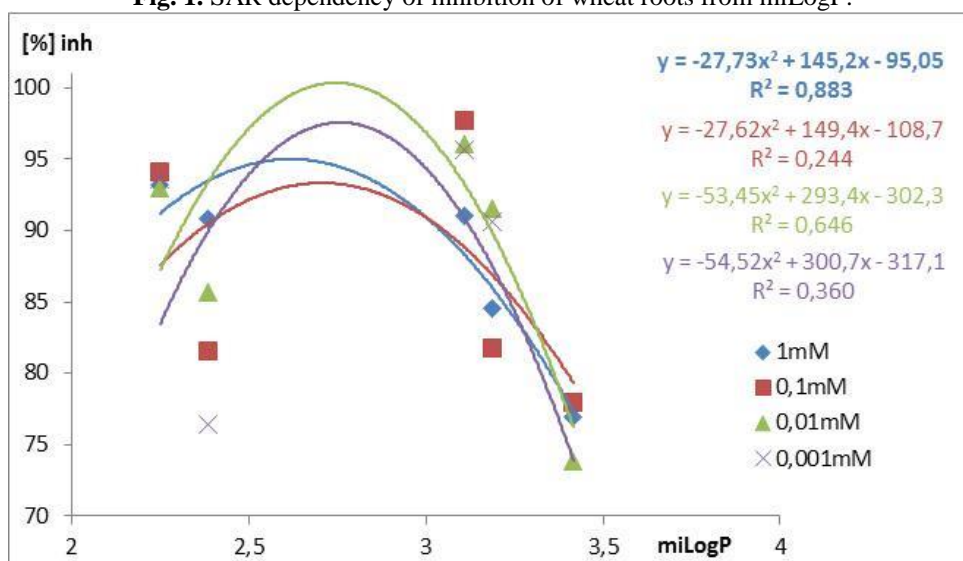


Fig. 2. SAR dependency of inhibition of wheat shoots from miLogP.

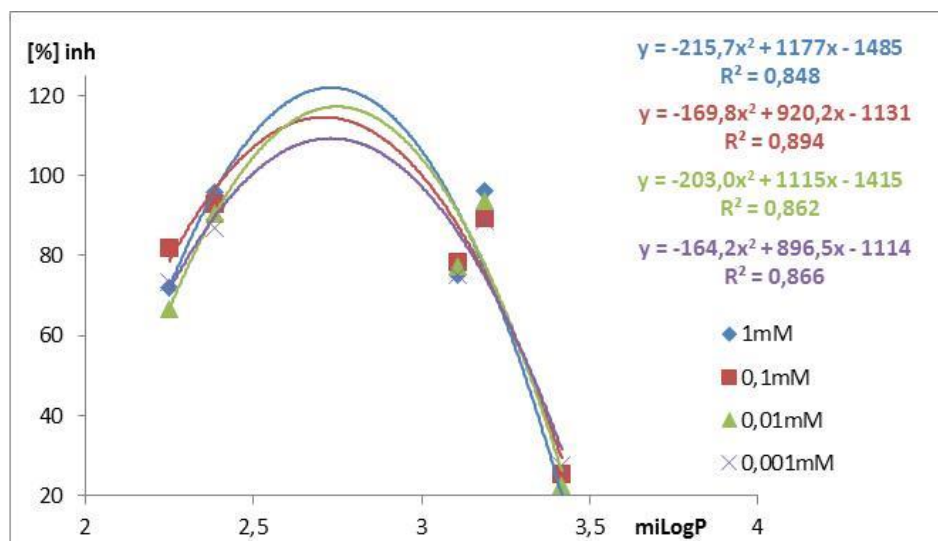


Fig. 3. SAR dependency of inhibition of cucumber roots from miLogP.

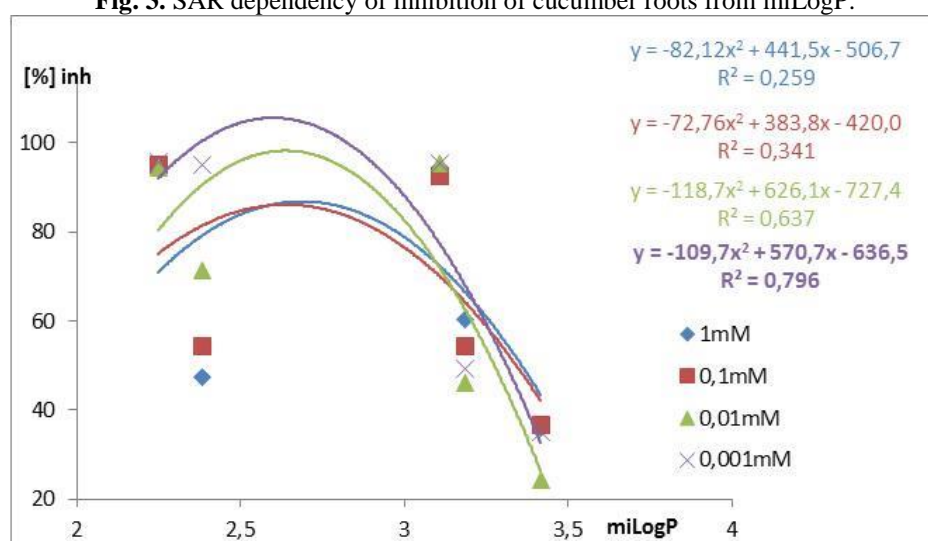


Fig. 4. SAR dependency of inhibition of cucumber shoots from miLogP.

As seen from the presented figures a second degree polynomial structure-activity dependency on the herbicidal effects from the corresponding miLogP is observed with R<sup>2</sup> in the range of 0.796 to 0.894.

**Conclusion.** Two new N-pyrrolylcarboxylic acids were synthesized *via* Paal-Knorr cyclization. The obtained structures were elucidated by IR and <sup>1</sup>H-NMR spectral data and their purity was proven by TLC characteristics and melting points. The corresponding phytochemical activity of the obtained compounds on wheat and cucumber cultivars in three concentrations was studied. No concentration dependence of the herbicidal effects was established for the evaluated compounds.

In addition a second degree polynomial structure-activity dependency of the herbicidal effects from the corresponding miLogP was determined with R<sup>2</sup> in the range of 0.796 to 0.894.

## EXPERIMENTAL PART

All commercial chemicals used in this study as starting materials and reagents were purchased from “Merck” (Darmstadt, Germany). The melting points were determined with a capillary digital melting point apparatus IA 9200 Electrothermal AZ9003MK4, Southend-on-Sea, UK. The IR spectra were registered on Specord IR-71, Carl Zeiss, Jena, Germany (KBr). The <sup>1</sup>H NMR spectra (250 MHz, 20 °C) were registered on a BrukerSpectrospin WM250 spectrometer (Faenlanden, Switzerland), using TMS as internal standard. All OH protons were D<sub>2</sub>O exchangeable.

TLC characteristics of the products were measured on aluminum sheets of silica gel 60 F<sub>254</sub>, Merck 1.05554 at ambient temperature using a mobile phase chloroform-ethanol (*R<sub>f</sub>* value for the new compounds at the relevant CHCl<sub>3</sub>-C<sub>2</sub>H<sub>5</sub>OH ratio is given below).

**General procedure for the synthesis of 1,4-dicarbonyl compounds.** Sodium (0.10 moles) was



dissolved in anhydrous ethanol (50 ml) and to the resulting solution, cooled to 20-25 °C, relevant 1,3-dicarbonyl compounds (0.10 moles) were added, ensuring that the temperature didn't exceed 30 °C. The mixture was stirred for 15-20 minutes. After cooling, the corresponding  $\alpha$ -brominated acetophenone (0.10 moles) was added in portions at a temperature not exceeding 30 °C. The mixture was stirred for 30-40 minutes, benzene (100 ml) were added and the resulting solution was washed successively with 5% HCl and water. The organic layer was dried with anhydrous sodium sulfate. The solvent was removed by rotary vacuum evaporator at a temperature below 45 °C. The residue consisted in the relevant 1,4-dicarbonyl compound as an oil, which was used directly in the next stage of condensation.

**General procedure for the synthesis of targeted N-pyrrolylcarboxylic acids:** 1,4-dicarbonyl compound (0.10 moles) and the  $\gamma$ -aminobutyric acid (0.12 moles) were dissolved in glacial acetic acid (50 ml). For the preparation of compound **1**, the reaction was performed at the boiling point of the mixture and for the preparation of compound **2** - at 60 °C. The reaction development was monitored by TLC. After reaction completion, the mixture was poured into water. The separated precipitate was filtered off, washed with water, dried and recrystallized from warm ethanol. The reaction time was varied from 2.30 hours (compound **1**) to 4.30 hours (compound **2**) (TLC control).

All compounds were soluble in warm ethanol, chloroform and dimethylsulfoxide, but insoluble in water and hexane.

**4-(3-diehtylcarbamoil-2-methyl-5-phenyl-pyrrol-1-yl)-butyric acid (1):** White solid, Yield 76%, mp 96-98 °C,  $R_f$  0.48 (10:0.4). IR spectrum (KBr),  $\nu$ ,  $\text{cm}^{-1}$ : 3600-2300 (COOH), 3350 (O-H), 1700, 1580 (C=O), 780, 730 ( $\text{C}_6\text{H}_5$ );  $^1\text{H}$  NMR (250 MHz,  $\text{CDCl}_3$ )  $\delta$ , ppm: 1.20 (t, 6H,  $J$  7.1 Hz,  $2 \times \text{NCH}_2\text{CH}_3$ ), 1.70-1.81 (m, 2H,  $\text{CH}_2\text{CH}_2\text{CH}_2\text{COOH}$ ), 2.15 (s, 3H,  $\text{CH}_3$ -2), 2.30 (t,  $J$  2.0 Hz, 2H,  $\text{CH}_2\text{CH}_2\text{CH}_2\text{COOH}$ ), 3.50 (q, 4H,  $J=7.1$ ,  $2 \times \text{NCH}_2\text{CH}_3$ ), 3.95 (t,  $J$  3.0 Hz, 2H,  $\text{CH}_2\text{CH}_2\text{CH}_2\text{COOH}$ ), 6.10 (s, 1H, H-4), 7.40-7.50 (m, 5H,  $\text{C}_6\text{H}_5$ ), 8.10 (s, 1H, COOH).

**4-[3-acetyl-5-(4-chloro-phenyl)-2-methyl-pyrrol-1-yl]-butyric acid (2):** White solid, Yield 84%, mp 162-164 °C,  $R_f$  0.46 (10:0.3). IR spectrum (KBr),  $\nu$ ,  $\text{cm}^{-1}$ : 3600-2400 (COOH), 3300 (O-H), 1720, 1695 (C=O), 830 ( $p\text{-C}_6\text{H}_4$ );  $^1\text{H}$  NMR (250

MHz,  $\text{CDCl}_3$ )  $\delta$ , ppm: 1.79-1.84 (m, 2H,  $\text{CH}_2\text{CH}_2\text{CH}_2\text{COOH}$ ), 2.17 (t,  $J$  2.0 Hz, 2H,  $\text{CH}_2\text{CH}_2\text{CH}_2\text{COOH}$ ), 2.30 (s, 3H,  $\text{COCH}_3$ ), 2.50 (s, 3H,  $\text{CH}_3$ -2), 3.98 (t,  $J$  3.0 Hz, 2H,  $\text{CH}_2\text{CH}_2\text{CH}_2\text{COOH}$ ), 6.30 (s, 1H, H-4), 7.15-7.25 (m, 4H,  $\text{C}_6\text{H}_4$ ), 7.44 (s, 1H, COOH).

### Phytochemical analyses

Both newly synthesized compounds were tested for potential herbicidal activity in a series of bioassays with the representatives of the monocotyledonous (wheat - *Triticum aestivum* L., cv. Sadovo-1) and dicotyledonous (cucumber - *Cucumis sativus* L., cv. Gergana) cultivars. The growth-regulating activity of compounds tested was determined in accordance with their influence on the growth of intact seedlings, grown in dark for 96 h ( $25 \pm 1$  °C) by measuring the coleoptile (hypocotyl respectively) and root length. The compounds were tested at 1 mM, 0.1 mM, 0.01 mM, and 0.001 mM concentrations. As a standard in the experiments was used total herbicide glyphosate (active ingredient in Roundup formulation, production of international company Monsanto) at 1 mM concentration.

All experiments were repeated three times with three replications for each concentration tested. The results reported in the tables are means of the values with a standard error (SE).

### REFERENCES

1. L. P. Gianessi, *Pest Management Science*, **69**, 1099 (2013).
2. J. R. Park, I. McFarlane, R. H. Phipps, G. Ceddia, *Plant Biotechnol. J.*, **9**, 2 (2011).
3. B. Buchanan, W. Gruissem, R. Jones, *Biochemistry & Molecular Biology of Plants. American Society of Plant Physiologists*, 1367 (2000).
4. E. Varejão, A. Demuner, L. Barbosa, R. Barreto, *Crop Protection*, **48**, 41 (2013).
5. S. Vladimirova, D. Todorova, I. Sergiev, *Pharmacia*, **61**, 28 (2014).
6. S. Vladimirova, A. Bijev, *Heterocyclic Commun.*, **20**, 111 (2014).
7. C. Paal, *Berichte der deutschen chemischen Gesellschaft*, **16**, 2865 (1883).
8. N. Kornblum, R. A. Smiley, R. K. Blackwood, D. C. Iffland, *J. Am. Chem. Soc.*, **77**, 6269 (1955).
9. F. Kröhnke, *Berichte der deutschen chemischen Gesellschaft*, **69**, 921 (1936).
10. C. Cox, *J. Pesticide Reform.*, **18**, 2 (1998).
11. P. Hetherington, T. Reynolds, G. Marshal, R. Kirkwood, *J. Exp. Bot.*, **50**, 1567 (1999).

## СИНТЕЗ И ОЦЕНКА НА ВРЪЗКАТА СТРУКТУРА-ФИТОХИМИЧНА АКТИВНОСТ НА НОВИ N-ПИРОЛИЛ КАРБОКСИЛНИ КИСЕЛИНИ

С. П. Владимирова<sup>1\*</sup>, М. Б. Георгиева<sup>2</sup>

<sup>1</sup>Катедра „Органичен синтез и горива”, Химикотехнологичен и металургичен университет, бул. „Климент Охридски“ 8, 1756 София, България

<sup>2</sup>Катедра „Фармацевтична химия”, Факултет по фармация, Медицински университет, ул. Дунав 2, 1000, София, България

Постъпила на 10 октомври, 2017 г.; приета на 8 май, 2017 г.

(Резюме)

Две нови N-пилолилкарбоксилни киселини са синтезирани чрез Паал-Кнор кондензация на  $\gamma$ -аминомаслена киселина и 1,4-дикарбонилни съединения. Структурите на получените съединения са изяснени чрез ИЧ и <sup>1</sup>H-ЯМР спектрални анализи, а чистотата им бе доказана посредством тънкослойна хроматография и температури на топене. Проучена е фитохимичната активност на съединенията спрямо сортове пшеница и краставица. И двете молекули са тествани при 4 концентрации за хербицидна активност, при което не е установена концентрационна зависимост. Инхибирането на растежа на надземните части и корените на най-ниската (0.001 mM) и най-високата (1 mM) концентрация на съединенията е съизмерима.

В допълнение бяха изчислени редица структурни параметри за целевите съединения и някои техни аналози. Зависимостта на хербицидните ефекти от съответния  $\text{miLogP}$  се описва с полином от втора степен, като  $R^2$  е в диапазона от 0.796 до 0.894.

## Comparative study of offset plate tone value reproduction using different measuring and image processing tools

Ž. Pavlović<sup>1\*</sup>, M. Pal<sup>1</sup>, T. Cigula<sup>2</sup>, R. Boeva<sup>3</sup>, I. Spiridonov<sup>3</sup>, T. Bozhkova<sup>3</sup>, M. Prica<sup>1</sup>

<sup>1</sup>University of Novi Sad, Faculty of Technical Sciences, Department of Graphic Engineering and Design, Novi Sad, Serbia

<sup>2</sup>University of Zagreb, Faculty of Graphic arts, Zagreb, Croatia

<sup>3</sup>University of Chemical Technology and Metallurgy, Department of Printing Arts, Pulp and Paper, Sofia, Bulgaria

Submitted November 30, 2016; Accepted May 8, 2017

The quality of tone values on offset printing plate is one of the crucial factors affecting the printed product quality. By implementing Computer to Plate systems tonal values are first formed on a printing plate's surface and therefore their size and shape are one of the crucial factors affecting the printed product quality. In particular, when producing printing plates, a rigorous quality control has to be performed, since any bulk and surface imperfection can have a large detrimental effect on tone value reproduction and thus on print sharpness, contrast, nonuniformity and other print properties.

The aim of this paper was to analyse measured results of two different measuring instruments and two different image processing software, determined by two different assessment methods. For direct analysis, of tone value parameters on the printing plate, we have used Techkon spectroplate measuring device with built-in software for image analysis. For indirect analysis, we have used Vitiny VT-300 digital microscope for image recording and microDot software (CC dot) for image analysis. Tools independent software-based image analysis, on all recorded images from both measuring devices, was accomplished using ImageJ, a public domain Java image processing program. This study has shown that indirect and independent image analysis-based evaluation methods proved to be a viable alternative to the established ones on built-in software method with Techkon spectroplate measuring device, providing a reliable tool for the monitoring of the tone value reproduction parameters of offset printing plate.

**Key words:** offset printing plate, measuring device, image-based software, TV reproduction

### INTRODUCTION

Although the market share of the offset printing is in recent years slightly decreasing mostly due to the emerging technologies of digital printing and flexography, it is still the market leader. The main advantages of the offset printing are relatively quick workflow and especially printing quality which stands as a standard which other technologies aim to achieve [1,2].

The offset printing is more complex in comparison to the other conventional printing techniques as gravure printing, flexography or letterset as the selective ink adsorption on the printing plate is achieved by different chemical properties of the printing and nonprinting areas. The printing areas are oleophilic and attract oil based printing ink, and the nonprinting areas are hydrophilic to adsorb water based fountain solution which prevents adsorption of the printing ink [3]. The main advantages of offset printing over other mentioned conventional printing technologies are plate price and the plate making process, which is relatively simple including, in principle, two step procedure, imaging and chemical processing [4,5]. Even more, recently plate producers put onto

market processless printing plates which are processed in a printing machine, meaning only imaging is done offline, in a platesetter [6].

With the Computer to Plate systems implementation the printing plate became first material to be used in the reproduction chain of the graphic product. One should control the platemaking process by visual and apparatus control to avoid any defects which would lead to reproduction outside standard tolerances, i.e. unacceptable final product quality [7]. Several possible unexpected costs in reproduction, before the printing process starts, could be detected and corrected with the standardized procedure of control [8]. To enable quick control of the produced printing plate and standardize procedures institutes and producers developed various control wedges. One of the first developed was the Ugra/Fogra Digital Plate Wedge [9]. Another problem to solve was to standardize measuring devices in order to solve various problems as a single plate may vary in contrast, tonal surface, the way of screening and their physical characteristics. Measuring devices called Plate Readers are used to control the tonal values in the halftone patches on printing plates [10]. There are many of these devices present on

\*) To whom all correspondence should be sent:

E-mail: zivkopvl@uns.ac.rs

the market, but they operate on the same principle: they are equipped with a digital camera which records detail image of halftone structure with high resolution. The obtained digital image is then processed and analysed using image processing software integrated in the measuring device. Depending on the software, beside the percentage of coverage of the plate with halftone dot, units can give information about on the corner and line screens of conventional halftone, dot diameter and magnified view of halftone images. In addition, as formation of new ink receptive layers are developed the Plate Readers were equipped with additional light sources which enable better contrast and more precision in measurements. The additional development of the measuring units made them more expensive and therefore less present in smaller print houses, which makes finding of the alternative plate making process control very important.

## MATERIALS AND METHODS

For the purpose of this research a set of three printing plates was made. The plates were chosen to include various system present on the market, a conventional plate imaged in a platesetter (CtCP plate), the Ipagsa CtcP Eco 88S (Ipagsa) – UV positive working plate (meaning the imaged areas

are removed during chemical processing of the plate), thermal CtP plate, the Fuji Brillia LH-PCE (Fuji), also positive working and photopolymer CtP plate, the Kodak Violet Print (Kodak), negative working plate (meaning the imaged areas stay on the aluminium base after chemical processing of the plate). All printing plates were imaged and chemically processed in defined conditions according to the producer's recommendations. The standardized Fogra CtP test form with tone value control strip was used (Fig 1). On the all prepared printing plates same control strip was analyzed (Fig 1, red marked). The control strip consisted of 21 test fields covering the tone value interval from 0 – 100 % with the step of 5 %.

In order to determine the printing plate's quality level, i.e. formation of the printing elements, the surface coverage value was analyzed. The coverage values were measured by the use of two hand-held units, one with built in software for image analysis, the Techkon spectroplate (Fig 2a, Techkon) and the other with commercial software for image analysis, the Vitiny VT-300 digital microscope (Fig 2 b., Vitiny). The Vitiny records the image which is analyzed by microDot software (CC dot). Both of these are easy to use and give instant results of the coverage values [11,12].

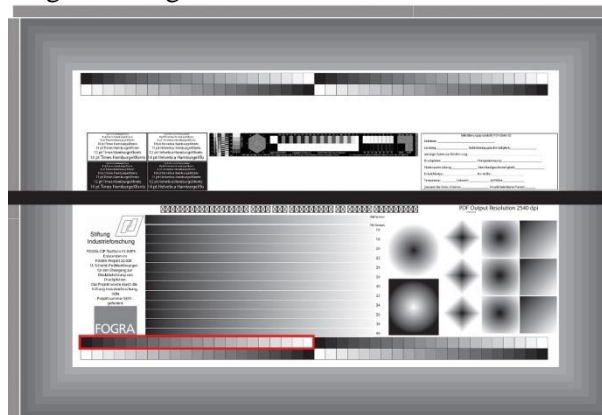


Figure 1. FOGRA CtP test form



Figure 2. Measuring devices: a) Techkon spectroplate; b) Vitiny VT-300 digital microscope.

As an alternative, the coverage values were obtained from image analysis using tools independent software-based image analysis, the

Wayne Rasband's ImageJ 1.5, a public domain Java image processing program [13] The image analysis

was performed on images recorded by both measuring devices, the Techkon and the Vitiny.

The ImageJ procedure for measuring coverage values consists of generally two steps. First images are converted into a black&white mode and in second step software calculates fraction of black/white pixels. In addition, as the surface of the printing plate is rough, some pixels could be too bright/dark leading to the need of removing these defects.

There are several methods to convert images in ImageJ, in this study two different approaches/methods were used: in method 1 (M1) the function “Make Binary” (Process > Binary > Make Binary) was used to convert image to black&white. Correction of small defects was then made using function “Despeckle” (Process > Noise > Despeckle) three times. In the method 2 (M2) additional correction was included due to the unevenness of the lightness on the surface when using microscope, function “Subtract Background” (Process> Subtract Background) and then the function “Make Binary” (Process > Binary > Make Binary) followed by the function “Remove Outliers” to remove defects (Process > Noise > Remove Outliers). The function “Subtract Background” was set to use the Rolling ball method with radius of 50 pixels and the function “Remove

Outliers” was set by radius 2 pixels and threshold 50, to remove defects (white or black holes in the printing area or nonprinting areas, respectively) smaller than 2 pixels.

The printing plate evaluation was conducted in few steps, first printing plate was cleaned of gum and each test field of the control strip was measured five times using Techkon by moving the camera opening inside the test field. Each image was also saved on the computer. The same procedure was conducted using Vitiny. The recorded images were processed with the ImageJ.

## RESULTS AND DISCUSSION

In Figure 3 one could see the difference between average measured values of the coverage values on the investigated printing plate samples using two commercial measuring systems, the Techkon and the Vitiny with microdot software. The difference ( $\Delta_{TV}$ ) was calculated using (1).

$$\Delta_{SV} = CV_{Sp} - CV_V [\%] \quad (1)$$

where  $CV_{Sp}$  is the coverage value (tone value) measured by Techkon and  $CV_V$  is the coverage value (tone value) measured by Vitiny with microdot software.

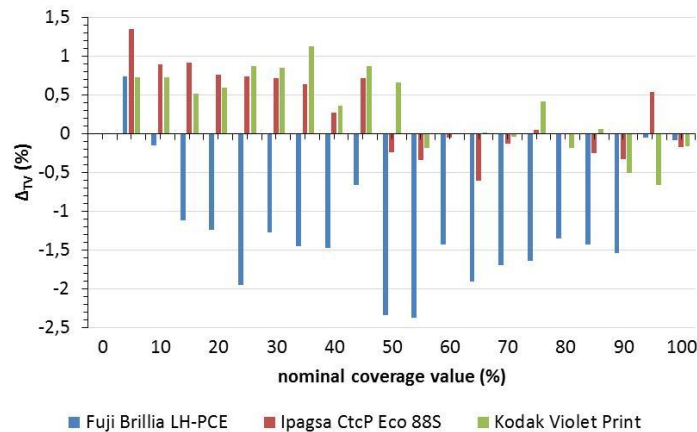


**Figure 3.** Differences in measured coverage values by using two commercial systems on all plate samples

The highest difference between values obtained from two measuring systems, the Techkon and the Vitiny with microdot software is visible by Fuji in the mid tonal range (round nominal value of 50%). The coverage values measured by the Techkon are lower than the values measured by the Vitiny with microdot software on the Fuji while on the other plates in lower nominal coverage values (under 50%) they are higher, and in higher nominal coverage values (over 50%) are lower.

Furthermore, by the Ipagsa and the Kodak almost all differences in coverage values over nominal value of 50% are up to 0.5% which is repeatability of the Techkon [14].

The differences in measured values between two measuring systems could be the consequence of the optical systems and illumination both units use. Observing Figures 4 and 5 one could see that Techkon images appear darker.

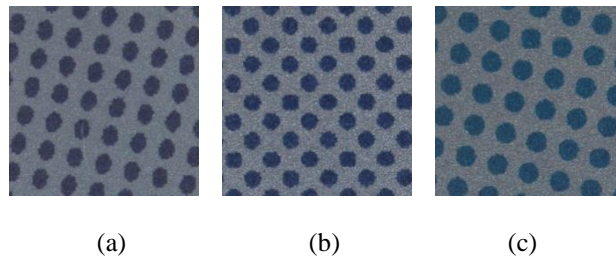


**Figure 4.** Images of 30% nominal coverage value field obtained by Spectroplate, a) Fuji, b) Ipagsa, c) Kodak

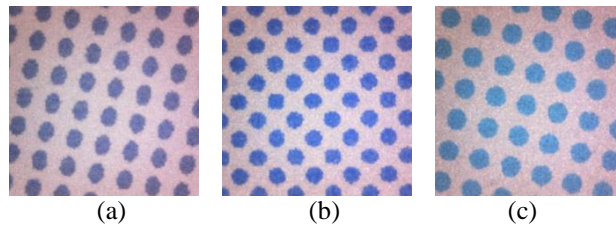


**Figure 5.** Images of 30% nominal coverage value field obtained by Vitiny. a) Fuji, b) Ipagsa, c) Kodak

Furthermore, the aluminium-oxide areas (nonprinting areas) are by Techkon dark bluish (Figure 4), while by the Vitiny they appear reddish (Figure 5). By the Fuji plate this improves contrast between the printing and the nonprinting areas by the images obtained from Vitiny making it easier to determine coverage value (algorithm of coverage values determination includes converting the image into a binary image). On the other two plates (Ipagsa and Kodak) the printing areas are at the Techkon images darker (Ipagsa, Figure 4b) or more to the cyan (Kodak, Figure 4c) which improves contrast of the image, i.e. difference between printing and the nonprinting areas. This in the end leads to the more similar results of the coverage values measured by both systems (Figure 3).

Differences between coverage values obtained from Techkon and from image analysis by ImageJ are calculated using equation (2).

$$\Delta_{TM} = CV_{Sp} - CV_{Mi} [\%] \quad (2)$$

where  $CV_{Sp}$  is the coverage value (tone value) measured by Techkon and  $CV_{Mi}$  is the coverage value (tone value) measured by ImageJ,  $i = 1$  means use of the method M1 and  $i = 2$  means use of the method M2.

In Figure 6 one could see the difference between coverage values obtained from Techkon and coverage values obtained from ImageJ analysis. The both ImageJ methods (M1 and M2) calculate higher results than Techkon.

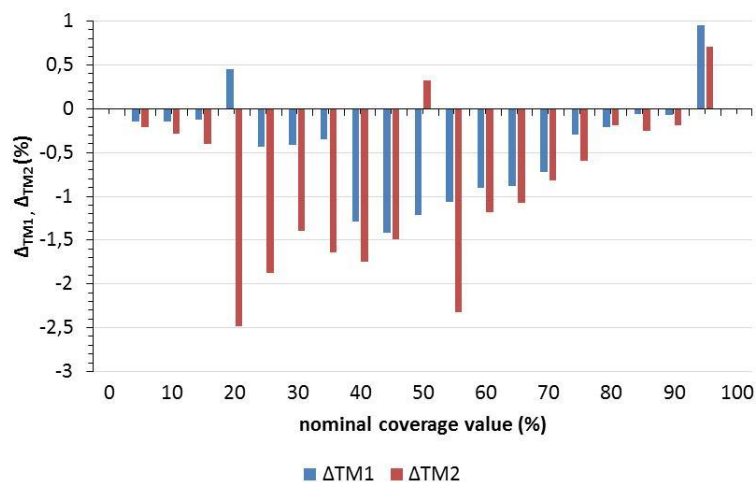


**Figure 6.** Differences in measured coverage values obtained from Techkon and ImageJ analysis of images recorded by Techkon on Fuji.

Higher differences can be noticed in the middle range of coverage values (30-70%), furthermore,

M2 computes higher values than M1 at almost all control fields (Figure 6).

The coverage values calculated by ImageJ analysis using M1, except ones measured on files with nominal coverage value of 5 and 95%, are nearly the same to the ones measured by Techkon on the Ipagsa (Figure 7), i.e. they are in the range of repeatability of Techkon [14]. The calculation of coverage values using M2 resulted with higher coverage values than Techkon. Higher differences (1-1.5%) can be seen at nominal coverage values between 50 and 70%.

The calculation of coverage values on Kodak differentiates to the values obtained by Techkon more than other two plates (Figures 6-8). Furthermore, on this plate values calculated using M2 are lower than the ones calculated using M1 at nominal coverage values from 20 – 100%. The difference between coverage value at control field on 5 and 95% nominal value are nearly 14% and go over the range presented in the graph in Figure 8.

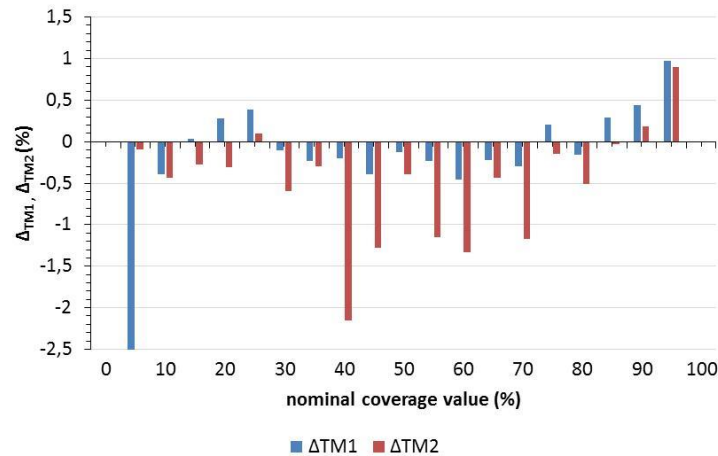


Figure 7. Differences in measured coverage values obtained from Techkon and ImageJ analysis of images recorded by Techkon on Ipagsa

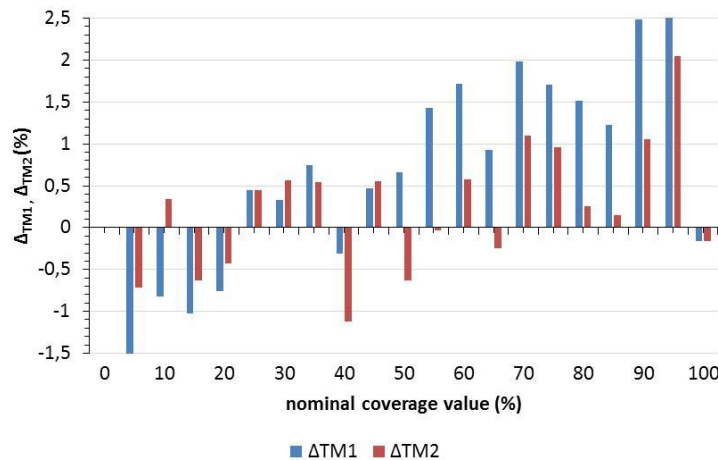


Figure 8. Differences in measured coverage values obtained from Techkon and ImageJ analysis of images recorded by Techkon on Kodak.

The ImageJ analysis using M2 significantly differ to the M1, as is mentioned before. Use of the “Subtract background” function removes a certain value of each pixel and is used at images with uneven illuminated background [15]. Although subtracting background should decrease coverage values, on Fuji and Ipagsa results show opposite. Reason for these results could lay in the second difference, use of the “Remove Outliers” instead of the “Despeckle” function. The “Despeckle” function replaces each pixel with the median value in its 3×3 neighbourhood [15], so if the defect is larger this could mean that this function would not remove it. On the other hand, function “Remove Outliers”

detects defects of certain size (which is defined by user) and replaces a pixel by the median of the pixels in the surrounding if it deviates from the median by more than a certain value (the threshold) [15].

Although both ImageJ methods could be used when analysing Techkon images, the uneven illumination of surface used by the Vinity (Figure 5) makes M1 unusable for analyse of its images, especially in the low and high nominal coverage value where differences are 10 or more percent (Figure 9).

The ImageJ function “Subtract Background” makes the image recorded by Vitiny even and could

be analysed. In contrast to the values obtained by analyse of Techkon images, one can see that analyse of Vitiny images results with coverage values lower than Techkon's on Fuji plate (Figures 7 and 10).

The values measured by Techkon and calculated using M2 are similar on Kodak with the difference to -1% in nominal coverage values lower than 50 and +1% in nominal coverage values over 50%. The same trend, values obtained by ImageJ M2 higher than the ones obtained by Techkon in nominal coverage values under 50% and lower in nominal coverage values over 50%, can also be noticed on Ipagsa (Figure 10).

The images recorded by Vitiny are brighter than the ones recorded by Techkon (Figures 4 and 5) which results with higher minimal and maximal grey values of an image, but also with higher contrast in an image (example on Fuji nominal value of 30% the difference between min and max

grey value is 141 and 164 on images recorded by Techkon and by Vitiny, respectively). Smallest contrast was seen at images recorded by Techkon on the Fuji and this probably results with higher coverage values as it is more difficult to detect the edge of the printing areas. Moreover, due to the characteristics of the laser beam [16] the printing elements on its edge has a bit lower colour intensity than in the middle. In images with higher contrast these edge areas will probably be assigned as black when converting image into Black&white. Lower differences in image contrast between images recorded by Techkon and Vitiny results with lower differences in coverage values as could be seen on Ipagsa and Kodak.

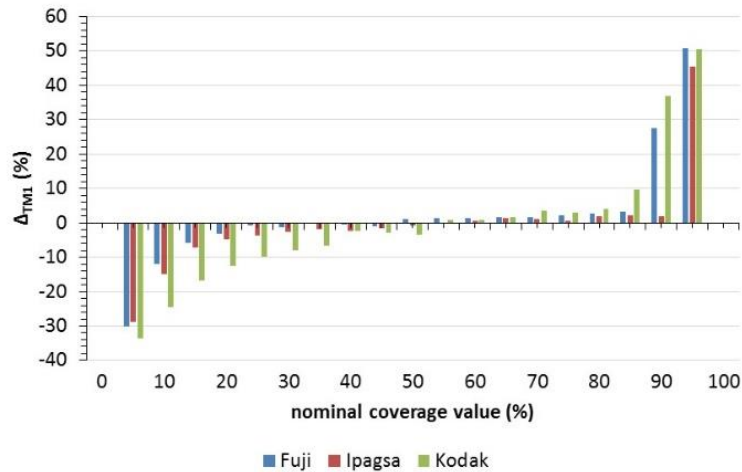


**Figure 9.** Differences in measured coverage values obtained from Techkon and ImageJ M1 analysis of images recorded by Vitiny on all plate samples

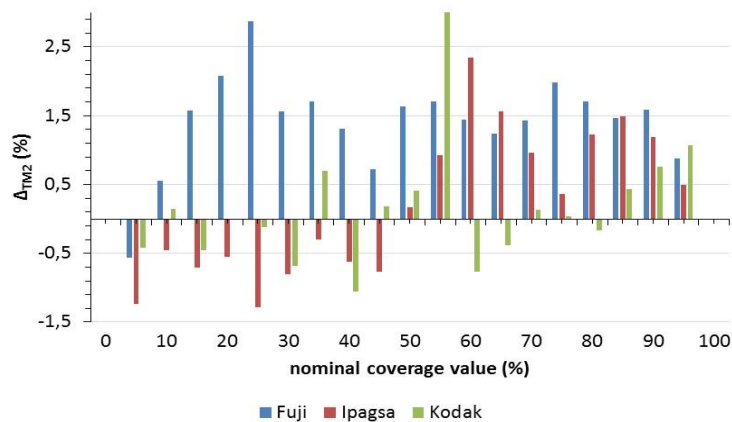


**Figure 10.** Differences in measured coverage values obtained from Techkon and ImageJ M2 analysis of images recorded by Vitiny on all plate samples.



## CONCLUSIONS

This research was conducted in order to investigate the usability of the alternative method in printing plate making process control. For the purpose of the research three different printing plates were prepared by imaging the UGRA/FOGRA test form. The prepared printing plates were then controlled using three different tools, hand held platerreader Techkon spectroplate with built-in image analysis software, Vitiny VT-300 digital microscope for image recording and commercial software microDot and ImageJ, free software for image analysis to analyse images recorded by both mentioned devices.

The results of this research showed that printing plate highly influences measurement of the coverage values. Comparing commercial devices differences between them are more than 1% on Fuji plate, but on other investigated plates is lower than 1%, moreover, almost negligible at control field of over 50% nominal coverage value. Comparison of ImageJ proposed methods to the Techkon measurements showed that better results (meaning closer to the Techkon values) are obtained when analysing Techkon images, where by the use M1 on Ipagasa differences are in the repeatability range of Techkon spectroplate. Analyse of the Vitiny images showed inability to use M1 as these images were uneven illuminated during recoding, which is especially visible in lowed (to 30%) and higher (over 80%) nominal coverage values.

This investigation proved the high impact of the printing plate to be measured and the influence of the image recording unit on the determination of the coverage values on a printing plate. Furthermore, the results have confirmed that ImageJ software could be used in control of the coverage values on a printing plate, but the image analysis procedure should be more tuned to diminish the variances in measurements and more adjusted it to enable use of ImageJ on all types of

the offset printing plates, making it affordable alternative in printing plate control.

**Acknowledgment.** This work was supported by the Serbian Ministry of Science and Technological Development, Grant No.: 35027 "The development of software model for improvement of knowledge and production in graphic arts industry.

## REFERENCES

1. <http://www.powerofinkjet.com/quality>
2. <http://www.landanano.com/nano-news/digital-printing-at-13000-b1-sph>
3. D.G. Wilson, Lithography Primer, Third Edition, PIA/GATFPress, Pittsburg, 2005.
4. H. Kipphan, Handbook of Print Media-Technologies and Production Methods. Springer; Berlin, Germany: 2001, pp. 206–226
5. Ž. Pavlović, S. Dedijer, S. Draganov, I. Karlović, I. Jurić, Printing on Polymers, Chapter Offset Printing, Elsevier Inc., Amsterdam, Zagreb, Croatia, 2015, pp. 217-238.
6. S. Mahović Poljaček, T. Cigula T., T. Hoffmann-Walbeck, T. Tomašegović, S. Riegel, *J. Graph. Eng. Des.* **6**, 23 (2015)
7. <http://www.printing.org/page/4268>
8. J. Poljak, G. Botella, C. Garcia, S. Mahović Poljaček, M. Prieto-Matías, F. Tirado, *Sensors*, **13**, pp 28-31,(2013).
9. Kontrollmittel, Ugra/Fogra-Digital-Plattenkeil, Fogra, München, Jan 2011
10. <http://www.offsetprintingtechnology.com/2015/control-of-ctp-plates-after-their-developement/>
11. <http://www.ccdotmeter.com/wp-content/uploads/2013/07/pressdot-brochure-090414.pdf>
12. <http://www.techkon.com/spectroplate-98.html>
13. <https://imagej.nih.gov/ij/>
14. [http://www.partxpres.com/files/spectrodens\\_manual.pdf](http://www.partxpres.com/files/spectrodens_manual.pdf)
15. <https://imagej.nih.gov/ij/docs/guide/146-29.html#toc-Subsection-29.14>
16. J. Alda, Laser and Gaussian Beam Propagation and Transformation, Encyclopedia of Optical Engineering 999, 2003, Marcel Decker, New York

## СРАВНИТЕЛЕН АНАЛИЗ НА ТОЧНОСТТА НА ВЪЗПРОИЗВЕЖДАНЕ НА РАСТЕРОВИЯ ТОН НА ПЕЧАТНИТЕ ФОРМИ ИЗПОЛЗВАЙКИ РАЗЛИЧНИ МЕТОДИ ЗА ИЗМЕРВАНЕ И ОБРАБОТКА НА ИЗОБРАЖЕНИЯТА

Ж. Павлович<sup>1\*</sup>, М. Пал<sup>1</sup>, Т. Цигула<sup>2</sup>, Р. Боева<sup>3</sup>, И. Спиридонов<sup>3</sup>, Т. Божкова<sup>3</sup>, М. Прица<sup>1</sup>

<sup>1</sup> *Университет на Нови Сад, Технически факултет, Катедра по графично инженерство и дизайн, Сърбия*

<sup>2</sup> *Загребски Университет, Факултет по Графични технологии, Загреб, Сърбия*

<sup>3</sup> *Химикотехнологичен и металургичен Университет, Катедра „Целулоза, хартия и полиграфия“, България*

Постъпила на 30 ноември, 2016 г.; Приета за печат на 8 Май, 2017 г.

(Резюме)

Точността на възпроизвеждане на растеровия тон на печатната форма е един от най-важните фактори за постигане на предвидими резултати и качество на печат. При съвременните технологии за директна експонация Компютър-Печатна форма, растеровите елементи се формират директно на повърхността на формата като от изключителна важност е коректното задаване на тяхната форма и размер. При експонирането на печатните форми е необходимо да се извършва строг и постоянен контрол по цялата им площ. Дори и най-малкото отклонение в някой от качествените показатели на експонацията може да доведе до неточност в растеровия тон, неравномерност по площта, липса на острота, контраст и др.

Целта на настоящата статия е да анализира резултатите от измерванията получени от две устройства и два различни метода и софтуера за анализ на изображенията. За директен анализ на печатните форми е използван прибор за измерване и заснемане - Techkon със вградения в него софтуер. За индиректен анализ е използван дигитален микроскоп Vitiny VT-300 със софтуер microDot (CC dot). Като допълнение е използван и независим от устройството софтуер за анализ на заснетите изображения- ImageJ. В статията са анализирани и сравнени получените резултати от различните методи и софтуери и е установена надеждността на алтернативните методи за анализ на качеството на печатните форми.

## Study of color characteristic changes of printed images under artificial ageing on different papers

I.T. Spiridonov<sup>1</sup>\*, R.K. Boeva<sup>1</sup>, I.V. Lozanova-Doncheva<sup>1</sup>, T.Ts. Bozhkova<sup>1</sup>,  
Ž. Pavlović<sup>2</sup>, G. Vladić<sup>2</sup>, N. Kašiković<sup>2</sup>, M. Stančić<sup>2</sup>, B. Tacheva<sup>1</sup>

<sup>1</sup>Department of Pulp, Paper and Printing Arts University of Chemical Technology and Metallurgy,

<sup>2</sup>Department of Graphic Engineering and Design, University of Novi Sad,  
Faculty of Technical Sciences, Novi Sad, Serbia

Submitted November 28, 2016; Accepted May 8, 2017

A comprehensive study of color characteristic changes of offset printed images have been performed. A specialized and designed for this research test form have been used. In real printing conditions on different papers have been printed the test form with big number of control strips and elements. The optical and color characteristics properties of different combinations of inks, paper and printing press were measured before and after artificial ageing time periods. The main goal of this paper is estimating and evaluation in real printing conditions on real papers the impact of artificial ageing of inks and papers.

**Key words:** color characteristics, offset printing, color difference, print quality, ageing of materials

### 1. INTRODUCTION

Examination of color characteristics of printed materials during the thermal ageing processes provides important information about preventive care, which should be undertaken for the purpose of preservation of printed materials kept in museums, libraries and archives and increase of their durability [1]. Until now there was not made enough experiments recording to the problems of aging and discoloring of offset prints. The main purpose of these studies is to follow the change of the color range and color difference arising on aging of prints.

For the determination of these parameters was needed to exposing the paper samples on artificial thermal ageing. The main goal is estimating and evaluation in real printing conditions on real papers the impact of artificial ageing of inks and papers.

### 2. EXPERIMENTAL

For the purpose of the experiment were used printing samples printed on 5 major types of paper for sheet and reel offset printing machines, according to [2].

- Paper type 1 and 2, responding to coated papers – glossy and mat;
- Paper type 3, responding to LWC paper /coated reel paper/;
- Paper type 4, responding to offset uncoated paper;
- Newspaper.

On paper samples have been measured the change of color characteristics and brightness of the sealing material, and the change in the 3D color ranges, depending to the time of artificial thermal aging.

#### A. Printing conditions and color measurement of printing samples

Printing was done in real production conditions with state-of-the-art-equipment. Implemented print forms were positive acting and were exposed by Computer to Plate System for direct exposure. Heat set reel offset printing presses Komori System 40 and sheet-fed offset printing press Heidelberg SpeedMaster 7.4-5 P+L was employed. The ink sequence was Black (K), Cyan (C), Magenta (M), Yellow (Y). After printing of all test copies, printing samples were selected meeting the optimal inking requirements and corresponding to all examinations, according to [2, 3, 4]. Color measurements were performed with spectrophotometer GretagMachbeth Spectrolino installed on a scanning table GretagMachbeth X-Y SpectroScan [5]. Measurement conditions – standard light source D50, measuring geometry 45°/0° or 0°/45°, 2° standard observer [6].

Paper samples with printed control scales (TC 6.02) containing 999 color fields of dimensions 5x5 mm were treated and subjected to thermal ageing. The fields have single, double, triple and quadruple overprinting of inks. Resulting colors are the most common one, in respect where of human eye is particularly sensitive. Control scales may be used to examine changes in color characteristics of a

\*) To whom all correspondence should be sent:

E-mail; i\_spiridonov@abv.bg

printed image on the respective paper during the artificial thermal ageing process.

**B. Artificial thermal ageing**

The color characteristics of 5 papers and printing samples were measured before and after artificial thermal ageing in cupboard at 105°C for 72 hours. The measurements were done on intervals: 2 hours, 4 hours, 6 hours, 12 hours, 24 hours, 36 hours, 48 hours and 72 hours.

The following parameters were measured:

- CIE L\*a\*b [7, 8, 9] color characteristics with spectrophotometer GretagMacbeth Spectrolino.
- Brightness of 5 papers was measured with apparatus ELREPHO-2000 on standard light source CIE D65, Brightness R<sub>457</sub>, according to [10].

**3. RESULT AND DISCUSSION**

**A. Color characteristics and brightness of investigated printed materials before thermal ageing**

where,  $\Delta E_{Sample/Original}^{Field}$  – color difference between a specific sample color field and the same field of the original untreated sample.

The results on Fig. 1 are showing relatively big change approx. 3,5 units of L in CIE L\* between 0 - 24 hours and 36 - 72 hours. The difference of CIE L\* is insignificant - about 1,5 units.

On the Fig. 2 the results shows sharp increase in the value of CIE a\* /between 24 and 36 hours of thermal ageing/, approx 1,6 units. The exception is

Color characteristics and brightness of five types of papers, have been measured before printing and artificial thermal ageing. The results are shown in Table 1.

**B. Color characteristics and brightness of investigated materials depending of time of artificial thermal ageing**

On next figures (Fig. 1, 2, 3) are presented graphic dependences of CIE L\* values CIE a\* and CIE b\* of paper before and after exposing of artificial thermal ageing.

In addition to color range changes, it is essential to study color changes expressed by the color difference ( $\Delta E$ ) resulting from thermal ageing as compared to untreated sample. For objectivity reasons, color difference was assessed using  $\Delta E_{AVERAGE}$  – mean arithmetic color difference of 999 measured fields between the specific sample and the original untreated sample, before and after thermal ageing period calculated by Formula 1:

$$\Delta E_{AVERAGE} = \frac{\Delta E_{Sample/Original}^{Field 1} + \Delta E_{Sample/Original}^{Field 2} + \dots + \Delta E_{Sample/Original}^{Field 999}}{999}, \tag{1}$$

for newspaper where CIE a\* difference between 36 and 72 hours is about 1 unit.

The experimental results shown on Fig. 4 presented constantly and uniformly increase of  $\Delta E_{ab AVERAGE}$  between 0 and 72 hours of ageing. In the Fig. 1, 2 and 3 the changes of CIE L\*, CIE a\* and CIE b\* are between specific time period of 12 hours. In Fig. 4 the resulting difference of  $\Delta E_{ab}$  which is generalizing the results of Fig. 1-3, shows constant difference in all ageing hours 0-72.

**Table 1.** Color characteristics of papers before ageing

Type of paper	CIE L*a*b*			Brightness, %	Mass of paper, g/m <sup>2</sup>
	L*	a*	b*		
Coated paper – glossy	99,99	-0,02	-0,19	97,19	130
Coated paper – mat	98,99	-0,30	2,86	91,70	130
LWC paper	97,49	0,48	-0,31	91,00	90
Uncoated offset paper	98,38	0,72	-2,21	97,64	80
Newspaper	90,25	0,07	10,34	58,88	45

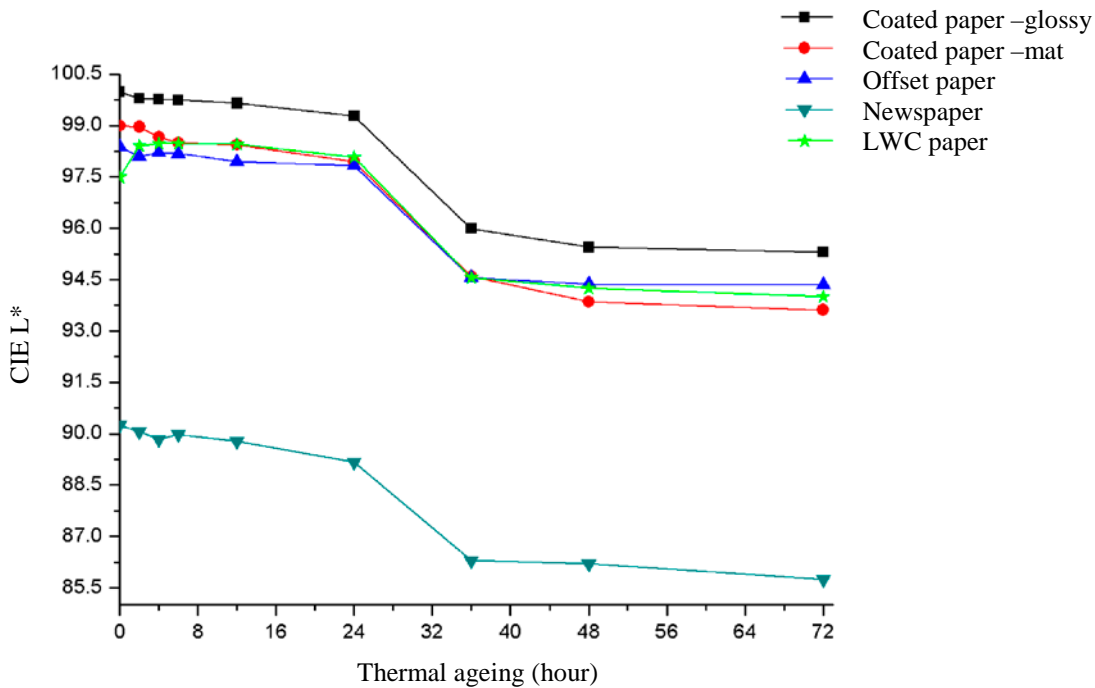


Fig.1. Depending of CIEL\* of papers on the thermal ageing

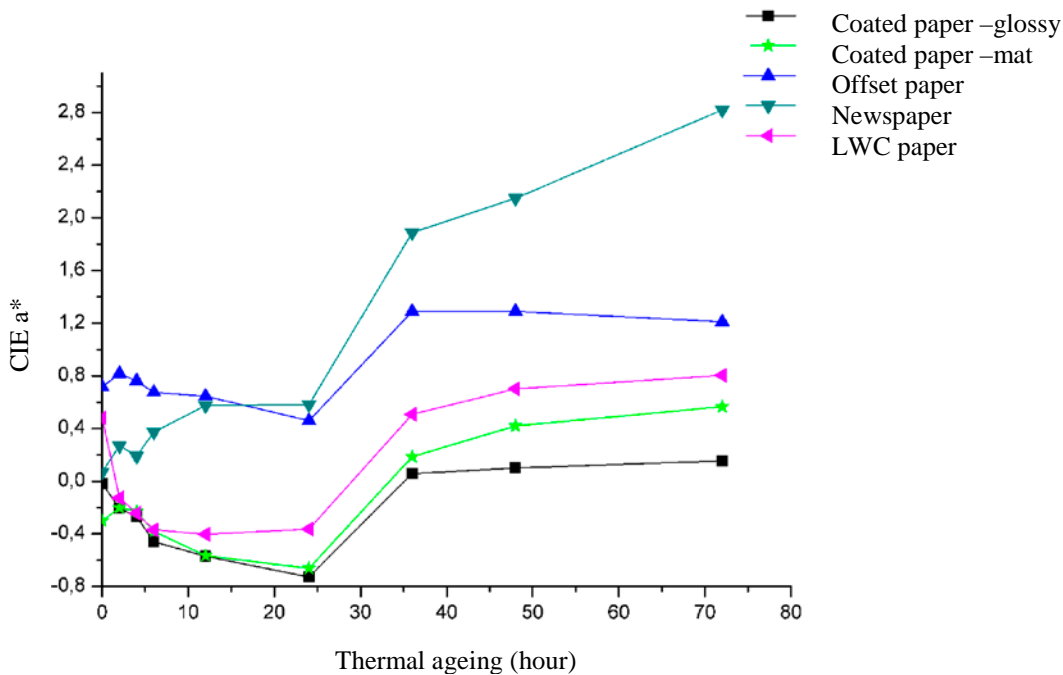


Fig.2. Depending of CIEa\* of papers on the thermal ageing.

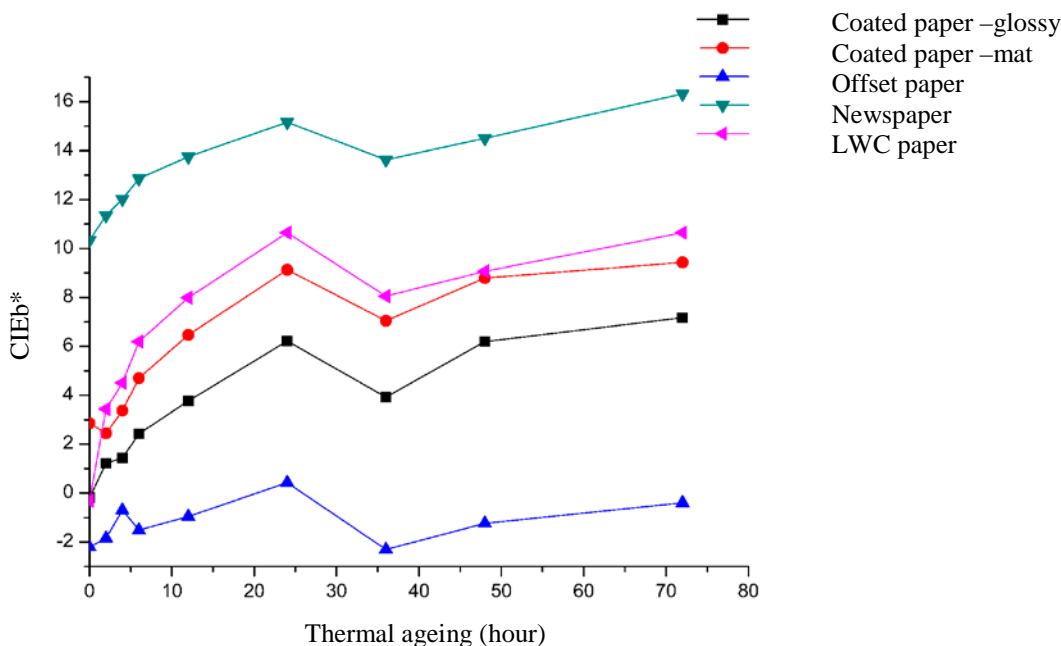


Fig.3. CIE b\* of papers depending of duration of the thermal ageing

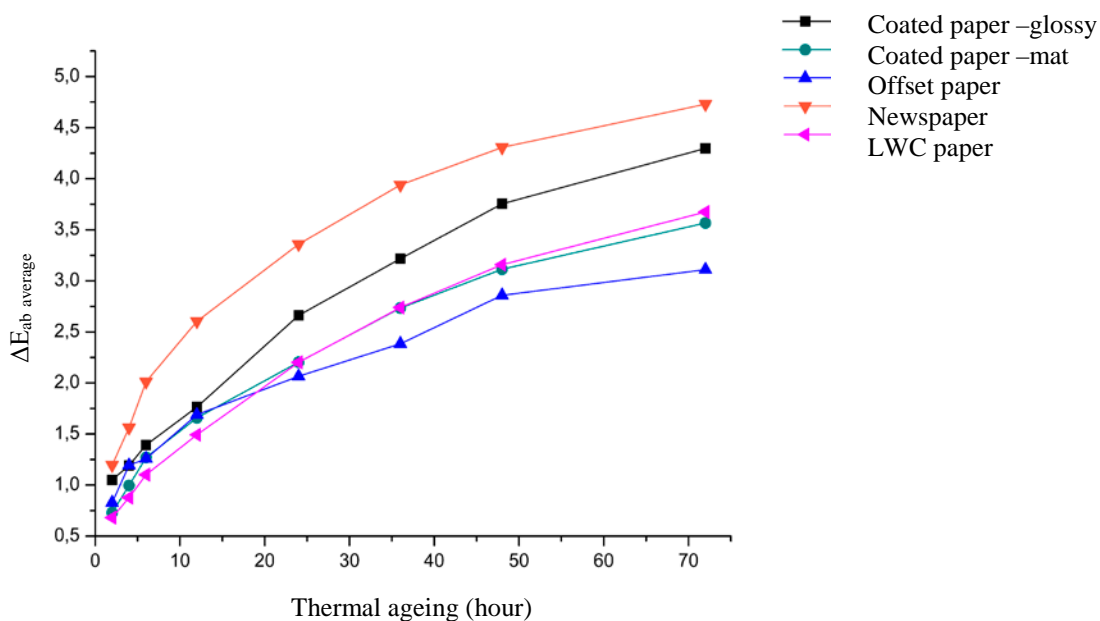


Fig.4. Depending of duration of the thermal ageing on average color difference

**C. Study of the change in 3D color range from different point of view depending of time of artificial thermal ageing**

Visualization of 3D color ranges of specific printing combination - ink - paper - printing technology is the most valuable method for estimation of color changes during some kind of process. Evaluation of changes in different color areas of 3D body of color range clearly shows the influence of thermal ageing on color zones =green, blue, yellow etc. the crossovers of the CIE L\* axis shows the influence of ageing on light, middle and dark tones.

The evaluation of changes of 3D color range for offset printed images in dependence of ageing time is innovative methodology developed by authors of this research. [11]

It is done a comparison of the color ranges from different point of view before and after exposing the paper 72 hours artificial thermal ageing.

On Fig. 5 are presented 3D color ranges from different point of view before and after exposing for 72 hours artificial thermal ageing for glossy coated paper.

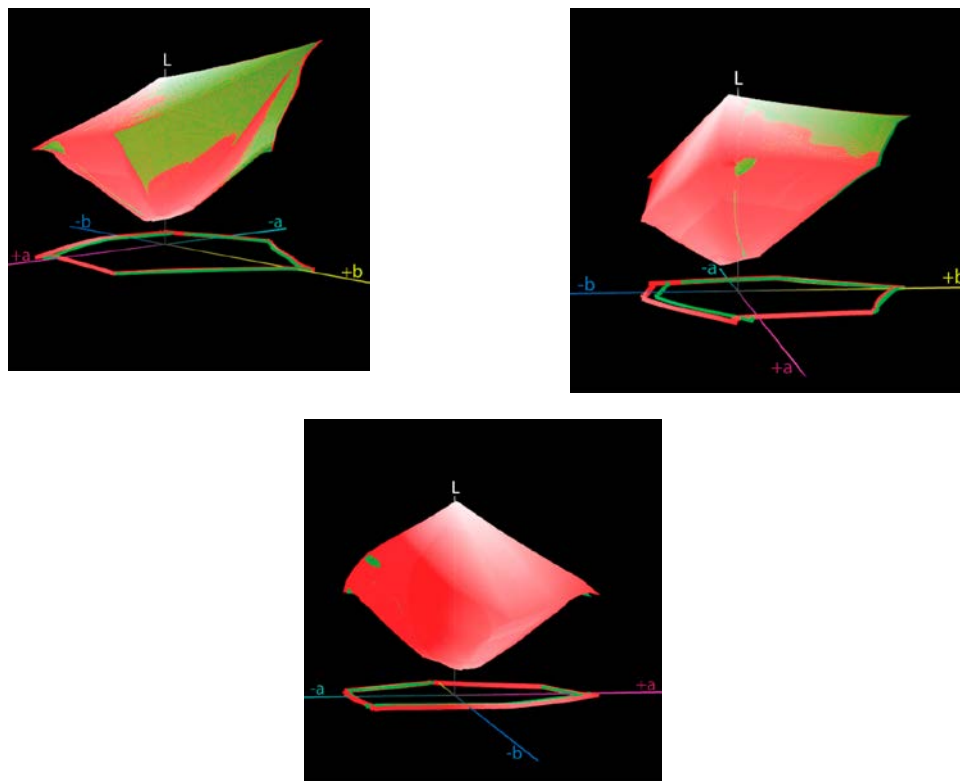


**Fig. 5.** 3D color range before (red) and after exposure (green) on 72 hours artificial thermal ageing on glossy coated paper.

The 3D color ranges shows relatively big changes for all colors after 72 hours of thermal ageing. For dark tones (L=18) smaller change is for yellow color, for some of the dark (L=25) and middle tones (L=50) the bigger change after thermal ageing is for blue and blue-violet colors. In light tones (L=63, L=90) color range before artificial thermal ageing is bigger for blue-violet, green and yellow colors compare to color range after ageing.

On Fig. 6 is presented 3D color ranges for coated paper – mat. For coated paper – mat in dark tones

(L=13 to L=25) color range before artificial thermal ageing is bigger compare to color range after 72 hours thermal ageing on 105°C for all colors. In dark tones (L=36), middle tones (L=50) and light (L=70) the bigger change of color range after thermal ageing is for green, blue-green and blue-violet colors. In light tones (L=82) and (L=90) 3D color ranges shows relatively big changes for all colors exception is for yellow-red colors. On Fig. 7 is presented 3D color ranges for offset uncoated paper.

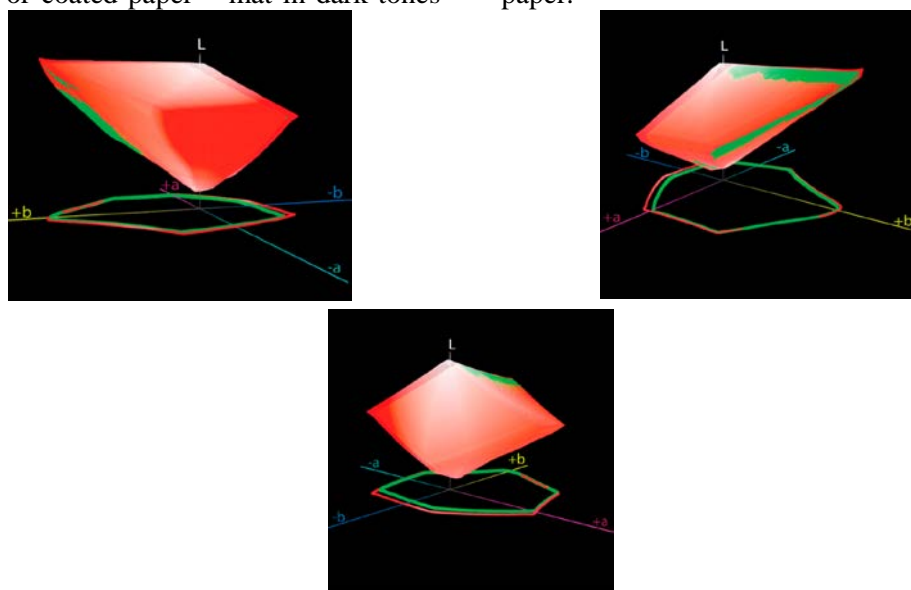


**Fig. 6.** 3D color range before (red) and after exposure (green) on 72 hours artificial thermal ageing for coated paper – mat.

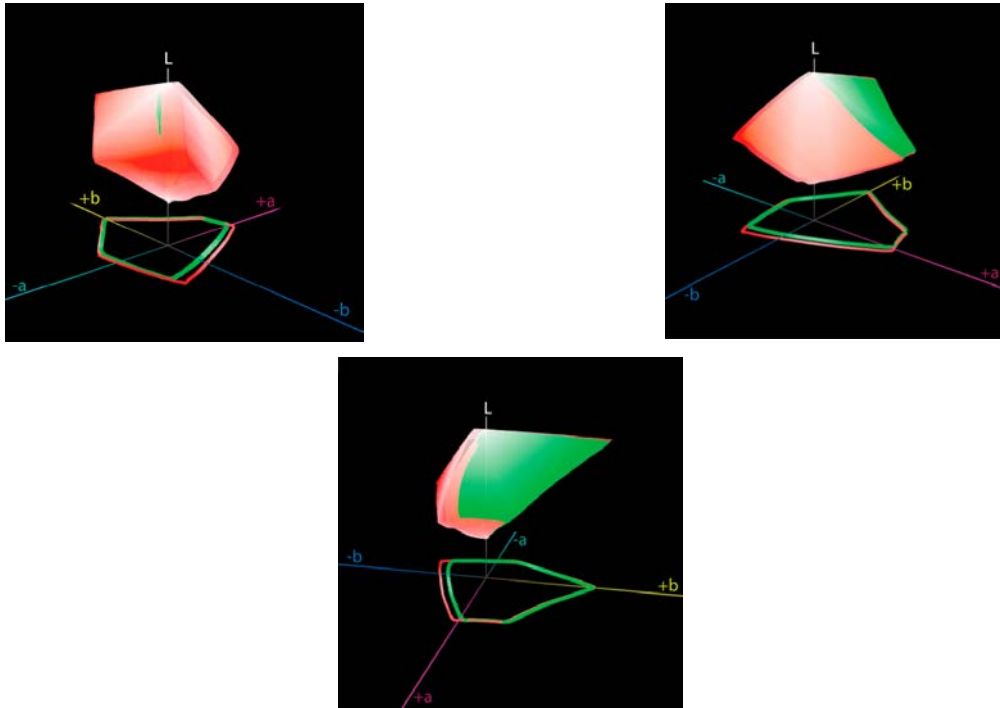


**Fig. 7.** 3D color range before (red) and after exposure (green) on 72 hours artificial thermal ageing for offset uncoated paper.

For offset uncoated paper for dark tones ( $L=29$ ) the bigger change in color range before thermal ageing compare to color range after 72 hours thermal ageing is for blue and blue violet colors. In dark tones ( $L=36$ ) the change in color range is smaller for yellow color. In middle and lights tones

the bigger change for color range is for blue-green and blue-violet colors.

On Fig. 8 is presented 3D color ranges for LWC paper.

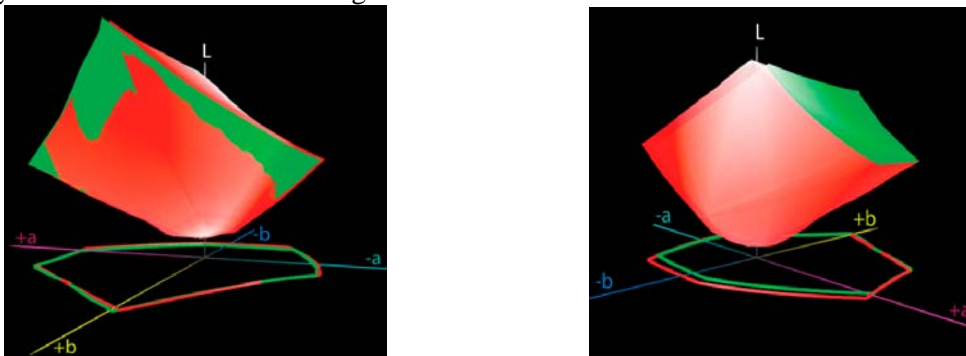


**Fig. 8.** 3D color range before (red) and after exposure (green) on 72 hours artificial thermal ageing for LWC paper.

For LWC paper in dark tones ( $L=13$ ) and ( $L=25$ ) color range before artificial thermal ageing is bigger compare to color range after 72 hours thermal ageing on  $105^{\circ}\text{C}$  for all colors. In some dark tones ( $L=36$ ) in middle tones ( $L=50$ ) and lights tones to ( $L=70$  shows relatively big changes in color range for blue-violet color, and in tones ( $L=83$  to  $L=90$ ) the change in color range is for yellow color.

On next Fig. 9 is presented 3D color ranges for news paper.

For newspaper dark tones ( $L=27$ ) color range before artificial thermal ageing is bigger for blue-violet color compare to color range after 72 hours thermal ageing on  $105^{\circ}\text{C}$ . In dark tones ( $L=36$ ) and middle tones ( $L=50$ ) there is change in color range for all color exception for yellow color. In light tones ( $L=63$ ,  $L=70$ ,  $L=83$ ) the bigger change in color range is for green-blue and blue-violet colors



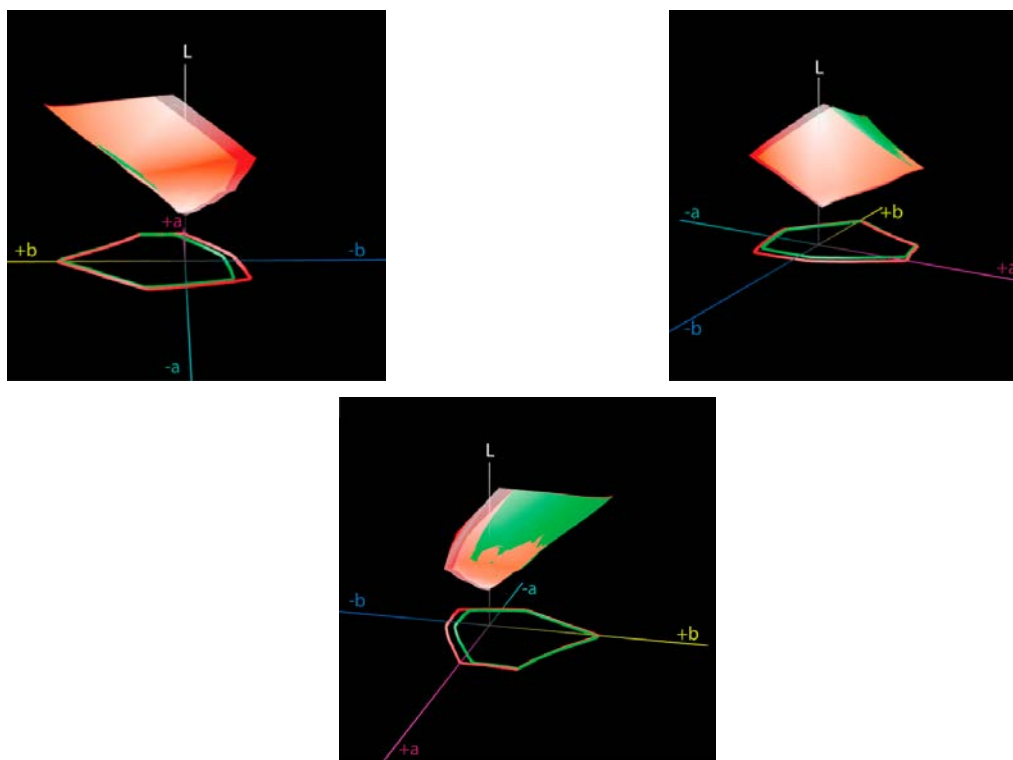


**Fig. 9.** 3D color range before (red) and after exposure (green) on 72 hours artificial thermal ageing for newspaper.

#### 4.CONCLUSIONS

In this research for a first time was created and implemented a methodology for ageing of colors and brightness and experimental in real printing condition for mostly used and certified by ISO main types of papers – coated paper – glossy and mat, offset paper, LWC paper and newspaper.

From this research found that with increase a time of exposure of artificial thermal ageing after 72 hours on 105°C for five types of papers brightness decreased.

The CIE L\* value is decreasing between 3,5 to 4,5 units after thermal ageing for all types of papers. The bigger difference of CIE L\* is between 24 to 36 hours for all types of papers. The value of CIE a\* increase between 24 and 36 hours for all types of papers, and value of CIE b\* is increase for all types of paper to 24 hour, and then between 24 and 36 hour decreased and after 36 hour increase. With increased the time of exposure to artificial thermal ageing color difference for all types of papers increase. The color difference for coated papers – glossy and mat and LWC paper, color difference on 36 hour is smaller compare to this between 24 and 48 hour of artificial thermal ageing.

In result of exposure on thermal ageing average color difference ( $\Delta E^*_{ab, average}$ ) increase for all types of papers.

The 3D color ranges shows relatively big changes in all colors after 72 hours of thermal ageing. The lights, middle and dark tones of color range before artificial thermal ageing is bigger

compare to color range after 72 hours thermal ageing on 105°C for blue-violet color.

After comparing color range of five types of papers before and after 72 hours exposure on artificial thermal aging at 105°C have been observed the following influence on color shifting during the ageing process:

In yellow-red color the small difference on color range was in offset paper and bigger for coated paper – mat and LWC paper.

For blue-red color the smallest color range have newspaper, and bigger coated paper – glossy. For green-blue colors bigger color range have LWC paper and smallest newspaper.

#### REFERENCES

1. G. Saikova, Base methods for restoration and conservation of paper, NHM, Sofia, 1990
2. ISO 12647-2:2004, Graphic technology – Process control for the production of half-tone color separations, proof and productions prints, Part 2: Offset lithographic processes.
3. N. Kachin, I. Spiridonov, *Cellulose Chemistry and Technology*, **39**, 255 (2004).
4. N. Kachin, I. Spiridonov, *Printing Processes, Part 1, Theoretical bases*, Pleiada, Sofia, 2000
5. Gretag Mackbeth, *Обзорный проспект технических и программных средств контроля цвета*, Легион группа, Москва 2000.
6. ISO 13656:2000, Graphic technology – Application of reflection densitometry and colorimetry to process control or evaluation of prints and proofs.
7. H. Kipphan, *Handbook of Print Media Technologies and Production Methods*, Berlin Springer, 2001.

*I.T. Spiridonov et al.: Study of color characteristic changes of printed images under artificial ageing on different papers*

8. K. Schlöpfer, *Farbmetrik in der Reproduktionstechnik und im Mehrfarbendruck*, 2. Auflage. UGRA. St. Gallen 1993.
9. H. Kipphan, *Color Measurement Methods and Systems in Printing, Technology and Graphic Arts Proceeding*, SPIE, Vol. 1912 (Color Hardcopy and Graphic Arts II). The Society for Optical Engineering (SPIE), Bellingham (WA), 278-298, 1993.
10. ISO 2470:2002, Paper, board and pulps - Measurement of diffuse blue reflectance factor (ISO brightness)
11. E. Petkova, I. Spiridonov, I. Lozanova-Doncheva, R. Boeva-Spiridonova, *Proc. 5th International GRID symposium*, Novi Sad, Serbia, p. 39-44, 2010.

## ИЗСЛЕДВАНЕ НА ПРОМЕНИТЕ В ЦВЕТОВИТЕ ХАРАКТЕРИСТИКИ НА ПЕЧАТНИТЕ ИЗОБРАЖЕНИЯ ПРИ ИЗКУСТВЕНО СТАРЕЕНЕ НА РАЗЛИЧНИ ХАРТИИ

И. Спиридонов<sup>1\*</sup>, Р. Боева<sup>1</sup>, И. Лозанова-Дончева<sup>1</sup>, Т. Божкова<sup>1</sup>,  
Ж. Павлович<sup>2</sup>, Г. Владич<sup>2</sup>, Н. Кашикович<sup>2</sup>, М. Станчич<sup>2</sup>, Б. Тачева<sup>1</sup>

*1 Химикотехнологичен и металургичен университет, Катедра „Целулоза, хартия и полиграфия“, България*

*2 Университет на Нови Сад, Технически факултет, Катедра по графично инженерство и дизайн, Сърбия*

Постъпила на 28 ноември, 2016 г.; Приета за печат на 8 май, 2017 г.

(Резюме)

В настоящата разработка е извършено е подробно изследване на промените в цветовите характеристики на офсетовите печатни изображения в процеса на изкуствено термично стареене. За целта е моделирана, експонирана и отпечатана специална тестова форма съдържаща голям брой различни контролни скали и елементи. Измерени са оптичните (денситометрични) и цветови характеристики на различните комбинации от мастило-хартия-печатна машина преди стареенето и след подлагане на стареене през различни времеви периоди. Основната задача на изследването е установяване и оценка в реални производствени условия на стареенето на различните комбинации от мастило и хартии за печат.

**Ключови думи:** цветови характеристики, офсетов печат, цветови разлики, качество на печата, стареене на материалите

## Ga(III) complexes of methoxy substituted aroylhydrazones: synthesis, characterization and DFT calculations

B. I. Nikolova-Mladenova<sup>1\*</sup>, S. E. Angelova<sup>2</sup>

<sup>1</sup> Department of Chemistry, Faculty of Pharmacy, Medical University-Sofia, 2 Dunav Str., 1000 Sofia, Bulgaria

<sup>2</sup> Institute of Organic Chemistry with Centre of Phytochemistry, Bulgarian Academy of Sciences, Acad. G. Bonchev str. bl.9, 1113 Sofia, Bulgaria

Submitted November 30, 2016; Revised April 27, 2017

The study reports the synthesis and physicochemical characterization of Ga (III) complexes with 3-, 4- and 5-methoxy substituted salicylaldehyde based aroylhydrazones designed by varying the position of methoxy group in salicylaldehyde moiety. The complexes were obtained by reaction of Ga(NO<sub>3</sub>)<sub>3</sub>.H<sub>2</sub>O with the ligands in 1:2 metal-to-ligand molar ratio. The coordination behaviour of 3-, 4- and 5-methoxysalicylaldehyde-4-hydroxybenzoylhydrazones towards Ga (III) ions was investigated at theoretical and experimental level. Density Functional Theory calculations with Becke's 3-parameter hybrid functional and 6-31+G (d,p) basis set were carried out to investigate the structural features of the methoxy substituted at different positions aroylhydrazones ligands and Ga (III) complexes. The predicted metal-ligand binding mode was confirmed by spectral data. The complexes are mononuclear with the Ga (III) ions being surrounded by two tridentate ligands. The analysis revealed coordination binding through deprotonated salicylaldehyde phenolic-oxygen, azomethine-nitrogen and amide-oxygen atoms. A general formula [Ga(L-H)<sub>2</sub>]<sub>2</sub>NO<sub>3</sub> for the complexes obtained was suggested on the basis of the experimental data.

**Key words:** gallium (III) complexes, aroylhydrazones, DFT calculations.

### INTRODUCTION

Over the last few years gallium was widely studied due to the versatile applications of this metal and its complexes as bioactive compounds, materials for optoelectronic devices, catalysts, etc. [1–3]. The ability of simple metal salt gallium (III) nitrate to inhibit tumor cell growth *in vitro* and *in vivo* provides a strong motivation for continued research into the development of new gallium compounds with antitumor activities [3–6]. However, in aqueous media and under physiological conditions, the small and highly charged Ga (III) ion hydrolyzes nearly completely over a wide pH range, forming various hydroxide species [1]. To prevent hydrolysis processes, coordination of gallium with polydentate organic ligands has been proposed since Ga (III) complexes possess improved oral bioavailability, hydrolytic stability and membrane penetration ability [1, 3]. Hydrazones are effective ligands as they easily form stable complexes with many metals. The coordination modes of the hydrazone ligands depend on different factors like reaction conditions, stability of the complex formed, number and nature of the substituents on hydrazone skeleton. Aroylhydrazones of the type R-CO-NH-N=CH-R', derived by condensation of aromatic aldehydes and acid hydrazides form a series of biologically active ligands used in medicinal chemistry

[7–10]. Furthermore, suitable substituents can improve the coordination properties. Especially interesting hydrazones were synthesized by salicylaldehyde (2-hydroxybenzaldehyde). The additional hydroxy group in the aldehyde part increases the number of donor atoms and enhances coordination ability of the ligands. Various derivatives of salicylaldehyde have been used in order to discover new pharmacologically active compounds [11–13]. The substitutions slightly change the compounds but give rise to a diversity of biological effects and various pharmacological and potential therapeutic properties. It has been demonstrated that the introduction of a methoxy group into a salicylaldehyde results in derivatives with high antiproliferative and antioxidant activity [13–15]. Hence the methoxy substituted hydrazones would be suitable to prepare cytotoxic Ga complexes.

In the study herein we describe the synthesis and physicochemical characterization of Ga (III) complexes with 3-, 4- and 5-methoxy substituted salicylaldehyde based hydrazones. DFT calculations were carried out to examine the coordination ability of methoxy hydrazones and to investigate how the position of the methoxy group in salicylaldehyde affects the structural features of the complexes. The obtained gallium complexes were characterized by elemental analysis, NMR- and IR-spectroscopy.

\*) To whom all correspondence should be sent:  
E-mail: boriananik@abv.bg

## EXPERIMENTAL PART

3-methoxysalicylaldehyde, 4-ethoxysalicylaldehyde, 5-methoxysalicylaldehyde and 4-hydroxybenzylhydrazone used for the preparation of the ligands 3-methoxysalicylaldehyde-4-hydroxybenzoylhydrazone (**L**<sup>1</sup>), 4-methoxysalicylaldehyde-4-hydroxybenzoylhydrazone (**L**<sup>2</sup>) and 5-methoxysalicylaldehyde-4-hydroxybenzoylhydrazone (**L**<sup>3</sup>) were purchased from Sigma-Aldrich and used without further purification. Gallium (III) nitrate monohydrate used for the synthesis of the complexes was purchased from Sigma-Aldrich. All other chemicals used were of analytical reagent grade.

The carbon, nitrogen and hydrogen contents of the compounds were determined by elemental analyses on Euro EA 3000 – Single, EuroVector SpA analyzer. The IR spectra were recorded on a Thermo Scientific Nicolet iS10 spectrophotometer in the range of 4000–400 cm<sup>-1</sup> as ATR. The <sup>1</sup>H NMR spectra were recorded on a Bruker Avance DRX 250 spectrometer in DMSO-d<sub>6</sub> as solvent, chemical shifts were referenced to the solvent signal. Chemical shifts (δ) are reported in parts per million (ppm), *J* values are given in Hz. Splitting patterns were indicated by the symbols: s (singlet), d (doublet), t (triplet) and m (multiplet).

The synthesis of the ligands was published in our previous works [13–14, 16].

The gallium (III) complexes were obtained by reaction of Ga(NO<sub>3</sub>)<sub>3</sub>·H<sub>2</sub>O with the ligands in 1:2 metal-to-ligand molar ratios using the following general procedure: Solution of gallium nitrate monohydrate (0.5 mmol) in methanol (50 mL) was added to the respective solutions of the ligands (1 mmol) in methanol (100 mL). The resulted solutions were stirred for 1 h at room temperature to complete the reaction and then were kept at room temperature for 48 h. During this time crystals of the product were obtained. Fine crystals were collected after filtration, washed with methanol and dried in a vacuum desiccator.

*Bis-(3-methoxysalicylaldehyde-4-hydroxybenzoylhydrazone) gallium (III) nitrate,*  
[Ga(L<sup>1</sup>-H)<sub>2</sub>](NO<sub>3</sub>)

Yield: 58%; Colour: Yellow-greenish; IR (ν cm<sup>-1</sup>): 3400 (OH<sub>hydrazide</sub>), 3200 (NH), 1607 (C=O), 1588 (C=N), 1391 (NO<sub>3</sub><sup>-</sup>). <sup>1</sup>H NMR (250 MHz, DMSO-d<sub>6</sub>) δ ppm: 3.77 (s, 3H, -OCH<sub>3</sub>), 6.83 (m, 2H, ArH<sub>hydrazide</sub>, 3H, ArH<sub>aldehyde</sub>), 7.90 (d, 2H, *J* = 8 Hz, ArH<sub>hydrazide</sub>), 8.76 (s, 1H, CH=N), 10.00 (s, 1H, OH<sub>hydrazide</sub>), 11.11 (s, 1H, NH). Calculated for [Ga(C<sub>15</sub>H<sub>13</sub>N<sub>2</sub>O<sub>4</sub>)<sub>2</sub>](NO<sub>3</sub>): C, 51.31; H, 3.73; N, 9.97. Found: C, 51.58; H, 3.89; N, 9.59.

*Bis-(4-methoxysalicylaldehyde 4-hydroxybenzoylhydrazone) gallium (III) nitrate,*  
[Ga(L<sup>2</sup>-H)<sub>2</sub>](NO<sub>3</sub>)

Yield: 65 %; Colour: Yellow-greenish; IR (ν cm<sup>-1</sup>): 3401 (OH<sub>hydrazide</sub>), 3179 (N-H), 1618 (C=O), 1593 (C=N), 1392 (NO<sub>3</sub><sup>-</sup>). <sup>1</sup>H NMR (250 MHz, DMSO-d<sub>6</sub>) δ ppm: 3.67 (s, 3H, -OCH<sub>3</sub>), 6.31 (s, 1H, ArH<sub>aldehyde</sub>), 6.35 (d, 1H, *J* = 8 Hz, ArH<sub>aldehyde</sub>), 6.86 (d, 2H, *J* = 8 Hz, ArH<sub>hydrazide</sub>), 7.31 (d, 1H, *J* = 9 Hz, ArH<sub>aldehyde</sub>), 7.80 (d, 2H, *J* = 6.5 Hz, ArH<sub>hydrazide</sub>), 8.56 (s, 1H, CH=N), 9.96 (s, 1H, OH<sub>hydrazide</sub>), 11.78 (s, 1H, NH). Calculated for [Ga(C<sub>15</sub>H<sub>13</sub>N<sub>2</sub>O<sub>4</sub>)<sub>2</sub>](NO<sub>3</sub>): C, 51.31; H, 3.73; N, 9.97. Found: C, 51.18; H, 3.95; N, 9.62.

*Bis-(5-methoxysalicylaldehyde 4-hydroxybenzoylhydrazone) gallium (III) nitrate,*  
[Ga(L<sup>3</sup>-H)<sub>2</sub>](NO<sub>3</sub>)

Yield: 62 %; Colour: Orange-greenish; IR (ν cm<sup>-1</sup>): 3370 (OH<sub>hydrazide</sub>), 3190 (N-H), 1616 (C=O), 1593 (C=N), 1392 (NO<sub>3</sub><sup>-</sup>). <sup>1</sup>H NMR (250 MHz, DMSO-d<sub>6</sub>) δ ppm: 3.70 (s, 3H, -OCH<sub>3</sub>), 6.80 (m, 2H, ArH<sub>hydrazide</sub>, 2H, ArH<sub>aldehyde</sub>), 7.00 (s, 1H, ArH<sub>aldehyde</sub>), 7.90 (d, 2H, *J* = 7.5 Hz, ArH<sub>hydrazide</sub>), 8.62 (s, 1H, CH=N), 9.97 (s, 1H, OH<sub>hydrazide</sub>), 10.80 (s, 1H, NH). Calculated for [Ga(C<sub>15</sub>H<sub>13</sub>N<sub>2</sub>O<sub>4</sub>)<sub>2</sub>](NO<sub>3</sub>): C, 51.31; H, 3.73; N, 9.97. Found: C, 51.51; H, 4.04; N, 9.62.

The B3LYP/31+G(d,p) (Becke's three-parameter hybrid exchange-correlation functional [17] with diffuse function augmented double-ζ polarized basis set) method was used to optimize the geometry of each ligand and metal complex. Local minima were verified by establishing that all vibrational frequencies are real. All calculations were performed using Gaussian 09 [18]. PyMOL molecular graphics software was used for generating the molecular graphics images [19].

## RESULTS AND DISCUSSION

The ligands 3-methoxysalicylaldehyde-4-hydroxybenzoylhydrazone (**L**<sup>1</sup>), 4-methoxysalicylaldehyde-4-hydroxybenzoylhydrazone (**L**<sup>2</sup>) and 5-methoxysalicylaldehyde-4-hydroxybenzoylhydrazone (**L**<sup>3</sup>), shown on Figure 1, were synthesized as already reported [13, 14, 16].

Three gallium (III) complexes with the ligands **L**<sup>1</sup>, **L**<sup>2</sup> and **L**<sup>3</sup> were prepared by a direct reaction of the hydrazones and gallium (III) nitrate monohydrate in absolute methanol with good yields (58–65 %) (Scheme 1).

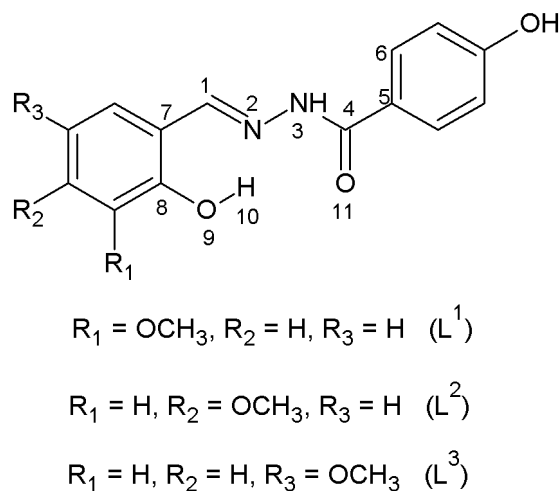
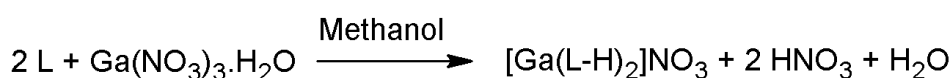


**Figure 1.** Structure of the 3-, 4- and 5-methoxy substituted ligands.



**Scheme 1.** Synthesis of the gallium (III) complexes with the ligands.

The complexes were characterized by elemental analysis as a basis for the determination of their empirical formulas. Experimental and calculated C, H, N values are in good agreement and reveal molar ratio metal:ligand = 1:2 in the complexes. Analyses suggest the following molecular formula of the compounds  $[\text{Ga}(\text{C}_{15}\text{H}_{13}\text{N}_2\text{O}_4)_2]\text{NO}_3$ . The data from the elemental analysis of the gallium (III) complexes are summarized in the Experimental section.

The coordination behaviour of 3-, 4- and 5-methoxysalicylaldehyde benzoylhydrazones towards Ga (III) ions was investigated at theoretical and

experimental level. DFT calculations were carried out to predict the molecular structure of the new gallium (III) complexes and to investigate how the position of the methoxy group in the salicylaldehyde affects the structural features of the complexes. The optimized geometry of the Ga-complex ions  $[\text{Ga}(\text{L}^1-\text{H})_2]^+$ ,  $[\text{Ga}(\text{L}^2-\text{H})_2]^+$  and  $[\text{Ga}(\text{L}^3-\text{H})_2]^+$  are shown on Figure 2.

Selected geometrical parameters for the studied ligands and complexes (bond lengths (Å) and angles (°)) are presented in Table 1.

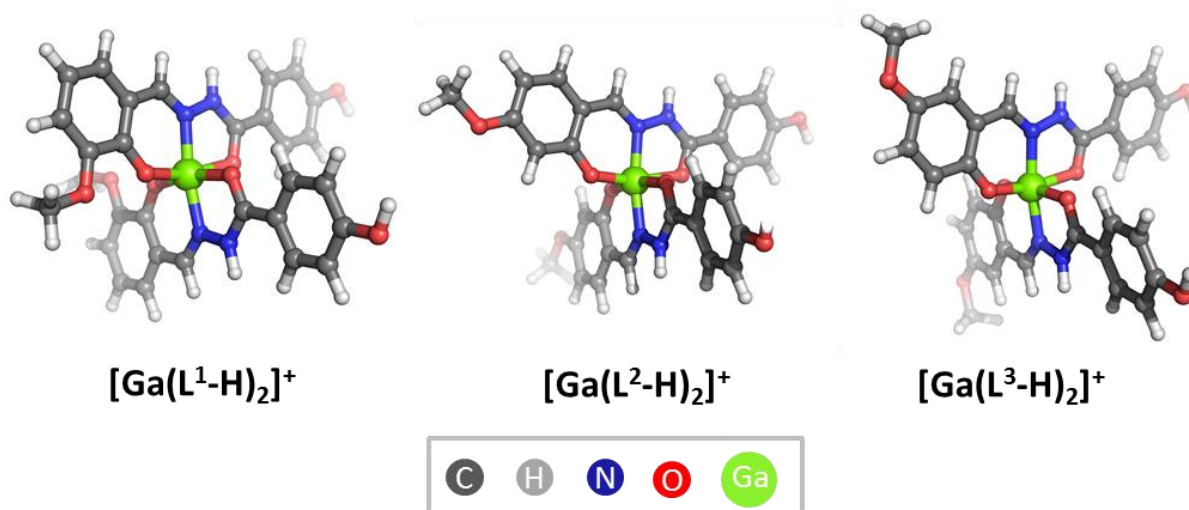


**Figure 2.** B3LYP/6-31+G(d,p) optimized geometries of the Ga (III) complexes.

**Table 1.** Selected B3LYP/6-31+G(d,p) calculated parameters for the ligands and complexes. Atom numbering is shown on Figure 1.

	Ligand			Complex		
	L <sup>1</sup>	L <sup>2</sup>	L <sup>3</sup>	[Ga(L <sup>1</sup> -H) <sub>2</sub> ] <sup>+</sup>	[Ga(L <sup>2</sup> -H) <sub>2</sub> ] <sup>+</sup>	[Ga(L <sup>3</sup> -H) <sub>2</sub> ] <sup>+</sup>
dipole moment, $\mu$ [D]	4.36	5.93	6.38	5.14	4.11	6.79
bond length [Å]						
C1-N2	1.290	1.291	1.291	1.305	1.308	1.307
N2-N3	1.359	1.361	1.359	1.376	1.377	1.377
N3-C4	1.388	1.387	1.389	1.357	1.357	1.357
C4-C5	1.497	1.496	1.496	1.463	1.464	1.464
C4-O11	1.223	1.224	1.223	1.263	1.262	1.263
C5-C6	1.406	1.406	1.406	1.410	1.410	1.464
C1-C7	1.453	1.448	1.451	1.421	1.415	1.420
C7-C8	1.416	1.428	1.416	1.432	1.446	1.434
C8-O9	1.343	1.346	1.350	1.303	1.309	1.309
O9-H10/O9-Ga	0.986	0.987	0.985	1.903	1.902	1.901
N1-Ga	-	-	-	2.014	2.022	2.024
O11-Ga	-	-	-	2.031	2.034	2.029
angle [°]						
C1-N2-N3	118.68	118.60	118.68	120.26	120.06	119.95
N2-N3-C4	120.21	120.17	120.09	116.40	116.14	116.23
N3-C4-O11	122.12	122.18	122.06	117.72	117.84	117.80
N3-C4-C5	114.99	114.97	115.03	120.39	120.11	120.14
C5-C4-O11	122.88	122.85	122.90	121.89	122.05	122.06
C1-C7-C8	121.37	122.18	121.83	121.92	122.99	122.15
dihedral angle [°]						
N2-C1-C7-C8	0.80	0.77	1.03	0.09	0.77	0.66
N3-C4-C5-C6	24.14	24.77	23.97	2.56	11.48	10.59

The phenyl ring in the ligand structure is rotated about 25 degrees ( $23.97^\circ$ – $24.77^\circ$ ), so the ligands are not planar. One mode of coordination with octahedral arrangement between the optimized structures of the deprotonated free ligands and the Ga cations was considered: the metal is bound to the oxygen atoms of salicylaldehyde phenolic and amide groups and to the azomethine nitrogen atom of each of the two ligands. In the resulting complexes the ligands are positioned almost perpendicularly to each other. The calculated Ga–O and Ga–N distances are indicative of a stronger interaction of Ga cations with the deprotonated OH-groups – in all cases the O9–Ga bonds ( $<2$  Å) are shorter than the O11–Ga and N1–Ga bonds ( $>2$  Å) (Table 1). Some structural changes are observed in the ligands upon complex formation, as the most pronounced one is the change observed in the L<sup>1</sup> structure – the ligand becomes almost planar (the N3–C4–C5–C6 dihedral angle changes from  $24.14^\circ$  to  $2.56^\circ$ ). Ga cation is positioned at almost equal distance from O9 and O11 atoms in all complexes. A little bit shorter N1–Ga bond is predicted for the [Ga(L<sup>1</sup>-H)<sub>2</sub>]<sup>+</sup> complex. The coordination realized between L<sup>1</sup> (with methoxy group in position 3) and Ga cation seems to be slightly stronger than that with the other ligands.

The predicted mode of coordination of the ligands to the gallium ions was verified by IR and <sup>1</sup>H NMR spectral data for the metal-free ligands as well as their Ga (III) complexes.

The ligands show a band at  $3300$ – $3360$  cm<sup>-1</sup> due to salicylaldehyde phenolic OH group. The absence of these bands in the IR spectra of the Ga (III) complexes supports the suggestion for deprotonation of the ligands during the coordination and displacement of a proton by the Ga (III) ion. The  $\nu(\text{C}=\text{O})$  band, observed at  $1634$ – $1662$  cm<sup>-1</sup> in the spectra of the ligands, is shifted to lower wavenumbers by  $18$ – $44$  cm<sup>-1</sup> in the gallium complexes, indicating coordination of the carbonyl group to the metal ion. The bands attributed to azomethine C=N group of the ligands ( $1602$ – $1608$  cm<sup>-1</sup>) were shifted by  $9$ – $20$  cm<sup>-1</sup> to lower wavenumbers in the spectra of the complexes ( $1588$ – $1593$  cm<sup>-1</sup>) indicating the involvement of N-atom of the azomethine group in the complex formation. Absorptions at  $1391$ – $1392$  cm<sup>-1</sup> in the spectra of the complexes were attributed to the nitrate group as counter-ion. The IR spectra of ligand L<sup>3</sup> and its Ga-complex are given on Figure 3.

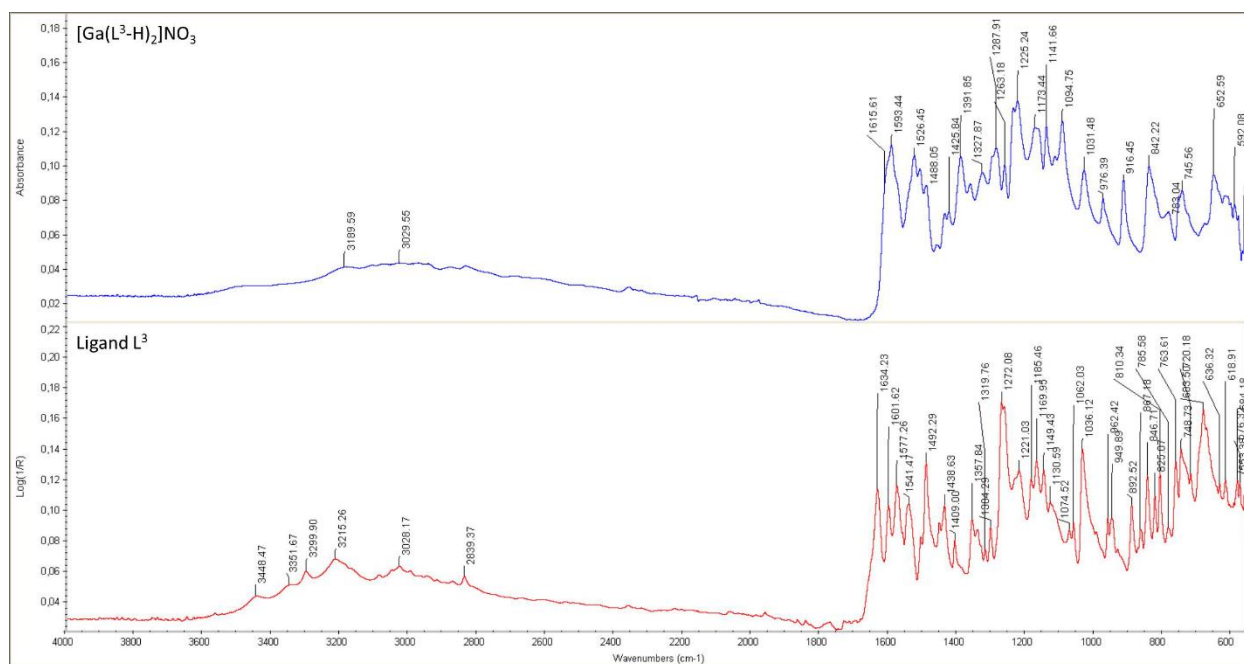


Figure 3. The IR spectra of ligand  $L^3$  and its Ga-complex.

$^1\text{H}$  NMR spectra of the Ga (III) complexes give additional information about structural changes in the ligands upon complexation. In the  $^1\text{H}$  NMR spectra of the ligands the signal for the proton of the salicylaldehyde phenolic OH group was observed as a singlet at 11.78-11.89 ppm. The disappearance of these signals in the  $^1\text{H}$  NMR spectra of the complexes supposes coordination of Ga (III) ion to the salicylaldehyde phenolic oxygen atom after deprotonation. The singlets at 8.51-8.61 ppm in the spectra of the ligands, assigned to azomethine group –  $\text{CH}=\text{N}$ , were downfield shifted (by 0.05-0.15 ppm) in the complexes to 8.56-8.76 ppm, indicating the involvement of the azomethine nitrogen in bonding with the Ga (III) ion. The signals for the protons of the methoxy-group in salicylaldehyde ring in the spectra of the complexes were slightly upshifted by 0.02-0.10 ppm compared to those of the ligands.

The observed changes in the experimental IR and  $^1\text{H}$  NMR spectra of the ligands and their Ga (III) complexes suggest that 3-methoxy-, 4-methoxy- and 5-methoxysalicylaldehyde-4-hydroxybenzoylhydrazones chelate the metal ions through deprotonated salicylaldehyde phenolic-oxygen, azomethine-nitrogen and amide-oxygen atoms and thus forming stable six-membered chelates.

### CONCLUSION

Three novel Ga (III) complexes with 3-, 4- and 5-methoxysalicylaldehyde-4-hydroxybenzoylhydrazone ligands were synthesized and structurally characterized. The analytical data reveal that complexes are mononuclear with molar ratio metal:ligand = 1:2 and general formula  $[\text{Ga}(\text{L}-\text{H})_2]\text{NO}_3$ . The ligands act as

tridentate ligands and chelate Ga (III) ion through deprotonated phenolic-oxygen, azomethine-nitrogen and amide-oxygen atoms forming a six-membered chelate ring. The molecular geometries of the ligands and gallium (III) complexes were studied at the B3LYP/6-31+G(d,p) level of theory. Selected geometrical parameters for the studied ligands and complexes are compared and the structural changes in the ligands upon complex formation are discussed. On the basis of the calculated Ga–O and Ga–N distances stronger interaction of Ga (III) with the deprotonated salicylaldehyde OH-groups can be concluded.

**Acknowledgements.** Financial support by the Medical University of Sofia (Council of Medical Science, Project №540/ 21.01.2016, Grant 49/2016) is gratefully acknowledged. The calculations were performed on the HPC system at IOCCP – BAS with the financial support of the Bulgarian Scientific Fund under Project “MADARA” (RNF01/0110, contract №DO02-52/2008).

### REFERENCES

1. L. R. Bernstein, in: The Use of Metals in Medicine, M. Gielen, B. R. T. Tiekink. (eds), vol. 14, John Wiley & Sons, Ltd., New York, 2005, 259.
2. F. Zhang, X. Liu, F. Huang, Z. Zhuo, L. Lu, Z. Xu, Y. Wang, X. Tao, W. Bian, W. Tang, , *Chin. Sci. Bull.*, **56**, 479 (2011).
3. M. A. Jakupec, M. Galanski, V. B. Arion, G. C. Hartinger, B.K. Keppler, *Dalton Trans.*, **2**, 183 (2008).
4. L. R. Bernstein, T. Tanner, C. Godfrey, B. Noll, *Met. Based Drugs*, **7**, 33 (2000).
5. P. Collyer, B. K. Keppler, C. Madoulet, B. Desoize, *Crit. Rev. Oncol. Hematol.*, **42**, 283 (2002).
6. M. A. Jakupec, B. K. Keppler, *Curr. Top. Med. Chem.*, **4**, 1575 (2004).

7. P. Ponka, D. Richardson, E. Baker, H. M. Schulman, J. T. Edward, *Biochim. Biophys. Acta*, **967**, 122 (1988).
8. E. Baker, D. R. Richardson, S. Gross, P. Ponka, *Hepatology*, **15**, 492 (1992).
9. D. R. Richardson, P. Ponka, *J. Lab. Clin. Med.*, **131**, 306 (1998).
10. J. L. Buss, E. Arduini, P. Ponka, *Biochem. Pharmacol.*, **64**, 1689 (2002).
11. D. B. Lovejoy, D. R. Richardson, *Blood*, **100**, 666 (2002).
12. D. R. Richardson, K. Milnes, *Blood*, **89**, 3025 (1997).
13. B. Nikolova-Mladenova N. Halachev, R. Iankova, G. Momekov, D. Ivanov, *J. Arzneim.-Forsch.*, **61**, 714 (2011).
14. B. Nikolova-Mladenova, G. Momekov, D. Ivanov, *Pharmacia*, **LVIII**, 41 (2011).
15. N. G. Hristova-Avakumova, B. I. Nikolova-Mladenova, V. A. Hadjimitova, *Bulg. Chem. Comm.*, **47**, 1053 (2015).
16. B. Nikolova-Mladenova, G. Momekov, D. Ivanov, A. Bakalova, *J. Appl. Biomed.*, in press (2017).
17. A. D. Becke, *J. Chem. Phys.*, **98**, 5648 (1993).
18. M. J. Frisch et al., Gaussian 09, Revision D.01; Gaussian, Inc., Wallingford CT, 2013.
19. The PyMOL Molecular Graphics System, Version 1.7.6.6 Schrödinger, LLC.

## Ga(III) КОМПЛЕКСИ С МЕТОКСИ-ЗАМЕСТЕНИ АРОИЛХИДРАЗОНИ: СИНТЕЗ, ОХАРАКТЕРИЗИРАНЕ И ИЗЧИСЛЕНИЯ С ТФП

Б.И. Николова-Младенова<sup>1\*</sup>, С.Е. Ангелова<sup>2</sup>

<sup>1</sup> Катедра „Химия“, Факултет по фармация, Медицински университет - София, ул. Дунав 2, София 1000, България

<sup>2</sup> Институт по органична химия с Център по фитохимия, Българска академия на науките, ул. Акад. Г. Бончев, бл. 9, София 1113, България

Постъпила на 30 ноември, 2016 г.; коригирана на 27 април, 2017 г.

(Резюме)

В това изследване се описва синтезът и физикохимичното охарактеризиране на Ga (III) комплекси с метокси заместени ароилхидразони, получени чрез вариране на мястото на метокси групата в салицилалдехидния фрагмент. Комплексите са получени чрез взаимодействие на Ga(NO<sub>3</sub>)<sub>3</sub>·H<sub>2</sub>O с лигандите в молно отношение метал:лиганд = 1:2. Координационното поведение на 3-, 4- и 5-метоксисалицилалдехид-4-хидроксibenзоилхидразоните спрямо Ga (III) йони беше изследвано теоретично и експериментално. За изследване на структурните характеристики на лигандите (метокси-заместени в различни позиции ароилхидразони) и Ga (III) комплекси бяха направени изчисления с използване на Теория на функционала на плътността, B3LYP функционал и базисен набор 6-31+G (d,p). Предсказаното координиране метал-лиганд беше потвърдено от спектралните данни. Комплексите са моноядрени, като Ga (III) йоните са свързани с два тридентатни лиганда. Доказаната координация е чрез кислороден атом от депротонираната алдехидна хидроксилна група, азотен атом от азометинова група и кислороден атом от amidна група. На базата на експерименталните данни за комплексите беше предложена обща формула [Ga(L-H)<sub>2</sub>]NO<sub>3</sub>.



## BULGARIAN CHEMICAL COMMUNICATIONS

### Instructions about Preparation of Manuscripts

**General remarks:** Manuscripts are submitted in English by e-mail or by mail (in duplicate). The text must be typed double-spaced, on A4 format paper using Times New Roman font size 12, normal character spacing. The manuscript should not exceed 15 pages (about 3500 words), including photographs, tables, drawings, formulae, etc. Authors are requested to use margins of 3 cm on all sides. For mail submission hard copies, made by a clearly legible duplication process, are requested. Manuscripts should be subdivided into labelled sections, e.g. **Introduction, Experimental, Results and Discussion**, etc.

**The title page** comprises headline, author's names and affiliations, abstract and key words.

Attention is drawn to the following:

a) **The title** of the manuscript should reflect concisely the purpose and findings of the work. Abbreviations, symbols, chemical formulas, references and footnotes should be avoided. If indispensable, abbreviations and formulas should be given in parentheses immediately after the respective full form.

b) **The author's** first and middle name initials, and family name in full should be given, followed by the address (or addresses) of the contributing laboratory (laboratories). **The affiliation** of the author(s) should be listed in detail (no abbreviations!). The author to whom correspondence and/or inquiries should be sent should be indicated by asterisk (\*).

**The abstract** should be self-explanatory and intelligible without any references to the text and containing not more than 250 words. It should be followed by key words (not more than six).

**References** should be numbered sequentially in the order, in which they are cited in the text. The numbers in the text should be enclosed in brackets [2], [5, 6], [9–12], etc., set on the text line. References, typed with double spacing, are to be listed in numerical order on a separate sheet. All references are to be given in Latin letters. The names of the authors are given without inversion. Titles of journals must be abbreviated according to Chemical Abstracts and given in italics, the volume is typed in bold, the initial page is given and the year in parentheses. Attention is drawn to the following conventions:

a) The names of all authors of a certain publications should be given. The use of “*et al.*” in the list of references is not acceptable.

b) Only the initials of the first and middle names should be given.

In the manuscripts, the reference to author(s) of cited works should be made without giving initials, e.g. “Bush and Smith [7] pioneered...”. If the reference carries the names of three or more authors it should be quoted as “Bush *et al.* [7]”, if Bush is the first author, or as “Bush and co-workers [7]”, if Bush is the senior author.

**Footnotes** should be reduced to a minimum. Each footnote should be typed double-spaced at the bottom of the page, on which its subject is first mentioned.

**Tables** are numbered with Arabic numerals on the left-hand top. Each table should be referred to in the text. Column headings should be as short as possible but they must define units unambiguously. The units are to be separated from the preceding symbols by a comma or brackets.

Note: The following format should be used when figures, equations, etc. are referred to the text (followed by the respective numbers): Fig., Eqns., Table, Scheme.

**Schemes and figures.** Each manuscript (hard copy) should contain or be accompanied by the respective illustrative material as well as by the respective figure captions in a separate file (sheet). As far as presentation of units is concerned, SI units are to be used. However, some non-SI units are also acceptable, such as °C, ml, l, etc.

The author(s) name(s), the title of the manuscript, the number of drawings, photographs, diagrams, etc., should be written in black pencil on the back of the illustrative material (hard copies) in accordance with the list enclosed. Avoid using more than 6 (12 for reviews, respectively) figures in the manuscript. Since most of the illustrative materials are to be presented as 8-cm wide pictures, attention should be paid that all axis titles, numerals, legend(s) and texts are legible.

The authors are asked to submit **the final text** (after the manuscript has been accepted for publication) in electronic form either by e-mail or mail on a 3.5” diskette (CD) using a PC Word-

processor. The main text, list of references, tables and figure captions should be saved in separate files (as \*.rtf or \*.doc) with clearly identifiable file names. It is essential that the name and version of the word-processing program and the format of the text files is clearly indicated. It is recommended that the pictures are presented in \*.tif, \*.jpg, \*.cdr or \*.bmp format, the equations are written using "Equation Editor" and chemical reaction schemes

are written using ISIS Draw or ChemDraw programme.

The authors are required to submit the final text with a list of three individuals and their e-mail addresses that can be considered by the Editors as potential reviewers. Please, note that the reviewers should be outside the authors' own institution or organization. The Editorial Board of the journal is not obliged to accept these proposals.

## EXAMPLES FOR PRESENTATION OF REFERENCES

### REFERENCES

1. D. S. Newsome, *Catal. Rev.–Sci. Eng.*, **21**, 275 (1980).
2. C.-H. Lin, C.-Y. Hsu, *J. Chem. Soc. Chem. Commun.*, 1479 (1992).
3. R. G. Parr, W. Yang, *Density Functional Theory of Atoms and Molecules*, Oxford Univ. Press, New York, 1989.
4. V. Ponec, G. C. Bond, *Catalysis by Metals and Alloys (Stud. Surf. Sci. Catal., vol. 95)*, Elsevier, Amsterdam, 1995.
5. G. Kadinov, S. Todorova, A. Palazov, in: *New Frontiers in Catalysis (Proc. 10th Int. Congr. Catal., Budapest, 1992)*, L. Guzzi, F. Solymosi, P. Tetenyi (eds.), Akademiai Kiado, Budapest, 1993, Part C, p. 2817.
6. G. L. C. Maire, F. Garin, in: *Catalysis. Science and Technology*, J. R. Anderson, M. Boudart (eds), vol. 6, Springer-Verlag, Berlin, 1984, p. 161.
7. D. Pocknell, *GB Patent 2 207 355* (1949).
8. G. Angelov, PhD Thesis, UCTM, Sofia, 2001.
9. JCPDS International Center for Diffraction Data, *Power Diffraction File*, Swarthmore, PA, 1991.
10. *CA* **127**, 184 762q (1998).
11. P. Hou, H. Wise, *J. Catal.*, in press.
12. M. Sinev, private communication.
13. <http://www.chemweb.com/alchem/articles/1051611477211.html>.

## CONTENTS

<i>Yu. Raynova, Kr. Idakieva, M. Guncheva, V. Uzunova, P. Ossowicz, E. Janus, I. Angelov, R. Tzoneva</i> , Hemocyanin from <i>Rapana thomasi</i> ana – structure and anti-breast cancer activity in a presence of cholinium amino acids.....	5
<i>Y. Raynova, S. Todinova, K. Idakieva</i> , Thermal stability of <i>Helix aspersa</i> maxima hemocyanin	12
<i>V.I. Iliev, D.V. Tomova, V.F. Georgiev, S.K. Rakovsky</i> , Promoting the oxidative removal rate of 4-chlorophenol on gold-doped TiO <sub>2</sub> /graphene photocatalysts under UV light irradiation.....	17
<i>T.T. Batakliiev, V.F. Georgiev, P.A. Karakashkova, M.V. Gabrovska, D.A. Nikolova, M.P. Anachkov, S.K. Rakovsky</i> , Gas phase ozone decomposition over co-precipitated Ni-based catalysts.....	24
<i>V.F. Georgiev, V. Iliev, A.E. Eliyas, T.T. Batakliiev, M.P. Anachkov, V.E. Serga, P.A. Karakashkova, S.K. Rakovsky</i> , Effectiveness of TiO <sub>2</sub> -based photocatalysts in the ozone assisted oxidative degradation of model wastewater contaminant adipic acid under UV-light irradiation.....	30
<i>M.P. Anachkov, P.A. Karakashkova, V.F. Georgiev, S.K. Rakovsky, L.S. Minchev, T.T. Batakliiev</i> , Kinetics and mechanism of the ozone reaction with cyclohexane in liquid phase.....	38
<i>A.H. Braga, J.B.O. Santos, J.M.C. Bueno, S. Damyanova</i> , Study of CoNi catalysts for ethanol steam reforming.....	45
<i>D.I. Ivanova, G.P. Ilieva, L.B. Fachikov</i> , Cold plastic deformation effects on the mechanical properties and corrosion behaviour of low-alloyed (2% Cr) steel.....	54
<i>E.N. Kolentsova, D.Y. Dimitrov, K.I. Ivanov, T.T. Tabakova, Y.G. Karakirova, K.K. Tenchev, G.V. Avdeev</i> , CO and VOCs oxidation over alumina supported Cu-Mn catalysts modified by cerium.....	59
<i>P.M. Miladinova, D.A. Todorova</i> , Synthesis and photophysical properties of a novel benzanthrone pH sensor based on internal charge transfer.....	67
<i>P. G. Velichkova, T. V. Ivanov, I. G. Lalov</i> , A study of the energy potential of vinasse.....	74
<i>U. Vrabič Brodnjak</i> , The effect of ultrasound treatment on soy protein and chitosan coating solution for packaging paper.....	79
<i>U. Vrabič Brodnjak, D. Muck</i> , Printing quality of chitosan-rice starch coated packaging paper.....	85
<i>N. Yotov, I. Valchev, S. Petrin, V. Savov</i> , Lignosulphonate and waste technical hydrolysis lignin as adhesives for eco-friendly fiberboard.....	92
<i>K. Dimitrov, V. Yavorova, M. Herzog, S. Nenkova</i> , Adhesives based on recycled polyurethane foam for wood based materials.....	98
<i>P.G. Velichkova, T.V. Ivanov, I.G. Lalov</i> , Magnetically assisted fluidized bed bioreactor for bioethanol production.....	105
<i>R. Boeva, G. Radeva, I. Spiridonov</i> , Obtaining of high yield fibrous material from hardwood and evaluation of their optical properties of in process of thermal treatment.....	110
<i>R. Boeva, I. Spiridonov, T. Bozhkova, D. Novakovic, B. Banjanin</i> , Evaluation of changes in the optical properties of high yield fibrous materials under thermal treatment.....	115
<i>R. Boeva, I. Spiridonov, G. Radeva</i> , Fast growing paulownia wood – perspective raw material for production of fibrous materials.....	121
<i>R. Boeva, I. Spiridonov, Ž. Pavlović, G. Vladić</i> , Investigation of color characteristics changes of semi chemical pulp samples in process of ageing.....	126
<i>N. Kašiković, M. Stančić, I. Spiridonov, D. Novaković, R. Milošević, D. Grujić, B. Ružičić</i> , The effect of washing temperature and number of washing cycles on the quality of screen printed textiles materials.....	130
<i>S. Dedijer, I. Tomić, I. Spiridonov, R. Boeva, I. Jurić, N. Milić, S. Đurđević</i> , Assessment of using ink - jet imprints in just noticeable color difference evaluation.....	140
<i>S. Dedijer, M. Pal, R. Boeva, I. Spiridonov, T. Bozhkova, V. Zorić, Ž. Zeljković</i> , Characterization of flexo and letterpress printing plate's surface roughness by indirect SEM image-based profilometry.....	148
<i>G. Vladić, N. Kašiković, I. Spiridonov, R. Boeva, I. Pinčjer, M. Stančić</i> , The colorimetric and	

microscopic analysis of differences in colorfastness to rubbing process caused by different composition of screen print inks.....	158
<i>T. Bozhkova, I. Spiridonov, A. Ganchev, R.Boeva- Spridonova</i> , Studies of technologies for exposing photopolymer plates in a controlled atmosphere and their application on a corrugated post print.....	163
<i>T. Bozhkova, R. Boeva, I. T. Spiridonov, J. Sapkota, Y. V. Nedelchev, N. Kašiković, S. Dedijer, M. Pal</i> , Improvement of physical-mechanical and optical properties of the packaging production trough coating with aqueous polymer dispersions in accordance with the environmental protection requirements.....	169
<i>A. Matev, P. Velez, S. Ismail, M. Herzog</i> , Preparing, properties and application of waterborne polyurethane-acrylate oligomer as a matrix in UV-cured fiberglasses.....	174
<i>D.A. Todorova, P.M. Miladinova</i> , Investigation on the influence of reactive dyes over the colour stability of offset printing paper during ageing.....	181
<i>D.A. Todorova, P.M.Miladinova, V.N. Blyahovski</i> , Dyeing of offset printing paper with new reactive dyes - influence over the paper properties and the ageing.....	187
<i>T. Bozhkova, I. Spiridonov, K. Shterev</i> , Overview of security printing types and trends in its future development.....	195
<i>I. Tzvetanska, V.Lasheva</i> New methods of protection during the conservation of books.....	202
<i>R.T.Cenkova, V. Lasheva</i> , Conservation and restoration of documents from the National Historical Museum fund by appropriate methods.....	206
<i>D.A. Todorova, V.G. Lasheva</i> , Study the possibilities of using silver nanoparticles in packaging paper.....	210
<i>S.P. Vladimirova, M.B. Georgieva</i> , Synthesis and SAR evaluation of the phytochemical activity of new N-pyrrolylcarboxylic acids.....	215
<i>Ž. Pavlović, M. Pal, T. Cigula, R. Boeva, I. Spiridonov, T. Bozhkova, M. Prica</i> , Comparative study of offset plate tone value reproduction using different measuring and image processing tools.....	221
<i>I.T. Spiridonov, R.K. Boeva, I.V. Lozanova-Doncheva, T.Ts. Bozhkova, Ž. Pavlović, G. Vladić, N. Kašiković, M. Stančić, B. Tacheva</i> , Study of color characteristic changes of printed images under artificial ageing on different papers.....	229
<i>B.I. Nikolova-Mladenova, S.E. Angelova</i> , Methoxy substituted aroylhydrazones and their Ga(III) complexes: synthesis, characterization and DFT calculations .....	237
<i>Instruction to the authors</i> .....	243

## СЪДЪРЖАНИЕ

Юл. Райнова, Кр. Идакиева, М. Гунчева, В. Узунова, П. Осовиц, Е. Янус, Ив. Ангелов, Р. Цонева, Структура и антитуморна активност на хемоцианин от <i>Rapana thomasiana</i> в присъствие на йонни течности на основата на холин и аминокиселини.....	11
Юл. Райнова, С. Тодинова, К. Идакиева, Термична стабилност на хемоцианин от охлюви <i>Helix aspersa maxima</i> .....	16
В.И. Илиев, Д.В. Томова, В.Ф. Георгиев, С.К. Раковски, Промотиране на скоростта на окислително отстраняване на 4-хлорфенол върху злато-дотирани TiO <sub>2</sub> /графен фотокатализатори при облъчване с ултравиолетова светлина.....	23
В.Ф. Георгиев, В. Илиев, А.Е. Елияс, Т.Т. Батаклиев, М.П. Аначков, В.Е. Серга, П.А. Каракашкова, С.К. Раковски, Ефективност на фотокатализатори на основата на TiO <sub>2</sub> в подпомогнато от озон окислително разграждане на адипинова киселина като моделен замърсител в отпадни води при облъчване с УВ светлина.....	37
Т.Т. Батаклиев, В.Ф. Георгиев, П.А. Каракашкова, М.В. Габровска, Д.А. Николова, М.П. Аначков, С.К. Раковски, Разлагане на озон върху сътуаени никел съдържащи катализатори в течна фаза.....	44
А.Х. Брага, Ж.Б.О. Сантуш, Ж.М.К. Буено, С. Дамянова, Изследване на катализатор от кобалт и никел за стийм-реформинг на етанол.....	53
Д.И. Иванова, Г.П. Илиева, Л.Б. Фачиков, Влияние на студената пластична деформация върху механичните свойства и корозионното поведение на нисколегирана (2% Cr) стомана.....	58
Е.Н. Коленцова, Д.Я. Димитров, К.И. Иванов, Т.Т. Табакова, Й.Г. Каракирова, К.К. Тенчев, Г.В. Авдеев, Окисление на СО и ЛОС върху нанесени на алуминиев оксид Cu-Mn катализатори, модифицирани с церий.....	66
П.М. Миладинова, Д.А. Тодорова, Синтеза и фото-физични свойства на нов рН-сензор с бензатрон на основата на вътрешен пренос на заряда.....	73
П.Г. Величкова, Т.В. Иванов, И.Г. Лалов, Изследване енергийния потенциал на винаса...	78
У. Вrabич Бродняк, Ефект на ултразвуково третиране на разтвори от соев протеин и хитозан за покрития върху опаковъчна хартия.....	84
У. Вrabич Бродняк, Д. Мук, Печатарски качества на опаковъчна хартия, покрита с хитозан и оризова скорбяла.....	91
Н. Йотов, И. Вълчев, Ст. Петрин, В. Савов, Лигносулфонат и отпадъчен технически хидролизен лигнин в ролята на свързващо вещество при производството на екологични плочи от дървесни влакна.....	97
К. Димитров, В. Яворова, М. Херцог, С. Ненкова, Лепила за дървесина базирани на рециклирани полиуретанови пени.....	104
П.Г. Величкова, Т.В. Иванов, И.Г. Лалов, Получаване на биоетанол в биореактор с магнитно асистиран флуидизиран слой.....	109
Р. Боева, И. Спиридонов, Г. Радева, Получаване на високодобивни влакнести материали от широколистна дървесина и оценка на техните оптични свойства в процеса на термична обработка.....	114
Р. Боева, И. Спиридонов, Т. Божкова, Д. Новакович, Б. Банжанин, Изследване на промените в оптичните свойства на високодобивните влакнести материали при термична обработка.....	120
Р. Боева, Г. Радева, И. Спиридонов, Бързорастящата дървесина от <i>Paulownia</i> - перспективна суровина за производство на влакнести материали.....	125
Р. Боева, И. Спиридонов, Ж. Павлович, Г. Владич, Изследване на промените в цветовете характеристики на образци от семи-целуозна маса в процеса на стареене.....	129
Н. Кашикович, М. Станчич, И. Спиридонов, Д. Новакович, Р. Милошевич, Д. Груджич, Б. Ружичич, Изследване на влиянието на температурата и броя цикли на изпиране върху качеството на текстилни материали със нанесени ситопечатни изображения.....	139

<i>С. Деджиер, И. Томич, И. Спиридонов, Р. Боева, И. Юрич, Н. Милич, С. Джурджевич,</i> Изследване и оценка на слабо забележими цветови разлики на отпечатъци получени чрез дигитален струен печат.....	147
<i>С. Деджиер, М. Пал, Р. Боева, И. Спиридонов, Т. Божкова, В. Зорич, Ж. Желькович,</i> Изследване на повърхностните характеристики на флексо и летърпрес печатни форми чрез SEM-базиран анализ.....	157
<i>Г. Владич, Н. Кашикович, И. Спиридонов, Р. Боева, И. Пинчиер, М. Станчич,</i> Колориметричен и микроскопски анализ на устойчивостта на цветовете на различни състави на ситопечатни мастила.....	162
<i>Т. Божкова, И. Спиридонов, А. Ганчев, Р. Боева-Спиридонов,</i> Изследване на технологии за експониране на фотополимерни форми в контролирана атмосфера и тяхното приложение при директен печат върху вълнообразен картон.....	168
<i>Т. Божкова, Р.Боева, И.Спиридонов, Я. Сапкота, Я.Неделчев, Н. Кашикович, С.</i> <i>Деджиер, М. Пал,</i> Подобряване на физико-механичните и оптичните свойства на опаковките чрез покритие с водни полимерни дисперсии в съответствие с изискванията за опазване на околната среда.....	173
<i>А. Матев, П. Велев, С. Исмаил, М. Херцог,</i> Изготвяне, свойства и приложение на вододиспергиран полиуретан-акрилатен олигомер като матрица за УВ-втвърдяващи се стъклопласти.....	180
<i>Д.А. Тодорова, П.М.Миладинова,</i> Изследване на влиянието на реактивни багрила върху стабилността на цвета на офсетова хартия за печат при стареене.....	186
<i>Д.А. Тодорова, П.М. Миладинова, В.Н. Бляховски,</i> Багрене на офсетова хартия за печат с нови реактивни багрила - влияние върху свойствата на хартия и стареенето.....	194
<i>Т. Божкова, И. Спиридонов, К. Щерев,</i> Обзорен преглед на видовете защиты в защитения печат и тенденции за бъдещото им развитие.....	201
<i>И. Цветанска, В. Лашева,</i> Нови методи за защита от биофактори при консервация на книги.....	205
<i>Р. Ценкова, В.Лашева,</i> Консервация и реставрация на документи чрез подходящи методи от фонда на националния исторически музей.....	209
<i>Д. Тодорова, В. Лашева,</i> Проучване възможностите за използване на сребърни наночастици в опаковъчна хартия.....	214
<i>С.П. Владимирова, М.Б. Георгиева,</i> Синтез и оценка на връзката структура- фитохимична активност на нови п-пироллил карбоксилни киселини.....	220
<i>Ж. Павлович, М. Пал, Т. Цигула, Р. Боева, И. Спиридонов, Т. Божкова, М. Прица,</i> Сравнителен анализ на точността на възпроизвеждане на растеровия тон на печатните форми използвайки различни методи за измерване и обработка на изображенията.....	228
<i>И. Спиридонов, Р. Боева, И. Лозанова-Дончева, Т. Божкова,</i> <i>Ж. Павлович, Г. Владич, Н. Кашикович, М. Станчич, Б. Тачева,</i> Изследване на промените в цветовете характеристики на печатните изображения при изкуствено стареене на различни хартии.....	236
<i>Б.И. Николова-Младенова, С.Е. Ангелова,</i> Ga(III)-комплекси с метокси-заместени ароилхидразони: синтез, охарактеризиране и изчисления с ТФП.....	242
<i>Инструкция за авторите</i> .....	243